

BINDING SERVICES
Tel +44 (0)29 2087 4949
Fax +44 (0)29 20371921
e-mail bindery@cardiff.ac.uk

RECYCLING IN SUBDUCTION ZONES: EVIDENCE FROM ECLOGITES AND BLUESCHISTS OF NW CHINA

SHAUN LAVIS

Submitted in partial fulfilment of the requirements for the degree of Ph.D.

Cardiff University

AUGUST 2005

UMI Number: U584737

All rights reserved

INFORMATION TO ALL USERS
The quality of this reproduction is dependent upon the quality of the copy submitted.

In the unlikely event that the author did not send a complete manuscript
and there are missing pages, these will be noted. Also, if material had to be removed,
a note will indicate the deletion.



UMI U584737
Published by ProQuest LLC 2013. Copyright in the Dissertation held by the Author.
Microform Edition © ProQuest LLC.
All rights reserved. This work is protected against
unauthorized copying under Title 17, United States Code.



ProQuest LLC
789 East Eisenhower Parkway
P.O. Box 1346
Ann Arbor, MI 48106-1346

ACKNOWLEDGEMENTS

I would first like to thank NERC for providing the funding for my PhD, and to Cardiff University, Department of Earth, Ocean and Planetary Sciences for its support. I am indebted to our Chinese colleagues, including Huaikun Li, Huichu Wang, Song Shuguang and Lifei Zhang, for their help and guidance during our field excursion to NW China.

For help collecting ICP and SEM data, a large thanks to Iain McDonald, Pete Fisher and Eveline De Vos. Many thanks to Andrew C Kerr for his supervision. I am very grateful to my supervisor Julien Pearce, who has been invaluable in making this thesis possible and for my scientific development. I would also like to thank Yaoling Niu, who originally proposed this work, for his enthusiasm and inspiration.

Thanks to the people who have helped make my PhD so enjoyable. To my current office mates Kevin Jones, Sarah Dare and Richard Lilly. To my good friend Darren Hirst, and a big big thanks to Graham Banks. I cannot begin to thank my wife Jenny enough here, but I can at least dedicate this work to her.

Abstract

The geochemical evolution of subducting oceanic crust (including both mafic and sedimentary components) has important implications for our understanding of the origin of mantle heterogeneity and the geochemistry of volcanic-arc basalts (VAB). However, knowledge of the actual geochemical evolution of the subducting oceanic crust is largely based on indirect evidence, such as the composition of VAB and our understanding of the geochemical properties of key trace elements. Certain kinds of blueschist belt are thought to consist of exhumed portions of subducted oceanic crust. It is therefore possible to derive direct evidence of the geochemical evolution of subducted oceanic crust by studying the metamorphic rocks (i.e. greenschists, blueschists and eclogites) of blueschist belts.

The bulk rock chemical analysis of greenschists, blueschists and eclogites from the western Tian Shan blueschist belt, Xingjiang Province, People's Republic of China (PRC), has enabled the geochemical effects of subduction zone metamorphism to be determined. Some eclogites from Tian Shan are thought to have undergone "ultra-high pressure metamorphism" (UHPM) at pressures >2.5GPa, and to have passed through the dehydration reactions associated with subduction zone processes. However, it is shown in this thesis that the eclogites have not been subjected to UHPM.

Novel approaches have been developed to interpret the geochemistry of metamorphic rocks, including a new method for identifying "immobile elements" and a method for identifying fresh (i.e. un-metamorphosed) chemically-similar samples from large published datasets. Protoliths of meta-basaltic rocks from Tian Shan are shown largely to originate from seamounts, continental volcanic arcs and basalts associated with attenuation of continental crust. Comparison of the chemistry of the metamorphosed rocks with likely protolith compositions has not revealed any systematic changes associated with subduction zone metamorphism.

To augment the information obtained from the Tian Shan rocks, samples were also analysed from the blueschist belts of the Qilian Mountains, Gansu/Qinhai Province, PRC. Protoliths of the meta-basaltic rocks were shown to be back-arc basin basalts and basalts associated with back-arc rifting. Comparison of the geochemistry between likely protolith and metamorphic rock compositions revealed no systematic changes. This indicates that no geochemical effects associated with subduction zone metamorphism.

It is shown, by comparing the Loss on Ignition (LOI) of carbonate-bearing meta-basaltic rocks with the H_2O content of H_2O-saturated MORB, that the blueschists and eclogites have not significantly dehydrated. Thus, no mobile phase with the capacity to transport fluid-mobile elements was present during subduction zone metamorphism.

The identification of no chemical changes associated with subduction zone metamorphism in this work is consistent with similar investigations that have recently been published. Ostensibly, such findings have important implications for our understanding of the origin of mantle heterogeneity and VAB compositions. However, the assumption that rocks from blueschist belts, such as those of the western Tian Shan blueschist belt, are analogous to actual deeply subducted oceanic crust is shown not to be valid. This may particularly be true with respect to differences between initial H_2O content of blueschists and eclogites compared with actual subducting altered oceanic crust. Consequently, any interpretations of the geochemical evolution of such rocks should not be extended to cover the evolution of actual subducting oceanic crust.

LIST OF CONTENTS

CHAPTER 1. Introduction **1**

1.1 Introduction 1
1.2 Principle Aims of Project 2
1.3 Outline of Thesis 4
1.4 Some Important Concepts and Terms 4
1.4.1 Subduction Zones and Evolution of the Oceanic Crust 4
1.4.1.1 Stage 1: Mid Ocean Ridges 5
1.4.1.2 Stage 2: Lithospheric Maturation 7
1.4.1.2 Stage 3: Passage to Volcanic Arc 7
1.4.2 Subduction Zone Metamorphism 8
1.4.2.1 The Blueschist Facies 12
1.4.2.1.1 P-T Conditions of the Blueschist Facies 12
1.4.2.1.2 Key Minerals of the Blueschist Facies 12
1.4.2.2 The Eclogite Facies 13
1.4.2.2.1 Key Minerals of the Eclogite Facies 14
1.4.3 The Occurrence of High P/T Rocks: Blueschist Belts 14
1.4.4 Mantle Heterogeneity Recycling Models 16
1.4.4.1 Isotope Geochemistry of Mantle Source End-Members 17
1.4.4.2 Trace Element Geochemistry of Mantle Source End-members 19
1.4.4.2.1 HIMU Trace Element Geochemistry 20
1.4.4.2.2 EM-1 Trace Element Geochemistry 21
1.4.4.2.3 EM-2 Trace Element Geochemistry 21
1.5 Summary 22

CHAPTER 2. Literature Review **23**

2.1 Introduction 23
2.2 What is a Subduction Zone Chemical Signature? 24
2.2.1 Evidence from the geochemistry of Volcanic Arc Rocks 26
2.2.2 Evidence from Experimental Investigations 26
2.2.3 The Subduction Zone Signature in Dehydrated Rocks 28
2.3 The Compatibility of Elements in Different Mineral Phases 28
2.3.1 Hydrous Calcium-Aluminosilicate Minerals 29
2.3.2 Mica Group Minerals 30
2.3.3 Other Minerals 31
2.4 Stability of Volatile-Bearing Phases in Subducting Crust 32
2.4.1 Some Terms, Concepts and Limitations 33
2.4.1.1 Continuous and Discontinuous Reactions 33
2.4.1.2 Fluid Production 34
2.4.1.3 Limitations of Phase Petrology 34
2.4.2 Devolatilisation of Subducting Lithologies 35
2.4.2.1 Devolatilisation Regimes in Meta-Basalts 37
2.4.2.1.1 High Dehydration and Fluid Production Rates 37
2.4.2.1.2 Low Dehydration Rates and Little Fluid Production 37

2.4.2.2 Devolatilisation Regimes in Pelites..... 39
2.4.2.3 Devolatilisation of Greywackes and Volcanoclastics..... 39
2.4.2.4 Devolatilisation of Serpentinised Peridotite..... 40
2.4.2.5 Carbonates.....40
2.5 Mobile Phase Production and Trace Element Partitioning..... 41
2.5.1 Predicting when Elements will be Mobilised by Dehydration Reactions..... 42
2.5.2 Predicting Element Mobility Resulting from Dehydration: Limitations..... 42
2.6 Constraints from the Geochemistry of High P/T metamorphic rocks..... 44
2.6.1 Bulk Rock Geochemistry..... 44
2.6.1.1 Meta-Sedimentary Rocks.....45
2.6.1.2 Meta-Mafic Rocks..... 47
2.6.1.2.1 Evidence for LILE removal from Meta-Mafic rocks.....47
2.6.1.2.2 Evidence for LREE Removal from Meta-Mafic Rocks.....47
2.6.1.2.3 Evidence for LILE Addition To Meta-Mafic Rocks.....49
2.6.1.2.4 Evidence for No Element Loss in Meta-Mafic Rocks..... 49
2.6.1.3 Summary..... 51
2.7 Fluid Composition: Measurement of Actual Subduction Zone Fluids..... 51
2.7.1 Fluid Inclusions.....53
2.7.1.1 Fluid Inclusions in Rock Forming Minerals..... 53
2.7.1.2 Fluid Inclusions in High Pressure Veins.....53
2.7.2 Composition of High Pressure veins..... 55
2.7.3 Evidence from Fluids Expelled at Convergent Margins..... 56
2.7.4 Summary..... 56
2.8 Synthesis..... 57

CHAPTER 3. The Geology of Field Areas..... 59

3.1 Introduction..... 59
3.2 Field Location 1: The Chinese Tian Shan.....60
3.2.1 Western Tian Shan HP-LT Belt..... 60
3.2.2 Geological Evolution of the Chinese Tian Shan..... 61
3.2.3 Petrology of the Blueschist Belt..... 62
3.2.3.1 Meta-Volcanic Rocks.....63
3.2.3.2 Meta-Volcanoclastic Rocks..... 64
3.2.3.3 Clastic Meta-Sedimentary Rocks.....64
3.2.4 P-T Evolution of the Tian Shan Blueschist and Eclogites..... 64
3.2.4.1 Peak P-T Conditions..... 64
3.2.4.2 Prograde Metamorphic Sequence..... 67
3.2.4.3 Retrograde Sequence..... 68
3.2.5 Exhumation of the Blueschist Belt..... 69
3.3 Area 2: North Qilian Shan..... 70
3.3.1 Geological Overview..... 71
3.3.2 Tectonic Evolution..... 73
3.3.3 Blueschist Belts..... 75
3.3.3.1 Southern High Grade Blueschist Belt..... 76
3.3.3.2 Northern Low-Grade Blueschist Belt..... 77
3.3.3.3 Relationship Between the Two Blueschist Belts..... 78

5.4 Field Work..... 78

CHAPTER 4. Bulk Rock Geochemical Analysis..... 79

4.1 Introduction..... 79
4.2 Aims..... 79
4.3 Feasibility Study of Dissolution Techniques for Trace Element Analysis 80
4.3.1 "Routine" HF-HNO_3 Dissolution Technique..... 80
4.3.1.1 Advantages..... 80
4.3.1.2 Disadvantages..... 80
4.3.2 High Pressure Bombs..... 80
4.3.2.1 Advantages..... 81
4.3.2.2 Disadvantages..... 81
4.3.3 Sodium Peroxide Sintering..... 81
4.3.3.1 Advantages..... 82
4.3.3.2 Disadvantages..... 82
4.3.4 Lithium Metaborate Fusion..... 82
4.3.4.1 Advantages..... 82
4.3.4.2 Disadvantages..... 83
4.3.5 Microwave Digestion..... 83
4.3.5.1 Advantages..... 83
4.3.5.2 Disadvantages..... 83
4.4 Choosing a Method..... 84
4.5 Testing the Method..... 84
4.5.1 Results of the Trial with $LiBO_2$-Fused Solutions..... 85
4.6 Optimising the Preparation Method..... 86
4.6.1 Identifying the Purest Flux..... 86
4.6.2 Choosing a Flux..... 89
4.6.3 Optimising the Flux-to-Sample Ratio..... 90
4.6.4 Sample Preparation Method..... 90
4.6.5 Reduction of Total Dissolved Solids in Flux-Bearing Solutions..... 91
4.8 Summary..... 92
4.9 Routine HF-$HNO3_3$ Analysis..... 92
4.9.1 Comparison Between $LiBO_2$-Fused and HF-HNO_3 Dissolved Solutions..... 93
4.9.2 Analysis of Lead and Some Low Abundance Elements..... 93
4.9.2.1 Method..... 94
4.9.2.2 Results..... 94
4.10 Summary..... 95
4.11 Results of Trace Element Data Acquisition..... 95
4.12 Discussion of Trace Element Data Quality..... 96
4.12.1 Limits of Detection and Quantification..... 96
4.12..3 Accuracy Estimates..... 97
4.13 Major Element Analysis..... 97
4.14 Results of Bulk Rock Geochemical Analysis..... 97

CHAPTER 5. Mineralogy of Metamorphic Rocks 1: Tian Shan..... 105

5.1 Introduction and Aims..... 105

5.2 Classification: Summary of Previous Work 105
5.3 Classification of rocks Collected for This Work 106
5.3.1 Meta-sedimentary Rocks 106
5.3.1.1 Glaucophane-Bearing meta-Sedimentary Rocks 107
5.3.1.1 Glaucophane Absent Meta-Sedimentary Rocks 109
5.3.1.3 Marble 109
5.3.2 Meta-Igneous Rocks 109
5.4 Mineral Chemistry 113
5.4.1 Methods 113
5.4.2 Garnet 113
5.4.3 Clinopyroxene 114
5.4.4 Amphibole 115
5.4.5 Other Minerals 115
5.5 Geothermometry 116
5.5.1 Introduction 116
5.5.2 Paragenetic Relationships 118
5.5.3 Geothermobarometric Calculations 121
5.5.3.1 The Garnet-Clinopyroxene Fe^{2+}-Mg Exchange Thermometer 121
5.5.3.2 The Garnet-Clinopyroxene-Phengite Barometer 122
5.5.3.3 Error Estimates 123
5.5.3.4 Results 125
5.6 Discussion of Geothermobarometry 127
5.6.1 Implications for this Investigation 127

CHAPTER 6. Mineralogy of Metamorphic Rocks 2: Qilian Shan 129

6.1 Introduction 129
6.2 Metamorphic Rock Classification: Summary of Previous Work 129
6.2.1 Southern High-Grade Blueschist Belt 129
6.2.2 Low-Grade Belt 130
6.3 Classification of Rocks Collected for This Work 130
6.3.1 Meta-Sedimentary Rocks 130
6.3.2 Meta-Igneous Rocks 131
6.3.2.1 High-Grade Belt 133
6.3.2.2 Low-Grade Belt 133
6.4 Pressure-Temperature Estimates 134
6.4.1 Previous Work P-T Estimates 134
6.4.2 P-T Calculations for Rocks Collected for this Investigation 134
6.4.2.1 Paragenetic Relationships 134
6.5.2.2 Geothermobarometric Calculations 136
6.5.2.3 Discussion of P-T Conditions 138

CHAPTER 7. Protolith Geochemistry 1: Tian Shan 140

7.1 Introduction: The Importance of the Protolith 140
7.2 Methodology 141
7.2.1 Meta-Igneous Rocks 142

7.2.2 Meta-Sedimentary Rocks 142
7.3 Screening for Meta-Cumulates among the Meta-Igneous Samples 143
7.4 Classification of Meta-Volcanic Rocks 144
7.5 Identifying Co-Genetic Samples 146
7.5.1 Group 1a and Group 1b 146
7.5.2 Group 2a and Group 2b 148
7.5.3 Group 2c and Group 2d 149
7.5.4 Group 3 149
7.5.5 Ultramafic Sample: TS02-34 150
7.5.6 Summary 150
7.6 Identifying Immobile Elements 151
7.6.1 Methodology 151
7.6.1.1 Theory 151
7.6.1.2 Application 152
7.6.1.3 Limitations 152
7.6.2 Results 153
7.6.2.1 General Outcome 153
7.6.2.2 Group 1a 155
7.6.2.3 Group 2a and Group 2b 156
7.6.2.4 Group 3 157
7.6.3 Summary and Discussion of Element Mobility 157
7.7 Tectonic Discrimination 158
7.7.1 Identifying Volcanic Arc Signatures 159
7.7.1.1 Group 1a and Group 1b 160
7.7.1.2 Group 2a and Group 2b 160
7.7.1.3 Group 2c and Group 2d 160
7.7.1.4 Group 3 161
7.7.2 Identifying WPB and MORB Signatures 161
7.7.2.1 Group 1a and Group 1b 162
7.7.2.2 Group 2c and Group 2d 162
7.7.2.3 Group 3 162
7.7.3 Summary of Tectonic Discrimination 163
7.7.3.1 Group 1a and Group 1b 163
7.7.3.2 Group 2a and Group 2b 163
7.7.3.3 Group 2c and Group 2d 163
7.7.3.4 Group 3 164
7.8 Finding Analogues from Large Datasets 164
7.8.1 The Sum of D-Squared Method 164
7.8.1.1 Absolute Comparison 165
7.8.1.2 Relative Comparison 165
7.8.1.3 Choosing which Elements to Compare 165
7.8.1.4 Compiling the Data Set of Potential Analogues 166
7.8.1.5 The Preferred Method for ΣD^2 Calculations 166
7.8.2 Results of the ΣD^2 Calculations 167
7.8.2.1 Group 1a 167
7.8.2.2 Group 2a and Group 2b 170
7.8.2.3 Group 3 172
7.8.2.4 Other Meta-Igneous Rocks 174

7.9 Summary and Discussion of Meta-Volcanic Rock Petrogenesis..... 179
7.9.1 Contaminated Basalts..... 179
7.9.2 Basalts Originating from a Volcanic Arc..... 180
7.9.3 Comparison with Previous Work on the Tian Shan Meta-Igneous Rocks..... 181
7.10 Geochemistry of Meta-Sedimentary Protoliths..... 182
7.10.2 Origin of the Meta-Sedimentary Rocks..... 185
7.10.2.1 Meta-Volcanoclastic Rocks..... 186
7.10.2.2 Geochemistry of Glaucophane-Bearing and Glaucophane Absent Meta-Sedimentary Rocks..... 187
7.10.3 Discussion of Sediment Petrogenesis..... 188
7.10.3.1 Does the Composition of Meta-Sedimentary Rocks Reflect the Protolith?..... 188
7.10.3.2 Tectonic Setting of the Protoliths..... 189
7.11 Geochemical Nature of the Protoliths: Summary..... 190

CHAPTER 8. Protolith Geochemistry 2: Qilian Shan..... 191

8.1 Introduction and Aims..... 191
8.2 Identifying Meta-Cumulates..... 191
8.3 Classification of Meta-Volcanic Rocks..... 191
8.2.3 Identifying Co-Genetic Samples..... 193
8.2.3.1 Subgroups of Group Q1 and Group Q2..... 193
8.2.3.2 Other Samples..... 195
8.2.4 Immobile Elements..... 196
8.2.5 Tectonic Discrimination..... 198
8.2.8.1 Identification of Volcanic Arc Signatures..... 198
8.2.5.2 Identification of Within-Plate Characteristics..... 199
8.2.6 Finding Analogues: Results of the ΣD^2 Calculations..... 200
8.2.6.1 Results of the ΣD^2 Calculations: Group Q1..... 200
8.2.6.2 Results of the ΣD^2 Calculations: Group Q1a..... 201
8.2.6.3 Results of the ΣD^2 Calculations: Group Q1b..... 202
8.2.6.4 Results of the ΣD^2 Calculations: Group Q2..... 203
8.2.7 Discussion of the Protolith Petrogenesis of the Qilian Shan Meta-Basalts..... 205
8.3 Geochemistry of the Protoliths 2: Meta-Sedimentary Rocks..... 206
8.4 Protolith Petrogenesis: Summary..... 208

CHAPTER 9. Geochemical Effects of Subduction Zone Metamorphism..... 209

9.1 Introduction..... 209
9.2 Aims..... 210
9.3 Method for Investigating Mass Transfer..... 210
9.4 Evidence for Mass Transfer from Meta-Igneous Rocks..... 213
9.4.1 Group 1a and Group 3 of the Chinese Tian Shan..... 213
9.4.1.1 No residual Subduction Zone Signature..... 213
9.4.1.2 Samples with Low $[Ba/Nb]_N$ and $[K/Nb]_N$ Ratios..... 215
9.4.2.3 Samples with Low $[Sr/Nd]_N$ Ratios..... 216
9.4.2 Group 2a and Group 2b of the Chinese Tian Shan..... 218
9.4.3 Meta-Basaltic Rocks of the North Qilian Shan..... 219

9.5 Evidence for Mass Transfer from Meta-Sedimentary Rocks..... 220
9.5.1 Evidence from Meta-Sedimentary Rocks of the Chinese Tian Shan Blueschist Belt..... 220
9.5.2 Evidence from Meta-Sedimentary Rocks of the Qilian Shan Blueschist Belts..... 221
9.6 Summary and Discussion of Evidence for Mass Transfer from Protoliths..... 222
9.6.1 Comparison with Other Work..... 224
9.7 Explaining the Lack of Residual Subduction Zone Signatures 1: Evidence from Protoliths..... 224
9.7.1 Tectonic Setting of Protolith Petrogenesis 1: Protoliths of the Chinese Tian Shan..... 225
9.7.1.1 Protoliths Originating from Seamounts..... 225
9.7.1.2 Protoliths Originating from Continental Volcanic Arcs..... 229
9.7.2 Tectonic Setting of Protolith Petrogenesis 2: Protoliths of the North Qilian Shan..... 230
9.7.2.1 Protoliths Originating from a Back Arc Basin..... 230
9.7.2.2 Protoliths Originating from Attenuated Continental Crust..... 231
9.7.3 Implications of the Evidence from Protoliths..... 233
9.8 Explaining the Lack of Residual Subduction Zone Chemical Signatures 2: Other Evidence..... 235
9.8.1 Lack of Systematic Sampling..... 235
9.8.2 Problems with the Behavior of LILEs..... 235
9.8.3 None of the Collected Rocks Underwent UHP Metamorphism..... 235
9.9 Summary..... 236

CHAPTER 10. Thesis Conclusions..... 237

10.1 Introduction..... 237
10.2 Identifying Immobile Elements and Samples Chemically Analogous to Protoliths... 237
10.2.1 Identifying Immobile Elements in Rocks with chemically Heterogeneous Protoliths.....
10.2.2 Identifying Fresh Rocks with Similar Compositions to Protoliths..... 238
10.3 Petrogenetic History of the Chinese Tian Shan HP-LT Rocks..... 239
10.3.1 Pre-metamorphic Petrogenesis..... 239
10.3.2 Metamorphic Petrogenesis of the Chinese Tian Shan HP-LT Rocks..... 240
10.4 Petrogenetic History of Rocks from the Qilian Shan HP-LT Belts..... 241
10.4.1 Pre-metamorphic Petrogenesis..... 241
10.4.2 Metamorphic Petrogenesis..... 242
10.5 Evidence for Chemical Recycling in Subduction Zones: Conclusions..... 242
10.6 Further Work..... 243

REFERENCES
APPENDIX 1
APPENDIX 2

LIST OF FIGURES

Figure 1.1 Schematic diagram illustrating some of the important processes effecting oceanic crust from its inception at a mid-ocean ridge until it is subducted beneath a volcanic arc..... 6

Figure 1.2 P-T diagram depicting the 8 commonly used metamorphic facies..... 9

Figure 1.3 Schematic P-T diagram showing the P-T paths of the three metamorphic facies series..... 10

Figure 1.4 Schematic diagram showing the principal differences between the Collsion type (A) and Pacific type (B) blueschist belts..... 15

Figure 1.5 A-F Some possible locations of mantle reservoirs and relationships to mantle dynamics. 17

Figure 1.6 A-D Representative isotopic data for the three OIB end-members HIMU, EM-1 and EM-2 and MORB..... 18

Figure 1.7 Primordial mantle normalised multi-element diagrams of selected trace elements for OIB end-member compositions (HIMU, EM-1 and EM-2)..... 20

Figure 2.1 Multi-element diagram of average island arc tholeiite normalised to "oceanic crust" compared with the residual crust after dehydration reactions..... 26

Figure 2.2 P-T diagram showing the four main devolatilisation regimes, and phase relations relevant for MORB compositions..... 36

Figure 2.3 Major phase stability boundaries for H_2O-saturated MORB compositions..... 38

Figure 3.1 Map of the Peoples Republic of China showing the locations of the two field areas..... 59

Figure 3.2 Locations and simplified geology of the western Tian Shan HP-LT belt..... 61

Figure 3.3 Model for the Paleozoic tectonic evolution of the Chinese Tian Shan and adjacent regions.... 62

Figure 3.4 A-C. Tectonic model for the exhumation of HP-LT metamorphic rocks in the Chinese Tian Shan..... 70

Figure 3.5 Sketch map of the distribution of blueschist belts in the North Qilian Shan, China..... 71

Figure 3.6 Revised geological map of the north Qilian Shan..... 74

Figure 3.7 Schematic diagram showing the tectonic evolution of the North Qilian Shan during the Early Paleozoic..... 75

Figure 4.1 Difference between certified and measured values for the international standard BIR-1..... 85

Figure 4.2 Comparison of $LiBO_2$ and HF-HNO_3 prepared samples using selected elements..... 93

Figure 5.1 Selected garnet analyses..... 114

Figure 5.2 Clinopyroxene analysis plotted on the Jd- Q-Ae (Jd = jadeite, Q = wollastonite + enstatite + ferrosilite + wollastonite) diagram of Morrimoto (1988)..... 114

Figure 5.3 Analyses of amphibole from rocks of the western Tian Shan plotted on a diagram for the general classification of amphibole from Leake et al. (1997)..... 115

Figure 5.4 SEM EDX spectrum profile for allanite from cores of clinozoisite..... 116

Figure 5.5 P-T estimates for rocks collected for this study based on mineral assemblage and paragenetic relationships..... 120

Figure 5.6 A & B Results of P-T calculations plotted on a P-T diagram with reaction curves and metamorphic facies..... 126

Figure 6.1 Petrogenetic grid displaying the facies diagram of Evans (1990) and petrogically significant univariant reaction curves..... 136

Figure 6.2 Results of the geothermobarometric calculations..... 137

Figure 7.1 A & B Flow diagram summarising the methodology for investigating the geochemical nature of: A) meta-igneous protoliths, and; B) meta-sedimentary protoliths..... 141

Figure 7.2 The Zr/Ti - Nb/Y diagram of Winchester & Floyd (1977) diagram of Pearce (1996).....144

Figure 7.3A-H N-MORB normalised multi element diagrams of the meta-basaltic rock subgroups..... 147

Figure 7.4 A & B A) Example of part of a correlation matrix with elements arranged according to compatibility, and B) a schematic representation of how the correlation coefficient might change as a function of decreasing K_{Nb}/K_X..... 152

Figure 7.5 A-D Nb-correlation diagrams for Groups 1a, sa, 2b and 3..... 154

Figure 7.6 Diagram showing the variation (defined as relative standard deviation: 1σ/mean*100) of selected elements in Group 1a..... 155

Figure 7.7 Diagram showing the variation (defined as relative standard deviation: 1σ/mean*100) of selected elements in Group 2a and Group 2b..... 157

Figure 7.8 Schematic diagram showing the three tectonic setting end-members for basalts and transitional settings..... 159

Figure 7.9 A & B A) the Th-Hf-Ta of Wood (1980). B) The Th/Yb vs. Nb/Yb diagram from Pearce & Pete (1995)..... 159

Figure 7.10 A & B A) the Zr-Ti-Y diagram of Pearce & Cann (1973), B) the Ti-V diagram of Shervais (1992)..... 161

Figure 7.11 Results of the ΣD^2 calculations showing three of the closest analogues for Group 1a..... 167

Figure 7.12 N-MORB normalised ratio-ratio diagrams of: A) $[La/Yb]_N$ against $[Th/Nb]_N$ and B) $[Th/Nb]_N$ against $[Hf/Sm]_N$..... 169

Figure 7.13 A & B N-MORB normalised diagrams of selected immobile trace element for Group 2a (A) and Group 2b (B), compared with analogues suggested by the ΣD^2 experiments..... 170

Figure 7.14 N-MORB normalised diagrams of selected trace elements comparing the results of the ΣD^2 method with Group 3..... 172

Figure 7.15 Comparison of $[Th/Nb]_N$ and $[Hf/Sm]_N$ ratios of Group 3 with fresh basalts from the Manus back arc basin (Sinton et al. 2003) and East Pacific Rise seamounts (Niu & Batiza 1997)..... 173

Figure 7.16 A-D N-MORB normalised multi-element diagrams for sample groups and their analogues... 175

Figure 7.17 A-D Scatter plots of elements considered immobile by John et al. (2004) illustrating the possible subgroups that can be made from their Group II eclogitic gabbros..... 177

Figure 7.18 La-correlation diagram for subgroup C from Group II of John et al., (2004)..... 178

Figure 7.19 A & B N-MORB normalised multi-element diagrams of selected elements for the meta-volcanoclastic rocks..... 186

Figure 7.20 GLOSS normalised multi-element diagrams for glaucophane-bearing (GBMS) and glaucophane- absent (GAMS) meta-sedimentary rocks..... 188

Figure 8.1 The modified Zr/Ti against Nb/Y Winchester & Floyd (1977) classification diagram of Pearce (1996)..... 192

Figure 8.2 A-D N-MORB normalised multi-element diagrams of the four meta-volcanic sub-groups from Qilian Shan..... 194

Figure 8.3 A-C N-MORB normalised multi-element diagrams for samples not belonging to the subgroups of Group Q1 or Group Q2..... 196

Figure 8.4 A-C Nb-correlation diagrams for the meta-basaltic groups..... 197

Figure 8.5 A & B Tectonic discrimination diagrams useful for identifying volcanic arc signatures..... 198

Figure 8.6 A & B Tectonic discrimination diagrams for identifying within-plate characteristics in basalts..... 199

Figure 8.7 N-MORB normalised multi element diagram showing the Group Q1 patterns and the data for the analogous samples..... 201

Figure 8.8 N-MORB normalised multi-element diagram for Group Q1a and the results of the ΣD^2 calculations..... 202

Figure 8.9 N-MORB normalised multi-element diagram for Group Q1b and analogue samples..... 203

Figure 8.10 N-M ORB normalised multi-element diagram showing the trace element pattern of Group Q2 and the patterns of the analogue samples..... 204

Figure 8.11 GLOSS-normalised multi-element diagrams showing the trace element pattern of Glaucophane Absent Meta-sedimentary rocks (GAMS) and Galucophane Bearing Meta-sedimentary rocks (GBMS)..... 208

Figure 9. Schematic multi-element diagrams showing an average Island Arc Basalt (IAB) composition normalised to N-MORB, and an estimate of the composition of "residual" oceanic crust after passing through dehydration reactions associated with subduction zone metamorphism..... 210

Figure 9.2. Schematic diagram illustrating the use of ratio-ratio diagrams to investigate the mobility of elements..... 212

Figure 9.3. N-MORB normalised ratio-ratio diagrams for Group 1a and Group 3 meta-basalts of the Chinese Tian Shan blueschist belt..... 214

Figure 9.4. Covariation diagrams between Sr and different LILEs..... 217

Figure 9.5. N-MORB normalised ratio-ratio diagrams for Group 2a and Group 2b meta-basalts of the Chinese Tian Shan blueschist belt..... 218

Figure 9.6. N-MORB normalised ratio-ratio diagrams for meta-basaltic groups of North Qilian Shan blueschist belts..... 219

Figure 9.6. N-MORB normalised ratio-ratio diagrams comparing the compositions of HP-LT meta-sedimentary rocks of the Chinese Tian Shan with the composition other sediments..... 221

Figure 9.7 A-D. N-MORB normalised ratio-ratio diagrams comparing the compositions of HP-LT meta-sedimentary rocks of the North Qilian Shan with the composition of other terrigeneous..... 222

Figure 9.8. Model for the incorporation of a seamount into an accretionary wedge, modified after Pickett et al. (1996)..... 227

Figure 9.9 Schematic diagrams showing the tectonic evolution of the North Qilian Mountains, and likely locations of the basaltic protoliths..... 232

Figure 9.10. Major phase stability boundaries in MORB saturated with H_2O..... 234

LIST OF TABLES

Table 1.1 Representative mineral assemblages for the high P/T facies series..... 11

Table 1.2 Summary of some characteristic rock-forming minerals of the blueschist and eclogite facies..... 11

Table 1.3 Summary of the classification of mode of occurrence of eclogites..... 13

Table 1.5 Summary of some characteristic trace element ratios for the three OIB end-members..... 22

Table 3.1 Summary of the findings of previous work investigating the P-T and PTt paths of the western Chinese Tian Shan HP-LT metamorphosed rocks..... 65

Table 3.2 Summary of the three key issues regarding the existence or non-existence of UHPM in the western Tian Shan metamorphic rocks..... 66

Table 4.1 Quantitative results of an experiment to find out the composition of two lithium metaborate fluxes..... 88

Table 4.2 Summary of data quality for the measurement of lead using 10% HCl and 10% HNO_3 as cleaning solutions before and in between sample analyses. 95

Table 4.4 Results of bulk rock geochemical analysis..... 98

Table 4.3 Summary of the data quality estimations for the elements analysed from solutions prepared by different methods..... 96

Table 5.1 Summary of different rock classification terms for metamorphic rocks collected from the western Tian Shan blueschist belt..... 106

Table 5.2 Summary table of sedimentary rocks with selected samples of each rock type..... 108

Table 5.3 Modal estimates (estimated visually) of selected blueschists and eclogitic rocks from the meta-igneous rocks..... 111

Table 5.4 Average P-T interception estimates from three eclogitic samples collected from the western Tian Shan blueschist belt..... 125

Table 6.1 Modal estimates of representative meta-sedimentary rocks..... 131

Table 6.2 Modal estimates for meta-igneous rocks from Qilian Shan..... 133

Table 6.3 Results of P-T calculations for the eclogitic sample Q02-08. See Chapter 5 for details of calculations..... 137

Table 7.1 Summary of the rationale behind the six stages used for predicting the geochemical nature, compositional variation and petrogenesis of meta-igneous protoliths..... 142

Table 7.2 Summary of samples with compositions indicative of an accumulated component..... 143

Table 7.3 Summary of the classification of the Tian Shan meta-volcanic rocks..... 145

Table 7.4 Summary of the evidence for the petrogenesis of Groups 1, 2 and 3..... 146

Table 7.5 Results of the ΣD^2 experiments showing three of the closest analogues for Group 1a..... 168

Table 7.6 Summary of the source of data and the petrogenesis of the analogue samples..... 171

Table 7.7 Summary of the location, rock type, tectonic setting and petrogenesis of the analogue samples..... 173

Table 7.8 Summary of the results of the ΣD^2 calculations for Groups 1b, 2c, 2d and the rodingite sample TS02-34..... 174

Table 7.9 Summary of the petrogenesis of the various meta-basaltic samples groups of the western Tian Shan blueschist belt..... 179

Table 7.10 Summary of rocks types identified in previous work on meta-igneous rocks of Tian Shan..... 182

Table 7.11 Summary of major element data , including data re-calculated on an LOI basis for meta-sedimentary rocks..... 187

Table 8.1 Summary of samples with compositions indicative of an accumulated component..... 191

Table 8.2 Summary of characteristic trace element ratios for the four meta-basaltic groups of Qilian Shan..... 193

Table 8.3 Summary table of the results of the ΣD^2 calculations..... 201

Table 8.4 Summary of the results of the ΣD^2 calculations for Group Q1b..... 203

Table 8.5 Summary of the results of the ΣD^2 calculations for Group 2 and important petrogenetic information for the analogues..... 204

Table 8.6 Major element content of meta-sedimentary rocks..... 207

Table 9.1. Summary of LOI data from the analogue samples..... 228

LIST OF PLATES

Plate 5.1 Photomicrographs of representative meta-sedimentary rocks..... 108

Plate 5.2 A and B Photomicrographs of representative meta-igneous rocks..... 111

Plate 5.3.A & B Back Scattered Electron (BSE) images of examples of inclusions in garnet..... 112

Plate 6.1 A & B. Photomicrographs of representative meta-sedimentary rocks..... 131

Plate 6.2 A-F Photomicrographs of representative meta-igneous rocks..... 132

CHAPTER 1

INTRODUCTION

1.1 INTRODUCTION

Geochemical investigations of Oceanic Island Basalts (OIB) have been fundamentally important in helping to develop our understanding of the chemical and physical geodynamics of the Earth's mantle. Ocean Island Basalts are generally more enriched in incompatible elements and radiogenic isotopes compared with basalts produced at other tectonic settings. Importantly, OIB isotope geochemistry is highly variable, and a number of compositional "end-members" can be identified, which also possess distinct trace element signatures. As the composition of OIB is largely inherited from mantle sources, it follows that there must be compositional end-members within the mantle itself. A number of mantle end-members have therefore been proposed to explain the chemical inhomegenity of OIB, i.e. Enriched Mantle-1 (EM-1), Enriched Mantle-II (EM-2), High-μ (HIMU), Depleted MORB Mantle (DMM) and others (e.g. White 1985; Zindler and Hart 1986; Hart et al. 1992).

The ultimate origin of mantle end-members is controversial. However, a clue to the origin of mantle end-members comes from the association of OIB with hotspot volcanism. This is because hotspot volcanism is thought to result from melting of rising and decompressing mantle plumes. Thus mantle plumes may themselves introduce chemical inhomogeneities into the otherwise chemically homogenous "ambient" mantle. OIB geochemistry may therefore be associated with the composition of mantle plumes.

Mantle plumes may explain the origin of chemically inhomogeneous mantle source regions, but what is the origin of mantle plumes? The generally accepted hypothesis is that mantle plumes are hot, buoyant material that rises from the deep mantle, perhaps as deep as the core-mantle boundary (e.g. Griffiths and Campbell 1990). Furthermore, these plumes contain oceanic crust that has been "recycled" back into

the deep mantle at subduction zones (e.g. Hofmann and White 1982). With respect to OIB geochemistry, the "recycling hypothesis" provides a powerful explanation, as the composition of mantle end-members may be explained in terms of the composition of the different components of recycled oceanic crust. For example, the isotopic systematics of EM-1, EM-2 and HIMU components in OIB may reflect incorporation of recycled pelagic sediments, terrigenous sediments and Mid Ocean Ridge Basalt (MORB), respectively (e.g. Weaver 1991).

Although generally accepted, recycling models have recently been questioned by Niu and O'Hara 2003. Among the problems identified by the latter authors are:

1) melting of recycled oceanic crust cannot produce the high-magnesian lavas often characteristic of OIBs;
2) ancient recycled oceanic crust should be isotopically too depleted to meet the required values of most OIB;
3) oceanic crust, as it subducts back into the deep mantle, should become depleted in water-soluble incompatible elements (e.g. Rb, Ba, Cs, U, Pb). Such material cannot be the source for OIB, which exhibit no or little depletion in water-soluble incompatible elements compared to immobile elements.

This thesis is concerned with the third of the points outlined above, and aims to test whether chemical modification at subduction zones depletes recycled oceanic crust in fluid-mobile trace elements.

It is not possible to sample oceanic crust after it has passed through the subduction zone into the deep mantle. Fortunately, there are geological features that expose rocks known to have undergone subduction zone metamorphism. These metamorphic rocks are known as blueschists and eclogites and are exposed in features known as blueschist belts. Blueschists and eclogites essentially follow the same pressure-temperature (P-T) changes as recycled oceanic crust, which subducts into the deep mantle. Thus, blueschists and eclogites can be considered analogues to recycled oceanic crust, and so provide a unique opportunity to observe the geochemical consequences of subduction zone metamorphism.

1.2 PRINCIPAL AIMS OF PROJECT

The ultimate aim of this project is to quantify the chemical modification of oceanic crustal materials resulting from subduction zone metamorphism. To achieve this aim, blueschists and eclogites have been collected from two mountain chains in NW China: 1) the Tian Shan mountains, and; 2) the Qilian Shan mountains (see Chapter 3). Eclogites from Tian Shan are thought by some to have subducted to extremely deep levels, perhaps up to ~150km, which may be the deepest yet recorded for subducted oceanic crust (exposed as eclogites) (e.g. Zhang et al. 2003b). If the depth estimates are correct, eclogites from Tian Shan should be the closest analogues to the material actually subducted into the deep mantle thus far collected. Blueschists and eclogites from Qilian Shan have not subducted to such deep levels, and so are not expected to provide a robust test for subduction zone chemical modification. Information from the rocks collected from Qilian Shan is therefore used to complement conclusions based on the Tian Shan rocks.

To evaluate the geochemical effects of subduction metamorphism, this thesis aims to achieve the following objectives:

1) determine the trace and major element composition of the collected blueschist and eclogites;
2) predict the composition of the rocks prior to metamorphism (i.e. predict the composition of protoliths);
3) compare the composition of the blueschists and eclogites with the composition of possible protoliths to identify any chemical modification resulting from subduction zone metamorphism;
4) determine the peak P-T conditions reached by the eclogites to evaluate the assumption that eclogites are analogous to the oceanic crust actually recycled into the deep mantle;
5) identify key minerals known to be important "sinks" for trace elements;
6) model OIB petrogenesis (i.e. model the mantle melting leading to OIBs) using subduction zone-modified source materials.

Before addressing these objectives, it is necessary to provide a brief outline of the structure of this thesis, and to introduce a number of important terms and concepts in greater detail.

1.3 OUTLINE OF THESIS

This chapter summarises some concepts and terminology important for understanding the rest of the thesis. Chapter 2 reviews previous literature relevant to the study of the geochemical effects of subduction zone metamorphism. Chapter 3 presents a geological and geographical overview of the blueschist belts of the Tian Shan and Qilian Shan mountain belts. This is followed by a summary of the methods used for the chemical analysis of the collected rocks in Chapter 4. The mineralogy and peak P-T conditions experienced by rocks collected from Tian Shan and Qilian Shan is then investigated in Chapters 5 & 6, respectively. Chapters 7 and 8 investigate the composition of the protoliths for rocks of the Tian Shan and Qilian Shan, respectively. In Chapter 9 the evidence from previous chapters is used to evaluate and explain the geochemical effects of subduction zone metamorphism. Finally, Chapter 10 summarises the principal conclusions of the thesis.

1.4 SOME IMPORTANT CONCEPTS AND TERMS

The scope of this work can be broadly divided into two areas of study: metamorphic petrology in the context of subduction zone metamorphism, and igneous petrology in the context of the origin of mantle chemical heterogeneity. The following two sections will introduce some important concepts and terms relevant to these two areas of study.

1.4.1 SUBDUCTION ZONES AND EVOLUTION OF THE OCEANIC CRUST

Subduction zones are three-dimensional features caused by the sinking (or downwelling) of one tectonic plate beneath another into the Earth's mantle. The surficial expression of downwelling is a convergent margin, and the surficial and crustal expressions of the subduction zone are volcanic arcs (Stern 2002 and references therein). Subduction is a major tectonic process, being described as being "the dominant physical and chemical system of the Earth's interior" (Stern 2002). Indeed, the sinking lithosphere provides most of the force required for the mobilisation of plates and the manifestation of spreading at mid ocean ridges.

At a subduction zone, the sinking plate (or lithosphere) is sometimes referred to as the "slab" or "subducting slab." As the slab subducts, it starts to thermally equilibrate

with the surrounding mantle (known as the mantle wedge) which is hotter (see Figure 1). This causes rocks in the slab to metamorphose, during which dehydration of certain hydrous minerals release fluids. These fluids trigger partial melting of the surrounding mantle, forming magmas that develop into the volcanic arc. As fluids (and dissolved chemical components) are removed, the remaining rocks of the slab can be considered as being "residual." These residual rocks then continue to subduct into the deep mantle, where they may reach the core-mantle boundary, be stored for 1-2 billion years and finally return to the lithosphere as part of a mantle plume (see Section 1.4.4 for further details).

This project ultimately aims to define the chemical changes associated with the dehydration reactions thought to take place during metamorphism of the slab. In order to determine chemical changes, it is vital to know both the composition of the residual material, and the composition of the starting material. There are a number of materials that can potentially be delivered to a subduction zone. However, in the context of lithospheric recycling models invoked by some workers in the field of OIB genesis, these materials can be divided into four categories: altered oceanic crust, pelagic sediments, terrigenous sediments, and serpentinised peridotites (Poli and Schmidt 2002; Schmidt and Poli 2004).

It is convenient to define three stages for the development of the oceanic lithosphere with respect to the four components listed above. These three stages represent important periods in the evolution of the oceanic lithosphere as it travels from spreading centre to subduction zone (Figure 1.1).

1.4.1.1 STAGE 1: Mid Ocean Ridges

Magmas are produced at mid-ocean ridges (MORs) by decompression melting of upwelling mantle. A simplified model of the rocks produced by decompression melting consists of an upper layer of pillow and flow basalts, overlying a sheeted dyke complex that overlies intrusive gabbros. Beneath the gabbros are residual mantle peridotites, which are dominantly clinopyroxene-poor lherzolites and harzburgites. As well as producing magma, mid-ocean ridges are also loci for active hydrothermal circulation and associated hydrothermal alteration (e.g. Alt 1995; Humphries et al. 1998).

The depth and intensity of hydrothermal alteration are a function of the thermal structure and permeability of the oceanic lithosphere. Consequently, pervasive hydrothermal alteration generally affects rocks from slow spreading centres more than those from fast spreading centres (due to the deep axial valleys and intense faulting associated with slow spreading MORs, but not fast spreading MORs).

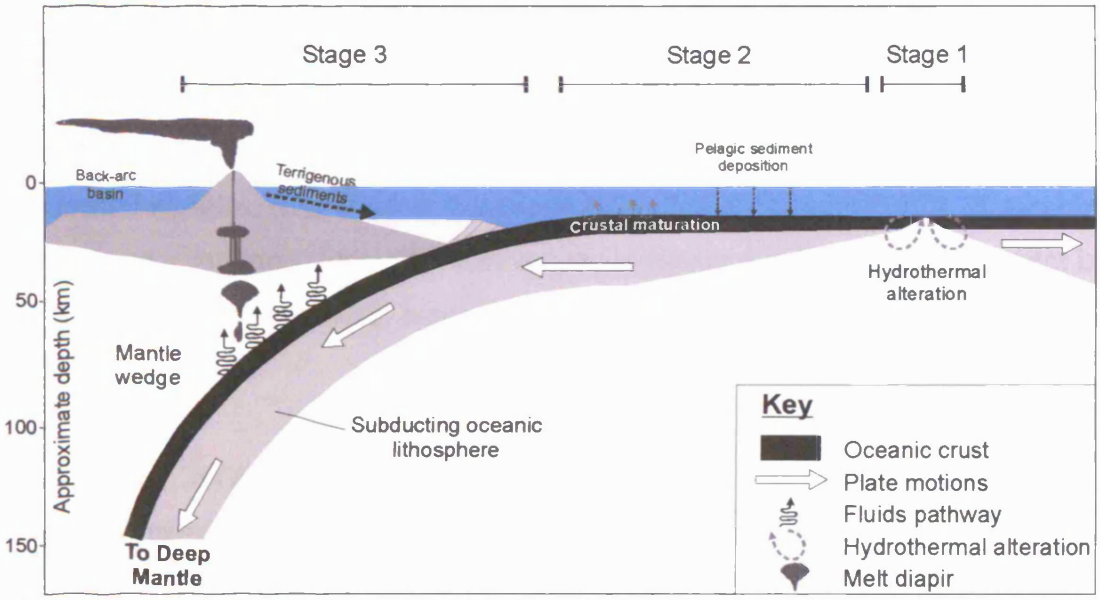


Figure 1.1. Schematic diagram illustrating some of the important processes affecting oceanic crust from its inception at a mid-ocean ridge until it is subducted beneath a volcanic arc, adapted from Stern (2002). Depth estimates are approximate. The lifetime of the oceanic crust is divided into three stages. At Stage 1 oceanic crust is formed where it is subsequently hydrothermally altered by circulating seawater. Some pelagic sediments and ore minerals may also be added to the crust during this stage. During Stage 2 the oceanic crust is weathered, by passive (and occasionally active) seawater circulation (e.g. Kelley et al. 2001). Pelagic sediments of various compositions also accumulate during this stage, perhaps forming thick sedimentary covers (e.g. Plank & Langmuir 1998). During Stage 3 many processes can happen: 1) At the onset of subduction, the oceanic lithosphere can bend, forming cracks and allowing circulation of seawater; 2) addition of terrigenous sediments, or offscraping of sediments onto the overlying plate; 3) compaction of sediments and removal of pore waters; 4) subduction zone metamorphism.

Chemically, the most important changes associated with hydrothermal alteration include: 1) major addition of H_2O (hydration) and CO_2 (carbonation) in the upper basaltic layer, and; 2) discontinuous hydration of the lower crustal sequences, including serpentinisation of peridotites (Poli & Schmidt, 2002). In fact, the volatile (i.e. $H_2O + CO_2$) budget of basalts and ultramafic rocks prior to subduction are to a large extent determined during hydrothermal alteration at spreading ridges, (Alt, 1995; Kerrick & Connolly, 2001a; Poli & Schmidt, 2002; see also Staudigel et al.

1989; Humphries et al. 1998). The largest reservoir for water storage is serpentinised ultramafic rocks, which contain up to 13 wt% H_2O (Scambelluri et al. 1995).

Sediments can also be added to the top of oceanic crust produced at mid ocean ridges. The potential compositional variation of the sediment is large, because sediment composition is largely source-dependent, e.g. biogenic sources will provide sediment with a different composition from that of detrital sediment. Furthermore, the relative proportions of different sediments will affect the composition of the sedimentary column as a whole. A sedimentary column can therefore contain many different sediment compositions that are deposited during the journey from the mid-ocean to continental margins, (e.g. Plank & Langmuir 1998; Poli & Schmidt 2002). If suitably distant from a continental margin, however, the terrigenous sedimentary component is likely to be negligible, with biogenic clays and oozes forming the predominant sediments.

1.4.1.2 STAGE 2: Lithospheric maturation

During the passage from MOR to the margins, the oceanic lithosphere is "weathered" by seawater (e.g. Kelley et al. 2001). Alteration away from axial hydrothermal systems consists of passive circulation, which can lead to precipitation of carbonates to depths of a few hundred metres (some active circulation may also take place). In addition to weathering processes, sediments of various compositions are continually added to the oceanic lithosphere, perhaps leading to a thick sedimentary column (e.g. Plank & Langmuir 1998).

1.4.1.3 STAGE 3: Passage to volcanic arc

At the onset of subduction a number of important processes begin to affect the oceanic lithosphere. These include:

1) offscraping of some of the sedimentary material to be incorporated into the accretionary prism;
2) addition of sedimentary material by erosion of the continental margin (e.g. von Huene & Scholl 1991).
3) compaction during the early stages of subduction, which releases much of the pore fluid from the sedimentary column (Bebout & Barton 1993; Bebout 1995).

4) flexing of the oceanic lithosphere, which can cause fracturing and thus further hydrothermal circulation and alteration (Schmidt 2004).

With continued subduction, dehydration reactions begin to take place throughout the lithosphere. The extent of dehydration is strongly dependent on the P-T path the rocks follow, with relatively low P/T ratio paths favouring more extensive dehydration.

Once dehydration reactions have released a fluid, it can alter any overlying rocks. For example, any fluid released from dehydration of the serpentinised peridotites can alter the overlying basaltic layers, and fluids from the basaltic and peridotite layers can alter the overlying sedimentary cover (Schmidt 2004).

1.4.2 SUBDUCTION ZONE METAMORPHISM

Metamorphism is the process where mineral assemblages of rocks change towards a new state of chemical equilibrium as the environmental conditions of the rocks are subjected to change. The main environmental conditions are pressure (P) and temperature (T), which generally both increase with increasing depth within the Earth. Rocks (igneous or sedimentary) that become metamorphosed are called protoliths. If a protolith is subjected to increasing P-T conditions the type of metamorphism is termed prograde, if the reverse is true, the metamorphism is termed retrograde. A fundamentally important concept in metamorphic petrology is that of metamorphic grade. Metamorphic grade is a measure of the intensity of the metamorphic event that has affected a given rock, and usually refers to the maximum P or T conditions of the event.

Assuming a closed system, changes in mineral assemblages with increasing grade can be systematic, leading to mineral assemblages characteristic of particular P-T conditions. Based on the repeated association between mineral assemblages and P-T conditions for rocks of similar bulk composition, Eskola (1921) defined a number of metamorphic facies. Turner (1981) gave a formal definition of metamorphic facies:

> "A metamorphic facies is a set of metamorphic mineral assemblages, repeatedly associated in space and time, such that there is a constant

and therefore predictable relation between mineral composition and bulk rock chemical composition."

The eight commonly used metamorphic facies are displayed in the P-T diagram of (Figure 1.2), where the fields for the blueschist and eclogite facies have been highlighted. The scheme of metamorphic facies adopted by various authors can differ, e.g. the prehnite-pumpellyite facies of Figure 1.2, includes the prehnite-pumpellyite, pumpellyite-actinolite and lawsonite-albite facies of other authors (Yardley 1989).

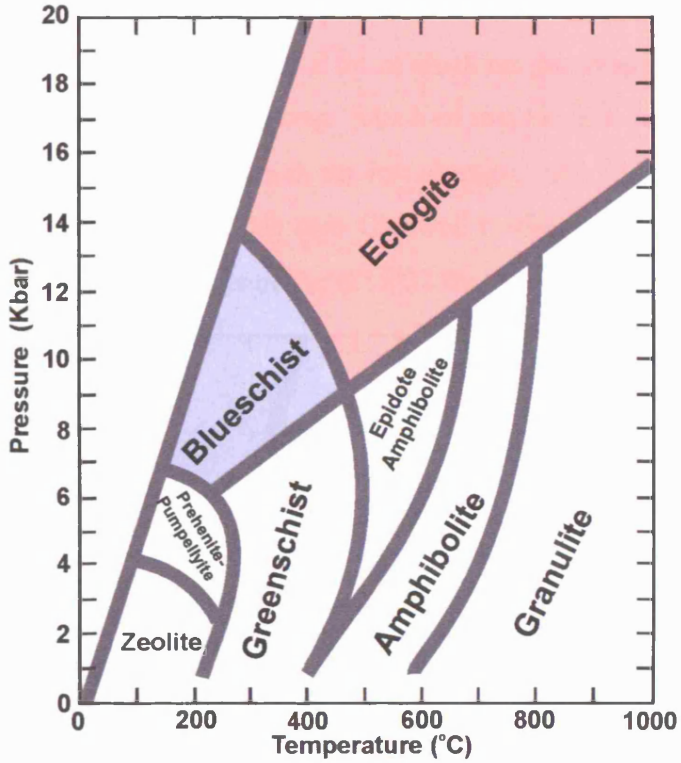


Figure 1.2 P-T diagram depicting the 8 commonly used metamorphic facies, after Spear (1990). Reactions that define the facies boundaries cover a considerable P-T range. The P-T field for the blueschist and eclogite facies have been highlighted in blue and red.

During progressive metamorphism, a rock will metamorphose under a series of successive facies, termed the metamorphic facies series. Miyashiro (1961) defined three metamorphic facies series: 1) the high P/T series; 2) the intermediate P/T series, and; 3) the low P/T series. These facies series are known to affect rocks during metamorphism in different tectonic environments (e.g. Miyashiro 1961).

The facies series encountered at a subduction zone is the high P/T type, because of the low geotherms resulting from the subduction of relatively cool lithosphere. The subduction zone metamorphic facies series involves progressive metamorphism along the series zeolite – prehnite – pumpellyite – blueschist –eclogite (Figure 1.3). High P/T paths may also intersect the greenschist facies. At particular P-T conditions, the chemical reactions that take place in a rock during metamorphism are governed by the composition of the rock. Consequently, rocks with different compositions will experience different chemical reactions, producing different mineral assemblages.

To fully understand high P/T metamorphism the effects of many variables need to be described. Consequently there has been a lot of work on the phase petrology of these facies at different bulk-rock compositions. Much of this work is beyond the scope of this study, and too broad to include in an introduction (see Miyashiro (1994) and Spear (1990) for detailed reviews, see also Carswell (1990) and Goddard (2001) for comprehensive discussions of rocks of the eclogite facies).

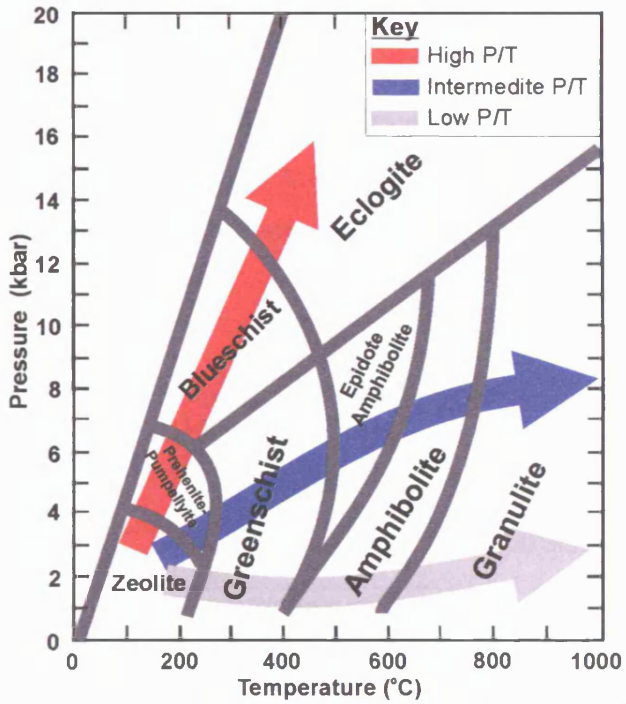


Figure 1.3. Schematic P-T diagram showing the P-T paths of the three metamorphic facies series. The high P/T metamorphic facies series uniquely affects rocks undergoing subduction zone metamorphism.

Although there are many different kinds of rocks that can be metamorphosed, it is convenient (and relevant to this work) to describe the mineral assemblages of two different rock types: meta-mafic rocks of broadly basaltic compositions, and pelites.

Furthermore, these rock types have been studied extensively in the field of metamorphic petrology and so are relatively well understood. Although somewhat simplified, characteristic mineral assemblages for different facies of the high P/T metamorphic facies series are given in Table 1.1.

Facies	Meta-mafic rocks	Peltic rocks (with quartz)
Zeolite	Zeolites: laumonite, analcite, heulandite, wairakite. Incompletely reacted relicts widespread.	Mixed-layer clays
Prehnite-Pumpellyite	Lower-T zone: Prehnite + pumpellyite ± chlorite ± albite ± epidote. Higher-T zone: Pumpellyite + actinolite. Higher-P zone: Lawsonite + albite.	Illite/muscovite + chlorite + albite + quartz Stilpnomelane, pyrophylite
Greenschist	Lower-T zone: Actinolite + epidote ± albite ± chlorite ± stilpomelene. Higher-T zone: Hornblende ± actinolite + albite + chlorite + epidote ± garnet	Lowest-T zone: Chlorite + muscovite + albite. Highest-T zone: Chlorite + muscovite + biotite + albite ± garnet Also, chloritoid, paragonite + muscovite + albite
Blueschist	Glaucophane ± lawsonite ± jadeitic pyroxene	Phengite + chlorite or talc + garnet. No biotite. Also Mg-chloritoid, carpholite.
Eclogite	Omphacite + garnet. No plagioclase, no lawsonite.	Talc + kyanite ± garnet ± phengite

Table 1.1 Representative mineral assemblages for the high P/T facies series. Adapted after Yardley (1989). Many other minerals will be present along with the minerals summarised above depending on P-T path, peak metamorphic grade and bulk rock compositions (including the activity of water).

As this project is primarily concerned with rocks of the blueschist and eclogite facies, only the key minerals associated with these facies are further summarised in Table 1.2. Furthermore, some important terms and concepts relevant to these facies are summarised in the following section.

Characteristic Mineral	Mineral Group	Chemical Characteristics	Eclogite?	Blue-schist?
Lawsonite	-	Hydrous Calcic-alumino silicate: $CaAl_2[SiO_7](OH)_2.H_2O$	✓	✓
Epidote	Epidote group	$Ca_2Fe^{3+}Al_2[Si_3O_{12}](OH)$	✓	✓
Glaucophane	Amphibole group	Sodic amphibole $Na_2(Mg_3Al_2)[Si_8O_{22}](OH)_2$ (end-member)	✓	✓
Phengitic mica	Mica group	Silica-rich muscovite with an Si:Al ratio >3:1	✓	✓
Jadeitic pyroxene	Pyroxene group	Sodic pyroxene endmember $NaAlSi_2O_6$	X	✓
Omphacite	Pyroxene group	Calcic-sodic pyroxene $(Ca,Na)(Mg, Fe^{2+}, Fe^{3+}, Al)[Si_2O_6]$	✓	✓
Kyanite		Al_2SiO_5 polymorph	✓	X
Coesite	Silica group	High pressure quartz polymorph	✓	X
Garnet	Garnet	General formula: $X_3Y_2Si_3O_{12}$ where: X = Fe, Mg, Ca or Mn; Y =Al or Fe.	✓	X

Table 1.2 Summary of some characteristic rock-forming minerals of the blueschist and eclogite facies. The list is not exhaustive, and does not include accessory minerals such as zircon and rutile but provides information on some of the key prograde minerals of each facies. Note that some characteristic minerals of the blueschist facies, such as glaucophane, are also stable in eclogite facies P-T conditions.

1.4.2.1 THE BLUESCHIST FACIES

According to Evans (1990), the blueschist facies, originally termed glaucophane schist facies by Eskola (1939), has perhaps met with the widest range of possible interpretations: from complete rejection of the facies, through restricted use, to comprehensive use. Subdivision of the facies include:

1) those of Evans (1990) which include the relatively high P/T lawsonite blueschist facies and the relatively low P/T epidote-blueschist facies;
2) those described by Maruyama (1994) as the low- and high-pressure subfacies.

1.4.2.1.1 P-T CONDITIONS OF THE BLUESCHIST FACIES

As can be seen from Figure 1.2, the P and T field of the blueschist facies ranges from approximately 6 to 14 kbar and 170 to 500°C, respectively. The blueschist P-T field is bounded on the low-P, low-T side by three facies: the prehnite-pumpellyite facies, the lawsonite-albite-chlorite facies (an intermediate facies defined by Turner (1981) with P conditions above those necessary to form zeolite but high enough to form lawsonite) and the greenschist facies. The boundary between the three latter facies and the blueschist facies is defined by the formation of glaucophanic amphibole (amphibole containing significant amounts of glaucophane amphibole) in rocks of broadly basaltic composition.

The upper P-T limit of the blueschist facies field is defined by the presence of the eclogite field. Miyashiro (1994) defines the boundary as being where meta-mafic rocks of broadly basaltic compositions begin to take on the assemblage omphacite + garnet (i.e. eclogite mineral assemblages).

1.4.2.1.2 KEY MINERALS OF THE BLUESCHIST FACIES

The most characteristic mineral of blueschist facies metamorphism of meta-mafic rocks is the sodic amphibole, glaucophane. This amphibole imparts a lilac blue colour to the rock, hence the term blueschist. Other important minerals for this facies include lawsonite, epidote, jadeitic pyroxene and phengitic muscovite (Table 1.1).

1.4.2.2 THE ECLOGITE FACIES

Along the high P/T metamorphic series, the eclogite facies will first be intercepted at P-T conditions of 9-14kbar and 300-450°C, respectively (Figure 1.3). The upper P-T limits of the facies are not defined, but rocks metamorphosed to pressures of 50 kbar, which corresponds to a depth of ~100-150km (see Liou et al. 2004), have been reported. The eclogite facies can be subdivided according to the temperatures of formation, after Carswell (1990):

1) low-temperature subdivision: ~450-550°C;
2) medium-temperature subdivision: 550-900°C;
3) high-temperature subdivision: 900- approx. 1600°C.

The mode of occurrence of eclogites can vary widely, including inclusions in kimberlite, associations with blueschist and associations with gneiss regions of otherwise amphibolite or granulite rocks. It is thus also possible to classify eclogites in terms of their mode of occurrence (see Table 1.2).

Type	Subgroup	Typical Localities	Details
Type I	Type Ia	Isle of Sifnos, Greece	Associated with blueschist facies regions. Relatively low temperature eclogites, metamorphosed under a relatively restricted range of P-T conditions.
	Type Ib	Dora Maria, western Alps	Associated with blueschist facies regions. Low-medium temperature eclogites. Metamorphism under a wider P-T range relative to Type Ia.
Type II	-	Nordfjord, western Norway	These eclogites are associated with apparently amphibolite or granulite facies gneiss regions (which may have originally been eclogite).
Type III	Type III.A	Kuruman kimberlites, western South Africa	Inclusions in kimberlitic rocks
	Type III.B	Salt Lake crater, Hawaii	Inclusions in basaltic rock
	Type III.C	Basal Gneiss Complex, western Norway	Inclusions in peridotitic rocks

Table 1.3. Summary of the classification of mode of occurrence of eclogites, based on that of Miyashiro (1994).

Eclogites that develop from subduction zone metamorphism belong to Type Ia.

A final possible classification for eclogites is for those that have metamorphosed under Ultrahigh Pressure Metamorphism (UHPM) conditions, and those that have metamorphosed under High Pressure Metamorphism (HPM). Ultrahigh Pressure Metamorphism refers to the metamorphism of rocks at P-T conditions high enough to stabilise certain key index minerals, such as coesite and diamond. These minerals are stable at minimum P-T conditions of 27kbar and 600°C respectively, which

corresponds to a depth of ~90km (e.g. Liou et al. 2004). High Pressure Metamorphism takes place at pressure below those of UHPM. This classification is important because eclogites collected from Tian Shan are thought by some (e.g. Zhang et al. 2002a and b; Zhang et al. 2003) to have undergone UHPM (see Chapter 3).

1.4.2.2.1 KEY MINERALS OF THE ECLOGITE FACIES

An eclogite is a rock of mafic composition that is mainly composed of omphacite and almadine-pyrope-grossular garnet. Carswell (1990) defined an eclogite as a rock consisting of >70 vol% garnet + omphacite. Other important minerals associated with eclogites include quartz, coesite, kyanite, amphibole (including glaucophane), phengite, paragonite, zoisite, epidote, rutile, graphite and diamond (e.g. Miyashiro 1994). Although the definition of eclogite as a rock type is restricted to rocks of mafic bulk compositions, other rock types can be metamorphosed under eclogite facies conditions.

1.4.3 THE OCCURRENCE OF HIGH P/T ROCKS: BLUESCHIST BELTS

High P/T ratio rocks are intimately associated with orogenic belts. Maruyama et al. (1996) coined the term "blueschist belt" to describe orogenic metamorphic belts containing blueschist facies rocks and other rocks of high P/T ratio, such as eclogite. As well as containing high P/T ratios rocks, these belts are tectonically significant because they are markers of "fossil subduction zones."

Blueschist belts may be found on all major continents and appear to have been produced throughout most of geologic time (see Maruyama et al. (1996) for a comprehensive review of the occurrence of blueschist belts in space and time). At present, blueschist belts can be found in the circum-Pacific and the Tethysian orogenic belts. Coesite (and sometimes diamond-bearing) UHPM rocks are also found in blueschist belts associated with continental-collision orogenic belts, such as the Western Alps, the Scandinavian Caledonides, central China and the Kokchetav Massif in northern Kazakhstan (Maruyama et al. 1996 and references therein).

Blueschist belts are divided into two types according to their protoliths: 1) the A-Type, or Collision Type, and; 2) B-Type, or Cordillerian Type, (sometimes also

known as the Pacific type). This classification scheme is particularly useful, because the protoliths used to define the blueschist belt types are known to have originated from contrasting tectonic settings prior to subduction. The A-type protoliths originate from a rifted (passive) continental margin, whereas the B-type protoliths originate from an active margin (Figure 1.4). The B-type blueschist belt is characterised by having an accretionary complex, a forearc basin, a huge tonalite-trondjeimite-granitoid (TTG) belt and a volcanic arc, all of which developed during subduction of oceanic lithosphere. The Collision type blueschist belt generally lacks these features, and also differs from the B-type belt in its larger size (e.g. Maruyama 1996).

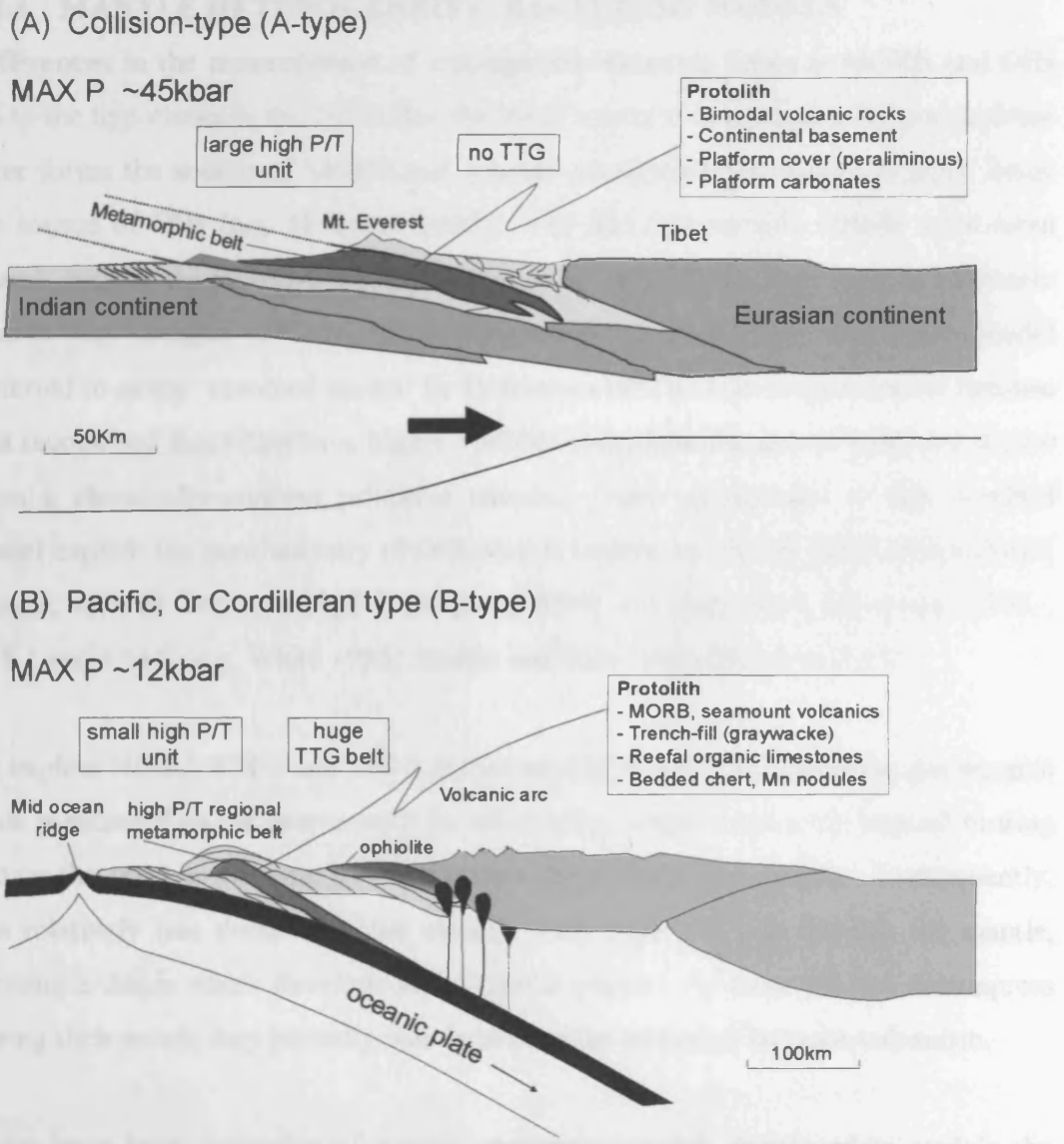


Figure 1.4. Schematic diagram showing the principal differences between the Collision type (A) and Pacific type (B) blueschist belts (simplified after Liou et al. 2004). The Pacific type (or Cordilleran type or B-type) is characterised by associations of an accretionary complex, a forearc basin, a huge tonalite-trondjeimite-granitoid (TTG) belt and a volcanic arc which developed during subduction of oceanic lithosphere. The Collision type blueschist belt generally lacks these features, and also differs from the B-type belt in that it is larger (e.g. Maruyama 1996).

As well as there being differences in the types of protoliths, there are some other first-order differences between the two different types of belt. The maximum pressures recorded in high P/T rocks from the A-type belt are generally much greater than those of the B-type (see Figure 1.4). Eclogites from the A-type blueschist belt commonly show evidence for UHPM, whereas UHPM rocks of the B-type are rare or perhaps absent (e.g. Liou et al. 2004). Another important difference is that rocks of the A-type belt generally show greater degrees of retrogression compared with the B-type rocks.

1.4.4 MANTLE HETEROGENEITY: RECYCLING MODELS

Differences in the concentration of incompatible elements between MORB and OIB led to the hypothesis in the 1970s that the Earth's mantle is layered: an upper depleted layer forms the source of MORB and a lower undepleted (or primitive) layer forms the source of OIB (e.g. Hofmann 1997). The fact that oceanic islands often form chains, such as the Hawaiian chain, indicates that OIBs result from melting of mantle plumes (e.g. Morgan 1971) which rise from the primitive mantle. This simple model (referred to as the 'standard model' by Hofmann (1997)) is no longer tenable because it is recognised that OIBs have highly variable compositions, and so could not derive from a chemically-uniform primitive mantle. Later adjustments to this standard model explain the geochemistry of OIB source regions by mixing between a depleted mantle, such as Depleted MORB Mantle (DMM) and three other reservoirs: HIMU, EM-1 and EM-2 (e.g. White 1985; Zindler and Hart 1986; Hart et al. 1992).

To explain HIMU, EM-1 and EM-2, Hofmann and White (1982) propose that oceanic crust is returned to the deep mantle by subduction, where eventually internal heating causes the crust to become less dense than the surrounding mantle. Consequently, this relatively less dense recycled oceanic crust begins to rise through the mantle, forming a diapir which develops into a mantle plume. As these plumes decompress during their ascent they partially melt becoming the source of hot spot volcanism.

There have been a number of mantle convection models developed to explain the chemical differences between the relatively depleted MORB and enriched OIB basalts (see Hofmann 1997 and Tackley 2000 for expanded review). These models generally differ in how they explain the origin of the enriched OIB sources and the depleted

MORB sources. However, they all generally invoke recycling of oceanic crust into the mantle and its incorporation into a mantle plume (see Figure 1.5 A-F).

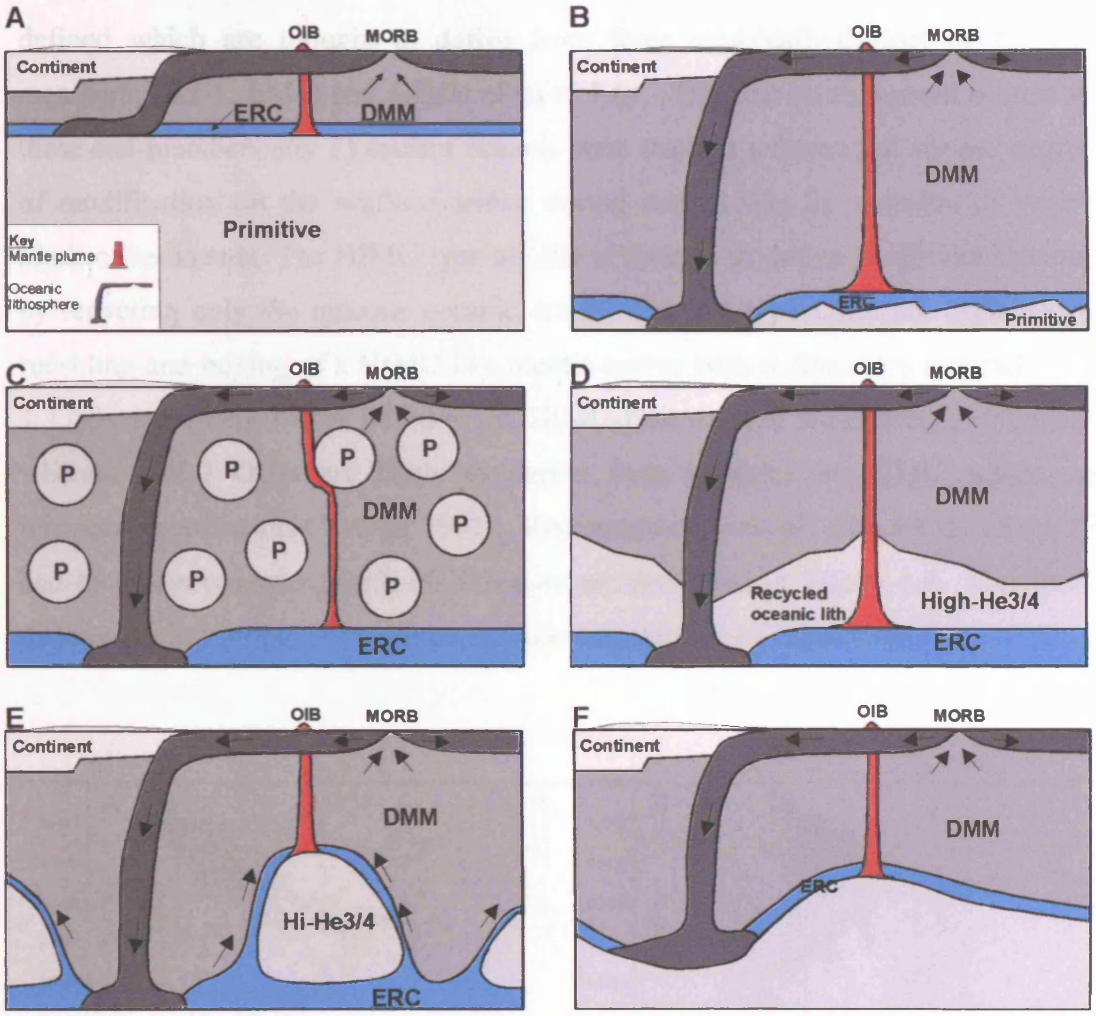


Figure 1.5 A-F. Possible locations for mantle reservoirs, modified from Tackley (2000) and references therein. Depleted MORB Mantle (DMM). High $^{3}He/^{4}He$ (here considered equivalent to primitive mantle). Enriched recycled crust (ERC). A) Typical geochemical model, layered at 660km depth; B) Typical geodynamic model, homogeneous except for some mixture of ERC and primitive material at the base; C) Primitive blob model with an added ERC layer; D) complete recycling model; E) Primitive Piles model. F) Deep primitive layer.

1.4.4.1 ISOTOPE GEOCHEMISTRY OF MANTLE SOURCE END-MEMBERS

Isotopic investigations have revealed geochemical variations in OIBs between different island chains (e.g. White, 1985, Allegre et al. 1987) and within island chains (Dupre et al. 1982; Woodhead and McCulloch 1989; Chauvel 1992). Isotopic differences between OIBs, defined by isotope ratios such as $^{87}Sr/^{86}Sr$, $^{143}Nd/^{144}Nd$ and

$^{206}Pb/^{204}Pb$ (and others), reflect differences in the parent daughter ratios in the mantle sources, which over time have evolved to distinct fields in isotope ratio space (e.g. White, 1985; Zindler & Hart, 1986; Dicken 1995; Hofmann 1997; Niu & O'Hara 2003). On the basis of these differences, three main OIB lava types have been defined which are thought to derive from three chemically-distinct mantle end-members; EM-1, EM-2 and HIMU (Figure 1.6). The commonly-agreed origins for these end-members are: 1) ancient oceanic crust that has experienced various degrees of modification on the seafloor and/or during subduction; 2) inclusion of various kinds of sediments. The HIMU type of OIB is thought to derive its distinct signature by recycling only the igneous oceanic crust. The EM-type OIBs are explained by recycling and mixing of a HIMU-like mantle source with sedimentary material. EM-1 OIBs are likely to be mixtures of HIMU-like sources with pelagic sediments, whereas EM-2 OIBs are likely to derive from mixtures of HIMU source and terrigenous sediments (Weaver 1991). Representative isotopic data for the three OIB end-members compared with MORB data are presented in Figure 1.6. Qualitative differences in isotopic composition are also summarised in Table 1.4.

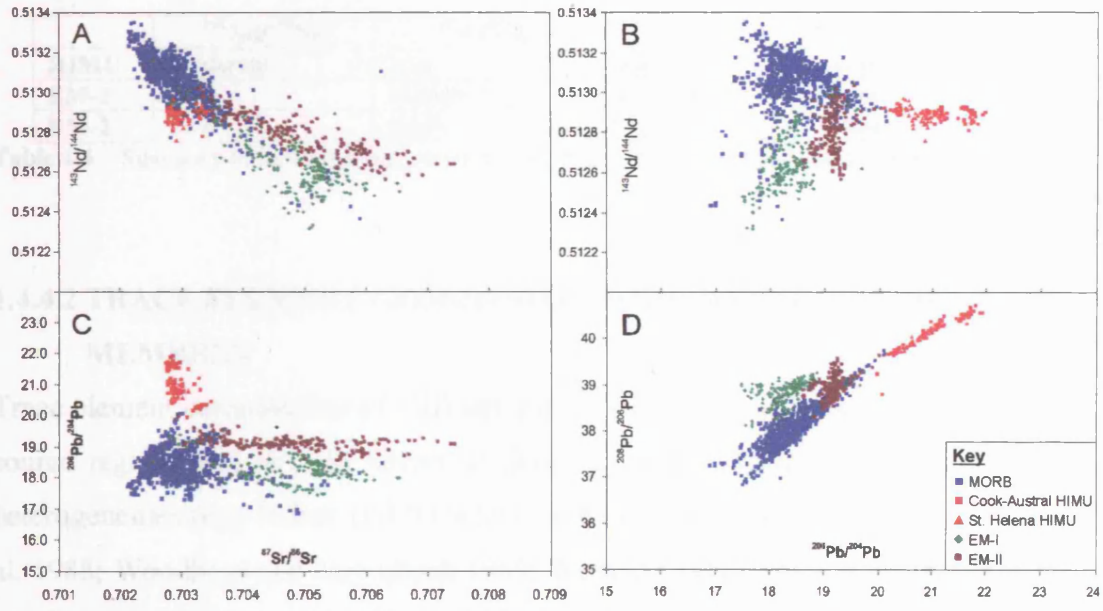


Figure 1.6 A-D Representative isotopic data for the three OIB end-members HIMU, EM-1 and EM-2 and MORB. Adapted from Stracke et al. (2003) and using data from the references therein.

HIMU-sourced (i.e. high μ, where μ = $^{238}U/^{204}Pb$) basalts form end-member compositions in Pb isotope space and are characterised by relatively high $^{206}Pb/^{204}Pb$ ratios (Figure 1.6 C), of generally >20.5 (Hart 1988). Other isotope ratios, such as $^{87}Sr/^{86}Sr$ and $^{143}Nd/^{144}Nd$, are MORB-like. Such high μ values suggest enrichment of U compared with Pb to have preceded eruption of the basalt in order for ^{206}Pb to accumulate by ^{238}U decay (Tatsumoto 1978; Hauri & Hart 1993). For HIMU basalts to have elevated radiogenic lead compositions, the ultimate source must have originally been enriched in U relative to Pb, which with time (on the order of 10^9 years), generated the radiogenic lead and high $^{206}Pb/^{204}Pb$ ratios.

Relative to HIMU, EM-1 basalts are elevated in $^{87}Sr/^{86}Sr$ and depleted in $^{143}Nd/^{144}Nd$ (Figure 1.6 A). Other important differences between EM-1 and HIMU include the low $^{206}Pb/^{204}Pb$ and $^{208}Pb/^{204}Pb$ ratios. Weaver (1991) proposes that the isotopic systematics are consistent with mixing a HIMU source with a few percent of ancient pelagic sediment. Compared to the other OIB end-member compositions, EM-2 lavas have the highest $^{87}Sr/^{86}Sr$ ratios. EM-1 differs from EM-2 in that it is enriched in radiogeneic lead (Figures 1.6 B-D) and has slightly higher $^{143}Nd/^{144}Nd$ ratios.

	$^{143}Nd/^{144}Nd$	$^{87}Sr/^{86}Sr$	$^{208}Pb/^{204}Pb$	$^{206}Pb/^{204}Pb$
HIMU	Moderate	Low	High	High
EM-1	Low	Moderate	Moderate	Low
EM-2	Low	High	Moderate	Moderate

Table 1.4. Summary of isotopic characteristics of OIB end-members described qualitatively.

1.4.4.2 TRACE ELEMENT GEOCHEMISTRY OF MANTLE SOURCE END-MEMBERS

Trace element compositions of OIB complement isotopic evidence for defining OIB source regions and provide further evidence for the ultimate origin of the mantle heterogeneities (e.g. Palacz and Saunders 1986; Weaver et al. 1986, 1987; Loubet et al. 1988; Woodhead and McCulloch 1989; Weaver 1991). Trace element abundance of OIB magmas are considerably variable, but show systematic variations that enable mantle sources to be fingerprinted in a similar fashion to isotopic fingerprinting. To summarise the differences between the different OIB end-members, Figure 1.7 A-C compares normalised multi-element diagrams of data from the respective basalts. Table 1.5 also summarises important trace element characteristics.

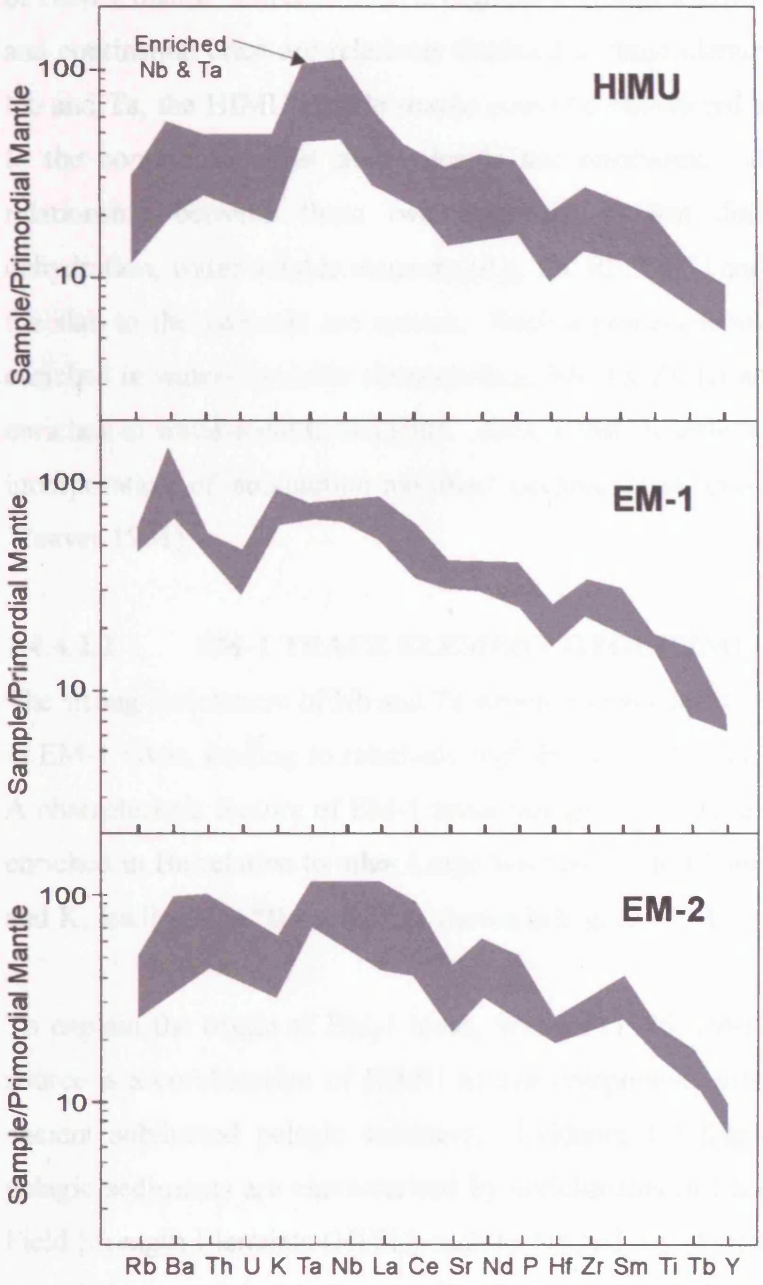


Figure 1.7. Primordial mantle normalised multi-element diagrams of selected trace elements for OIB endmember compositions (HIMU, EM-1 and EM-2). Adapted from Weaver (1991). The plotted HIMU OIB data are taken from volcanic rocks from Saint Helena, Raivavae and Rurutu; EM-1 OIB are from volcanic rocks from Gough; EM-2 OIB are for volcanic rocks from Samoa and Tahaa.

1.4.4.2.1 HIMU TRACE ELEMENT GEOCHEMISTRY

Perhaps the most characteristic trace element feature of HIMU basalts is the enrichment in Nb and Ta relative to Rb, Ba Th, U and the Light Rare Earth Elements (LREE) (Weaver, 1991; Woodhead 1996). HIMU basalts are the only terrestrial basalts to display such enrichment of Nb and Ta (Weaver 1991). This enrichment can be expressed by a number of trace element ratios, such as the sub-N-MORB La/Nb and Ba/Nb ratios (see Table 1.5).

Niobium and Ta enrichment of HIMU OIBs may provide a clue to the ultimate origin of HIMU mantle sources. This is because it is well known that volcanic arc magmas and continental crust are relatively depleted in these elements. Thus, with respect to Nb and Ta, the HIMU mantle source could be considered a complementary reservoir to the continental crust and volcanic arc reservoirs. A possible model for the relationship between these two reservoirs is that during subduction and slab dehydration, water-soluble elements (e.g. Ba, Rb, Cs, U and perhaps Th) are lost from the slab to the volcanic arc system. Such a process would leave the slab relatively enriched in water-insoluble elements (e.g. Nb, Ta, Zr, Hf and Ti) and the volcanic arc enriched in water-soluble elements. Thus, HIMU mantle sources can be generated by incorporation of subduction-modified oceanic crust into the ambient mantle (e.g. Weaver 1991).

1.4.4.2.2 EM-1 TRACE ELEMENT GEOCHEMISTRY

The strong enrichment of Nb and Ta which is characteristic of HIMU basalts is absent in EM-1 lavas, leading to relatively high Ba/Nb, K/Nb, La/Nb ratios (see Table 1.5). A characteristic feature of EM-1 lavas recognised by Weaver (1991), is that they are enriched in Ba relative to other Large Ion Lithophile Elements (LILE) such as Rb, Cs and K, leading to a "Ba-spike" as shown in Figure 1.7 B.

To explain the origin of EM-1 lavas, Weaver (1986, 1991) speculates that the EM-1 source is a combination of HIMU source components mixed with small amounts of ancient subducted pelagic sediment. Evidence for this comes from the fact that pelagic sediments are characterised by enrichments in LILEs and depletions of High Field Strength Elements (HFSE) such as Nb and Ta. Furthermore, pelagic sediments are relatively enriched in Ba (e.g. Ben Othman et al. 1989).

1.4.4.2.3 EM-2 TRACE ELEMENT GEOCHEMISTRY

Although similar to EM-1, EM-2 basalts differ in terms of ratios such as Rb/Nb, Ba/Th, Ba/Nb and Ba/La (Table 1.5). Important characteristics for EM-2 are the relatively high Th/Nb and Th/La compared with EM-1 and the less pronounced Ba enrichment. Like EM-1 lavas, Weaver (1991) proposed that these features may be explained by mixing a mantle source consisting of sedimentary and HIMU components. However, differences in the trace element compositions between EM-1

and EM-2 effectively rules out pelagic sediment as an important component in EM-2 mantle sources. On the other hand, the similarities between the chemical characteristics of terrigenous sediments and EM-2, such as the high LILE/HFSE and the lack of a strong Ba-enrichment, provide evidence that terrigenous sediment may be a component in EM-2 source regions.

	Zr/Nb	La/Nb	Ba/Nb	Ba/Th	Rb/Nb	Th/Nb	Th/La	Ba/La
Primordial mantle	14.8	0.94	9.0	77	0.91	0.117	0.125	9.6
Normal MORB	30	1.07	4.3	60	0.36	0.071	0.067	4.0
Continental crust	16.2	2.2	54	124	4.7	0.44	0.204	25
HIMU OIB								
Saint Helena	4.5	0.69	5.9	77	0.38	0.078	0.112	8.7
Mangaia	3.8	0.77	6.5	64	0.38	0.101	0.131	8.4
Tubuaii	3.2	0.72	4.9	49	0.35	0.093	0.133	6.9
Rurutu	5.0	0.77	5.3	63	0.38	0.083	0.107	6.8
Raivavae	4.2	0.66	5.4	68	0.38	0.080	0.121	8.3
EM-1 OIB								
Hole 525A	11.4	1.19	17.7	-	-	-	-	14.9
Walvis Hole 527	8.4	0.92	12.7	-	-	-	-	15.1
Ridge Hole 528	6.1	0.87	14.7	-	-	-	-	16.9
Hole 530A	5.9	0.64	5.6	-	-	-	-	8.8
Gough	6.8	0.97	16.1	154	0.99	0.105	0.110	16.6
Tristan da Cunha	4.2	0.86	11.4	103	0.88	0.108	0.128	13.2
Kerguelen	5.3	1.14	14.4	126	1.17	0.122	0.107	13.5
EM-2								
Tutuila, Samoa	7.3	0.89	7.3	67	0.59	0.111	0.126	8.3
Upolu, Samoa	4.5	1.09	11.0	84	0.76	0.133	0.122	10.4
Tahaa, Society	6.5	0.97	10.9	71	0.85	0.157	0.163	11.3

Table 1.5. Summary of some characteristic trace element ratios for the three OIB end-members. Estimates for N-MORB, Primordial mantle and continental crust also included. Adapted from Weaver (1991).

1.5 SUMMARY

This thesis aims to test the validity of "recycling models" which have been used by some workers to explain the geochemistry of ocean island basalts. To test recycling models, this work will evaluate the geochemical effects of subduction zone metamorphism by investigating the geochemistry of blueschists and eclogites from two mountain chains of NW China. Having identified any geochemical effects of subduction zone metamorphism, the possibility of recycled oceanic crust forming part of the source regions of OIB will then be evaluated.

CHAPTER 2

LITERATURE REVIEW

2.1 INTRODUCTION

This chapter reviews previous work that has attempted to identify or predict the geochemical effects of subduction zone metamorphism. Because of the great depths at which HP-LT metamorphism takes place, and the consequent lack of direct sampling, much of the previous work is speculative, drawing on evidence from a number of different fields of study. These include: 1) the geochemistry of volcanic arc basalts (VAB); 2) experiments under HP-LT conditions; 3) the trace element geochemistry of high pressure minerals; 4) phase petrology; 5) the geochemistry of subduction zone metamorphosed rocks and fluids. This review covers each of these fields of study and aims to identify any consistencies and inconsistencies between them.

A useful starting point in this review is to ask the question "what might the geochemical signature of HP-LT metamorphism look like?" Perhaps the clearest picture comes from the characteristic geochemistry of volcanic arc magmas. The distinctive LILE and LREE enrichment relative to HFSE and HREE characteristics of arc magmas (e.g. McCulloch and Gamble, 1991; Tatsumi et al. 1986; Pearce and Peate, 1995; Brenan et al. 1995; Kogiso et al. 2000) is evidence that the residual slab rocks are LILE and LREE-depleted while being HFSE- and HREE-enriched (e.g. Niu et al. 1999). In addition to VAB geochemistry, experimentation is also a useful source of geochemical evidence for the effects of subduction zone metamorphism. Although few in number, dehydration experiments have been important in placing constraints on the geochemistry of high P/T metamorphism under controlled conditions. In this review, results from studies on VAB geochemistry and evidence from experiments are used to place first order constraints on the geochemical signature of HP-LT metamorphism.

After defining what is meant by a HP-LT metamorphic chemical signature, the review reviews what is known about the mineralogical basis of HP-LT metamorphism. This is because the stability of minor, often hydrous phases ultimately controls chemical differentiation in subducting slabs (e.g. Poli and Schmidt 2002). Knowledge of the trace element geochemistry of these minerals, coupled with phase petrological investigations, can therefore be used to constrain the likely location of chemical differentiation in P-T space. For example, if it were known that certain trace elements were concentrated in a particular hydrous phase, it would be possible to predict the liberation of those trace elements by knowing when that mineral will dehydrate.

Having defined what is meant by a HP-LT metamorphic chemical signature, and outlined the phase petrological basis of chemical differentiation, the review turns to previous studies on actual HP-LT rocks and fluids. It is not possible to sample actual eclogites that subduct into the deep mantle, but HP-LT rocks (such as blueschists and eclogites) are useful analogues as they have followed similar P-T paths, and presumably undergone similar dehydration histories. Furthermore, blueschists and eclogites can contain fluid inclusions and high pressure veins, formed from fluids that must have been present during growth of the metamorphic minerals. Chemical analysis of the composition of blueschists and eclogites, and of associated fluid inclusions and high pressure veins, therefore gives a unique opportunity to observe the chemistry of rocks and fluids associated with subduction zone metamorphism.

Based on the above considerations, this review is broadly divided into five sections:

- Section 2.2 discusses evidence constraining the signature of chemical differentiation associated with subduction metamorphism;
- Sections 2.3 and 2.4 discuss the trace element geochemistry of high P/T metamorphic minerals and the phase petrology of subduction zone metamorphism;
- Section 2.5 discusses previous work on the chemical composition of rocks that are known to have undergone subduction zone metamorphism and fluids thought to be associated with HP-LT metamorphism;
- Section 2.6 presents a synthesis of the important findings of the previous sections.

2.2 WHAT IS A SUBDUCTION ZONE CHEMICAL SIGNATURE?

As noted above, VAB geochemistry is strong evidence for chemical modification of the subducting slab. This section aims to provide a clear picture of the geochemical characteristics this modification may leave in the residual subducting slab, using evidence from volcanic arc magma geochemistry and from dehydration experiments.

2.2.1 EVIDENCE FROM THE GEOCHEMISTRY OF VOLCANIC ARC MAGMAS

In the widely-accepted model, hydrated oceanic crust and sediment dehydrate to produce fluids that migrate into the mantle wedge. This fluid or "slab component" lowers the mantle wedge solidus to produce magmas. The incompatible trace element characteristics of these magmas largely reflect those of the slab component (e.g. Gill, 1981; McCulloch and Gamble, 1991; Stolper and Newman, 1994; Pearce and Peate, 1995; Sobolev and Chaussidon, 1996; Elliott et al. 1997; Iwamori, 1998). Volcanic arc magmas are generally enriched in LILE (and sometimes LREE) relative to HFSE and HREE, a characteristic unlikely to be inherited from the ambient mantle (e.g. Pearce and Peate 1995). Elements such as LILE must therefore be supplied by the slab component, and so the subducting slab itself must be correspondingly depleted in these elements (Niu et al. 1999, 2002; Niu and O'Hara 2003).

Niu et al. (1999) provided a schematic diagram illustrating what the residual chemical characteristics of subducted oceanic crust might look like (Figure 2.1). From this diagram, it can be seen that water-soluble incompatible elements such as Ba, Rb, Th, U, K, Pb and Sr should be relatively depleted in the residual crust. In contrast, water-insoluble elements, such as Ti, Zr, Hf, Nb and Ta, should be relatively enriched (or less depleted). Thus residual oceanic crust should have low ratios of fluid-mobile elements to fluid immobile elements, compared with reservoirs such as MORB (or indeed any basalt produced predominantly by partial melting). Such ratios may include Th/Nb, Ba/Zr and Rb/Ta.

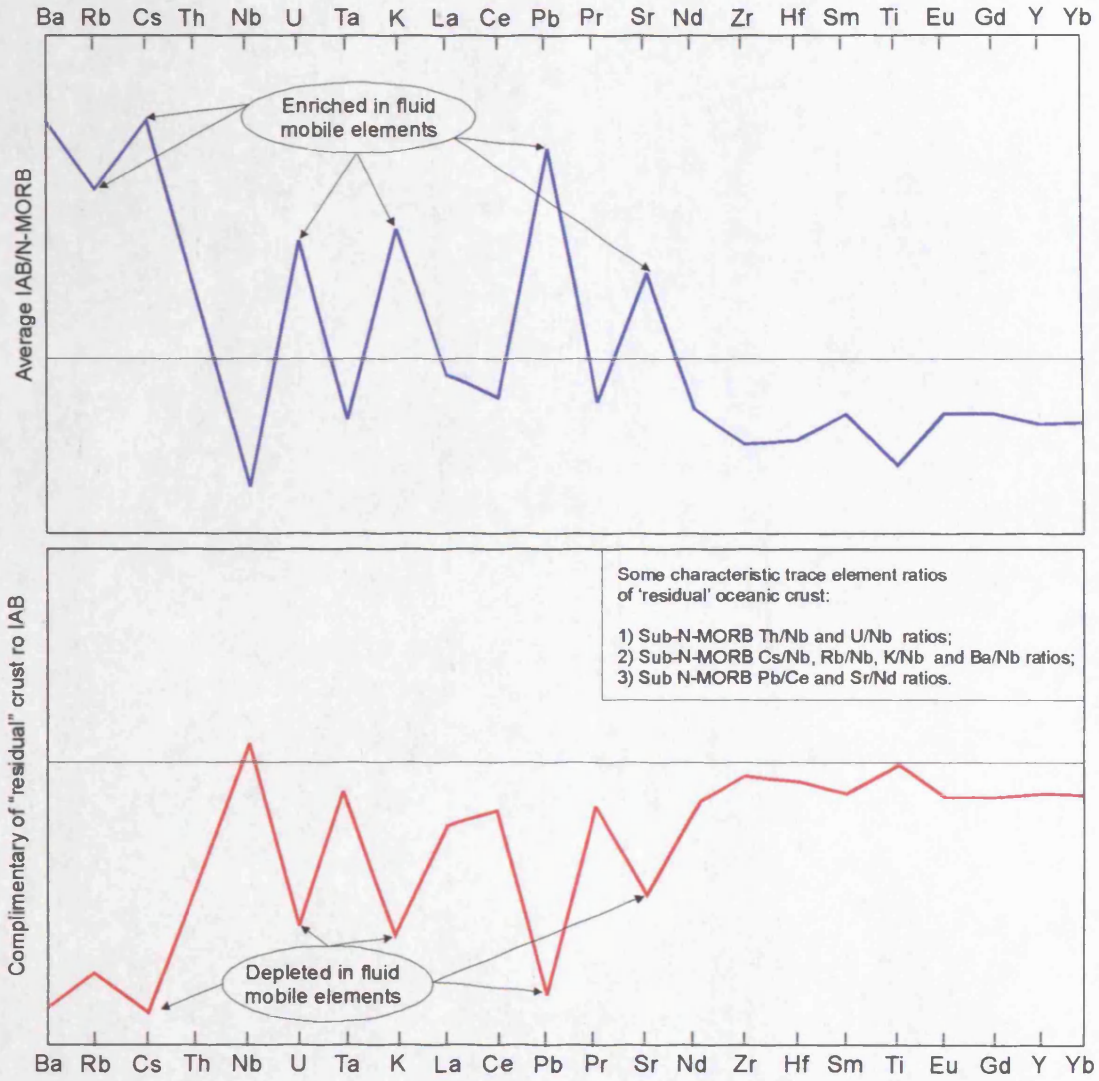


Figure 2.1. Multi-element diagram of average island arc tholeiite (broadly equivalent with volcanic arc basalts) normalised to "oceanic crust" (a calculated mixture of surficial basalts, feeder dykes and gabbros) compared with the residual crust after dehydration reactions (adapted from Niu and O'Hara 2003). It can be seen that water soluble elements, such as Rb, Ba, Th, U, Pb and Sr are depleted in the residual crust, compared with oceanic crust and VAB. As this chemical signature is thought to result from dehydration reactions during HP-LT metamorphism, it is here used to define the potential geochemical signature of subduction zone metamorphism (see text for further discussion).

2.2.2 EVIDENCE FROM EXPERIMENTAL INVESTIGATIONS

There are a number of experiments that have determined the equilibrium partitioning of elements between different minerals and melts/fluids (e.g. Brenan et al. 1995a,b). However, during actual dehydration processes in the slab, any mass transfer would be more complicated than simple equilibrium mineral/fluid (or melt) partitioning (Kogiso et al. 1997a). This is because dehydration in actual subducting slabs would take place under "open system" conditions, with the potential for changing fluid

compositions, non-equilibrium partitioning, phase dissolution and recrystalisation (e.g. Keppler 1996). Furthermore, some trace elements could be transported along grain boundaries, and so mineral/fluid (or melt) partitioning may not be relevant at all. Such problems have led a small number of workers to investigate experimentally the geochemical effects of dehydration on different lithologies under open system conditions. These include mafic lithologies (e.g. Kogiso et al. 1997), serpentinites (e.g. Tatsumi 1986) and sediments (e.g. You et al. 1996; Johnson and Plank 1999).

Kogiso et al. (1997a) performed repeated open-system dehydration experiments on natural mafic amphibolite. These experiments showed that dehydration should increase ratios such as Th/Pb, U/Pb and Sm/Nd and decrease Rb/Sr ratios in the slab. In general, elements with large ionic radii, i.e. LILEs, LREE, Th and U, were readily transported during open-system dehydration processes. Such findings are consistent with the predictions of element mobility during subduction processes from VAB geochemistry. However, the experiments were performed on natural amphibolite, which is thought to metamorphose under lower P/T ratio conditions (i.e. follow a hotter geotherm) than those expected at mature subduction zones. It follows that the experiments of Kogiso et al. (1997a) cannot solely be relied on for evidence of the chemical modification resulting from dehydration.

Johnson and Plank (1999) performed dehydration experiments on pelagic red clay sediments at 20-40 kbar and 600-1000°C. The results show that, below the solidus, elements such as Rb, Sr, Ba and Pb are the most mobile. However, Th and Be only become significantly mobile at the solidus, where they behave with partition coefficients similar to that of Rb (a condition required by VAB geochemistry).

In contrast to Johnson and Plank (1999), You et al. (1996) performed hydrothermal experiments investigating the chemical modification resulting from sediment-fluid interaction (as opposed to sediment dehydration). Although the experiments were conducted at relatively low T conditions of 25-350°C and 800°C, the results are generally consistent with those of Johnson and Plank (1999). Fluid-mobile elements such as Cs, Li, Pb, and Rb are readily mobilised, although Be was also found to be mobilised under these conditions, in contrast to the results of Johnson and Plank

(1999). Other results include a slight de-coupling of LREE from HREE, and HFSE immobility.

Tatsumi et al. (1986) conducted dehydration experiments on synthetic serpentine spiked with 11 trace elements (Cs, Rb, K, Ba, Sr, La, Sm, Tb, Y, Yb and Nb) at 12 kbar and 850°C. The results clearly show that elements with large ionic radii (e.g. Cs, Rb, K, Ba, Sr, and La) are readily mobilised by aqueous fluids.

2.2.3 THE SUBDUCTION ZONE SIGNATURE IN DEHYDRATED ROCKS

Qualitatively, the predictions from VAB studies and experimental investigations are generally consistent. Put simply, elements such as LILE should be readily mobilised, and the LREE should be less readily mobilised (perhaps being decoupled from the heavier REE) from the slab. Furthermore, HFSE and HREE should remain immobile during dehydration.

Rocks that that have been metamorphosed under high P/T conditions and experienced dehydration reactions should therefore be characterised by relatively low LILE/HFSE and LILE/HREE ratios, and "normal" HREE/HFSE ratios. For example, a metamorphosed and dehydrated MORB should exhibit sub-N-MORB ratios of Ba/Nb, Cs/Zr, Rb/Yb and La/Yb, and MORB-like Nb/Yb and Zr/Nb ratios (obviously a large number of other ratios could be used, but those presented above are adequate to express the point). As a guide to what a subduction zone signature in subduction zone metamorphosed lithologies might look, the schematic diagram of Niu et al. (1999) may therefore prove to be very useful (see Figure 2.1).

2.3 THE COMPATIBILITY OF ELEMENTS IN DIFFERENT MINERAL PHASES

The subducting slab is composed of an assemblage of minerals that undergoes continuous and discontinuous transformations during subduction zone metamorphism (Poli and Schmidt 2002). Of the potentially large number of minerals that can coexist in rocks metamorphosed to blueschist and eclogite facies, a relatively small number of minerals have been found to control the bulk rock trace element budget, including:

1) hydrous calcium aluminosilicate minerals (e.g. epidote, zoisite, lawsonite);

2) mica group minerals (e.g. phengite);
3) other minerals, including rutile, zircon, titanite and (metastable) pre-metamorphic minerals.

The major mineral constituents of blueschist and eclogite facies rocks are generally not considered important sinks for trace elements, apart from garnet, which is important for the HREE (e.g. Tribuzio et al. 1996; Spandler et al. 2003). The major element composition and nomenclature of the amphiboles of high P/T metamorphic rocks are highly variable and numerous (see Leake et al. 1997). However, amphibole is not considered a major host of trace elements in high P/T metamorphosed rocks. For example, barrositic amphibole (Na-rich hornblende) was shown by Zack et al. (1998, 2002a) to contain moderate amounts of Ba, Rb, Pb, Sr, MREE and small concentrations of Th, U, LREE and HREE. Similarly Spandler et al. (2003) found very small concentrations of these trace elements in eclogites and blueschists from New Caledonia. Clinopyroxenes, such as jadeite and omphacite, also often constitute major proportions of high P/T mineral assemblages. However, these minerals have also been shown to contribute small proportions of the whole rock trace element budget of blueschists and eclogites (Tribuzio et al. 1996; Zack et al. 2002a; Spandler et al. 2003).

2.3.1 HYDROUS CALCIUM ALUMINOSILICATE MINERALS

In this section, four important calcium aluminosilicate minerals are considered: epidote, zoisite/clinozoisite; allanite and lawsonite. Studies of the trace element composition of these minerals have been remarkably consistent: in general these minerals can be important sinks for Sr, Pb, U, Th and LREE.

Zoisite can contain significant concentrations of REE Sr, U, Pb, Th (e.g. Domanik et al. 1993; Nagasaki and Enami 1998; Brunsmann et al. 2001; Becker et al. 1999; Spandler et al 2003). For example, Nagasaki and Enami (1998) showed that in the rocks investigated, up to 70% of the bulk rock budget of Sr can be contained in this mineral (that is in the absence of other major Ca-bearing phases). With regards to the REE content of zoisite, Brunsmann et al. (2001) detected significant concentrations (e.g. <100ppm for individual REE) in meta-basalts from the Tauern Window, Austria. However, not all REE were found to be enriched to the same degree. The effects of

lanthanide contraction were apparent, as indicated by estimated partition coefficients increasing from $D_{La}^{zoisite/fluid} = 0.08 \pm 0.02$ to $D_{Eu}^{zoisite/fluid} = 0.8 \pm 0.4$ (Brunsmann et al. 2001). Similarly Becker et al. (1999), who reviewed data from a wide range of sources to obtain partition coefficients for calculating the composition of a fluid released from eclogites, found that epidote-group minerals can be significant sinks for U and Pb. Becker at al. (1999) also showed that Pb, Sr and U can be up to two orders of magnitude higher in zoisite/epidote than in coexisting omphacite, while Sm and Nd can be up to 3 orders of magnitude higher, confirming the findings of previous workers such as Brunsmann et al. (2001). The high affinity of U, Pb, Sr, Th and the LREE with zoisite was also shown by Zack et al. (1998) in a Laser Ablation ICP-MS analysis of eclogites from Trescolmen, Switzerland.

Lawsonite is also an important sink for Sr, LREE and Pb in rocks that have followed relatively cool P-T paths (lawsonite is stable during relatively cool P-T paths, along hotter P-T paths other Ca-Al-silicate minerals, such as epidote, will form instead). Nagasaki and Enami (1998) estimate that Sr would principally be distributed between epidote (or zoisite) and lawsonite if the two minerals coexist. Spandler et al. (2003) found that lawsonite contained >90% Sr, 30% LREE (of the whole-rock budget), as well as significant proportions of Th and other REE. Similarly Tribuzio et al. (1996) showed that lawsonite contains nearly the entire whole rock LREE budget.

Allanite is also an important LREE, Th and U sink, under lawsonite-blueschist conditions (e.g. Spandler et al. 2003). Similarly, Tribuzio et al. (1996) and Zack et al. (2002a), showed that allanite is very important LREE (and Th and U) host in eclogitic rocks. Furthermore, Hermann (2002) showed that allanite is an important host of LREE, carrying >90% of the whole-rock budget, as well as 75% of the U and Th whole-rock budget.

2.3.2 MICA GROUP MINERALS

The trace element characteristics of phengite are well documented (e.g. Domanik et al. 1993; Schmidt, 1996; Sorensen et al. 1997; Becker et al. 1999; Bebout, 1999; Zack et al. 2001, 2002a; Hermann 2002; Spandler et al. 2003). There is a general

agreement among these authors that phengite can accommodate significant proportions of LILE, especially K, Ba, Rb and Cs.

For example, in a microprobe study of variably metamorphosed rocks from the Franciscan Complex and Catalina Schist, Domanik et al. (1993) found that phengite is the principal host of Rb, Ba, B and Be. Sorensen et al. (1996) also showed that phengite can be a significant host of LILE by demonstrating that whole-rock K/Ba ratios fall on an array defined by the K/Ba ratios of phengite. Similarly, Zack et al. (1998; 2001), who studied eclogites from Trescolmen of the Central Alps, showed that phengite is the dominant host of LILE in eclogites, containing up to 90% of the total whole-rock budget.

2.3.3 OTHER MINERALS

Rutile is a common accessory phase in many high pressure rocks (Zack et al. 2002b and references therein; Becker et al. 2000). The ability of rutile to accommodate highly charged elements such as Nb and Ta in its lattice is well documented (e.g. Jenner et al. 1993; Brenan, et al. 1994; Stalder et al. 1998; Becker et al. 2000; Foley et al. 1999; Zack et al. 2002b; Spandler et al. 2003). It is proposed by these authors (as well as others) that this mineral is responsible for retaining Nb and Ta in the slab, and hence leading to high LILE/Nb and LILE/Ta ratios observed in VAB.

Brenan et al. (1994) carried out experiments on rutile-aqueous fluid partitioning of Nb, Ta, Hf, Zr, U and Th at 1-2 GPa and 900-1100°C. Using a combination of electron microprobe and Laser Ablation Microprobe (LAM), Zack et al. (2002b) measured the above elements (and many other elements including Mo, Sn, Sb, W, Al, Si, Ca, V, Cr, Mn, Fe, and Pb) from eclogites and garnet mica schists from Trescolmen in the Central Alps. Both methods clearly show that rutile is an important sink for HFSE (including W) and Sb. Zack et al. (2002b) showed that, when present, rutile can accommodate >90% of the whole-rock content of Ti, Nb, Sb, Ta and W. Furthermore, it is even possible to accurately calculate bulk rock compositions of Nb and Ta based on LAM analysis and modal estimates of rutile. Brenan et al. (1994) obtained similar results, indicating that just small proportions of rutile (~0.2 wt%) in metabasites or pelagic sediments is sufficient to prevent HFSE enrichment of the

mantle wedge. Results of Stalder et al. (1998) also showed that rutile can fractionate HFSE (especially Nb and Ta) from other trace elements.

Results of rutile/fluid partitioning are also in agreement with those of rutile/melt partitioning. Foley et al. (2000) found extremely high D_{Nb} and D_{Ta} of 100-500 during melting of a tonalite at 1.8-2.5 GPa. In contrast, D_{Zr} and $D_{Hf} \sim 5$, while all other trace elements analysed had $D^{rutile/melt}$ of less than 0.1. In the absence of rutile, titanite is the major Nb and Ta host, and can also be important for the REE, especially the MREE and HREE (e.g. Tribuzio et al. 1996; Spandler et al. 2003)

While rutile, and titanite, are clearly important sinks for Nb and Ta, zircon is generally accepted as being a sink for another petrologically-significant HFSE pair: Zr and Hf. Zack et al. (2002b) conclude that Zr and Hf bulk rock compositions are strongly determined by zircon. Similarly, Hermann (2002) and Rubatto and Hermann (2003) showed that zircon can accommodate >90% of the Hf and Zr budget of eclogite facies rocks.

Pre-metamorphic minerals, such as pargasite, augite and apatite can retain large amounts of trace elements (up to 20%) in blueschists and eclogites that have metamorphosed along low-T geotherms (Spandler 2003).

2.4 STABILITY OF VOLATILE-BEARING PHASES IN SUBDUCTING CRUST

As discussed above, a relatively small number of often hydrous phases generally control the trace element budget of subducting oceanic crust. These phases are only stable under certain P-T conditions and, as prograde metamorphism proceeds, they undergo devolatilisation reactions. Devolatilisation reactions produce a fluid, or more generally a mobile phase, which may be able to move from the slab into the mantle wedge, leaving the slab chemically differentiated.

The phase petrology of different subducting lithologies has relatively recently received a great deal of attention. These studies are highly complex and involve investigation of the effects of many variables, such as:

1) differences of subduction zone geotherms;

2) temperature gradients across the subducting lithosphere;
3) different bulk rock compositions of subducting lithologies, and variation over different scales;
4) inhomogenous degrees of oxidation in the subducting lithosphere;
5) the transport of aqueous fluids throughout the subducting lithosphere;
6) whether melts, aqueous fluids or fluids/melts beyond the 'second critical endpoint' (i.e. a mobile phase that exists under conditions where the distinction between a solute-rich aqueous fluid and a hydrous silicate melt no longer exists) are generated during devolatilisation reactions;
7) the attainment of chemical equilibrium on different scales;
8) reaction kinetics, which, if slow enough, may preserve minerals beyond their stability field;
9) whether reactions are continuous or discontinuous;
10) the reliability of thermodynamic data at high P/T conditions.

As a consequence of the variables listed above there is a large body of literature relevant to the study of phase petrology of subduction zone metamorphism, a review of which is beyond the scope of this work. Two recent reviews, however, give an up to date account of phase petrological studies relevant to subduction zone metamorphism: Poli and Schmidt (2002) and Schmidt and Poli (2004). The following summary is largely based on these two reviews, with other references cited where necessary. However, before continuing with the summary it is necessary to explain some terms, concepts and limitations relevant to the phase petrology of subduction zone metamorphism.

2.4.1 SOME TERMS, CONCEPTS AND LIMITATIONS

2.4.1.1 CONTINUOUS AND DISCONTINUOUS REACTIONS

Fluid production in the slab during subduction zone metamorphism is controlled by a succession of continuous and discontinuous reactions. Discontinuous reactions mark the appearance or disappearance of a phase, whereas continuous reactions change the composition and modal abundance of phase (or phases). Both kinds of reaction are of similar importance in terms of the volume of fluid production. Minerals that exhibit extensive solid solution, such as amphibole, micas and garnet, react continuously, resulting in continuous fluid production over several tens of kilometres depth. In

contrast, discontinuous reactions tend to take place over a restricted depth range of a few kilometres.

2.4.1.2 FLUID PRODUCTION

A fluid will only be produced if a given rock volume is fully fluid-saturated, a condition not required for the stability of hydrous phases. If fluid saturation is not achieved at the beginning of subduction, fluid-absent reactions involving hydrous phases will take place. These reactions have the form: $A + V_1 = B + V_2$ (where A and B are volatile free phases, and V_1 and V_2 are volatile-bearing phases (either hydrous phases or carbonates) and no fluid will be produced. During prograde metamorphism, the volume of fluid able to be stored in hydrous minerals generally decreases. Fluid saturation can be achieved via continuous or discontinuous reactions, and so any part of the slab can eventually become fluid saturated during metamorphism. The point at which saturation is reached depends on initial water content, pressure and temperature.

2.4.1.3 LIMITATIONS OF PHASE PETROLOGY

The approach of phase petrology is to assume equilibrium conditions and homogeneous bulk rock compositions throughout the system under investigation. However, the layers of the oceanic crust (i.e. the simplified stratigraphy of a sediment layer, a mafic layer and a peridotite layer) are not likely to be chemically homogeneous. Furthermore, chemical equilibrium cannot always be assumed. To a first approximation, the effect of these complications is to add to the continuous nature of mineral reactions in the subducting crust. Thus a fluid *pulse* may be smeared over a relatively large depth range.

Another problem with phase petrology studies is that, below 2.2-2.4 GPa (before the amphibole-out and chlorite-out reactions), most information comes from studying natural samples. This is because the kinetics of many important reactions are too slow to allow experimental study, and so the processes taking place at $P < 2.2$-2.4 GPa cannot be observed under controlled conditions. Consequently, calculations using thermodynamic data from experiments conducted below ~2.2-2.4 GPa can give possibly inaccurate results. For example, thermodynamic modelling of MORB in the blueschist facies becomes less accurate when incorporating amphibole solid-solution.

Thus, the calculated amphibole modal abundance and stability range of 4-5 GPa is much greater than observed in experiments and natural eclogites, where amphibole is stable to 2.3-2.8 GPa. It is only under the P-T conditions where amphibole and chlorite react out that kinetics are sufficiently high to allow experimental study, and to observe processes taking place under controlled conditions.

2.4.2 DEVOLATILISATION OF SUBDUCTING LITHOLOGIES

Devolatilisation reactions that take place during subduction zone metamorphism are strongly dependent on the P-T path taken by the subducting crust. Four P-T regimes producing mobile phases in oceanic crust can be resolved (after Schmidt and Poli 2004):

1) **High dehydration rates at low-to-medium pressures (<2.5GPa) and low temperatures (<600°C).** Under these conditions, hydrous phases are often abundant in oceanic crust and dehydration reaction lines (in P-T space, see Figure 2.2) are perpendicular to typical subduction zone P-T paths. All subducted lithosphere undergoes high dehydration rates during the earlier stages of subduction.
2) **Medium to low dehydration rates at medium-to-high pressures (2.5-10 GPa) and low temperatures (500-850°C).** Dehydration rates are relatively low because hydrous phases are reduced in volume by previous devolatilisation, and because dehydration reaction lines (in P-T space) are often subparallel to typical subduction zone geotherms. In this P-T range, mobile phases become denser as a result of dissolution of more material.
3) **Melting**, the volume of which is largely dependent on the availability of H_2O, and the composition of which is strongly pressure-dependent. Melting regimes can be further subdivided:
   i. **Flush melting (1-4 GPa, 650-850°C).** Under these conditions, additional fluid is required from underlying dehydrating lithologies to initiate melting in otherwise fluid-undersaturated lithologies, e.g. dehydration reactions in serpentinised peridotite could initiate fluid-saturated melting in the overlying mafic crust.
   ii. **Fluid-absent melting at high temperatures (800-900°C).** Under these relatively low P/T ratio conditions, volatile-bearing phases begin to melt, e.g. at pressures of 1-2.5 GPa, amphibole will produce an adakitic melt (with Na

contents > K contents). At higher pressures (P = 2.5-5 GPa), phengite will melt producing melts with K>Na.

4) **Dissolution at high P, high T (>5 GPa, T>800°C).** Under these conditions, the differences between a melt and a fluid no longer exist, i.e. there is a chemical continuum between melts and fluids. Given favourable fluid-rock ratios, continuous dissolution processes can dissolve hydrous phases and leach hydrophile species out of rocks.

The rocks collected for this work are not expected to have undergone metamorphism with peak pressures >10GPa and temperatures >>650°C (see Chapters 3, 5 and 6) and so the summary will be concerned only with the first two dehydration regimes outlined above.

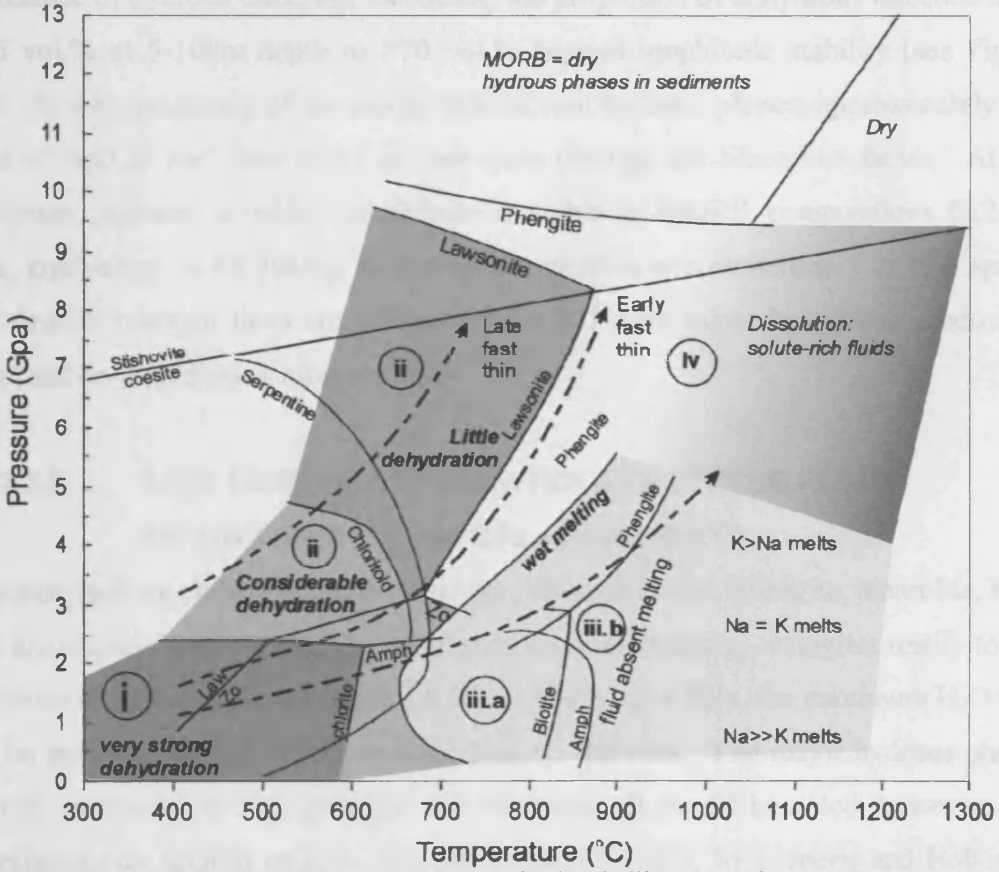


Figure 2.2 P-T diagram showing the four main devolatilisation regimes, and phase relations generally relevant for MORB (adapted from Schmidt and Poli 2004). P-T regions for high dehydration rates are limited by the stability of amphibole and the wet solidus. The P-T region for moderate dehydration is limited by lawsonite and zoisite stability. The curved, stippled arrows indicate cold-intermediate temperature subduction zones. Note that the geotherms intersect mineral stability lines at greater angles under relatively low P-T conditions. Under higher P-T conditions the geotherms become almost parallel, this is especially clear for the relationship between geotherm and lawsonite stability.

2.4.2.1 DEVOLATILISATION REGIMES IN META-BASALTS

In this section the effects of the two relatively low-T devolatilisation regimes on the phase petrology of meta-basalts (or MORB-like composition) is presented.

2.4.2.1.1 HIGH DEHYDRATION AND FLUID PRODUCTION RATES

During early subduction, and after pore fluid has been expelled, the principal hydrous phases in oceanic crust are prehnite, zeolites and pumpellyite, contributing to a bulk-rock H_2O content of 8-9 wt% (Peacock 1993). After reaching depths of 15km, oceanic crust enters blueschist facies conditions, under which the principal hydrous phases are chlorite, Na-rich amphiboles (glaucophane and barrosoisite), phengitic mica, lawsonite or zoisite and paragonite. Bulk rock H_2O contents are ~6 wt% under these conditions. Continuous and discontinuous reactions gradually reduce the modal abundance of hydrous minerals, increasing the proportion of anhydrous minerals from 5-25 vol.% at 5-10km depth to >70 vol.% beyond amphibole stability (see Figure 2.3). As a consequence of the modal reduction of hydrous phases, approximately 4-6 wt% of H_2O is lost from rocks as they pass through the blueschist facies. At the maximum pressure at which amphibole is stable in MORB compositions (2.2-2.4 GPa, equivalent to 65-70km), dehydration reactions are numerous. In P-T space, dehydration reaction lines are oblique to the P-T path taken by typical subducting slabs, and so dehydration rates are high.

2.4.2.1.2 LOW DEHYDRATION RATES AND LITTLE FLUID PRODUCTION (2.4-10 GPa and 500-800°C)

Minerals such as chloritoid, epidote/zoisite, lawsonite, talc, phengite, staurolite, OH-rich topaz associated with UHP (sometimes diamond-bearing), eclogites testify to the existence of hydrous phases above 2.4 GPa. Above ~2.4 GPa, the maximum H_2O that can be stored in meta-basaltic oceanic crust is ~1.5wt%. The major hydrous phases are talc, lawsonite, zoisite, phengite and chloritoid. It should be noted, however, that experiments on MORB up to ~2.2-3.4GPa and 625-750°C by Forneris and Holloway (2003) indicate that chloritoid is a metastable phase only, and so perhaps chloritoid is not an important hydrous phase in meta-basalts under these conditions.

Under relatively cool geotherms, lawsonite is the major H_2O-bearing phase (12wt% H_2O) and may contain >50 wt% of the bulk rock water budget. Under warmer geotherms up to ~3.3GPa, zoisite is the stable hydrous Ca-Al-silicate. Talc is a relatively minor phase in MORB but becomes more abundant in bulk compositions with high X_{Mg}, such as magnesium gabbros. Phengite is also an important hydrous phase, as well as being the carrier of essentially all the K_2O at pressures <5GPa.

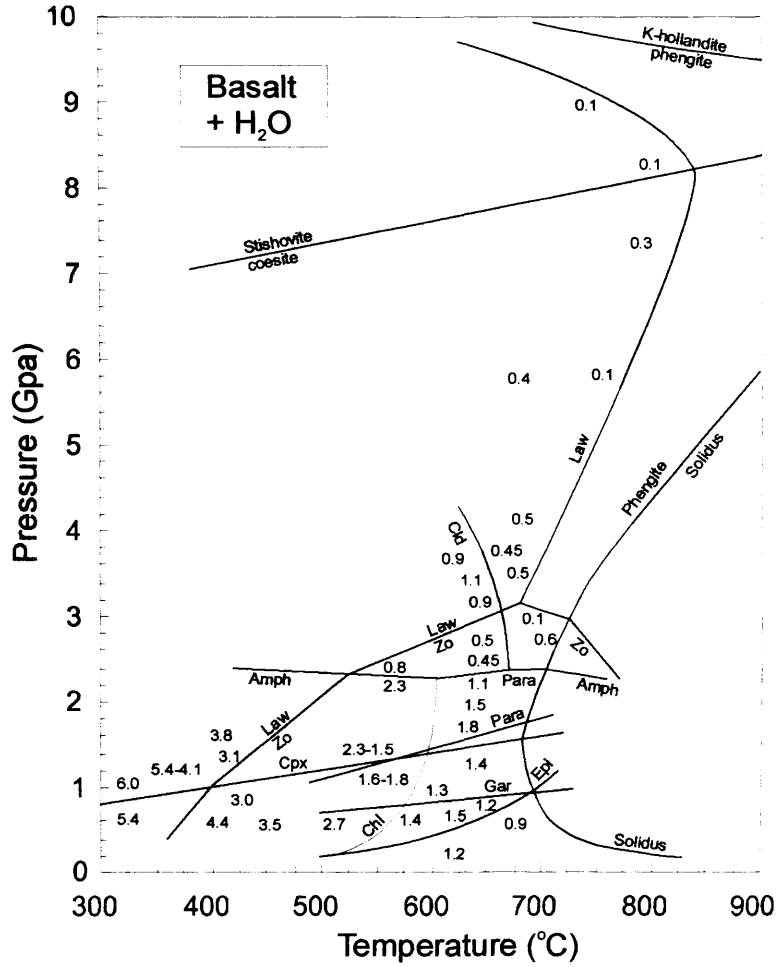


Figure 2.3 Major phase stability boundaries for H_2O-saturated MORB compositions. Numbers refer to amount of H_2O stored in hydrous phases (in wt%). Phase boundaries and H_2O contents below 550°C are from natural blueschists, all other data are based on experiments (after Schmidt and Poli 1998).

Above 2.4GPa, continuous reactions dominate over discontinuous reactions and most reaction curves are subparallel to typical subduction geotherms. Consequently dehydration reactions take place over large depth intervals, and so fluid production rates are low. The hydrous phases with the greatest stability in oceanic crust are lawsonite and phengite which can persist into the stishovite (a high pressure quartz polymorph) stability field at which pressures exceed 7 GPa at temperatures greater

than 500°C. The breakdown of these minerals effectively marks the end of major dehydration reactions for subducting meta-basaltic rocks.

2.4.2.2 DEVOLATILISATION REGIMES IN PELITES

In contrast to MORB, where dehydration reactions below 2.4GPa can lead to significant dehydration, metamorphism of pelites to 2.5-3.3GPa does not necessarily result in the loss of stored H_2O. The potassic micas, biotite and phengite, are the most important hydrous phases, carrying up to 4-4.5 wt% bulk rock H_2O. Other hydrous phases include chloritoid, talc, staurolite and chlorite (Poli and Schmidt 2002). The stability of these phases depends on X_{Mg}, which varies widely in sediments (e.g. Plank and Langmuir 1998). Under relatively low X_{Mg}, biotite is expected to react to form garnet + phengite-bearing assemblages at pressures above 2.5-3.2GPa; under higher X_{Mg} biotite can persist to 4GPa. Phengite, however, is stable up to 8-9 GPa (Domanik and Holloway 1996; Ono 1998). The proportion of hydrous phases, and consequently the H_2O content, present in meta-pelites is dependent on the proportion of quartz, which can be highly variable.

Compared with MORB, our knowledge of the phase petrology of meta-pelites under high P/T conditions is fragmentary, requiring further experimental work to constrain the nature of hydrous phases between the pressure interval 2-4GPa. However, to a first approximation, meta-pelites contain less H_2O than MORB during the low-P blueschist facies, but more H_2O than MORB when P>2.5GPa.

2.4.2.3 DEVOLATILISATION OF GRAYWACKES AND VOLCANOCLASTICS

The bulk rock geochemistry of graywackes and volcanoclastic rocks approximates to that of volcanic andesite and dacites (Plank and Langmuir 1998). From a phase petrological point of view, graywackes and volcanoclastics may be treated as being intermediate between MORB and pelite. For example, the high K_2O contents of graywackes and volcanoclastics promotes the stability of K-micas (phengite and/or biotite), with the corollary that dehydration reactions are similar to those of pelites. However, graywackes and volcanoclastics can also have significant Ca-contents, promoting the stability of amphiboles and leading to similar dehydration reactions observed for MORB. It should be noted that, compared to the MORB and pelite

systems, reactions for graywacke and volcanoclastic rocks are shifted in P-T space due to differences in bulk rock composition.

2.4.2.4 DEVOLATILISATION OF SERPENTINISED PERIDOTITE

Any subduction path taken by a slab is likely to keep serpentine stable up to pressures of >2.5GPa (Ulmer and Trommsdorff 1995). Consequently the mineral assemblage of serpentine + chlorite (+ olivine + clinopyroxene) will remain stable, producing little or no fluid, up to pressures of 3-6 GPa where, depending on temperature, serpentine will break down.

2.4.2.5 CARBONATES

Although H_2O and CO_2 are the two major volatile species subducted, the discussion so far has been concerned only with dehydration reactions. This is because the mass of H_2O subducted at many trenches is much greater than that of CO_2. Furthermore, many trench sediments do not contain significant proportions of carbonate rocks, and so, generally speaking, CO_2 is not a major volatile component in subducting oceanic lithosphere. However, carbonate can be introduced to mafic oceanic crust prior to subduction during hydrothermal alteration (at mid ocean ridges for example). It is therefore necessary to outline the effects of CO_2 on hydrous mineral stability, fluid composition and carbonate stability.

In general, the succession of stable carbonates with increasing pressure is calcite – dolomite – magnesite, with aragonite replacing calcite under low-T high-P paths. Experimental data on the high pressure stability limits of carbonates are few. Domanik and Holloway (2000) identified magnesite in a pelite metamorphosed to 6-11 GPa. Under sub-solidus conditions between 5GPa and 9GPa, dolomite reacts to form magnesite and $CaCO_3$ polymorphs (Luth 2001). In contrast to this, however, Molina and Poli (2000) identified magnesite in H_2O-CO_2-bearing basalts at P-T conditions of ~2GP and 665-850°C.

Carbonates present in oceanic crust under the P-T conditions necessary for dehydration reactions can enlarge the stability field of hydrous phases. This is true during melting and dehydration reactions (Molina and Poli 2000).

2.5 MOBILE PHASE PRODUCTION AND TRACE ELEMENT PARTITIONING

Devolatilisation of oceanic crust during subduction is a process controlled by continuous and discontinuous reactions in lithologies of heterogeneous bulk compositions. Such processes and chemical heterogeneity, together with thermal gradients which exist across the different oceanic layers, promote continuous but not constant fluid/melt production (generally fluid for P <10GPa and T<800°C). This mobile phase production generally decreases with increasing depth below the arc, with peaks in fluid production resulting from significant discontinuous reactions. However, despite fluid flux being continuous, it does not necessarily follow that trace elements are transported continuously off the slab. As a consequence of slow solid state diffusion in minerals, the only trace elements that can be mobilised are probably those that are hosted by decomposing phases (which may breakdown by discontinuous reactions). It is therefore possible to delimit a number of cases for trace element residence in subducting oceanic crust:

1) Extremely soluble trace elements such as B and Be (e.g. Bebout et al. 1993; Bebout 1995) with mineral/fluid partition co-efficients <<1. Such elements may show a continuous decrease in concentration in fluid produced at successively greater depths. Furthermore, the concentration of such elements may be very low at moderate depths due to effective removal of these elements at shallower depths.
2) Trace elements with partition co-efficients of ~1, which will show a constant concentration in fluids produced over increasing depths.
3) Trace elements that are strongly compatible in hydrous phases (e.g. zoisite, lawsonite) but only moderately compatible in anhydrous phases (e.g. clinopyroxene, garnet). During dehydration of such phases, trace elements will strongly partition into the fluid, causing a variation in their (i.e. the trace element) concentration that is not proportional to the fluid flux.
4) A trace element may be strongly partitioned into phengite (such elements include Cs, Rb and Ba) and so is only released at great pressures where phengite breaks down (along typical subduction P-T paths).
5) A trace element strongly partitions into garnet and/or clinopyroxene and so continues to subduct into the deep mantle.

2.5.1 PREDICTING WHICH ELEMENTS WILL BE MOBILISED BY DEHYDRATION REACTIONS

This marks the end of the summary of the reviews by Poli and Schmidt (2002) and Schmidt and Poli (2004). Based on the phase petrology, partitioning behaviour and the trace element geochemistry of mineral phases discussed above, it is possible to predict which elements may be liberated by dehydration reactions during subduction to <10GPa.

Elements such as MREE-HREE and HFSE are highly compatible in non-hydrous phases such as garnet and rutile. Such elements are not likely to be mobilised by dehydration reactions at high, medium or low dehydration rates, and so will be recycled into the deep mantle. Allanite, zoisite and lawsonite largely host elements such as LREE, Pb, Sr and Th and U. Such minerals are not likely to break down until ~3.3 GPa (zoisite) or 7 GPa (lawsonite). Allanite is stable to >4.5 GPa and 1050°C (Hermann and Green 2001; Hermann 2002). Elements such as the LILEs will be almost entirely hosted by phengite, and so are not likely to be released until ~7GPa at ~500°C.

2.5.2 PREDICTING ELEMENT MOBILITY RESULTING FROM DEHYDRATION: LIMITATIONS

From the evidence presented in the previous sections it appears that continuous dehydration should liberate trace elements according to the decomposition of their host phases. That is, fluids evolved during dehydration continuously escape from the slab with compositions directly controlled by the phase petrology and trace element geochemistry of certain hydrous phases. However, this is an unrealistic picture. Spandler et al. (2003) show that, although the analysed eclogites show evidence for significant dehydration (apparent from the relatively low volatile content compared with blueschists), trace element contents are essentially the same as the protoliths. Spandler et al. (2002) propose that as hydrous minerals breakdown, the liberated trace elements are incorporated in other major and accessory phases, thus decoupling them from the fluid. For example, the breakdown of lawsonite should produce allanite by the reaction:

Lawsonite + Diopsite + Garnet ($gr_{20}py_{80}$) → Garnet ($gr_{40}py_{60}$) + Allanite + Fluid

Any trace elements released by decomposition of lawsonite that are incompatible in garnet will be taken up by allanite. Supporting evidence for such a process (i.e. uptake of trace elements by hydrous phases) is the existence of multiply zoned epidote grains. Trace element-rich zones in epidote probably formed in response to decomposition of other trace element-rich phases (such as lawsonite). In contrast, trace element-poor zones formed during decomposition of trace element-poor phases, such as amphibole (Spandler et al. 2003).

Another limitation with the phase petrological approach to predicting trace element liberation is that the fluid may not be in equilibrium with other rocks as it moves throughout the slab. Thus it remains possible that the fluid composition could be modified by dissolving other phases, or by trace element partitioning into stable phases.

The predictions made in previous sections also suffer from not taking into account any externally-derived fluid. The addition of such fluids will raise fluid:rock ratios above those expected from dehydration reactions alone. If fluid:rock ratios become high enough, the system resembles intense hydrothermal alteration processes. Hydrothermal alteration can involve very high fluid:rock ratios and a fluid that is often able to dissolve mineral phases in the host rock. Any element can be mobilised if there are no stable phases into which it can partition, and if it is soluble in the fluid. Therefore, any element can potentially be mobilised in a body of rock subjected to pervasive hydrothermal alteration (e.g. Niu and Lesher 1991). Fluid:rock ratios and the composition of flowing fluids in real slabs cannot be predicted by phase petrology because of the possibility of externally-derived fluids (e.g. Scambellui and Philippot 2001). Consequently, the predictions of the mobility of elements based on the stability of phases made above should be regarded as an end-member possibility.

Another limitation for element mobility is whether the fluids produced by dehydration are able to flow away from the reaction loci. If fluid is not able to leave the reaction loci, dissolved trace elements will not be mobilised from the volume of reacting rock. It is beyond the scope of this review to cover fluid flow in the deep crust, further details of which can be found in Ague (2004). In general, however, eclogite can retain ~1-2vol% of fluid in interstitial spaces between minerals up to depths of at least

150km (Mibe et al. 2003). If the volume of fluid produced is greater, fluid flow can be channelised along hydrofractures and/or pre-existing fractures, or by porous flow throughout the rock. During porous flow, fluids can continuously equilibrate with the rock matrix along the flow path, such that the rock matrix controls the fluid composition. In contrast, during channelised flow fluid:rock ratios are much greater such that the fluid interacts less with the rocks. The initial composition of the fluid is therefore retained to a greater extend in channalised fluids than fluids travelling by porous flow (Manning 2004).

2.6 CONSTRAINTS FROM THE GEOCHEMISTRY OF HIGH P/T METAMORPHIC ROCKS

In this section the evidence for or against a subduction zone chemical signature obtained by the chemical analysis of high P/T metamorphic rocks from the published literature is reviewed. As outlined in the previous chapter, it is likely that protoliths are highly heterogeneous with respect to their lithology. Correspondingly, investigations into the geochemistry of high P/T metamorphic rocks have found large protolith heterogeneity (see especially Spandler et al. 2004). In addition to analysing a wide range of protolith compositions, investigations into high P/T rocks have also included the analysis of metamorphic veins and fluid inclusions. To cover these wide ranging studies, this section is divided into three subsections:

1) the bulk rock geochemistry of high P/T metamorphic rocks,
2) the chemistry of high P/T metamorphic veins,
3) the chemistry of fluid inclusions.

2.6.1 BULK ROCK GEOCHEMISTRY

During the course of this project the number of studies investigating the bulk rock geochemistry of high P/T metamorphic rocks has increased dramatically. The list of studies investigating the bulk rock geochemistry of a variety of high P/T metamorphic rocks now includes: Sorensen and Grossman (1989); Kullerud et al. (1990); Bebout and Barton (1993, 2002); Bebout (1995); Arculas et al. (1999); Volkova and Budanov (1999); Bebout et al. (1999); Cruciani et al. (2003); Becker et al. (2000); Buisigny et al. (2003); Chalot-Prat et al. (2003); Sadofsky and Bebout (2003); Spandler et al. (2004); John et al. (2004); and Breeding et al. (2004). Evidence from this research is not consistent, with some authors finding that:

1) LILE elements are removed from the rocks (e.g. Becker et al. 1999; Arculus et al. (2002);
2) LILE elements are added to rocks (e.g. Sorensen and Grossman 1989);
3) no evidence for element mobilisation (e.g. Chalot-Prat et al. 2003; Cruciani et al. 2002; Spandler et al. 2004).

To further consider these findings this section is broadly divided into a section concerned with meta-sedimentary rocks and a section examining meta-mafic rocks.

2.6.1.1 META-SEDIMENTARY ROCKS

The geochemistry of meta-sedimentary rocks has been reported by Bebout (1995), Busigny et al (2003), Arculus et al. (1999), Bebout et al. (1999), Sadofsky and Bebout (2003) and Breeding et al. (2004). Some previous workers report that chemical differentiation of meta-sedimentary rocks is strongly dependent on the prograde P-T path taken by the protoliths. Bebout et al. (1999) showed that amphibolite facies meta-sedimentary rocks that followed a relatively low P/T path, were depleted in the relatively fluid-mobile elements B, Cs, As and Sb by ~ 80-90%. In contrast, despite being relatively depleted in elements such as B and Cs, rocks following a lower-T path (lawsonite-albite and lawsonite blueschist facies) tended to retain volatile elements to a greater degree. Mass transfer of LILE away from meta-sediments was also recognised by Arculus et al. (1999). Arculus et al (1999) examined clinozoisite-bearing metamorphic rocks (metamorphosed along higher-T geotherms than lawsonite-bearing rocks) and discovered that 50-85% of the Rb, Ba and Sr were lost from pelitic schist (compared with continental crust).

Later work by Sadofsky and Bebout (2003) on lawsonite blueschist meta-sedimentary rocks from the Franciscan Complex and the Western Baja terrain, western USA, generally confirm the results of Bebout et al. (1999). However, Sadofsky and Bebout (2003) reported fluid-mobile elements present at concentrations indistinguishable from those of the protoliths. Similarly, high pressure and ultra-high pressure meta-sedimentary rocks from the Schists Lustrés nappe (western Alps), which followed relatively low thermal gradients, have K, Rb and Cs compositions that are indistinguishable from likely protoliths (Busigny et al. 2003).

In terms of P-T conditions typical of mature subduction zones, results from amphibolite facies meta-sedimentary rocks (e.g. Bebout et al. 1999) may not be representative, as mature subduction zones are generally cooler (e.g. Peacock 1996). However, evidence for chemical differentiation of lower-T meta-sedimentary rocks is not consistent. A problem with working with meta-sediments is that protolith compositions are highly variable, with the corollary that estimates of chemical modification are intrinsically flawed, especially if the modification is slight (Sadofsky and Bebout 2003; Breeding et al. 2004). Unless protolith compositions have been rigorously estimated, which is not the case for those studies that identified LILE mobilisation, evidence for chemical differentiation must be treated with caution.

Given the problem outlined above, and based on the work of Sadofsky and Bebout (2003) and Busigny et al. (2003), it may be concluded that the evidence does not support chemical differentiation during low-T metamorphism. However, metasomatic alteration of mafic and ultramafic blocks in some mélange zones show evidence of alteration by LILE-enriched fluids. These fluids are thought to have equilibrated with meta-sedimentary rocks (e.g. Sorensen and Grossman 1989) thus chemical differentiation should take place during high P/T metamorphism.

The problems associated with heterogeneous protolith compositions led Breeding et al. (2004) to undertake chemical analysis of a single continuous meta-sedimentary layer. The bulk rock chemistry of the protolith of this layer was not thought to vary significantly along strike. This layer was metasomatically altered at one end, which was in contact with a meta-ultramafic mélange, with the effects of alteration decreasing away from the mélange. By comparing unaltered and altered sediment from this single layer, the problems associated with variable protolith compositions were minimised. Results from Breeding et al. (2004) clearly show that elements such as the LILEs, Pb and U are removed from the altered part of the meta-sedimentary layer. Such observations are the first clear evidence for the mobilisation of LILE, Pb and U by fluids from meta-sediments during subduction under 'typical' subduction zone conditions. It should be noted, however, that this alteration is associated with a melange zone, which is unlikely to be representative of all rocks undergoing subduction zone metamorphism.

2.6.1.2 META-MAFIC ROCKS

Evidence for element mobilisation of meta-mafic rocks (i.e. rocks of broadly basaltic composition, including gabbros) during subduction zone metamorphism is generally inconsistent. A number of studies have provided evidence for chemical changes associated with subduction zone metamorphism:

1) LILE (and perhaps Th and U) removal (e.g. Bebout 1995; Bebout et al. 1993, 1999; Arculus et al. 1999; Becker et al. 2000);
2) LREE (and to a lesser extent, LILE) removal (e.g. John et al. 2004);
3) LILE addition (e.g. Sorensen and Grossman 1989; Sorensen et al. 1997).

In contrast, some recent studies suggest that there is no element transfer associated with high P/T metamorphism, even for the fluid-mobile LILEs (e.g. Chalot-Prat et al. 2003; Spandler et al. 2004; Cruciani et al. 2002). Based on the all differences outlined above, this section is divided into four sections.

2.6.1.2.1 EVIDENCE FOR LILE REMOVAL FROM META-MAFIC ROCKS

Arculus et al. (1999) analysed pelitic and mafic rocks metamorphosed to a peak of 1.3-2 GPa (equivalent to ~45-60km depth) and $\leq$ 600°C. Meta-basaltic eclogites revealed loss of Rb, Ba and Sr of between 50-80% compared with estimates of E-MORB and OIB by Sun and McDonough (1989). Similarly, Becker et al. (2000) showed that 95-98% of K, Rb and Ba are lost compared with Nb and Th, and that U and Pb are also lost, although to a much lesser extent. Although ostensibly showing the existence of extensive LILE depletion resulting from subduction zone metamorphism, the results of Arculus et al. (1999) and Becker et al. (2000) may not be as conclusive as they seem. In both cases, the composition of protoliths has not been rigorously estimated, and so quantitative results may not be valid (Spandler et al. 2004).

2.6.1.2.2 EVIDENCE FOR LREE REMOVAL FROM META-MAFIC ROCKS

The results from John et al. (2004) may also point to the presence of a subduction zone geochemical signature in eclogites. This case however differs from the previous two studies in that the elements affected are not principally LILEs, but Light Rare

Earth Elements (LREE, i.e. La-Sm), U and (possibly) Th (although LILE are depleted in some eclogites). John et al. (2004) compared the composition of gabbroic eclogites with partially metamorphosed and non-metamorphosed co-magmatic gabbros. The eclogites, which are thought to have metamorphosed up to 2.6-2.8 GPa and 630°C - 690°C, display a distinct depletion of LREE relative to HFSE. According to John et al. (2004), the LREE were decoupled from HFSE and HREE, a feature not explicable by igneous fractionation processes. Thus fluids must have decoupled the LREE from HFSE during metamorphism (in particular, during eclogitisation).

There are three reasons why the results of John et al. (2004) are potentially very important:

1) implications for explaining implicit VAB geochemistry;
2) implications for recycling models explaining OIB petrogenesis;
3) implications for other studies of the geochemical effects of subduction zone metamorphism (including this work).

At the time of writing this thesis, the work of John et al. (2004) was newly published, and so there was no appraisal of their findings in the literature. Consequently, it proved necessary to confirm the conclusions of John et al. (2004) in this work. In Chapter 7 the data from John et al. (2004) are re-evaluated, and show that a central pillar of their hypothesis may be incorrect. In Chapter 7 I demonstrate that, although the LREE are depleted relative to HFSE on N-MORB normalised multi-element diagrams, the LREE are not *decoupled* (in the sense of not correlating) from HFSE. The principal implication of this is that the magmatic relationship between such elements (i.e. their behaviour as controlled by their compatibility) is preserved in the eclogites. Thus there is no need to invoke metasomatic alteration by fluids.

Furthermore, similar signatures to those observed in the gabbroic eclogites are also identified in blueschists from Tian Shan and Qilian Shan (this study), and so it is not necessary that such characteristics develop during eclogitisation. Most importantly, however, similar bulk-rock chemical characteristics have been observed in fresh gabbros and dolerites from the Oman ophiolite, recently analysed by Lilley et al. (in prep). Preliminary laser ablation analysis of these rocks has also revealed similar chemical characteristics in igneous amphibole. An alternative explanation for the

chemical characteristics of the eclogitic gabbros of John et al. (2004) is that the protoliths were similar to the Oman gabbros. If this is correct, the protoliths of the gabbroic eclogites developed their bulk rock chemical characteristics by accumulation of amphibole a distinctive LREE-depleted composition.

2.6.1.2.3 EVIDENCE FOR LILE ADDITION TO META-MAFIC ROCKS

Sorensen et al. (1997) investigated whole-rock and phengite geochemistry of low-T eclogite and related rocks from mélange of two subduction zone complexes. These rocks had been metasomatised, as manifest chemically by distinct LILE enrichment relative to the otherwise MORB-like REE and HFSE compositions. This LILE enrichment was hosted by phengitic mica, thought to have crystallised from a fluid that equilibrated with meta-sedimentary rocks (and hence became relatively LILE-enriched). Models, based on the LILE composition of phengite, indicate that 1-40 wt% of phengite added to MORB can produce the observed LILE enrichment of bulk-rock geochemistry (Sorensen et al. 1997).

2.6.1.2.4 EVIDENCE FOR NO ELEMENT LOSS IN META-MAFIC ROCKS

Three recent papers provide significant evidence that there is no chemical differentiation resulting from high P/T metamorphism. Chalot-Prat et al. (2002) analysed eclogitic rocks metamorphosed at up to 1.3 GPa from the Western Alps. Based on the trace element patterns of these rocks, Chalot-Prat et al. (2002) conclude that no significant element transfer, and no Sr and Nd isotope exchange, took place during metamorphism. Spandler et al. (2004), who analysed rocks metamorphosed up to 1.9 GPa, arrived at the same conclusion. Interestingly, the study by Spandler et al. (2004) is unique in that non-metamorphosed equivalents of the meta-basaltic rocks also exist in the field location. Thus Spandler et al. (2004) were able to avoid problems associated with unknown protolith compositions discussed above. Similar conclusions on element mobility were made by Cruciani et al. (2002) who analysed meta-mafic rocks metamorphosed to amphibolite facies from NE Sardinia, Italy. High concentrations of LILE elements and Th exist in these rocks, implying that they were not removed during metamorphism.

Although not as comprehensive as those above, and in some cases not explicitly looking for metamorphic geochemical signatures, four other investigations have provided evidence that high P/T metamorphism of meta-mafic rocks does not result in a distinctive geochemical signature. Relatively dehydrated meta-basaltic amphibolites analysed by Bebout (1995) exhibit major element, trace element and isotopic signatures indistinguishable from those of altered seafloor basalts. Similar results are also shown by Kullerud et al. (1990) who, although identifying post-magmatic element mobility, do not identify trace element mass loss. Similarly, meta-basaltic blueschists and eclogites from the Fan-Karategin blueschist belt, Tajikistan, and the western Tian Shan blueschist belt, NW China do not show evidence for a subduction zone signature in the context outlined in section 2.1 (e.g. Volkova and Budanov 1999; Gao and Klemd 2003).

During the 1980's and up to 1996, the mobility of REE was actively debated (e.g. see Shatsky et al. 1990). The general consensus based on evidence from metamorphic rocks was that the REE were immobile, although study by Griffin and Bruekner (1985) argued against this (Shatsky et al. 1990 and references therein). Shatsky et al. (1990) analysed the REE content of mafic eclogites (which have experienced various degrees of amphibolite facies overprints) from a number of locations: Kokhchetav Massif (northern Kazackstan), the Atbashi range (southern Tian Shan, Kirgizia), and Koralpe (Autrian Alps). From these rocks, Shatsky et al. (1990) conclude that the REE are essentially immobile during metamorphism, with 30-60% of the LREE being stored in intergranular spaces.

In a similar study, Tribuzio et al. (1996) examined the REE content of eclogitic and blueschist Fe-gabbros from Ligurian metaophiolite, NW Italy, metamorphosed at 2GPa and ~500°C. By comparing the distribution of REE in metamorphic minerals to their distribution in fresh gabbros, and by using mass balance calculations, Tribuzio et al. (1996) obtained similar results to Shatsky et al. (1990). The REE remained essentially immobile during high P/T metamorphism; however, they argued that minor phases, not intergranular spaces, were the sinks for LREE.

2.6.1.3 SUMMARY

From the work above it is clear that there is no consensus on the geochemical effects of subduction zone metamorphism. Perhaps the principal difficulty with identifying a distinct signature is the chemical variation in the protolith (e.g. Spandler et al. 2003, 2004). Unless the composition of the protolith is rigorously determined, erroneous estimates of chemical modification will always result. For an example of some of the mistakes that can be made by not fully appreciating the possible protolith chemical variation, see the comment and reply papers of Liebscher (2004) and Spandler et al. (2004).

Interpretation of LILE systematics is most seriously affected by variations in the protolith, as these elements are highly susceptible to mobilisation during pre-subduction metasomatism (e.g. Staudigel et al. 1996; Staudigel 2004). Such elements can be removed or added depending on the type of alteration a body of rock has been subjected to (i.e. different temperatures, fluid:rock ratios, compositions of the metasomatic fluid). As the type of pre-subduction alteration cannot be independently predicted (i.e. independent of the geochemistry of metamorphic rocks), it is not reliable to conclude that the LILE composition of high P/T rocks result solely from metamorphism.

2.7 FLUID COMPOSITION: MEASUREMENT OF ACTUAL SUBDUCTION FLUIDS

Fluids are generally thought to be the principal mobile phase transporting elements from the subducting oceanic lithosphere to mantle wedge. Despite their importance for the genesis of VAB, little is known about the actual fluids that pass from subducting lithosphere to mantle wedge (Manning 2004). Perhaps the largest barrier to our knowledge of these fluids is the fact it is not possible to directly sample fluids produced at high pressures and great depths. Methods for predicting the composition of fluids include inverse modelling from the composition of VAB and experimentation. However, the former method can only reveal part of the fluid flow system, while the latter has proven to be extremely difficult, due to the high P and T conditions required to reproduce the conditions of high P/T metamorphism (Manning 2004).

Fortunately, there are three different kinds of direct evidence for the likely composition of the fluids: 1) fluid inclusions in high-pressure minerals and veins; 2) the chemistry of high pressure veins; 3) fluid expelled at serpentine-mud volcanoes at convergent margins. A brief introduction to these 3 sources of fluid is provided below.

Fluid inclusions found in high P/T meta-mafic rocks (e.g. Philippot and Selverstone 1991; Scambelluri, 1995; Nelson, 1995; Philippot et al. 1998; Scambelluri et al. 1998; Becker et al. 1999; Gao and Klemd, 2001, and Fu et al. 2001), meta-sedimentary rocks (e.g. Philippot et al. 1995) and meta-ultramafic rocks (Scambelluri et al. 1995, 2001) often preserve information about the chemistry of fluids present during subduction. As well as containing a fluid, fluid inclusions commonly contain a vapour phase and mineral "daughter" phases. As these phases must have originally been dissolved (although some reaction with the host mineral phase can take place), the original fluid composition must have contained the components that now form the daughter minerals.

In addition to fluid inclusions, eclogite facies rocks often contain high pressure veins (Barnicoat and Fry 1986, Becker et al. 1999; Gao and Klemd 2001). These veins are thought to have formed by precipitation of minerals from an aqueous fluid during high P/T metamorphism (e.g. Gao and Klemd 2001). Thus the composition of the vein should reflect that of the fluid, allowing for constraints to be placed on the composition of fluids during high P/T metamorphism.

Another source of evidence for the composition of subduction zone fluids comes from hydrothermal vents and serpentine-mud volcanoes at convergent margins. These features are often supplied with fluids from the subduction zone (although the fluid is generally thought to originate from relatively shallow depths), allowing for fluids thought to be associated with HP/LT metamorphism to be sampled. It is noted, however, that it is not possible to predict with what material the fluid expelled at mud volcanoes last equilibrated. It therefore follows that the assumption that the composition of such fluids is representative of dehydration fluids may not be strictly valid.

2.7.1 FLUID INCLUSIONS

Fluid contained in fluid inclusions can be considered as rough analogues of the actual fluid produced during a dehydration event (although some modification takes place, e.g. P-T estimates from fluid inclusions rarely match those from minerals (Fu et al. 2002)). Unfortunately, fluid inclusion studies have not provided comprehensive trace element data for subduction zone fluids. The focus of fluid inclusion studies has been on salinity, P-T estimation and the daughter crystal phase assemblage (i.e. what minerals have precipitated in the fluid inclusion). These studies have revealed a fundamental difference between the composition of fluid inclusions found in B-type HP-LT rocks (formed by oceanic lithosphere subduction) and those found in A-type HP-LT rocks (formed by continent-continent collision) (Gao and Klemd 2001; Manning 2004). Fluids trapped during oceanic subduction are commonly low salinity aqueous fluids (Giaramita and Sorensen 1994; El-Shazly and Sisson 1999; Gao and Klemd 2001), whereas fluids trapped during continent-continent collision are generally of high salinity (Scambelluri et al. 1998; Svensen et al. 1998; Xiao et al. 2000). In addition to these differences, two general types of fluid inclusions can be discerned: inclusions associated with rock forming minerals, and inclusions associated with high pressure veins.

2.7.1.1 FLUID INCLUSIONS IN ROCK FORMING MINERALS

Primary fluid inclusions in rock-forming minerals, such as garnet and omphacite, of high P/T rocks are relatively rare. These fluid inclusions are thought to be composed of fluids either released during replacement of precursor minerals, or remnants of fluid expelled during previous dehydration (Philippot and Scambelluri 1996; Scambelluri and Philippot 2001). In general, rock-forming mineral-hosted fluid inclusions are low salinity aqueous fluids + CO_2 vapour. However, relatively high salinity fluids of 17-21 and 32-45 wt% have been recorded in Monviso and Rocciavre eclogites (Scambelluri and Philippot 2001). Other highly saline inclusions in eclogites from Norway contain up to 18 solid phases, some of which are Pb-bearing (Svensen et al. 1999).

2.7.1.2 FLUID INCLUSIONS IN HIGH PRESSURE VEINS

Fluid inclusions in minerals of high pressure veins are the most abundant types of fluid inclusion (Scambelluri and Philippot 2001). Fluid inclusions in high pressure

veins are generally associated with eclogites, providing evidence that fluids are ubiquitous during eclogitisation of slab components, i.e. the sedimentary, mafic and ultramafic "layers" (Philippot and Selverstone, 1991; Becker et al. 1999; Gao and Klemd 2001; Scambelluri and Philippot 2001). It is also noteworthy that high-pressure veins are often not associated with blueschists, indicating that free fluid is more abundant in the eclogite facies (Gao and Klemd 2001).

Fluid inclusions in veins associated with A-type mafic and ultramafic eclogites of the Alps are relatively saline, with salt concentrations up to 50 wt%. These inclusions also contain many solid phases, such as: calcite + dolomite + anhydrite + barite + rutile + sphene + baddeleyite + monzanite + Fe-oxides (Philippot and Selverstone 1991); carbonates + Fe-Ti oxides + rutile + apatite + mica + zoisite + Ca-sulphates + kyanite + omphacite + glaucophane ± quartz ± ilmenite ± magnetite (Selverstone et al. 1992; Scambelluri et al. 1997, 1998). Philippot and Selverstone, (1991) argue that the presence of Ti-bearing daughter minerals is strong evidence that HFSE can be mobilised during subduction zone metamorphism in the presence of highly saline fluids.

In contrast to the highly saline fluid inclusions discussed above, Gao and Klemd (2001) found low salinity ± solid-bearing fluid inclusions in B-type eclogites of the Chinese Tian Shan mountains. These primary fluid inclusions were found in high pressure veins thought to have formed as a result of dehydration during the eclogite-blueschist transition. Similarly, Giaramita and Sorensen (1994) identified low salinity (1.2-5.3 wt% NaCl equivalent) fluid in inclusions from B-type eclogites of the Domincan Republic and California, USA. It is also noteworthy that, in contrast to the inclusions found in A-type eclogites, the inclusions from B-type eclogites do not contain high proportions of daughter crystals. This indicates that fluids, prior to being trapped in inclusions, contain more dissolved solids in the A-type regimes than in B-type regimes.

The difference between the fluid composition of inclusions of A- and B-type eclogites is likely to reflect first order differences in fluid-flow regimes (Giarimita and Sorensen 1994). An obvious difference between the two regimes is whether the fluid

is derived from external sources, or internally as a result of dehydration. To determine the source, methods comparing the oxygen-isotope between fluid (or veins) and host rock can be used (e.g. Gao and Klemd 2001). It is beyond the scope of this work to review these findings, but it should be noted that cross-comparisons between fluids of A- and B-type eclogites requires caution (Manning 2004).

2.7.2 COMPOSITION OF HIGH PRESSURE VEINS

High pressure veins are important sources of information about fluid compositions, because their constituent minerals are thought to have precipitated from a fluid (Becker et al. 1999). Thus the composition of a high pressure vein is related to the composition of the fluid from which it precipitated. In general, mineral assemblages of high pressure veins are similar to the host rock, including minerals such as phengite, kyanite, quartz, zoisite and clinopyroxene (Scambelluri and Philippot 2001; Becker et al. 1999; Gao and Klemd 2001). This indicates that the fluids were solute-rich (Scambelluri and Philippot 2001). Such fluids could explain the presence of Ti-bearing phases in fluid inclusions, as such solute-rich fluids have similar transport capacity to melts, which can dissolve Ti-phases (e.g. Brenan et al. 1995).

Becker et al. (1999) presented a comprehensive major, isotopic, trace and mineralogical analysis of high pressure veins and eclogitic host rocks collected from Munchberg Gneiss Massif, Germany and Trescolmen, central Alps, Switzerland. In this study it was found that the high pressure veins were rich in kyanite and phengite, indicating that the fluid must have been dominated by SiO_2 and Al_2O_3, compared with components such as FeO, MgO and CaO. Furthermore, similar isotopic compositions between the veins and host rock require an internal source of the fluids.

To determine the trace element composition of the fluid, the compositions of the veins were compared with that of the host rocks. To a first approximation, the trace element patterns of the veins were complementary to the host rocks. The veins were enriched in Cs, Rb, Ba, K and Pb, depleted in Nb, REE, Zr, Ti and neither enriched nor depleted in Sr, Th and U relative to the host rocks. The host rocks were correspondingly depleted in Rb, Ba (but not Cs) and K (although one host rock sample was not depleted in K), and relatively enriched in REE and HFSE.

2.7.3 EVIDENCE FROM FLUIDS EXPELLED AT CONVERGENT MARGINS

Samples of subduction zone fluids are available from fluids expelled at serpentine-mud volcanoes at non-accretionary convergent margins (e.g. Fryer et al. 1999; Mottl et al. 2004). Such fluids are thought to derive from moderate depths below the fore-arc, e.g. 10-15 km (Silver et al. 2000) and are sometimes associated with blueschist fragments (e.g. Yamamoto et al. 1995; Fryer et al 1999). Fluids expelled at non-accretionary margins are especially significant, as their chemistry is not modified by reaction with thick piles of sediments in the accretionary prism, as would happen at accretionary margins (Fryer et al. 1999; Silver et al. 2000). Unfortunately however, analysis of a wide range of elements in these fluids has not been completed, with elements such as Ca, Na, K, Rb, Sr and Si being commonly analysed.

A recent study of five serpentine-mud volcanoes in the Mariana forearc showed that pore water chemistry varies systematically with depth to the slab-mantle interface (Mottl et al. 2004). Close to the trench (where the depth to the slab is minimum), the fluids are enriched in Ca and Sr relative to seawater, whereas carbonate alkalinity, sulphate, Na/Cl ratios, K, Rb and B are all less than that of seawater. With increasing depth to the slab-mantle interface, the above trends become reversed. To explain these trends, Mottl et al. (2004) speculate that B, Cs, K and Rb originate from the top of the slab, and are progressively released as the slab increases in temperature (i.e. as it subducts).

2.7.4 SUMMARY

Previous work investigating the composition of subduction zone fluids is broadly divided between those who consider that elements such as Ti and other HFSE can be mobilised (as evidenced by the presence of rutile in fluid inclusions) and those who do not. The apparent paradox requires further investigation. It is clear that fluid composition is a function of many variables, and can be modified by interaction with melt and rock it travels through the slab (e.g. Scambelluri and Philippot, 2001). The ultimate trace element composition of subduction zone fluids is likely to be determined by the history of the fluid during its circulation in the slab. This, as noted by Scambelluri and Philippot, (2001), is a complex area and has not been investigated thoroughly.

Although data on the trace element composition of fluid inclusions are generally lacking, new spectroscopic methods and ICP-MS techniques are being applied to fluid inclusions in high P/T rocks, mantle wedge xenoliths and arc magmas. The results should give new insights into the initial and final conditions of the fluid processes operating during subduction zone metamorphism (Manning 2004).

2.8 SYNTHESIS

From the range of work outlined above, it is clear that there is much conflicting evidence on the effects of subduction zone metamorphism. Phase petrological studies are useful for our understanding of the mineralogical basis of dehydration and can be used as an end-member constraint for trace element mobilisation. However, these studies remain over-simplified compared with the "real world" as shown by the work of Spandler et al (2004).

Chemical analysis of HP-LT metamorphosed rocks have not yielded consistent results, with some workers finding evidence for loss of LILE and/or LREE, some gain of LILE and some no change at all. Clearly, the range of composition of the protoliths, especially for meta-sedimentary rocks, severely restricts the possibility for identifying small chemical changes. This is especially true as alteration of the protoliths is likely to have happened prior to subduction (e.g. on the ocean floor). In the context of the chemical signature outlined in Section 2.1, it is possible to conclude that the compositions of HP-LT rocks do not show clear evidence of a dehydration chemical signature.

Two possibilities may explain the lack of chemical signatures: 1) HP-LT rocks (especially those metamorphosed to pressures <2.5GPa) may not have become fluid-saturated; 2) trace element partitioning into minerals fractionated the elements liberated, decoupling them from the fluid (e.g. Spandler et al. 2004). With regard to 1) if the protoliths did not undergo pervasive sea-floor alteration prior to metamorphism, the H_2O content may be significantly below that of saturation. It may also be possible that some rocks never became fluid-saturated throughout their HP-LT metamorphic history. For example, Figure 2.3 shows that a lawsonite-bearing meta-basalt can contain 3.8 wt% H_2O at conditions up to ~2.4GPa and <500°C. Such

pressures are above the upper P-limit for B-type subduction zones (Maruyama et al 1996), and so any protoliths with H_2O concentrations <3.8 wt% may not dehydrate even up to the eclogite facies. Obviously this scenario applies to situations where fluid is not introduced from external sources.

Regarding possibility 2), the point is that if minerals are present during dehydration reactions into which element can partition, the rock will retain its protolith geochemistry. Consequently, no residual dehydration signature will develop.

The geochemical analyses of fluids should provide vital evidence for understanding the geochemistry of HP-LT rocks. Unfortunately, there are very few comprehensive chemical analyses. The work carried out on fluids can be broadly divided into those that find evidence for HFSE mobilisation, as evidenced by daughter phases such as rutile, and those that do not find such evidence. However, studies that find large daughter mineral abundance, and evidence for high Total Dissolved Solids (TDS), in subduction zone fluids have analysed inclusions present in A-type rocks. As noted by Manning (2004), there are fundamental differences between inclusions associated with A-type and B-type subduction. As this study is concerned with B-type subduction (as are recycling models in the context of OIB genesis), the evidence from inclusions associated with A-type subduction may not be relevant.

A consistent finding amoung fluid studies is that elements such as Ba, Rb Cs, Na and K (i.e. the fluid-mobile elements) are often dissolved in the fluids. This is consistent with the geochemical behaviour of such elements (hence the term fluid mobile elements). However, because of the lack of geochemical data for the protolith, it is not known whether these elements are enriched in the fluid relative to the host rock.

CHAPTER 3

THE GEOLOGY OF FIELD AREAS

3.1 INTRODUCTION

Blueschist, eclogite and greenschist facies rocks were collected from paleo-subduction zone complexes of two major mountain ranges in NW China (Figure 3.1): Tian Shan, and; Qilian Shan ("shan" translates as mountain). In this Chapter an overview of the geology of the field areas and a summary of previous work carried out on rocks collected from these areas are given.

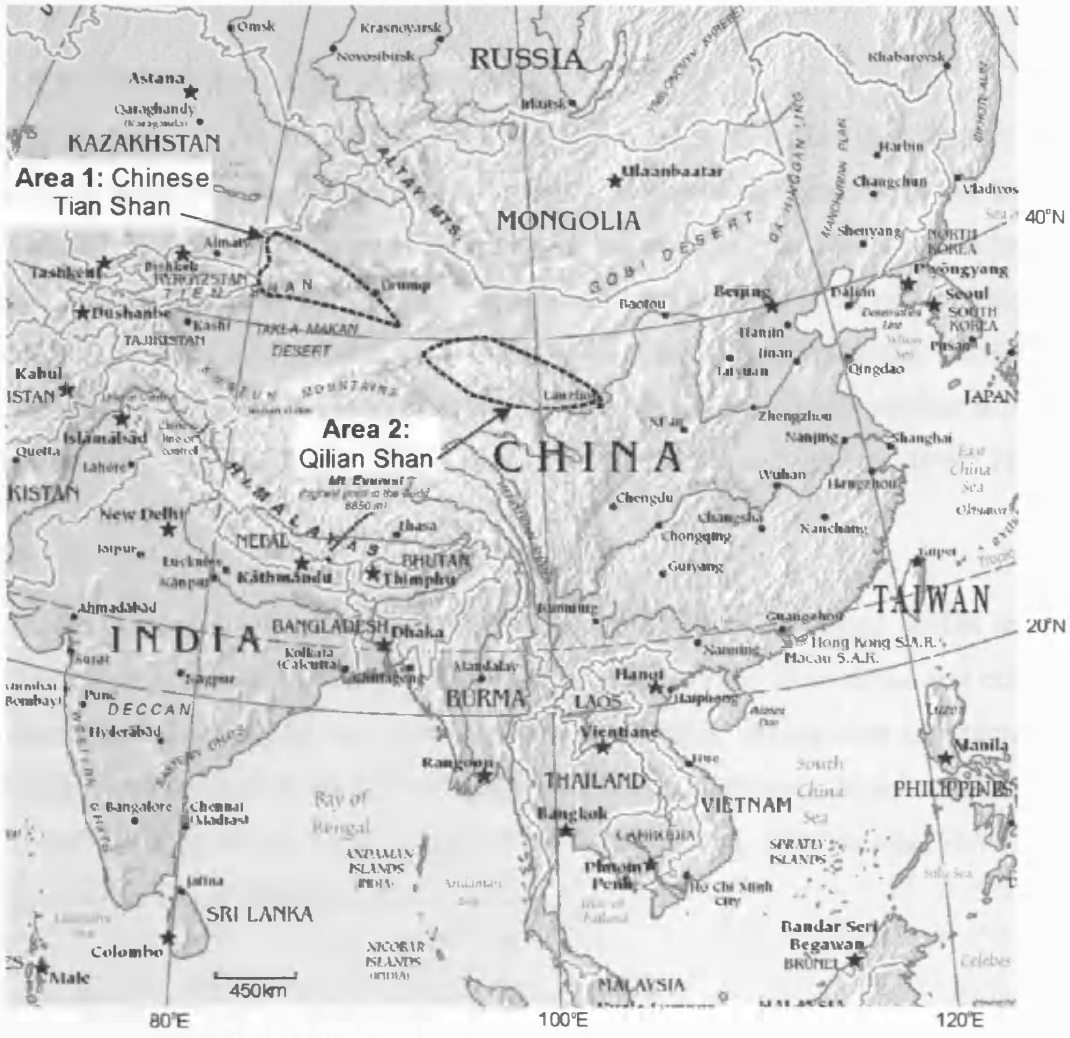


Figure 3.1. Map of the Peoples Republic of China showing the locations of the two field areas (image taken from http://encyclopedia.fablis.com/index.php/China).

3.2 FIELD AREA 1: CHINESE TIAN SHAN

The Tian Shan[1] is a major mountain range of central Asia that extends east-west for about 2500km from Xinjiang, NW China across Kyrgyzstan and into Tajikistan (Sobolev et al 1986; Gao et al. 1995; Volkova and Budanov 1999). The Chinese Tian Shan (which forms part of the eastern tip of the Tian Shan) is an eastward-pointing wedge-shaped block defined by two major faults, the Southern Central Tian Shan suture (SCTS) and Northern Central Tian Shan suture (NCTS) (Windley et al. 1990; Allen et al. 1992). As shown in Figures 3.1 and 3.2a, the Chinese Tian Shan extends from the China-Kazakhstan border until the two faults converge about 1500km to the east (Allen et al. 1992; Gao et al. 1998, 1999). The Chinese Tian Shan separates two microcontinental blocks, known as the Junggar craton (to the north) and the Tarim craton (to the south). A microplate, known as the Yilli-central Tian Shan Plate (YCTP) intervenes between these two blocks (see Figures 3.2a and 3.3).

3.2.1 WESTERN TIAN SHAN HP-LT BELT

The collision of the Tarim plate and YCTP formed a blueschist belt known as the western (or Chinese) Tian Shan HP-LT belt. As shown in Figure 3.3a this lozenge-shaped belt extends for at least 200km along the strike of the SCTS, and is bounded by ductile shear zones and brittle reverse or strike-slip faults (Gao et al. 1998). The belt may also correlate with belts located westwards in Kazakhstan (such as the Atbashy eclogite-bearing blueschist belt), and the Fan-Karategin blueschist belt of the south Tian Shan, Tajikistan (Tagiri et al. 1995; Volkova & Budanov, 1999; Zhang et al. 2002a,b).

The discontinuous Western Tian Shan blueschist belt is contained within an early Palaeozoic accretionary wedge, composed of greenschists, blueschists and eclogites, dismembered ophiolitic slices and Late Silurian marbles. Blueschists and intercalated eclogites crop out as small discrete pods (15-25 cm in diameter), boudins (0.2-0.5 to 5 x 20m^2) thin layers (2-50cm in size) or massive blocks (~2km^2 in plan view) within greenschist facies country rocks.

[1] Tian Shan is also spelt Tien Shan, Tienshan and Tianshan.

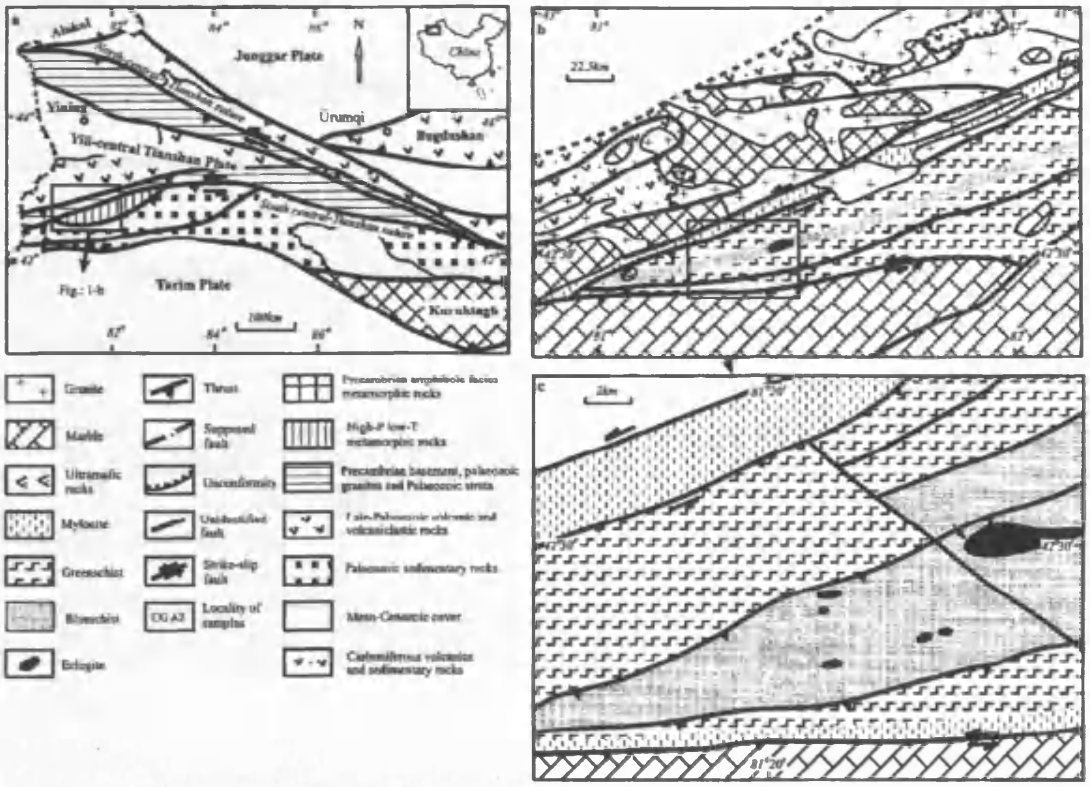


Figure 3.2. Locations and simplified geology of the western Tian Shan HP-LT belt (after Gao et al. 1999).

3.2.2 GEOLOGICAL EVOLUTION OF THE CHINESE TIAN SHAN

As shown in Figure 3.3, formation of Tian Shan, (as well as adjacent regions including parts of the Siberian, Tarim and Kazakhstan-Yilli plates) took place throughout the Palaeozoic (Burrett, 1974: Burtman, 1975: Colemen, 1989: Caroll et al. 1990, Gao et al. 1997, 1998). During the Late Cambrian-Middle Ordovician an ocean, known as the Paleo-Junggar ocean, was subducting southwards beneath the combined YCTP and Tarim plates. Subduction of the Paleo-Junggar ocean continued until early Silurian times, during which the southern regions of the YCTP began to extend and rift, forming the Paleo-South Tian Shan ocean (PSO). During the late Silurian/Early-Carboniferous the PSO, which now separated the YCTP and Tarim plates, subducted under the south margin of the YCTP, forming a continental volcanic arc. Collision between the Tarim plate and YCTP took place during the Early Carboniferous and produced island-arc volcanics, intrusives and HP-LT rocks now exposed along the SCTS. The fate of the Paleo-Junggar ocean is less well understood. Subduction is thought to have waxed and waned until Late Devonian times, when there is strong evidence that it subducted under the YCTP, e.g. extensive Early

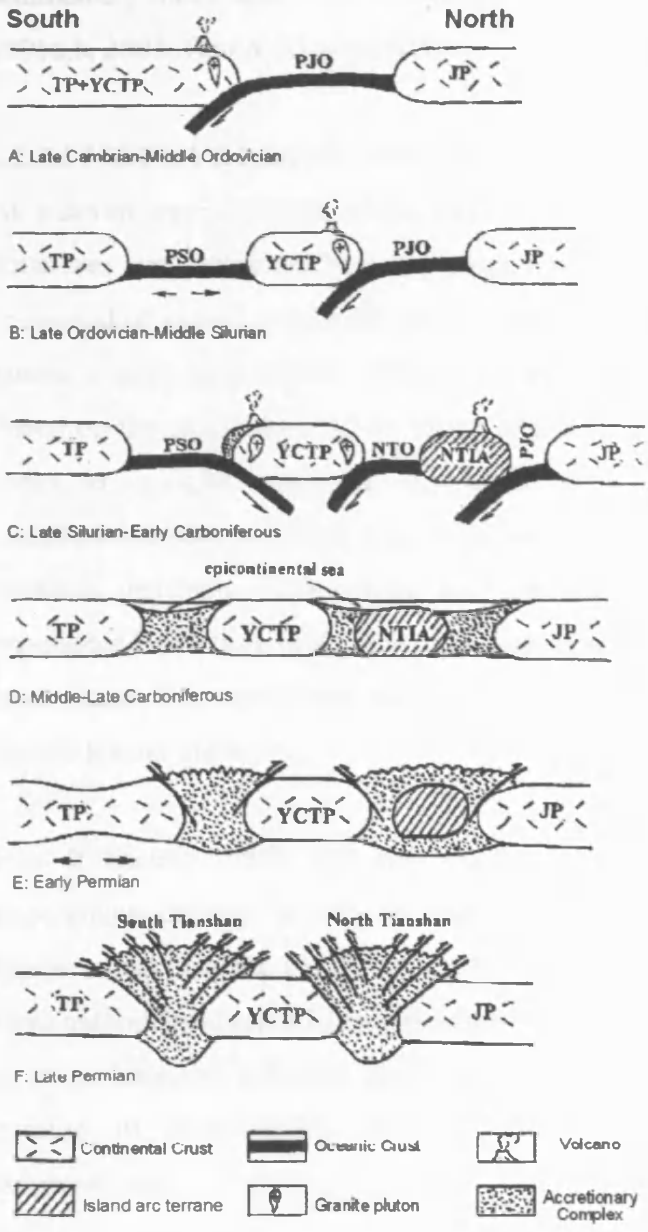


Figure 3.3 Model for the Palaeozoic tectonic evolution of the Chinese Tian Shan and adjacent regions, modified after Gao et al. (1998). Abbreviations: TP = Tarim Plate; YCTP = Yilli-central Tian Shan Plate; JP = Junggar Plate; PJO = Paleo-Junggar Ocean; PSO = Paleo-South Tian Shan Ocean; NTO = North Tian Shan back-arc basin NTIA = North Tian Shan Island arc.

Carboniferous volcanic-arc related rocks exposed along the north Tian Shan active margin (Allen, et al. 1992). An island-arc (the North Tian Shan Arc) and back-arc basin developed in response to this subduction. Subduction of the back-arc basin under the YCTP resulted in collision between the arc and YCTP towards the end of the Early Carboniferous (Xiao et al. 1992; Gao et al. 1998, 1999). Consumption of the Paleo-Junggar basin was contemporaneous with this collision. The Junggar, Tarim and YCTP were then all accreted to Eurasia during the Middle Carboniferous.

3.2.3 PETROLOGY OF THE BLUESCHIST BELT

Four broad types of HP-LT metamorphic rock can be found in the western Tian Shan blueschist belt: 1) meta-volcanic rocks, 2) meta-volcanoclastic rocks; 3) clastic meta-

sedimentary rocks, and 4) marbles (e.g. Gao et al. 1995; Gao et al. 1999; Zhang et al. 2001a,b, 2003; Gao & Klemd 2003).

3.2.3.1 META-VOLCANIC ROCKS

At outcrop meta-volcanic rocks principally occur as massive layers, but pillow structures are occasionally well preserved. Meta-volcanic rocks are typically composed of garnet, omphacite, zoisite, epidote, phengite, paragonite, Na-amphibole, quartz, titanite and rutile in different modal proportions (e.g. Gao & Klemd, 2003). Based on the proportions of the above minerals, Gao & Klemd (2003) classified the rocks as eclogite, epidosite, omphacite and blueschist, although many other classification schemes have also been proposed (see Chapter 5 for more details). Contacts between these rocks are gradual, indicating that these lithologies experienced identical peak P-T conditions (Gao et al. 1999) and that the different assemblages may result from the protoliths being of differing bulk compositions (e.g. Gao & Klemd 2003).

Gao & Klemd (2003) and Gao et al. (1993, 1995) have reported whole rock geochemical data of the meta-volcanic rocks. Volkova & Budanov (1999) analysed similar rocks from the Fan-Kerategin belt, of the southern Tian Shan, Tajikistan. All these authors used series of tectonic discrimination diagrams to show that the majority of blueschists and eclogites have meta-basaltic E-MORB compositions. A smaller number of meta-basaltic samples have N-MORB and OIB trace element compositions.

On the basis of "strong correlations" on Zr-Ti-Nb tectonic discrimination diagrams Gao & Klemd (2003) propose that the N-MORB, E-MORB and OIB rocks had a common igneous origin, or "a single geochemical source," Gao & Klemd (2003). A suitable tectonic setting for such a source would be a seamount close to an active spreading centre; a modern equivalent may be the seamounts of the east Pacific Rise, perhaps similar to those investigated by Niu & Batiza (1997) and Niu et al. 2002).

The notion that the western Tian Shan Blueschist Belt extends to the Fan-Kerategin, blueschist belt of Tajikistan, is supported by the occurrence of meta-volcanic blueschists with similar compositions to those of the western Tian Shan. Variably-

enriched REE patterns and evidence from discrimination diagrams, allowed Volkova & Budanov, (1999) to distinguish two kinds of blueschist: 1) a blueschist with an alkali basalt protolith, and; 2) tholeiitic meta-basalts. Alkali meta-basalts are chemically similar to OIB whereas the tholeiitic meta-basalts are akin to E-MORB. As with Gao et al. (1999, 2003) Volkova & Budanov (1999) conclude that both these lithologies were formed as a result of seamount volcanism close to a spreading centre.

3.2.3.2 META-VOLCANOCLASTIC ROCKS

Meta-volcanoclastic rocks either form the bulk of the country rock in which eclogitic bodies outcrop, or as blueschist layers (e.g. Gao and Klemd 2003). Geochemically the meta-volcanoclastics are similar to the meta-volcanic rocks of OIB and E-MORB affinity. This indicates that the original volcanoclastic sediment was derived from the protoliths of the meta-volcanic rocks.

3.2.3.3 CLASTIC META-SEDIMENTARY ROCKS AND MARBLES

Clastic meta-sedimentary rocks include omphacite-bearing quartz mica schist, relatively pure quartzites (up to 85% vol quartz), and chlorite-mica-quartz schists with glaucophane relicts. Such rocks crop out with meta-volcanoclastic rocks and marbles, indicating that the meta-sedimentary rocks were subducted as a coherent unit. Carbonate rich rocks include impure marbles, pure marbles and banded marbles, the latter with bands of almost pure carbonate and pelitic bands.

3.2.4 P –T EVOLUTION OF TIAN SHAN BLUESCHISTS AND ECLOGITES

3.2.4.1 PEAK P-T CONDITIONS

The determination of the peak pressure-temperature conditions that affected the western Tian Shan blueschist belt has recently received considerable attention (e.g. Gao et al. 1995, 1999; Klemd et al. 2002; Klemd 2003; Wei et al. 2003; Zhang et al. 2002a, 2002b, 2003) and is highly controversial (see Table 3.1, for a summary of the findings to date). The controversy centres on whether the rocks underwent ultra-high-pressure metamorphism (UHPM). Some authors claim peak pressures up to 5.07 GPa, equivalent of depths of >150km (Zhang et al. 2003), whilst other suggest pressures of ~ 2.0GPa, which is equivalent to ~60km depth (e.g. Gao and Klemd 2003).

AUTHOR	DETAILS OF METAMORPHIC STAGES.
Gao et al. (1999)	**Prograde** 1. Pre-peak lawsonite-blueschist facies metamorphism 2. Epidote blueschist facies metamorphism: 347-451°C at 1.2GPa 3. Peak eclogite facies: 530 ± 50°C and 1.4-2.1 GPa **Retrograde** 4. Retrogression back through epidote-blueschist facies 5. Final retrogressive stage through the greenschist facies
Klemd et al. (2002)	**Prograde** 1. Pre-peak lawsonite-blueschist facies metamorphism 2. Transition into epidote-blueschist facies conditions 3. Peak eclogite facies conditions: 490-570 °C 1.8 - 2.1GPa **Retrograde** 4. Epidote-blueschist facies conditions 5. Near isothermal decompression into the epidote-amphibolite facies: 470-570 °C and 0.8-1.4 GPa
Zhang et al . (2002a)	1. Pre-peak eclogite facies 356-443°C and 8-1.0GPa 2. Peak UHPM eclogite facies: 496-598°C P>2.5GPa 3. Near isothermal decompression passing through the epidote-blueschist facies.
Zhang et al. (2002b)	1. Peak eclogite metamorphism: 525-607 °C and 2.7-2.8GPa 2. Other stages are the same as for Zhang et al. (2002a)
Zhang et al. (2003)	1. Peak metamorphism at 560-600°C and 4.95-5.07 GPa 2. Retrograde blueschist facies overprint
Wei et al. (2003)	3. Peak prograde metamorphism took place at 550-580°C at 1.6-1.9 GPa 4. Post peak pressures, temperatures increased leading to conditions of 610-630°C at 1.7-1.8GPa.

Table 3.1 Summary of the findings of previous work investigating the P-T and PTt paths of the western Chinese Tian Shan HP-LT metamorphosed rocks.

High P/T rocks without evidence for UHPM were described by Gao et al. (1995,1999), Klemd et al. (2003), Wei et al. (2003) and Gao & Klemd (2003). The controversy over the existence of evidence for UHPM started in 2002 when Zhang et al. (2002a, b) published two papers reporting evidence for UHPM. Interestingly, the papers of Zhang et al. (2003a, b) neglected to comment on the previous findings, and "comment" and "reply" papers were soon published in *American Mineralogist* in 2003, (i.e. Klemd 2003; Zhang et al. 2003).

As noted by to Klemd et al. (2003), the conclusion of Zhang et al (2002a,b) that all western Tian Shan eclogite experienced UHPM is based on three key features: (1) radial cracks surrounding mono- or polycrystalline quartz grains in garnet, resulting from dilation associated with the coesite-quartz transition; (2) quartz exsolution lamellae in omphacite; (3) magnesite inclusions in dolomite and glaucophane. Thus the controversy is over the existence (or not) of UHP "markers" such as index minerals (e.g. microdiamond, magnesite and coesite) and exsolution lamellae in omphacite. A summary of the arguments for and against UHPM is given in Table 3.2).

ISSUE	COMMENT (Klemd 2003)	REPLY (Zhang et al. 2003)
The former existence of coesite	Although polycrystaline and mosaic-textured, the quartz inclusions of (Zhang et al. 2003a) do not have the characteristic texture of palisade quartz surrounding polycrystalline quartz (± coesite relicts) indicative coesite phase change. Therefore, the inclusions surrounded by radial cracks described by Zhang et al (2002a) do not necessarily indicate UHP conditions. Other mechanisms, such as dilation of quartz, without phase change, may explain the radial fractures.	The polycrystaline quartz inclusion in garnet from some rocks of the western Tian Shan ARE surrounded by palisade quartz. Consequently, the textures of the quartz inclusions are characteristic of coesite decomposition, and hence UHPM conditions.
Quartz exsolution lamellae in omphacite	Two issues are here raised: i) similar features to the quartz exsolution lamellae described by Zhang et al. (2002a) are re-interpreted as tubular fluid inclusions; ii) the conditions for the exsolution of quartz in clinopyroxene are disputed and so cannot be used as a geobarometer. Furthermore, quartz exsolution has been reported for non UHPM granulites.	i) Laser-raman spectroscopy and microscopic investigations of omphacites do show that they contain quartz exsolution lamellae. ii) other workers have shown the usefulness of quartz exsolution as a useful barometer.
Magnesite inclusions in dolomite	Three issues are here raised: i) textural evidence from the rocks examined do not support the order of reaction necessitated by the reaction to form magnesite proposed by Zhang et al. (2003b). ii) phase equlibria calculations performed by Zhang et al. (2002b) neglected to include minerals present in the specimen, and consequently overestimated the pressure conditions; iii) magnesite itself does not imply UHPM as it occurs in non-UHPM eclogites. It has also been shown to form at P ≥ 18kbar (e.g. Poli & Schmidt 2002).	i) textural relationships do support the necessary order of reaction; ii) calculations performed with the observations of Klemd (2003) in mind, but calculated using a value of 607°C, and not 470°C as used by Klemd et al. (2003), gives a P value of ~25kbar; iii) magnesite has been observed in many UHP eclogites and mantle rocks.

Table 3.2. Summary of the three key issues regarding the existence or non-existence of UHPM in the western Tian Shan metamorphic rocks. See Klemd (2003) and Zhang et al. (2003) for a more detailed discussion of these points. It is noted that the reply to the issue of the existence of magnesite at P≥ 18kbar (after Poli & Schmidt 2002) is not discussed by Zhang et al. (2003).

From Table 3.2, it can be seen that the issues raised by Klemd (2003) seem to be countered by Zhang et al. (2003). There are, however, still a number of issues that remain uncertain:

1) **Coesite:** Although Zhang et al. (2002) state that the quartz inclusions do exhibit palisade quartz, their Figure 3 (a photomicrograph of radial cracks in garnet surrounding an inclusion) does not unambiguously show this. Perhaps textural evidence from a larger number of quartz inclusions is required. Although it is possible to form a single grain of quartz from coesite via transitional textures, depending on the extent of retrogression, the existence of coesite relicts still remains a possibility. It may therefore be appropriate to use laser Raman Spectroscopic techniques to unambiguously identify the presence of any coesite relics.

2) The crystallisation of magnesite at lower pressures, as shown by Poli & Schmidt (2002), is not addressed by Zhang et al. (2003).
3) Another important aspect of this controversy, as noted by Klemd (2003), is that Zhang et al. (2003b) assert that all the Tian Shan rocks experienced UHPM. Zhang et al. (2003b) refute this, maintaining that that they only implied some of the rocks have experienced UHPM. However, Zhang et al. (2002a,b) can be read as implying that all HP-LT rocks of Tian Shan are UHP, as their description of the field occurrence of UHPM eclogites is almost identical to that of others describing the occurrence of non-UHPM rocks.

It could simply be that the authors on both sides of the dispute have sampled different rocks. Ultimately, this controversy could be settled by an inter-laboratory examination of the relevant samples by workers on both sides of the argument. It is beyond the scope of this thesis to determine whether the rocks collected by the workers above have or have not undergone UHPM. Rather, the task of thesis is to determine whether the rocks collected *for this work* underwent UHPM. This is undertaken in Chapter 5.

3.2.4.2 PROGRADE METAMORPHIC SEQUENCE

As shown in Table 3.1, much work has been published on the P-T paths taken by the Chinese Tian Shan HP-LT rocks. Consequently, many different models exist that employ a wide range of terminology. Rather than compare and contrast these models, this section summarises the general prograde sequence, which to a first approximation, is common to all models (apart from the peak pressure conditions).

In general, the prograde sequence ranges from the greenschist facies (the country rocks in which the blueschists and eclogites occur) to the eclogite facies. Some of the greenschist facies rocks contain sodic amphibole relicts in albite, indicating that some of these rocks underwent high pressure metamorphism (Gao et al. 1999). The post-greenschist P-T path can be divided into three stages:

1) **Low-T blueschist facies.** Omphacite-bearing blueschists contain box-shaped pseudomorphs of clinozoisite+paragonite+quartz. The standard interpretation of such inclusions is the former existence of lawsonite (Evans, 1990; Gao et al. 1999).

This suggests that the early stages of prograde metamorphism were in the relatively cool lawsonite-blueschist facies.

2) Higher-T blueschist facies metamorphism. The disappearance of lawsonite and appearance of clinozoisite and paragonite (as inclusions in garnet and in the groundmass as porphyroblasts) suggests that temperatures increased, pushing the P-T path from the Lawsonite-Blueschist facies into the Epidote-Blueschist facies. Gao et al. (1999) suggest the following reactions, after Heinrich & Althaus (1988):

$$Jd + 4Lws \rightarrow 2Zo + Pg + Qtz + 6H_2O$$

$$4Lws + Ab \rightarrow 2Zo + Pg + 2\ Qtz + 6H_2O.$$

Geothermobarometric analysis of the zoisite + paragonite inclusions have predicted temperatures of 345-445°C at 10kbar 347-451°C at 12kbar. Pressure estimates, based on the jadeite component of omphacite inclusions, indicate a minimum of between 8 and 12 kbar at 350-450°C Gao et al. (1999).

3) Eclogite facies metamorphism The transition from blueschist facies to the eclogite facies was probably marked by reactions such as Gln + Czo → Gnt + Omp + Pg + Qtz+ H_2O as indicated by features such as prism-shaped aggregates of omphacite, paragonite and quartz pseudomorphing after glaucophane. Peak eclogite conditions are discussed above.

Gao et al. (1999) noted that eclogites occur as intimate intercalations in blueschist layers, indicating that these rocks shared a common P-T path (see also Klemd et al. 2002). It therefore follows that some rocks may have been metamorphosed to eclogite facies conditions, despite their blueschist facies mineral assemblage.

3.2.4.3 RETROGRADE SEQUENCE

Detailed evaluation of the retrograde stage was provided by Klemd et al. (2002). Two stages can be identified:

1) Epidote amphibolite facies. Post eclogite facies, temperatures increased while pressures remained the same, or slightly decreased (i.e. the path approximates

to an isothermal decompression path), moving the rocks into epidote-amphibolite facies. Evidence for this comes from the higher $Fe^{2+}/(Fe^{2+} + Mg)$ composition of garnet rims compared with cores (Klemd et al. 2003). Modelling the mineral assemblages of glaucophane-bearing and hornblende-bearing eclogites also led Wei et al. (2003) to conclude that a temperature increase, coupled with a slight pressure decrease, occurred post eclogite facies.

2) Greenschist facies metamorphism. A final retrograde stage resulted from passing from the epidote-amphibolite facies to the greenschist facies. This stage is likely characterised by hydration reactions such as:

$$\text{Na-amp} + \text{Czo} + \text{Qtz} + H_2O \rightarrow \text{Ab} + \text{Act} + \text{Chl}$$

This reaction was found to take place at 7-8kbar and 350°C – 450°C by Maruyama et al. (1986).

3.2.5 EXHUMATION OF THE BLUESCHIST BELT

On the basis of pressure-temperature-time (P-T) constraints, it was found that the post-peak P-T path of the HP-LT rocks involved an almost isothermal decompression path. Following this, the rocks were subjected to an epidote-amphibolite facies overprint (Klemd et al., 2002; Gao and Klemd 2003), similar to Alpine-tectonic regimes (Ernst 1988). This is in contrast to previous work identifying the P-T path as being a clockwise loop, indicative of Franciscan, or B-type, subduction (e.g. Gao et al. 1999).

Gao and Klemd (2003) propose that the HP-LT rocks were exhumed to moderate crustal levels by a "wedge extrusion" mechanism between 344-331Ma (Figure 3.4B). After being transported to moderate crustal depths, the HP-LT rocks were further exhumed by major thrusts resulting from a later stages of continent-continent collsion (Gao et al. 2000). After 331Ma, the HP-LT rocks were underlain by a major shear zone, which may have exhumed the rocks to even shallower levels, preserving them from greenschist facies overprints.

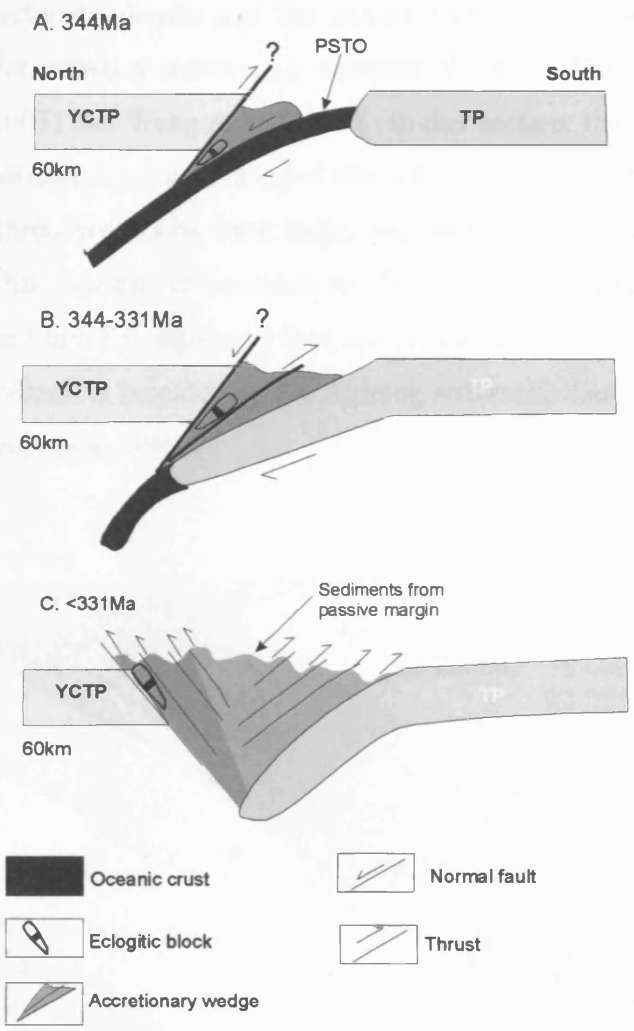


Figure 3.4 A-C. Tectonic model for the exhumation of HP-LT metamorphic rocks in the Chinese Tian Shan (modified after Gao & Klemd 2003). TP = Tarim Plate; YCTP =Yilli-Central Tian Shan Plate; PSTO = Paleo-Tian Shan Ocean.

3.3 AREA 2: NORTH QILIAN SHAN

3.3.1 GEOLOGICAL OVERVIEW

The North Qilian Shan is a SW-NE trending mountain chain, forming part of the Qilian Mountain (or Fold) System situated on the northern margin of the Qinghai-Xizhang (Tibet) Plateau. The Qilian Fold System is itself a subdivision the Caledonian Qinling-Qilian-Kunlun Tectonic belt, (Li et al. 1978 Wu et al. 1993), otherwise known as the Kunlun-Qinling fold system (e.g. Huang et al. 1980; Wu et al. 1993).

Details of the tectonic subunits and the terminology used for describing the Qilian fold system differ between authors e.g. compare Wu et al. (1993) and Song (1996) with Xia et al (2003) and Wang et al. (2005). In this section, the scheme of Wu et al. (1993) is used because they have mapped blueschist belts. The Qilian Fold System is separated from three massifs by three large, deep seated faults (Figure 3.5): 1) to the north, the Alashan Massif is bounded by the Longshou Mountain Fault; 2) the southern Qaidam Massif is separated by a major (nameless) boundary fault; 4) to the east, the Tarim Massif is bounded by the Altintag strike-slip fault (Wu et al. 1993 and references therein; Song 1996).

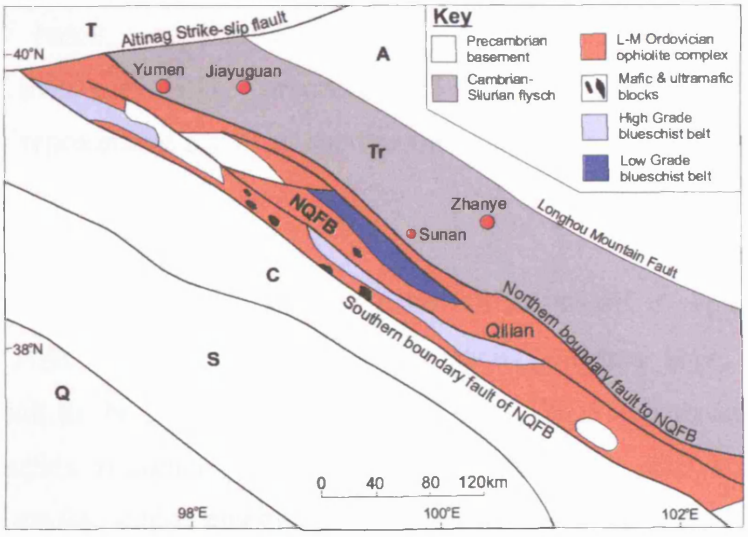


Figure 3.5. Sketch map of the distribution of blueschist belts in the North Qilian Shan, China (simplified after Wu et al. 1993). A, Alashan Massif; T, Tarim Massif; Tr, Transition zone; NQFB, North Qilian Fold Belt; C, Central Qilian Massif; S, South Qilian Fold belt; Q, Qaida Massif.

Huang et al. (1980) divides the Qilian Mountain system into four tectonic subunits (belts), which are also separated by deep-seated faults: 1) Corridor Transition Belt; 2) North Qilian Eugeosynclinal Fold Belt; 3) Qilian Median Rise or Central Qilian Massif; 4) South Qilian Geosynclinal Fold Belt. The following sections are a summary of these subunits after Wu et al. (1993) and Song, (1996).

Corridor transition belt (CTB). Between the Alashan Massif and the North Qilian Fold Belt is an area of the Hexi Corridor known as the Corridor Transition belt (CTB). The CTB is thought to have been the passive margin on the south of the Alashan Massif during the Early Palaeozoic. Evidence for this includes the fact that

most rocks of CTB are sedimentary (indicating stable sedimentary environments), and that the CTB shares the same Precambrian basement as the Alashan Massif.

North Qilian fold belt (NQFB). Located south of the Corridor Transition belt, the North Qilian Fold Belt is separated from the Central Qilian Massif, to the south, by a large fault. Importantly, the NQFB contains two blueschist belts, known as the High-grade and Low-grade blueschist belts, which occur in Middle Cambrian and Lower to Middle Ordovician rocks.

The NQFB consists of a wide range of rock types and associations: 1) ophiolitic sequences, including associated sediments; 2) an island-arc volcanic sequence, consisting of basalt, andesite, dacite and rhyolite; 3) sedimentary sequences, consisting of meta-greywacke, carbonates and peltic rocks. These sequences are interpreted as representing a typical subduction complex (e.g. Wu et al. 1993; Song 1996).

Central Qilian Massif (CQM). The Central Qilian massif is separated from the North Qilian Fold Belt to the north by the southern boundary fault, and the South Qilian Fold Belt to the south by an un-named fault. The Precambrian metamorphic basement complex is similar to that of the Qaidam, Tarim and Alashan Massifs, consisting of gneiss, schist, amphibolite, graphitic marble and migmatites. Zircons from a migmatitic granite of the CQM yield a U-Pb date of 2469Ma, similar to ages obtained for Tarim and Qaidam Massifs respectively (Wang & Chen, 1987). This indicates that the Central, Qiadam and Alashan massifs may have been contemporaneous.

South Qilian Massif (SQM). The South Qilian Massif is situated between the Qaidam Massif, further to the south, and Central Qilian Massif, to the north (Figure 3.5). Greywacke and interlayered crystalline limestone, sandstone, siltstone, shale and basic-acid volcanic rocks, make up the dominant lithologies, with Devonian molasse developed locally. These associations have been interpreted as having formed in an intercontinental basin, which developed during the Ordovician and Silurian. Granitic intrusions during the Caledonian and Indo-Sinian orogenies (Wang

& Chen, 1987) have been interpreted by Xiao et al. (1988) as the remnants of a back-arc basin of the North Qilian Subduction Belt.

3.3.2 TECTONIC EVOLUTION

The tectonic model and geological maps presented by Wu et al. (1993) and Song (1996) have recently been subjected to re-evaluation on the basis of ophiolite and other igneous rock geochemistry (e.g. Xia et al. 2003; Wang et al. 2005). These recent studies have concluded that a back-arc basin must have existed during the evolution of the North Qilian from middle Ordovician to the end of the Ordovician (Figures 3.6 B and C).

Figure 3.7, summarises the tectonic model of Wang et al. (2005) for the time period middle Ordovician-Silurian. Unfortunately, the tectonic subdivision, and hence geological map, of the North Qilian mountains presented by Wang et al. (2005) is very different to that of Wu et al. (1993) and Song (1996), and it is very difficult to cross correlate between maps (e.g. compare Figure 3.5 With 3.6). It is also very difficult to understand their tectonic model in the context of previous geological maps (e.g. the map of Wu et al. (1993) as shown in Figure 3.5). A brief outline of the work of Wang et al. (2005) is therefore given below.

Wang et al. (2005) split the North Qilian Shan into the North China Block, North Qilian Orogenic Belt (NQOB), Central Qilian block and South Qilian Orogenic Belt (Figure 3.6). The North China Block and the Central Qilian Block generally correlate with the Alashan Massif and Central Qilian Massif, respectively (as defined in Figure 3.5).

The NQOB is divided into the Northern Terrane and the Southern Terrane, which are divided by a volcanic rock belt. The Northern Terrane is composed of mafic lavas, pyroclastic rocks, clastic sedimentary rocks, and minor ophiolites thought to have formed in a back arc basin. The Northern terrane is roughly equivalent to the northern margin of the North Qilian Fold Belt and part of the Corridor Transition Zone as defined by Wu et al. (1993). The southern terrane consists of a subduction zone accretionary complex of ophiolites, blueschists, eclogites, phengite schists and

sedimentary rocks. The Southern terrane is roughly equivalent to the southern margin of the North Qilian Fold Belt as defined by Wu et al. (1993).

This volcanic rock belt is composed of mafic and felsic volcanic rocks. The mafic rocks have compositions similar to rocks produced at either mature island arcs, or arcs built on thin continental crust. The calc-alkaline felsic rocks have compositions indicative volcanic arc rocks derived from a depleted mantle. Based on the composition of these volcanic rocks, Wang et al. (2005) conclude that there must have been an island arc separating the Northern and Southern terranes.

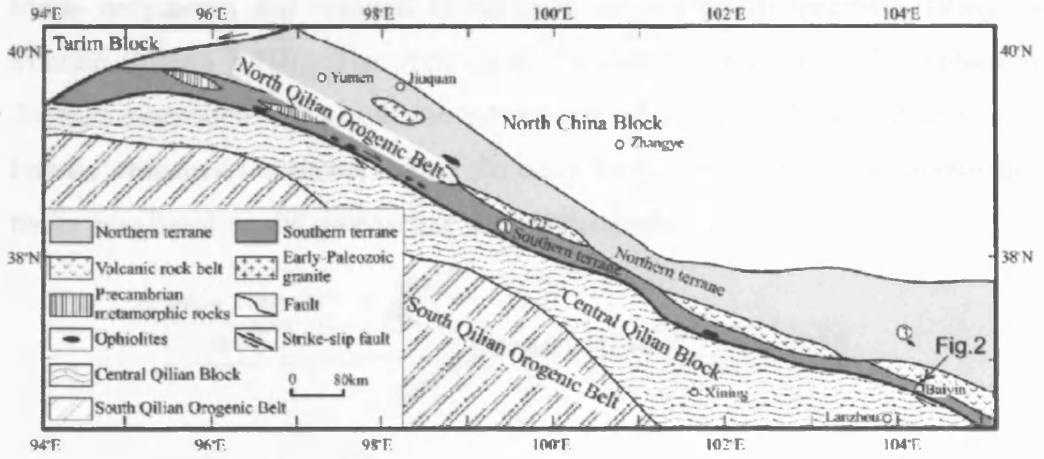


Figure 3.6 Revised geological map of the north Qilian Shan, after Wang et al. (2005). It is very difficult to accurately cross correlate the geology of this map with that of Wu et al. (1993) without further information.

Wang et al. (2005) have developed a tectonic model to explain the Middle Ordovician-Silurian geology of the North Qilian Shan (Figure 3.7 A-D). However, the following model also uses previous work by Wu et al. (1993) and Song (1996) to fill in the pre-middle Ordovician tectonics:

1) The [Late] Precambrian China Platform was undergoing rifting from early to Middle Cambrian times.
2) Continued rifting through to the late Cambrian and early Ordovician produced a small ocean basin.
3) During the Middle Ordovician (Figure 3.7A), the oceanic crust was subducting northwards below what is now the southern margin of the Alashan Massif. This continued into the middle-late Ordovician, producing an ophiolitic melange and

HP-LT metamorphism. Blueschist metamorphism was dated at 460-440Ma by Wu et al. (1993).

4) Continued subduction in the Middle-Late Ordovician (Figure 3.7B) eventually led to rifting and the development of back arc spreading. The rifted Alashan Massif (equivalent to the North China Block) crust developed into an island arc, under which the earlier paleo-ocean continued to subduct (Figure 3.7C).
5) The ocean crust of the back arc basin must also have began to subduct during the mid-late Ordovician. This subduction was to the North below southern margin of what is now the Alashan Massif (Figure 3.7C)
6) Initial orogenesis and residual ocean-basin sedimentation occurred during the Silurian (Figure 3.7D). The thick flysch deposits are thought to be syntectonic deposits associated with a collision between the island-arc and the continent.
7) Intense orogenesis occurred during the early Devonian, where large, deep-seated faults developed, as did greenschist facies retrograde metamorphism.

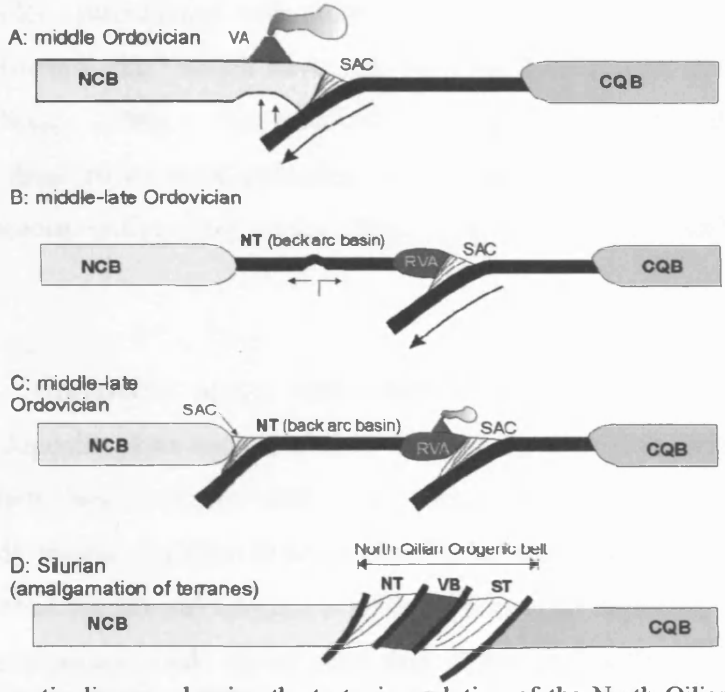


Figure 3.7. Schematic diagram showing the tectonic evolution of the North Qilian Shan during the early Paleozoic (modified after Wang et al. 2005). SAC, Subduction accretionary complex; VA, volcanic arc; RVA, rifted volcanic arc; NT, Northern Terrane; ST, Southern Terrane, VB, volcanic rock belt; NCB, North China block; CQB, Central Qilian Block.

3.3.3 BLUESCHIST BELTS

Qilian Shan contains two early Palaeozoic belts which, on the basis of mineral assemblages, have been classified as High-grade and Low-grade blueschist belts (see

Figure 3.5). In the 1970s, the general geology and petrology of the High-grade blueschist belt were first studied (Xiao et al. 1974, 1978; Wang & Liu, 1981) and later, further studies took place after the discovery of eclogitic blocks in the blueschist belt. The Low-grade blueschist belt was first discovered in 1990 (Wu et al. 1993) as a feature distinct from the High-grade belt.

3.3.3.1 SOUTHERN HIGH GRADE BLUESCHIST BELT

The southern High-grade blueschist belt crops out in Qilian county, Qinghai Province, approximately 40km northwest from Qilian. The high-grade blueschist belt is located in the Changma and Qilian regions of the west-central part of the Qilian mountains, and extends discontinuously for approximately 500km in a NW-SE direction. In the Qilian region, the belt is exposed along the Black and Qilian rivers and extends for 100Km, NE-SW. Thrust faults cut the belt into three slices, A, B and C, which all consist of blueschist facies rocks, eclogite, gabbro and serpentinised and carbonatised ultramafic rocks. Intercalated with these rocks are bimodal volcanic rocks from "a previous continental rift," which have also been subducted with the aforementioned lithologies (Song, 1996). Geochemical investigations have indicated that the protoliths to these rocks were ophiolitic, island-arc volcanic rocks, graywacke and pelitic & siliceous sedimentary rocks, (Xiao et al. 1978; Wu, 1980; Wang & Liu, 1981).

Graywacke. Graywacke occurs with olisthostrome deposits in all three slices, representing deposits of an ancient trench. In slice A, the olistholiths include blocks of marble, chert, basic volcanic rock, acid volcanic rock and serpentinite held in a siliceous sandy matrix. In Slice B limestone blocks, that contain gravitational sliding structures, extend for several kilometres within graywacke deposits. Slice C consists of a turbidite sequence made up of chert and graywacke with numerous silica-rich marble olistholiths (Xu et. al., 1994).

Ophiolites. Ophiolitic sequences occur as blocks of serpentinite, gabbro, pillow lava and ferromagnesian chert, which together with the graywacke and volcanic rocks, constitute an ophiolitic melange. Radiolarian fossils discovered in chert in the Baijingsi area are thought to be of Early Ordovician Age (Wu et. al., 1993), and

indicate that the ophiolitic melange and the subduction complex formed during the early Ordovician.

Eclogites. Eclogites occur as blocks and lenses in all sub units of the high-grade belt. The upper P-T limits of eclogite metamorphism is estimated at 0.8 ±0.1 GPa and 340-410°C, respectively (Wu et al 1993). Wide ranging garnet compositions have led Wu et al. (1993) to conclude that the eclogite is type C according to the classification of Colemen et al. (1965).

High-grade blueschist. High-grade blueschist can be found in all sub units of the high grade subduction complex. Mineral assemblages in such blueschists vary according to the composition of the protolith. In meta-greywacke, assemblages such as glaucophane + phengite + garnet + albite + quartz are common, whereas in mafic volcanic rocks glaucophane + epidote + chlorite + albite phengite assemblages are more common. In highly siliceous rocks, assemblages such as phengite + quartz ± glaucophane ± garnet or chloritoid + phengite + quartz are typical (Song 1996).

3.3.3.2 NORTHERN LOW-GRADE BLUESCHIST BELT

The low-grade blueschist belt trends parallel to the high-grade belt and consists of ophiolitic blocks, greywacke, siliceous slate and low-grade meta-mafic, meta-intermediate and meta-felsic blueschists.

Ophiolite blocks. Ophiolites and including sediments can be found throughout the shallow level subduction complex. Geochemically, the ophiolites are similar to transitional-type MORB (E-MORB), which based on associated fossils in sediments, formed no earlier than the late Ordovician (Song 1996).

Low grade blueschists. Low-grade blueschists occur as a lenticular body (20km long, 1km wide) that trends NE-SW in the general area of Sunan county (Figure 3.5). Based on mineral assemblages, three zones can be recognised: 1) the pumpellyite + glaucophane ± lawsonite zone; 2) the prehnite zone; 3) the chlorite + albite zone. The zones trend parallel to the regional structures, and are defined by late thrust faults which formed imbricate slices (Wu et al. 1993). Metamorphic minerals in sedimentary rocks rarely appear. Based on the composition of glaucophane and

chlorite, Wu et al (1993) estimated peak P-T conditions of 0.4-0.7GPa and 150-250°C.

3.3.3.3 RELATIONSHIP BETWEEN THE BLUESCHIST BELTS

The relationship between the High- and Low-grade blueschist belts remains uncertain, as does the mode of formation. Feng and He (1995), hypothesise that the High-grade blueschist belt formed as a result of ocean crust subduction, while the Low-grade belt is a product of back-arc basin subduction. However, Song (1996) concludes that there is insufficient evidence to deny or confirm this hypothesis. Instead, Song (1996) proposes that the belts originated from the same subduction zone. Supporting evidence for this includes the fact that both belts contain ophiolitic melange, and that blueschists formed around the same time (460-440Ma). Furthermore, Song (1996) hypothesise that as P-T regimes are different in the high and low-grade belt the rocks must have formed at different levels in the same subduction zone. However, recent work, although not explicitly explaining the origin of the high and low-grade blueschist belts, does seem to support the former existence of a back-arc basin (e.g. Xia et al. 2003; Wang et al. 2005), lending credence to the hypotheses of Feng and He (1995).

5.4 FIELD WORK

Samples were collected from the field areas described above during the summer of 2002. Samples collected from Qilian Shan during this time were intended to complement the sample set collected by Yaoling Niu and our Chinese collaborators in 1998. Our sampling method aimed to collect blueschists and eclogites that derived from volcanic and sedimentary protoliths. Fresh samples that showed no, or little, evidence for retrogressive metamorphic overprints were preferentially selected. This was to minimise any geochemical effects brought about by hydration reactions during retrogression. Where possible samples were collected from outcrop, but this was not always possible in the Tian Shan because outcrops are often high in the mountains, where the risks of an accident are high. As a result greenschists, blueschists and eclogites were often collected from boulders at the base of the mountains. Our sampling may be therefore be considered "random," as no outcrop or cohesive blueschist body was systematically sampled.

CHAPTER 4

BULK ROCK GEOCHEMICAL ANALYSIS

4.1 INTRODUCTION

The analysis of geological samples by Inductively Coupled Plasma–Optical Emission Spectroscopy (ICP-OES) and Inductively Coupled Plasma – Mass Spectrometry (ICP-MS) requires that the samples are first dissolved. Consequently, it is fundamentally important that complete dissolution of all mineral phases takes place (e.g. Yu et al. 2001; Meisel et al. 2001; Diegor et al. 2001; Totland et al. 1992, 1995). However, complete sample dissolution by certain routine techniques can be inhibited by the presence of refractory minerals such as rutile and zircon (e.g. Becker et al. 1999, Meisel et al. 2001 and references therein; Münker et al. 2001).

Prior to trace element analysis, it was known that the rocks of the collected sample sets contained refractory phases, including zircon and rutile. It was therefore necessary to carry out further research into the methods available for complete sample dissolution. The following is a summary of the methods used to obtain bulk rock trace element data.

4.2 AIMS

The essential aim of this chapter is to describe the methods used for collecting and assessing the quality of bulk rock geochemical data. To achieve this aim, the following objectives will be met:

1) Carry out a feasibility study to identify dissolution method/s that are both able to dissolve the rocks and be available to this project;
2) Experiment with the different method/s identified by the feasibility study;
3) Develop and optimise the chosen dissolution technique to ensure high quality data;
4) Acquire, and assess the quality of, bulk rock geochemical data.

4.3 FEASIBILITY STUDY OF DISSOLUTION TECHNIQUES FOR TRACE ELEMENT ANALYSIS BY ICP-MS

There are a variety of methods that have been developed to dissolve geological samples for solution analysis by ICP-MS. These include:

1) The "routine" hydrofluoric acid–nitric acid ($HF-HNO_3$) dissolution method, which uses an acid mixture to dissolve samples at relatively low pressures and temperatures (~125°C);
2) the "High Pressure Bomb" method (i.e. reaction vessels capable of withstanding temperatures >150°C and pressures greater than 70bar), used by Becker et al. (2000) and discussed by Diegor et al. (2001) and Yu et al. (2001);
3) Sodium peroxide (Na_2O_2) sintering (e.g. Meisel et al. 2001; Yu et al. 2001);
4) Lithium metaborate ($LiBO_2$) fusion, and, if required, chemical separation (e.g. Ulfbeck et al. 2003; Yu et al. 2001);
5) High temperature microwave-assisted dissolution methods (e.g. Yu et al. 2001).

4.3.1 "ROUTINE" $HF-HNO_3$ DISSOLUTION TECHNIQUE

The $HF-HNO_3$ dissolution method is the routine method used at Cardiff University, and is described in greater detail in APPENDIX 1. The method essentially consists of dissolving samples in a $HF-HNO_3$ mixture at about 125°C in Teflon® vials.

4.3.1.1 ADVANTAGES

Being the routine method at Cardiff University all the equipment and reagents for this method are readily available. The method is tried and tested, and the composition of the reagents is well characterised.

4.3.1.2 DISADVANTAGES

This method will not dissolve refractory phases such as zircon (e.g. Yu et al. 2001).

4.3.2 HIGH PRESSURE BOMBS

The High Pressure Bomb Method works on the principle that sample digestion takes place more efficiently at higher pressures and temperatures. High pressure bombs consist of an outer pressure-resistant (usually) steel vessel that contains an inner

chemically-inert reaction vessel, often composed of PTFE (polytetrafluoethene). Once loaded with the sample and reagents, the bomb is sealed and placed in an oven for heating.

4.3.2.1 ADVANTAGES

This method is known to dissolve refractory phases (Becker et al. 1999; Yu et al. 2001). The reaction vessel is also resistant to strong acids and will not contribute contaminants to the sample. This method uses the same reagents as the routine Hf-HNO_3 method, and so the blank contribution is identical to the routine HF-HNO_3 method.

4.3.2.2 DISADVANTAGES

High pressure bombs can take about 3 days dissolution time per sample (Ulfbeck et al. 2003; H. Becker, perrs. comm.). In order to dissolve the ~80-90 samples, along with blanks, repeats and standards, as well as a period of experimentation, many bombs would be required to keep the whole process time-efficient. This highlights another important disadvantage in that the bombs are very expensive. Furthermore, the bombs would require an oven to be fitted in a fume cupboard, in case of the unlikely event of a bomb becoming ruptured and leaking HF.

4.3.3 SODIUM PEROXIDE SINTERING

As with other alkali salts (e.g. lithium metaborate), sodium peroxide is known to break minerals down during intense heating. The general method for using sodium peroxide is as follows (adapted from Meisel et al. 2001 and Yu et al. 2001).

1) A mixture of Na_2O_2 and sample powder is heated to ~500°C in glassy carbon crucibles for 0.5 hours.
2) When cooled, de-ionised water is added until the vigorous reaction stops.
3) Undissolved hydroxides are removed by centrifugation and dissolved in HCl. The supernatant is decanted into a volumetric flask
4) The solution containing the, now-dissolved, Fe-hydroxides is added to the supernatant and made up to volume.

4.3.3.1 ADVANTAGES

This method is effective at dissolving refractory phases (Meisel et al. 2001; Yu et al. 2001), and does not introduce elements with large memory effects into the ICP-MS instrument. Another advantage is the relatively low cost of the reagent, and the fact that no special equipment is required, other than a furnace, graphite crucibles and a centrifuge (all of which are available to this project).

4.3.3.2 DISADVANTAGES

Disadvantages of this method include the high blank content of the sodium peroxide, as noted by Yu et al. (2001) and apparent from assays given for the compound in a variety of catalogues. Yu et al. (2001) also found that the method could not be used for HFSE, because of high levels of these elements in the procedural blanks. A further disadvantage is the large amount of sample handling that is required to prepare the final solutions, which increases the possibility of contamination. In addition, HCl is used to dissolve the Fe-hydroxides, which could lead to the formation of Cl-complexes and cause molecular interference during analysis by ICP-MS.

4.3.4 LITHIUM METABORATE FUSION

The lithium metaborate fusion method is essentially the same as the preparation method for ICP-OES solutions (see APPENDIX 1, for more details). Lithium metaborate digests sample powders during high temperature fusion to produce a "glass." This glass can then simply be dissolved in dilute nitric acid. This dissolution method has been successfully used to dissolve resistant phases for the isotopic analysis of Hf and Nd (e.g. Ulfbeck et al. 2001) and Hf (e.g. Le Fevre & Pin, 2001).

4.3.4.1 ADVANTAGES

The main advantage of this method is the relatively short time required to prepare and analyse a large number of samples. Accurate, reproducible results can be obtained, providing a pure flux can be found. Furthermore, the reagents are affordable and all the apparatus required is available to this project, as it is used for preparing solutions for major element analysis by ICP-OES.

4.3.4.2 DISADVANTAGES

Disadvantages with this method include the purity of the flux, which has been found to vary from batch to batch (Ulfbeck et al. 2003). Another disadvantage is the high Total Dissolved Solids (TDS) of the prepared solutions. This can give rise to memory effects, and premature furring of the instrument's components with subsequent loss of sensitivity. One further disadvantage is that the presence of relatively high concentrations of boron may favour the formation of complexes, and give rise to molecular interference.

4.3.5 MICROWAVE DIGESTION

Microwave digestion uses the high temperatures that can be produced in microwave ovens to aid the rapid dissolution of samples (the actual temperatures that can be safely used depend on the amount of pressure the reaction vessels can withstand). The method is similar to the routine HF-HNO_3 dissolution, the essential difference being that the reaction vessels are placed in a microwave oven for additional heating.

4.3.5.1 ADVANTAGES

The method requires only the reagents that are used in routine HF-HNO_3 dissolution, and these are well constrained in terms of their blank contribution. Reaction vessels, a microwave and some of the necessary equipment for the microwave, already exist at Cardiff University.

4.3.5.2 DISADVANTAGES

An important disadvantage is that the method must be made safe, as hot HF will be under pressure in the microwave reaction vessels. Ideally, each vessel should have a pressure monitor, which will cause the microwave to stop and alert the user to a vessel breach. Additionally, the microwave should be housed in a fume cupboard so that any gas escape can be made safe.

Another important disadvantage is that, according to Yu et al. (2001), the microwave dissolution method is not suitable for geological materials because refractory minerals do not dissolve. It is noted however that Yu et al. (2001) restricted the dissolution times to <1 hour, and longer dissolution times may be yield better results.

4.4 CHOOSING A METHOD

From the information above, and published work on the geochemistry of eclogites (e.g. Becker et al. 1999), the high pressure bomb method should be the most suitable method for dissolution of the samples. This is mainly due to two factors: 1) low blank contributions compared with alkali salt methods; and 2) the capacity to dissolve all phases. As discussed however, individual bombs are expensive, and many would be required for efficient time management. Furthermore, additional equipment would be required for safe operation of the bombs. With these considerations in mind it was decided to investigate the potential of other techniques first.

Although microwave-assisted dissolution techniques have the potential to dissolve refractory phases, the safety conditions discussed in section 4.3.5.2, could not be met at the time of this work. The potential of other methods was therefore assessed before going ahead with any experiments using the microwave.

Having postponed experiments with the high pressure bomb and microwave-assisted methods, the alkali salt methods were left to be compared. The Na_2O_2 sintering method requires more sample handling and more equipment than the $LiBO_2$ fusion method (e.g. centrifugation, dissolving precipitates with HCl). Furthermore, acquiring pure (i.e. reagent with low abundance contaminants) Na_2O_2 is difficult compared with the pure $LiBO_2$ fluxes available. It was therefore decided to experiment with solutions prepared by the $LiBO_2$ fusion method.

4.5 TESTING THE METHOD

A reconnaissance experiment was designed to establish whether meaningful results could be obtained from $LiBO_2$-fused solutions at all. Solutions that had previously been prepared for ICP-OES were chosen and diluted a further 5 times, to reduce the TDS, and spiked with Tl. To assess the quality of the data, the international standard BIR-1 was run. Although the certified values for BIR-1 are not all well constrained, comparison of measured and certified values provide a guide as to the effectiveness of the method. Other independent data quality checks included smooth REE curves and correlation between geochemically similar elements, e.g. Nb & Ta and Hf & Zr, (not shown).

4.5.1 RESULTS OF THE TRIAL WITH $LiBO_2$-FUSED SOLUTIONS

A summary of the results of the trial is given in Figure 4.1. In Figure 4.1, the results are presented as the difference, in percent, between the certified and measured values of the international standard BIR-1. In order to plot the highly variable results on a log-scale graph, the percentage differences have been re-scaled so that they are all positive, with the magnitude of the difference remaining the same.

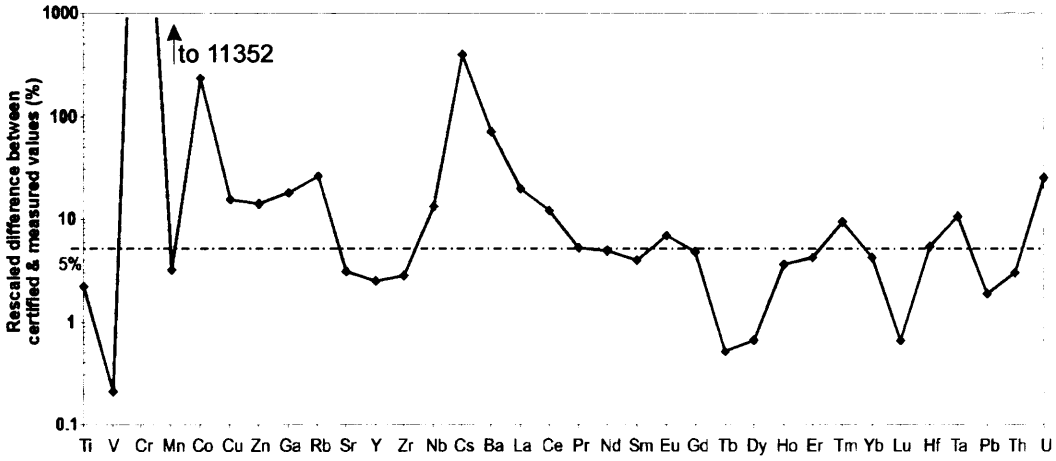


Figure 4.1. Difference between certified and measured values for the international standard BIR-1. The difference between the two values has been re-scaled so that all values are positive and can be plotted on a log-scale graph. The 5% line has been highlighted to mark a conservative estimate of instrument precision for most elements. Note that the majority of elements plot below the 10% line, with certain elements, especially Co, Cu, Zn, Ga, Rb, Cs, Ba and La plotting above this line.

From Figure 4.1, it can be seen that the majority of the elements plot below 10% difference between the certified and measured values. These elements include the REE, Ti, V, Sr, Y, Zr, Hf, Pb and Th. A large number of these elements also plot below the 5% line. This indicated that, for these elements, the method could produce reliable results.

A particular important outcome from the experiment was that the elements associated with refractory phases (especially Zr and Hf) can be successfully analysed by this method. Tantalum and niobium, however, gave compositions >10% different to the certified values, at 11% and 13% respectively. It was not known at this stage if this was significant, and so this discrepancy was investigated further in subsequent experiments.

Certain elements plot well above the 10% line. These include Cr, Co, Cu, Zn, Ga, Rb, Cs, Ba, U and La. Poor Cs results are expected because Cs is volatile at the

temperatures used during flux fusion (e.g. Yu et al. 2001). Poor Ba (+69% different) and Rb (+26%) results may be due to the preparation method used for the solutions, as this was not designed for trace element analysis. The cause of poor Cr, Co, Cu, Zn, Ga and U results was less clear, and may be due to poor certified values. This and other possibilities were investigated in subsequent experiments.

Another significant result is that of lead, which appears to have been measured accurately (Figure 4.1). Poor lead results could be expected because of volatility (e.g. Yu et al. 2001), contamination, or high blank levels in the flux. Inspection of the calibration curves showed that the apparently-accurate Pb results may not be real (i.e. the accurate Pb results are fortuitous), because the curves were poorly defined.

Despite the relatively poor results for some elements, the experiment was successful in showing that elements associated with refractory phases, and other elements such as REE, can be analysed by this method. It is also worth noting that the experiment was successful for solutions that were prepared by a method that was not designed for trace element analysis, and so the potential for significant improvement was very high.

4.6 OPTIMISING THE PREPARATION METHOD

After this relatively successful experiment with the ICP-OES solutions, it was decided to continue with, and develop, the dissolution method. It was anticipated that this method would provide HFSE data, which would then be augmented by data from solutions prepared by the HF-HNO_3 method. It was therefore not considered necessary to experiment with the other dissolution techniques discussed in Section 4.3.

Before proceeding with the $LiBO_2$ fusion method, it was necessary to optimise the sample preparation procedure. The aim of optimising the method was to minimise both the blank contribution, and the potential for contamination.

4.6.1 IDENTIFYING THE PUREST FLUX

The first step was to identify the purest flux available. Two fluxes were obtained: 1) Ultrapure SPEX CertiPrep 100% lithium metaborate; 2) Spectroflux ultraclean 100%

lithium metaborate. Both fluxes were prepared for testing for their purity by dissolving a mass of flux equal to that commonly used in $LiBO_2$-flux fusion methods. The method was as follows.

1) In clean Teflon beakers, 0.4 ±0.0005g of flux was dissolved in 2 mls concentrated nitric acid.
2) The solution was spiked and made up to $100cm^3$ with 18.2MΩ water.

After running on the ICP-MS, a simple comparison of the counts for each element between the fluxes (not shown) could identify the purest flux. However, it is also important to measure the abundance of the contaminants in the flux to see if these are at levels high enough, relative to rock samples, to cause potential problems. To obtain quantitative results, two calibration standards and a calibration-independent standard (JB-1a) were carefully prepared and analysed. The calibration-independent standard was included to check the accuracy of the quantitative results.

A difficulty with the above method is that the procedural blanks (for calibration) and calibration standards are likely to be contaminated because they have been prepared by fusion in a general laboratory. The calibration solutions are therefore likely to have higher element abundance, compared with the flux solutions prepared by dissolving flux in nitric acid in the clean lab. To account for this, calibration lines were constructed by either using procedural blank data, or simply forcing the calibration curve through the origin. However, comparisons between the two methods for calibration curve construction showed no significant differences in quantitative results. The results are given in Table 4.1.

In terms of accuracy (assuming that the lab-certified JB-1a values are in fact accurate), Table 4.1 shows that the analysis has been generally consistent with the lab-certified measurement of JB-1a. Results of the JB-1a analysis are in general about ±10% different from the lab-measured values. Notable exceptions include Zn (-119.26%), Co (49.55%), Cu (-63.75%). Ta (19.0%) and Pb (535.57%). Poor results for Co, Cu and Zn have been encountered before. This indicates that there is a systematic problem associated with the analysis of these elements by this method.

Such a problem may be molecular interference due to the formation of boron-complexes (e.g. $Ti^{48} + B^{11} = Co^{59}$).

Poor Ta results have previously been encountered (see Section 4.5.1), which also points to systematic problems with this element. Such problems may be related to molecular interference or due to the low abundance of this element in JB-1a. With these possibilities in mind, Ta data quality was carefully monitored in subsequent analyses.

Element	Mean SPEX	Mean Sprectroflux	JB1a (measured)	Difference* (%)
TiO_2 (wt%)	0.00	0.00	1.29	-2.06
V	7.61	7.56	197.13	-1.90
Cr	65.70	65.78	429.67	8.18
MnO (wt%)	0.00	0.00	0.14	0.97
Co	-0.20	-0.20	19.25	49.55
Cu	6.44	9.71	95.39	-63.75
Zn	27.88	32.54	147.48	-119.26
Ga	0.32	0.19	19.60	-10.01
Rb	0.08	0.15	35.63	10.74
Sr	1.22	1.62	430.09	4.72
Y	0.14	0.17	23.00	3.11
Zr	5.68	0.86	137.24	4.30
Nb	0.86	0.36	28.08	-3.20
Cs	0.07	0.09	1.12	4.87
Ba	9.68	5.42	464.31	9.43
La	0.01	0.22	35.71	8.19
Ce	0.03	0.04	60.86	7.26
Pr	0.00	0.01	7.77	-7.93
Nd	0.01	0.02	23.25	12.63
Sm	0.00	0.01	4.75	5.85
Eu	0.00	0.00	1.42	5.74
Gd	0.00	0.02	4.50	6.19
Tb	0.00	0.00	0.61	14.75
Dy	0.00	0.00	3.92	2.94
Ho	0.00	0.00	0.67	14.15
Er	0.00	0.00	1.92	11.58
Tm	0.00	0.00	0.34	-2.27
Yb	0.00	0.01	1.95	6.36
Lu	0.00	0.04	0.31	2.72
Hf	0.10	0.01	3.30	5.75
Ta	0.00	0.00	1.42	18.98
Pb	2.83	3.29	-29.15	535.57
Th	0.01	0.04	7.87	8.29
U	0.01	0.02	1.59	0.69

Table 4.1. Quantitative results of an experiment to find out the composition of two lithium metaborate fluxes. All results in ppm except where otherwise stated. The results are averages of three repeated preparations and analyses of the respective flux.

*For an estimate of the accuracy of the analysis, measured JB-1a data was compared with the lab certified JB-1a values (repeated analysis of JB-1a at Cardiff University). The difference is defined as the percent difference between the measured and certified values.

The poor lead results also confirm previous difficulties with this element, such as poorly defined calibration curves (Section 4.5.1). The possible causes of poor lead analysis include Pb-contamination of reagents and standards, high Pb levels in the flux and Pb-volatility during fusion. Addition of Pb from the air in the general laboratory may also contribute to poor Pb analysis.

In terms of the flux composition, Table 4.1 shows that for most elements there is little significant difference between the two fluxes at the ppm level. Nevertheless, there are differences between the flux for certain elements. Zirconium has a higher concentration in the SPEX flux with 5.7ppm compared with 0.9ppm for Spectroflux. However the use of average values is misleading because, throughout the experiment, the concentration of Zr (and Hf) steadily fell. The SPEX samples were prepared and analysed first, and so it is suggested that the high Zr (and relatively high Hf) values are due to memory effects, either in the instrument, or in the lab-ware. Niobium and Ba are also higher in the SPEX flux, and do not decrease throughout the experiment. The final important difference is with La, which more abundant in the Spectroflux flux with an abundance of 0.2ppm.

4.6.2 CHOOSING A FLUX

Table 4.1 shows that at the ppm level the two fluxes are very similar. The most important differences (for this project) are the high Nb abundance in the SPEX flux and higher La abundance in the Spectroflux flux. High quality niobium analysis is especially important because of the potential difficulties in dissolving rutile (the principal Nb-bearing phase) by the HF-HNO_3 dissolution method. A further problem with the SPEX flux is that the material was very crystalline (powdered SPEX flux was not available at the time of this work) and did not absorb the non-wetting agent very well, resulting in spitting during heating. It would be possible to powder the SPEX flux, but this would require additional handling, increasing the chance of contamination. It was therefore decided that the Spectroflux flux would be chosen. The potentially high La levels, and poor Ta results, would be monitored during subsequent analyses. It is also noted that at 0.2 ppm, compared with 2.5ppm for N-MORB (Sun & McDonough 1989), the La abundance in the flux is not highly significant unless the samples to be analysed are highly depleted relative to N-MORB.

4.6.3 OPTIMUM FLUX-TO-SAMPLE RATIO

With the flux chosen, experiments were performed to minimise the amount of flux used during dissolution of the sample powders. This is important for two reasons:

1) dilution of the solution prior to analysis, to reduce TDS, could be minimised and so the abundance of elements in the solution maximised.
2) reduction of blank contribution from the flux.

To test for the minimum ratio of flux-to-sample required for dissolution, different ratios were mixed, fused and then dissolved in 50ml of 4%HNO_3 (as used for preparation of solutions for ICP-OES analysis). Any material that did not dissolve after a sufficient time was assumed to be non-fused rock powder. The minimum effective flux-to-sample ratio was found to be 2:1. It was discovered that better results could be achieved by adding the LiI non-wetting agent as a solid to the mixture, (instead of a LiI solution, which can rapidly evaporate and spit during heating). By adding LiI powder, it became clear that the glass formed a more cohesive ball that stuck less to the crucible walls during fusion, compared with mixtures that had LiI solution added. It is likely that, because of the reduced sticking, more effective mixing between flux and sample could be achieved, and so less flux was required. Furthermore, the molten glass was more readily poured from the crucibles.

4.6.4 SAMPLE PREPARATION METHOD

Results from previous experiments have shown evidence for contamination of Ba, Rb, Pb and Zr, and so a method was developed to minimise potential contamination. Minimising potential contamination was especially important because the samples would be exposed in a general laboratory. The preparation method was as follows:

1) Platinum crucibles were boiled in 20% hydrochloric acid
2) The crucibles were then rinsed with milli-Q water, nitric acid, then a final rinse of milli-Q water and stored in an air-tight container (to avoid contamination from airborne particles).

3) 0.1000± 0.0005g of sample powder, 0.2000±0.0005g flux and 0.035± 0.0005 lithium iodide (LiI) non-wetting agent (approximately equivalent to 4 drops of 25% m/v LiI solution) was added to the crucibles.
4) The mixture was then fused and dissolved by the same method used in the ICP-OES solution preparation (see APPENDIX 1).

To avoid Zr and Hf memory effects in the apparatus, as indicated by the flux analysis (see section 4.6.1), an extra stage washing was used. For this, clean 20% HCl was used to rinse the labware (i.e. beakers, volumetric flasks etc), followed by thorough rinsing with milli-Q water.

4.6.5 REDUCTION OF TOTAL DISSOLVED SOLIDS IN FLUX-BEARING SOLUTIONS

Further testing of solutions prepared by lithium metaborate fusion on the ICP-MS showed that the high TDS can affect the sensitivity of the instrument. Furthermore elements with large memory effects can be introduced to the instrument, especially when a large number of samples are analysed.

To reduce the TDS of the flux-bearing solutions, two methods are possible. The first involves dissolving the glass produced during fusion in HF-HNO_3, as in the manner reported by Yu et al (2001). This method removes Si and B as fluoride complexes, and hence reduces TDS. Yu et al. (2001) found that Si could be removed by up to 36% and B up to 61% in solutions containing dissolved basalt.

The other method has the potential to remove most of the undesired material from the solution to be analysed. This method is presented in Ulfbeck et al. (2003) and involves precipitating iron compounds from the solution by raising the pH using ammonia. The theory is that high charged cations, such as HSFE, will be strongly adsorbed onto the surface of the Fe-compounds (mostly Fe-hydroxides). Once the precipitate has formed it is separated from the remaining solution by centrifugation, and dissolved. The resulting solution can then be prepared for analysis, or can be passed through an ion exchange column to allow for more control over what elements will be present in the analyte.

The method was originally a step in an Hf and REE separation procedure from Ulfbeck et al. (2003). The Hf yield for the method was >90%, after passing the solution through an ion exchange column. Such results were very encouraging, and so this method was first to be evaluated.

Although precipitating a compound was met with some success for basaltic samples, it was unsuccessful for samples with smaller Fe-abundance (e.g. relatively pure quartzites). Furthermore it would be difficult to obtain data for procedural blanks by this method as the Fe abundance would be particularly low in these solutions. In fact, to precipitate Fe-compounds in procedural blanks, Fe would have to be added to the solutions, further increasing the chance of contamination and producing unrepresentative procedural blanks.

With these considerations in mind, and after further successful experimentation on the ICP-MS, it was decided that no TDS reduction would be required, as long as the number of samples to be analysed was not >30-40. If required, however, and in terms of keeping the handling of the samples to a minimum, time management and keeping the addition of reagents to a minimum, the recommended method for TDS reduction would be the HF-HNO_3 digestion.

4.8 SUMMARY

Dissolution of samples using fusion with lithium metaborate can produce accurate, reproducible results for a number of elements. However, certain elements cannot be analysed for by this method (e.g. Cs, Pb), requiring analysis of solutions prepared by different methods (see below). If analysed by the flux method, elements such as La, Rb and Ta need to be carefully monitored to ensure the quality of the data. Results of the analysis of the collected unknown samples are presented in Table 4.4.

4.9 ROUTINE HF-HNO_3 ANALYSIS

To analyse for lead, some low abundance elements and the elements that were not analysable in $LiBO_2$-fused solutions, sample powders were also dissolved using the routine HF-HNO_3 dissolution method (see APPENDIX 1 for details). As well as analysing for these elements, it was also possible to test the efficiency of the HF-HNO_3 dissolution method on dissolving refractory phases. Figure 4.2 presents the

results of the first trial of selected lithium metaborate fused samples with the same samples prepared by HF-HNO_3 dissolution.

4.9.1 COMPARISON BETWEEN $LiBO_2$-FUSED AND HF-HNO_3-DISSOLVED SOLUTIONS

Comparison of the two preparation methods in Figure 4.2, shows that the HF-HNO_3 solutions are relatively depleted in Zr and Hf. This is expected for rocks containing zircon. An unexpected outcome is that rutile has dissolved in solutions prepared by the HF-HNO_3 dissolution method, as shown by the equal abundance of Ti, Nb and Ta in both solutions. Furthermore, the equal abundance of HREE indicates that garnet has similarly dissolved in the HF-HNO_3 solutions.

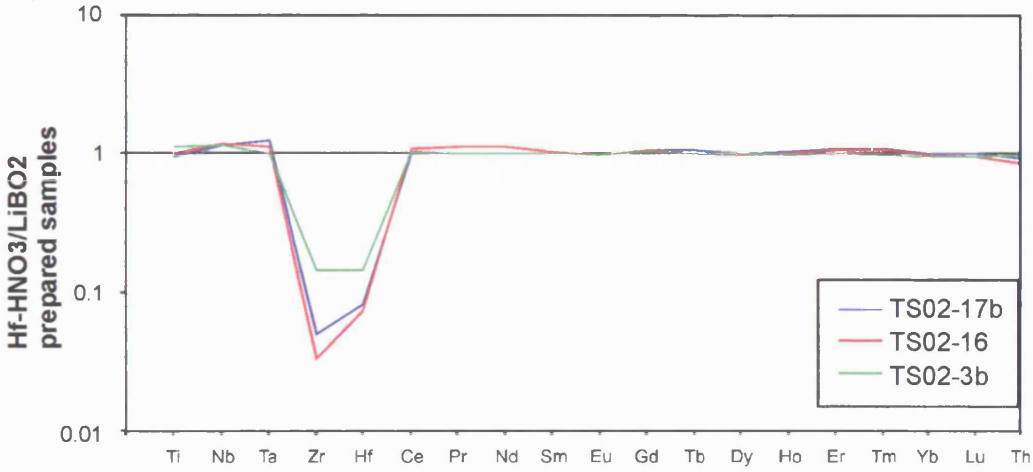


Figure 4.2. Comparison of $LiBO_2$ and HF-HNO_3 prepared samples using selected elements. Important features include the relative depletion of Hf and Zr in the HF-HNO_3 prepared samples and the equal abundance of Ti, Nb and Ta in both solutions. This shows that zircon has not dissolved and rutile has. Another important outcome is the approximately equal abundance of all other elements shown on the diagram.

The samples analysed were among the most depleted in the sample set, and so it is also noteworthy that the two methods have produced similar results, even though the $LiBO_2$ solutions have higher blanks and TDS.

4.9.2 ANALYSIS OF LEAD AND SOME LOW ABUNDANCE ELEMENTS

Some (but not all) analyses of the HF-HNO_3 solutions highlighted a problem with Pb, which sometimes produced poor calibration curves. These poor calibration curves are likely to have resulted from lead contamination of the standard solutions. There are three main possibilities for the source of lead contamination:

1) the apparatus, including the ICP-MS instrument (e.g. the solution uptake tubes);
2) the reagents;
3) unfiltered air in the laboratories.

It was expected that, of these possible sources the instrument and lab apparatus were the main Pb-contributors, because these apparatus are constantly exposed to Pb-bearing solutions. A procedure was therefore developed to clean all of these apparatus.

4.9.2.1 METHOD

To minimise lead and other contaminants in the blank and apparatus, additional washing procedures were necessary. As well as the usual HNO_3 washing stages, a stage of washing with HCl for both the lab apparatus and the ICP-MS instrument was used. A brief outline of the method is given below, which was adapted from the advice given by T. Barry (pers. comm.).

1) To the sample dissolution vials, 1ml of concentrated HCl (1.2 s.g. PRIMAR HCl) was added, and the vials heated at 125°C overnight. After cooling, the vials were rinsed with milli-Q water.
2) All volumetric flasks and sample bottles were first washed in 15M HNO_3. After rinsing with milli-Q water, 20% HCl was added and the flasks vigorously shaken and finally rinsed with milli-Q water.
3) The ICP-MS instrument was rinsed with 10% PRIMAR HCl for about one hour before analysis of unknown samples. The instrument was also rinsed between each sample with 10% HCl.

To evaluate the new method, solutions prepared were compared with the samples prepared by the routine cleaning methods (which uses only HNO_3 to clean apparatus and the ICP-MS instrument).

4.9.2.2 RESULTS

The first indication that HCl was having an effect on the ICP-MS apparatus was during the cleaning stage prior to analysis. When the HCl was introduced, the count rate on a variety of elements (including Pb) increased dramatically. The count rates

then slowly decreased until they reached a minimum, which reflected the composition of the HCl. Important results from the experiment include the lower detection and quantification limits for lead as predicted (see Table 4.2), as well as more accurate lead results.

METHOD	Limit of Detection	Limit of Quantification	JB-1a (measured)	JB-1a (certified)	JB-1a (lab certified)
With HCl washing	0.02	0.06	6.85	7.20	6.9
With HNO_3 washing	0.11	0.38	12.49	7.20	6.9

Table 4.2. Summary of data quality for the measurement of lead using 10% HCl and 10% HNO_3 as cleaning solutions before and in between sample analyses. All values in ppm. Limit of detection (LOD) and limit of quantification (LOQ) are 3σ and 10σ respectively of 10 repeated analysis of the procedural blank used in the calibration line. Note that for the HCl-cleaned run that LOD, LOQ are lower and the accuracy estimates are closer than for the HNO_3 cleaned analysis.

The effects of Cl-complexes on data accuracy was generally minor, restricted to a small number of elements, particularly V, Zn and Cr. Data for these elements (see Table 4.4) were therefore collected by different methods (e.g. ICP-OES, ICP-MS using solutions prepared by HF-HNO_3 dissolution).

4.10 SUMMARY

The bulk rock trace element data collected for this work, and presented in Section 4.11 and Table 4.4, is a compilation from a number of sample preparation and apparatus cleaning methods. The majority of routinely-analysed elements can be obtained by using solutions prepared by the $LiBO_2$-fusion method, which dissolves refractory phases such as zircon. The routine HF dissolution method will not dissolve zircon, but will dissolve other refractory phases such as rutile, ilmenite and titanite. This method however, does not always produce accurate lead data, without additional cleaning of the ICP-MS instrument. Washing with clean HCl is advised, especially for highly depleted samples. It is also advised that Nb and Ta be carefully monitored during analysis of $LiBO_2$-fused solutions.

4.11 RESULTS OF TRACE ELEMENT DATA ACQUISITION

Results for the collected sample set are presented in Table 4.4. The following is a summary of the methods used and statistical data for the elements that have been analysed for by ICP-MS. The data are presented in Table 4.3.

	METHOD	LOD (ppm)	LOQ (ppm)	RSD* (%)	Average JB-1a	JB-1a (lab-cert)	Difference (%)
Sc	HCl washed	0.02	0.08	1.21	29.41	28.33	3.80
Nb	HCl washed	0.00	0.02	0.97	30.26	27.84	8.68
Ta	HCl washed	0.00	0.00	1.75	1.84	1.76	4.96
Pb	HCl washed	0.02	0.06	2.22	7.18	6.69	7.26
Rb	HCl washed	0.02	0.05	0.90	41.78	39.92	4.67
Cs	HCl washed	0.00	0.01	0.82	1.28	1.19	7.59
V	$LiBO_2$-fused	0.66	2.20	4.64	207.89	193.46	7.46
MnO	$LiBO_2$-fused	0.51	1.69	4.91	0.15 wt%	0.15 wt%	2.98
Zn	$LiBO_2$-fused	0.82	2.73	3.75	80.41	74.26	8.29
Ga	$LiBO_2$-fused	0.02	0.08	4.39	18.80	17.82	5.49
Sr	$LiBO_2$-fused	0.30	1.00	1.40	460.80	451.38	2.09
Y	$LiBO_2$-fused	0.42	1.42	2.23	24.20	23.74	1.95
Zr	$LiBO_2$-fused	0.06	0.19	2.03	145.32	143.40	1.33
Ba	$LiBO_2$-fused	0.41	1.36	2.27	512.49	512.64	-0.03
La	$LiBO_2$-fused	0.01	0.04	4.36	39.19	38.89	0.75
Ce	$LiBO_2$-fused	0.01	0.02	4.11	66.69	65.62	1.63
Pr	$LiBO_2$-fused	0.00	0.01	3.94	7.38	7.20	2.56
Nd	$LiBO_2$-fused	0.01	0.02	3.71	26.42	26.61	-0.70
Sm	$LiBO_2$-fused	0.01	0.02	3.83	5.16	5.05	2.13
Eu	$LiBO_2$-fused	0.00	0.01	3.73	1.55	1.51	2.60
Gd	$LiBO_2$-fused	0.03	0.10	4.75	4.84	4.80	0.87
Tb	$LiBO_2$-fused	0.01	0.03	3.54	0.73	0.72	1.24
Dy	$LiBO_2$-fused	0.00	0.01	3.65	4.15	4.04	2.90
Ho	$LiBO_2$-fused	0.00	0.00	3.90	0.81	0.78	3.56
Er	$LiBO_2$-fused	0.00	0.01	4.45	2.17	2.17	-0.01
Tm	$LiBO_2$-fused	0.00	0.00	4.78	0.33	0.33	-1.65
Yb	$LiBO_2$-fused	0.00	0.01	3.45	2.12	2.08	1.87
Lu	$LiBO_2$-fused	0.00	0.01	3.66	0.32	0.32	-1.52
Hf	$LiBO_2$-fused	0.00	0.01	3.66	3.56	3.50	1.60
Th	$LiBO_2$-fused	0.00	0.01	4.62	8.60	8.58	0.17
U	$LiBO_2$-fused	0.00	0.02	3.44	1.74	1.62	6.96
Cr	HNO_3 washed	0.28	0.94	2.23	428.15	467.97	-8.51
Co	HNO_3 washed	0.01	0.04	1.90	37.90	38.16	-0.69
Cu	HNO_3 washed	2.08	6.93	0.74	55.46	58.25	-4.79

Table 4.3. Summary of the data quality estimations for the elements analysed from solutions prepared by different methods. LOD and LOQ are calculated from 10 repeated analysis of the procedural blank used in the calibration curves, based on 3σ and 10σ respectively. All elements in ppm unless otherwise stated. RSD* (Relative Standard Deviation, defined as: 1σ/mean * 100) values are calculated from repeated analysis of multiple preparations of JB-1a. HCl and HNO_3-washed refer to HF-HNO_3-dissolved samples that have been prepared and analysed in apparatus washed with HCl and HNO_3 respectively.

4.12 DISCUSSION OF TRACE ELEMENT DATA QUALITY

4.12.1 LIMITS OF DETECTION AND QUANTIFICATION

Limits of detection and quantification were calculated from 10 repeat analysis of the procedural blank used in the calibration curve, based on 3σ and 10σ respectively.

Limits of quantification are generally <1ppm with particularly good results for REE. Notable exceptions include Cu (6.93ppm), Ba (1.36ppm), Y (1.42ppm), Zn

(2.73ppm), MnO (1.69ppm) and V (2.2 ppm). In general these quantification limits are below the abundance of the respective elements in the samples of the sample sets. Where the measured value is below these values, the element in question is used with caution during data interpretation.

4.12.2 PRECISION ESTIMATION

Precision has been estimated by the analysis of multiple preparations of JB-1a. Errors associated with sample preparation, as well as instrument precision are thereby included in the precision estimates of Table 4.3. In all cases, the RSD is below 5% indicating that the results can be considered precise.

4.12.3 ACCURACY ESTIMATES

Accuracy estimates are shown in Table 4.3 under the column heading % difference. This column is the difference in percent between the average JB-1a value from multiple analysis compared with the lab-certified value. From Table 4.3 it can be seen that that for the elements analysed all are within ±10% of the lab-certified values. Certain elements however, have differences approaching ±10%, including Cr (-8.51), Zn (8.29) and Nb (8.68).

4.13 MAJOR ELEMENT ANALYSIS

Details of the preparation and analysis methods for major element analysis are presented in APPENDIX 1. The complete major element data for collected sample sets, along with trace element data are presented in Table 4.4.

4.14 RESULTS OF BULK ROCK GEOCHEMICAL ANALYSIS

Table 4.4 shows the complete bulk rock geochemical dataset for samples of this thesis. In Table 4.4 the samples have been divided into different groups according to geochemistry, see Chapter 7 and 8 for the details of these groups. Furthermore, each sample in Table 4.4 has been assigned a rock type; see Chapters 5 and 6 for the definition and characteristics of these rock types.

	Group 1a															Group 1b		Group 2a
	TSO2-01	TSO2-02	TSO2-03A	TSO2-03B	TSO2-04	TSO2-05	TSO2-09	TSO2-35	TSO2-38	TSO2-41	TSO2-42	TSO2-47	TSO2-48	TSO2-99	105-1	TSO2-36	110-3	TSO2-12
Rock type	B	B	B	E	E	B	G	B	B	B	B	E	B	B	B	B	B	B
(wt%)																		
SiO_2	48.57	52.63	44.17	51.29	46.54	47.19	52.35	49.07	49.53	46.90	47.82	46.99	47.54	47.08	47.54	48.01	49.75	49.06
TiO_2	2.45	2.83	3.72	2.15	3.52	2.38	1.76	2.80	2.25	3.80	3.31	2.40	1.62	2.21	3.02	2.60	1.76	1.00
Al_2O_3	14.84	13.13	13.91	9.38	14.38	14.90	14.21	17.44	14.04	14.06	13.38	14.82	18.44	12.89	17.88	18.50	16.22	17.80
$Fe_2O_3^*$	14.60	14.47	14.93	11.63	14.47	11.04	9.81	13.01	12.95	13.30	12.99	8.56	10.16	9.83	14.57	14.42	11.33	11.92
MnO	0.08	0.24	0.15	0.11	0.18	0.14	0.10	0.09	0.17	0.16	0.19	0.07	0.18	0.11	0.19	0.13	0.18	0.16
MgO	6.81	5.36	6.06	5.47	4.05	8.03	6.90	4.63	4.91	3.31	6.79	4.18	3.71	5.73	3.94	4.70	3.93	6.15
CaO	6.85	7.24	7.25	11.90	9.44	6.06	9.67	7.71	8.91	8.31	8.77	15.11	10.04	14.35	7.11	5.71	11.15	5.46
Na_2O	3.50	3.29	2.72	3.55	3.14	3.66	3.72	3.81	3.33	3.22	2.88	3.28	3.82	3.51	2.54	2.99	3.05	5.25
K_2O	1.34	0.74	1.40	0.08	1.41	1.18	0.11	1.05	1.15	2.26	1.04	0.12	0.36	0.32	1.92	2.33	1.63	0.18
P_2O_5	0.39	0.55	0.64	0.44	0.59	0.50	0.27	0.36	0.26	0.70	0.49	0.33	0.24	0.25	0.56	0.16	0.47	0.13
LOI	1.56	0.78	3.68	3.59	1.78	3.50	1.20	1.20	2.29	3.87	1.16	2.80	2.90	2.90	1.37	1.89	1.30	1.72
Total	100.99	101.27	98.63	99.59	99.50	98.58	100.10	101.17	99.79	99.89	98.83	98.66	99.01	99.17	100.64	101.45	100.76	98.82
(ppm)																		
Sc	35.8	28.2	26.9	16.7	25.9	19.9	24.7	29.9	33.5	27.4	25.6	35.4	27.2	28.5	31.3	48.9	32.5	43.8
V	152	97	120	177	168	170	236	287	301	293	305	327	201	240	285	318	239	344
Cr	80	10	93	65	26	223	269	36	53	nd	105	215	24	171	23	159	178	nd
Co	40	34	49	30	37	46	38	46	37	29	37	51	29	19	41	51	25	35
Cu	36	28	40	23	32	25	60	47	72	44	41	82	51	32	16	20	68	145
Zn	116	122	106	85	136	98	72	137	97	133	114	63	74	90	128	87	46	63
Ga	23	22	20	15	25	20	22	27	23	29	29	27	20	19	26	21	19	16
Rb	40.2	17.6	27.1	0.9	28.2	23.1	1.8	22.5	30.4	52.6	22.8	1.9	6.8	7.1	37.1	59.9	40.7	1.1
Sr	366	209	268	316	129	406	195	398	233	134	465	656	343	342	390	248	191	218
Y	40.15	49.92	36.62	34.66	52.01	31.48	22.06	39.01	38.26	61.17	49.90	30.12	28.31	22.83	50.92	42.18	28.98	17.68
Zr	190.5	271.0	179.7	151.6	296.2	157.4	158.2	207.4	198.4	245.0	196.4	169.1	147.5	243.2	175.3	181.5	138.8	50.4
Nb	18.18	31.63	35.09	14.85	37.63	37.32	14.85	24.96	16.25	41.25	25.49	19.94	13.76	24.28	27.40	11.21	13.91	2.09
Cs	1.0	0.8	0.8	0.0	1.6	0.8	0.1	0.6	0.8	1.4	0.5	0.1	0.3	0.2	1.0	1.7	0.9	0.2
Ba	204.7	189.8	351.1	9.2	358.8	250.0	35.4	252.7	299.5	544.7	260.6	32.9	68.8	87.0	818.8	704.8	240.0	23.6
La	23.85	32.52	31.62	19.72	33.51	34.19	22.81	27.89	20.15	43.66	28.80	24.44	13.22	20.26	27.83	11.36	16.23	6.11
Ce	52.88	71.73	69.44	43.26	74.16	71.79	47.75	65.53	45.19	98.03	64.67	53.96	29.41	42.89	62.78	29.09	33.60	14.07
Pr	7.08	9.47	9.80	6.12	10.02	9.49	6.37	8.65	6.05	13.00	8.85	7.14	3.96	5.66	8.40	4.36	4.61	2.24
Nd	30.62	40.26	41.95	26.59	43.51	37.76	25.97	36.34	25.40	54.19	38.14	29.69	16.86	22.60	34.83	19.96	18.88	10.63
Sm	7.51	9.41	10.25	6.94	10.30	8.05	5.95	8.94	6.41	13.14	9.62	7.07	4.30	4.83	8.31	5.66	4.45	3.18
Eu	2.52	2.98	3.09	2.28	3.11	2.54	1.97	2.74	2.11	3.93	2.92	2.42	1.50	1.55	2.78	2.08	1.45	1.12
Gd	7.96	9.79	10.06	6.69	10.48	7.56	5.75	8.59	6.92	13.27	9.40	6.89	4.60	4.91	8.59	6.16	4.39	3.53
Tb	1.27	1.55	1.53	1.12	1.66	1.16	0.85	1.27	1.14	2.09	1.52	1.02	0.80	0.73	1.46	1.11	0.74	0.56
Dy	7.32	8.80	8.24	6.66	9.22	6.33	4.44	7.19	6.76	11.55	8.76	5.71	4.92	4.00	8.83	7.18	4.61	3.31
Ho	1.39	1.71	1.52	1.33	1.77	1.19	0.80	1.39	1.31	2.10	1.68	1.08	0.97	0.76	1.73	1.49	0.93	0.70
Er	3.50	4.52	3.79	3.37	4.64	3.04	2.00	3.71	3.41	5.26	4.46	2.76	2.58	1.95	4.41	4.05	2.51	2.01
Tm	0.48	0.67	0.53	0.49	0.69	0.45	0.30	0.54	0.49	0.74	0.64	0.39	0.36	0.26	0.62	0.62	0.36	0.32
Yb	2.54	3.91	3.16	2.87	4.03	2.71	1.82	3.42	3.09	4.52	3.87	2.39	2.35	1.70	3.95	4.01	2.29	2.08
Lu	0.36	0.56	0.50	0.40	0.58	0.40	0.28	0.49	0.47	0.67	0.56	0.36	0.35	0.26	0.57	0.61	0.34	0.32
Hf	4.49	5.96	4.55	3.86	6.40	3.31	3.74	4.45	4.50	5.23	4.27	3.85	3.40	5.29	3.72	4.18	3.72	1.51
Ta	1.17	1.99	2.22	1.02	2.15	2.28	0.92	1.58	1.02	2.56	1.62	1.27	0.86	1.65	1.66	0.72	0.83	0.12
Pb	3.5	3.5	4.7	3.4	2.7	nd	3.4	3.9	2.5	2.9	4.9	4.1	2.5	3.6	3.4	1.5	2.5	2.4
Th	2.24	3.14	2.78	1.69	3.19	3.58	2.59	2.57	1.84	4.65	2.87	2.11	1.20	2.07	2.65	0.74	1.46	0.81
U	0.54	0.83	0.76	0.48	0.85	0.84	0.46	0.60	0.54	1.30	0.79	0.65	0.43	0.52	0.60	0.19	0.17	0.26

Table 4.4. Results of bulk rock geochemical analysis of meta-basaltic samples collected from the Chinese Tian Shan blueschist belt. See Chapter 7 for details of the sample groups. Rock types: G = Greenschist; B = Blueschist; E = Eclogite, GBMS = Glaucophane–Bearing Meta-sedimentary rocks, GAMS = Glaucophane-Absent Meta-sedimentary rocks. See Chapter 5 for definitions of these rock types. Fe_2O_3- all Fe as Fe_2O_3. Major element data for samples from Qilian (labelled "Q98-x" or "Q02-x") is summed to 100% on an LOI-free basis.

	Group 2a			Group 2b								Group 2c			Group 2d			Group 3
	TS02-23	TSO2-28	TSO2-30	TSO2-50	TSO2-21A	TSO2-26	TSO2-27	TSO2-43	TSO2-46	TS02-54	TSO2-62	TSO2-55	TSO2-57	TSO2-58A	TSO2-15A	TSO2-15B	TSO2-34	TSO2-16
Rock type	B	E	B	B	B	E	B	B	B	E	B	B	E	E	E	B	Rodingite	B
(wt%)																		
SiO_2	46.65	46.24	48.26	46.17	55.76	47.79	48.61	49.88	52.92	46.41	56.24	44.49	43.95	46.45	46.88	46.99	34.01	47.49
TiO_2	0.59	0.83	0.94	0.97	1.13	1.06	0.96	1.55	0.79	1.04	0.68	1.23	0.97	0.96	2.78	2.80	1.56	2.27
Al_2O_3	15.02	14.84	17.06	15.26	16.16	13.94	13.21	13.88	17.20	13.83	16.34	15.28	13.75	12.28	13.23	13.49	18.19	11.24
Fe_2O_3	7.77	10.17	8.59	9.45	11.83	12.25	11.80	15.48	9.55	9.43	7.65	11.20	10.21	10.22	18.39	18.50	27.33	22.62
MnO	0.13	0.18	0.12	0.14	0.20	0.22	0.17	0.24	0.16	0.14	0.09	0.19	0.19	0.15	0.32	0.34	0.69	0.31
MgO	7.52	7.61	6.60	4.80	4.00	6.99	8.56	5.35	5.66	5.86	4.82	6.70	5.98	5.81	4.15	4.39	3.51	4.84
CaO	12.15	13.58	12.24	14.19	4.49	11.79	10.40	9.91	7.90	14.57	3.67	12.02	14.33	14.05	8.62	8.52	10.33	9.82
Na_2O	2.78	3.75	3.58	3.41	4.58	3.46	2.68	3.04	4.77	4.68	7.35	2.13	3.53	4.78	3.09	3.04	0.19	1.70
K_2O	0.43	0.11	0.59	0.19	0.75	0.19	0.20	0.11	0.35	0.11	0.46	0.19	0.07	0.02	0.17	0.31	0.08	0.07
P_2O_5	0.09	0.07	0.07	0.17	0.11	0.08	0.13	0.13	0.07	0.12	0.14	0.14	0.18	0.05	0.88	0.93	0.07	0.16
LOI	5.94	3.16	1.49	5.60	1.15	1.84	1.92	0.41	1.47	4.83	2.05	5.11	6.20	4.38	0.32	0.76	5.46	0.23
Total	99.06	100.55	99.52	100.35	100.16	99.61	98.64	99.98	100.84	101.03	99.51	98.68	99.36	99.14	98.83	100.07	101.42	100.75
(ppm)																		
Sc	36.8	47.4	48.2	35.9	39.9	47.7	44.2	47.2	41.3	46.5	29.3	47.1	41.5	45.6	39.0	38.9	74.7	52.0
V	251	280	312	291	290	295	279	421	264	315	257	336	301	312	201	218	339	827
Cr	156	430	490	302	nd	89	101	nd	153	441	nd	315	462	517	nd	nd	142	28
Co	38	37	31	34	27	35	42	44	38	48	24	43	45	48	36	34	47	56
Cu	75	69	53	57	114	34	46	73	120	75	49	85	78	92	77	44	6	114
Zn	61	78	55	68	97	82	86	103	74	95	66	76	67	84	140	133	165	160
Ga	14	14	17	17	18	15	14	19	15	15	17	15	15	15	22	24	14	20
Rb	10.0	1.2	22.1	3.8	12.2	3.4	4.0	2.0	5.9	1.1	3.8	2.1	0.6	0.7	6.1	14.0	1.1	1.1
Sr	142.6	171.0	153.8	341.2	187.1	73.5	150.5	95.2	156.7	130.6	76.5	168.7	196.1	89.7	91.4	97.2	134.9	60.6
Y	22.35	26.90	29.69	31.17	33.62	37.83	31.54	47.04	17.60	27.08	13.94	36.26	30.10	19.14	91.04	93.42	160.54	57.61
Zr	29.2	41.3	43.7	54.5	89.5	76.2	67.2	103.5	54.8	57.8	57.3	72.5	55.0	63.7	119.0	148.7	94.3	102.9
Nb	1.04	1.20	1.15	1.77	3.64	2.45	2.20	1.56	1.54	2.21	1.69	1.82	1.92	3.11	9.49	9.21	1.43	1.17
Cs	0.6	0.2	2.4	0.6	0.4	0.1	0.2	0.2	0.3	0.4	0.3	0.3	0.2	0.2	0.7	1.4	0.2	0.3
Ba	77.6	11.4	208.8	313.6	197.0	70.5	43.3	24.1	111.2	16.1	114.5	26.3	12.3	10.5	35.3	86.1	11.4	8.8
La	3.15	3.01	3.33	3.07	6.45	5.54	5.45	3.33	4.09	2.46	4.26	2.50	2.11	1.77	17.01	15.86	3.90	2.19
Ce	7.17	7.65	8.23	8.61	15.39	12.52	12.49	10.65	9.70	6.82	10.20	7.86	5.92	5.10	44.98	41.08	8.43	8.17
Pr	1.09	1.24	1.34	1.46	2.33	1.77	1.75	1.97	1.48	1.16	1.53	1.46	1.05	0.85	7.80	7.11	1.30	1.63
Nd	5.43	6.36	6.96	7.57	10.99	7.99	7.78	10.57	7.05	6.06	6.97	7.86	5.56	4.34	40.54	37.05	6.27	9.46
Sm	2.04	2.37	2.58	2.72	3.36	2.62	2.51	4.01	2.22	2.17	1.95	2.93	2.13	1.48	13.00	11.94	2.73	4.15
Eu	0.81	0.91	0.95	1.10	1.17	0.91	0.83	1.42	0.79	0.79	0.70	1.10	0.85	0.54	4.60	4.30	2.20	1.58
Gd	2.84	3.13	3.31	3.55	4.06	3.71	3.48	5.24	2.49	2.84	2.17	4.02	3.15	2.11	16.82	15.15	7.74	5.98
Tb	0.55	0.61	0.65	0.72	0.78	0.81	0.70	1.06	0.44	0.56	0.35	0.81	0.66	0.46	3.03	2.71	2.56	1.23
Dy	3.74	4.13	4.49	4.70	5.24	5.66	4.90	7.17	2.81	4.02	2.16	5.60	4.56	3.09	19.07	17.10	21.80	8.53
Ho	0.80	0.92	1.01	1.01	1.10	1.26	1.07	1.60	0.60	0.87	0.45	1.22	0.98	0.64	4.03	3.59	5.20	1.83
Er	2.22	2.64	2.90	2.88	3.02	3.57	3.06	4.58	1.72	2.51	1.29	3.47	2.87	1.64	11.17	9.85	15.47	5.05
Tm	0.35	0.41	0.43	0.44	0.47	0.55	0.48	0.72	0.27	0.40	0.20	0.55	0.44	0.24	1.72	1.50	2.53	0.81
Yb	2.39	2.74	2.85	2.88	3.24	3.63	3.21	4.84	1.80	2.60	1.33	3.59	2.99	1.49	10.98	9.54	16.70	5.57
Lu	0.48	0.43	0.42	0.43	0.51	0.58	0.49	0.76	0.28	0.41	0.20	0.53	0.45	0.24	1.72	1.50	2.44	0.89
Hf	0.89	1.19	1.25	1.38	2.34	2.03	1.83	2.77	1.50	1.48	1.52	1.82	1.41	1.71	3.78	4.29	2.64	2.74
Ta	0.06	0.08	0.07	0.11	0.22	0.17	0.15	0.10	0.09	0.13	0.10	0.13	0.12	0.15	0.61	0.58	0.08	0.09
Pb	2.3	1.2	2.4	4.0	2.9	2.8	1.9	1.5	2.7	0.8	1.4	2.4	1.1	0.8	1.5	1.5	3.0	0.8
Th	0.42	0.38	0.43	0.23	0.87	1.61	2.09	0.22	0.68	0.20	0.75	0.14	0.16	0.20	1.45	1.26	0.06	0.13
U	0.28	0.19	0.21	0.24	0.49	0.56	0.47	0.07	0.34	0.15	0.54	0.09	0.27	0.09	0.44	0.38	0.07	0.04

Table 4.4. continued.

	Group 3				Volcanoclastic									GBMS			GAMS	
	TSO2-17b	TSO2-20	TSO2-32A	TSO2-33	117-1	106-3B	TSO2-29	TSO2-53	TSO2-52	106-14	105-12	106-3a	TSO2-06	984-1	TSO2-14	TSO2-18	TSO2-08	TSO2-11
Rock type	E	E	E	E	E	B	E	B	B	B	E	B	B	B	B	B	G	G
(wt%)																		
SiO_2	52.98	46.55	46.44	51.32	48.13	76.66	52.65	53.19	52.09	41.17	47.49	47.84	40.96	41.06	56.11	65.68	47.49	48.46
TiO_2	1.58	1.56	1.71	1.34	0.80	0.31	0.74	0.79	0.91	2.40	2.86	2.44	2.48	0.72	0.69	0.42	3.85	1.82
Al_2O_3	11.71	14.07	13.60	12.68	10.78	3.86	14.98	13.88	13.67	15.27	15.51	14.53	14.96	13.70	16.85	12.98	19.04	14.06
Fe_2O_3	15.34	18.15	16.68	14.10	11.76	4.27	7.03	11.03	12.34	11.16	12.20	12.23	13.18	7.89	9.41	7.73	15.06	11.48
MnO	0.20	0.30	0.26	0.22	0.14	0.03	0.11	0.18	0.15	0.21	0.16	0.16	0.14	0.14	0.11	0.08	0.05	0.14
MgO	4.93	6.02	6.62	5.62	5.99	3.60	5.73	5.14	4.45	3.19	6.71	5.56	4.29	3.95	4.25	2.22	1.61	6.59
CaO	9.65	10.87	11.33	10.10	14.80	6.10	9.96	7.29	7.67	15.70	8.48	9.98	8.93	19.82	3.64	1.97	4.02	8.62
Na_2O	3.06	2.19	2.60	2.95	3.38	1.58	4.84	3.83	4.48	0.41	3.23	1.83	2.99	2.92	4.24	5.12	1.95	3.04
K_2O	0.06	0.20	0.08	0.27	0.06	0.03	0.44	0.10	0.03	0.07	0.93	1.24	3.63	0.04	0.44	0.25	2.12	1.05
P_2O_5	0.12	0.13	0.10	0.11	0.07	0.15	0.14	0.13	0.09	0.56	0.42	0.19	0.35	0.09	0.17	0.12	0.44	0.22
LOI	0.69	0.34	0.19	0.39	4.13	3.38	2.11	4.83	3.61	10.14	1.21	4.16	8.13	10.22	3.63	2.41	3.84	3.69
Total	100.32	100.40	99.60	99.09	100.04	99.97	98.72	100.39	99.49	100.28	99.20	100.17	100.04	100.55	99.52	98.98	99.47	99.17
(ppm)																		
Sc	46.7	53.5	54.0	50.4	43.3	6.6	34.8	37.3	41.7	19.6	23.9	23.0	25.6	35.4	29.5	28.1	30.2	27.4
V	504	515	456	346	332	81	221	291	380	199	243	217	226	263	159	73	86	184
Cr	26	13	35	65	nd	nd	215	4	nd	140	141	68	206	459	25	4	92	210
Co	49	53	45	44	37	16	29	37	44	30	38	26	49	30	14	10	22	40
Cu	52	92	86	25	30	19	35	88	48	28	25	42	28	36	19	47	17	75
Zn	86	113	120	90	102	36	48	121	109	69	104	84	120	69	77	48	185	71
Ga	20	20	17	18	18	6	16	16	18	30	25	24	20	17	14	16	28	17
Rb	0.3	11.6	0.4	5.0	0.6	0.9	16.6	1.9	0.9	1.0	16.5	24.4	103.9	2.6	7.4	4.4	71.2	23.6
Sr	36.8	128.3	125.2	122.7	87.0	129.1	96.4	144.7	170.3	1762.8	325.7	509.1	137.5	317.6	201.5	63.2	163.8	215.0
Y	43.89	54.97	43.01	45.89	26.41	12.58	24.57	24.39	31.39	34.93	36.47	45.06	37.09	22.09	20.71	22.99	44.71	22.00
Zr	86.5	79.3	79.3	84.2	42.4	33.1	86.1	51.3	69.4	190.4	258.7	217.9	171.6	45.6	74.2	71.0	230.6	131.8
Nb	0.91	1.09	0.74	0.94	0.49	3.24	2.58	0.96	1.19	22.58	29.40	26.77	26.93	1.12	4.51	3.43	35.01	15.87
Cs	0.0	0.7	0.1	0.2	0.1	0.0	0.2	0.3	0.1	0.1	0.7	0.9	3.0	0.4	0.3	0.4	2.4	0.9
Ba	1.6	51.4	10.8	76.2	5.1	19.5	78.0	140.8	26.5	32.3	799.3	570.3	770.5	7.5	620.1	68.0	923.5	141.2
La	2.13	2.08	1.79	2.38	1.16	15.51	11.45	2.58	3.75	27.09	29.21	32.03	27.60	2.70	8.17	6.84	28.53	16.74
Ce	8.18	7.62	6.23	8.33	4.04	33.30	23.87	6.74	9.76	61.45	63.62	69.37	60.62	7.52	16.23	14.55	66.44	36.75
Pr	1.64	1.51	1.22	1.62	0.80	4.03	3.07	1.12	1.64	7.99	8.40	8.94	8.40	1.29	2.44	2.12	9.13	5.16
Nd	9.47	8.74	7.10	9.29	4.62	15.73	12.62	5.62	8.10	32.94	34.17	35.60	34.68	6.65	10.69	9.14	39.36	22.00
Sm	3.78	3.60	2.84	3.66	1.96	3.14	3.30	1.99	2.84	7.93	8.01	7.89	7.79	2.28	2.99	2.53	9.79	5.49
Eu	1.34	1.41	1.11	1.33	0.89	0.83	0.91	0.69	0.94	2.52	2.64	2.61	2.49	0.86	1.23	0.75	3.11	1.86
Gd	4.90	5.20	4.49	4.81	2.81	2.45	3.71	2.58	3.52	7.38	8.18	7.99	7.56	2.82	3.80	2.83	9.46	5.48
Tb	0.95	1.09	0.94	0.99	0.59	0.36	0.63	0.54	0.68	1.18	1.24	1.30	1.23	0.53	0.74	0.54	1.52	0.87
Dy	6.55	7.85	6.47	6.89	4.23	2.21	3.98	3.67	4.59	6.70	6.72	7.62	7.17	3.60	4.95	3.73	8.73	4.89
Ho	1.41	1.71	1.45	1.57	0.92	0.49	0.82	0.80	1.02	1.22	1.29	1.55	1.39	0.77	1.12	0.80	1.73	0.94
Er	3.89	4.85	4.17	4.45	2.58	1.46	2.34	2.36	3.03	3.02	3.17	4.02	3.54	2.15	3.35	2.23	4.53	2.37
Tm	0.62	0.77	0.68	0.70	0.42	0.24	0.36	0.38	0.49	0.44	0.45	0.57	0.52	0.35	0.55	0.36	0.68	0.34
Yb	4.25	5.42	4.18	4.67	3.01	1.61	2.41	2.48	3.25	2.86	2.74	3.37	3.16	2.51	3.63	2.59	4.23	2.03
Lu	0.68	0.86	0.64	0.71	0.50	0.25	0.47	0.40	0.50	0.43	0.42	0.49	0.46	0.40	0.59	0.41	0.61	0.29
Hf	2.33	2.03	2.29	2.30	1.25	0.84	2.21	1.46	1.85	4.34	5.98	4.96	3.45	1.24	3.33	1.99	5.19	3.56
Ta	0.07	0.07	0.05	0.07	0.03	0.21	0.19	0.06	0.07	1.60	1.83	1.60	1.66	0.07	0.30	0.20	2.17	0.99
Pb	0.3	0.8	1.2	0.6	1.4	1.3	8.1	1.9	2.2	17.2	3.3	3.5	2.3	1.3	4.3	1.7	9.1	2.6
Th	0.10	0.10	0.08	0.11	0.06	1.02	3.68	0.40	0.55	3.20	3.31	4.64	2.72	0.21	3.10	1.36	3.20	1.58
U	0.03	0.03	0.03	0.05	0.02	0.26	0.99	0.16	0.22	1.07	0.82	0.84	0.70	0.23	1.09	0.65	0.83	0.39

Table 4.4. continued.

	GAMS				
	986-1	TSO2-10	TSO2-13	TSO2-19	TSO2-56
Rock type	G	G	G	G	G
(wt%)					
SiO_2	71.28	69.66	68.14	60.37	59.55
TiO_2	0.36	0.52	0.70	0.81	0.57
Al_2O_3	8.81	12.45	13.64	17.96	13.27
Fe_2O_3	3.77	4.70	5.25	7.44	5.16
MnO	0.20	0.08	0.07	0.10	0.05
MgO	1.81	2.02	2.24	3.70	3.13
CaO	5.01	1.74	2.11	1.29	5.95
Na_2O	1.23	1.81	3.25	2.36	2.10
K_2O	0.70	2.40	1.78	3.22	1.66
P_2O_5	0.05	0.17	0.22	0.16	0.12
LOI	8.22	3.84	1.71	3.51	7.21
Total	101.44	99.39	99.11	100.91	98.77
(ppm)					
Sc	6.6	10.5	15.9	19.1	19.6
V	51	71	109	121	107
Cr	11	26	50	91	20
Co	9	11	13	19	10
Cu	68	19	24	26	40
Zn	198	98	63	99	286
Ga	10	16	16	24	18
Rb	28.6	108.6	81.5	168.9	36.4
Sr	368.7	105.0	191.6	172.9	122.1
Y	42.83	25.82	28.06	35.95	12.75
Zr	105.4	176.3	308.7	188.8	133.8
Nb	9.08	10.68	12.97	15.39	4.47
Cs	1.2	4.9	3.6	7.6	2.0
Ba	128.6	599.3	454.7	902.2	425.9
La	25.27	37.87	32.74	43.96	7.42
Ce	57.74	72.20	70.27	86.36	15.90
Pr	7.43	8.41	8.38	10.28	2.07
Nd	28.66	30.20	31.02	36.85	8.38
Sm	6.58	5.45	6.19	7.30	1.98
Eu	1.84	1.23	1.41	1.57	0.49
Gd	6.23	4.85	5.15	6.40	1.89
Tb	1.07	0.71	0.80	1.03	0.33
Dy	6.77	4.09	4.83	6.11	2.12
Ho	1.40	0.85	0.96	1.24	0.44
Er	3.75	2.45	2.59	3.48	1.26
Tm	0.57	0.40	0.41	0.55	0.21
Yb	3.47	2.47	2.82	3.63	1.57
Lu	0.47	0.38	0.45	0.55	0.26
Hf	2.89	4.47	7.64	5.04	3.55
Ta	0.55	0.73	0.83	1.01	0.31
Pb	94.7	20.8	15.8	15.2	198.3
Th	6.41	10.50	9.65	14.06	4.33
U	1.50	2.12	2.45	2.48	1.14

Table 4.4. continued.

	Group Q1						Group Q1a					Group Q1b			Group Q2			
	Q02-32b	Q98-34	Q02-34	Q98-35	Q98-40	Q98-149	Q02-22	Q98-117	Q98-122	Q98-127	Q98-128	Q98-119	Q98-125	Q98-126	Q02-02	Q98-113	Q98-114	Q98-116
Rock type	PP	B/S	PP	PP	B/S	B/S	B/S	B/S	B/S	B/S	B/S	B/S	B/S	B/S	B/S	B/S	BS	B/S
Wt%																		
SiO_2	50.81	49.36	50.21	49.73	51.18	48.40	49.10	48.99	50.34	47.17	47.83	47.66	49.10	49.08	52.31	48.75	49.28	48.71
TiO_2	1.13	1.27	1.45	1.23	1.54	2.01	1.07	1.00	1.35	1.67	1.72	2.02	1.61	1.72	1.02	0.74	0.94	1.20
Al_2O_3	15.21	18.42	15.66	17.94	16.49	14.93	17.34	18.14	19.83	16.85	16.91	18.09	18.88	16.56	15.98	20.89	18.01	18.27
Fe_2O_3	9.74	12.72	11.65	11.69	12.44	16.69	12.98	9.88	11.69	16.07	14.07	15.57	12.59	12.38	8.73	9.24	9.97	10.05
MnO	0.17	0.24	0.19	0.28	0.19	0.31	0.09	0.16	0.17	0.38	0.22	0.21	0.20	0.24	0.14	0.24	0.19	0.17
MgO	7.63	9.63	7.08	10.13	7.42	7.25	4.94	8.50	4.59	7.11	7.48	4.87	5.55	6.63	8.33	7.38	8.75	8.24
CaO	11.70	4.44	9.49	4.99	6.61	7.19	9.38	9.54	7.76	6.69	8.36	8.68	7.81	8.89	8.39	8.58	9.17	9.10
Na_2O	3.17	2.94	4.05	2.61	3.79	2.66	3.93	2.98	1.14	2.34	2.01	1.97	2.92	2.97	4.22	2.42	3.06	1.70
K_2O	0.32	0.79	0.06	1.19	0.13	0.34	1.01	0.60	2.71	1.32	1.10	0.71	1.12	1.24	0.75	1.63	0.46	2.32
P_2O_5	0.12	0.18	0.17	0.22	0.21	0.22	0.16	0.20	0.41	0.42	0.30	0.22	0.23	0.29	0.12	0.14	0.17	0.25
Total	100.00	100.00	100.00	100.00	100.00	100.00	100.00	100.00	100.00	100.00	100.00	100.00	100.00	100.00	100.00	100.00	100.00	100.00
ppm																		
Sc	41.2	36.0	38.1	37.9	41.8	41.9	38.7	30.3	37.5	40.4	38.2	39.6	36.6	33.9	33.4	24.2	29.1	30.1
V	278	271	303	229	260	443	208	190	143	229	248	269	213	219	220	196	188	201
Cr	366	400	299	354	157	96	354	444	330	285	162	219	315	278	347	299	446	327
Co	36	47	42	44	54	47	42	38	56	41	41	36	41	44	32	39	64	43
Ni	127	130	126	90	66	46	205	142	112	115	56	63	98	116	91	81	169	122
Cu	40	57	47	206	57	57	32	57	55	80	52	26	48	53	45	59	126	52
Zn	18	81	97	70	71	80	79	55	83	107	76	67	78	82	95	108	96	77
Ga	15	17	17	15	14	17	18	14	18	15	16	20	17	15	15	19	15	17
Rb	5.2	14.0	0.3	18.5	1.2	3.0	21.1	8.5	65.2	19.4	22.2	12.9	15.1	17.3	22.1	28.2	6.1	37.6
Sr	116.2	77.0	33.4	75.4	68.0	183.1	394.6	215.5	436.9	176.4	301.1	224.5	205.7	124.2	197.7	352.9	256.6	372.2
Y	29.33	21.86	39.27	24.86	29.58	35.04	28.75	18.90	27.33	35.99	30.97	38.36	28.18	29.32	24.14	14.92	18.46	20.14
Zr	78.5	60.8	97.1	83.1	96.2	99.2	65.3	57.7	78.2	114.7	102.6	144.5	105.3	116.0	81.2	52.6	54.6	79.2
Nb	2.16	1.33	2.02	2.21	3.04	4.06	4.12	2.73	2.73	4.60	3.95	5.04	3.40	4.15	4.56	3.53	4.47	8.88
Cs	0.5	3.4	0.1	2.2	0.4	0.2	0.8	0.2	3.3	1.5	1.4	1.1	1.1	1.7	0.4	1.1	0.2	1.0
Ba	55.3	125.0	9.2	88.7	25.2	47.8	128.7	78.7	259.3	152.4	261.9	62.8	89.4	87.8	146.6	259.5	66.6	389.9
La	3.35	2.17	3.74	3.52	3.52	4.66	5.15	4.78	5.26	7.61	7.12	7.34	4.60	4.90	10.46	9.45	5.98	10.72
Ce	9.30	7.05	10.79	10.24	10.81	13.20	12.13	12.07	13.71	18.39	18.24	20.79	14.15	15.18	22.12	19.89	13.90	23.80
Pr	1.61	1.28	1.92	1.69	1.85	2.15	1.92	1.77	2.12	2.64	2.68	3.51	2.28	2.49	2.93	2.50	1.90	3.10
Nd	8.17	6.90	10.05	8.50	9.47	10.38	9.01	8.05	10.16	11.87	12.39	17.22	11.23	11.99	12.18	10.09	8.27	12.70
Sm	2.67	2.45	3.44	2.77	3.22	3.59	2.89	2.37	3.21	3.43	3.66	5.28	3.51	3.69	2.99	2.41	2.28	3.16
Eu	0.94	0.91	1.23	1.13	1.16	1.27	1.14	0.87	1.19	1.23	1.29	1.95	1.34	1.32	0.99	1.21	0.85	1.12
Tb	0.64	0.60	0.91	0.65	0.80	0.89	0.74	0.54	0.76	0.87	0.84	1.13	0.79	0.82	0.60	0.48	0.50	0.63
Gd	3.32	3.38	4.56	3.61	4.43	4.79	3.85	3.09	4.22	4.60	4.80	6.56	4.47	4.67	3.34	2.88	2.87	3.73
Dy	4.40	4.11	6.04	4.41	5.41	6.19	4.73	3.55	5.13	6.06	5.62	7.33	5.21	5.31	3.82	2.87	3.35	4.00
Ho	0.99	0.89	1.32	0.97	1.16	1.35	1.01	0.77	1.09	1.44	1.25	1.53	1.13	1.18	0.83	0.59	0.74	0.81
Er	2.83	2.59	3.78	2.87	3.33	3.97	2.78	2.17	3.00	4.41	3.70	4.35	3.24	3.43	2.37	1.73	2.15	2.23
Tm	0.45	0.39	0.59	0.42	0.49	0.59	0.43	0.31	0.42	0.68	0.58	0.64	0.47	0.50	0.38	0.27	0.33	0.33
Yb	2.89	2.50	3.84	2.71	3.10	3.78	2.76	1.98	2.62	4.40	3.79	4.00	2.99	3.14	2.40	1.75	2.10	2.07
Lu	0.43	0.38	0.58	0.41	0.48	0.58	0.42	0.30	0.39	0.68	0.57	0.61	0.45	0.46	0.37	0.27	0.32	0.31
Hf	1.90	1.85	2.50	2.20	2.56	2.83	1.61	1.60	2.16	3.08	2.73	3.65	2.63	2.91	1.94	1.48	1.53	2.08
Ta	0.14	0.09	0.13	0.14	0.20	0.27	0.24	0.14	0.17	0.27	0.23	0.33	0.22	0.27	0.26	0.22	0.25	0.52
Pb	0.6	0.7	0.9	0.5	0.6	3.2	1.4	3.0	33.1	8.6	25.4	6.5	2.2	0.7	4.5	6.7	4.8	13.6
Th	0.30	0.12	0.29	0.42	0.53	0.68	0.49	0.64	0.80	1.18	1.02	0.38	0.27	0.34	2.50	2.13	1.01	1.83
U	0.09	0.09	0.11	0.17	0.20	0.19	0.54	0.17	0.31	0.50	0.31	0.14	0.10	0.11	0.40	0.61	0.32	0.50

Table 4.4. continued.

	Group Q2						GAMS						GBMS					
	Q98-118	Q98-140	Q98-147	Q98-135	Q98-144	Q98-152	Q98-42	Q98-121	Q98-142	Q02-05	Q02-08B	Q02-10A	Q98-120	Q98-134	Q98-136	Q98-139	Q98-143	Q98-148
Rock type	B/S	B/S	B/S	B/S	B/S	B/S	G/S	G/S	G/S	G/S	B/S	B/S	B/S	G/S	B/S	B/S	B/S	B/S
wt%																		
SiO_2	51.00	47.37	50.37	55.49	52.17	50.89	77.96	72.07	90.86	75.34	64.61	56.26	55.89	68.10	60.48	67.67	72.05	88.46
TiO_2	0.78	1.09	1.47	2.03	2.01	1.96	0.34	0.52	0.05	0.53	0.80	0.73	1.31	0.58	0.49	0.74	0.57	0.12
Al_2O_3	17.88	16.26	18.52	13.50	15.06	15.20	9.33	12.08	1.44	9.80	11.92	11.82	15.41	15.24	17.97	12.08	13.90	3.22
Fe_2O_3	9.61	10.08	15.07	14.54	16.32	16.75	4.15	6.76	1.54	6.34	7.27	14.30	11.56	4.44	8.75	6.89	3.93	5.55
MnO	0.25	0.25	0.21	0.13	0.25	0.23	0.09	0.22	1.18	0.27	0.14	0.25	0.18	0.07	0.19	0.08	0.03	0.37
MgO	8.73	5.14	6.39	5.96	5.21	5.42	1.51	3.20	2.04	3.54	5.07	7.38	6.70	3.97	4.09	4.53	1.64	1.04
CaO	7.67	14.12	3.32	2.48	4.75	5.87	0.56	1.32	2.26	1.47	5.75	4.56	3.83	0.88	0.31	2.66	1.59	0.12
Na_2O	2.78	2.57	1.41	2.61	1.62	2.10	0.02	0.80	0.04	1.26	2.67	4.20	2.27	1.95	1.86	1.75	1.13	0.26
K_2O	1.16	2.83	3.04	3.01	2.27	1.25	5.80	2.89	0.50	1.30	1.60	0.34	2.64	4.57	5.68	3.40	5.05	0.79
P_2O_5	0.13	0.29	0.21	0.25	0.33	0.33	0.25	0.14	0.08	0.14	0.17	0.17	0.21	0.20	0.18	0.19	0.12	0.06
Total	100.00	100.00	100.00	100.00	100.00	100.00	100.00	100.00	100.00	100.00	100.00	100.00	100.00	100.00	100.00	100.00	100.00	100.00
ppm																		
Sc	28.7	27.9	45.6	34.7	44.7	39.1	7.7	17.2	1.8	17.6	26.0	22.1	26.2	9.5	26.9	10.1	10.2	3.7
V	199	152	254	316	403	326	39	102	0	109	159	145	209	33	183	126	45	25
Cr	313	493	140	66	93	73	100	137	47	136	399	421	1193	35	41	322	39	27
Co	35	38	46	42	39	44	13	19	18	21	57	20	27	8	25	9	8	20
Ni	90	211	82	62	48	73	48	53	14	52	97	238	128	13	17	122	19	23
Cu	674	25	96	70	116	120	7	46	4	61	36	19	10	14	21	14	5	56
Zn	132	67	111	90	149	102	47	56	19	54	58	102	74	50	78	55	34	50
Ga	15	13	15	19	20	18	9	11	3	11	14	11	15	18	16	13	18	4
Rb	20.9	39.5	55.5	72.0	46.8	22.8	115.6	64.6	12.3	44.0	7.3	67.1	61.2	87.4	151.4	42.5	163.1	20.7
Sr	210.6	251.0	84.5	89.7	197.4	285.1	70.4	83.8	343.8	41.7	241.6	32.3	173.5	40.5	48.7	170.0	175.2	23.1
Y	17.84	22.58	21.17	35.87	48.47	35.12	12.89	14.49	3.36	17.14	28.91	22.71	34.63	26.02	19.44	24.65	37.80	5.09
Zr	64.2	73.4	89.9	173.3	136.0	153.1	82.3	73.0	12.9	76.0	165.0	94.3	256.1	240.3	154.4	156.5	256.0	41.9
Nb	4.31	7.82	5.93	14.25	16.04	15.35	5.29	6.79	0.59	3.54	4.87	5.13	15.18	13.31	13.02	4.86	14.95	1.40
Cs	0.7	2.3	2.9	2.9	2.0	1.1	5.6	3.1	1.3	2.2	0.4	4.2	3.7	2.4	3.5	2.5	4.2	1.2
Ba	167.9	273.1	413.0	1045.0	530.0	236.1	1027.4	414.4	269.2	304.2	345.4	50.9	356.5	435.2	799.0	498.6	510.7	319.8
La	10.61	9.22	10.15	19.84	20.02	20.02	12.49	13.78	1.67	13.19	29.96	11.24	32.94	26.71	35.97	25.13	35.92	5.13
Ce	22.85	19.30	22.82	46.97	42.48	45.28	23.27	30.62	3.35	29.82	62.75	24.93	74.00	62.31	72.45	54.14	79.15	9.64
Pr	2.88	2.68	3.24	5.94	6.29	5.99	3.03	3.50	0.42	3.46	7.50	3.09	8.91	7.29	8.50	6.52	9.42	1.27
Nd	11.35	11.19	13.99	23.86	26.69	23.75	11.20	12.82	1.69	13.03	28.01	11.91	31.61	26.47	28.94	23.92	34.24	4.85
Sm	2.71	2.85	3.76	5.95	6.63	5.85	2.36	2.64	0.50	2.79	5.68	2.77	6.23	5.19	5.19	4.99	6.90	1.07
Eu	0.97	1.02	1.25	1.62	1.74	1.67	0.54	0.59	0.17	0.70	1.25	0.76	1.38	0.83	0.99	1.18	1.29	0.29
Tb	0.53	0.58	0.72	1.08	1.25	1.05	0.36	0.41	0.12	0.46	0.78	0.63	0.92	0.70	0.58	0.71	0.99	0.15
Gd	3.15	3.23	4.02	6.36	7.00	6.25	2.34	2.46	0.67	2.61	4.87	3.11	5.46	4.28	3.94	4.34	5.95	0.97
Dy	3.36	3.67	4.35	6.92	7.79	6.76	2.24	2.71	0.72	2.90	4.90	4.04	6.20	4.54	3.44	4.39	6.11	0.92
Ho	0.71	0.78	0.92	1.43	1.65	1.40	0.46	0.56	0.13	0.59	0.98	0.85	1.32	0.98	0.72	0.87	1.22	0.19
Er	1.98	2.14	2.54	4.01	4.55	3.99	1.34	1.64	0.30	1.60	2.69	2.35	3.80	3.10	2.11	2.33	3.37	0.52
Tm	0.29	0.34	0.41	0.59	0.73	0.59	0.20	0.25	0.04	0.26	0.43	0.37	0.58	0.51	0.32	0.37	0.56	0.08
Yb	1.82	2.14	2.62	3.71	4.48	3.78	1.28	1.61	0.29	1.77	2.95	2.42	3.70	3.57	2.17	2.58	4.12	0.56
Lu	0.27	0.32	0.39	0.56	0.68	0.58	0.20	0.25	0.05	0.27	0.44	0.37	0.57	0.55	0.34	0.45	0.69	0.08
Hf	1.76	1.64	2.75	4.75	3.51	4.16	2.21	2.00	0.37	2.02	4.28	2.47	6.87	6.83	4.18	4.22	6.89	1.02
Ta	0.24	0.48	0.37	0.87	0.94	0.92	0.40	0.45	0.04	0.24	0.36	0.35	1.00	0.89	0.89	0.34	1.04	0.10
Pb	3.5	7.5	7.7	4.1	11.9	8.8	9.3	9.6	25.7	5.0	3.3	15.6	14.1	5.4	13.8	24.8	13.2	11.4
Th	2.30	1.48	0.98	5.29	3.63	3.23	5.04	5.59	0.51	5.07	9.19	4.03	14.62	10.39	15.78	8.73	10.29	1.71
U	0.56	0.69	0.38	1.20	1.03	0.91	1.14	0.64	0.03	0.63	1.63	0.93	1.57	1.31	1.91	2.70	2.49	0.39

Table 4.4. continued.

	GBMS	Other				
	Q98-150	Q98-131	Q98-133	Q98-138	Q02-11	Q02-08A
Rock type	B/S	G/S	B/S	B/S	G/S	Ec
wt%						
SiO_2	53.29	55.38	45.12	48.56	58.94	49.81
TiO_2	1.18	0.32	2.50	0.09	0.89	1.47
Al_2O_3	16.82	13.78	21.01	4.91	16.01	13.21
Fe_2O_3	14.71	10.15	15.21	39.47	9.27	10.38
MnO	0.27	0.14	0.10	0.74	0.19	0.31
MgO	4.71	12.61	3.66	2.77	7.28	5.35
CaO	3.33	2.08	1.79	0.60	2.14	13.35
Na_2O	1.85	4.99	3.17	2.18	4.42	4.22
K_2O	3.52	0.43	5.95	0.57	0.71	0.28
P_2O_5	0.32	0.13	1.47	0.10	0.15	1.61
Total	100.00	100.00	100.00	100.00	100.00	100.00
ppm						
Sc	24.2	31.7	31.8	26.6	19.0	28.1
V	160	161	173	156	133	227
Cr	147	258	176	6749	495	457
Co	23	24	34	238	33	32
Ni	69	97	66	4492	289	117
Cu	67	52	24	10	33	17
Zn	75	41	126	168	85	48
Ga	16	10	24	6	17	17
Rb	46.3	7.5	85.3	8.2	26.1	5.6
Sr	168.7	66.7	154.4	8.1	113.7	292.1
Y	31.73	5.41	27.37	4.37	10.34	27.15
Zr	170.2	33.6	356.6	17.1	90.6	55.6
Nb	15.26	0.59	92.89	0.18	6.94	4.40
Cs	2.7	0.9	3.7	0.5	1.6	0.3
Ba	265.9	113.1	1300.7	176.9	228.2	57.9
La	16.91	0.62	87.38	1.47	20.56	16.05
Ce	39.11	1.70	183.59	0.90	44.08	34.71
Pr	4.86	0.26	21.87	0.26	5.39	4.80
Nd	18.28	1.29	77.42	1.01	19.93	20.63
Sm	4.25	0.47	12.64	0.24	3.94	5.64
Eu	1.22	0.18	3.38	0.09	0.86	1.67
Tb	0.82	0.14	1.13	0.06	0.44	0.89
Gd	4.56	0.70	8.72	0.32	3.12	5.94
Dy	5.57	0.95	6.10	0.45	2.22	4.72
Ho	1.23	0.21	1.13	0.11	0.42	0.91
Er	3.74	0.63	2.91	0.36	1.18	2.42
Tm	0.58	0.10	0.41	0.06	0.20	0.39
Yb	3.98	0.70	2.50	0.42	1.50	2.45
Lu	0.65	0.12	0.38	0.06	0.25	0.39
Hf	4.29	1.06	8.40	0.38	2.89	1.36
Ta	0.94	0.03	4.94	0.01	0.48	0.31
Pb	11.9	4.4	6.3	4.6	12.1	16.2
Th	5.97	0.13	16.57	0.26	8.68	2.72
U	1.54	0.13	3.84	0.65	1.29	1.62

Table 4.4. continued.

CHAPTER 5

MINERALOGY OF METAMORPHIC ROCKS 1: TIAN SHAN

5.1 INTRODUCTION AND AIMS

Mineral assemblages of metamorphic rocks carry important information on the nature of the protolith, and the pressure and temperature (P-T) conditions experienced by the rock. As discussed in Chapter 3 (Section 3.2.4), the issue of whether rocks from the western Tian Shan underwent ultra-high pressure metamorphism (UHPM) is highly controversial, and so it is essential that the P-T conditions of the rocks collected for this investigation are determined. Furthermore, as outlined in Chapter 2, particular trace elements are carried in particular mineral phases, and so the presence or absence of such phases will be important for interpreting trace element geochemistry.

In this Chapter the petrography of rocks collected from the western Tian Shan blueschist belt is investigated, in order to:

1) classify the rocks collected for this work. The classification aims to include rock type, e.g. meta-igneous, meta-sedimentary, and metamorphic grade, such as blueschist, eclogite. For example a blueschist with a basaltic protolith would be classified as a blueschist meta-basalt;
2) analyse mineral compositions to positively identify mineral phases;
3) determine the peak P-T conditions experienced by rocks collected for this work, compare with previous work and discuss any implications relevant to the aims of the thesis.

5.2 CLASSIFICATION: SUMMARY OF PREVIOUS WORK

From previous work (e.g. Gao et al. 1999; Klemd et al. 2002), it is clear that eclogites *sensu stricto* (i.e. garnet + clinopyroxene >70 vol% (Carswell 1990)) are very rare in the western Tian Shan blueschist belt. Furthermore, mineral assemblages in general are highly variable such that it has not been possible for previous workers to classify rocks simply as greenschists, blueschists or eclogites. Consequently many

classification schemes have been developed to describe rocks from the western Tian Shan blueschist belt (Table 5.1).

Reference	Rock Classification Schemes
Gao et al. (1999)	1) omphacite-garnet epidosite; 2) garnet-omphacite bearing quartzite, and 3) metabasic blueschists, which are further subdivided into omphacite-present and omphacite-absent blueschist.
Zhang et al. (2001)	1) massive glaucophane-epidote eclogites and glaucophane-paragonite eclogites; 2) schistose or gneissic mica eclogites; 3) banded calcite eclogites; 4) pillow glaucophane eclogites; 5) garnet–omphacite quartzites.
Klemd et al. (2002)	1) garnet omphacitite; and 3) garnet-omphacite blueschists.
Zhang et al. (2002a)	Classified rocks according to field relationships as well as petrography: 1) Type I eclogites are interlayered with mafic blueschist; 2) Type II eclogites are thought to be metamorphosed pillow structures; 3) Type III eclogites are banded calcite/dolomite rocks occurring as lenticular bodies within marbles.
Gao & Klemd (2003)	Classify the rocks as: (1) eclogite; (2) epidosite; (3) omphacitite; (4) blueschist; (5) metavolcanoclastic rocks; (5) metaquartzite.
Wei et al. (2003)	Classify rocks as: (1) glaucophane-eclogite, and; (2) hornblende-eclogite

Table 5.1. Summary of different rock classification terms for metamorphic rocks collected from the western Tian Shan blueschist belt.

As can be seen from Table 5.1, there are many classification schemes for the metamorphic rocks of the western Tian Shan. These schemes are not consistent between different workers. Indeed these schemes are often further subdivided so that even individual rocks receive unique names. For the objectives of this work, such specific schemes are not required and so a simple classification scheme has been used. The scheme used aims to cover rock type (i.e. meta-sedimentary or meta-igneous), and describe the peak metamorphic facies the rocks likely experienced (e.g. blueschist, eclogite). In this respect, the classification scheme here used most closely resembles that of Gao & Klemd (2003).

5.3 CLASSIFICATION OF ROCKS COLLECTED FOR THIS WORK

5.3.1 META-SEDIMENTARY ROCKS

To a first order, meta-sedimentary rocks can be recognised by their high modal quartz and carbonate contents. The meta-sedimentary rocks have very heterogeneous mineral assemblages, which display no evidence of having been partially melted (i.e. these rocks are not migmatites). Some rocks are almost pure carbonates, and others are mixtures of carbonate, quartz and other silicates such as chlorite. The meta-sedimentary rocks can be split into three general groups:

1) glaucophane-bearing meta-sedimentary (GBMS) rocks, some of which are interpreted as originally being volcanoclastic rocks;
2) glaucophane absent meta-sedimentary (GAMS) rocks;
3) marble.

5.3.1.1 GLAUCOPHANE-BEARING META-SEDIMENTARY ROCKS

This rock type has highly variable mineral proportions. Assemblages dominated by quartz + carbonate + white mica (often K-mica) with glaucophane distributed throughout the rock, have been interpreted as meta-sedimentary, e.g. 986-1 contains ~80% quartz and can be considered a meta-quartzite. The proportion of glaucophane, and other high-pressure phases such as zoisite, varies from several volume percent to rare individual grains in garnet. When high-pressure phases are rare, they are often only recognisable with use of scanning electron microscope (SEM) techniques, such as analysing inclusions in garnet by SEM-Energy Dispersive Spectroscopy (EDS).

Glaucophane-bearing meta-sedimentary rocks are often foliated, as defined by orientated mica and amphibole grains. Other important textures include tabular inclusions of paragonite + zoisite/clinozoisite in garnet, which indicates the former existence of lawsonite (see Section 5.3.2). These rocks are also often heavily retrogressed, with chlorite replacing garnet and sodic amphibole, and albite replacing large proportions of the groundmass.

In contrast to the clearly meta-sedimentary samples, some other rocks with high modal quartz and carbonate contents also contain distinct domains with meta-igneous-like assemblages (Plate 5.1). These rocks are here interpreted as being sedimentary in origin, perhaps originally being a combination fragments of igneous rock combined with carbonate and other sedimentary material (e.g. quartz). The term meta-volcanoclastic is used to describe these rocks. In support of this interpretation, similar rocks, containing metamorphosed mafic and calcareous clastic domains, from the Seve Nappes of the Scandinavian Caledonides were described by Kullerud et al. (1990) who interpreted them as being pyroclastic in origin.

	GAMS		GBMS		Meta-volcanoclastic	Banded marble	
	TS02-19	TS02-13	TS02-14	TS02-18	106-03	Pelitic band	Pure carbonate
Garnet	5	5	10	10	25	10	1
Omphacite							
Blue amphibole	1		45	5	25	3	
Green Amphibole		3		5	5		
Epidote							
Clinozoisite		2			5	2	
White mica	35	25	15		10	20	
Chlorite	5	5	4	10	1	5	
Quartz	30	25	15	25	15	10	
Albite	20	25	4	30	5	5	
Rutile					2		
Titanite	1	2	2	2	2	1	
Carbonates	1	5	2	5	2	40	99
Opaques	2	3	2	4	3	4	

Table 5.2 Summary table of sedimentary rocks with selected samples of each rock type. Mode estimates (in vol%) were derived by visual estimation. GAMS = Glaucophane Absent Meta-sedimantry rocks; GBMS = Glaucophane Bearing Meta-sedimentary rocks.

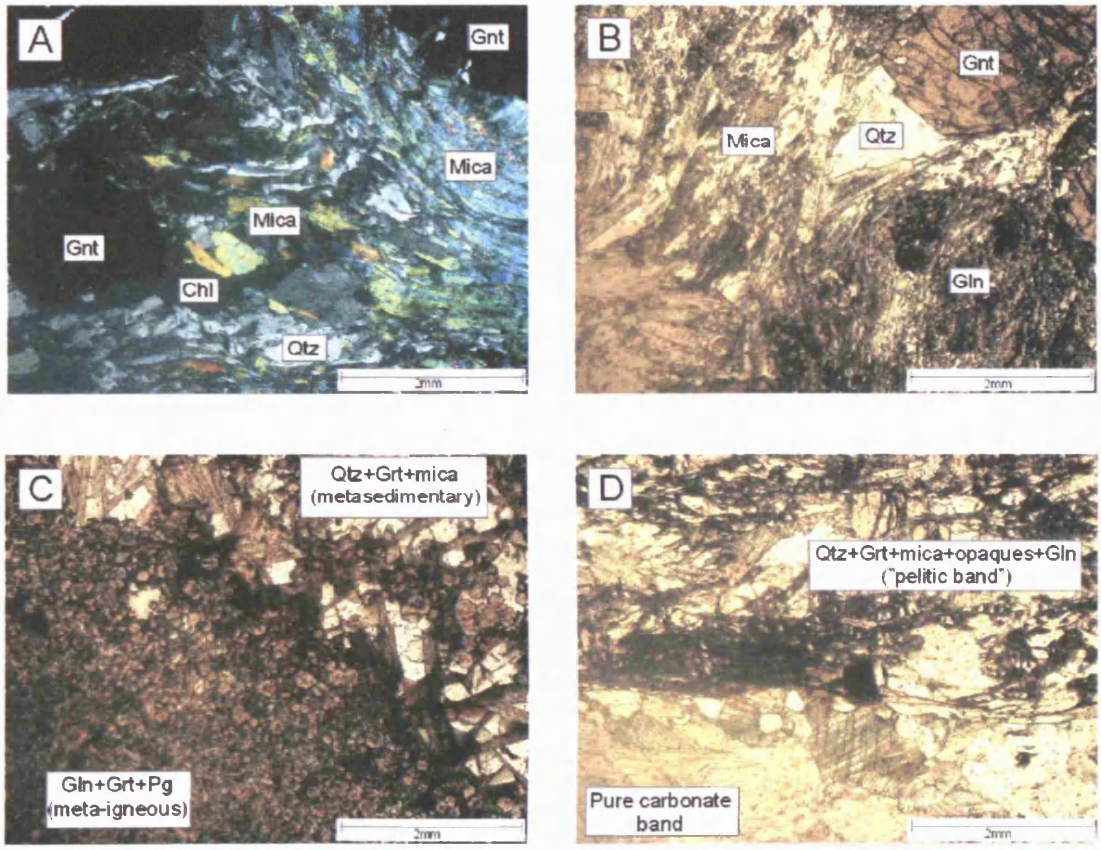


Plate 5.1. Photomicrographs of representative meta-sedimentary rocks. A) Photomicrograph taken in crossed polars of a GAMS showing the general mineral assemblage and aligned mica, defining the foliation. B) Photomicrograph in plane-polarised light of a GBMS, showing the general mineral assemblage. Note that glaucophane and quartz occur throughout the rock, i.e. not in distinct domains as for meta-volcanoclastic rocks. C) Photomicrograph in plane-polarised light of meta-volcanoclastic rock. Note the distinct differences between meta-sedimentary (i.e. large proportions of quartz+mica+garnet) and meta-igneous domains (i.e. with the assemblage glaucophane+garnet+white mica+clinozoisite). D) Photomicrograph taken in plane-polarised light of banded marble. The relatively pure marble and pelitic bands are clearly recognisable.

5.3.1.2 GLAUCOPHANE ABSENT META-SEDIMENTARY ROCKS

This rock type is characterised by the assemblage quartz + K-mica + garnet + albite + chlorite, which is similar to the garnet-mica schists commonly associated with "Barrovian zone" metamorphism, (which is typically of higher temperature, for a given pressure, than subduction zone metamorphism). It is for this reason that the rock type has been separated from the "glaucophane-bearing meta-sedimentary rocks."

Large proportions of garnet porphyroblasts are often replaced by chlorite (see Plate 5.1). Inclusions in garnet of high P/T metamorphic index minerals, such as glaucophane, indicate that these rocks have in fact undergone subduction zone metamorphism. Other notable inclusions in garnet include rare tabular inclusions of paragonite + zoisite/clinozoisite, which indicate the former existence of lawsonite (see Section 5.3.2 for discussion of the implications of this).

5.3.1.3 MARBLE

Carbonate (i.e. dolomite and calcite) is a conspicuous component that is present almost ubiquitously in all types of samples collected for this work. Indeed, it was immediately clear in the field that marble is a very common rock type in the western Tian Shan. Almost pure marble can be found, as well as banded carbonates composed of bands of pure carbonate and bands of peltic material (see Plate 5.1D). The pelitic bands contain minerals such as glaucophane and garnet, confirming that this rock type underwent subduction zone metamorphism.

5.3.2 META-IGNEOUS ROCKS

Meta-igneous rocks are here broadly divided into two groups: blueschists and eclogites, with a small number of samples being classified as greenschists. Only a very small number of samples, however, can be termed eclogites according to the classification of Carswell (1990). This is because: 1) some of the rocks simply do not (and likely did not) contain the necessary proportions of omphacite and garnet; 2) other rocks contain significant proportions of minerals such as calcite, which effectively "dilute" the proportion of omphacite and garnet, and; 3) some rocks (which may have been eclogite) have retrogressed and contain large proportions of

retrogressive albite and Na- and/or Ca-amphiboles. For these reasons, rocks with relatively high modal proportions of garnet and omphacite are termed eclogitic, see Table 5.3.

In both blueschists and eclogitic rocks, the common rock-forming prograde minerals include sodic amphibole, omphacite, white mica, clinozoisite/zoisite, epidote, garnet, quartz and carbonates in various modal proportions (see Table 5.3). Phengitic and paragonite mica both constitute "white mica," but are indistinguishable in thin section, requiring identification by SEM-EDS. Blueschists are essentially composed of sodic amphibole, omphacite, garnet, white mica and clinozoisite/zoisite. Sample TS02-01 also contains large subhedral chloritoid porphyroblasts that engulf all other matrix minerals, indicating that these porphyroblasts are a retrogressive feature. See Table 5.3 for summary of the minerals present and mode estimates in selected blueschists.

Common accessory minerals in blueschists and eclogites include zircon, apatite, pyrite, titanite, rutile and rare barite. Allanite was also detected in some samples (by SEM EDS), where it forms the core of clinozoisite porphyroblasts. Minerals formed during retrogression are also common, the most common of which are calcic-amphiboles and albite. Titanite is also a common retrograde mineral, which replaces rutile. Based on mineral assemblages, modal proportions, and the fact that some of the samples were collected from metamorphosed pillow structures, the meta-igneous rocks are likely to be mafic in composition (e.g. they are meta-basaltic).

Texturally, the meta-igneous rocks can be described as plurifacial, i.e. their mineral assemblages are not indicative of one metamorphic facies. These rocks generally contain complex fine-grained matrices, often composed of 10-50μm grains of omphacite + sodic amphibole + Ca-amphibole + albite, which indicate the influence of multiple facies. Dispersed throughout the matrix, garnet, glaucophane and clinozoisite/zoisite often form poikiloblastic porphyroblasts of various sizes. The eclogites are essentially unfoliated, although, as reported in Gao & Klemd, (2003), phengitic mica can sometimes define a weak foliation.

	Blueschist		Eclogitic rocks	
Mineral	TS02-36	TS02-35	TS02-32a	TS02-20
Garnet	5	10	35	30
Omphacite	5	5	40	20
Blue Amphibole	50	50	10	25
Green Amphibole				
Epidote				
Clinozoisite	20	20	3	5
White mica	10	5	1	5
Chlorite				
Quartz	3	3	5	3
Albite	3	2	1	10
Rutile			2	
Titanite	2	3		
Carbonates				
Opaques	2	2	3	2

Table 5.3. Modal estimates (estimated visually) of selected blueschists and eclogitic rocks from the meta-igneous rocks. All values in vol%.

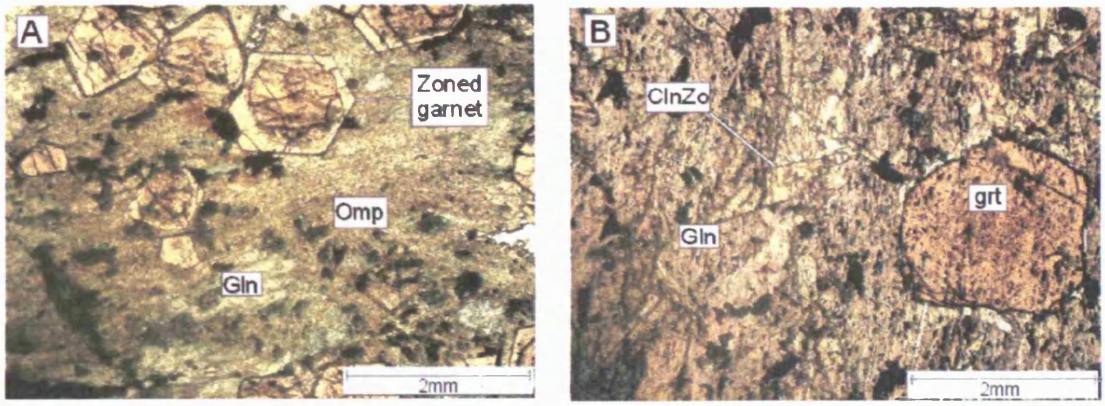


Plate 5.2 A and B. Photomicrographs of representative meta-igneous rocks. A) Photomicrograph taken in plane-polarised light of an eclogitic meta-igneous rock (TS02-32a), composed of garnet+omphacite+ glaucophane. This rock contains very small modal proportions of mica and is the only true eclogite sampled. 3) Photomicrograph taken in plane polarised light of a blueschist meta-igneous rock (TS02-35), composed essentially of glaucophane+garnet+zoisite+ white mica.

There is evidence for both late (i.e. post peak P-T conditions) and early carbonate mineralisation in these rocks. The early carbonate can be found pervasively throughout the rock, in some cases within minerals such as garnet or glaucophane. Such textures indicate the presence of carbonates (dolomite and carbonate) in the rocks prior to metamorphism. Perhaps the carbonates were incorporated into the rocks during eruption (particularly for those erupted as pillow basalts) on the seafloor, or during any post-magmatic alteration. Other carbonate minerals are found

associated with veins that cut through high-pressure assemblages, and so must post-date peak metamorphism.

Inclusions in garnets include zoisite, omphacite, glaucophane, rutile/titanite and quartz. Of particular petrological interest, however, are the common (almost ubiquitous) tabular inclusions in garnet containing clinozoisite/zoisite + paragonite ± amphibole ± quartz (Plate 5.3A). Such an association suggests that these minerals have replaced lawsonite, because: 1) lawsonite commonly displays a tabular habit; 2) inclusions of pg + czo can be formed by the breakdown of lawsonite according to the following reactions (after Heinrich & Althaus 1988):

1) lawsonite + jadeite → paragonite + clinozoisite + H_2O + Qtz;
2) lawsonite + albite → paragonite + clinozoiste + H_2O + Qtz.

The location of these reactions in P-T space has been investigated (e.g. Heinrich & Althaus 1988; Tropper & Manning 2004) and can used to place constraints on the P-T path of a given rock (see Section 5.5.2)

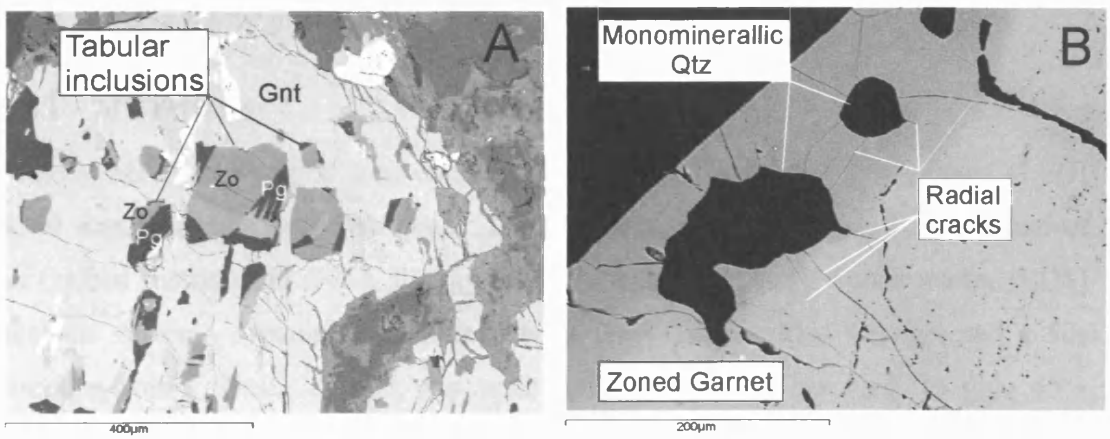


Plate 5.3.A & B. Back Scattered Electron (BSE) images of examples of inclusions in garnet. A) Tabular inclusions of paragonite + clinozoisite/zoisite in garnet. B) Inclusions of mono-minerallic quartz surrounded by radial fractures in the rim of zoned garnet.

Another notable inclusion in garnets, shown in Plate 5.3B, is quartz surrounded by radial cracks. Such inclusions occur in a very limited number of samples, with the best examples in sample TS02-32a. Radial cracks surrounding quartz inclusions in garnet are significant because they can indicate the transformation of the high-P

polymorph coesite to lower-P quartz polymorphs during decompression (e.g. Chopin 1984). As coesite is an index mineral for ultra-high pressure metamorphism (e.g. Schreyer 1995), it is important to determine whether these cracks did in fact result from the transition coesite-quartz.

Two other characteristics, in addition to radial cracks in garnet, can also be associated with the coesite-quartz transition. These include: 1) coesite relicts in the quartz inclusions; 2) palisade (i.e. radiating quartz fibres) quartz surrounding a core of polycrystalline quartz (± coesite relicts). However, analysis by SEM-EDS and optical microscopy have established that the radial cracks surround pure silica monominerallic inclusions, i.e. there is an absence of any other minerals, including coesite relicts. Furthermore, the texture of palisade quartz surrounding a core of polycrystalline quartz is absent. This, at least to a first order, may indicate that coesite did not form in these rocks, although it is possible to produce a single crystal of quartz via sequential changes of coesite given sufficient retrogression (e.g. Mosenfelder 1997; Zhang et al. 2003a).

5.4 MINERAL CHEMISTRY

5.4.1 METHODS

Mineral chemical analysis was completed using the Cambridge Instruments (LEO) S360 scanning electron microscope. The analytical instrumentation is comprised of an Oxford Instruments INCA Energy Energy Dispersive X-ray Spectrometry (EDS) analysis system. Operating conditions were 20kV accelerating voltage, and a 50s counting time. Beam current was optimised, using a Co standard, to give 45% deadtime. Raw data was corrected using a ZAF correction (Z = atomic number correction; A = absorption correction; F = fluorescence correction) procedure, performed by INCA Energy+ software. Calibration of the instrument was achieved using natural and synthetic standards provided by Micro-Analysis Consultance LTD.

5.4.2 GARNET

The full range of garnet analysis, from meta-igneous and meta-sedimentary rock types, are shown in Figure 5.1, see APPENDIX 2, for the complete garnet dataset, and

mineral formula calculations. Garnet compositions correspond with the Group C eclogite classification of Coleman (1965), with compositions of <30 mol% pyrope. In most meta-igneous rocks, garnets are zoned from core to rim, which is expressed chemically by a distinct increase of the pyrope content and a slight increase in the content of Grs + And (see the schematic vector in Figure 5.1). Such an increase in Mg (pyrope) content, from core to rim, has been described by previous workers for similar rocks of the western Tian Shan, and is thought to represent slightly increasing temperatures during slightly decreasing pressures (e.g. Klemd et al. 2003). This zonation is less apparent (and often absent) in garnets from the meta-sedimentary samples.

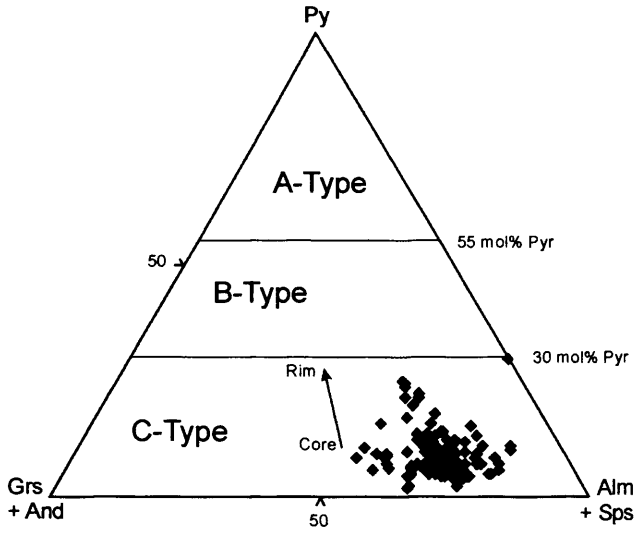


Figure 5.1 Selected garnet analyses, from data presented in Appendix 2, plotted on the Pyr-(Alm+Sps)-(Grs+And) diagram of Coleman et al. (1965). The vector arrow is a schematic representation of the general chemical difference between cores and rims of euhedral garnet grains. Py = pyrope; Grs = Grossular; And = Andradite; Alm = Almandine; Sps = Spessartine.

5.4.3 CLINOPYROXENE

The full data set and structural formula calculations for clinopyroxenes are given in Appendix 2. Most of the clinopyroxenes analysed plot in the omphacite composition field of the diagram of Morimoto (1988). A small number of samples, however, plot in the aegerine-augite field (Figure 5.2). No systematic chemical zoning was observed in the clinopyroxenes,

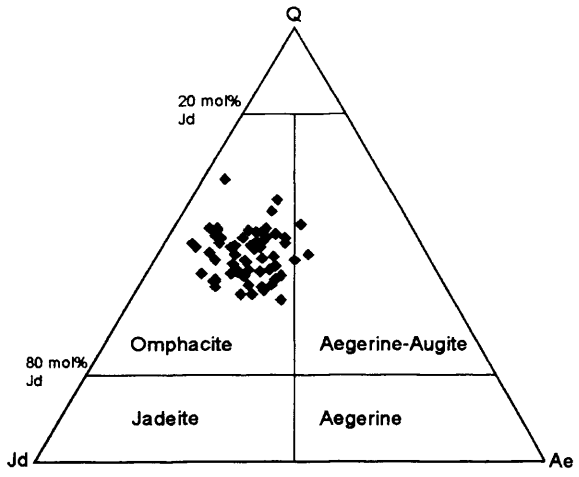


Figure 5.2 Clinopyroxene analysis plotted on the Jd-Q-Ae (Jd = jadeite, Q = wollastonite + enstatite + ferrosilite + wollastonite) diagram of Morrimoto (1988). Mineral analysis normalised according to the method presented in Morimoto (1988).

although it is apparent from analysis of multiple grains, (from one sample), that omphacite exhibits considerable chemical heterogeneity on the thin section scale. This has been observed by previous workers, who interpreted this as being indicative of chemical disequilibrium (e.g. Klemd et al. 2003).

5.4.4 AMPHIBOLE

Amphibole from blueschists, eclogites and the rare greenschists from the western Tian Shan, consists of glaucophane, actinolite and barroisite/katophorite and magnesio-hornblende, according to the general amphibole classification diagram of Leake et al. (1997) (Figure 5.3). Compositionally, blue (sodic) amphiboles in the Tian Shan rocks generally have $Al^{VI}/Fe^{3+} \geq 1$, making them glaucophane *sensu stricto*. Green amphiboles, which predominantly replace glaucophane, are highly variable in composition, ranging from Si = 7.87pfu (per formula unit) in the actinolite composition field, to Si = 6.8pfu in the barroisite/katophorite field.

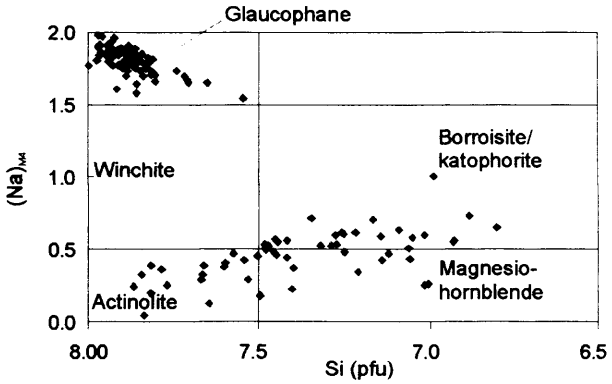


Figure 5.3. Analyses of amphibole from rocks of the western Tian Shan plotted on a diagram for the general classification of amphibole from Leake et al. (1997). Amphibole analysis normalised according to the method recommended by Leake et al. (1997). See Appendix 2, for the full amphibole analysis dataset.

5.4.5 OTHER MINERALS

White mica is predominantly paragonite in meta-igneous rocks, see APPENDIX 2, with phengitic mica rare or even absent in some samples. The Si content of phengite is variable, although always >3pfu, ranging from 3.29, to 3.63pfu. This is generally in the composition range of phengitic mica reported in previous studies of similar rocks from the western Tian Shan, although Si contents of >3.6 are rare (e.g. Gao et al. 1999; Klemd et al. 2003; Wei et al. 2003). Si-contents in paragonite range from 2.97, to 3.02 pfu and Na-contents vary from 0.79-1 pfu.

Clinozoisite is almost ubiquitous in the rocks (see APPENDIX 2 for analysis). Allanite often forms fine inclusions in the centre of zoisite. The size of the allanite

crystals, as well as their Rare Earth Element-bearing compositions, however, hampered analysis by SEM-EDS often giving totals <50% (this was also reported for allanite analysis of different rocks by Spandler et al. (2004)). A SEM-EDS profile is therefore shown in Figure 5.4 to display allanite compositions qualitatively. Albite, which is interpreted to be formed during uplift by the breakdown of Na-pyroxene or amphibole, occurs as essentially end-member (i.e. pure) as indicated by SEM-EDS spectra.

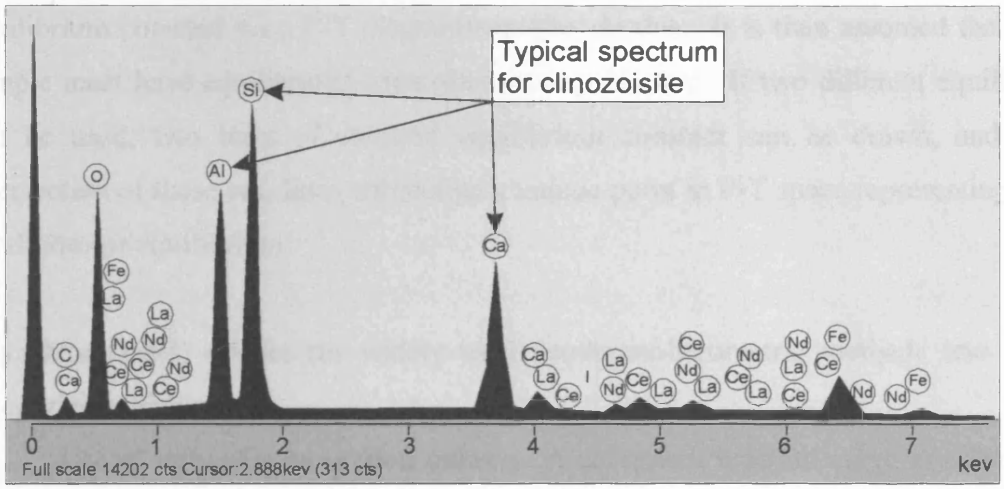


Figure 5.4. SEM-EDS spectrum profile for allanite from cores of clinozoisite. The spectrum is similar to that clinozoiste (with high count rates for O, Al, Si, Ca and Fe), but differs in that rare earth elements occur in detectable quantities in allanite.

5.5 GEOTHERMOBAROMETRY

5.5.1 INTRODUCTION

Geothermobarometry is concerned with estimating the pressure (geobarometry) and temperature (geothermometry) conditions of rock forming processes, such as metamorphism, usually through various types of mineral equilibria. Geothermobarometry is based on the fact that equilibrium constants of certain key reactions are dependent on pressure and temperature. A good geobarometer will have equilibrium constants that are strongly dependent on pressure (resulting from large volume changes between reactants and products) but not temperature. A good geothermometer will not be pressure sensitive (only small volume changes result from reactions) but be highly sensitive to temperature changes (as a result of large changes

in other thermodynamic quantities, such as entropy and enthalpy between reactants and products).

To carry out a geothermobarometric investigation, the equilibrium constant is measured by acquiring mineral composition data, using instruments such as the electron microprobe or an SEM EDS. The relevant thermodynamic quantities are known from experimental calibrations, and so it is possible to calculate P-T conditions from the measured equilibrium constant. Plotting lines of constant equilibrium constant on a P-T diagram can also do this. It is then assumed that the sample must have equilibrated somewhere along this line. If two different equilibria can be used, two lines of constant equilibrium constant can be drawn, and the intersection of these two lines will define a unique point in P-T space representing the conditions of equilibrium.

Miyashiro (1994) divides the widely used geothermobarometric methods into four categories, which are:

1) **Use of univariant reaction curves.** A univariant reaction curve is a line on phase diagram that describes the point at which a reaction will take place. Experiments designed to investigate the breakdown of certain minerals in P-T space (and the formation of others) have provided much information of the stability range of key metamorphic minerals. This is important, because if it can be demonstrated that certain reactions have taken place, then it follows that the rock must have passed through the necessary P-T conditions.
2) **Solvus geothermometers.** Under the necessary conditions (usually relatively high temperatures), usually immiscible mineral end members form homogeneous mixtures, e.g. under high temperatures, plagioclase can be soluble in alkali feldspar forming one mineral grain. If the conditions change (e.g. the temperature drops) the mineral end-members will exsolve forming two distinct substances (e.g. plagioclase and alkali feldspar mineral grains). Such exsolution is the cause of textural features such as perthites, where plagioclase exists as intergrowths within alkali feldspar. If textural features, such as perthites, can be identified in a rock, it follows that the rock must have been under the P-T conditions necessary for mineral end-member micibility at some point in its history. Such thermometers have not been used in this study.

3) **Fe-Mg exchange geothermometers.** The exchange of Fe and Mg between Fe and Mg-bearing phases (e.g. garnet and omphacite) causes little change in volume of the relevant phases, and so is not sensitive to pressure. Such reactions are, however, sensitive to changes in temperature, which has led to the development of calibrated exchange thermometers. Such an exchange thermometer has been used for this study, which is based on the exchange between Fe and Mg between omphacite and garnet.

4) **Solid-solid reaction barometers.** Many solid-solid reactions involve solid solution minerals, and are both pressure and temperature sensitive. If the temperature can be predicted (e.g. by methods utilising Fe-Mg exchange) such solid-solid reactions can be used as good geobarometers.

Three samples were selected for geothermobarometry. These are: 1) TS02-32a which contains quartz inclusions in garnet surrounded by radial cracks; 2) TS02-33, an eclogitic rock, and; 3) TS02-20, also an eclogitic rock.

These rocks were selected principally on the basis of their eclogitic assemblages (i.e. high modal proportions of omphacite and garnet), and because they are not significantly overprinted by lower-P minerals. TS02-32a was also chosen because of the presence of radial cracks surrounding quartz inclusions in garnet.

5.5.2 PARAGENETIC RELATIONSHIPS

Textural features, mineral assemblage and composition data are important in constraining the P-T path of the blueschists and eclogites collected for this work. The almost ubiquitous tabular paragonite + zoisite/clinozoisite inclusions in garnet is evidence for the previous existence of lawsonite (see Section 5.3.2). The almost ubiquitous presence of zoisite/clinozoisite + paragonite in the matrix may also have resulted from the breakdown of lawsonite in response to increasing temperature. It is therefore likely that the prograde path of these rocks followed a relatively cool geotherm that passed through the lawsonite- blueschist facies. A subsequent increase in temperature caused lawsonite to break down according to the reactions suggested in Section 5.3.2. As a number of studies have estimated the position of the reaction curves (for the lawsonite-out reactions) in P-T space (e.g. Heinrich & Althaus 1988;

Poli & Schmidt 1995), constraints can be placed on the P-T path taken by the Tian Shan rocks.

In addition to the presence of zoisite/clinozoiste + paragonite inclusions in garnet, the absence of kyanite is also important. The location of the univariant curve for the reaction: paragonite = omphacite + kyanite + H_2O in P-T space has been investigated (e.g. Holland 1970; Tropper & Manning 2004) and can be used to place constraints on the maximum pressure conditions. Others studying Tian Shan blueschists and eclogites, have used this curve to show that because kyanite is absent, P-T conditions must have been below those necessary for this reaction to have taken place. Such maximum-P predictions are, however, highly reliant on the assumed a_{H2O} and can be subject to large uncertainty, e.g. at 700°C, varying a_{H2O} from 0.2–1 can move the position of the reaction curve by approximately +1.5GPa (e.g. Tropper & Manning 2004).

The presence of coesite in the eclogitic rocks collected for this study is not confirmed, although there is a possibility that coesite reverted entirely to quartz. However the lack of kyanite, which forms from the reaction discussed above at lower pressures than coesite (see Figure 5.5), suggests that coesite was never present in these rocks.

The univariant reaction: coesite→quartz in P-T space is well constrained (e.g. Hemingway et al. 1998; see also Figure 5.5), and so the absence of coesite suggests P-T conditions below that necessary for the reaction to take place. The univariant reaction line for the transition of coesite to quartz occupies a high P-region of the P-T diagram in Figure 5.5, than the reaction Pg = Omp+Ky+H_2O, and so the observation of no kyanite is consistent with the observation of no coesite.

The eclogitic mineral assemblages of Grt+Omp+Gln+Zo/Czo+Pg±Phe corresponds to the "Glaucophane eclogite" as defined by Wei et al. (2003), which covers a temperature range from ~530-620°C and a pressure range of ~15-20Kbar. This temperature range is calculated for the full system of NCFMASH (i.e. Na_2O-CaO,FeO,MgO,Al_2O_3-SiO2-H_2O), and gives an upper temperature limit compared with the P-T pseudosections, calculated for a specified bulk composition, presented in

Wei et al. (2003). Because of the lack of kyanite, this assemblage is representative of the maximum P-T conditions experienced by the rocks in this study.

Plotting the temperature estimates based on the mineral assemblage of glaucophane eclogite from Wei et al. (2003) on a P-T diagram, which shows the P-T location of the univariant reaction lines discussed above and the facies diagram of Evans (1990), an upper-P limit of ~22Kbar is given (see Figure 5.5). This corresponds to a depth of burial of ~75Km, and is clearly not UHP.

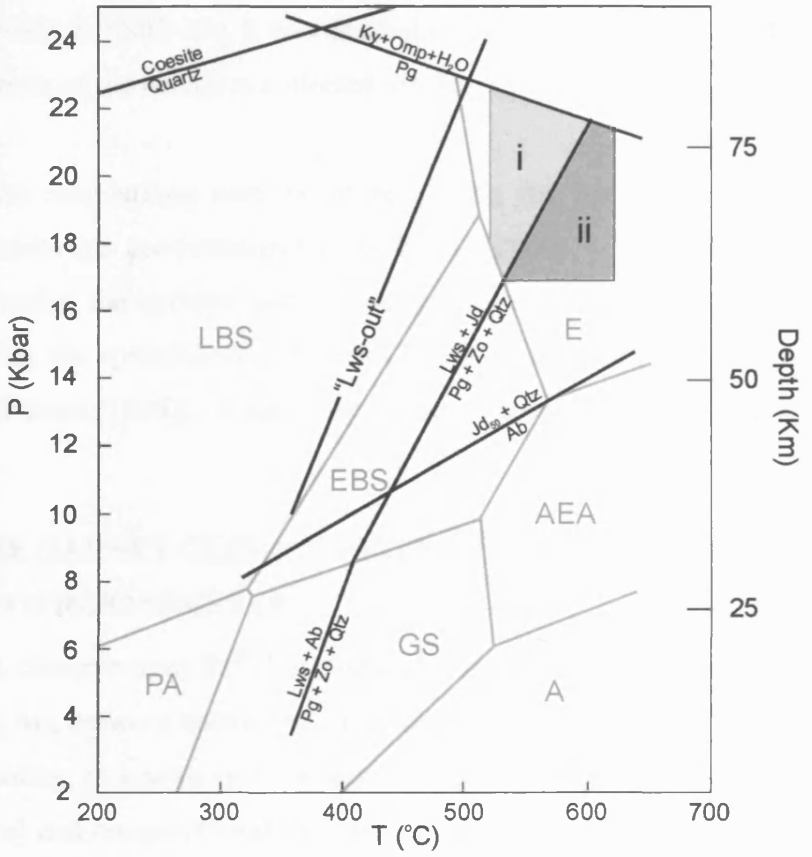


Figure 5.5. P-T estimates for rocks collected for this study based on mineral assemblage and paragenetic relationships. The shaded area covers the maximum thermal stability range for "glaucophane eclogite" as calculated by Wei et al. (2003). The lower pressure limit is set arbitrarily, as it is the maximum pressure limit that is in question. The shaded area is divided into two regions (i and ii) based on the location of the lws + jd = Pg + zo + qtz reaction curve. Note that the upper pressure limits, set by the Pg = Ky+Omp+H_2O is ~22Kbar, which is below that necessary for UHPM.

Adapted from Gao et al. (1999), with: coesite-quartz reaction curve from Mirwald and Massonne (1980); Law + Jd = Pg + Zo + Qtz and Law + Jd = Pg + Zo + Qtz from Heinrich & Althaus (1988); the "lawsonite out" curve, after Poli & Schmidt (1995), is based on the same reactions as for Heinrich & Althaus (1988). Fields for the metamorphic facies is after Evans (1990): LBS=lawsonite blueschist; EBS = epidote blueschist; AEA = albite-epidote-amphibolite facies; E =eclogite facies; A = amphibolite facies; GS= greenschist facies; PA = pumpellyite-actinolite facies.

5.5.3 GEOTHERMOBAROMETRIC CALCULATIONS

Evidence from paragenetic and textural relationships above has revealed no evidence for UHP metamorphism. However, Zhang et al. (2003b) found that use of geobarometers, such as the garnet-clinopyroxene-phengite barometer of Waters & Martin (1993), on magnesite-bearing eclogites yield P estimates of 24.6-28.9Kbar at a T range of 525-607°C. These P-T estimates were calculated for kyanite-absent paragonite-bearing rocks (Zhang et al. 2002). It may therefore be the case that evidence for UHPM metamorphism is present in compositions of relevant minerals. For this reason, and because the presence or absence of coesite cannot be ruled out unambiguously in TS02-32a, it was decided to try such methods to further confirm the P-T conditions of the eclogites collected for this work.

Temperature calculations were performed using the updated garnet-clinopyroxene Fe^{2+}-Mg exchange geothermometer of Ravna (2000). Pressure calculations were performed using the updated garnet-clinopyroxene-phengite geobarometer of Waters (1996), using the spreadsheet of Ravna (2004), (which uses different garnet activity models to Waters (1996)). A summary of these calculations is given below.

5.5.3.1 THE GARNET-CLINOPYROXENE Fe^{2+}-Mg EXCHANGE GEOTHERMOMETER

The garnet-clinopyroxene Fe^{2+}-Mg exchange thermometer is based on the partitioning of Fe^{2+} and Mg between coexisting garnet and clinopyroxene (in this case omphacite). The partitioning is known to be a function of both physical conditions (particularly temperature) and compositional variations in the phases involved (e.g. Ellis & Green 1979; Ravna 2000 and references therein). This has led to the development of a number of calibrations for the calculation of metamorphic temperatures, the most recent of which is by Ravna (2000). The equations for calculating temperatures from Ravna (2000) are:

$$T(^{o}C) = [(1939.9 + 3270X_{Ca}^{Grt} - 1396(X_{Ca}^{Grt})^2 + 3319X_{Mn}^{Grt} - 3535(X_{Ca}^{Grt})^2 + 1105X_{Mg\#}^{Grt} - 3561(X_{Mg\#}^{Grt})^2 + 2324(X_{Mg\#}^{Grt})^3 + 169.4P(GPa)/(\ln K_D + 1.223)] - 273$$

- 5.1

Where: $K_D = (Fe^{2+}/Mg)^{Grt} / (Fe^{2+}/Mg)^{cpx}$; X_{Ca}^{Grt} = Ca/(Ca+Mn+Fe^{2+}+Mg) in garnet; X_{Mn}^{Grt} = Mn/(Ca+Mn+Fe^{2+}+Mg) in garnet, and; $X_{Mg\#}^{Grt}$ = Mg(Mgt+Fe^{2+}) in garnet.

In the case of element partitioning, the equilibrium constant is expressed as the "distribution coefficient." The distribution coefficient (K_D) for the partitioning of Fe^{2+} and Mg (i.e. ln K_D) is calculated using the expression:

$$\ln K_D = \ln [(Fe^{2+}/Mg)^{Grt}/(Fe^{2+}/Mg)^{cpx}]$$

- 5.2

5.5.3.2 THE GARNET CLINOPYROXENE-PHENGITE BAROMETER

The Garnet-Cpx-Phengite barometer is based on the following reaction between minerals commonly associated with eclogites (Ravna & Terry 2004):

6diopside + 3muscovite = 2grossular + 1pyrope+ 3celedonite

The reaction shown above produces the celedonite end member (a mica-end member richer in Si than pure muscovite). During increasing compression, the proportion of celedonite increases in muscovite. Muscovites with high celedonite contents are termed phengites, and it is the celedonite component that is often measured indirectly by measuring the Si-content of muscovite.

A calibration for the above reaction was provided by Waters & Martin (1993) based on the thermodynamic data of Holland & Powell (1990).

$$P(kbar) = 28.050 + 2044T - 0.003539T \,.\, \mathrm{Ln}K$$

- 5.3

Where T = temperature in Kelvin.

ln$K$ is calculated using the equation:

$$\ln K = 6 \ln a_{prp} - \ln a_{prp} - 2 \ln a_{grs} + 3 \ln\left(\frac{X_{Al,M1}.(4-Si)}{X_{Mg,M1}.(Si-2)}\right)$$

- 5.4

Where: $\ln a_{di}$ is the activity (i.e. a thermodynamic quantity expressing the effective concentration of a substance in a system) of diopside; $\ln a_{prp}$ and $2\ln a_{grs}$ refer to the activities of the respective garnets.

Si = silicon atoms per formula unit of a mica analysis normalised to 12 oxygens. $X_{Al,M1}$ and $X_{Mg\ M1}$ refers to the proportion of Al and Mg on the M1 cation sites of the mica molecule.

For this work, a spreadsheet constructed by Ravna (2004) has been used, which calculates the interception of the lines of constant equilibrium constant between the garnet-clinopyroxene geothermometer, and the garnet-pyroxene-phengite geobarometer. A modification to this spreadsheet has been made so that it can calculate temperatures assuming all Fe as Fe^{2+}. The following activity models are used by this spreadsheet:

1) the activity model for the phengite solid solution of Holland & Powell (1998);
2) the clinopyroxene activity model of Holland (1990);
3) the garnet activity model of Ganguley et al. (1996).

5.5.3.3 ERROR ESTIMATIONS

Because of the inherent limitations in data quality of SEM-EDS techniques compared with electron microprobe techniques (e.g. see Waters 2004), the P-T estimates of this section are not intended to be definitive. The principal aim of performing these calculations is to further establish whether or not these rocks have undergone UHPM, not to define the P-T conditions to within a few °C or kbar. However, care has been taken to estimate the margin of error for the P-T estimations calculated in this section.

Errors have been estimated for the calculated P-T conditions by using:

1) the variation of calculated P-T estimates for omphacite-garnet pairs of each individual sample.
2) the error calculated for the intersection of geobarometer and geothermometer published in Ravna & Terry (2004).

By considering the two aspects above errors for precision 1) and accuracy 2) are estimated. It is suggested that by combining 1) and 2), maximum error is estimated, which will cover the following factors (after Waters 2004):

1) **Uncertainty related to the thermobarometric calculation.** This can result from uncertainties in the position in P-T space of equilibrium between phases, and can be considered an accuracy error. If a calibration has been derived from a self-consistent thermodynamic data set, it can be possible to estimate this uncertainty. In this study, the errors calculated using the program THEROCALC of Ravna & Terry (2004) have been used.
2) **Uncertainty related to mineral chemical analysis.** This uncertainty is related to the accuracy of the analysis of minerals by electron probe techniques.
3) **Uncertainty in the relationship between activity and composition.** This is uncertainty is difficult to quantify, and may result from inappropriate assumptions in calculations used to estimate activity from compositions.
4) **Geological error.** These are "human errors" introduced by selection of, for example, mineral phases that were not in chemical equilibrium at the stage of interest in the rock's history. Alternatively, these errors could arise by the rock not being fully equilibrated.
5) A large additional source of error is with the estimation of Fe^{2+} and Fe^{3+}. For example, Ravna (2000) stated, "...Fe-poor omphacites (in some eclogites) are notoriously problematic, as even fairly small variations in any of the analysed elements may give substantial variations in the calculated Fe^{2+}/Fe^{3+} ratio based on stoichiometry." In terms of calculated temperatures, Ravna (2004) shows how this problem can lead to temperature estimates (using the Grt-Cpx Fe-Mg exchange thermometer (of Ravna 2000)) to vary from ~650 to 920°C using homogeneous omphacite from a single sample. As P-T estimates in this work are estimated by the interception of equilibrium curves for the geotheromometer and the geobarometer, large errors on both P and T will likely result.

It became clear very quickly that the results of geothermometric calculations are highly sensitive to estimates of Fe^{2+} and Fe^{3+} content of omphacite. In light of problems associated with the oxidation states of Fe, two geothermometric calculation runs were performed using different assumptions: 1) all Fe in omphacite as FeO –

which appears to be the method adopted by previous workers on similar rocks (e.g. Gao et al. 1999); 2) that Fe^{2+} and Fe^{3+} can be calculated in omphacite by charge balance. The same error estimates outlined above are applied to both of these estimates.

5.5.3.4 RESULTS

Results of the calculations are presented in Table 5.4. From this Table it can be seen that sample TS02-32a gives the highest average P-T estimates, whether iron is considered as entirely Fe^{2+} or whether Fe^{2+} and Fe^{3+} are calculated by charge balance. The maximum pressure calculated for this sample is 22.4kbar. The maximum pressure calculated for the whole data set is 24.2kbar at T= 633.1°C for TS02-33, although such maximum (and minimum) P-T estimates are generally shown by a small number of "outlying" mineral pairs in each sample.

a) Fe = Fe^{2+} (total)									
		P kbar				T°C			
SAMPLE	n	Ave	Rsd	Max	Min	Ave	Rsd	Max	Min
TS02-32a	23	20.1	9.6	20.9	16.1	551.6	21.5	908.8	390.1
TS02-33	29	19.0	10.5	24.2	15.5	455.2	18.2	633.1	318.3
TS02-20	18	14.5	20.4	23.8	11.4	444.0	23.4	723.9	290.9

b) Fe = Fe^{2+} & Fe^{3+} (calculated)									
		P kbar				T°C			
SAMPLE	n	Ave	Rsd	Max	Min	Ave	Rsd	Max	Min
TS02-32a	23	19.1	6.6	22.4	17.2	441.1	15.7	644.3	325.0
TS02-33	29	18.3	7.8	22.2	15.6	348.7	15.0	445.7	249.5
TS02-20	18	15.5	14.8	23.1	13.1	349.3	29.9	701.8	265.9

Table 5.4. Average P-T interception estimates from three eclogitic samples collected from the western Tian Shan blueschist belt. Calculations assuming all Fe as FeO give higher T estimates in nearly all cases. See main text for details of calculations.

The range of P-T estimates (minus the outliers- which are here interpreted to be anomalous) are plotted on a P-T diagram in Figure 5.6 A & B along with 2σ error ellipses. From this diagram the differences in P-T estimates are readily observed. Calculations involving estimation of the oxidation state of iron yield lower-T estimates. This is apparent from Equation 5.1, where high Fe^{2+} in omphacite lowers K_D and hence raises temperature estimates. As the proportions of Fe^{2+} and $Fe^{3+}$are not actually known, the true temperature range must lie between the estimates presented in Figures 5.6 A & B (i.e. between all Fe as Fe^{2+} and $Fe^{2+} = Fe_{tot} - Fe^{3+}$).

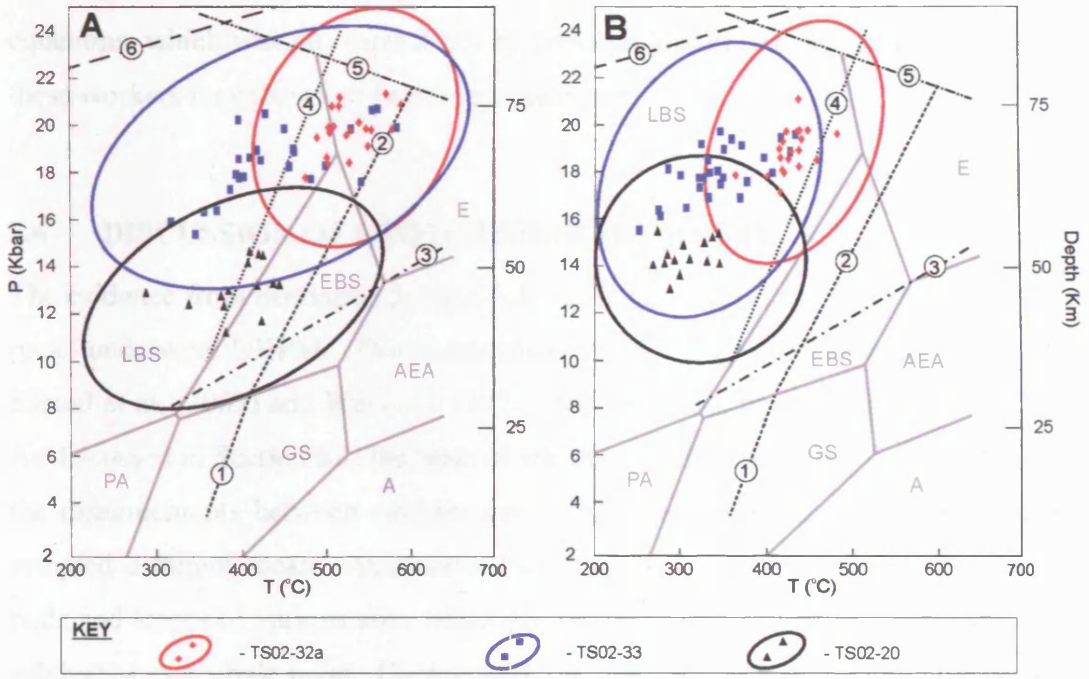


Figure 5.6 A & B. Results of P-T calculations plotted on a P-T diagram with reaction curves and metamorphic facies. **A)** Results for calculations treating Fe as $Fe^{2+}_{(tot)}$; **B)** Results for calculations using estimates of Fe^{2+}/Fe^{3+}. 2σ error ellipses are based on a combination of: 1) errors calculated by THERMOCALC for the intersection of the equilibrium curves for the geothermometer and geobarometer by Ravna & Terry (2004), and; 2) the variation in calculated P-T conditions from different mineral pairs in each sample (minus the 'outlying' samples). The reaction curves are: 1) and 2) Law + Jd = Pg + Zo + Qtz of Heinrich & Althaus (1988); 3) Alb = Jd + qtz of Holland (1983); 4) Law + Jd = Pg + Zo + Qtz of Poli & Schmidt (1995); 5) Pg = Ky + Jd+ H_2O of Holland (1979); 6) coesite-quartz reaction curve from Mirwald and Massonne (1980). Fields for the metamorphic facies is after Evans (1990): LBS=lawsonite blueschist; EBS = epidote blueschist; AEA = albite-epidote-

Using the average values for TS02-32a calculated for estimated Fe^{2+} and Fe^{3+} and Fe as FeO_{tot} respectively, the maximum P-T conditions are T = 441.1-551.6°C and P = 19.1 - 20.1kbar. Such estimates are not consistent with UHPM, as even the maximum pressure estimates (shown by the anomalous mineral pairs) do not indicate unambiguous UHPM (i.e. >25kbar). These pressure estimates compare well with results from some previous workers who put maximum pressures at ca 21kbar (e.g. Gao et al. 1999; Klemd et al. 2003; Wei et al. 2003). The P-T conditions calculated in this section also compare well with the limits suggested by paragenetic relationships in Section 5.5.2. However, temperature estimates from this study (especially from calculations using estimated Fe^{2+} and Fe^{3+}), are generally below that of previous workers who estimate temperatures of ca. 580°C at ~20kbar (e.g. Gao et al. 1999; Klemd et al. 2003; Wei et al. 2003). The lower T estimates of this study are the result

of using estimates of the proportions of Fe^{2+} and Fe^{3+} in omphacite in the P-T equations, which was not carried out by previous studies. Temperatures reported by these workers may therefore be overestimates.

5.6 DISCUSSION OF GEOTHERMOBAROMETRY

The evidence from Sections 5.5.2 and 5.5.3 does not support the proposition that these rocks underwent UHPM. This is consistent with finding of Gao et al. (1995, 1999) Klemd et al. (2002) and Wei et al. (2003), but not Zhang et al. (2002a, 2002b, 2003). As discussed in Section 5.1, the issue of whether UHPM took place is contentious and the disagreements between workers may simply be explained by the fact that they sampled different rocks. As described in Chapter 3, eclogites and blueschists form pods and lenses of various size, which presumably requires that these rocks were not subducted as a single mass. Consequently, it is not the case that that all the pods and lenses necessarily subducted to the same depths. Thus, there may be rare pods and lenses containing UHP eclogites that were sampled by some workers, but not others (including the contributors to this work).

There is also evidence that temperatures have been overestimated by previous workers, who seem to have assumed all Fe to be Fe^{2+} in their geothermometric calculations. Lower peak temperatures may also be supported by the differences in the position of the Law+Omp = Zo+Pg+H_2O reaction curves. The more recent estimates of the position of this curve, that of Poli & Schmidt (1995) for basaltic systems, is close to 100°C lower than that of Heinrich & Althaus (1988) at 20Kbar. The lower-T limit may therefore be ~100°C below that predicted by the lawsonite-out reaction curve of Heinrich & Althaus (1988) based on paragentic relationships, as used by some previous workers (e.g. Gao et al. 1999; Klemd et al. 2003).

5.6.1 IMPLICATIONS FOR THIS INVESTIGATION

The lack of any evidence for UHPM in the rocks collected from the western Tian Shan, has important implications for the original aims of this work. It was initially supposed that UHP eclogites would be sampled, and that these would be analogous of rocks that subduct beyond the Benioff-zone and into the deep mantle. It is, however,

apparent that the rocks collected for this work could not have subducted to depths >>75Km, and cannot be considered analogues to oceanic crust that has passed through the "subduction filter." Consequently, the trace element geochemistry of these rocks will not necessarily reflect the net effects of subduction zone metamorphism as initially supposed.

CHAPTER 6

MINERALOGY OF METAMORPHIC ROCKS 2: QILIAN SHAN

6.1 INTRODUCTION

This chapter investigates the mineralogy of and predicts the P-T conditions reached by the metamorphic rocks collected from the North Qilian Shan blueschist belts. The aims of this Chapter, and methods used, are identical to those of Chapter 5, which investigated the mineralogy of rock collected from the Chinese Tian Shan.

6.2 METAMORPHIC ROCK TYPE CLASSIFICATION: SUMMARY OF PREVIOUS WORK

There are only two studies of the mineral assemblages of metamorphic rocks from Qilian Shan that are available in English, i.e. Wu et al. (1993) and the field trip guide of Song (1996), which is largely based on Wu et al. (1993). The following summary draws almost exclusively from these references (other references are cited where necessary).

6.2.1 SOUTHERN HIGH-GRADE BLUESCHIST BELT

Previous studies have used a relatively simple classification scheme to describe the rocks from the high-grade blueschist belt, namely: 1) meta-mafic blueschists and eclogites; 2) meta-siliceous blueschists, and; 3) meta-greywacke blueschists.

Meta-siliceous rocks have the assemblage phe + qtz ± gln ± gnt ± cld. The meta-greywackes have the assemblage gln + phe + gnt + alb + qtz, with very high proportions of phengite and quartz. Blueschist meta-mafic rocks have the assemblage gln + ep + chl + alb ± phe ± gnt. The eclogites can be subdivided into: 1) schistose eclogite with the assemblage gnt + cpx + gln ± phe ± phe, and; 2) granular eclogite with weaker schistosities and an assemblage of gnt +cpx ± gln. Both kinds of eclogite have been strongly overprinted by greenschist facies minerals, such as chlorite, actinolite and albite.

6.2.2 LOW GRADE BELT

The low-grade belt consists of blueschists and lower-grade metamorphic rocks, such as greenschists and rocks of the prehenite-pumpellyite facies. Importantly, the blueschists contain lawsonite, which is not reported in rocks of the higher-grade belt. There are three important mineral assemblages that characterise the mafic meta-igneous rock, of the low-grade blueschists:

1) pumpellyite + glaucophane + chlorite + albite + quartz;
2) pumpellyite + glaucophane + chlorite + albite;
3) glaucophane + lawsonite.

High-pressure minerals, such as glaucophane, rarely appear in meta-sedimentary rocks of the low-grade belt and have typical assemblages of chlorite + epidote + muscovite + albite + quartz.

6.3 CLASSIFICATION OF ROCKS COLLECTED FOR THIS WORK

6.3.1 META-SEDIMENTARY ROCKS

The meta-sedimentary rocks of this study are similar to those collected by previous workers. The classification of these rocks in this work, however, follows that of Chapter 5, where siliceous meta-sediments were divided into glaucophane-bearing and glaucophane-absent (i.e. garnet-mica schists) rock types.

Only one meta-sedimentary sample was recovered from the low-grade belt, the sample consisting essentially of quartz + white mica + accessory minerals such as zircon. No other HP-LT index minerals, such as glaucophane or lawsonite, are present in this meta-siliceous sample. Meta-sedimentary samples with high-pressure index minerals are common in the high-grade belts. These rocks have variable proportions of the minerals qtz + phe + gln + chl (see Table 6.1 and Plate 6.1 A). Garnet-mica schists (GAMS) from the high-grade belt are dominated by the assemblage qtz + phe + gnt, with garnet replaced by chlorite in various proportions (see Table 6.1 and Plate 6.1 B).

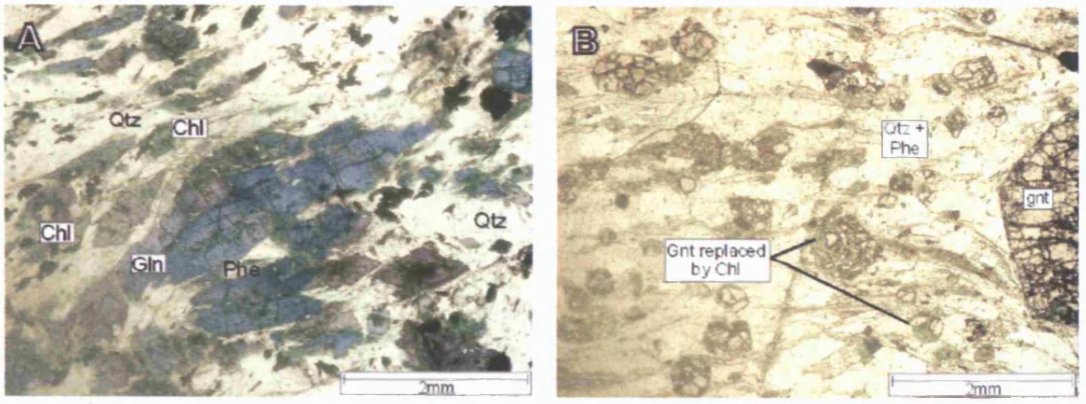


Plate 6.1 A & B. Photomicrographs of representative meta-sedimentary rocks. A) Photo-micrograph taken in plane polarised light of a glaucophane-bearing meta-greywacke with the assemblage Qtz + Phe + Gln + Chl. B) Photomicrograph taken in plane-polarised light of a glaucophane-absent meta-greywacke with the assemblage Qtz + Phe + Gnt + Chl.

	Glaucophane-bearing		**Glaucophane-absent**	
	Q98-143	Q98-136	Q98-142	Q98-121
Garnet		2		10
Omphacite				
Blue Amphibole	15	20		
Green Amphibole		2		
Epidote				
Clinozoisite				
White mica	35	40	5	15
Chlorite		3		5
Quartz	40		80	60
Albite	2			2
Rutile				1
Titanite	1	1		
Carbonates	5		10	
Pumpellyite				5
Opaques	2	2	5	2

Table 6.1. Modal estimates (performed by visual estimation) of representative meta-sedimentary rocks. All values in volume %.

6.3.2 META-IGNEOUS ROCKS

The meta-igneous blueschists and eclogites are similar to those collected by other workers (as summarised in Section 6.2). Based on mineral assemblages (particularly the relatively small modal proportion of quartz), the rocks are meta-mafic blueschists and eclogites.

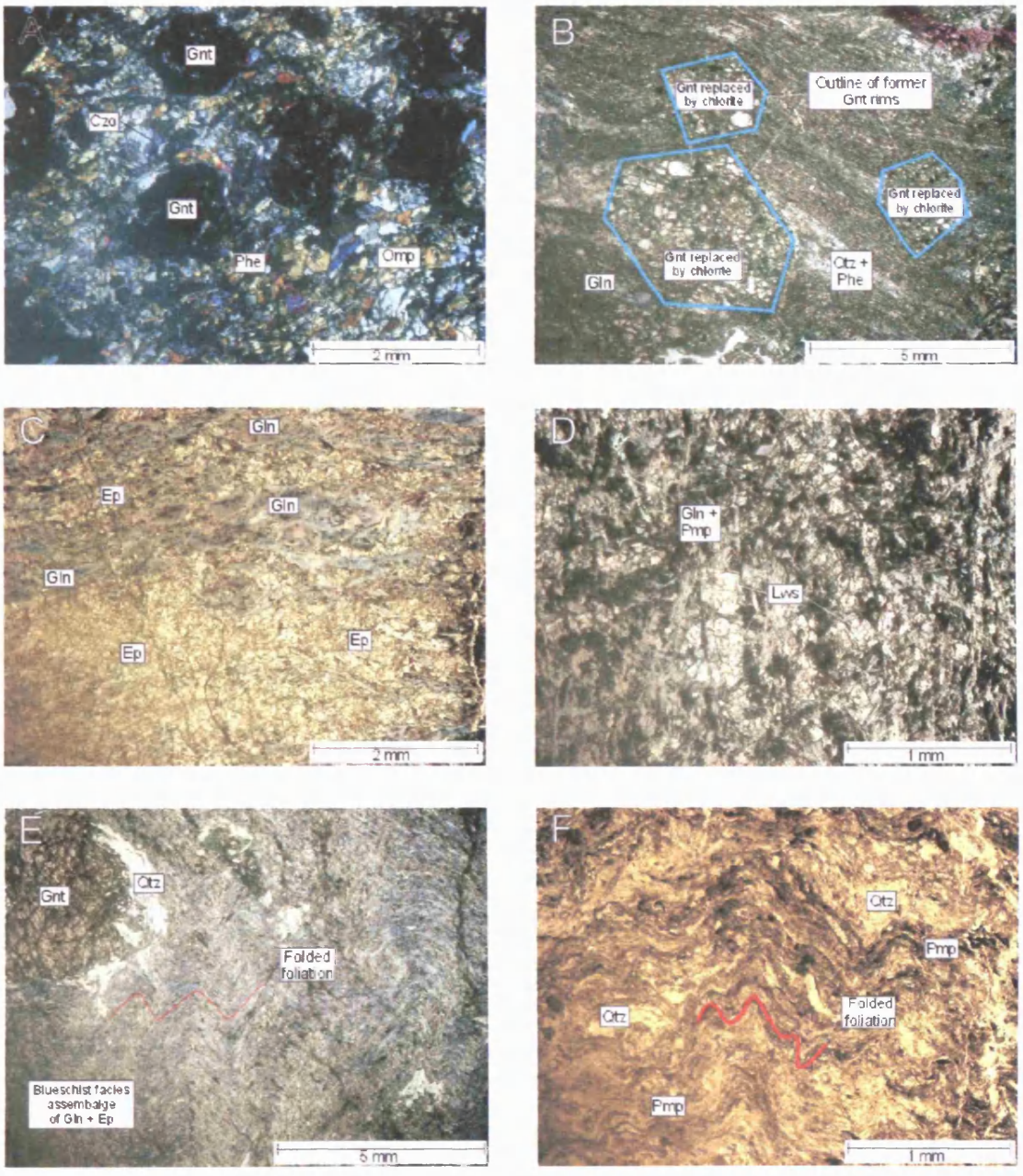


Plate 6.2 A-F. Photomicrographs of representative meta-igneous rocks. A) Photomicrograph taken in crossed polars of the only "fresh" eclogitic assemblage collected from Qilian Shan for this study. B) Photomicrograph taken in plane-polarised light (PPL) of a retrogressed eclogite. Garnets in this rock type are often replaced by large proportions of chlorite. The groundmass, however, is still made up of large proportions of glaucophane and omphacite. C) Photomicrograph taken in PPL of the common blueschist assemblage of glaucophane + epidote. D) Photomicrograph taken in ppl of an example of a blueschist from the Low-grade blueschist belt. This sample essentially consists of lawsonite + glaucophane + pumpellyite. E) Photomicrograph of a garnet-bearing blueschist taken in PPL. This sample has been deformed at least two times, with a foliation (as defined by epidote and glaucophane) being folded to develop a weak crenulation cleavage. F) Photomicrograph taken in PPL of an example of a sample from the prehenite-pumpellyite facies (from the low-grade blueschist belt) showing textures consistent with multiple deformation stages. The foliation is folded forming a crude crenulation cleavage.

	Low-grade blueschist	High-grade blueschist	Garnet blueschist	Fresh Eclogite
	Q02-34	Q02-22	Q98-135	35
Garnet			10	40
Omphacite				2
Blue Amphibole	30	50	45	
Green Amphibole				
Epidote		40		
Clinozoisite				5
White mica		5	25	10
Chlorite			4	1
Quartz			10	3
Albite	5	2		
Rutile				1
Titanite		1	3	
Carbonates				
Opaques	5	2	3	2
Pumpellyite	35			
Lawsonite	25			

Table 6.2. Modal estimates for meta-igneous rocks from Qilian Shan. All values are vol% and have been estimated visually. Low-grade blueschist refers to a lawsonite-bearing blueschist from the low-grade blueschist belt. All other samples from the high grade belts.

6.3.2.1 HIGH-GRADE BELT

The high-grade blueschists are predominantly composed of the assemblage gln + ep + chl ± gnt ± czo, with rut + ttn + zrn as the more common accessory minerals. In contrast to rocks of the Chinese Tian Shan, these rocks commonly lack paragonite, and the principal mica is phengitic (as indicated by SEM-EDS). Furthermore, there is no evidence for lawsonite (e.g. tabular inclusions of Pg + Czo in garnet) in the high-grade mafic rocks. Minerals formed during retrogression, most commonly chlorite, often replace prograde minerals such as glaucophane and garnet.

Although not ubiquitous (see Plates 6.2 A & C), these rocks often have evidence for multiple deformation events, such as folded foliations, that produce crude crenulation cleavages (see Plate 6.2 E & F). Other deformation textures include pressure shadows containing qtz ± phe around garnets, typically in foliated blueschists or eclogites.

6.3.2.2 LOW-GRADE BELT

Meta-igneous rocks of the low-grade belt have assemblages indicative of the lawsonite-blueschist facies and the prehnite-pumpellyite facies. Rocks of the blueschist facies generally consist of pmp + gln + law + ab, together with accessory titanite and magnetite (see Plate 6.2 D & F). Some rocks also contain relict igneous-

clinopyroxene. Rocks from the low-grade belt are fine-grained with lawsonite sometimes forming porphyroblasts with sizes <10mm^2 in diameter (Plate 6.2 D). Some samples have been multiply deformed with at least two stages of deformation recognisable at the thin section scale, producing a foliation that was subsequently folded (see Plate 6.2 F).

6.4 PRESSURE -TEMPERATURE ESTIMATES

6.4.1 PREVIOUS WORK P-T ESTIMATES

Using garnet-clinopyroxene geothermometry, with the calibrations of Krogh (1988), Wu et al.(1993) estimated maximum temperatures of 340 ±10°C for eclogites from the high-grade blueschist belt. Pressure estimates made using a number of geobarometers (excluding the Gnt-Cpx-Phe barometer), give a range of 8±1 kbar (Wu et al. 1993). Using the Si-content of phengite, Wu et al. (1993) obtain an upper P estimate of 9-9.5 kbar, which is considered "on the high side."

With regard to the low-grade belt, the appearance of certain index minerals, such as lawsonite and pumpellyite, were used by Wu et al. (1993) to constrain the P-T conditions to 4-7 kbar and 150-250°C, respectively.

Previous workers have not used the Gnt-Cpx-Phe geobarometer for rocks of the Qilian Shan. This is most probably because of the scarcity of fresh eclogites from which garnet-omphacite pairs can be analysed. However, a fresh eclogite was collected for this investigation, and so it is now possible to undertake a geothermobarometric investigation using the recent geothermobarometric calibrations. See Chapter 5 for an overview of the methods and calculations used.

6.4.2 P-T CALCULATIONS FOR ROCKS COLLECTED FOR THIS INVESTIGATION

6.4.2.1 PARAGENTIC RELATIONSHIPS

As with the Tian Shan rocks, minerals such as kyanite and coesite are absent from the Qilian rocks. This is a problem for upper-pressure limit estimations because the absence of lawsonite means that the reaction Law + Jd = Pg + Omp + H_2O + Qtz

cannot have been significant for these rocks. The corollary is that the univariant curve for the formation of kyanite from paragonite cannot be used to place upper pressure limits (as it is for the Tian Shan rocks). The transition, quartz-coesite, may be used as an upper pressure limit, but this reaction takes place at relatively high pressures, and so use of this transition may not yield accurate upper pressure limits.

Another potentially useful univariant reaction curve for upper pressure limit estimation is that marking the decomposition of clinozoisite/zoisite. A curve for the reaction gln+czo = gnt+omp+H_2O was given by Liu et al. (1997), but this curve has a strong negative slope in P-T space and is therefore not suitable for placing upper pressure limits. Poli & Schmidt (1997), however, plot a clinozoisite/zoisite-out reaction curve based on the reaction diopside + zoisite + $garnet_{(1)}$ = $garnet_{(2)}$ + water in the CFMASH system (the subscripts (1) and (2) refer to garnets of "composition 1" and "composition 2"). For a range of garnet compositions, the P-T conditions covered by this reaction are 15-30 kbar at 560-790°C. Because of this large pressure range (15kbar), these invariant curves may not be suitable for estimating upper pressure limits as the stability field of zoisite is "potentially huge" (Poli & Schmidt 2002), and can extend to pressure greater than the quartz/coesite transition (see Figure 8.1). Based on these various reaction curves, estimations of upper pressure limits based on paragenetic information are inherently inaccurate for rocks collected from Qilian Shan.

In terms of the P-T path, the absence of lawsonite in rocks of the high-grade belt show that they have followed a hotter geotherm than rocks the low-grade blueschist belt. Importantly however, the eclogitic mineral assemblages are similar to those of the glaucophane eclogite of Wei et al. (2003), the maximum thermal stability range of which is 530-620°C. This temperature range is used, together with the reaction curve for the transition coesite–quartz, to place upper pressure limits of ca. 25-27kbar on the Qilian eclogites (see Figure 6.1).

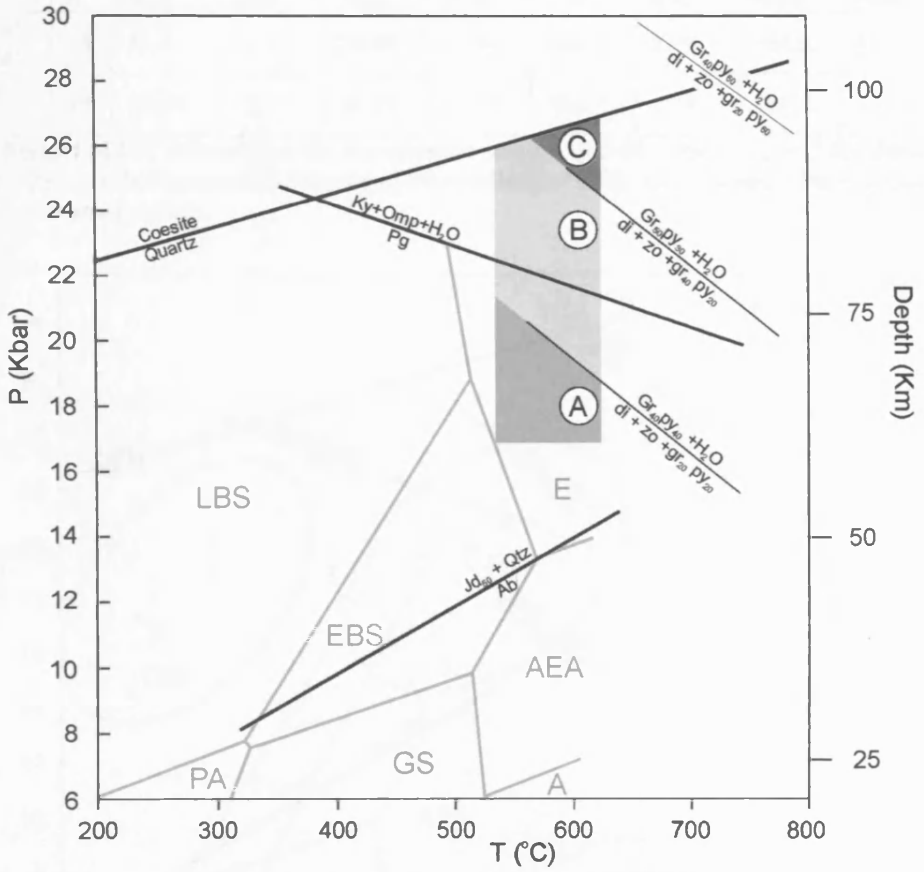


Figure 6.1 Petrogenetic grid displaying the facies diagram of Evans (1990) and petrologically significant univariant reaction curves. Shaded areas labelled A, B C refer to upper pressure limits based on the zoisite-out reaction. As can be seen, zoisite is stable over a wide range of P-T conditions. Upper pressure limits for the rocks of the North Qilian Shan are likely to be inaccurate, due to the absence of kyanite forming reactions from paragonite, the large stability field of clinozoisite/zoisite and the high pressure quart-coesite transition. Due to the uncertainties regarding the position in P-T spare where zoisite would actually react out, the curve for the coesite-quartz transition is used to provide upper pressure limits of ca. 25-27kbar. Temperature limits are given by the thermal stability range of the "glaucophane eclogite" of Wei et al (2002).

Coesite-quartz reaction curve from Mirwald and Massonne (1980); Ab =Jd + qtz after Holland (1980); Di + Zo + Gr_x Py_x = Gr_y Py_y + H_2O after Poli & Schmidt (2002). Fields for the metamorphic facies is after Evans (1990): LBS = lawsonite blueschist; EBS = epidote blueschist; AEA = albite-epidote-amphibolite facies; E = eclogite facies; A = amphibolite facies; GS = greenschist facies; PA = pumpellyite-actinolite facies.

6.5.2.2 GEOTHERMOBAROMETRIC CALCULATIONS

The results of the geothermobarometric calculations are summarised in Figure 6.2, and Table 6.3.

		P Kbar				T°C			
	n	Ave	Rsd	Max	Min	Ave	Rsd	Max	Min
Calculated Fe^{2+} & Fe^{3+}	**10**	17.4	12.1	20.08	12.94	286.4	27.9	368.0	81.3
All Fe as Fe^{2+}	**10**	20.91	13.7	26.27	17.59	706.7	17.9	986.2	593.9

Table 6.3. Results of P-T calculations for the eclogitic sample Q02-08. See Chapter 5 for details of calculations. Rsd = relative standard deviation (rsd = std/mean*100); Ave = mean; Max = maximum values; Min = minimum values.

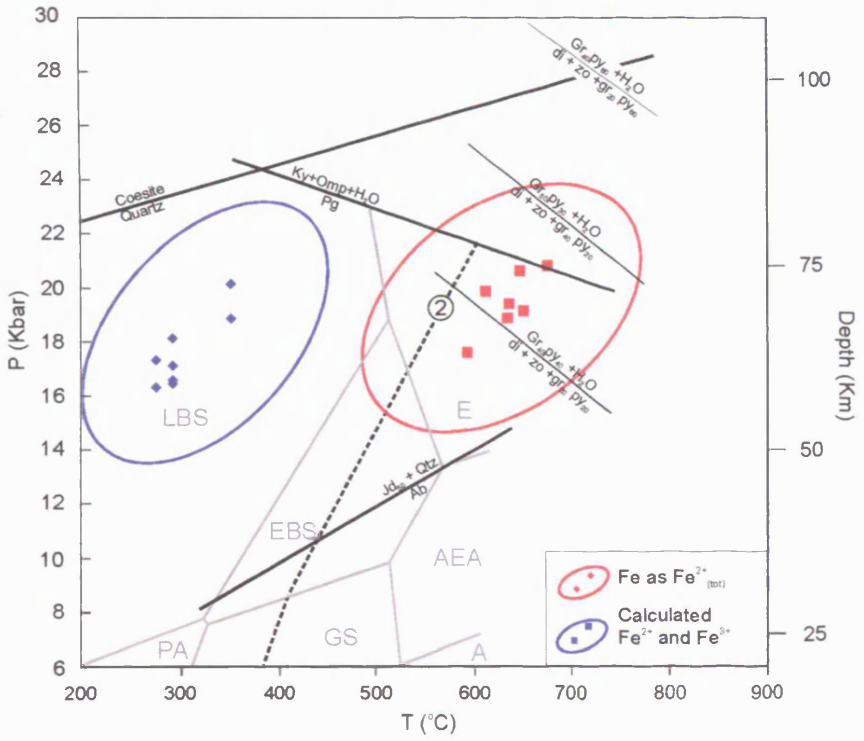


Figure 6.2 Results of the geothermobarometric investigation for calculations treating Fe as $Fe^{2+}_{(tot)}$ and calculated Fe^{2+}/Fe^{3+}. Results for calculations using Fe^{2+}/Fe^{3+} give significantly lower temperature results that are not consistent with evidence from paragentic relationships. Results for calculations treating Fe as Fe^{2+} between 600-700°C and 17-22kbar, which is much hotter than other calculations, and consistent with paragentic evidence. Pressure estimations are relatively similar between the two methods.

From Table 6.3 and Figure 6.2 it can be seen that there are considerable differences in temperatures between those calculations using estimated Fe^{2+}/Fe^{3+} and those assuming all Fe to Fe^{2+} (see Chapter 5 for explanation of the P-T calculations). The average temperature for all Fe as Fe^{2+} is 706.7°C, compared with 286.4°C for estimated Fe^{2+}/Fe^{3+}, a considerable difference of ~400°C. The maximum temperature calculated is 986.2°C. Pressure estimates are less variable, as can be seen from the lower rsd values of 12.1-13.7% (compared with 17.9-27.9% for temperatures). Average pressure estimates range from 17.4 kbar to 20.9 kbar for assumed Fe^{2+}/Fe^{3+} and all Fe as Fe^{2+}, respectively. The highest pressure calculated is 27.9kbar from the same mineral pair as the maximum-T estimate, which indicates that this mineral pair

unrepresentative of the data set as a whole (and so the results from this mineral pair is excluded from Figure 6.2).

Figure 6.2 shows the results of the P-T calculations without data from the anomalous mineral pairs. From Figure 6.2 it can be seen that the estimates using calculated Fe^{2+} and Fe^{3+} compositions place the rocks well within the lawsonite blueschist field with P-T conditions of 18kbar and 300°C respectively. This is inconsistent with the absence of evidence for the presence (or former presence) of lawsonite in these rocks. Higher-T estimates, from calculations assuming all Fe as Fe^{2+}, put the P-T conditions at ca. 8-22kbar and 600-700°C, respectively. Such conditions are within the eclogite field, beyond even the highest temperature estimate for the stability of lawsonite. The lack of evidence for the presence of lawsonite indicate that the Qilian Shan rocks metamorphosed along a hotter geotherm than the Tian Shan rocks, and that calculations assuming all Fe as Fe^{2+} give relatively more accurate T estimates in this case. However, it is unlikely that all Fe exists in the +2 state, and so the actual T conditions reached by the eclogite must be lower than that indicated by the calculations assuming all Fe to be Fe^{2+}.

6.5.2.3 DISCUSSION OF P-T CONDITIONS

Although not indicating UHPM, the P-T conditions calculated for the eclogitic sample sampled in this work are significantly greater than those proposed for eclogites by other workers. The P-T conditions predicted by this work are firmly within the eclogite field, whereas previous workers put P-T conditions for eclogites at 8±1kbar which is not high enough for the eclogite facies according to the diagrams of Spear (1990) or Evans (1990). It is therefore likley that previous pressure estimates were too low and that the estimates of this work are more accurate.

Previous workers have proposed that the low-P and high-P blueschist belts were originally part of the same subduction zone, with the low-P belt being relatively shallow, and the high-P relatively deep in the subduction zone (see Chapter 3). However, the difference in the P-T paths followed by the two belts excludes the possibility of them being contemporaries in the same subduction zone. The absence of lawsonite in the high-P belt indicates a hotter geotherm than the low-P belt.

Evidence from geochronology indicates that metamorphism in the low-P and high-P belts was roughly contemporaneous (e.g. Song 1996), so any cooling (of ~100-200°C) would have had to have occurred in the time it took for the protoliths of the high-P belt to subduct to ~75km.

CHAPTER 7

PROTOLITH GEOCHEMISTRY 1: TIAN SHAN

7.1 INTRODUCTION: THE IMPORTANCE OF THE PROTOLITH

As outlined in Chapter 2, it is fundamentally important to predict the compositional variation of protoliths of altered/metamorphosed rocks in order to determine the geochemical effects of alteration/metamorphism (e.g. Gresens 1967; Grant 1986; MacLean & Kranidiotis 1987; MacLean 1990; Bebout & Barton 1993; Humphries 1998; Becker et al. 2000; Sadofsky & Bebout 2003; Spandler et al. 2003, 2004a, 2004b; Breeding et al. 2004; Niu 2004). Furthermore, understanding the nature of protoliths aids classification of the blueschist belt (e.g. Maruyama et al. 1996) and reconstruction of the tectonic evolution of the orogen (e.g. Volkova & Budanov 1999, Dobretsov 2000). Consequently, this chapter investigates the geochemistry, petrogensis and tectonic origin of the protoliths of rocks collected from the western Tian Shan blueschist belt.

As stated in Section 2.6, a fundamental difficulty of predicting the compositional variation of protoliths is that there is often no available information on their composition prior to alteration/metamorphism. Why assume the composition of a blueschist/eclogite has any semblance to its protolith when it may have been hydrothermally altered, dehydrated and/or melted during metamorphism?

In the case of hydrothermally altered rocks, many workers have successfully predicted the composition of the protolith and so have been able to determine chemical changes resulting from alteration (e.g. Gresens 1967, Grant 1986, MacLean 1990, MacLean & Kranidiotis 1987, Mountain et al. 1995; Humphries 1998). This is because hydrothermal alteration can be restricted to veins and vein haloes, and so unaltered equivalents (i.e. rocks representative of the protoliths) can often be identified at a distance. However, rocks that have undergone subduction zone metamorphism are often pervasively metamorphosed and have been removed from their original tectonic environment, so unaltered equivalents rarely exist. Fortunately, there are a number of

geochemical arguments which can be used to link the composition of the metamorphic rock with that of its protolith.

7.2 METHODOLOGY

With the considerations outlined above in mind, a methodology has been developed in order to determine whether the composition of a metamorphic rock is likely to be representative of its protolith. This methodology is outlined in Figure 7.1.

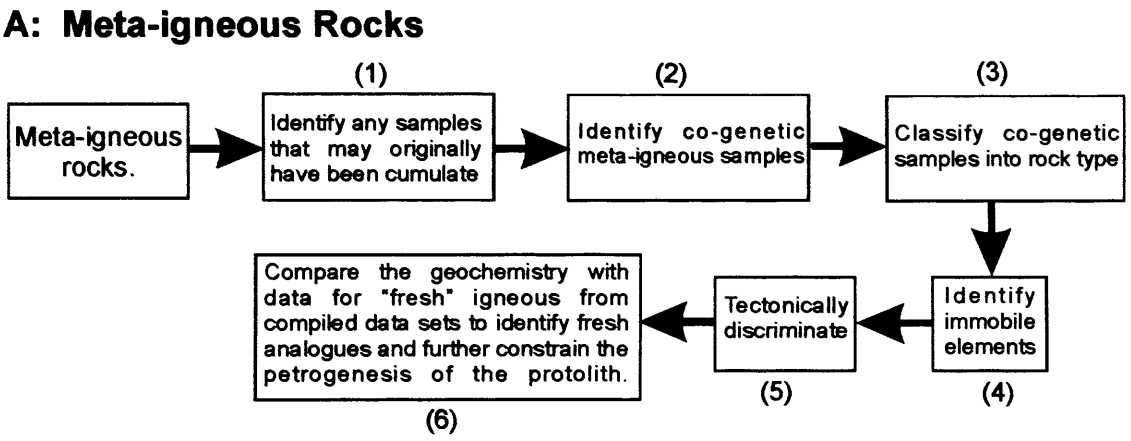


Figure 7.1 A & B. Flow diagram summarising the methodology for investigating the geochemical nature of: A) meta-igneous protoliths, and; B) meta-sedimentary protoliths. The rationale behind each stage for meta-igneous rocks is summarised in Table 7.1, see Section 7.2.2 for an outline of the rationale for investigating meta-sedimentary rocks.

Figure 7.1 illustrates the division of the methodology into two main stages: 1) investigations of meta-igneous rocks, and; 2) investigation of meta-sedimentary rocks. This is necessary because the methodology works by identifying relationships between chemical elements in co-genetic rocks (i.e. rocks that are genetically related by petrological processes). In the case of igneous rocks, these relationships are defined by a few known geochemical processes that are relatively well constrained (e.g. partial melting, fractional crystallisation). In contrast, the relationships between elements in sedimentary rocks may be defined by a large number of sedimentary processes (e.g. chemical weathering, sorting and mixing during transportation etc). These are very difficult (if not impossible) to constrain without detailed knowledge of

the composition of parent rocks, which cannot be known a priori. Consequently, it may not be possible to investigate the nature of meta-sedimentary protoliths by relying solely on relationships between chemical elements. What can be said about the petrogenesis and tectonic origin of meta-sedimentary protoliths is therefore limited.

7.2.1 META-IGNEOUS ROCKS

A summary of the rationale behind the stages shown in Figure 7.1A is given in Table 7.1.

STAGE	RATIONALE
1	Cumulate refers to those rocks that do not represent melt compositions. This can include rocks that result from accumulation of crystals, such as some gabbros, or rocks with high proportions of phenocrysts. As such rocks are not representative of their melts, the relationships between different trace elements (and their concentration) cannot be explained by processes such as partial melting or fractionation. Consequently, the geochemistry of cumulates has to be interpreted differently from that of frozen melts. Finally many diagrams such as classification diagrams and discrimination diagrams, cannot be used for cumulates. For these reasons, any cumulate rocks will be treated differently from volcanic rocks.
2	It is here assumed that samples with similar compositions are likely to be co-genetic and to have shared similar petrogenetic histories. It is possible that compositions of co-genetic samples could reflect either that of the protolith or be chemically "reset" compositions resulting from alteration/metamorphism. Either way, by observing the relationships between key trace elements it is possible to distinguish between these two possibilities.
3	It is important to classify the co-genetic samples into rock type, so that certain tectonic discrimination diagrams can be used.
4	Immobile elements preserve geochemical information about the protolith. It is therefore very important to establish which elements have remained immobile.
5	By knowing the tectonic environment, constraints can be put on the processes operating during the petrogenesis of the protoliths, and hence the potential chemical variation can be predicted.
6	By comparing the immobile element geochemistry with a variety of "fresh" (i.e. not significantly altered/metamorphosed samples) it is possible to identify analogous samples in the geological record. As additional information is often known about fresh samples, e.g. their tectonic origin, mineralogy, outcrop relationships etc, evidence for their petrogenesis is more complete, and can be used as a guide to interpret the metamorphic rocks.

Table 7.1. Summary of the rationale behind the six stages used for predicting the geochemical nature, compositional variation and petrogenesis of meta-igneous protoliths.

7.2.2 META-SEDIMENTARY ROCKS

Because of the large chemical variation in fresh subducting sediments (e.g. Plank and Langmuir 1998), previous workers on meta-sedimentary rocks (e.g. Sadofsky & Bebout 2003) have generally found that it is not possible to identify one "kind" of protolith. Consequently, it is very difficult to identify changes between sedimentary protoliths and their meta-sedimentary equivalents, especially if the changes are relatively minor (Sadofsky & Bebout 2003). With regard to the petrogenesis and tectonic origin of meta-sedimentary rocks, some workers (e.g. Bhatia & Crook 1986)

claim it is possible to tectonically discriminate sediments using diagrams similar to those used for discrimination of volcanic rocks. However, as noted in Section 7.2, and argued in Section 7.10, it is unlikely that these diagrams are useful for meta-sedimentary rocks that have been removed from their depositional environment. As a result, any interpretations about the petrogenesis and tectonic origin of meta-sedimentary rocks collected for this study are kept to a minimum.

7.3 SCREENING FOR META-CUMULATES AMOUNG THE META-IGNEOUS SAMPLES

During metamorphism the mineral assemblage and textures of a protolith are often destroyed. The identification of cumulate rocks, or strongly phyric rocks, is therefore not always possible by analysis of thin sections or hand specimens. Meta-cumulates, however, can be identified geochemically by following the suggestions of Pearce (1996), which are based on the concentrations of the following key (and often immobile) elements:

1) Al_2O_3: >20wt% Al_2O_3 may indicate significant plagioclase accumulation;
2) Sc: >50ppm may indicate clinopyroxene accumulation;
3) Ni: >200ppm may indicate olivine accumulation.

An examination of the meta-igneous sample data of Table 4.4 (see Chapter 4) has shown that the concentrations of these key elements are generally below the limits suggested by Pearce (1996). However, there are a small number of samples that do show evidence of an accumulated component. These are shown in Table 7.2.

SAMPLE	Ni (ppm)		SAMPLE	Sc (ppm)
TS02-17b	429.42		TS02-16	51.99
TS02-36	265.79		TS02-20	53.53
TS02-57	202.62		TS02-32	54.01
TS02-46	211.72		TS02-33	50.44
			TS02-34	74.67

Table 7.2. Summary of samples with compositions indicative of an accumulated component. Nickel abundance over 200ppm and Sc abundance over 50ppm are indicative of olivine and clinopyroxene accumulation, respectively. There are no samples with >20 wt% Al_2O_3 indicative of plagioclase accumulation.

In subsequent sections, the samples listed in Table 7.2 are shown to have basaltic bulk rock compositions (apart from sample TS02-34). This indicates that these rocks may have originally been phyric, with the high Ni samples being olivine-phyric, and high-Sc samples being clinopyroxene-phyric.

Sample TS02-34 is composed essentially of garnet, and based on analyses of the thin section and hand specimen, has been classified as a rodingite. Furthermore, the protolith may have been an ultramafic rock, as indicated by the low silica content of 34.39 wt%, high Fe_2O_3 of 27.33 and high Sc.

7.4 CLASSIFICATION OF META-VOLCANIC ROCKS

Having screened for cumulate samples, it is now possible to meaningfully classify the igneous rocks into rock type. This is undertaken by plotting the modified Winchester and Floyd (1977) Zr/Ti - Nb/Y diagram of Pearce (1996). This diagram is equivalent to the Total Alkalis Silica (TAS) classification diagram of Le Maitre et al. (1989), but uses immobile elements instead of easily mobilised alkalis.

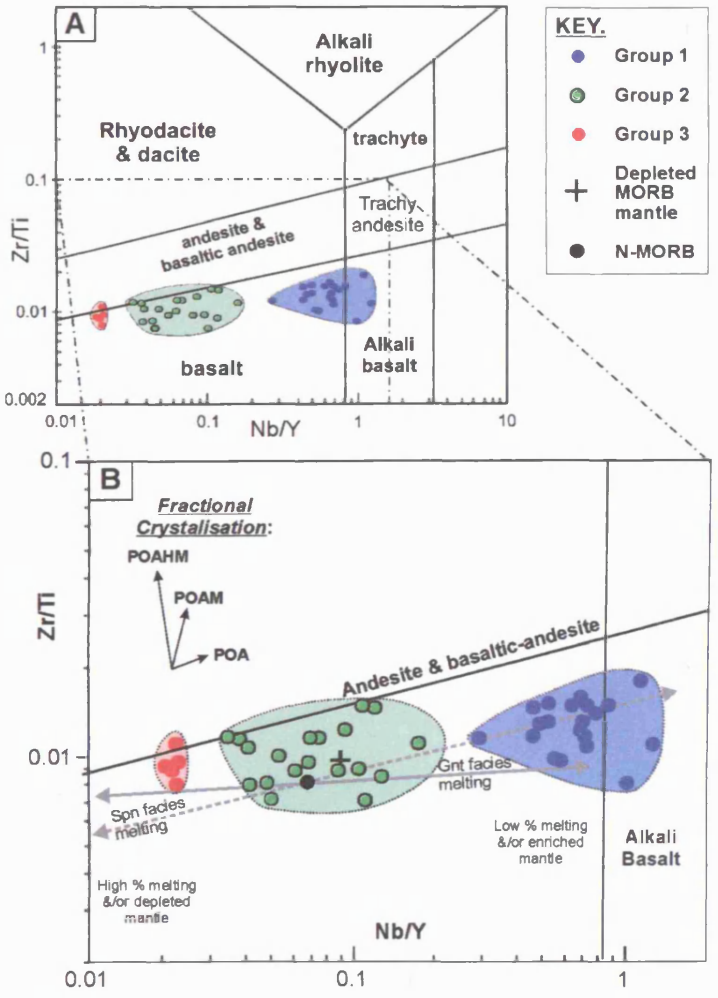


Figure 7.2. A & B.
A) the Zr/Ti - Nb/Y diagram of Winchester & Floyd (1977) diagram of Pearce (1996).

B) close-up of A) showing the three chemically distinct sample groups identified in the Chinese Tianshan meta-igneous rocks. Schematic melting vectors, MORB Mantle and fractionation vectors are from Pearce (1996).

Crystal fractionation acronyms:
P= plagioclase;
O= olivine;
A= augite;
H= hornblende;
M= magnetite.

On Figure 7.2 the meta-volcanic samples plot predominantly in the sub-alkalic basalt field, with a small number of samples in the alkali basalt field. The samples form three distinct clusters with small ranges of Zr/Ti ratios and large ranges of Nb/Y

ratios. These groups are referred to as Group 1, Group 2 and Group 3 (see the highlighted groups in Figure 7.2). The groups are made up of samples from multiple metamorphic facies, indicating that they have not been produced by chemical modification resulting from metamorphism.

Group 1 has Nb/Y ratios that range from 0.3 to 1.19 which, for a small number of samples, crosses from the sub-alkali basalt field into the alkali-basalt field. Group 2 Nb/Y ratios cover a greater range of 0.03-0.16 with a mean of 0.08, indistinguishable from the MORB estimate of Sun & McDonough (1989). Group 3 has the lowest Nb/Y ratio of 0.02, with negligible variation. Interestingly Group 3 contains all the basaltic samples that were shown to have evidence for clinopyroxene accumulation in Section 7.3.

As well as Figure 7.2, other classification diagrams, such as the Al-Fe+Ti-Mg diagram of Jensen (1976) and the TAS diagram of Le Maitre (1989), have shown that the majority of samples have basaltic compositions. These diagrams have been omitted for clarity. These diagrams are also considered less reliable, because the elements/compounds used as plotting parameters can be more readily mobilised than those used in Figure 7.2. Basaltic major elements compositions can also be discerned for these samples in the major element data shown in Table 4.4 (Chapter 4), two of which are reproduced in Table 7.3.

	PROTOLITH	Mean Nb/Y	MgO-Range	SiO_2-Range
GROUP 1	Transitional tholeiitic – alkaline basalt	0.64	3.31 - 8.06	44.17 - 53.01
GROUP 2	Sub-alkaline basalt	0.07	8.56-9.95	46.17 – 56.24
GROUP 3	Depleted sub-alkaline basalt, often clinopyroxene-phyric	0.02	4.84 – 6.62	47.49 – 52.98

Table 7.3. Summary of the classification of the Tian Shan meta-volcanic rocks. Note that samples with SiO_2 >52 wt% would plot outside of the basalt field in the TAS diagram. Only a small number of samples however plot with SiO_2>52wt%, and it cannot be ruled out that silica was added to these rocks during metamorphism/alteration. As addition of silica would not effect ratios between immobile elements, the classification derived from Figure 7.2 is preferred over the TAS diagram.

It may be argued that Figure 7.2 shows that the different groups form a trend line that can be explained by igneous processes. These processes may include partial melting as indicated by the melting vectors in Figure 7.2. However, the fact that the groups do not overlap, combined with evidence from other diagrams (see below) suggests

that this is not the case. It is more likely that the different groups derive from different sources.

That distinct groups do exist suggests that samples within a certain group may be co-genetic. If the different groups are different in terms of their source, Figure 7.2 provides some first order evidence as to their petrogenesis. This information is summarised in Table 7.4.

	PETROGENESIS
GROUP 1	High Nb/Y ratios of Group 1 indicate low degrees of partial melting, an enriched source or a combination of both, with variation in Zr/TiO_2 perhaps produced by fractional crystallisation, variations in source composition or contamination.
GROUP 2	The range of Nb/Y ratios of Group 2, which spans the MORB mantle estimate, suggests a similar degree of melting and/or source depletion to N-MORB mantle.
GROUP 3	The low Nb/Y ratios of Group 3 can result from high degree partial melts of MORB Mantle (MM) and/or a depleted mantle source. The effects of clinopyroxene phenocrysts (as indicated in Section 7.3), however, will also lower Nb/Y ratios because Y is more compatible in clinopyroxene than Nb (e.g. Green 1994). If the low Nb/Y ratios for Group 3 do reflect source depletion, then these ratios will be further decreased by clinopyroxene accumulation.

Table 7.4. Summary of the evidence for the petrogenesis of Groups 1, 2 and 3 from Figure 7.2.

7.5 IDENTIFYING CO-GENETIC SAMPLES

Although Figure 7.2 only indicates the presence of three distinct groups, the normalised multi-element diagrams of Figure 7.3 A-H show that further subdivisions are possible. Group 1 is subdivided into Groups 1a and 1b. Group 2 is subdivided into Groups 2a, 2b, 2c and 2d, and Group 3 is not further subdivided.

7.5.1 GROUP 1a & GROUP 1b

Figures 7.3 A & B are N-MORB normalised multi-element diagrams of the subgroups of Group 1. Group 1a, which contains the majority of samples from Group 1, has a general trace element pattern that is enriched relative to N-MORB and has an overall slope from left to right. The slope shows a smooth enrichment of $[LREE]_N$ relative to $[HREE]_N$, leading to high average $[La/Yb]_N$ ratios of 11.1 (the subscript N refers to MORB normalised values). This may indicate the trace element signature of melts that were produced from a garnet-bearing mantle source.

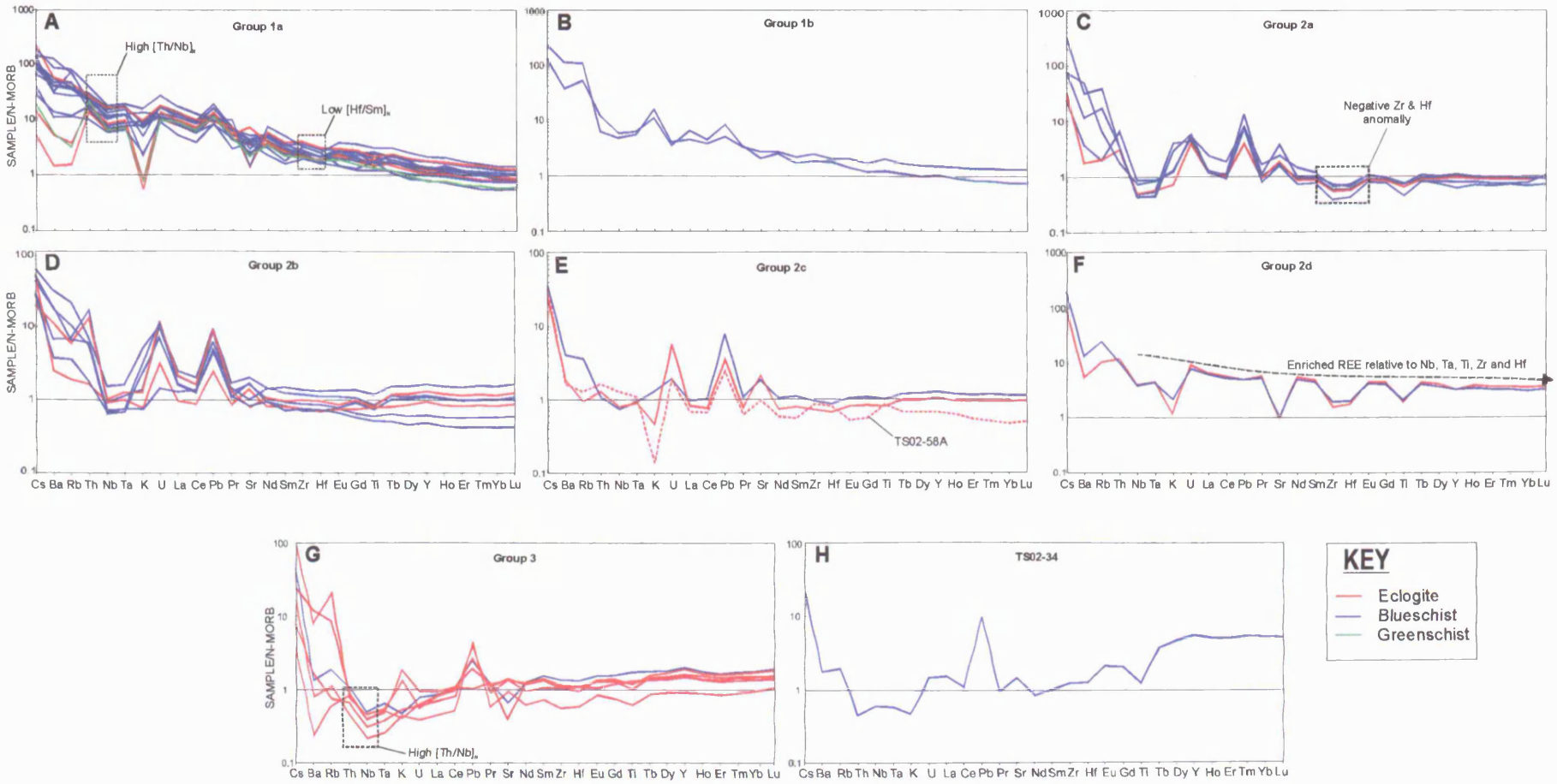


Figure 7.3 A-H. N-MORB normalised multi-element plots of the meta-basaltic rock sub-groups (A-G) and the rodingite sample TS02-34 (H). N-MORB values are taken from Sun & McDonough (1989), and the element order is from Pearce & Peate (1995).

It is obvious from Figure 7.3A that certain elements deviate significantly from a smooth curve. These elements can be ordered into two groups: 1) LILE anomalies, showing depletions or enrichments of Cs, Rb, Ba, K, Pb and Sr; and 2) HFSE anomalies, with depletions of Nb and Ta relative to Th and U, and depletions of Zr and Hf relative to Sm and Nd. As LILEs are readily mobilised by aqueous fluids, the LILE anomalies are likely to have resulted from interaction with fluids during alteration/metamorphism. This possibility is further examined in Section 7.6, below. However, it is worth noting that some (but not all) eclogitic samples show a depletion of Rb, Cs, Ba, and K relative to the blueschist samples.

With regard to the HFSE anomalies, the depletion of Nb relative to Th and U (see Figure 7.2A) is a characteristic feature of this group. Any interpretation of the petrogenesis of Group 1a must be able to explain the depletion of Nb compared to Th and U. Certainly, high $[Th/Nb]_N$ ratios are not expected for dehydrated oceanic crust, as Nb is often immobile and Th should be mobilised from the slab, if the temperature is high enough (e.g. Pearce & Peate, 1995). This would result in low $[Th/Nb]_N$ ratios, not the high ratios of 1.5-3.4 observed for this group. As with high $[Th/Nb]_N$ ratios, the slight depletion of Hf and Zr relative to adjacent elements is characteristic of this group. Ratios of $[Hf/Sm]_N$ best represent this anomaly. Again, any petrogentic models must explain the slightly low $[Hf/Sm]_N$ ratios, which average at 0.77 for Group 1a.

As shown in Figure 7.3B, Group 1b is less enriched in incompatible elements compared with Group 1a. The trace element pattern slopes from left to right, but with a shallower gradient than Group 1a, as illustrated by $[La/Yb]_N$ ratios of 3.5-8.6. Another similarity with Group 1a is the high $[Th/Nb]_N$ ratio, which averaging at 1.66, is slightly lower than for Group 1a. Large ion lithophile elements, such as Cs, Rb, Ba, K and Pb (but not Sr) all show positive anomalies compared with REE and HFSE.

7.5.2 GROUP 2a & GROUP 2b

With large depletions of Nb and Ta relative to Th and U and relatively enriched LREE, Groups 2a and 2b have trace element patterns characteristic of volcanic-arc basalts (VAB). The principal differences between these two groups are the presence (Group 2a) or absence (Group 2b) of negative Zr and Hf anomalies. Another

difference between the two groups is the slight enrichment of MREE-HREE shown by Group 2a compared to some Group 2b samples.

As with Groups 1a and 1b, Groups 2a and 2b have highly variable LILE abundance compared to the HFSE and REE. In contrast, trace element patterns for the HFSE and REE are generally parallel, indicating that fractional crystallisation of similar parental magmas may be important in controlling the geochemical variation within a group.

7.5.3 GROUP 2c & GROUP 2d

There are only three samples that make up Group 2c (Figure 7.3 E). Assuming the sampling is random this indicates that Group 2c rocks are relatively rare in the metamorphic belt. Group 2c is similar to MORB in REE and HFSE compositions, with $[La/Yb]_N$ of 0.9-1.5. Sample TS02-58A may be slightly different from the other samples as can be seen most clearly by the relative enrichment of Hf and Zr to adjacent elements, and by the depletion of REE compared with the other two members of the group. As with previous groups, the LILE elements Cs, Ba, Rb, K, Pb and Sr show both positive and negative anomalies.

Group 2d is a single sample composed of two parts, eclogite and blueschist, that were divided and analysed separately. On Figure 7.3 F Group 2d shows enriched REE with an abundance of ~3-6 times that of N-MORB. However, the REE trend is flat, with an average $[La/Yb]_N$ ratio of 1.96. Perhaps the most striking feature of the Group 2d trace element pattern is that the REE are enriched relative to Nb, Ta, Zr, Hf and Ti.

7.5.4 GROUP 3

This group is characterised by being depleted relative to MORB in Th, Nb, Ta, La Ce and U, and enriched in MREE-HREE. The overall depleted pattern is reflected in low average $[La/Yb]_N$ ratios of 0.54. The highly incompatible elements Cs, Ba Rb and Th are all enriched relative to Nb and Ta (apart from one sample that is depleted in Ba). Disregarding the LILEs which are may have been mobilised, this enrichment leads to high $[Th/Nb]_N$ ratios (of 1.7-2.3), as is characteristic of Group 1a and 1b. Another characteristic feature is the depletion of Hf and Zr relative to Sm, Nd and Eu, which is again similar to Group 1a.

Group 3 contains the samples with high Sc that may be indicative of clinopyroxene accumulation. This could explain the enrichment of MREE-HREE relative to N-MORB and low $[Hf/Sm]_N$ ratios, as these elements are more compatible in clinopyroxene relative to LREE and Zr and Hf (e.g. Green 1994).

7.5.5 ULTRAMAFIC SAMPLE: TS02-34

This sample is the only ultramafic rock collected. The trace element pattern (Figure 7.2H) shows large enrichments in Cs, Ba, Rb, and Pb. Disregarding these LILEs, the pattern shows a progressive depletion with increasing incompatibility, apart from Ti, which shows a negative anomaly. The HREE are particularly enriched, with values ~5 times that of MORB.

7.5.6 SUMMARY

Groups 1 and 2 can be further divided into subgroups. Group 1a is characterised by an enriched, rightward-dipping pattern with high $[La/Yb]_N$ ratios, high $[Th/Nb]_N$ ratios and low $[Hf/Sm]_N$ ratios. Although enriched in incompatible elements, Group 1b is not as enriched as Group 1a, and has slightly lower $[Th/Nb]_N$ ratios. Group 2 can be subdivided into four groups, two of which (Groups 2a & 2b) have patterns characteristic of volcanic arc rocks, a N-MORB like group consisting of three samples (Group 2c), and a sample (divided into two) with unusual trace element patterns (Group 2d). Group 3 rocks are depleted relative to MORB in the more incompatible elements (i.e. from Cs to La), but the probable presence of accumulated clinopyroxene in the protoliths may have raised the abundance of MREE-HREE to a level above that of MORB.

In all samples LILEs are much more variable than HFSE or REE and often display negative or positive anomalies. This indicates that LILE may have been mobilised at some point in their petrogenetic history. However, there is no systematic variation in LILEs with metamorphic grade (e.g. not all eclogites show negative LILE anomalies), which may indicate that metamorphism has not caused negative LILE anomalies. Furthermore, none of the multi-element diagrams for the groups show the trace element pattern thought to be indicative of the "residual subduction signature" (as discussed in Section 2.2). Element mobility is further investigated in Section 7.6.

7.6 IDENTIFYING IMMOBILE ELEMENTS

In the previous sections, it has been assumed that certain elements have remained immobile during alteration and/or metamorphism. The aim of this section is to establish whether these assumptions are valid. In order to achieve this aim it has been necessary to first develop a methodology which is summarised below.

7.6.1 METHODOLOGY

7.6.1.1 THEORY

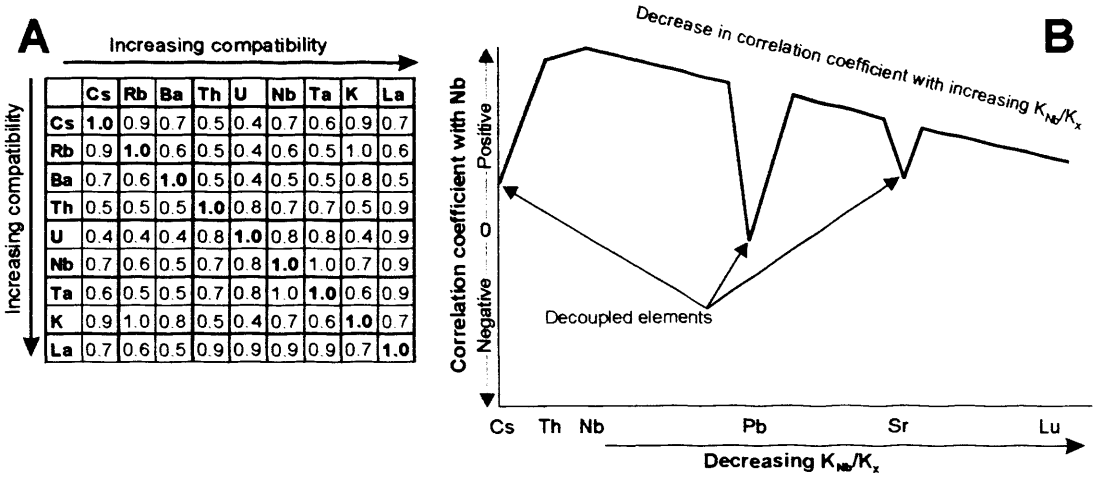
A useful method for identifying immobile elements was presented by Cann (1970) who investigated the compositions of altered and fresh oceanic basalts by using matrices of correlation coefficients (r) between different incompatible elements. Cann (1970) showed that immobile elements had a similar abundance in the altered rocks compared with the unaltered rocks but, more importantly, that these elements were strongly correlated with each other. Mobile elements on the other hand, did not have a similar abundance in the unaltered and altered rocks, and furthermore did not correlate with the immobile elements.

The observations of Cann (1970) may be explained by noting that incompatible elements with similar partition coefficients (K), e.g. Rb and Nb, can be considered to behave essentially the same during magmatic processes. Thus they often positively correlate with each other. But if one of these elements, such as Rb, is mobilised during alteration, the positive correlation will be lost, and Rb can be described as being "decoupled" from Nb. Not all immobile elements, however, will necessarily show good correlation if their partition coefficients are very different from each other. For example the correlation coefficient for the covariation of Nb and Ta (i.e. $r_{Nb\text{-}Ta}$) is likely to be higher than $r_{Nb\text{-}Yb}$. The task therefore becomes one of distinguishing between poor correlation brought about by mobilisation, and poor correlation brought about by differences in partition coefficients.

To help distinguish between the two processes outlined above, it is necessary to know whether r varies together with differences in K. For example if the correlation between Nb and other elements is investigated, does r vary predictably with K_{Nb}/K_x (where the subscript x refers to a given element)?

7.6.1.2 APPLICATION

To help answer the above question, this approach uses a matrix of correlation coefficients. In this matrix elements have been arranged according to their compatibility during mantle melting (i.e. arranged in the same order as often used in normalised multi-element diagrams) (Figure 7.4 A). Niobium is the most incompatible of the elements commonly found to be immobile, and is often placed towards the extreme left of normalised multi-element diagrams (e.g. Figures 7.3A-G). As such, Nb is the ideal element with which to investigate the relationship of r with differences in compatibility because if r does vary with K_{Nb}/K_x, a leftward sloping curve should result (Figure 7.4B).



	Cs	Rb	Ba	Th	U	Nb	Ta	K	La
Cs	**1.0**	0.9	0.7	0.5	0.4	0.7	0.6	0.9	0.7
Rb	0.9	**1.0**	0.6	0.5	0.4	0.6	0.5	1.0	0.6
Ba	0.7	0.6	**1.0**	0.5	0.4	0.5	0.5	0.8	0.5
Th	0.5	0.5	0.5	**1.0**	0.8	0.7	0.7	0.5	0.9
U	0.4	0.4	0.4	0.8	**1.0**	0.8	0.8	0.4	0.9
Nb	0.7	0.6	0.5	0.7	0.8	**1.0**	1.0	0.7	0.9
Ta	0.6	0.5	0.5	0.7	0.8	1.0	**1.0**	0.6	0.9
K	0.9	1.0	0.8	0.5	0.4	0.7	0.6	**1.0**	0.7
La	0.7	0.6	0.5	0.9	0.9	0.9	0.9	0.7	**1.0**

Figure 7.4 A & B. A) Example of part of a correlation matrix with elements arranged according to compatibility, and B) a schematic representation of how the correlation coefficient might change as a function of decreasing K_{Nb}/K_X (where the subscript "x" refers to another element), and if certain elements (such as Cs, Pb and Sr) are de-coupled (i.e. mobilised) from Nb.

Although it is possible to simply calculate r in the matrix, it has been necessary to visually inspect covariation diagrams in each group to make sure that "outliers" do not adversely effect the correlation coefficients. As the correlation between different elements is investigated by this method many samples are required. Consequently, only the samples from Groups 1a, 2a, 2b and 3 can be investigated using the method outlined above. Also, by knowing the number of samples (n) in each group it is possible to compare r with a known "critical value." A critical value is a value of r above which a correlation is statistically significant at the given level of confidence.

7.6.1.3 LIMITATIONS

The method outlined above requires that relatively simple magmatic processes were in operation during the magmatic history of the protoliths. Because the elements are

arranged according to their compatibility during spinel lherzolite melting, it is necessary that partitioning during melting in the spinel facies, and subsequent fractional crystallisation, were the dominant processes controlling protolith chemical variation. However this idealised picture is very likely to be an over-simplification because other processes could have had an effect on the composition of the melt. These include: 1) crustal contamination/mixing with other melts; 2) subduction zone enrichment; and 3) melting in the garnet facies (especially relevant for Group 1a: see Section 7.5.1). In addition to these, a potentially severe limitation is that of source variation, because the samples were not collected from a single lava flow, i.e. the rocks of a given group do not derive from a single evolving magma. In fact, because of the sampling method, the rocks forming a group could derive from lavas that erupted in different locations of a larger geographical area, and/or were erupted at different times. As it is unlikely that the source compositions in a given geographical area remain constant throughout space and time, it is possible that poor correlation could result from differences in source composition. Such a factor is likely to decouple certain elements from Nb, perhaps leading to the false conclusion that these elements have been mobilised. Nevertheless, by drawing on other evidence, whether or not other processes have had an effect can be determined. Such evidence may include: 1) correlation with other elements (including major elements); 2) the differences in variability (i.e. the Relative Standard Deviation (rsd = standard deviation/mean*100)) between different elements; and 3) comparisons with the results of other investigations into the mobility of elements.

7.6.2 RESULTS

7.6.2.1 GENERAL OUTCOME

Results from the method outlined above are shown in Figure 7.5 A-D. To a first order Figures 7.5 A-D are successful in distinguishing between immobile and mobile elements. Elements such as the LILEs generally show relatively low r in each diagram, whereas REE, Ta, U, Th, Zr and Zr have relatively high r. This is best shown in Figure 7.4 D for Group 3 and generally agrees with the results of other investigations into the mobility of elements (see Chapter 2). There are however a number of unexpected results which have been highlighted in Figure 7.5A-D, and which require further investigation.

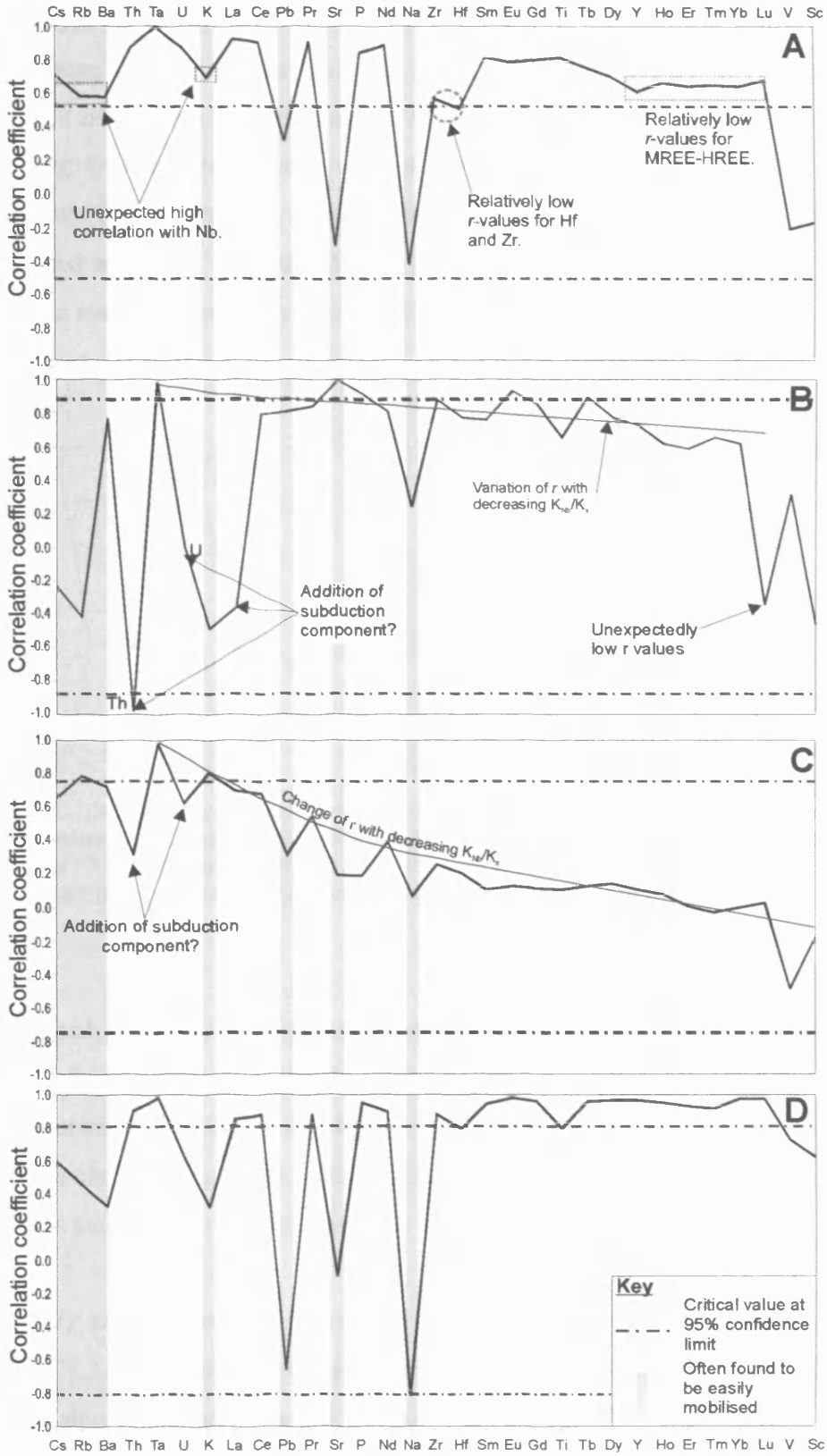


Figure 7.5 A-D. Nb-correlation diagrams for: A) Group 1a (n=15); B) Group 2a (n= 4); C) Group 2b (n= 7); D) Group 3 (n= 6). Note that the elements that are often found to be mobile consistently show relatively low correlation coefficients, indicating they have been de-coupled from Nb. To a first order, the elements often found to be immobile show greater r than the mobile elements and often positively correlate with Nb. There are, however, many elements that show unexpected behaviour: see text for more details.

7.6.2.2 GROUP 1a

From Figure 7.5A, it can be seen that the HFSE and REE all display a statistically significant correlation with Nb (at the 95% confidence limit, n=15). There are three interesting features about some of these elements: 1) the relatively low correlation coefficients for Zr and Hf; 2) the relatively low r for MREE-HREE, and 3) the unexpected high r for Cs, Ba, Rb and K. Figure 7.6 shows the variation (i.e. the rsd defined as standard deviation/mean*100) of the elements in Group 1a.

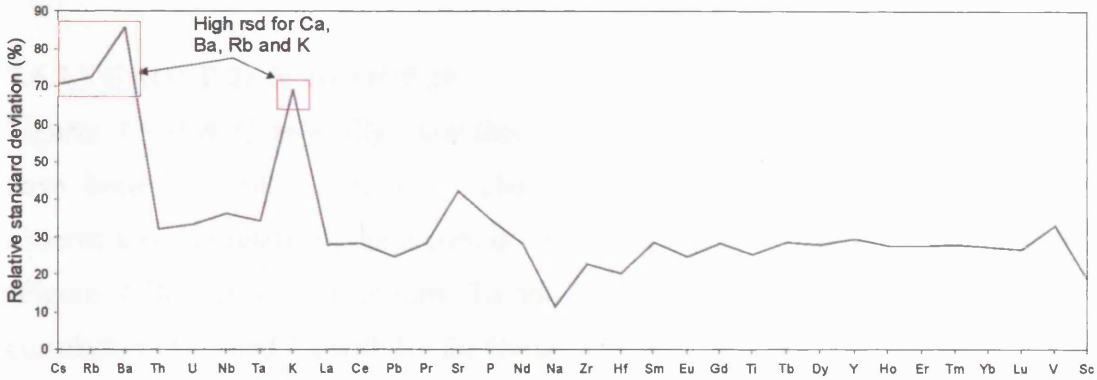


Figure 7.6. Diagram showing the variation (defined as relative standard deviation: 1σ/mean*100) of selected elements in Group 1a. The elements that are shown to be coupled with Nb have a relatively stable rsd of <35%, whereas Ba, Rb, Ca and K have much higher variation of >60%, suggesting that these elements have in fact been mobilised, see text for further information.

With regard to 1), the variation of Zr and Hf is relatively low at 22.8% and 20.3% respectively (Figure 7.6), which is similar to the REE, Nb and Ta. This, and the fact that r is statistically significant despite being relatively low for Zr and Hf, suggests that these elements have not been mobilised. It is therefore likely that the relatively low r was caused during their magmatic history, perhaps by contamination.

As with Zr and Hf, the REE from Dy-Lu show relatively low correlation coefficients in Figure 7.5A. These elements positively correlate with Nb, and so are still coupled, and also show relatively low rsd values (Figure 7.6). The relatively low r for these elements may therefore point to another factor being important during the petrogenesis of Group 1a protoliths. Such a factor may be the presence of garnet in the melt source regions, as shown in Section 7.5.1 by the steeply dipping REE curves. This is consistent with the unexpectedly low r for the HREEs as they are more

compatible in garnet compared with LREE, and so are more readily decoupled from Nb.

The LILEs Cs, Ba, Rb and K show statistically significant correlations with Nb in Figure 7.4A, which would be unexpected if these had been mobilised in aqueous fluids. However, trace element patterns of Figure 7.3A and the diagram of Figure 7.6 show that these elements are highly variable, which would not be expected for fresh basalts. It is therefore likely that these elements have been mobilised in some samples.

7.6.2.3 GROUP 2a & GROUP 2b

Figures 7.5 B & C generally show that elements such as Cs, Ba, Rb, K, Pb, Sr, Na have been decoupled from Nb. There are, however, a number of unexpected observations: 1) relatively high correlation for Cs, Ba and Rb with Nb for Group 2b (Figure 7.5b); 2) in both groups, Th and U both are decoupled from Nb; 3) low correlation of La and Lu with Nb for Group 2a.

To help investigate the causes of points 1) and 2) above, Figure 7.7 plots the variation (rsd) of each element. It can be seen that elements such as Cs, Ba, Rb, K and, to a lesser extent Pb and Sr, are more variable compared with Ta, REE, Zr and Hf (the latter elements having variability generally <40%). This indicates that they have been mobilised. With regard to point 2) Figure 7.7 shows that Th and U are more variable than REE, Nb, Ta etc in Group 2b, whereas these elements are not more variable than Nb, Ta, REE etc in Group 2a. This may appear to suggest that Th and U have been mobilised in Group 2b, but not Group 2a. However, caution must be used when interpreting the correlation between these elements for Group 2a and Group 2b on Figure 7.5 B & C, because the trace element patterns (Section 7.5) are similar to the characteristic volcanic arc signature. As previously discussed, the order of elements along the x-axis of the Nb-correlation diagram was chosen on the basis of their relative compatibility for simple partitioning during melting/fractionation. It may therefore be the case that Th and U are decoupled because they were delivered to the source regions by subduction zone fluids/melts that were not chemically homogenous.

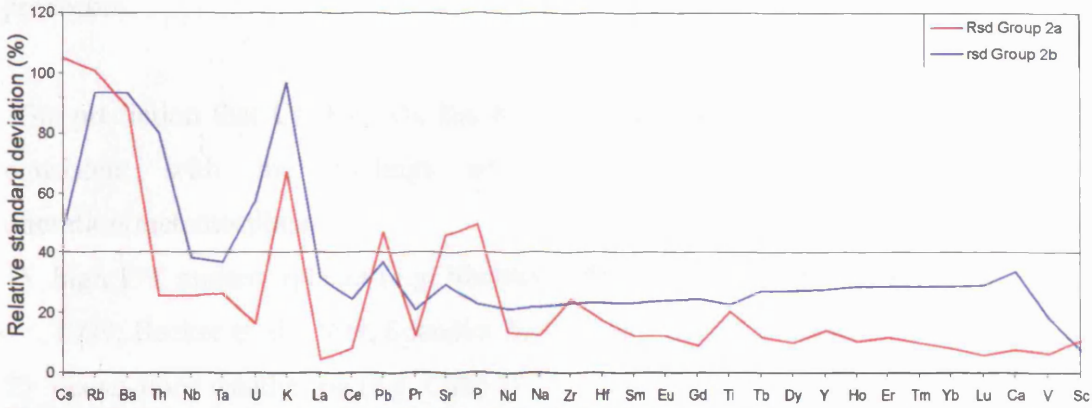


Figure 7.7. Diagram showing the variation (defined as relative standard deviation: 1σ/mean*100) of selected elements in Group 2a and Group 2b. The elements that are shown to be coupled with Nb have a relatively constant rsd of <40%. The elements that show lower than expected *r* with Nb, such as Ba, Rb, Ca and K have a much higher variation of >60%. Furthermore, Th and U also show greater variation than Nb, Ta and REE etc in Group 2b, which, although suggesting that they may have been mobilised, can be explained by igneous processes that are known to be in operation at volcanic arcs.

With respect to point 3), low *r* for La and Lu is unexpected because of the relatively high correlation for other REE, such as Ce and Yb. It is difficult to explain why these elements have anomalously low *r*, especially as Figure 7.7 shows La & Lu to have similar variability (rsd) to Nb, Ta and other REE. Based on the low rsd for these elements, it is unlikely that they have been mobilised.

7.6.2.4 GROUP 3

The Nb-correlation diagram of Figure 7.5D works particularly well for Group 3, with the HFSE and REE generally showing statistically-significant positive correlation with Nb. This indicates that these elements have remained immobile. Also, the elements usually considered as being easily mobilised show low positive or negative *r*, indicating that they have been mobilised.

7.6.3 SUMMARY & DISCUSSION OF ELEMENT MOBILITY

The overall picture from the correlation diagrams (Figure 7.5 A-D) is that the LILEs Cs, Ba, Rb, Pb, Sr, K and Na have become decoupled from Nb to some extent. In contrast, HFSE and REE are not decoupled from Nb, apart from Th and U in the sample groups that display trace element patterns with volcanic arc signatures. As outlined in previous sections, the picture is not quite that simple but, where

"anomalous" correlations exist these can often be explained in terms of igneous processes.

The prediction that Cs, Ba, Rb, Na, K, Sr and Pb have been mobilised is generally consistent with the findings of other workers on different kinds of alteration/metamorphism:

1) high P/T metamorphism (e.g. Shatsky 1990; Volkova & Budanov 1999; Arculus 1999; Becker et al. 1999; Spandler 2003, 2004a, 2004b; Chalot-Prat et al. 2003)
2) ocean-floor weathering (e.g. Cann 1970; Humphries et al. 1998)
3) volcanic arc geochemistry (e.g. Pearce & Peate 1995)
4) hydrothermal alteration (e.g. Mountain et al. 1995)
5) serpentinisation of abyssal peridotites (e.g. Niu 2004)

It is therefore suggested that the LILEs have been mobilised (either by being added or removed from the rocks), and that the HFSEs and REE have remained immobile. The use of these HFSE and REE in subsequent discrimination and covariation diagrams will therefore reveal information about the petrogenesis of the protolith.

Before further investigating the immobile elements it is necessary to discuss the mobility of V because, as seen in Figure 7.5A-D, V has been included on the correlation diagrams. Vanadium was included because it is one of the few moderately compatible elements used in discrimination diagrams. Furthermore, its sensitivity to oxidation state causes it to behave differently during igneous processes compared to the incompatible elements usually used. From Figure 7.5 it is clear that V is decoupled to some extent from Nb in all sample groups. However, because of the geochemical properties of this element, it should not be expected to be coupled to Nb. By observing the variation (rsd) of V (Figures 7.6 and 7.7) it can be seen that V varies to a similar degree as the immobile elements, suggesting that V has also remained immobile.

7.7 TECTONIC DISCRIMINATION

Tectonic discrimination diagrams have been used to distinguish between the three end-member tectonic settings (Figure 7.8): 1) volcanic arc settings; 2) mid-ocean ridge settings, and; 3) within plate settings.

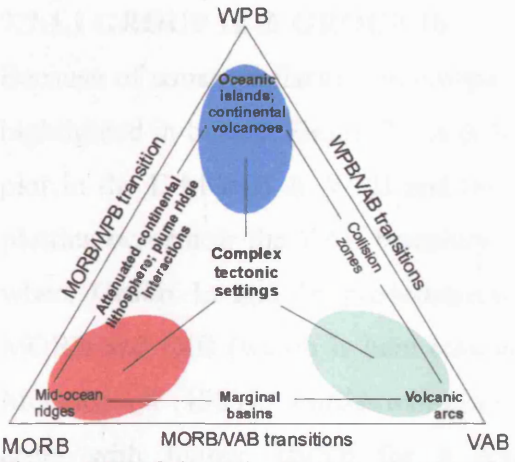


Figure 7.8. Schematic diagram showing the three tectonic setting end-members for basalts and transitional settings, adapted from Pearce (1996). Acronyms: MORB – Mid-ocean ridge basalt; WPB – within-plate basalt; VAB – volcanic-arc basalt.

It can be seen from Figure 7.8 that a number of transitional tectonic environments between the end-member settings exist: 1) within-plate (WP)/mid-ocean ridge (MOR) transitions; 2) mid-ocean ridge/volcanic arc (VAB) transitions; 3) volcanic arc/within-plate transitions. In the case of transitional or complex tectonic settings, evidence other than the diagrams themselves is often needed to positively identify the setting from which a rock originates (e.g. Pearce 1996).

Four discrimination diagrams that use immobile elements were found to be particularly useful in determining the tectonic origin of the protoliths for the various groups. These are split into those that can identify volcanic-arc signatures, and those that can discriminate between MORB and WPB signatures.

7.7.1 IDENTIFYING VOLCANIC ARC SIGNATURES

Figure 7.9 A & B shows: A) the Th-Hf-Ta diagram of Wood (1980), and; B) the Th/Yb against Nb/Yb diagram of Pearce & Peate (1995). Both these diagrams are particularly useful at discriminating volcanic arc basalts from other tectonic settings.

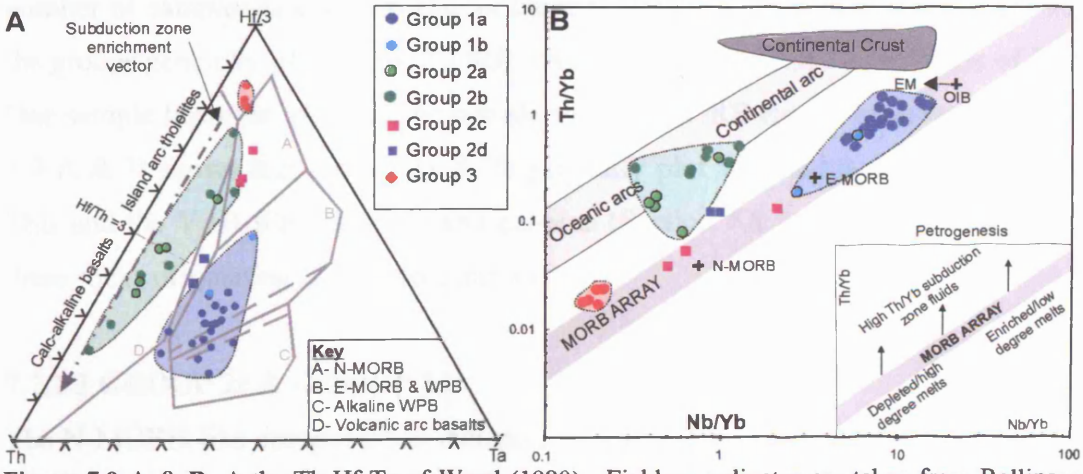


Figure 7.9 A & B A the Th-Hf-Ta of Wood (1980). Field co-ordinates are taken from Rollinson (1993) and the schematic subduction zone enrichment vector is taken from Pearce (1996). B The Th/Yb vs. Nb/Yb diagram from Pearce & Peate (1995). N-MORB, E-MORB and OIB are estimates from Sun & McDonough (1989) and the continental crust field is based on the data of Gao et al. (1997), Wedenpohl (1995) and Rudnick & Fountain (1995).

7.7.1.1 GROUP 1a & GROUP 1b

Because of some similarities in composition Group 1a and Group 1b have both been highlighted in blue in Figure 7.9 A & B. On Figure 7.9 A, the groups predominantly plot in the E-MORB & WPB and the WPB field, with a small number of samples plotting on or near the VAB boundary. A similar picture can be seen in Figure 7.9B, where Group 1a and 1b predominantly plot on the MORB array between the E-MORB and OIB (which is here considered as similar to WPB) estimates of Sun & McDonough (1989). Furthermore, a small number of samples plot off the MORB array with higher Th/Yb for a given Nb/Yb, which is indicative of either contamination with continental crust or the addition of a subduction component. As indicated on Figure 7.9B, EM-type OIB (either EM-1 or especially EM-2) tend to have higher Th/Yb ratios for a given Nb/Yb ratio than the MORB array. Thus a third possibility is that some Group 1a rocks have an EM-type OIB signature. In summary, the diagrams of Figures 7.9 A & B generally show that samples range in composition from E-MORB to WPB, with some samples being relatively Th-enriched.

7.7.1.2 GROUP 2a & GROUP 2b

There is no clear geochemical difference between Group 2a and 2b in terms of the variables used in Figure 7.9 A & B, and so to simplify matters they have been highlighted as one group (the green field surrounding the data points). On Figure 7.9 A Group 2a and 2b trend towards high Th compositions along the subduction enrichment vector (i.e. across the calc-alkaline and tholeiitic VAB fields). A small number of samples also plot within or close to the N-MORB field. On Figure 7.9B the groups generally plot off the MORB array, towards the high Th/Nb ratios of VAB. One sample however, plots on the boundary of the MORB array. In summary, Figure 7.9 A & B shows that Group 2a & 2b generally plot with VAB-like compositions. This and the VAB-like trace element patterns (Section 7.8.2), is strong evidence for these rocks originating from a volcanic arc.

7.7.1.3 GROUP 2c & GROUP 2d

The N-MORB-like compositions indicated by normalised multi-element diagrams for Group 2c are generally confirmed by the fact that this group plots in the field for N-MORB in Figure 7.9A and within the MORB array of Figure 7.9 B. Two of these samples plot close to the estimate for N-MORB, and one sample (TS02-58A), plots

closer to the estimate of E-MORB. In contrast Group 2d plot in a position equidistant from the fields for VAB and E-MORB & WPB (Figure 7.9 A) and with relatively high Th/Yb ratios, off the MORB array (Figure 7.9B).

7.7.1.4 GROUP 3

On Figure 7.9 A, Group 3 forms a cluster of data points that plot from the boundary of the N-MORB field to a position equidistant between the N-MORB and VAB fields. Figure 7.9 B shows that Group 3 has slightly elevated Th/Yb ratios compared to the MORB array at a given Nb/Yb ratio. The fact that Group 3 does not plot in a field on Figure 7.9A may therefore be due to slightly elevated Th composition relative to Hf and Ta. Such evidence, along with the trace element patterns discussed in Section 7.5.3, shows that a high-Th content component must have been important during the protolith petrogenesis. Such a component could derive from either subduction zone (i.e. slab-derived) fluids or from contamination with continental crust.

7.7.2 IDENTIFYING WPB AND MORB SIGNATURES

Having identified rocks with a clear VAB signature, attention is now turned to further investigating groups that do not show clear VAB signatures, i.e. Groups 1a, 1b, 2c, 2d and possibly 3. Sample groups with clear VAB signatures are omitted from Figures 7.10 A &B for clarity. This is here undertaken by using the diagrams of Pearce & Cann (1973) and Shervais (1992) (Figure 7.10A & B).

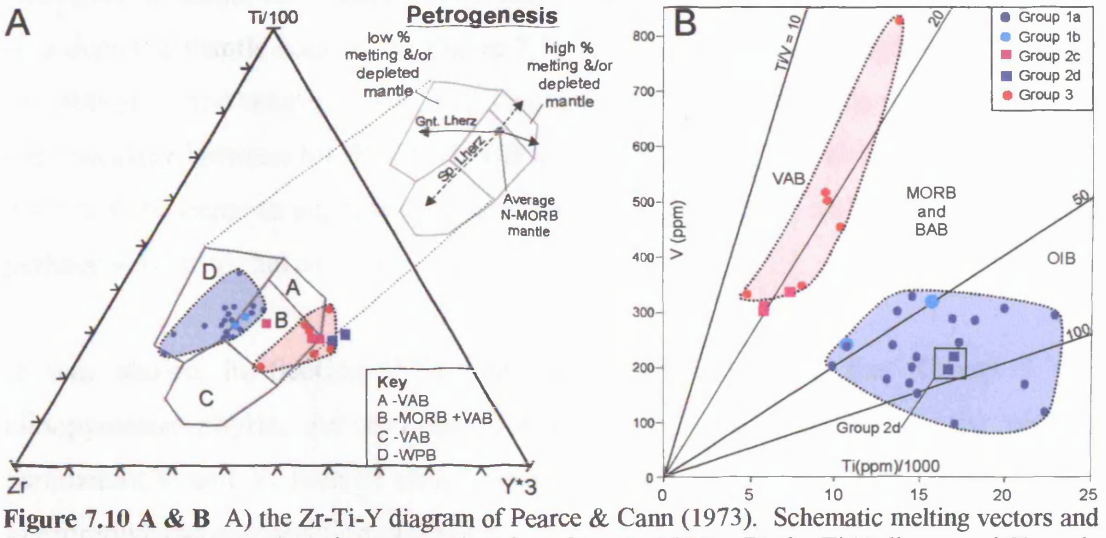


Figure 7.10 A & B A) the Zr-Ti-Y diagram of Pearce & Cann (1973). Schematic melting vectors and the average MORB mantle estimate are taken from Pearce (1996). B) the Ti-V diagram of Shervais (1992). This diagram was also included because of the use of the compatible element V, in contrast to other diagrams that use more incompatible elements.

7.7.2.1 GROUP 1a & GROUP 1b

Figure 7.10 A shows that Group 1a data predominantly plot in the WPB field, whereas a small number of samples and Group 1b plot in the MORB + VAB field. Similarly, on Figure 7.10B, some of these samples plot with a Ti/V ratio of <50 in a field for MORB/BABB, whilst others plot with Ti/V ratios >50 in the OIB (i.e. WPB) field. Such evidence is consistent with the results from the discrimination diagrams of Figure 7.9 A & B, and the trace element patterns of Section 7.5.1, in that Group 1a and 1b consist predominantly of transitional alkali basalts with E-MORB-WPB characteristics.

7.7.2.2 GROUP 2c & GROUP 2d

Group 2c plots across the MORB & VAB field in Figure 7.10A and, with Ti/V ratios of ~20, on the boundary between the VAB and the MORB & BABB fields in Figure 7.10B. In Figure 7.10A, Group 2d is unusual in that it plots entirely outside any field, towards relatively high Y concentrations. On the other hand, Figure 7.10B also shows Group 2d plotting in the OIB field, which is inconsistent with trace element patterns (Section 7.5.3), and discrimination diagrams (Figure 7.9 A & B).

7.7.2.3 GROUP 3

Although Group 3 generally plots in the MORB & VAB field in Figure 7.10A, some samples plot with Y contents above that of any field. According to the schematic petrogenesis model for Figure 7.10A, this could result from high degree partial melts or a depleted mantle source. In Figure 7.10B, Group 3 plot with high V contents, up to ~800 ppm, and relatively low Ti giving Ti/V ratios of ~20. This puts the group on the boundary between MORB & BABB and VAB fields. The evidence from Figure 7.10 A & B seems to suggest that these rocks have a "weak" volcanic arc signature, perhaps similar to that of a back-arc basin.

It was shown in Section 7.3.1 that Sc contents indicate that Group 3 was clinopyroxene-phyric. As the diagrams of Figure 7.10A & B use the plotting parameters V and Y, both of which are partitioned significantly into clinopyroxene, interpreting the composition of Group 3 has to be undertaken with care. On Figure 7.10 A & B, clinopyroxene accumulation would shift the samples towards enriched Y & V compositions respectively, relative to their true melt composition. Although this

may be true, the indication of a volcanic-arc signature, as revealed by ratios such as Th/Nb and Th/Yb, is consistent with the evidence of Figure 7.10 A & B.

7.7.3 SUMMARY OF TECTONIC DISCRIMINATION

7.7.3.1 GROUP 1a & GROUP 1b

According to the tectonic discrimination diagrams, the samples of Group 1a are variably-enriched E-MORB-like basalts. Some samples are enriched in Th (as also identified in the N-MORB normalised multi-element diagrams of Section 7.5.1) which may be explained by:

1) contamination with continental crust;
2) addition of a subduction component;
3) originating from an EM-type mantle (which is ultimately thought to gain its enriched Th from incorporation of subducted sedimentary material, (e.g. Weaver 1991; Hoffmann 1997).

Group 1b is enriched to a lesser extent than Group 1a, and shows no large Th enrichment (or VAB signature). On the basis of the diagrams used above, the samples of Group 1b are E-MORB.

7.7.3.2 GROUP 2a & GROUP 2b

Although they have different trace element patterns (see section 7.5.2), Group 2a and 2b are shown by the discrimination diagrams to have similar characteristics. Although they are VAB, it is uncertain whether they are continental or oceanic VAB. According to Figure 7.9A & B, a small number of samples are similar to N-MORB, which is inconsistent with trace element patterns showing all samples as having high $[Th/Nb]_N$ ratios.

7.7.3.3 GROUP 2c & GROUP 2d

Group 2c rocks have N-MORB-like trace element patterns (with the exception of TS02-58A, which has a marked Zr and Hf enrichment). An N-MORB setting is also generally shown by discrimination diagrams. Group 2d rocks are highly unusual. They have broadly basaltic compositions, but do not have a composition characteristic of any one setting (in terms of the parameters used by the discrimination diagrams).

Of particular interest are the enriched trace element patterns, which show the REE to be enriched relative to Ti, Hf and Zr.

7.7.3.4 GROUP 3

The tectonic discrimination of Group 3 can be affected by the geochemical effects of clinopyroxene phenocrysts in the protolith. However, evidence from trace element patterns and discrimination diagrams point to a depleted N-MORB-like protolith, which has a "weak" volcanic-arc signature. Such a signature may be expected for rocks originating at back-arc basins.

7.8 FINDING ANALOGUES FROM LARGE DATASETS

7.8.1 THE SUM OF D-SQUARED METHOD

When interpreting geochemical data it is often useful to know whether it resembles any data previously published. The "Sum of the Difference Squared" (ΣD^2) method is a useful way of doing this. The ΣD^2 method calculates the difference between the concentration of elements, or ratios between elements, of different samples using a simple equation. The difference can be calculated in two ways:

1) by calculating the actual difference in concentration of elements between different samples (e.g. subtracting the concentration of Ba in one sample from the concentration of Ba in another) here termed "absolute comparison";
2) by calculating the percentage difference between elements in different samples, here termed "relative comparison."

Before summarising the methods outlined above, it is necessary to first outline the terminology used in the subsequent sections:

1) the sample of the new geochemical dataset under investigation (i.e. results of analyses for this study), to which the published sample data is to be compared, is here termed "unknown";
2) samples that make up the database of published data are termed "possible analogues" or "potential analogues";

3) if a sample of the published database is found to be similar to the unknown, it is termed "analogue" or an "analogous sample."

7.8.1.1 ABSOLUTE COMPARISON

A selection of elements are chosen for comparison, and the difference between that element in the unknown and possible analogue is calculated. This is termed the difference "D" or "D-value." D-values for each of the elements are then squared, to remove negative results, and the result is termed D^2. The D^2 values for each element are then summed, and the product is termed ΣD^2 (see equation 7.1).

$$\Sigma D^2 = (X^a_U - X^a_A)^2 + (X^b_U - X^b_A)^2 + (X^c_U - X^c_A)^2 \ldots \quad (7.1)$$

Where: X^a_u is the concentration of element, or ratio, "a" in the unknown, and; X^a_A is the concentration of element, or ratio, "a" in the potential analogue.

7.8.1.2 RELATIVE COMPARISON

This calculation is similar to the equation for the absolute difference, only this time the difference (D) represents a percentage difference between two samples:

$$\text{Percentage difference } (\Sigma D^2_{\%}) = (\sqrt{(X^a_u - X^a_A)^2})/ X^a_u * 100 \quad (7.2)$$

$$\Sigma D^2_{\%} = (\sqrt{(X^a_u - X^a_A)^2})/ X^a_u) * 100 + (\sqrt{(X^a_u - X^a_A)^2})/ X^a_u) * 100 \ldots. \quad (7.3)$$

Where: X^a_u is the concentration of element or ratio "a" in the unknown, and X^a_A is the concentration, or ratio, of element "a" in the potential analogue.

7.8.1.3 CHOOSING WHICH ELEMENTS TO COMPARE

The choice of elements used for the ΣD^2 method has a fundamentally important effect on the quality of the outcome. Four factors were found to be particularly important when comparing the compositions of metamorphic, or altered, rocks with possible analogues:

1) only immobile elements should be used, to avoid the result reflecting the effects of alteration;
2) it is advisable to use elements that can be routinely analysed by a number of techniques (e.g. x-ray fluorescence, ICP-MS) because certain elements, such as Ta, Hf, cannot be accurately analysed for by some techniques. Thus, a potentially large number of samples will not be compared if such elements are used in the calculation.
3) high abundance elements can be analysed more accurately, and it is therefore advisable to choose elements that are relatively abundant, e.g. relatively high abundance REE, Nb instead of Ta etc.
4) the elements chosen should represent a wide range of geochemical properties. If all the elements are geochemically similar, then they are all likely to have similar compositions in the unknown and a potential analogue, and so ΣD^2 will be "weighted." An example would be the similarities between MORB and IAT in terms of MREE and HREE (e.g. Pearce & Peate 1995). If just these elements were compared between such rocks the ΣD^2 would be low (indicating similarity), even though the rocks may be significantly geochemically different.

7.8.1.4 COMPILING THE DATA SET OF POTENTIAL ANALOGUES

The data set was made by compiling data from petrological databases available on the World Wide Web at http://petdb.ldeo.columbia.edu/petdb/ and http://georoc.mpch-mainz.gwdg.de/. Some other data from recent publications and data absent from the electronic databases were also added. A database of >30 000 altered and fresh samples from a wide range of tectonic settings has been compiled from these sources. The database covers a wide range of rock types, from ultramafic to felsic, including granites, cumulates (e.g. gabbros), hydrothermally altered rocks, and sediments, which were analysed by different techniques.

7.8.1.5 THE PREFERRED METHOD FOR ΣD^2 CALCULATION

As there are many different ways in which the ΣD^2 method can be carried out, there are potentially many different solutions. Consequently, different combinations of the

methods were used. Of these methods, the relative comparison using both element abundance and element ratios was found to be most useful. This was because:

1) differences in elemental abundance in the unknown and the possible analogues that were brought about by fractionation, or partial melting, could be "seen through" by using certain trace element ratios. Thus it was possible to compare chemical signatures representing different sources and signatures brought about by contamination.
2) particular characteristics of the unknown could be "exaggerated" when deciding between a number of possible analogues, e.g. the Th/Nb ratio was useful in deciding between which of a small number of potential analogues most closely resembles Group 1a.

7.8.2 RESULTS OF THE ΣD^2 CALCULATIONS

7.8.2.1 GROUP 1a

From the results of the ΣD^2 calculations presented in Figure 7.11 and Table 7.3, it is clear that the analogues share many similarities with Group 1a. These are:

1) overlapping trace element patterns in Figure 7.11A, and similar $[Th/Nb]_N$ and $[Sm/Hf]_N$ ratios (Table 7.3);
2) two of the analogues have been classified as transitional alkaline basalts, and one as a basalt, which is similar to the classification of Group 1a
3) the tectonic setting for the analogues is a within plate setting, which is what is predicted for Group 1a in Section 7.7.

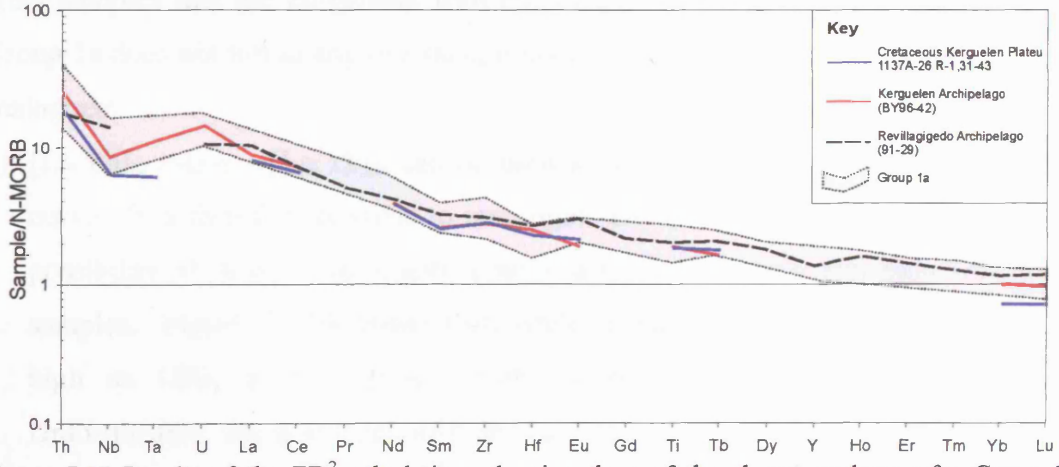


Figure 7.11 Results of the ΣD^2 calculations showing three of the closest analogues for Group 1a. Normalisation values are from Sun & McDonough (1989). See caption of Table 7.4 for details of data sources.

Sample (ref)	Location	Rock type	$[Th/Nb]_N$	$[Hf/Sm]_N$	Tectonic Setting	PETROGENESIS
90-78 (1)	Revillagigedo Archipelago/ Pacific ocean	Transitional alkali basalt	1.22	0.72	Volcanic island developed on mid-ocean ridge post-spreading.	Melts produced by similar degrees of melting of a homogenous mantle source were contaminated by "oceanic crustal components"
BY96-42 (2)	Kerguelen Archipelago	Aphyric, low-Mg basalt	2.79	0.96	Emergent part of the Kerguelen large igneous province	Mixing between magmas of a depleted mantle and magmas from the enriched Kerguelen plume. No evidence for contamination with continental crust.
1137A-26R-1, 31-43 (3)	Cretaceous Kerguelen plateau	Transitional-alkali basalt	2.89	0.91	Oceanic plateau	Magmas derived from the Kerguelen plume, and subsequently contaminated by incorporation of continental crust.

Table 7.5 Results of the ΣD^2 experiments showing three of the closest analogues for Group 1a. References: (1) Bohrson & Reid (1995); (2) Doucet et al. (2002); (3) Ingle et al.(2002). Relevant trace element ratios and major element characteristics are discussed in the main text.

The summary of petrogenesis given in Table 7.4 shows that contamination plays a role in the petrogenesis of the analogues from the Revillagigedo archipelago and the Cretaceous Kerguelen plateau. In contrast, the petrogenesis of the analogues from the Kerguelen archipelago does not involve any contamination (Ingle et al. 2002). However, as noted by Weaver et al. (1991) and Kamber & Collerson (2000), a role for contamination of any basalts related to the Kerguelen plume may be ultimately preserved, as the EM-1 character of the plume is well established. This may also explain the poor Zr and Hf correlation with Nb noted in Section 7.6.2.2.

Figure 7.12 A & B compares the characteristic trace element ratios of Group 1a with other samples that are co-genetic with the analogues. It can be seen that although Group 1a does not fall in any one field, it does show a number of similarities with the analogues:

1) $[La/Yb]_N$ ratios - $[La/Yb]_N$ can be used as a measure of the slope of the REE curve. It is therefore possible to investigate the REE curve of Group 1a, and the possibility of there being a garnet signature, by comparing this ratio with other samples. Figure 7.12A shows that, while Group 1a does not have $[La/Yb]_N$ as high as OIB, it does have similar ratios (of ~7-15) to the analogues. Unfortunately, the possibility of high $[La/Yb]_N$ ratios expressing garnet signatures in the analogue data is not discussed explicitly in the relevant papers.

Nevertheless, smooth REE curves with supra-N-MORB La/Yb ratios are good evidence for there being a garnet signature in the Group 1a geochemistry.

2) high $[Th/Nb]_N$ and low $[Hf/Sm]_N$ ratios - Figure 7.12A shows that the uncontaminated Kerguelen plateau samples best match the $[Th/Nb]_N$ ratios of Group 1a, whereas Figure 7.12 B shows that the samples from the Revillagigedo archipelago most closely match the range of $[Hf/Sm]_N$ ratios.

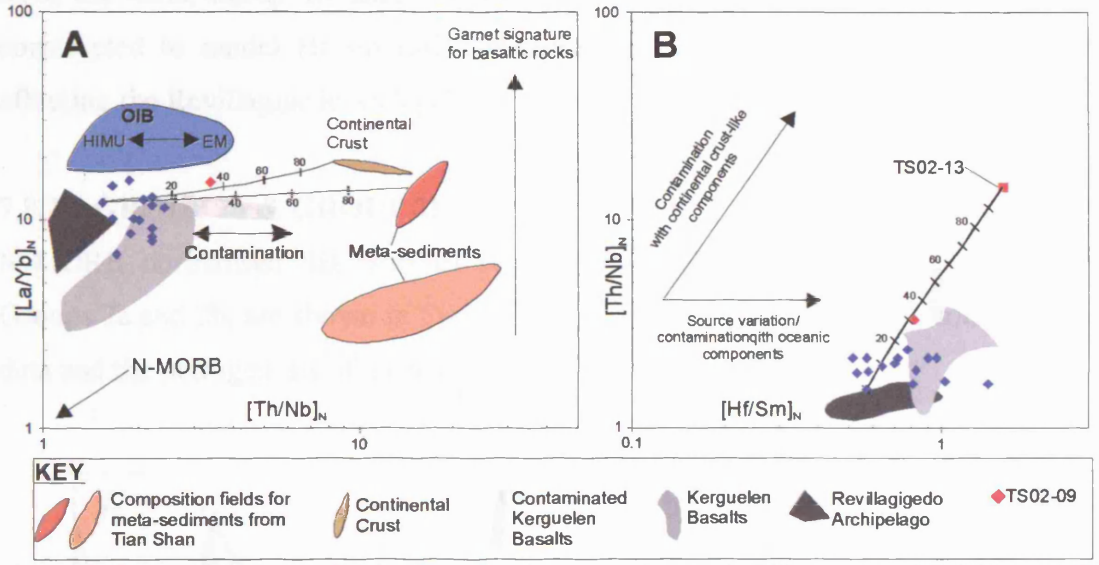


Figure 7.12 N-MORB normalised ratio-ratio diagrams of: A) $[La/Yb]_N$ against $[Th/Nb]_N$ and B) $[Th/Nb]_N$ against $[Hf/Sm]_N$. Normalisation values are from Sun & McDonough (1989). Fields for continental crust are constructed using data from Gao et al. (1998), and the fields for meta-sedimentary rocks are taken from this study, see section 7.10. On Figure 7.12A modelled mixing trends were derived by mixing the sample with the lowest Th/Nb ratio from Group 1a with either continental crust or the meta-sedimentary sample TS02-13 (collected from Tian Shan). On Figure 7.12B mixing trends were calculated using the same sample from Group 1a as used in Figure 12A, however only TS02-13 is used as an end-member because of the similarities of this sample with continental crust.

As contamination may have played an important role in the petrogenesis of the analogue samples, a mixing model is shown in Figures 7.12 A & B. This model uses the Group 1a sample with the lowest Th/Nb ratio and two potential sources of contamination: 1) continental crust, and; 2) a meta-sediment collected from Tian Shan (TS02-13). These sources have been considered because: 1) continental crust is thought to contaminate the Kerguelen plume (e.g. Ingle et al. 2002); 2) sedimentary material may have been incorporated into the protoliths of Group 1a during eruption, and; 3) because unfortunately only the geochemistry of the contaminant for the Cretaceous Kerguelen samples can be estimated.

As can be seen from Figures 7.12 A & B, Group 1a does not trend along the mixing lines. One sample however, TS02-09, plots at a distance away from the other samples on the mixing line with continental crust, but this single sample cannot be used as conclusive evidence for mixing. Figure 7.12 B shows that although Group 1a does not follow the mixing line, it does have a similar trend to the Revillagigedo archipelago samples. Also TS02-09 again plots on the mixing line at a point away from the main Group 1a sample cluster. Unfortunately, a mixing line cannot be constructed to model Hf/Sm ratios because the geochemistry of the contaminant affecting the Revillagigedo archipelago basalts is unknown.

7.8.2.2 GROUP 2a & GROUP 2b

N-MORB normalised diagrams of selected trace elements samples analogous to Groups 2a and 2b, are shown in Figure 7.13 A & B. A summary of the source of the data and the petrogenesis of the analogues is given in Table 7.5.

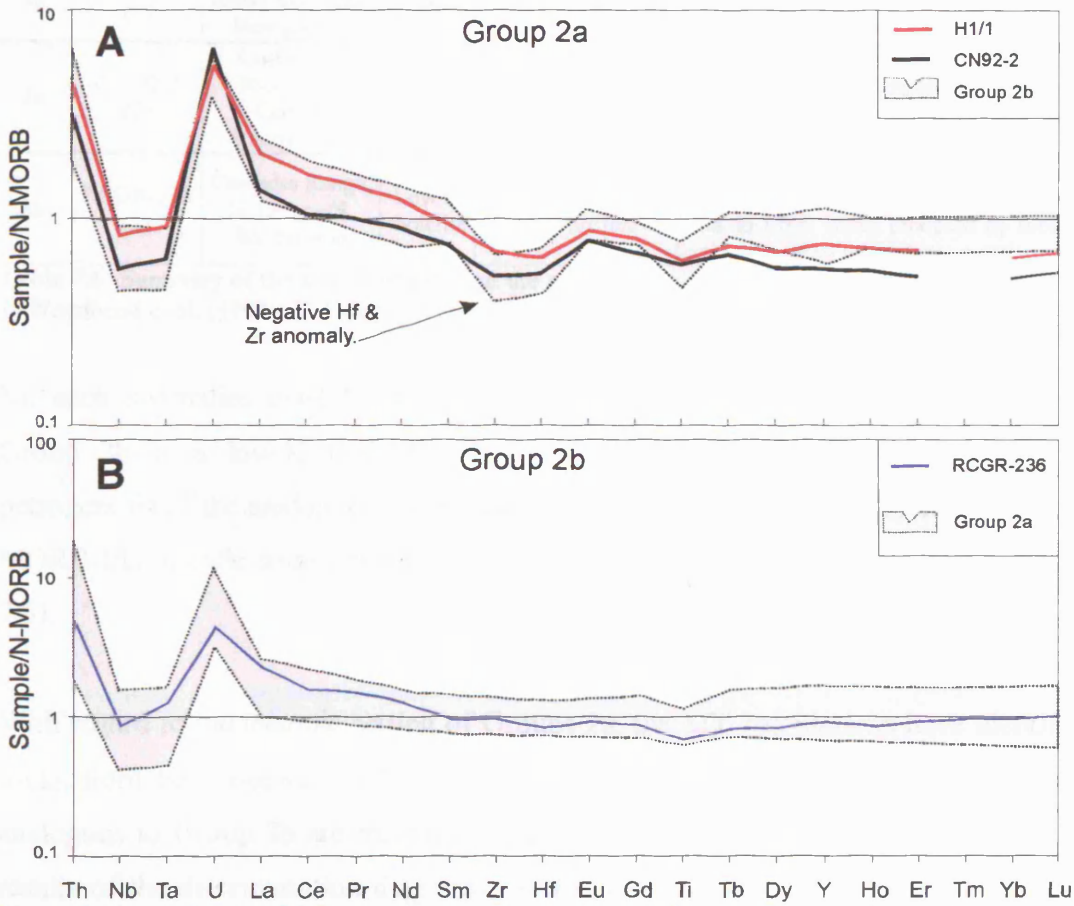


Figure 7.13 A & B. N-MORB normalised diagrams of selected immobile trace element for Group 2a (A) and Group 2b (B), respectively, compared with analogues suggested by the ΣD^2 experiments. Note the similar trace element patterns, including the relative depletion of Hf and Zr for Group 2a.

The overlapping trace element patterns of Figure 7.13A indicate that the ΣD^2 calculations have successfully identified chemical analogues for Group 2a. Importantly, these analogues display the same relative depletions of Zr and Hf that characterise Group 2a. Unfortunately these characteristic features are not discussed explicitly in the relevant publication (see Table 7.5). For example, the Zr and Hf depletions of the sample from the New Britain Arc are explained in terms of a general HFSE depletion of the mantle, (which resulted from melting events prior to the eruption of the analogues). Additionally, the Zr and Hf depletions of the sample from the Central American arc are not discussed at all. Despite the lack of any explanation of the depletions of Zr and Hf in the analogue samples, the ΣD^2 calculations have revealed that these characteristics can be recognised in basalts from both oceanic and continental arc settings.

Group	Sample (reference)	Location	Rock Type	Tectonic Setting	PETROGENESIS
2a	H1/1 (1)	New Britain Island arc/ Papua New guinea	Basalt	Island Arc	Extremely low HFSE concentrations (relative to N-MORB) resulted from depletion of the mantle source by prior melting events.
2a	CN-92-2 (2)	Costa Rica Nicaragua/ Central American arc	Basalt	Continental volcanic arc	N-MORB-like source with variable contributions from subducting slab reflecting different subducting sediment compositions and proportions.
2b	RCGR-236 (3)	Cascades Range, N. Oregon/S. Washington	Low-K tholeiite	Continental volcanic arc	Low-K tholeiites associated with rifting of the arc. Lavas are essentially MORB-like, with enrichments in LILE being produced by melting of subduction-modified lithospheric mantle.

Table 7.6 Summary of the source of data and the petrogenesis of the analogue samples. References: 1) Woodhead et al. (1998); 2) Thomas et al. (2002); 3) Conrey et al. (1997).

No such anomalies exist for Group 2b (Figure 7.13B). The closest analogue for Group 2b is a low-K tholeiitic VAB from the Cascades Range, USA. The petrogenesis of the analogue is relatively straight forward, involving melting of an N-MORB-like mantle source that was modified by slab-derived fluids/melts (see Table 7.5).

With regard to the tectonic setting of Groups 2a, the ΣD^2 calculations have identified rocks from both oceanic and continental volcanic arc settings, whereas the rocks analogous to Group 2b are from a continental arc. These findings are similar to the results of the discrimination diagrams, in that it is not possible to clearly determine whether Group 2 as a whole originates from a continental or oceanic volcanic arc.

This ambiguity probably results from the many processes in operation during petrogenesis at volcanic arcs. Apart from fractionation and partial melting, the relevant processes include the nature of the source region, contamination during ascent of melts, and components added to the mantle source regions from the subducting slab. Consequently, in order to determine whether Group 2a originates from a continental or oceanic arc, it necessary to use other, non-geochemical, information, this is further discussed in Section 7.9.

7.8.2.3 GROUP 3

The ΣD^2 calculations have been successful in identifying Group 3 analogues, as can be seen by the overlapping trace element patterns in Figure 7.14. Two samples in particular closely resemble the Group 3 pattern. These show the increasing depletion with increasing incompatibility and the high $[Th/Nb]_N$ and low $[Hf/Sm]_N$ ratios that are characteristic of Group 3. The slight negative Ti anomaly seen in Group 3 is also present for the Manus BABB samples, but not for the seamount samples. Important differences between Group 3 and the analogue samples are that in Group 3 the HREE are more enriched, and U, Th, Nb and Ta are more depleted. This may be explained by the majority of Group 3 protoliths being clinopyroxene-phyric (as suggested in Section 7.5.4), as clinopyroxne phenocrysts would enrich the HREE and deplete Th and Nb bulk rock geochemistry.

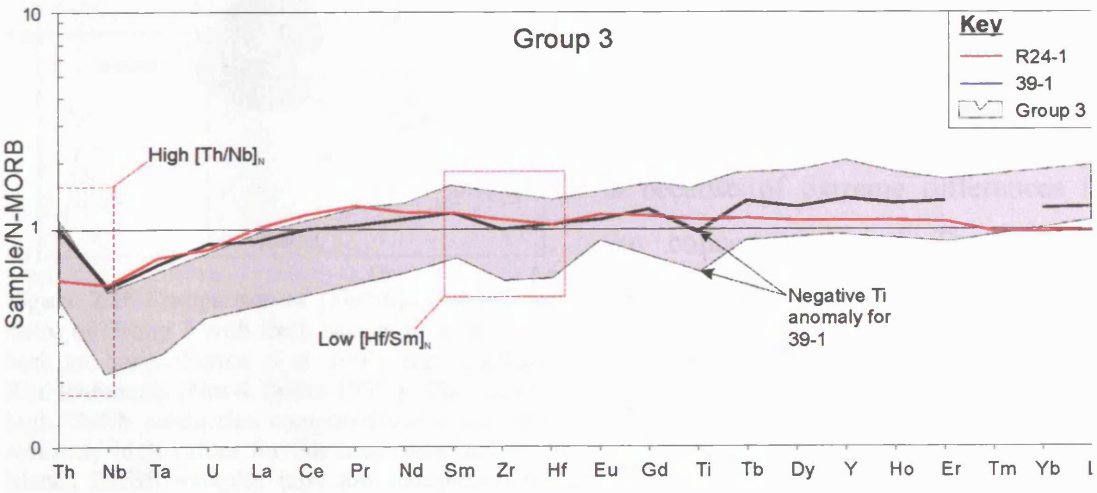


Figure 7.14 N-MORB normalised diagrams of selected trace elements comparing the results of the ΣD^2 method with Group 3. See Table 7.6 for a summary of the location, tectonic setting and petrogenesis of the analogues.

Sample (Ref)	Location	Rock Type	Tectonic Setting	$[Th/Nb]_N$	$[Hf/Sm]_N$	PETROGENESIS
39-1 (1)	Manus back arc basin, Papua New Guinea	Low-K_2O tholeiitic basalt	Back-arc basin spreading centre	1.85	0.89	N-MORB-like basalts, more depleted than typical N-MORB, were derived from a mantle depleted by previous melting events. Although MORB-like, volcanic arc signatures (e.g. enrichment of LILE) are also apparent for these basalts.
R24-1 (2)	Off axis Seamounts near the East Pacific Rise	Tholeiitic basalt	Off axis seamount	1.05	0.89	A range of depleted and enriched basalt compositions are produced by melting-induced mixing between melts from enriched and highly depleted (relative to typical MORB mantle) mantle components.

Table 7.7. Summary of the location, rock type, tectonic setting and petrogenesis of the analogue samples. References: 1) Sinton et al. (2003); 2) Niu & Batiza (1997).

To fully explain the petrogenesis of Group 3 protoliths, it is necessary to understand the causes of the high $[Th/Nb]_N$ and low $[Hf/Sm]_N$ ratios. These ratios are investigated in Figure 7.15, which shows that the closest analogues are from the Manus Back-arc Basin. The principal difference between Group 3 and the off axis seamount lavas from the East Pacific Rise is that $[Th/Nb]_N$ ratios of Group 3 are much higher for a given $[Hf/Sm]_N$ ratio. This is significant because high $[Th/Nb]_N$ ratios may indicate a subduction signature or perhaps contamination with continental crust-like materials.

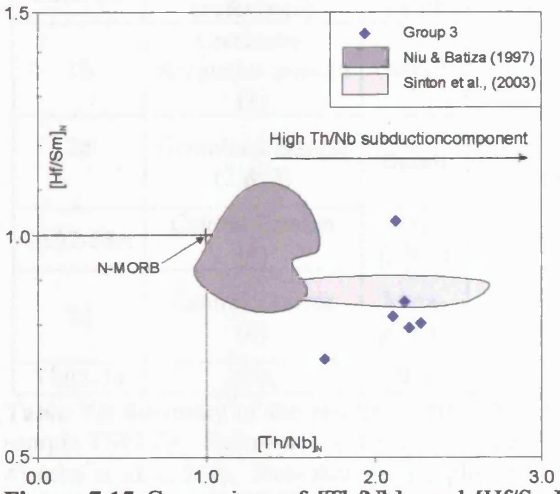


Figure 7.15 Comparison of $[Th/Nb]_N$ and $[Hf/Sm]_N$ ratios of Group 3 with fresh basalts from the Manus back arc basin (Sinton et al. 2003) and East Pacific Rise seamounts (Niu & Batiza 1997). The vector for high Th/Nb subduction components is based on the relatively high values for this ratio displayed by the Manus BABB samples (and the interpretations of Sinton et al. 2003).

The possibility of mixing with continental crust-like components and with meta-sediments from Tian Shan, to produce the characteristic trace element ratios has been investigated, but is not shown on Figure 7.15. This is because of extreme differences in the concentrations of Th and Nb between the contaminants and Group 3. Very small proportions of <1% contaminant are required to cover the range of $[Th/Nb]_N$ in group 3 rocks. Furthermore, the mixing curves do not "fit" the Group 3 trend. This points to an important precaution in interpreting Group 3 rocks: only small amounts of any contaminant are required to significantly change the characteristic element ratios.

7.8.2.4 OTHER META-IGNEOUS ROCKS

Groups 1a, 2a, 2b and 3 make up the majority of the meta-volcanic samples collected from Tian Shan. Other samples are few in number and show large degrees of chemical heterogeneity, restricting the potential for a detailed investigation of their petrogenesis. However, the ΣD^2 calculations were successful in finding analogues for Groups 1b and 2c (Figure 7.16 A & B, and Table 7.7). Unfortunately, no analogues could be found for the rodingite sample TS02-34.

As noted previously, Group 2c contains the sample TS02-58a, which has been shown to have certain characteristics different from other samples in the group (such as enriched Hf and Zr relative to REE). Such characteristics are "complimentary" to Group 2d, which is depleted in Zr and Hf with respect to the REE (Figure 7.16D). Although the ΣD^2 calculations did not identify any analogues for Group 2d and TS02-58a, gabbroic eclogites with similar characteristics were recently investigated by John et al. (2004) (Figure 7.16 C & D, and Table 7.6).

GROUP	LOCATION (reference)	ROCK TYPE	TECTONIC SETTING	PETROGENESIS
1b	Cretaceous Kerguelen plateau (1)	Basalt	Large igneous province (WPB)	Contamination of plume and Indian ocean mantle by continental crust.
2c	Greenland margin (2 & 3)	Basalt	Rifted continental margin	MORB-like lavas emplaced after rifting and subsequently contaminated with continental crust.
TS02-58A	Central Zambia (4)	Meta-gabbro	Orogenic belt	Reaction of the gabbro with REE-rich fluids which initiated eclogitisation.
2d	Central Zambia (4)	Meta-gabbro	Orogenic belt	During dehydration of gabbro REEs were liberated to the fluid, leaving the gabbro depleted in these elements.
TS02-34	N/A	N/A	N/A	N/A

Table 7.8 Summary of the results of the ΣD^2 calculations for Groups 1b, 2c, 2d and the rodingite sample TS02-34. References: (1) Frey et al. 2002; (2) Brooking et al. (1999); (3) Larsen et al. (1999) 4) John et al. (2004). Note that the samples from John et al. (2004) were not identified by the ΣD^2 method. N/A – not available, i.e. no analogous samples found.

From the overlapping trace element patterns on Figure 7.16 A, it can be seen that the ΣD^2 calculations have identified samples from the Kerguelen plateau as being chemically similar to Group 1b. This is consistent with the analogues identified for the chemically similar Group 1a. Furthermore, the petrogenesis of Group 1b analogues (see Table 7.6) is thought to involve contamination of the mantle source with continental crust (Frey et al. 2002).

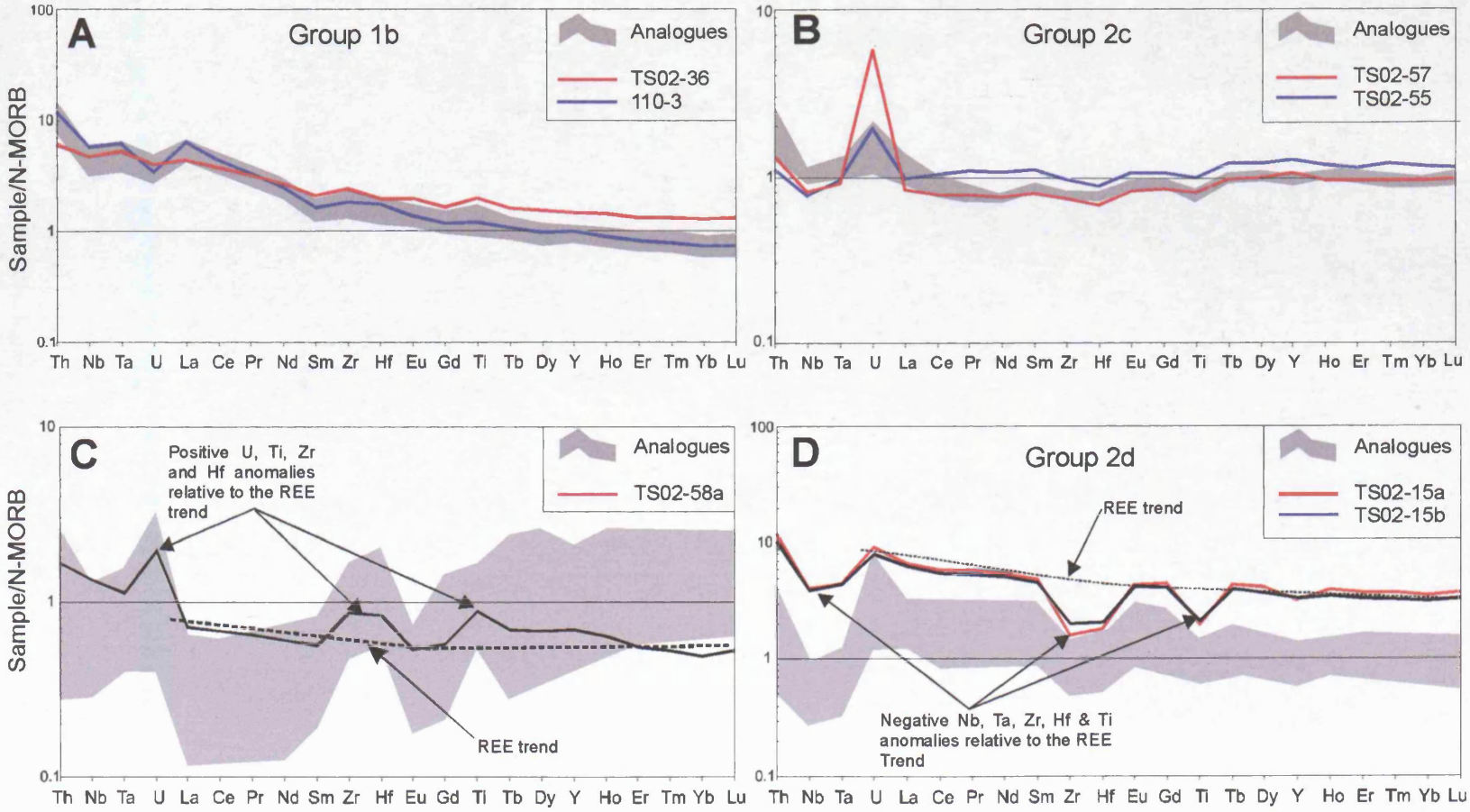


Figure 7.16 A-D. N-MORB normalised multi-element plots of: A) Group 1b and analogues; B) Group 2c and analogues; C) TS02-58a and similar eclogites from central Zambia (their Group II) analysed by John et al. (2004), and; D) Group 2d and similar eclogites from central Zambia recently analysed by John et al. 2004).

The analogues for Group 2c meta-basalts are basalts originating from the Greenland margin. From Figure 7.16 B it can be seen that these Greenland margin basalts have similar trace element patterns to Group 2c, including the relative enrichments of U and Th. The identification of these analogues is significant because their petrogenesis (see Table 7.6) involves the contamination of N-MORB-like lavas with continental crust, which is consistent with the findings for Group 1a and 1b.

As previously discussed, the enrichments of elements such as Zr and Hf relative to the REE of TS02-58a can be considered complementary to the depleted Zr Hf relative to the REE of Group 2d (compare Figure 7.16 C & D). Such contrasting geochemical signatures were also identified in Zambian eclogitic meta-gabbros by John et al. (2004) (Figure 7.16 C & D).

With regard to the petrogenesis of the Zambian eclogites, John et al. (2004) infer that these geochemical signatures were developed from fluids that existed during fluid-induced eclogitisation of the primary gabbros. According to their interpretation, these fluids de-coupled, or fractionated, the LREE from HFSE from co-genetic samples. It therefore follows that the meta-gabbros have a residual subduction zone chemical signature (i.e. a chemical signature resulting from subduction zone metamorphism). Such a hypothesis is ostensibly supported by the fact that a REE "source" (i.e. samples enriched in Zr and Hf relative to REE) and "sink" (i.e. samples depleted in Zr and Hf relative to REE) exist in the Zambian meta-gabbros.

As the apparent existence of eclogites with residual subduction zone signatures is highly relevant to this work, it was necessary to confirm the findings of John et al. (2004) by re-examining their data using the methods developed for previous sections of this work. A brief re-examination of the data is given below.

In this section, only the eclogites named as Group II by John et al. (2004) are further investigated. John et al. (2004) state that "The characteristic feature of this group is an unusual decoupling of LREE (La-Gd) from the HREE and HFSE." Later they state that, "Magmatic processes alone do not decouple the LREE from the HREE and HFSE. Instead, the observed fractionation in the Group II eclogites must have occurred during reaction of the rocks with aqueous fluid." Therefore a suitable test

for this hypothesis is whether the LREE really have been decoupled from HFSE and LREE. If it can be established that the LREE still correlate with the HFSEs in this group, then the LREE have not been de-coupled (or mobilised) from the HREE or HFSE.

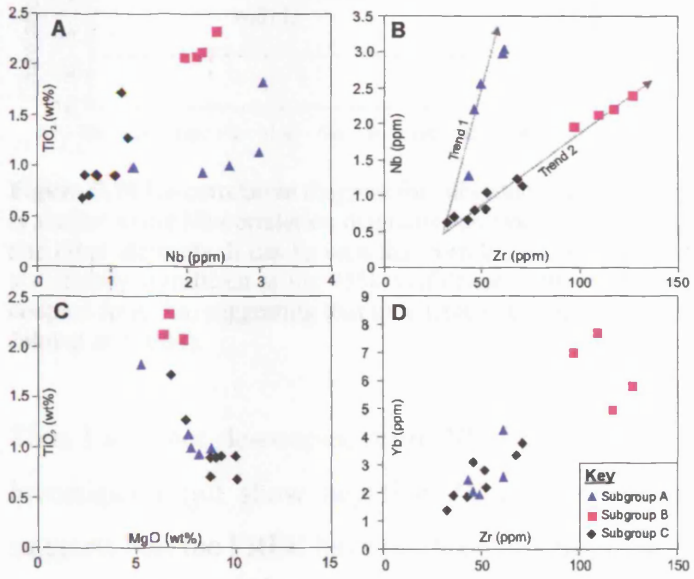


Figure 7.17 A-D Scatter plots of elements considered immobile by John et al. (2004) illustrating the possible subgroups that can be made from their Group II eclogitic gabbros.

The first task was to determine whether the samples of Group II are co-genetic by investigating the relationships between different HFSE and HREE (which are thought to be immobile, and hence reflect the protolith composition). After examining co-variation diagrams (see Figure 7.17 A-D), it was found that the variation of Group II-D could not be explained by the samples being simply co-genetic, i.e. the samples are not related by simple fractionation or partial melting processes. This is best illustrated by the two trends identified in Figures 7.17 B, which uses Zr as an index of fractionation. On the basis of Figure 7.17 A-D, at least two, and possibly three, subgroups can be identified.

To investigate the correlation of LREE with HFSE and HREE, Figure 7.18 is a simplified La (a LREE) correlation diagram, using the subgroup from Figure 7.17 A-D with the most samples. This diagram is similar to the Nb-correlation diagrams of section 7.6, but investigates correlation of elements with La instead of Nb. It can be seen from Figure 7.18 that La positively correlates with most of the HREE and HFSE (excluding U). There is very little difference between the $r_{La\text{-}Nd}$ (0.79), $r_{La\text{-}Zr}$ (0.8) and $r_{La\text{-}Lu}$ (0.79), and often the correlation is statistically significant at the 95% confidence limit.

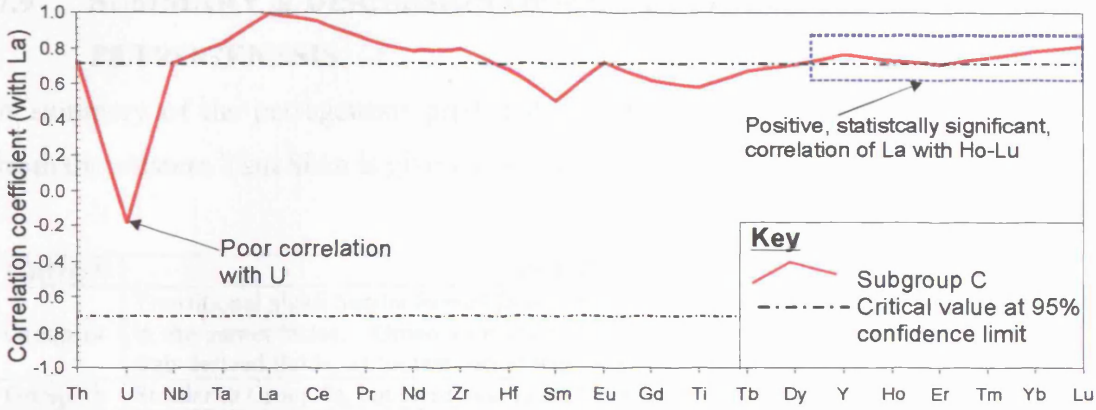


Figure 7.18 La-correlation diagram for subgroup C from Group II of John et al., (2004). This diagram is similar to the Nb-correlation diagrams described in Section 7.6, but shows the correlation between La and other elements. It can be seen that correlation coefficients of HREE, Th, Nb and Ta with La are all statistically significant at the 95% confidence limit. It follows that these elements have not been de-coupled from La, suggesting that they have not been mobilised. These findings are contrary to that of John et al. (2004).

Thus La is not de-coupled from Nb, Ta, Zr, Hf, Th and the HREE in the samples investigated (all show negative Zr and Hf anomalies, see Figure 7.16D). This suggests that the LREE have not been mobilised, and that the trace element patterns in Figures 7.16 C & D reflect the composition of the protolith.

In apparent support of this reappraisal of the data of John et al. (2004) is the fact that a Tian Shan blueschist sample (TS02-15b) carries a similar trace element signature to some of the gabbroic eclogites (see Figure 7.16D). This is significant because the trace element signatures of the gabbroic eclogites are supposed to develop during eclogitisation (John et al. 2004), so a blueschist with such a signature is contradictory. Furthermore new geochemical data (Lilley et al. in prep) of unaltered basalts and dolerites from the Oman ophiolite also show trace element signatures similar to those of the gabbroic eclogites of John et al. (2004). Thus, igneous processes can produce the geochemical features discussed in this section, although an explanation of these processes is out of the scope of this thesis.

In conclusion, although samples with similar compositions to Group 2d and TS02-58a do exist, their characteristic trace element patterns are not likely to have developed during subduction zone metamorphism. It is anticipated that investigation of the basalts and dolerites from the Oman ophiolite will shed light on the igneous processes that can produce the geochemical characteristics discussed in this section.

7.9 SUMMARY & DISCUSSION OF META-VOLCANIC ROCK PETROGENESIS

A summary of the petrogenesis predicted for each group of meta-basalts identified from the western Tian Shan is given in Table 7.7.

GROUP	PETROGENESIS
Group 1a	Transitional alkali basalts formed from melts with trace element patterns indicating melting in the garnet facies. Group 1a is relatively enriched in Th which may originate from: 1) slab-derived fluids; 2) contamination with continental crust; 3) EM-type mantle source.
Group 1b	Similar to Group 1a, but these basalts are less enriched.
Group 2a	Slab-derived fluids were added to a depleted MORB mantle in either a continental or oceanic arc.
Group 2b	Slab derived fluids were added to a MORB-like mantle at continental volcanic arc setting.
Group 2c	(Not TS02-58A) Basalts from N-MORB-like mantle source were contaminated by continental crust.
Group 2d	(Including TS02-58A) Uncertain igneous petrogenesis, but trace element patterns were not likely to have developed as a result of eclogitisation.
Group 3	Clinopyroxene-phyric basalts melted from a highly depleted MORB mantle, perhaps in a back arc basin. Basalts slightly enriched in Th indicating either contamination or a subduction component.

Table 7.9. Summary of the petrogenesis of the various meta-basaltic samples groups of the western Tian Shan blueschist belt.

From Table 7.8, it can be seen that the petrogenesis of Groups 1a, 1b and 1c is thought to involve some kind of contamination, perhaps with continental crust. Contamination may also play a role in the petrogenesis of Group 3, although this cannot be stated with any certainty (see below). Group 2a originated from either a continental or oceanic volcanic arc and Group 2b from a continental arc. It is thus possible to divide the groups into: 1) those involving contamination, and; 2) those that originating from a volcanic arc.

7.9.1 CONTAMINATED BASALTS

There is evidence for continental crust-like materials having contaminated the basalts of Group 1a, 1b and 1c. A possible setting for such contamination would be a passive continental margin such as the Greenland margin, as predicted for Group 1c. At such a setting, the crust can be relatively thick, which would explain why some samples (i.e. Group 1a) show garnet signatures. Alternatively, the garnet signatures may have developed by melting below a seamount which developed close to a continental margin. Such a setting also makes sense for the tectonic evolution of the Tian Shan orogeny (see Chapter 9). This is because any basalts erupted on the northern (passive) margin of the Tarim plate would be among the last oceanic material to be

subducted below the (active) margin of the Yilli-central Tian Shan plate. Furthermore, the positive topography of a seamount may have aided the incorporation of Group 1a rocks into an accretionary prism, where they were subsequently metamorphosed (see Chapter 9 for more details).

7.9.2 BASALTS ORIGINATING FROM A VOLCANIC ARC

It is not possible to tell geochemically whether Group 2a originated from an oceanic or continental volcanic arc. If it is assumed that its protoliths originated from an oceanic arc, the logical question would be: "what is the current location of that arc?" Although the relative high buoyancy of an intra-oceanic arc would cause it to resist complete subduction, it is possible for "young" arcs (i.e. <20Ma old) to subduct, if their thickness is <15Km (Cloos 1993) or <16Km Boutelier et al. (2003). It may therefore be the case that the arc simply subducted. However, given the lack of any evidence for the thickness of this hypothetical intra oceanic arc, it not certain whether this was the case. The alternative hypothesis is that the island arc accreted to the south side of the Yilli-Central Tian Shan Plate (see Chapter 3 for a review of the collision tectonics of the Chinese Tian Shan). It is apparent from previous workers however, that such an accreted arc does not exist (e.g. Allen et al. 1992; Gao et al. 1998; Gao & Klemd 2003). Given that the characteristics of both Groups 2a and 2b can be produced at a continental volcanic arc, and the absence of any accreted oceanic arc, it is therefore possible that Group 2a & 2b protoliths both originated from a continental volcanic arc.

Evidence from trace element patterns, tectonic discrimination and the results of the ΣD^2 experiments have all testified to the difficulty of identifying the tectonic setting in which protoliths of Group 3 were produced. The difficulty results from two important features:

1) the likelihood of the protoliths being clinopyroxene-phyric reduces the effectiveness of many tectonic discrimination diagrams;
2) the highly depleted nature of the samples makes them susceptible to modification by even small proportions of contamination. This can affect important elemental ratios such as Th/Nb.

Two tectonic settings have been suggested for Group 3 protoliths: 1) a back-arc basin; 2) a seamount setting proximal to a spreading ridge. If a back-arc basin is assumed then it is necessary that a back arc basin subducted beneath the southern margin of Yilli-central Tian Shan (YSTS) margin. It therefore follows that the accompanying arc must have collided with the southern active margin of the YCTS plate. However as discussed above, there is no evidence for an accreted oceanic arc in the vicinity of the western Tian Shan blueschist belt. In the absence of an accreted arc, a different setting is required. A setting such as the EPR seamounts, which are proximal to a spreading ridge (as suggested by the ΣD^2 calculations), is not preferred because of the relatively high Th/Nb ratios of Group 3. Either a subduction component or contamination with continental crust is necessary to explain the geochemistry of Group 3. It may therefore be that the tectonic origin of Group 3 is similar to that of Groups 1a, 1b and 1c, i.e. a passive continental margin. Furthermore, as highly depleted tholeiitic basalts can be produced at a seamount setting (e.g. Niu & Batiza 1997, 2002) it may also follow that Group 3 was similarly erupted from a seamount.

7.9.3 COMPARISON WITH PREVIOUS WORK ON TIAN SHAN META-IGNEOUS ROCKS

From this work, it is clear that compositionally-diverse meta-igneous rocks are present in the western Tian Shan blueschist belt. Table 7.9 shows two previous studies of meta-igneous blueschists and eclogites from Tian Shan which also recognised diverse meta-igneous compositions (i.e. Gao & Klemd 2003; Volkova & Budanov 1999). However, the compositional diversity reported in these studies is not as great as reported for this work. For example Gao & Klemd (2003), who collected rocks from the same field area as this study, did not report rocks of volcanic arc affinity or highly depleted MORB-like basalts, whereas Volkova & Budanov (1999) found E-MORB, OIB and VAB, but not N-MORB. Common to both of these previous studies is the existence of OIB, which is not confirmed by this study.

REFERENCE	LOCATION	ROCK TYPES	PROPOSED TECTONIC SETTING
Gao & Klemd (2003)	Chinese Tian Shan	N-MORB, E-MORB and OIB	Seamount formed in proximity to a spreading ridge
Volkova & Budanov (1999)	Tajikistan	E-MORB, OIB and volcanic arc	The E-MORB and OIB erupted on a seamount which resulted from plume-type volcanism. Volcanic arc rocks formed continental volcanic arc
Li et al. (2003)	Chinese Tian Shan	Rodingite	Rodingites formed during exhumation by alteration of eclogite by fluids derived from "secondary" serpentinisation of surrounding ultramafic rocks.

Table 7.10. Summary of rocks types identified in previous work on meta-igneous rocks of Tian Shan

In terms of the tectonic origin of OIB and E-MORB meta-basalts, Gao & Klemd (2003) and Volkova & Budanov (1999) both predict a seamount setting. However, although the former assume a setting proximal to a spreading ridge, whereas the latter suggest a within-plate plume-related seamount.

Finally, rodingites have recently been reported by Li et al. (2003) from the western Chinese Tian Shan blueschist belt. These have been interpreted as resulting from "secondary serpentinisation" during exhumation of the subducted oceanic plate" (Li et al. 2003). This is in contrast to the usual ocean-floor metamorphic origin of these rocks.

7.10 GEOCHEMISTRY OF META-SEDIMENTARY PROTOLITHS

As outlined in Section 7.2 it is much more difficult to interpret the bulk rock geochemistry (e.g. the likely compositional variation, the tectonic origin of the sedimentary material) of protoliths of meta-sedimentary rocks than of meta-igneous rocks. In this section, the potential problems with interpreting the bulk-rock geochemistry of meta-sedimentary rocks in general are explored. Following this is an examination of the geochemistry of meta-sedimentary samples collected for this work.

Previous work on the provencing of comprehensive geochemical datasets from subduction zone-metamorphosed meta-sedimentary rocks is restricted to one publication: Sadofsky & Bebout (2003). Other works include Li et al. (2004), Cingolani et al. (2003) and Kiminami & Ishihama (2003), but these have focused on "slightly" metamorphosed meta-sedimentary rocks (i.e. not eclogites or blueschists). Work on non-metamorphosed rocks include McLennon et al. (1983); Bhatia & Crook

(1986), Yang et al. (2003), Cullers (2000), Plank & Langmuir (1998), Othman et al. (1989) and Spinelli & Underwood (2004). Although all of these studies attempt to determine the provenance (i.e. tectonic setting) of the sedimentary rocks, two are particularly important in laying the foundations for the current methods of tectonically discriminating the provenance of sediments: 1) Bhatia & Crook (1986), and; 2) McLennan et al. (1993).

Based on the geochemistry of rocks from Palaeozoic turbidite sequences of eastern Australia, a number of discrimination diagrams were proposed by Bhatia & Crook (1986): La-Th; La-Th-Sc; La/Y-Sc/Cr; Th-Sc-Zr/10, and; Th-Co-Zr/Th. It is these diagrams that are often used by workers to investigate the provenance of sedimentary rocks (e.g. Cingolani et al. 2003 and Li et al. 2004). As well as proposing discrimination diagrams, Bhatia & Crook (1989) discuss the theoretical framework under which the diagrams operate. It is therefore convenient to refer to this framework to offer a critique of the methods used when tectonically discriminating the provenance of sediments. There are four factors of the framework that require discussion:

1) are different tectonic settings defined by a few rock types with distinct chemical characteristics?
2) can any distinct chemical characteristics of the parent rock be imparted to the sediments that derive from them? If so, what elements are useful for linking the composition of the sediment to its parent rock?
3) what are the geochemical effects of transportation and diagenetic processes?
4) do any sampled sedimentary rocks necessarily derive from only one tectonic setting?

With regard to 1), Bhatia & Crook (1986) distinguish four end-member tectonic settings: 1) oceanic island arc; 2) continental island arc; 3) active continental margin; 4) passive continental margin. Is it necessary that these tectonic end-members are composed of rocks with unique geochemical characteristics? For example are there definite geochemical differences between the composition of continental island arcs and active continental margins? As also noted by Cingolini et al. (2003) it is not necessarily the case that such settings are composed of one rock type (e.g. the accretion of oceanic flood basalts, or ophiolite to active continental margins). The

study made by Bhatia & Crook (1986) only compares sediments of eastern Australia; other settings from around the world are not compared. The database of Bhatia & Crook (1986) is therefore restricted. The corollary is that while the discrimination diagrams of Bhatia & Crook (1986) are good for discriminating between eastern Australian turbidite sequences, they are not well tested for distinguishing between sediments from different tectonic settings. Further work, which would compare data from a large database of rocks of tectonic end-member settings from around the world, is required to test the possibility of tectonic discriminating sediments.

Factors 2) and 3) relate to the relationships between the geochemistry of the parent rock and sediments that derive from them. Based on the work of McLennon et al. (1983), Bhatia et al. (1986) state that certain elements (e.g. La, Ce, Nd, Y, Th, Zr, Nb, Ti and Sc) are transferred quantitatively from the weathered parent material to the sediment. For example, sediments with high "ferromagnesian element" abundance (i.e. Al, Fe, Ti, Mg, Sc, V, Co, Zn, Ga) are likely to have derived from relatively mafic (e.g. basaltic, andesitic) parent materials. In contrast, sediments with a low abundance of ferromagnesian elements may have weathered from more felsic rocks, such as granites or granitic gneiss.

Based on the transfer of the above elements from parent to sedimentary rock McLennon et al. (1983) showed that the REE geochemistry of Archaean sedimentary rocks differs from post-Archaean rocks. This can be explained by there being a more mafic crust during the Archaean relative to post-Archaean time periods. Perhaps this is true, but there appears to be very little recent evidence regarding whether certain elements can be transferred quantitatively from parent rock to sediment. Beyond distinguishing between felsic and mafic parent rocks, is it possible to preserve any distinct chemical signatures from these rocks in the sediments?

A number of the elements listed above are often used to "see through" the effects of alteration and weathering (see Section 7.6 for an example of this when investigating altered igneous rocks). Furthermore, a number of these elements are concentrated by certain weathering-resistant minerals, e.g. Zr in zircon, and so Zr concentrations will reflect the proportion of zircon. Thus even if Zr is quantitatively transferred from parent rock to sediment, the concentration Zr in the sedimentary rock will be

controlled by sedimentary processes (e.g. sorting). The use of Zr in discrimination diagrams may not therefore be valid. It is beyond the scope of this work to investigate experimentally the geochemical relationships between parent rock and sediment during weathering, transportation, diagenesis etc.

A final problem is whether the sedimentary components of a sedimentary rock must derive from one tectonic setting. This is particularly relevant to meta-sedimentary rocks that have undergone subduction zone metamorphism, as subduction zones can bring material produced at one tectonic setting in contact with that produced at another e.g. pelagic sediments subducted beneath an active continental margin. As discussed by Spandler (2004c), mixing between different lithologies and sedimentary materials is likely to be common at subduction zones, where the "subduction blender" is in operation.

As a result of the above problems, it is not clear whether it is possible to tectonically discriminate meta-sedimentary rocks. In this light it is perhaps significant that the analysis of subduction-related meta-sediments by Sadofsky & Bebout (2003) and Breeding et al (2004) did not use tectonic discrimination methods. In fact Breeding et al. (2004) did not attempt to interpret the geochemistry of the protoliths at all. Instead, when reaching conclusions on the provenance of the meta-sedimentary rocks, Sadofsky & Bebout (2003) only state that "... metasedimentary rocks are similar in lithology and geochemistry to clastic sediments outboard of many subduction zones."

More work is required on whether it is possible to tectonically discriminate sediments. This would require a large geochemical data set, as well as empirical evidence for the nature of elemental transfer between parent rock and sediment. It is out of the scope of this study to provide such further work.

7.10.2 ORIGIN OF THE META-SEDIMENTARY ROCKS

Meta-sedimentary rocks have been identified by examination of hand specimens and thin sections. These examinations have shown that: 1) some rocks are intercalated igneous and sedimentary rocks that were subsequently metamorphosed (these have been classified as meta-volcano-clastic rocks); and 2) others are quartz-rich meta-sedimentary rocks. This section deals with these two rocks types separately.

7.10.2.1 META-VOLCANOCLASTIC ROCKS

The major element composition (on an LOI-free basis and normalised to 100%) of the meta-volcanoclastic rocks generally resembles basaltic compositions, with SiO_2 and $Na_2O + K_2O$ ranging from 44.57-55.66 wt% and 0.53-7.2 wt%, respectively. One sample however, (106-3b) has much higher silica content of 79.37 wt%, reflecting the high modal proportion of quartz in the sample. Trace element compositions are investigated in Figure 7.19 A & B.

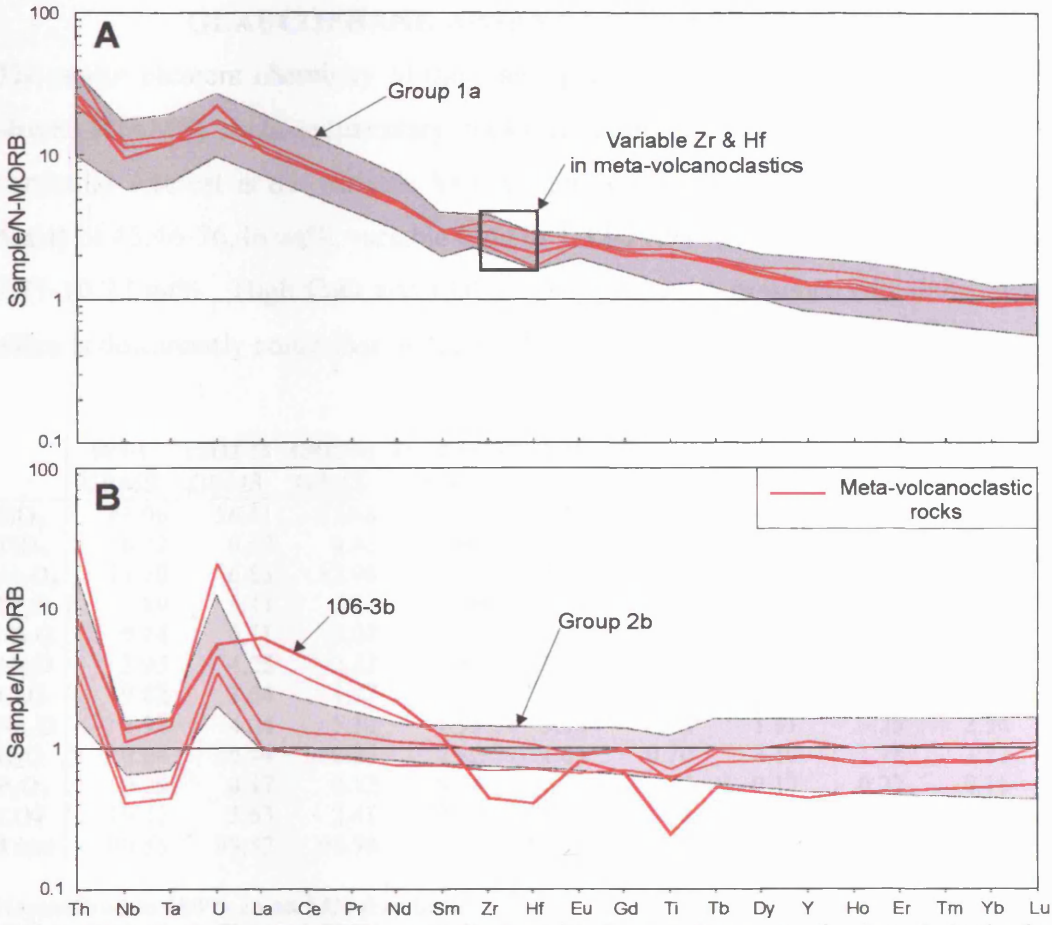


Figure 7.19 A & B. N-MORB normalised multi-element diagrams of selected (and often immobile) elements for the meta-volcanoclastic rocks. A) meta-volcanoclastic rocks with trace element signatures similar to Group 1a (WPB basalts). Note the relatively variable Zr & Hf compositions, which may reflect the modal proportion of zircon. B) meta-volcanoclastic rocks with trace element signatures similar to Group 2b (volcanic arc basalts). Note that sample 106-3b differs from the other samples in Fig. 7.19B by having a marked depletion of Zr, Hf and Ti.

As can be seen from the N-MORB-normalised multi-element plots of Figure 7.19A & B, there are two general trace element patterns for the suspected meta-volcanoclastic rocks: 1) a pattern that resembles a volcanic-arc signature, and 2); a pattern that resembles the enriched within-plate basalts (WPB) signature of Group 1a of the meta-basaltic samples.

As the trace element signatures of the meta-volcanoclastic rocks resemble those of Groups 1a and 2b, it follows that the igneous component must be composed of fragments that formed during eruption of the protoliths, perhaps on the ocean floor. The sedimentary component of these rocks is essentially composed of carbonates and quartz.

7.10.2.2 GEOCHEMISTRY OF GLAUCOPHANE-BEARING & GLAUCOPHANE-ABSENT META-SEDIMENTARY ROCKS

The major element chemistry of the glaucophane-bearing (GBMS) and glaucophane absent (GAMS) meta-sedimentary rocks is highly variable (see Table 7.10). Of particular interest is the variable SiO_2 content (normalised to 100% on an LOI-free basis) of 45.46-76.46 wt%, variable CaO of 1.32-21.94 wt% and LOI that ranges from 1.71-10.22 wt%. High CaO and LOI values reflect the presence of calcite, whereas silica is dominantly controlled by the modal quartz proportions.

	984-1	TSO2-14	TSO2-18	TSO2-08	TSO2-11	986-1	TSO2-10	TSO2-13	TSO2-19	TSO2-56
	GBMS	GBMS	GBMS	GAMS	GAMS	GAMS	GAMS	GAMS	GAMS	GAMS
SiO_2	41.06	56.11	65.68	47.49	48.46	71.28	69.66	68.14	60.37	59.55
TiO_2	0.72	0.69	0.42	3.85	1.82	0.36	0.52	0.70	0.81	0.57
Al_2O_3	13.70	16.85	12.98	19.04	14.06	8.81	12.45	13.64	17.96	13.27
Fe_2O	7.89	9.41	7.73	15.06	11.48	3.77	4.70	5.25	7.44	5.16
MnO	0.14	0.11	0.08	0.05	0.14	0.20	0.08	0.07	0.10	0.05
MgO	3.95	4.25	2.22	1.61	6.59	1.81	2.02	2.24	3.70	3.13
CaO	19.82	3.64	1.97	4.02	8.62	5.01	1.74	2.11	1.29	5.95
Na_2O	2.92	4.24	5.12	1.95	3.04	1.23	1.81	3.25	2.36	2.10
K_2O	0.04	0.44	0.25	2.12	1.05	0.70	2.40	1.78	3.22	1.66
P_2O_5	0.09	0.17	0.12	0.44	0.22	0.05	0.17	0.22	0.16	0.12
LOI	10.22	3.63	2.41	3.84	3.69	8.42	3.84	1.71	3.51	7.21
Total	100.55	99.52	98.98	99.47	99.17	101.64	99.39	99.11	100.91	98.77
Normalised to 100% on an LOI-free basis										
SiO_2	45.46	58.51	68.01	49.66	50.75	76.46	72.90	69.96	61.98	65.04
TiO_2	0.80	0.72	0.43	4.03	1.91	0.39	0.54	0.72	0.83	0.62
Al_2O_3	15.17	17.57	13.44	19.91	14.73	9.45	13.03	14.00	18.44	14.49
Fe_2O	8.73	9.81	8.00	15.75	12.02	4.04	4.92	5.39	7.64	5.64
MnO	0.15	0.11	0.08	0.05	0.15	0.21	0.08	0.07	0.10	0.05
MgO	4.37	4.43	2.30	1.68	6.90	1.94	2.11	2.30	3.80	3.42
CaO	21.94	3.80	2.04	4.20	9.03	5.37	1.82	2.17	1.32	6.50
Na_2O	3.23	4.42	5.30	2.04	3.18	1.32	1.89	3.34	2.43	2.29
K_2O	0.04	0.46	0.26	2.22	1.10	0.75	2.51	1.83	3.30	1.81
P_2O_5	0.10	0.18	0.12	0.46	0.23	0.05	0.18	0.23	0.17	0.13
Total	100	100	100	100	100	100	100	100	100	100

Table 7.11 Summary of major element data (all values in wt%), including data re-calculated on an LOI basis (to remove the "diluting" effects of carbonate and fluid that may be present in the rock) for glaucophane-bearing meta-sediments (GBMS), and glaucophane-absent metasediments (GAMS). See Chapter 5 for description of the different rock types. LOI = loss on ignition.

Although trace element patterns (Figure 7.20) of GAMS and GBMS are quite variable, they are similar to GLOSS, the data of Sadofsky & Bebout (2003) and the terrigenous (e.g. volcanoclastic turbidites, clastic turbidites) samples from Plank & Langmuir (1998). Slight differences between GAMS and GBMS are also revealed. GBMS tend to be more depleted than GAMS, with greater depletion being present for the more incompatible elements such as Th and Nb.

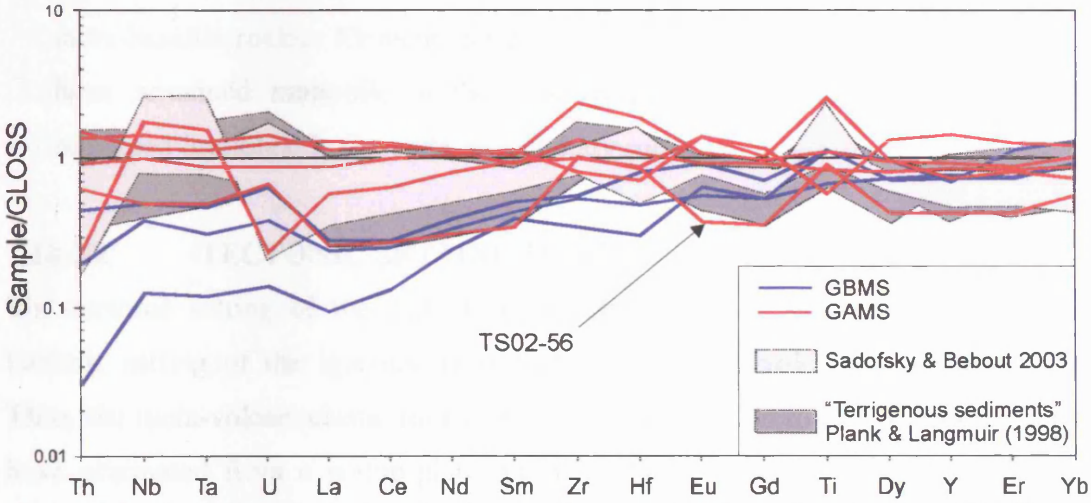


Figure 7.20 GLOSS normalised multi-element diagrams for glaucophane-bearing (GBMS) and glaucophane- absent (GAMS) meta-sedimentary rocks. GLOSS values are from Plank & Langmuir (1998). Data from Sadofsky & Bebout (2003) are of metamorphosed clastic sediments from the Franciscan and the Western Baja Terrane subduction complexes. "Terrigenous sediments" refers sediments termed volcanio-clastic turbidites, clastic turbidites, turbidites and volcanoc-clastic sediment, by Plank & Langmuir (1998).

7.10.3 DISCUSSION OF SEDIMENT PETROGENESIS

7.10.3.1 DOES THE COMPOSITION OF META-SEDIMENTARY ROCKS REFLECT THE PROTOLITH?

Interpreting the geochemistry of metamorphosed clastic sediments, Sadofsky & Bebout (2003) stated: "The rocks analysed as part of this study do demonstrate significant protolith heterogeneity that may complicate the assessment of small degrees of element loss, and it is difficult to prove unequivocally that certain elements were not present in metamorphic fluids." However, the similarities between the sediments of Sadofsky & Bebout (2003) and the terrigenous sediments of Plank & Langmuir (1998) led them to conclude that even the fluid-mobile trace elements are "...present at concentrations indistinguishable from the protoliths." Similar problems are encountered here with the likely heterogeneous nature of the protolith. Nevertheless, a number of lines of evidence suggest that the trace elements used in

this section to interpret the meta-sedimentary rocks have remained essentially immobile:

1) there is no evidence for melting in these rocks (see Chapter 5);
2) there are a number of similarities between the composition of the meta-sedimentary rocks and fresh and metamorphosed rocks of other studies (e.g. Sadofsky & Bebout 2003, and; Plank & Langmuir 1998);
3) the sedimentary protoliths would have followed similar P-T trajectories to the meta-basaltic rocks. Elements such as Th, U, Nb and REE have been shown to have remained immobile in the meta-basaltic rocks, and so they may have remained immobile in the meta-sedimentary rocks.

7.10.3.2 TECTONIC SETTING OF THE PROTOLITHS

The tectonic setting of the meta-volcanoclastic rocks is inexorably linked to the tectonic setting of the igneous rocks that provided the volcanoclastic component. Thus, the meta-volcanoclastic rocks with compositions akin to that of Group 1a must have originated from a within-plate setting. On the other hand, the clastic quartz component to Group 1a rocks must have derived from a subaerial source, such as a continental margin or island arc. If the quartz was derived from a continental source, it is further evidence to support the hypothesis that Group 1a protoliths originated from a continental margin. Furthermore, the carbonate component suggests these rocks formed in relatively shallow water, perhaps on a seamount. In support of this is the observation reported Chapter 3 that marbles are abundant in the blueschist belt-perhaps these marbles are a "carbonate cap" to the seamount (e.g. Volkova & Budanov 1999).

The meta-volcanoclastic rocks with compositions similar to Group 2b are however not quite so easily explained. This is because of the similarities between volcanic arc and continental crust trace element signatures. However, based on the conclusion that meta-basalts with volcanic arc signatures must have originated from a continental volcanic arc, it is possible to infer that these meta-volcanoclastic rocks may have originated at an active continental margin.

The difficulties in tectonically discriminating meta-sedimentary rocks by bulk rock geochemistry have been outlined above. On the basis of these difficulties it is only

possible to make broad statements regarding the tectonic provenance of GAMS and GBNS. The quartz-rich nature of these meta-sedimentary rocks, together with their geochemical similarities with "terrigenous sediments" of Plank & Langmuir (1998), leads to a similar conclusion as Sadofsky & Bebout (2003): the GAMS and GBNS rocks are similar to clastic sediments outboard of many subduction zones.

7.11 GEOCHEMICAL NATURE OF THE PROTOLITHS: SUMMARY

It has been shown that elements such as Th, U, Nb, Ta, REE, Zr and Hf have remained essentially immobile during the petrogenetic history of the meta-igneous rocks. It is also likely that such elements have remained immobile during the petrogenetic history of the meta-sedimentary rocks. It has therefore been possible (within limits discussed in the relevant Sections above) to predict the tectonic setting and petrogenesis of the protoliths. A summary and discussion of the nature of these protoliths is given in Section 7.9 and 7.10.3. By knowing the geochemical nature of the protoliths, it is possible to: 1) investigate the nature of any element mobility (as indicated for elements such as Rb, Ba, Cs), and; 2) to reconstruct the tectonic evolution of the blueschist belt. This will be undertaken in Chapter 9.

CHAPTER 8

PROTOLITH GEOCHEMISTRY 2: QILIAN SHAN

8.1 INTRODUCTION & AIMS

This Chapter has identical aims and uses identical methods to the previous Chapter, which investigated the protoliths of rocks from the western Tian Shan. These aims are essentially to investigate the geochemical nature of the protoliths of rocks collected from the Qilian Shan blueschist belts. This Chapter however, also aims to establish whether the protoliths from the high- and low-grade blueschist belts originated from the same setting. This is necessary because of the uncertainties regarding the relationship between these belts as discussed in Chapter 3.

8.2 IDENTIFYING META-CUMULATES

A small number of samples show evidence for accumulated olivine and plagioclase (Table 8.1). Sample Q98-138 has a Ni-content of 4492 ppm. Based on this and the fact that this sample is chromite-rich (see Chapter 6) and has a high bulk-rock Fe_2O_3 content of38.95 wt%, the protolith is likely to have been an ultramafic rock. Samples Q02-11 and Q02-10A have high Ni concentrations of 288.5 ppm and 238.0 ppm, respectively. As these two samples have otherwise basaltic bulk rock compositions, it is likely that the protoliths were olivine-phyric. Only Q98-133 shows any evidence of plagioclase accumulation, with an Al_2O_3 content of 21.39 wt%. No samples show evidence of having significant accumulated clinopyroxene.

SAMPLE	Ni (ppm)		SAMPLE	Al_2O_3 (wt%)
Q98-138	4492			
Q02-11	288.5		Q98-133	21.39
Q02-10A	238.0			

Table 8.1 Summary of samples with compositions indicative of an accumulated component. Nickel abundance over 200 ppm and Al_2O_3 abundance over 20 wt% is indicative of olivine and plagioclase accumulation, respectively (Pearce 1996). There are no samples with compositions indicative of significant clinopyroxene accumulation (i.e. Sc >50 ppm).

8.3 CLASSIFICATION OF META-VOLCANIC ROCKS

Two chemically distinct groups (Group Q1 and Group Q2), and a small number of samples that do not fit either group, can be identified on the Zr/Ti against Nb/Y classification diagram of Figures 8.1A & B. These two groups, which are made up of

rocks from multiple metamorphic facies, plot in the basalt field and are similar in terms of Zr/Ti ratios, but differ most clearly in Nb/Y ratios. Group Q1 has relatively low Nb/Y ratios that range from 0.05-0.14, whereas Group Q2 ranges from 0.19-0.44. Both groups have sub-alkalic compositions, with Group Q1 having Nb/Y ratios similar to the estimate of MORB mantle and N-MORB, while Group Q2 has slightly more enriched compositions. The other samples (i.e. the green circles in Figure 8.1A) show a large variation in composition, plotting in the basaltic andesite, basalt and alkali basalt fields. These samples are further considered in Section 8.2.3.

The classification according to Figures 8.1 A & B is broadly consistent with the major element data (see Table 4.4, Chapter 4) and the TAS diagram (not shown) as most samples (apart from two samples with basaltic-andesite compositions) have SiO_2 <52 wt% and $Na_2O + K_2O$ <6 wt%.

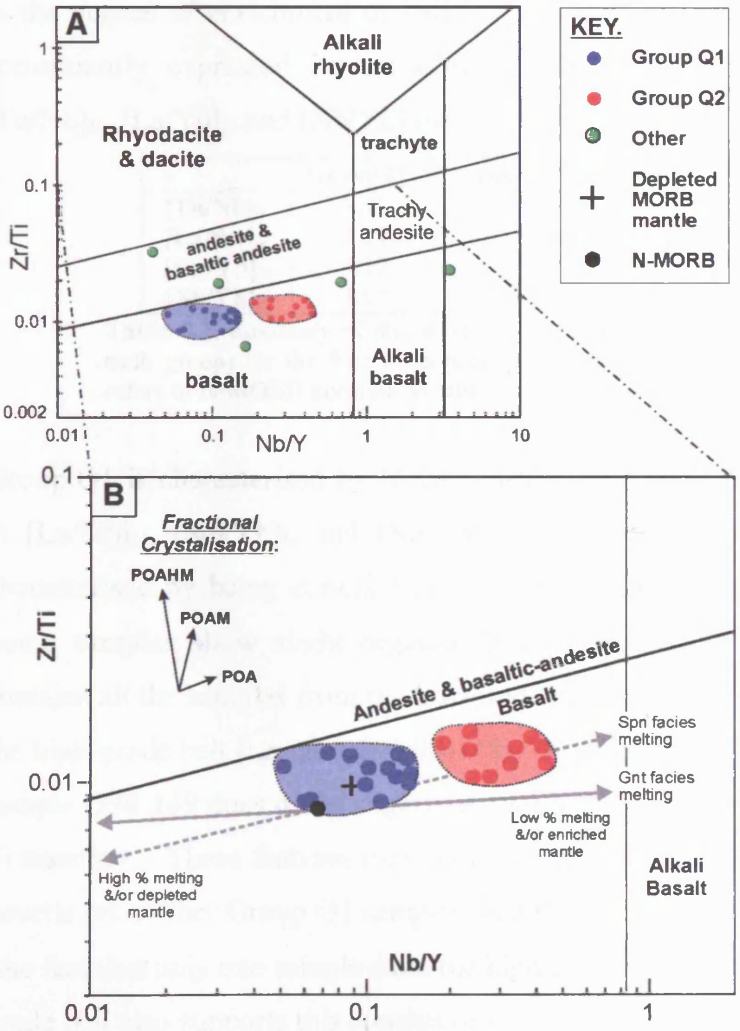


Figure 8.1. A & B. (A) The modified Zr/Ti against Nb/Y Winchester & Floyd (1977) classification diagram of Pearce (1996). (B) Close-up of (A) showing the two chemically distinct meta-basaltic groups that were sampled from the Qilian Shan blueschist belts. Schematic melting vectors for melting in the garnet (Gnt) and spinel (Spn) facies and fractional crystallisation vectors, as well as the estimation of depleted MORB Mantle are from Pearce (1996). N-MORB estimate after Sun & McDonough (1989).

Fractional crystallisation acronyms:
P= plagioclase;
O= olivine;
A= augite;
H= hornblende;
M= magnetite.

8.2.3 IDENTIFYING CO-GENETIC SAMPLES

Of the samples making up Groups 1 and 2, four geochemically distinct sub-groups can be identified. These groups are shown on the N-MORB-normalised multi-element diagrams of Figure 8.2A-D. The small number of samples that do not form part of Group 1 and Group 2 are shown in Figure 8.3A-C. To a first approximation, these Figures show that trace element patterns all have characteristics similar to the trace element patterns of volcanic arc basalts (i.e. enrichment in Th, U and LREE relative to Nb, Ta, Zr, HF and HREE). The LILEs (Cs, Ba, Rb, K etc) are not considered further in this section, because they are easily mobilised.

8.2.3.1 SUBGROUPS OF GROUP Q1 AND GROUP Q2

Figure 8.2A-D shows that Group Q1 can be broken down into three subgroups, namely, Group Q1, Group Q1a and Group Q1b, whereas Group Q2 is not subdivided. The key differences between Groups Q1, Q1a, Q1b and Q2 are related to differences in the degree of enrichment of LREE, Th and U over Nb, Ta and HREE. This is conveniently expressed in terms of a number of trace element ratios, such as $[Th/Nb]_N$, $[La/Yb]_N$ and [Nb/Yb] (see Table 8.2).

	Group Q1	Group Q1a	Group Q1B	Group Q2
$[Th/Nb]_N$	2.93	4.51	1.51	6.36
$[La/Sm]_N$	1.21	2.02	1.41	3.48
$[Sm/Yb]_N$	1.12	1.21	1.42	1.64
$[Nb/Yb]_N$	1.02	1.57	1.62	3.94

Table 8.2. Summary of characteristic trace element ratios (average value from each group) for the four meta-basaltic groups of Qilian Shan. The suffix "N" refers to N-MORB normalised ratios.

Group Q1 is characterised by N-MORB-like REE and HFSE compositions reflected in $[La/Sm]_N$, $[Sm/Yb]_N$ and $[Nb/Yb]_N$ ratios close to unity. This group is also characterised by being enriched in Th giving high average $[Th/Nb]_N$ ratios of 2.93. Some samples show slight negative Y & Ti anomalies. Importantly, Group Q1 contains all the samples from the low-grade blueschist belt, and only one sample from the high-grade belt (i.e. sample Q98-149). Although chemically similar to Group Q1, sample Q98-149 does differ slightly in that it is relatively enriched and has a positive Ti anomaly. These features may indicate that the protolith of Q98-149 was not co-genetic with other Group Q1 samples, and that the chemical similarities are fortuitous (the fact that only one sample from the high-grade belt matches samples from the low-grade belt also supports this conclusion).

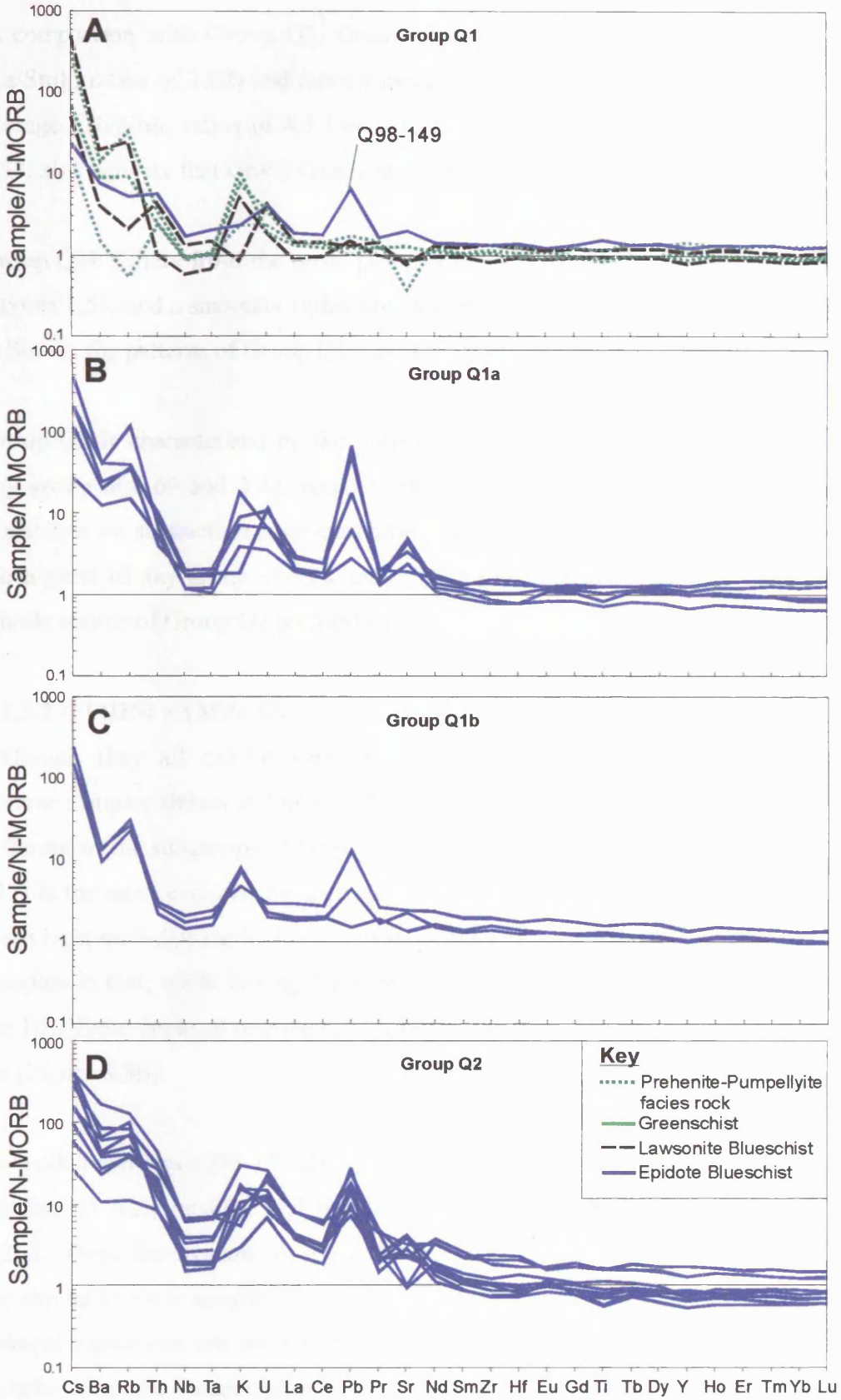


Figure 8.2 A-D. N-MORB normalised multi-element diagrams of the four meta-volcanic sub-groups from Qilian Shan. Normalising values are taken from Sun & McDonough (1989) and the order of elements is based on the order of compatibility during the melting of spinel lherzolite after Pearce & Peate (1995).

In comparison with Group Q1, Group Q1a is more LREE enriched (with average $[La/Sm]_N$ ratios of 2.02) and more enriched in U and Th relative to Nb and Ta, e.g. average $[Th/Nb]_N$ ratios of 4.5 (see Table 8.1). Other ratios, such as $[Nb/Yb]_N$ of 1.57, also indicate that Group Q1a is more enriched than Group Q1.

Group Q1b differs from the other groups in that it has the lowest average $[Th/Nb]_N$ ratio of 1.51, and a smoother rightward sloping REE curve (e.g. contrast the inflection at Sm for the patterns of Group Q1a and Group Q2 in Figure 8.2 B & D).

Group Q2 is characterised by the highest average $[Th/Nb]_N$ and $[La/Sm]_N$ ratios of any group at 6.69 and 3.48, respectively. Other ratios, thought not to be strongly dependent on subduction zone enrichment, such as $[Nb/Yb]_N$ and $[Sm/Yb]_N$ are also the highest of any group at 3.48 and 3.94, respectively. This may indicate that the mantle source of Group Q2 protoliths was more enriched than for other groups.

8.2.3.2 OTHER SAMPLES

Although they all exhibit supra-N-MORB $[Th/Nb]_N$ ratios, the compositionally diverse samples shown in Figure 8.3 A-C have trace element characteristics that are different to the subgroups of Group Q1 and Group Q2. For example, sample (Q98-133) is the most enriched meta-basalt sampled with $[Nb/Yb]_N$ ratios of 48.55, and a steep rightward-dipping REE curve (Figure 8.3A). Sample Q02-11 differs from other samples in that, while having super N-MORB $[Th/Nb]_N$ ratios similar to Group Q2, the HREE are depleted relative to N-MORB, and the REE curve is concave from Tb-Lu (Figure 8.3B).

Two other samples (Q98-131 and Q98-138) and one sample (Q02-08) are exceptional because of their positive and negative Hf and Zr anomalies, respectively (Figure 8.3C). These features are not shown by any other samples from Qilian, although they are similar to some samples from Tian Shan. As discussed in Chapter 7, similar trace element signatures are shown by Zambian eclogites as well as fresh gabbros and dolerites from the Oman Ophiolite.

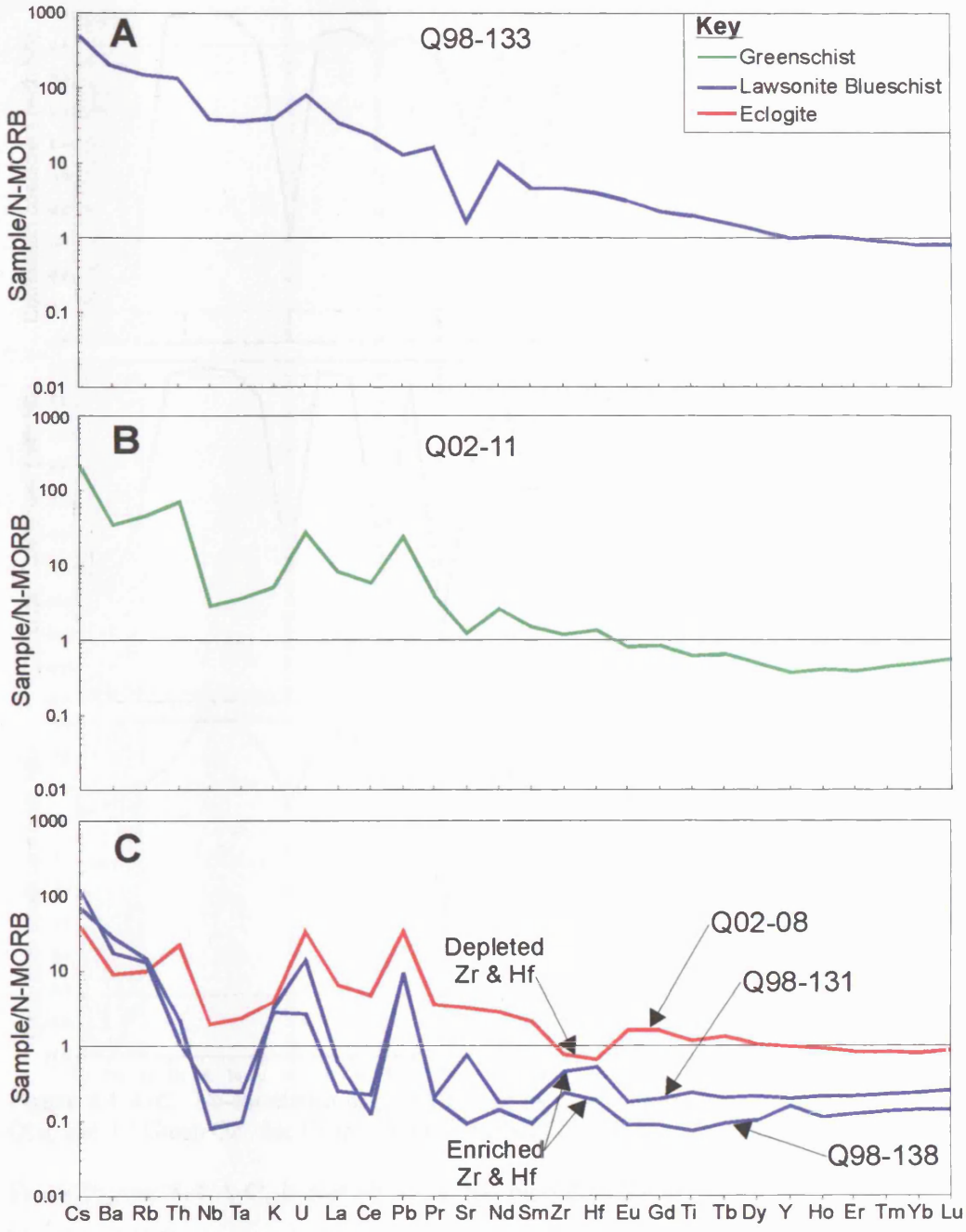


Figure 8.3 A-C. N-MORB normalised multi-element diagrams for samples not belonging to the subgroups of Group Q1 or Group Q2.

8.2.4 IMMOBILE ELEMENTS

The large number of samples that make up Group Q1, Q1a and Group Q2, allow for a meaningful investigation into the correlation between different elements. The methods used in this section are explained in Chapter 7. Nb-correlation diagrams for these groups are presented in Figure 8.4 A-C.

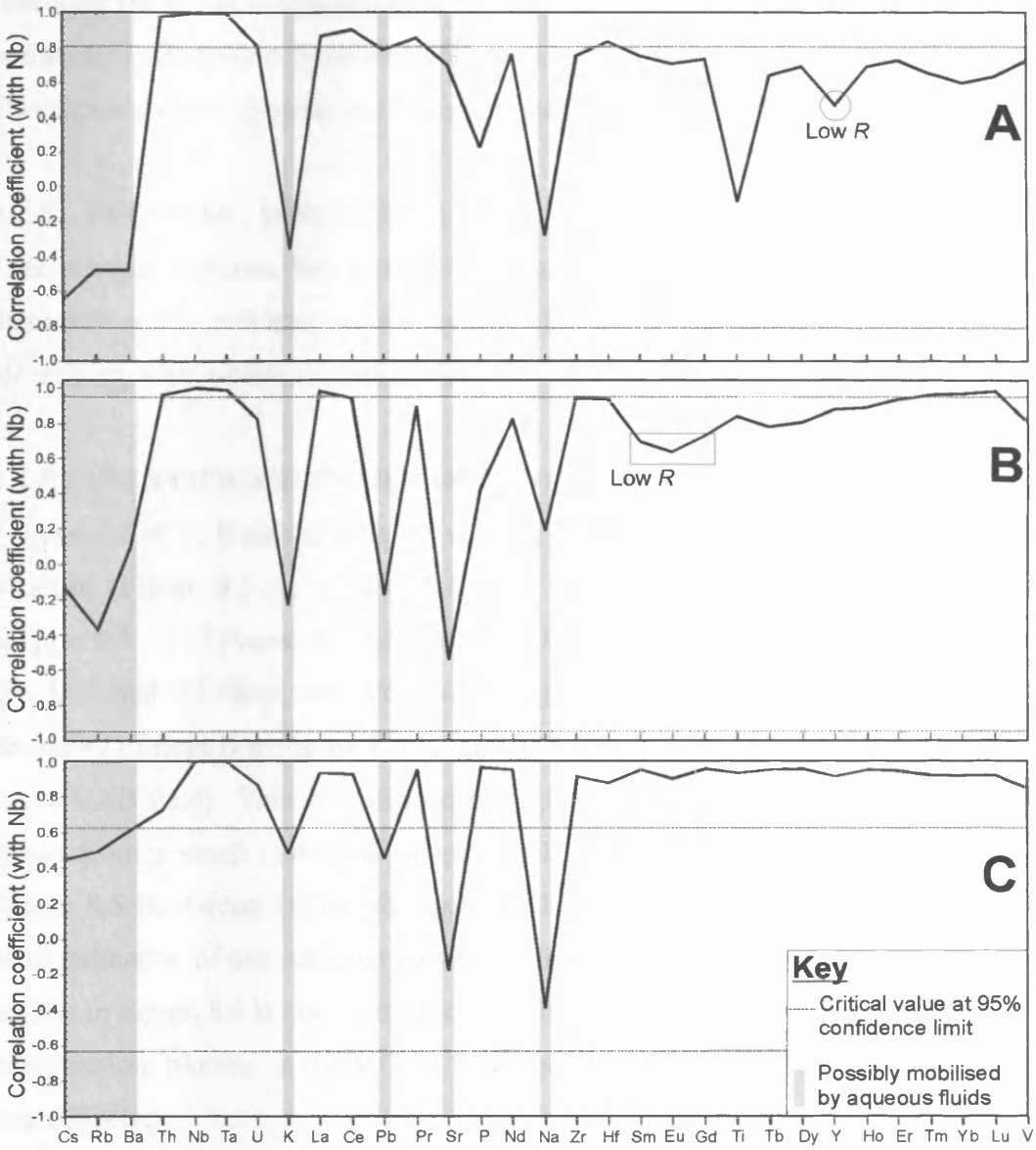


Figure 8.4 A-C. Nb-correlation diagrams for the meta-basaltic groups. A) Group Q1; B) Group Q1a, and; C) Group Q2. See Chapter 7 for an explanation how Nb-correlation diagrams work.

From Figure 8.4 A-C, it can be seen that elements such as Cs, Rb, Ba, K, Pb, Sr and Na (i.e. LILE elements) repeatedly show relatively poor correlation with Nb. This indicates that they have been de-coupled from Nb, perhaps during alteration by aqueous fluids or dehydration. The REE and HFSE elements, such as Ta, Hf and Zr, all give relatively high positive correlation coefficients. Exceptions to this include: 1) poor correlation for Hf, Sm and Eu in Figure 8.4 B, and; 2) poor correlation between Nb and Ti in Figure 8.4 A. The poor correlation of Nb with Ti may have resulted from fractionation of Ti-magnetite from the melt (there are also slight negative Ti-anomalies for some of the samples of Group Q1, see Figure 8.2A). However, in general it is clear that that the REE and Ta, Th, U, Zr and Hf are coupled with Nb,

reflecting the relationships expected between such elements in magmatic systems. It is therefore likely that these elements have remained immobile and can be used to investigate the petrogenesis and tectonic setting of the protoliths.

8.2.5 TECTONIC DISCRIMINATION

This section explores the tectonic setting of the protoliths using discrimination diagrams, and is split into two sections: 1) identifying volcanic arc signatures, and; 2) identifying within-plate characteristics.

8.2.5.1 IDENTIFICATION OF VOLCANIC ARC SIGNATURES.

Figures 8.5 A & B aim to identify volcanic arc signatures by using the Th-Hf/3-Ta diagram (Figure 8.5 A) of Wood (1980), and the Th/Yb against Nb/Yb diagram (Figure 8.5 B) of Pearce & Peate (1995). From Figure 8.5A, it is clear that Groups Q1, Q1a and Q2 show volcanic arc-like signatures, plotting in and generally on the boundary of field D in Figure 8.5 A (although Group Q1 trends from the MORB field to the VAB field). This is confirmed by higher (Th/Yb)/(Nb/Yb) ratios of the groups (apart from a small umber of samples) relative to the MORB array, as shown in Figure 8.5 B. Group Q2 has the highest Th/Yb ratio and plot in the part of the arc field indicative of calc-alkaline basalts in Figure 8.5 A, and continental volcanic arc basalts in Figure 8.5 B. In contrast to the other Groups, Group Q1b has a MORB-like composition, plotting in the MORB field and the MORB array in Figure 8.5 A & B, respectively.

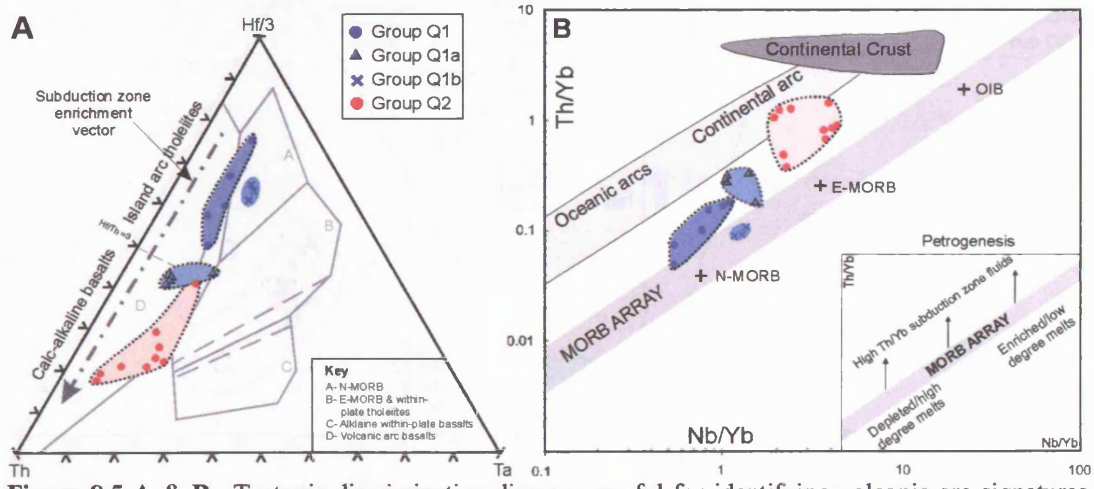


Figure 8.5 A & B. Tectonic discrimination diagrams useful for identifying volcanic arc signatures. A) the Th-Hf-Ta diagram of Wood (1980). B) the Th/Yb against Nb/Yb diagram of Pearce and Pete (1995). The protoliths generally have a volcanic arc signature, with a few other samples having composition similar to N-MORB.

It is important to emphasise that, although Figures 8.5 A & B indicate that Groups Q1, Q1a and Q2 have volcanic arc signatures, the signature is not "strong" for all samples. This is because many samples plot on the boundary between MORB and VAB fields, e.g. the boundary of Field D and the MORB array on Figures 8.5 A & B, respectively. This may be explained by the protoliths forming at a considerable distance from a subduction zone where signatures from slab-derived fluids/melts smaller in magnitude. Such a setting may be a back-arc basin.

The different degrees of enrichment between the Groups are clearly shown on Figure 8.5 B by the different Nb/Yb ratios. In this respect, Group Q1a has N-MORB-like compositions, Group Q1a and 1b have supra-N-MORB Nb/Yb ratios below that of E-MORB, and Group Q2 has supra-E-MORB, sub OIB, Nb/Yb ratios.

8.2.5.2 IDENTIFICATION OF WITHIN PLATE CHARACTERISTICS

In order to identify any within-plate characteristics Figures 8.6 A & B use the Ti-Y-Zr diagram of Pearce & Cann (1973) and the V against Ti diagram of Shervais (1982). Although these diagrams distinguish between the groups, they do indicate that there is no WPB-character for these rocks, as they all plot in, or on the boundary of, the MORB and VAB field. It is however significant that Figure 8.6B shows that Ti/V ratios of all groups are higher than those of VAB, with all groups plotting in the MORB/BABB field (and one sample from Group Q1b plotting in the OIB field).

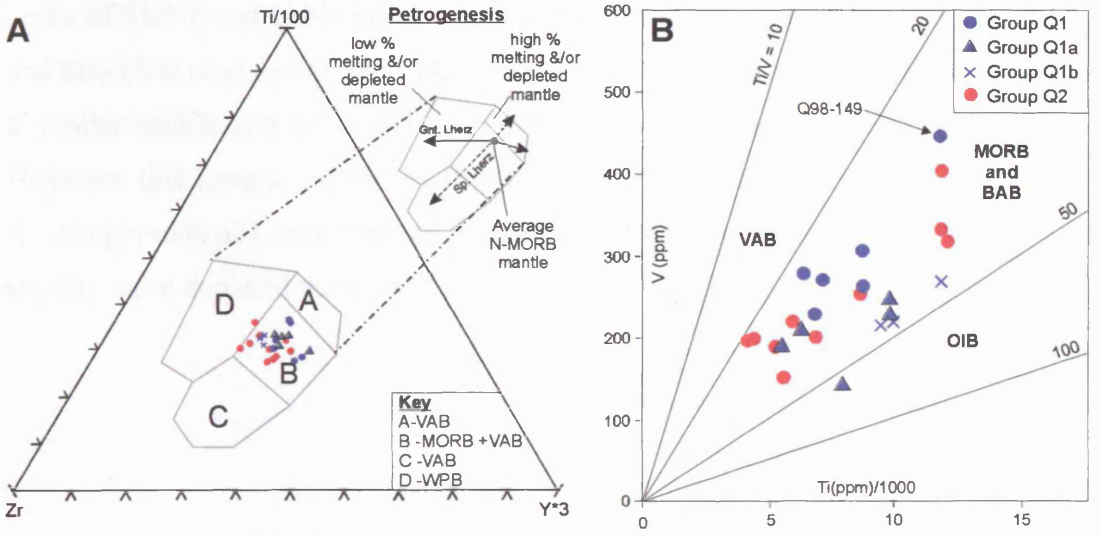


Figure 8.6 A & B. Tectonic discrimination diagrams for identifying within-plate characteristics in basalts. A) the Zr-Ti/100-Y*3 diagram of Pearce & Cann (1970). B) the V against Ti (ppm)/1000 diagram of Shervais (1982).

Ratios of Ti/V are thought to be partially controlled by the oxygen fugacity of the melting regime (e.g. Shervais 1982). Ratios of Ti/V above that of VAB is therefore further evidence suggesting that the volcanic-arc signature is not "strong" in some rocks, and may reflect generation of the protoliths in a back-arc basin.

8.2.6 FINDING ANALOGUES: RESULTS OF ΣD^2 CALCULATIONS

As completed for the rocks collected from the Chinese Tian Shan, calculations comparing the compositions of the metamorphic rocks of Qilian Shan with published data have been completed. See Chapter 7 for a detailed description of the methods used.

8.2.6.1 RESULTS OF THE ΣD^2 CALCULATIONS: GROUP Q1

Unfortunately the ΣD^2 calculations did not identify any one sample, or group of samples, that closely match Group Q1. However, it is clear from Figure 8.7 and Table 8.3 that a number of samples from different back-arc basins have similar trace element characteristics.

The analogue from the East Scotia Ridge (sample D2G) generally shows a similar trace element pattern to Group Q1, but differs in that it is much less enriched in U. This is shown by the low $[U/Nb]_N$ ratio of 1.87 for D2G compared with 2.87 for Group Q1. Sample 102DS-1b from the Bransfield Strait, Antarctica, is similar in terms of Th/Nb and U/Nb ratios to group Q1, but differs in that the REE curve from and Sm-Yb is slightly steeper. The sample from the Havre Trough (18DR-1) also has a similar enrichment of U over Nb (with a $[U/Nb]_N$ ratio of 2.91) to Group Q1. However this sample differs in that the REE curve is steeper from La-Sm, with $[La/Sm]_N$ ratios of 1.66 compared with 1.21 for Group 1. The MREE-HREE are also slightly more depleted than Group Q1 (Figure 8.7 and Table 8.3)

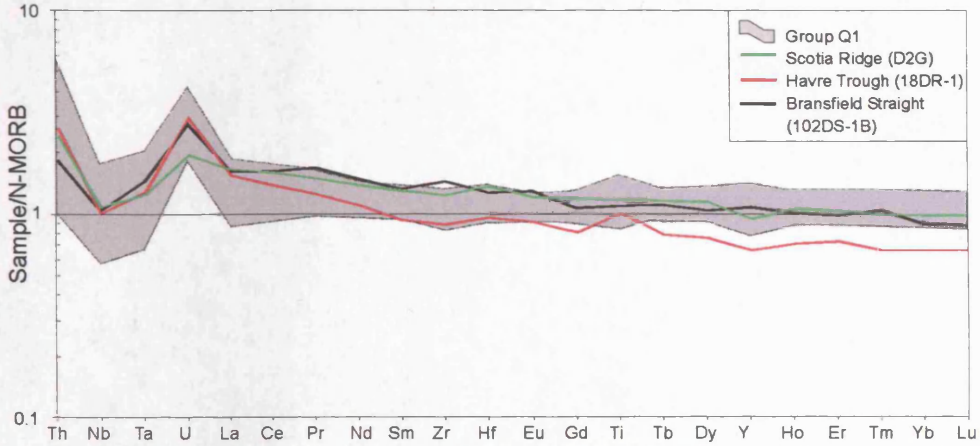


Figure 8.7 N-MORB normalised multi element diagram showing the Group Q1 patterns and the data for the analogous samples. See caption for Table 8.3 for source of the data and Table 8.3 for a summary of the petrogenesis of each sample. N-MORB normalising values are from Sun & McDonough (1989).

SAMPLE (reference)	ROCK TYPE	LOCATION	TECTONIC SETTING	PETROGENESIS
102DS-1B (1)	Basaltic Andesite	East Scotia Ridge, southern Atlantic ocean	Back-arc basin	Basalts produced by melting of an N-MORB-like mantle with a subduction component added during active back-arc spreading.
18DR-4 (2)	Basalt	Havre Trough, southern Pacific ocean	Back-arc basin	Basalts produced by melting of a Pacific-like MORB mantle with a subduction component added during active back-arc spreading.
D2G (3)	Basalt	Bransfield strait, Antarctica	Back-arc basin	Basalts produced during the transition of rifting to spreading taking place in an ensialic back-arc basin.

Table 8.3. Summary table of the results of the ΣD^2 calculations, references: 1) Fretzdorff et al. (2002); 2) Haase et al. (2002); 3) Keller et al. (2002).

In terms of the tectonic setting and petrogenesis of the protoliths, Table 8.3 is significant because it shows that the analogue samples all originate from a back-arc basin. Furthermore, each of the analogues were melts derived from a depleted (or otherwise N-MORB-like) mantle. This is strong evidence supporting the hypothesis made in Section 8.2.5 that the protoliths of each group (including Group Q1) may have originated in a back-arc basin.

8.2.6.2 RESULTS OF THE ΣD^2 CALCULATIONS: GROUP Q1a

Results of the ΣD^2 calculations for Group Q1a were more conclusive than for Group Q1 with the closest analogues for Group Q1a being basalts from the Siberian traps. A large number of samples from the Siberian Traps (from rocks analysed in different

publications) repeatedly gave the lowest ten ΣD^2 values. Analogous samples were identified from other tectonic settings, including:

1) large igneous provinces such as the North Atlantic Igneous Complex and the Kerguelen Plateau.
2) volcanic arcs such as the Honshu and Cascades arcs.

However, no one sample from the above locations gave repeatedly low ΣD^2 values, and so they have not been included in Figure 8.8.

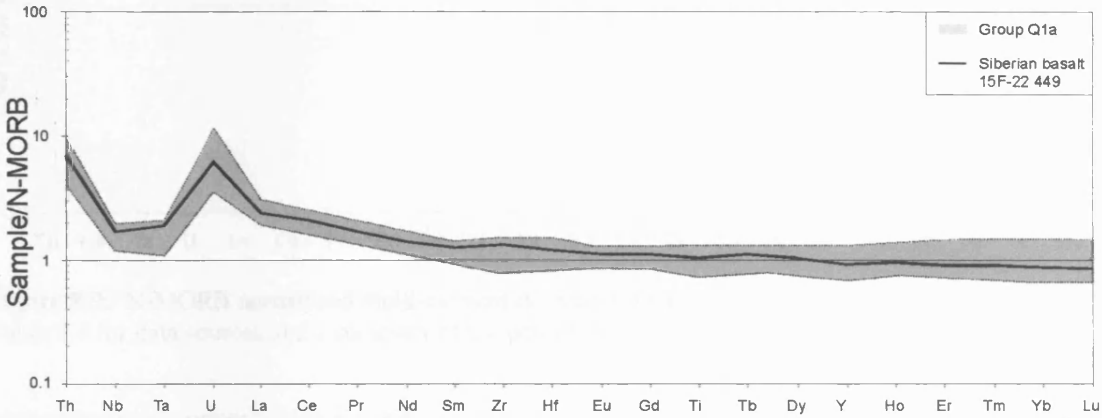


Figure 8.8. N-MORB normalised multi-element diagram for Group Q1a and the results of the ΣD^2 calculations. Data for the analogue samples from the Siberian Traps are taken from Hawkesworth et al. (1995).

The petrogenesis of the closest analogue samples from the Siberian Traps involves a three component source and open system differentiation (Hawkesworth et al. 1995). The three components are mantle material from both the lithosphere and the underlying asthenosphere, and contamination by a deep-seated continental crustal melt. The tectonic setting for the analogues is a within plate setting (i.e. within continental crust), which is in contrast to the back-arc basin setting hypothesised in Section 8.2.5.1, and the setting indicated for Group Q1. However, a WPB setting and contamination with continental crust may explain the supra-N-MORB $[Th/Nb]_N$ ratios and super VAB Ti/V ratios of Group 1a rocks.

8.2.6.3 RESULTS OF THE ΣD^2 CALCULATIONS: GROUP Q1b

Although not similar in all respects, the analogues identified by the ΣD^2 calculations have trace element patterns that are broadly similar to Group Q1b. Three of these analogues are shown in Figure 8.8 and summarised in Table 8.4.

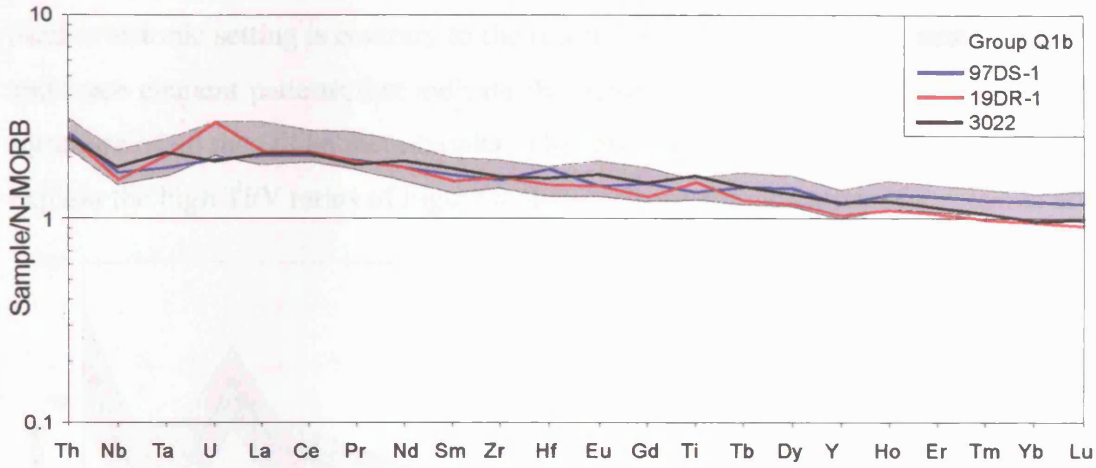


Figure 8.9. N-MORB normalised multi-element diagram for Group 1b and analogue samples. See Table 8.4 for data sources and a summary of the petrogenesis for each analogue sample.

SAMPLE (reference)	ROCK TYPE	LOCATION	TECTONIC SETTING	PETROGENESIS
3022 (1)	Tholeiitic basalt	Disko island and Nuusuaq, West Greenland.	Attenuated continental crust.	Contamination of tholeiitic magmas by assimilation of continental crust.
97DS-1 (2)	Basalt	East Scotia Ridge, Southern Atlantic ocean.	Back-arc basin.	Unmodified MORB-like mantle source modified by subduction components to give BABB.
19DR-1 (3)	Basalt	Havre Trough, Southern Pacific ocean.	Back-arc basin.	Relatively low degree melting of a Pacific-like MORB mantle source modified by subduction components to give BABB.

Table 8.4. Summary of the results of the ΣD^2 calculations for Group Q1b. References: 1) Lightfoot et al. (1997); 2) Fretzdorff et al. (2002), and; 3) Haase et al. (2002).

The analogues identified by the ΣD^2 calculations do not originate from the same tectonic setting, with sample 3022 coming from attenuated continental crust, and the other two samples from back-arc basins, (interestingly, the same back-arc basins as the analogue samples for Group Q1). Similar tectonic settings to these have been identified for Group Q1 and Group Q1a.

8.2.6.4 RESULTS OF THE ΣD^2 CALCULATIONS: GROUP Q2

The first interesting thing to note about the Group 2 analogues identified by the ΣD^2 calculations is that they all share a similar petrogenesis and tectonic setting. The three

analogues summarised in Figure 8.9 and Table 8.5, are all thought to have been produced by assimilation of continental crust by MORB-like magmas (apart from sample MV-1 which is indirectly contaminated by continental crust, see Table 8.5) during crustal attenuation.

Such a tectonic setting is contrary to the results from tectonic discrimination diagrams and trace element patterns that indicate that Group Q2 has the strongest volcanic arc signature of all the Qilian meta-basalts. However, as for Group Q1a, this setting may explain the high Ti/V ratios of Figure 8.6b, which are not indicative of a volcanic arc.

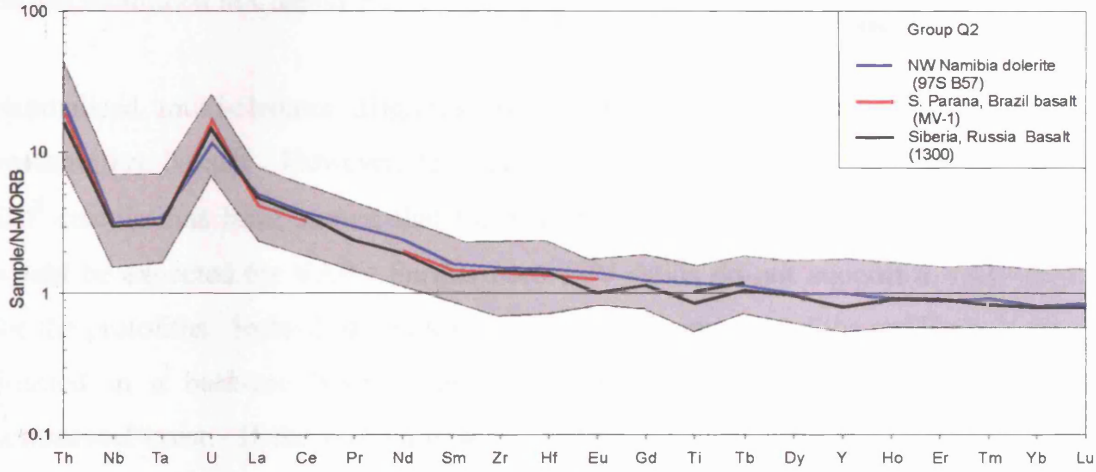


Figure 8.10. N-M ORB normalised multi-element diagram showing the trace element pattern of Group Q2 and the patterns of the analogue samples. See Table 8.5 for references and a summary of the petrogenesis of the analogue samples.

SAMPLE (reference)	ROCK TYPE	LOCATION	TECTONIC SETTING	PETROGENESIS
97SB57 (1)	Dolerite	Southern Etendeka region, NW Namibia	Attenuated continental crust	MORB-like magmas generated by melting beneath continental crust were subsequently contaminated with continental crust.
MV-1 (2)	Basalt	Southern Paraná, Brazil	Attenuated continental crust	MORB-like asthenospheric melts mixed with other magmas that had been contaminated with continental crust and the resulting magma differentiated.
1300 (3)	Basalt	Siberia, Russia	Attenuated continental crust	Melts from a Transitional-MORB-like mantle were contaminated by the overlying continental crust.

Table 8.5. Summary of the results of the ΣD^2 calculations for Group 2 and important petrogenetic information for the analogues. References: 1) Thompson et al. (2001); 2) Peate & Hawkesworth (1996), and; 3) Lightfoot et al. (1990).

8.2.7 DISCUSSION OF THE PROTOLITHS PETROGENESIS OF QILIAN META-BASALTS

As defined by the classification diagram of Figures 8.1 A & B, the meta-volcanic rocks are generally meta-basalts with a small number of basaltic-andesites and an ultramafic sample. Nb-correlation diagrams have shown that the majority of trace elements have remained immobile, especially the REE and HFSE. However, elements such as Cs, Rb, Pb, Sr and Ba (i.e. LILEs) have been de-coupled (i.e. mobilised) at some stage in the petrogenetic history of the metamorphic rocks. The nature of this mobility (e.g. whether mass has been transferred away or to the rocks) is further examined in Chapter 9.

Normalised multi-element diagrams indicate that the meta-basalts are similar to volcanic arc basalts. However, tectonic discrimination diagrams and results of the ΣD^2 calculations have shown that the volcanic-arc signature is not as "strong" as would be expected for VAB. Furthermore Ti/V ratios do not support a VAB origin for the protoliths. Instead of a volcanic-arc setting, some protoliths are likely to have erupted in a back-arc basin, whereas others erupted during the attenuation of continental crust. If the protoliths were contaminated by continental crust, it must have happened under relatively low pressures given the lack of garnet signatures in trace element patterns (apart from one sample with a steep REE pattern, see Figure 8.3A).

In support of the hypothesis that some protoliths formed during the attenuation of continental crust, Song (1996) showed that bimodal volcanic rocks are interbedded with two of the faulted blueschist belts. These bimodal rocks are thought to be the products of previous continental rifting (Song 1996 and references therein), and also thought to be involved in the subduction complex. Thus there is an intimate association between rocks produced by continental rifting (i.e. attenuation) and the high-P belt.

In summary, the protoliths of the four meta-basaltic groups were likely derived from the following settings:

Group Q1: Back-arc basin

Group Q1a: Attenuated continental crust

Group Q1b: Attenuated continental crust/back-arc basin
Group Q2: Attenuated continental crust

On the basis of this work there also appears to be clear geochemical differences between the protoliths of the relatively low-P belt, which are here shown to have originated from a back-arc basin, and the rocks of the high-grade belts, which generally show evidence for having originated from attenuated continental crust. Geochemical evidence for differences between meta-basalts of the relatively high-P and low-P belts is further confirmation of evidence from mineralogical investigations (Chapter 5) showing that these rocks are different. Consequently, it is unlikely that the high-P and low-P belts were part of the same subduction zone. Such a finding, and the tectonic origin of the protoliths in general, has important implications for understanding the tectonic formation of the Caledonian fold belt of the North Qilian Shan. However, the distribution of the blueschist belts needs to be reconciled with recent geological maps (i.e. the maps of Xia et al. 2003; Wang et al. 2005), in order to better understand the evolution of the North Qilian Shan.

Another important outcome of the previous sections is the identification of rocks with positive and negative Zr and Hf anomalies (Figure 8.3C). Although not so clear, Nb and Ta may also be slightly enriched in two samples (relative to LREE). Examples of such trace element signatures are difficult to find in the literature, e.g. the lack of analogues identified by the ΣD^2 calculations in Chapter 7. However rocks from the Tian Shan, eclogites from Zambia (e.g. John et al. 2004) and fresh gabbros and dolerites from the Oman Ophiolite all show similar trace element signatures. The identification of such signatures in rocks collected from a diverse range of settings may be evidence that such rocks are more common than what is indicated by the literature. Elements such as Nb, Ta, Hf and Zr are important in our understanding of basalt petrogenesis, and so rocks with the signatures described above may prove useful in improving our petrogentic models.

8.3 GEOCHEMISTRY OF THE PROTOLITHS 2: META-SEDIMENTARY ROCKS

The limitations for investigating the geochemistry of meta-sedimentary rocks were outlined in Chapter 7, where it was shown that geochemical methods cannot

unambiguously determine the tectonic origin of the protolith. It is within the limitations outlined in Chapter 7 that the protoliths of meta-sedimentary rocks from the North Qilian Shan are investigated.

Major element chemistry of meta-sedimentary rocks (on an LOI-free, normalised to 100% basis) is highly variable (see Table 8.6) with SiO_2 ranging from 53.29-90.86 wt% reflecting modal quartz proportions. Two samples in particular are silica rich, these are Q98-148 and Q98-142 with SiO_2 of 88.46 wt% and 90.86 wt%, respectively. Overall there appears to be little difference between the major element composition of Glaucophane Absent Meta-sedimentary rocks (GAMS) and Glaucophane Bearing Meta-sedimentary rocks (GBMS). However, the Al_2O_3 content of many GBMS is slightly elevated relative to GAMS (Table 8.6).

Sample	Q98-42	Q98-121	Q98-142	Q02-05	Q02-10A	Q98-120	Q98-134	Q98-136	Q98-150	Q98-148	Q98-143	Q02-08B	Q98-139
Rock type	GAM	GAM	GAM	GAM	GAM	GBMS	GBMS	GBMS	GBMS	GBMS	GBMS	GBMS	GBMS
SiO_2	77.96	72.07	90.86	75.34	56.26	55.89	68.10	60.48	53.29	88.46	72.05	64.61	67.67
TiO_2	0.34	0.52	0.05	0.53	0.73	1.31	0.58	0.49	1.18	0.12	0.57	0.80	0.74
Al_2O_3	9.33	12.08	1.44	9.80	11.82	15.41	15.24	17.97	16.82	3.22	13.90	11.92	12.08
Fe_2O_3	4.15	6.76	1.54	6.34	14.30	11.56	4.44	8.75	14.71	5.55	3.93	7.27	6.89
MnO	0.09	0.22	1.18	0.27	0.25	0.18	0.07	0.19	0.27	0.37	0.03	0.14	0.08
MgO	1.51	3.20	2.04	3.54	7.38	6.70	3.97	4.09	4.71	1.04	1.64	5.07	4.53
CaO	0.56	1.32	2.26	1.47	4.56	3.83	0.88	0.31	3.33	0.12	1.59	5.75	2.66
Na_2O	0.02	0.80	0.04	1.26	4.20	2.27	1.95	1.86	1.85	0.26	1.13	2.67	1.75
K_2O	5.80	2.89	0.50	1.30	0.34	2.64	4.57	5.68	3.52	0.79	5.05	1.60	3.40
P_2O_5	0.25	0.14	0.08	0.14	0.17	0.21	0.20	0.18	0.32	0.06	0.12	0.17	0.19
Total	100	100	100	100	100	100	100	100	100	100	100	100	100

Table 8.6 Major element content of meta-sedimentary rocks. The data have been recalculated on an LOI-free basis and normalised to 100%, allowing the lithological variations between different samples to be compared. All values in wt%.

In the Global Subducting Sediment (GLOSS)-normalised multi-element diagram of Figure 8.10, the Qilian Shan meta-sedimentary rocks generally show parallel trace element patterns. Although chemically similar, the GAMS tend to be slightly more depleted than the GBMS. Patterns for GAMS and GBMS are both similar to the data of Sadofsky & Bebout (2003) in particular, although there are also similarities with the terrigenous sediments of Plank & Langmuir (1998). Interesting similarities with Sadofsky & Bebout (2003) include enriched positive Zr, Hf and Ti relative to GLOSS. The silica rich samples discussed above are depleted compared with the other samples as a result of quartz effectively diluting the "shale" component (i.e. material other than quartz grains).

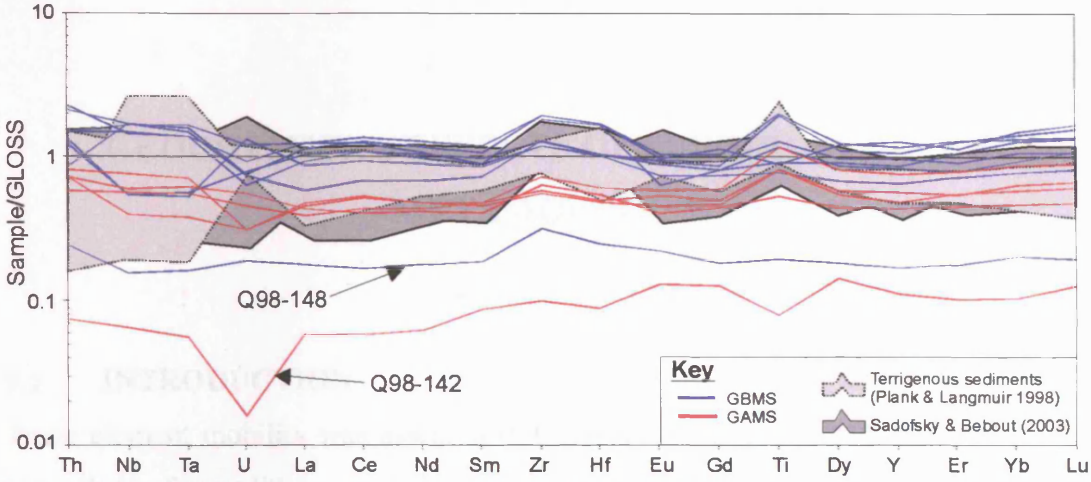


Figure 8.11. GLOSS-normalised multi-element diagrams showing the trace element pattern of Glaucophane Absent Meta-sedimentary rocks (GAMS) and Galucophane Bearing Meta-sedimentary rocks (GBMS). Meta-sedimentary rocks of Sadofsky and Bebout (2003) and terrigenous sediments of Plank and Langmuir (1998) are also shown for comparison. GLOSS values from Plank and Langmuir (1998).

From the similarities with rocks of Sadofsky & Bebout (2003) and the terrigenous sediments of Plank & Langmuir (1998) it is clear that the Qilian meta-sedimentary rocks are similar to clastic sediments outboard of many subduction zones. It is therefore likely that the composition of the meta-sedimentary rocks reflects that of the protolith (in terms of the elements used in Figure 8.10).

8.4 PROTOLITH PETROGENESIS: SUMMARY

As discovered in Chapter 7, it has also been shown in this Chapter that elements such as Th, U, Nb, Ta, REE, Zr and Hf have remained essentially immobile during the petrogenetic history of the meta-igneous rocks. It is also likely that such elements have remained immobile during the petrogenetic history of the meta-sedimentary rocks. It has therefore been possible (within limits discussed in the relevant Sections in Chapter 7) to predict the tectonic setting and petrogenesis of the protoliths. A summary and discussion of the nature of the meta-basaltic protoliths is given in Section 8.2.7. See Chapter 7 for a discussion of the limitations of interpreting the geochemistry of meta-sedimentary rocks. By knowing the geochemical nature of the protoliths, it is possible to investigate the nature of any element mobility (as indicated for elements such as Rb, Ba and Cs), and to reconstruct the tectonic evolution of the blueschist belt. This will be undertaken in Chapter 9.

CHAPTER 9

GEOCHEMICAL EFFECTS OF SUBDUCTION ZONE METAMORPHISM

9.1 INTRODUCTION

Trace element mobility was assessed in Chapters 7 and 8, where it was shown that, regardless of protolith composition, elements such as REE and HFSE (including Th and U) have remained essentially immobile. It was also shown in these chapters that the LILEs often show evidence of having mobilised from their protoliths. Furthermore, Chapters 7 and 8 rigorously investigated the composition of the protoliths, and identified analogue samples (i.e. non-metamorphosed samples with compositions likely to be similar to the actual protoliths). Thus having established element mobility and identified protolith compositions, it is now possible to investigate in more detail the nature of element mobility.

Before investigating the mobility of elements, it is important to reiterate what form the expected residual subduction zone geochemical signatures might take. In Chapter 2, a diagram of the expected trace element pattern for the residual subduction zone signature was given. This diagram is reproduced here for reference (Figure 9.1).

As shown by Niu et al. (2002), the geochemistry of a subducting slab should, to a first approximation, be complementary to the geochemistry of volcanic arc basalts (see Figure 9.1A & B). In terms of trace element ratios Niu et al. (2002) predict that the residual slab should be characterised by Th/Nb, Ba/Nb, U/Nb, Pb/Ce ratios (among others) less than N-MORB (Figure 9.1B). The diagram and predictions of Niu et al. (2002) are used in this Chapter as a guide to what form a residual subduction zone signature should take.

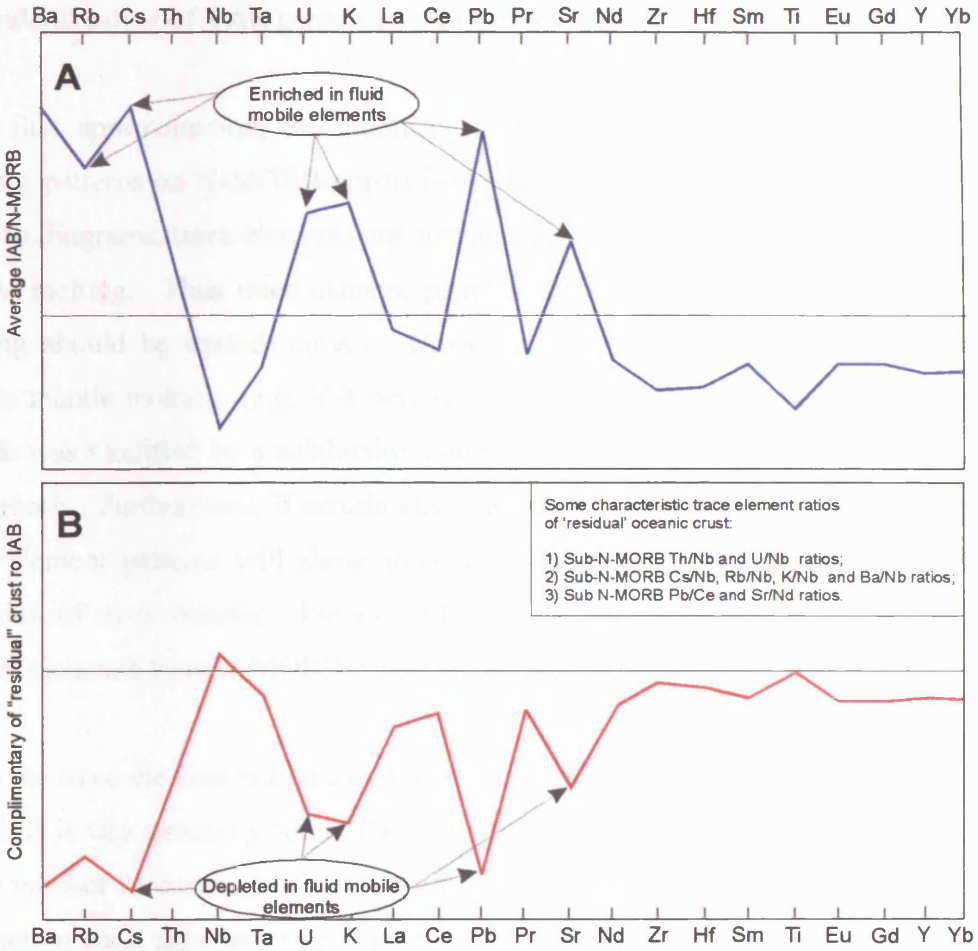


Figure 9.1 A and B. Schematic multi-element diagrams showing an average Island Arc Basalt (IAB) composition normalised to N-MORB (A), and an estimate of the composition of "residual" oceanic crust after passing through dehydration reactions associated with subduction zone metamorphism (B). Modified after Niu et al. (2002) and Niu and O'Hara (2003). See Chapter 2 for more details of the "residual subduction zone signature."

9.2 AIMS

There are essentially three aims of this Chapter: 1) to determine whether mobile elements have been added to or removed from the protoliths during metamorphism; 2) to explain the causes of any mass transfer; 3) to evaluate the implications the findings of this work have for the oceanic crust recycling models that attempt to explain OIB petrogenesis.

9.3 METHOD FOR INVESTIGATING MASS TRANSFER

Caesium, Ba, K, Rb, Sr and Pb are investigated in this section because these elements often show evidence for mobilisation from protoliths (as shown in Chapters 7 and 8).

In addition to these elements, U and Th are included because of their importance in our understanding of VAB genesis (see Figure 9.1A and Chapter 2).

To a first approximation, the mobility of elements can be established from trace element patterns on N-MORB-normalised multi-element diagrams. This is because, on such diagrams, trace elements are arranged according to their compatibility during mantle melting. Thus trace element patterns for rocks produced by simple mantle melting should be smooth curves. However, if a rock has not been produced by simple mantle melting, (e.g. if it was also contaminated), or the composition of the mantle was modified by a subduction component, the trace element patterns will not be smooth. Furthermore, if certain elements are added or removed from a rock the trace element patterns will show anomalies, the polarity of which depends of the direction of mass transfer. For example, Figure 9.1B shows how removal of fluid mobile elements from N-MORB results in pronounced negative anomalies.

From the trace element patterns on normalised multi-element diagrams (see Chapters 7 and 8) it was generally found that the LILEs had positive anomalies, except in a small number of cases. Such patterns do not correspond with the expected residual subduction zone signature (e.g. Figure 9.1B). Furthermore, these diagrams did not reveal any systematic variation between the LILE composition of greenschist, blueschist and eclogite facies rocks. It follows that, to a first approximation, the N-MORB normalised multi-element diagrams do not show clear evidence for residual subduction zone signatures in the rocks collected for this work.

Despite the lack of clear evidence for residual subduction zone signatures, this Chapter aims to investigate the LILE (and Th and U) composition of the rocks in greater detail. This is achieved by comparing the composition of the metamorphic rocks with their analogue samples, and altered oceanic crust.

Instead of reproducing normalised multi-element diagrams for the collected samples, the method adopted for determining the mobility of an element in this Chapter is similar to that used by Becker et al. (2000). In this method, ratios of elements of similar incompatibility during moderate degrees of mantle melting, such as Rb/Nb and Pb/Ce, are used. The numerator in these ratios is a readily mobilised element

(e.g. one of the LILEs, such as Rb), while the denominator is element that is not easily mobilised (e.g. one of the HFSEs, such as Nb). These ratios are plotted on "ratio-ratio" diagrams (see Figure 9.2).

Elements such as Rb and Nb are not greatly fractionated from each other by moderate degrees of partial melting or fractional crystallisation. It is therefore possible to "see through" compositional variation brought about by the latter processes. It follows that, on ratio-ratio diagrams, the size of the compositional variation fields of co-magmatic protoliths is minimised. Consequently, any variation brought about by non-magmatic processes (e.g. alteration) becomes readily recognisable, as the data points will plot outside of the composition fields defined by the protoliths (Figure 9.2). Furthermore, by normalising the ratios to N-MORB, it is possible to compare the composition of metamorphosed rocks with the expected residual subduction zone signature, such as that illustrated in Figure 9.1B.

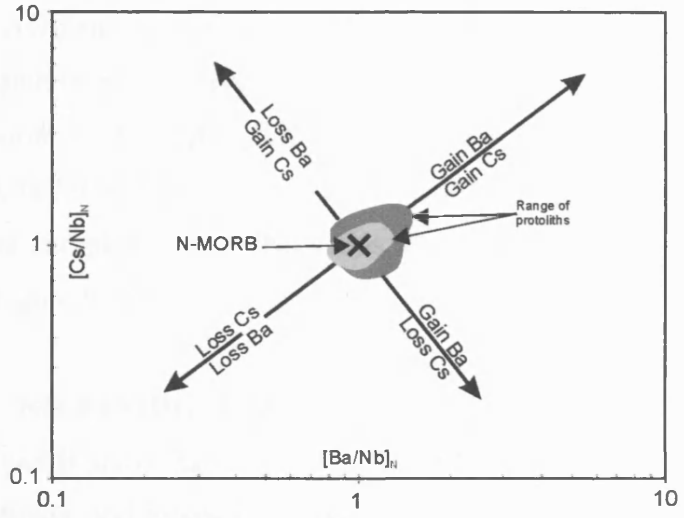


Figure 9.2. Schematic diagram illustrating the use of ratio-ratio diagrams to investigate the mobility of elements. The diagram illustrates four schematic vectors for the modification of N-MORB if Ba/Nb and Cs/Nb ratios change as a result of alteration and/or metamorphism.

Ratio-ratio diagrams can also be used for meta-sedimentary rocks, despite the fact that these rocks have a very different petrogenesis to meta-igneous rocks (e.g. See Chapter 7). The comparison of meta-sedimentary rock compositions with N-MORB allows for the identification of residual subduction zone signatures in the context outlined by Figure 9.1B.

9.4 EVIDENCE FOR MASS TRANSFER FROM META-IGNEOUS ROCKS

Chapters 7 and 8 showed that protolith compositions were likely to be highly heterogeneous in both the North Qilian and Chinese Tian Shan blueschist belts. However, a number of samples shared certain characteristics allowing for the identification of distinct geochemical groups (a smaller number of samples did not share geochemical characteristics with any of the groups). In this section the samples from the larger groups from the two field locations are examined, as the protolith compositions for these groups are generally better defined.

9.4.1 GROUP 1a AND GROUP 3 OF THE CHINESE TIAN SHAN

Figures 9.3 A-D are ratio-ratio diagrams comparing Groups 1a and 3 meta-basalts with their analogues, N-MORB and Altered Oceanic Basalt (AOB). From these diagrams three important features can be recognised:

1) data points plotted on the diagrams of Figures 9.2A-D generally fall within the fields for AOB or the analogues of Groups 1a and 3, indicating that there are no residual subduction signatures;
2) a small number of samples have Ba/Nb ratios and K/Nb ratios less than their analogues, N-MORB or AOB, in Figure 9.2 A & D, respectively;
3) some other samples have Sr/Nd ratios less than their analogues, N-MORB and AOB, in Figure 9.2C.

9.4.1.1 NO RESIDUAL SUBDUCTION ZONE SIGNATURE

Figures 9.3A and B show that $[Ba/Nb]_N$, $[Rb/Nb]_N$, $[U/Nb]_N$ and $[Th/Nb]_N$ ratios tend to plot in the fields, and follow the trends, of the analogues rather than those of AOB. The small range of $[Th/Nb]_N$ and $[U/Nb]_N$ ratios which overlap the analogue fields in Figure 9.2B is expected, as these elements were shown to have remained immobile in Chapter 7. In contrast, Figures 9.3 C and D show that the majority of data points fall in the overlapping fields of AOB and the analogues. There is no obvious systematic difference in the composition of blueschists and eclogites, showing that metamorphic grade has not affected the ratios used in Figures 9.3 A-D.

In general, the data points for the metamorphic rocks have values greater than N-MORB, and either plot in the fields for AOB and/or in the field of the analogues in

Figures 9.3 A-D. This is generally true for blueschists and eclogites. Thus, the compositional variation in the metamorphic rocks, in terms of the ratios used in Figures 9.3 A-D, can be produced in the protoliths, by pre-metamorphic igneous and alteration processes. Based on the similarity between protoliths and metamorphic rocks, and the lack of systematic differences between blueschists and eclogites, it is possible to make the general conclusion that no residual subduction zone signature exists in these rocks. However, some samples do plot with ratios below that of N-MORB, AOB and their analogues. These samples are discussed in the following two sections.

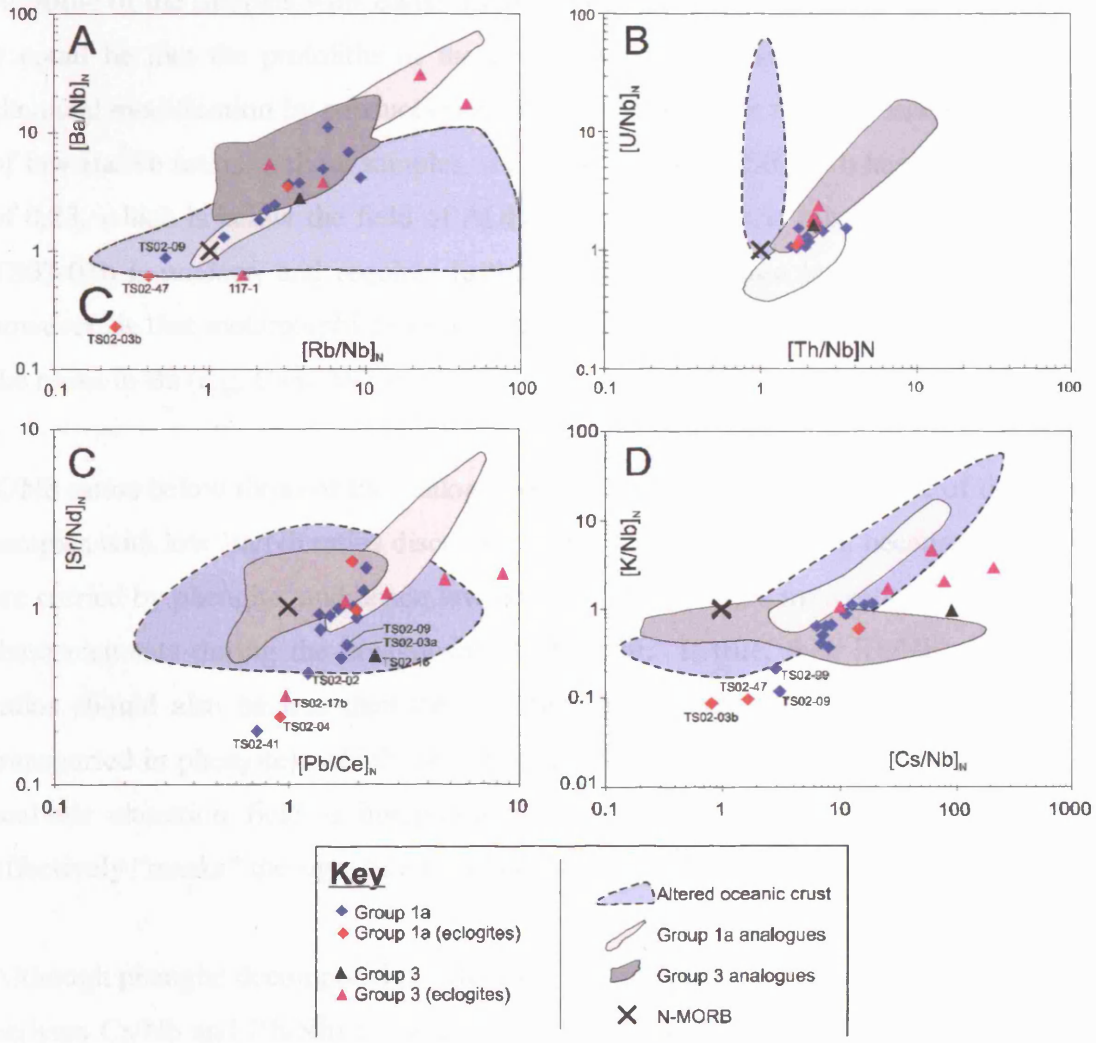


Figure 9.3 A-D. N-MORB normalised ratio-ratio diagrams for Group 1a and Group 3 meta-basalts of the Chinese Tian Shan blueschist belt. Also included are the fields for the analogues identified in Chapter 7, and Altered Oceanic Basalt (AOB). Data for the fields of AOB taken from Staudigel et al. (1996) and Kelley et al. (2003). Analogue fields are constructed by tracing around the composition fields defined by the data of: Bohrson & Reid (1995), Doucet et al. (2002) and Ingle et al.(2002) for Group 1a, and; Sinton et al. (2003) and Niu & Batiza (1997) for Group 3.

9.4.1.2 SAMPLES WITH LOW $[Ba/Nb]_N$ and $[K/Nb]_N$ RATIOS

Some samples plot with $[Ba/Nb]_N$ and $[K/Nb]_N$ ratios less than their analogues, N-MORB or AOB. These samples are generally from Group 1a (i.e. the samples TS02-09, TS02-03b and TS02-47), and have been labelled in Figures 9.3 A and D. On Figure 9.3 A only one sample (TS02-03b) plots clearly outside of the analogue and AOB fields, while the other labelled samples plot on the boundary of the AOB field. On Figure 9.3 D three samples plot with $[K/Nb]_N$ ratios of ~0.2, which is below any of the fields for the analogues MORB or AOB.

As some of the samples with Ba/Nb ratios less than N-MORB plot in the AOB field, it could be that the protoliths of these were affected by seafloor alteration. Thus chemical modification by subduction zone metamorphism is not necessarily the cause of low Ba/Nb ratios in these samples. However, sample TS02-03b has a Ba/Nb ratio of 0.23, which is below the field of AOB. The cause for the relatively low ratio for TS02-03b is unclear, and requires further investigation, (see below). A possibility however, is that metamorphism to greenschist facies on the ocean floor has depleted the rocks in Ba (e.g. Cann 1970).

K/Nb ratios below those of the analogue or AOB fields are characteristic of the same samples with low Ba/Nb ratios discussed above. This is significant because Ba and K are carried by phengite, and hence low Ba/Nb or K/Nb ratios may reflect liberation of these elements during the breakdown of phengite. If true, then Rb/Nb and Cs/Nb ratios should also be less than the protoliths and/or AOB (as Rb and Cs are also transported in phengite), which they are not. However, it could be the case that the seafloor alteration field is unrepresentative of the protoliths in this respect, and effectively "masks" the signature from phengite decomposition.

Although phengite decomposition offers an explanation for low Ba/Nb and K/Nb (and perhaps Cs/Nb and Rb/Nb) ratios in some HP-LT rocks, it is unlikely that phengite decomposition took place. This is because the P-T conditions reached by the rocks collected from the Chinese Tian Shan have been shown to be well below that required for phengite breakdown (see Chapter 5 and Figure 9.10). Two possibilities may explain the low ratios: 1) the ratios are a reflection of an altered protolith not represented by the AOB fields in the Figures 9.2 A and D; 2) Ba and K (perhaps also

Cs and Rb) were lost from the rocks prior to the crystallisation of white mica, e.g. from clay minerals present in altered protoliths during the earlier stages of subduction.

9.4.1.3 SAMPLES WITH LOW $[Sr/Nd]_N$ RATIOS

The samples with Sr/Nd ratios less than their analogues, N-MORB and AOB in Figure 9.3 C are not the same as those with low K/Nb and Ba/Nb ratios in Figures 9.3 A and D (apart from the sample TS02-09). This indicates that the cause of the low K/Nb and Ba/Nb ratios differs from the cause of low Sr/Nd ratios. Strontium is principally carried by Ca-Al-silicates such as zoisite and lawsonite, and so the decomposition of these hydrous minerals may lead to the liberation of Sr. Chapter 5 showed that lawsonite was formerly present in the HP-LT rocks collected from the Chinese Tian Shan. However, the decomposition of lawsonite produced two other hydrous minerals, namely zoisite/clinozoisite and paragonite. These other hydrous minerals could therefore immediately scavenge any fluid liberated by lawsonite decomposition. As Sr is compatible in zoisite/clinozoisite, it is also likely that Sr was taken up by such minerals and not removed from the HP-LT rocks. Furthermore, zoisite/clinozoisite is thought to be stable until it reacts out at P~ 4 GPa, which is significantly greater than the pressures reached by the Chinese Tian Shan samples. Therefore zoisite/clinozoisite decomposition is also unlikely to have caused the low Sr/Nb ratios.

It is possible to test whether low Sr/Nd ratios are the result of the breakdown of hydrous Ca-Al-silicate minerals, by investigating the co-variation of Sr with other LILE elements. Those LILEs compatible in hydrous Ca-Al-silicates, such as Pb and Ca, should correlate with Sr, whereas those LILEs not compatible in such phases, such as Rb, Ba and Cs (which are compatible in phengite) should not correlate with Sr. This scenario should be true unless there is a coupled breakdown of phengite and Ca-Al-silicates, which is not expected because of the different stability fields of these minerals. The covariation of Sr with other LILEs (as well as the covariation between other LILEs) in Group 1a is investigated in Figures 9.4 A-E.

Figures 9.4 A-E show the variation of Sr with other LILE elements. Figure 9.4 A shows that for the samples with low Sr/Nd ratios, Sr forms a positive correlation with Pb (as highlighted by the dashed line). This is the expected signature if the abundance

of Sr and Pb was determined by the breakdown of minerals such as lawsonite. However, Figures 9.4 B, D and E indicate that Sr correlates with Ba, Rb and Cs (also highlighted by the dashed line in the relevant figure). Such correlations would not be expected if the abundance of Sr was determined by the breakdown of hydrous Ca-Al-silicates. Figures 9.4 D and E reveals that the trend for some of the labelled samples (i.e. those indicated by the dashed line) follow the AOB field trend (which is "forked" on these diagrams). This may indicate that the low Sr/Nd ratios discussed above are a product of seafloor alteration prior to metamorphism.

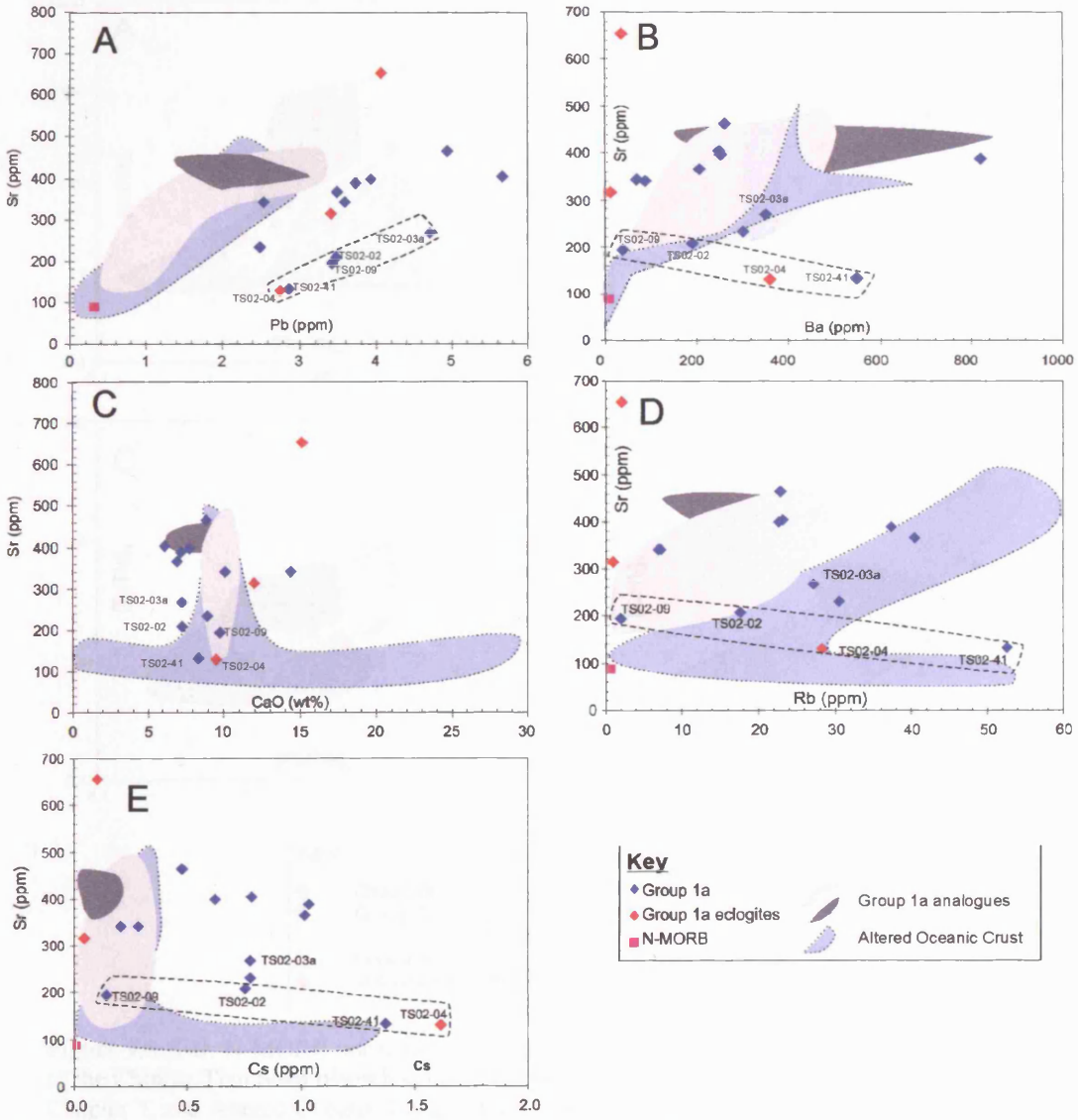


Figure 9.4 A-E. Covariation diagrams between Sr and different LILEs. On these diagrams the samples with low Sr/Nd ratios (labelled on the diagrams) often correlate with other LILEs. Correlation of Sr with other LILEs, such as Rb, Cs and Ba, is not expected if the breakdown of Ca-Al-silicate minerals has caused low Sr/Nd ratios in some samples. Analogue fields are constructed by tracing around the composition fields defined by the data of: Bohrson & Reid (1995), Doucet et al. (2002) and Ingle et al. (2002) for Group 1a, and; Sinton et al. (2003) and Niu & Batiza (1997) for Group 3.

9.4.2 GROUP 2A AND 2B OF THE CHINESE TIAN SHAN

Figures 9.5 A-D are ratio-ratio plots for Groups 2A and 2B of the Chinese Tian Shan blueschist belt. On Figures 9.5 A and B the samples of Groups 2a and 2b plot in the fields defined by the analogues, indicating subduction metamorphism has not significantly affected these samples. Figure 9.5 C however, show that many samples do not plot in the analogue fields but plot in the AOB fields, indicating that these samples may have been altered prior to metamorphism. On Figure 9.5 D many samples from Groups 2a and 2b have Cs/Nb ratios greater than N-MORB, AOB and the analogue fields.

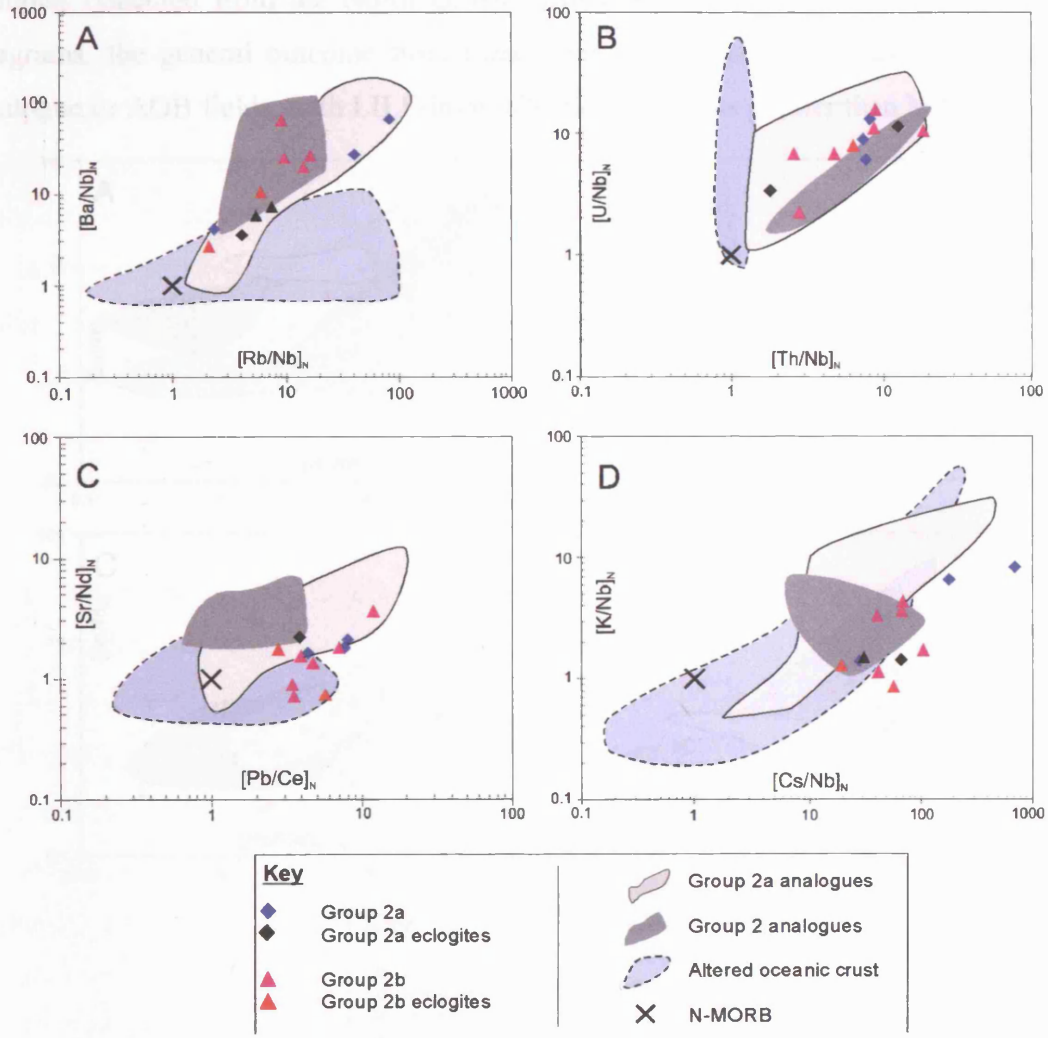


Figure 9.5 A-D. N-MORB normalised ratio-ratio diagrams for Group 2a and Group 2b meta-basalts of the Chinese Tian Shan blueschist belt. Also included are the fields for the analogues identified in Chapter 7, and Altered Oceanic Basalt (AOB). Data for the fields of AOB taken from Staudigel et al. (1996) and Kelley et al. (2003). Analogue fields are defined by the data of Woodhead et al. (1998), Thomas et al. (2002) and Conrey et al. (1997).

Figures 9.4 A-D indicate that the LILE/immobile element ratios of Groups 2a and 2b of the Chinese Tian Shan are similar to the analogues and AOB. Furthermore, all ratios are generally greater than N-MORB. Thus there is no clear evidence for a residual subduction zone signature in these rocks. This conclusion is further validated by the fact that there are no systematic differences between the LILE/immobile element ratios of blueschist and eclogite facies rocks.

9.4.3 META-BASALTIC ROCKS OF THE NORTH QILIAN SHAN

Figures 9.6A-D are N-MORB normalised ratio-ratio plots for the meta-basaltic samples collected from the North Qilian Shan blueschist belts. As with previous diagrams, the general outcome from these diagrams is that data points plot in the analogue or AOB fields, with LILE/immobile element ratios greater than N-MORB.

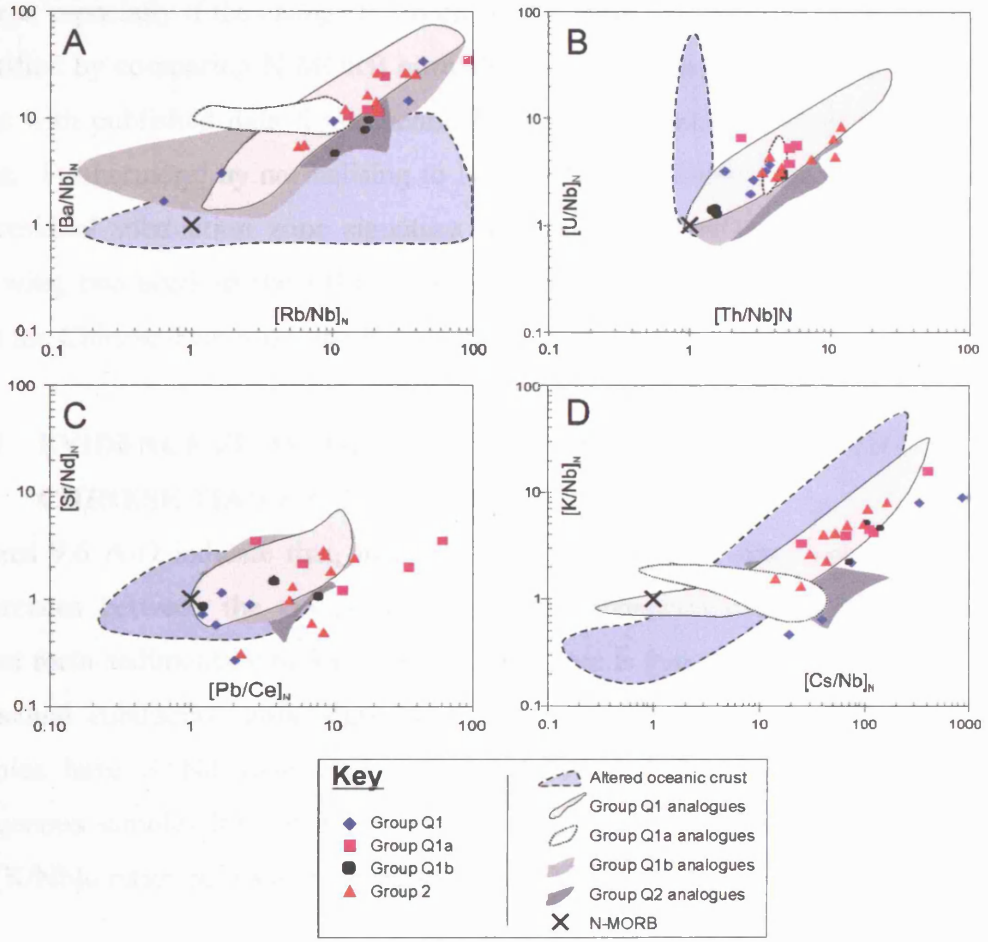


Figure 9.6 A-D. N-MORB normalised ratio-ratio diagrams for meta-basaltic groups of North Qilian Shan blueschist belts. Also included are the fields for the analogues identified in Chapter 8, and Altered Oceanic Basalt (AOB). Data for the fields of AOB taken from Staudigel et al. (1996) and Kelley et al. (2003). Analogue fields are defined the data of: Fretzdorff et al. (2002), Haase et al. (2002) and Keller et al. (2002) for Group Q1; Hawkesworth et al. (1995) for Group Q1a; Lightfoot et al. (1997), Fretzdorff et al. (2002) and Haase et al. (2002) for Group Q1b, and; Thompson et al. (2001); 2) Peate & Hawkesworth (1996), and; 3) Lightfoot et al. (1990) for Group Q2.

On Figures 9.6A and B the data from all the sample groups generally plot in the anlogue fields. However, one sample from Group Q1 plots in the field for the analogues of Group 1b, with a Rb/Nb ratio less than N-MORB (Figure 9.6A). Figures 9.6 C and D differ from the previous two figures in that many more samples plot outside of the analogue and AOB fields. Most of the latter have LILE/immobile ratios greater than any other field. However, Figure 9.6C also highlights the fact that two samples have $[Sr/Nd]_N$ ratios less than AOB and the analogue fields.

9.5 EVIDENCE FOR MASS TRANSFER FROM META-SEDIMENTARY ROCKS

As discussed in Chapter 7, it is very difficult to accurately predict the composition of the protoliths of meta-sedimentary rocks. This complicates the identification of mass change, especially if the change has been small. However, large mass changes can be identified by comparing N-MORB normalised ratios of the HP-LT meta-sedimentary rocks with published data from chemically-similar sediments and meta-sedimentary rocks. Furthermore, by normalising to N-MORB the existence, or non-existence, of the residual subduction zone signature (Figure 9.1B) can be established. In the following two sections the LILE compositions of meta-sedimentary rocks collected from the Chinese Tian Shan and North Qilian Shan are investigated.

9.5.1 EVIDENCE FROM META-SEDIMENTARY ROCKS OF THE CHINESE TIAN SHAN BLUESCHIST BELT

Figures 9.6 A-D indicate that, in terms of the ratios used, there are no systematic differences between the compositions of Glaucophane-bearing and Glaucophane-absent meta-sedimentary rocks. Furthermore, there is generally no clear evidence for a residual subduction zone signature. However, Figure 9.6 C shows that some samples have Sr/Nd ratios below those of N-MORB, a feature also of some terrigenous samples from Plank and Langmuir (1998). One sample in Figure 9.6 D has $[K/Nb]_N$ ratios below any analogue field and MORB.

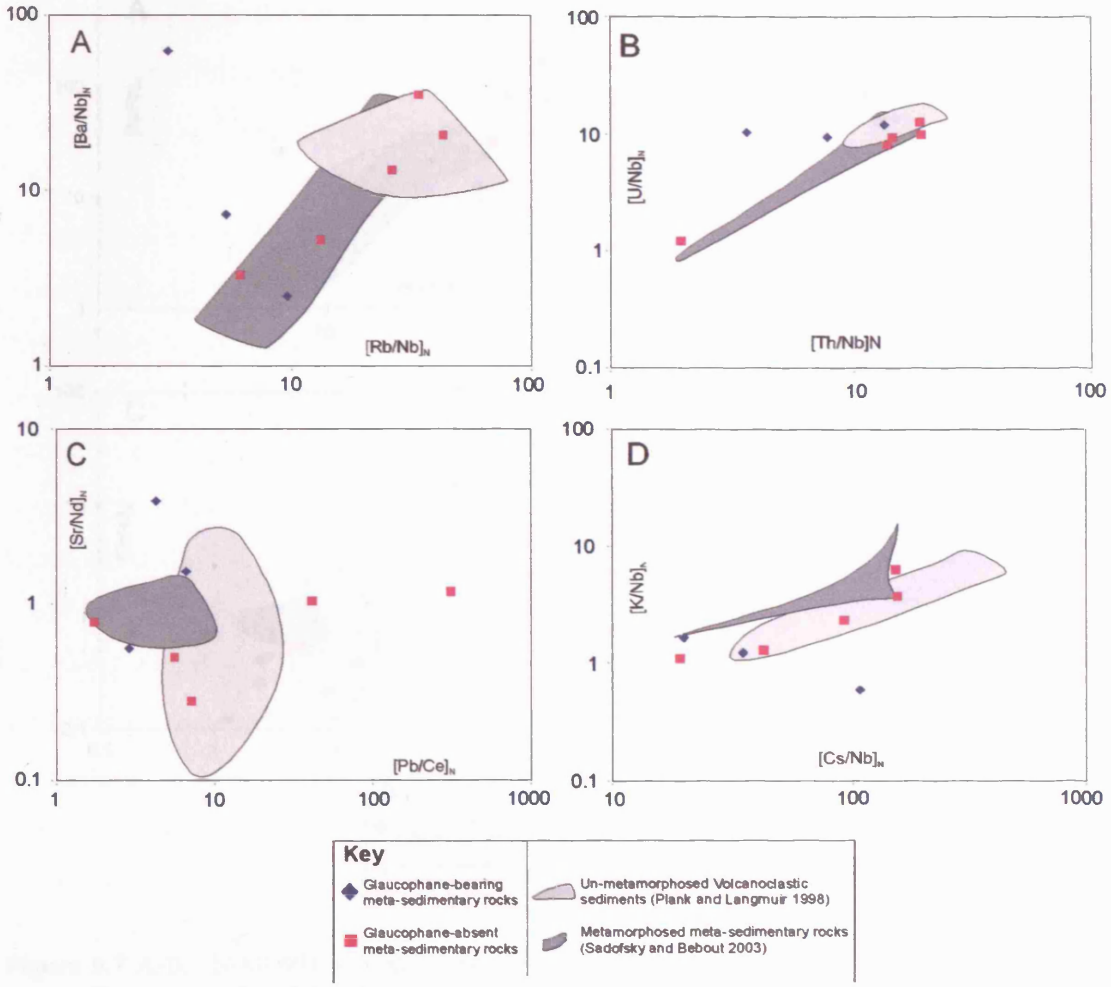


Figure 9.6 A-D. N-MORB normalised ratio-ratio diagrams comparing the compositions of HP-LT meta-sedimentary rocks of the Chinese Tian Shan with the composition of terrigenous sediments (Plank and Langmuir 1998), and the low-grade meta-sedimentary rocks of Sadofsky and Bebout (2003).

9.5.2 EVIDENCE FROM META-SEDIMENTARY ROCKS OF THE NORTH QILIAN SHAN BLUESCHIST BELTS

On Figures 9.7 A-D the data for the Qilian Shan meta-sedimentary rocks forms a wide scatter of points (which is similar to Figures 9.6 A-D for the Tian Shan samples). In general, the LILE/immobile element ratios are greater than those of N-MORB, with only one sample having values less than N-MORB (Figure 9.7C). Thus the expected residual subduction zone signature is absent in the Qilian meta-sedimentary samples.

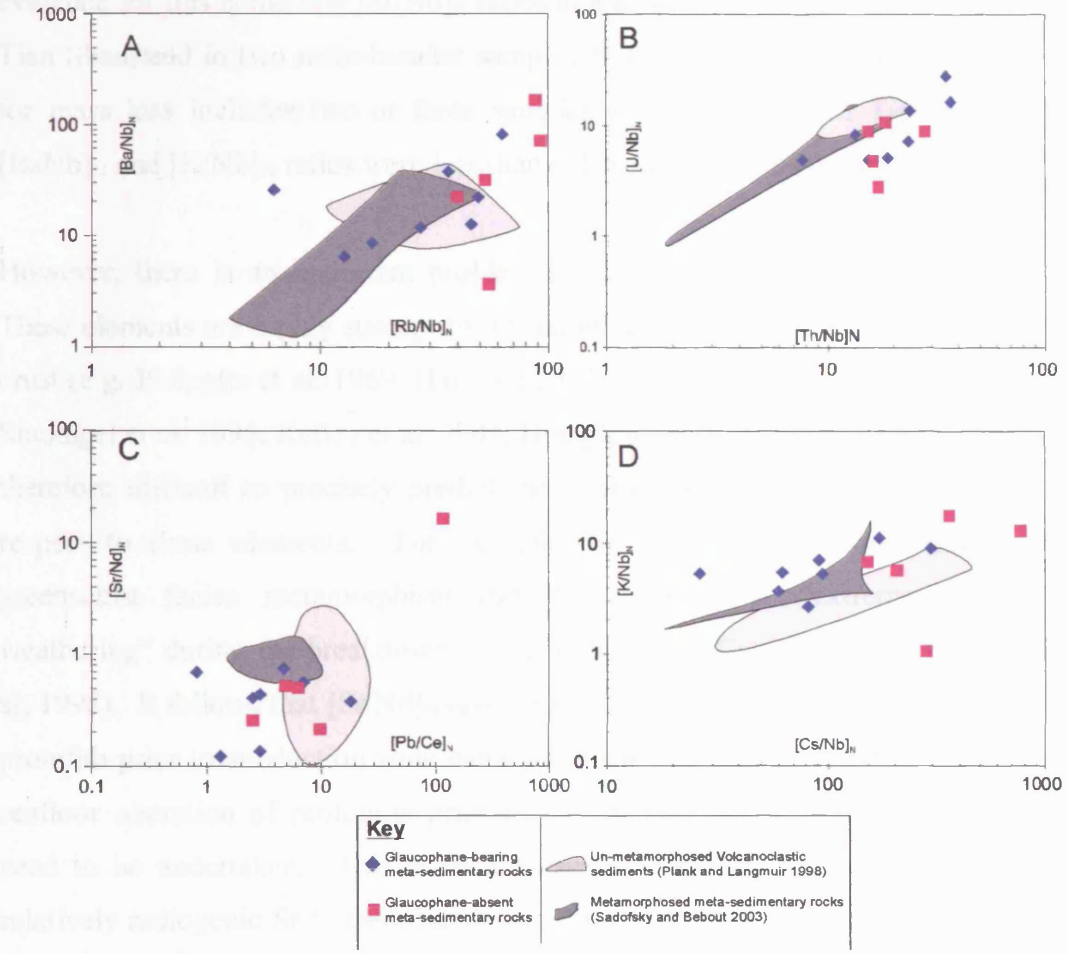


Figure 9.7 A-D. N-MORB normalised ratio-ratio diagrams comparing the compositions of HP-LT meta-sedimentary rocks of the North Qilian Shan with the composition of terrigeneous sediments of Plank and Langmuir (1998), and low-grade meta-sedimentary rocks of Sadofsky and Bebout (2003).

9.6 SUMMARY AND DISCUSSION OF EVIDENCE FOR MASS TRANSFER FROM PROTOLITHS

In general, the previous sections of this Chapter have revealed no clear evidence for residual subduction zone signatures in the rocks of this study. This is particularly true for elements such as U, Th and the LREE, which have been shown to have remained immobile since the igneous petrogenesis of the protoliths. Immobility of U, Th, and the LREE in the blueschists and eclogites is significant as these elements are thought to be transferred from the slab to the source regions of arc magmas (e.g McCulloch and Gamble 1991, Pearce and Peate 1995).

The only indication for element loss consistent with the expected residual subduction zone metamorphic signature is LILE loss in some samples. Ostensibly, the clearest

evidence for this is the low $[Sr/Nd]_N$ ratios in a number of samples of Group 1a from Tian Shan, and in two meta-basaltic samples from Qilian Shan. The other evidence for mass loss includes two or three samples from Group 1a of Tian Shan where $[BaNb]_N$ and $[K/Nb]_N$ ratios were less than either the protoliths or AOB.

However, there is an important problem in estimating mass change of the LILEs. These elements are highly susceptible to mobilisation during alteration of the oceanic crust (e.g. Philpotts et al. 1969; Hart et al. 1970; Cann 1970; Pearce and Cann 1973; Staudigel et al. 1996; Kelley et al. 2003; Humphries et al. 1998; Staudigel 2004). It is therefore difficult to precisely predict the composition of an altered protolith with respect to these elements. For example, Sr can removed from basalts during greenschist facies metamorphism (on the seafloor) or "extreme ocean floor weathering" during the breakdown of plagioclase (e.g. Cann 1970 and Humphries et al. 1998). It follows that $[Sr/Nd]_{N\text{-}MORB}$ ratios <1 could be caused by alteration of the protolith prior to subduction zone metamorphism. To further evaluate the effects of seafloor alteration of protoliths prior to metamorphism, Sr isotope analysis would need to be undertaken. This is because seafloor alteration can quantitatively add relatively radiogenic Sr to fresh basalt (e.g. Staudigel 2004). It should be possible to recognise the effects of seafloor alteration on LILE elements by investigating the correlation of these elements with Sr isotopes.

More robust evidence for a residual subduction zone signature could come from elements such as LREE, U and Th. This is because these elements are not generally susceptible to moderate degrees of seafloor alteration (Pearce and Cann 1973; Staudigel 1996; Staudigel 2004). However, the LREE and Th are often enriched in arc lavas implying that they are mobilised from the slab during subduction (e.g. McCulloch and Gamble 1991; Pearce and Peate 1995). Therefore decoupling and depletion of LREE, U and Th from HREE and HFSE in subduction zone-metamorphosed rocks would be relatively robust evidence for a residual subduction zone signature. No such evidence exists for the rocks collected from the two field locations of NW China.

It is also noteworthy that LILE depletion does not seem to be related to metamorphic grade, indicating that the blueschist-eclogite transition does not produce LILE mass

loss. This fact combined with 1) the problems inherent in interpreting LILE mass change, 2) the lack of clear evidence for LILE mass loss in the samples, and 3) no evidence for LREE, U or Th mass loss, leads to the conclusion that there is no evidence for a residual subduction zone signature in the rocks collected for this work.

9.6.1 COMPARISON WITH OTHER WORK

In Chapter 2 the previous work on geochemistry of blueschist and eclogites was divided into works that showed evidence for:

1) LILE (and perhaps Th and U) removal during HP/LT metamorphism (e.g. Bebout 1995; Bebout et al. 1993, 1999; Arculus et al. 1999; Becker et al. 2000);
2) LREE (and LILE, to a lesser extent) removal during HP/LT metamorphism (e.g. John et al. 2004);
3) LILE addition during HP/LT metamorphism (e.g. Sorensen and Grossman 1989; Sorensen et al. 1997).
4) no mass loss, even for the fluid-mobile LILEs (e.g. Cruciani et al. 2002; Chalot-Prat et al. 2003; Sadofsky and Bebout 2003; Spandler et al. 2004).

The results of this investigation are consistent with the works that show no evidence for mass loss (i.e. Cruciani et al. 2002; Chalot-Prat 2003; Sadofsky and Bebout et al. 2003; Spandler et al. 2004).

9.7 EXPLAINING THE LACK OF RESIDUAL SUBDUCTION ZONE CHEMICAL SIGNATURES 1: EVIDENCE FROM PROTOLITHS

To explain the lack of the expected residual subduction signature in the rocks collected for this study, it is necessary to return to the protoliths. This is because residual subduction zone signatures are expected to develop by the dehydration of seafloor altered basalt and sediments (see Chapter 1). Thus the initial assumption that the protoliths of rocks collected for this study are analogous to seafloor-altered basalt and sediments requires confirmation.

Seafloor-altered basalts of the upper oceanic crust can contain up to 10 wt% H_2O in the form of hydrous minerals, as pore fluids and as exchangeable H_2O bound to mineral surfaces (Staudigel 2004). Under blueschist or eclogite facies conditions (but

below ~2.5GPa), 10wt% H_2O is significantly greater than the expected H_2O content of H_2O-saturated MORB, which is about 3-4.1 wt% at P-T conditions between 1-2GPa and 400-500°C, respectively (see Figure 9.10). Thus, an AOB with an initial H_2O content of 10wt% must dehydrate during metamorphism up to blueschist/eclogite facies. Assuming the evolved fluid can escape, it is possible to remove fluid soluble elements from oceanic crust by dehydration of AOB with originally high H_2O contents (e.g. >4.1 wt%).

As H_2O loss is necessary for generating a mobile phase (in the absence of externally derived fluid) during HP-LT metamorphism, it is fundamentally important to establish whether the protoliths of the collected rocks were analogous to AOB with respect to initial H_2O content. The following two sections aim to further investigate the geological setting in which the protoliths formed, to determine whether the H_2O content of the protoliths was sufficient to generate a mobile phase during HP-LT metamorphism.

9.7.1 TECTONIC SETTING OF PROTOLITH PETROGENESIS 1: PROTOLITHS OF THE CHINESE TIAN SHAN

Geochemical investigations have shown that the meta-basaltic protoliths from the Chinese Tian Shan generally originated from two contrasting tectonic settings, namely: 1) seamounts, perhaps close to a continental margin (Groups 1a, 1b, 1c and perhaps 3), and; 2) a continental volcanic arc (Group 2a and 2b).

9.7.1.1 PROTOLITHS ORIGINATING FROM SEAMOUNTS

The accretion of the protoliths of Groups 1a, 1b, 1c and 3 into an accretionary wedge may have been similar to that depicted in Figure 9.8 A-C. In this model, a seamount enters the trench and undergoes normal faulting and subsidence (Figure 9.8 A and B). With continued subduction these processes result in the dismemberment of the seamount and the development of distinct blocks (Figure 9.8 C).

This model can explain a number of features of the HP-LT rocks exposed in Chinese Tian Shan blueschist belt (see Chapter 3):

1) **pods and lenses of blueschists and eclogites.** The dismemberment of the seamount produces blocks of different sizes, which may continue to subduct to depths where blueschist and eclogite facies metamorphism can take place. These blocks can then be exhumed by "wedge extrusion processes" during later continental collision (e.g. Gao and Klemd 2003, see Chapter 3).

2) **The presence of basalts and marbles.** In addition to meta-basalts and meta-sedimentary rocks, carbonates are very common in the Chinese Tian Shan blueschist belt. Furthermore, carbonates were found to be common accessory minerals in meta-basalts and meta-sedimentary rocks. Seamounts form positive bathymetry on the seafloor, perhaps reaching depths above the Carbonate Compensation Depth, and so allowing the precipitation of carbonates. Thus, the association of extensive marble and meta-basalt outcrops at the Chinese Tian Shan blueschist can be explained by the incorporation of a seamount capped with carbonate into an accretionary wedge.

2) **lack of evidence for sheeted dike complex.** Igneous features such as pillow basalts are preserved in blueschists and eclogites at the Chinese Tian Shan blueschist belt. However, another important igneous feature associated with oceanic crust is lacking, i.e. sheeted dikes. Sheeted dikes are not associated with seamounts (e.g. Schiffman and Staudigel 1994), and so their absence is fully consistent with the model illustrated in Figures 9.8 A-C.

Although some seamounts form near mid-ocean ridges, e.g. seamounts associated with the East Pacific Rise (see Niu and Batiza 1997), seamounts often form in intra-plate settings. The magmatic system giving rise to seamounts differs from the magmatic system at mid ocean ridges. Seamounts are thought to derive from magmas originating from a hotspot which rise to the plate surface along fractures (e.g. Batiza 1982). In contrast magmas are produced at mid-ocean ridges by decompression melting of mantle which rises in response to plate separation at spreading centres.
Because of the contrasting magmatic systems at Mid Ocean Ridges and seamounts, there are differences between the lithologies and structural features in volcanic edifices produced at these two environments (Schiffman and Staudigel 1994).

Consequently, hydrothermal circulation at these two settings differs because of the importance of structural and lithologic features in controlling hydrothermal circulation. Seamount edifices lack the deep fracture systems present at mid-ocean ridges, with the corollary that vertical fluid convection is relatively minor. Hydrothermal circulation at seamounts is more likely to be limited to lateral flow along permeable horizons, such as volcanogenic breccias (Schiffman and Staudigel 1994).

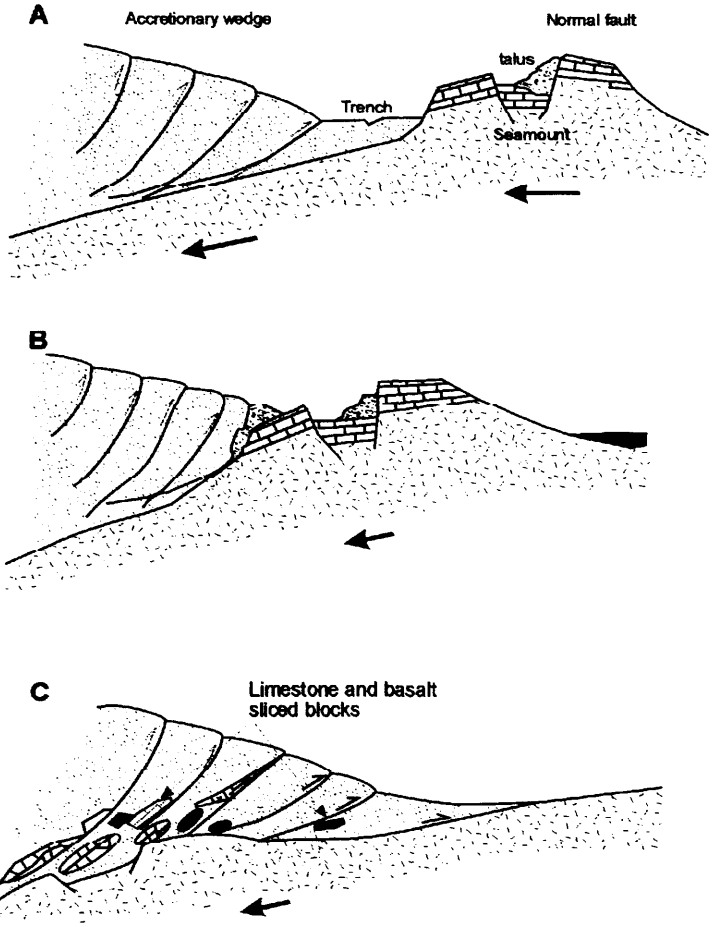


Figure 9.8. Model for the incorporation of a seamount into an accretionary wedge, modified after Pickett and Robertson (1996). According to this model, pods and lenses of limestone and basalt are produced during dismemberment of the seamount at the onset of subduction. After continued subduction, these lenses and pods become metamorphosed, and are later exhumed as HP-LT pods and lenses, perhaps by a "wedge extrusion" mechanism, as suggested by Gao and Klemd (2003).

The lack of vertical circulation in seamounts may restrict pervasive hydrothermal alteration to certain horizons. This may be particularly true if individual lava flows were very thick, thus isolating large bodies of relatively impermeable rock from permeable horizons. If true, it follows that hydrothermal alteration of a seamount need not be pervasive, resulting in volcanic rocks less altered than those of Altered

Oceanic Crust (in the sense used by Staudigel et al. 1996 and Kelley 2003). Furthermore, large cohesive bodies of relatively unaltered rocks are more likely than the weaker permeable horizons to survive dismemberment processes that take place during seamount accretion (Figure 9.8). In conclusion, it is unlikely that the rocks with seamount protoliths were analogous to AOB, and that meta-basaltic protolith H_2O contents were relatively low.

Such a conclusion is supported by the LOI data from the analogue samples that were identified in Chapter 7. Unfortunately, LOI data is only given for the data of Doucet et al. (2002), whereas LOI can only be inferred for the other analogue data by summing together the major element data and subtracting from 100%. It should be noted, however, that the accuracy of Inferred- Loss on Ignition (I-LOI) is dependent on the accuracy of the major element analysis, and that in the absence of actual LOI values, I-LOI should be treated only as a guide. Furthermore, LOI/I-LOI should not be considered necessarily representative of H_2O content because of the potential for other volatiles, such as carbonates and sulphides/sulphates. Another problem with the LOI of the analogue samples is that it represents a "snapshot" of the evolution of an analogue, i.e. after an analogue is erupted there remains the potential for seafloor alteration and modification of LOI. LOI/I-LOI of the analogues are therefore used as a guide to the H_2O content of the protoliths. LOI and I-LOI data the analogues of Groups 1a and 3 are given in Table 9.1.

Reference	Group	Ave LOI/I-LOI	RSD*	Max	Min	No. Samples
Doucet et al. (2002)	1a	2.97 wt%	45.08	6.69 wt%	0.64 wt%	30
Ingle et al. (2002)	1a	0.38 wt%	247.65	3.05 wt%	-1.2 wt%	17
Bohrson and Reid (1995)	1a	1.32 wt%	23.08	2.06 wt%	0.87 wt%	27
Niu and Batiza (1997)	3	0.29 wt%	14.33	0.41 wt%	0.19wt%	80

Table 9.1. Summary of LOI data from Doucet et al. (2002) and inferred LOI (I-LOI) (i.e. 100- Σmajor elements) from Niu and Batiza (1997), Ingle et al. (2002) and Bohrson and Reid (1995). RSD* - Relative Standard Deviation; Max- Maximum value; Min- Minimum value.

From Table 9.1 it can be seen that samples with LOI greater than 4 wt% are extremely rare, with average LOI or (I-LOI) ranging from 0.29 wt% to 2.97 wt%. Only a small number of samples from Doucet et al. (2002) have samples with LOI >4.0 wt%. Thus, the protoliths of Group 1a and Group 3 were unlikely to have H_2O contents greater than H_2O-saturated MORB at the maximum P-T conditions reached during

their metamorphism (i.e. 3-4.1wt%). Further evidence for this comes from Sinton et al. (2003), (the source of data for the analogues of Group 3 protoliths) who found H_2O contents of <1.9wt% in basalts from the Manus back arc basin, Papua New Guinea.

Low protolith H_2O contents have important implications for dehydration reactions, because H_2O saturation, and hence dehydration, would take place at greater depths for seamount lavas than AOB (see below). It is therefore possible to conclude that the response of lavas from seamounts during HP-LT metamorphism is not analogous to that of AOB during HP-LT metamorphism. Consequently, the geochemistry of the collected HP-LT seamount basalts cannot be used to evaluate the validity of "recycling models" (i.e. models that explain the geochemistry of OIBs by AOB recycling).

9.7.1.2 PROTOLITHS ORIGINATING FROM CONTINENTAL VOLCANIC ARCS

Incorporation of the continental volcanic arc protoliths into the Chinese Tian Shan paleo-accretionary wedge, may have involved erosion of the volcanic arc during subduction. Erosion of volcanic arcs is known to take place at convergent margins where sediment thickness in the trench is relatively shallow, at < 500m (e.g. Le Pichon et al. 1993). Seamount subduction is also known to cause erosion of the fore arc region (e.g. Cloos 1993). Thus a subducting seamount could cause the erosion necessary to incorporate the volcanic arc protoliths. There may therefore be a causal link between the subduction of a seamount, which gave rise to the seamount protoliths, and the incorporation of volcanic arc protoliths, although there is no direct evidence for this.

As with seamounts, the igneous petrogenesis of volcanic arc protoliths differs from rocks produced at mid ocean ridges. Basaltic volcanism at a volcanic arc does not take place at a mid ocean ridge. The extensive and pervasive hydrothermal alteration associated with mid ocean ridges is therefore not likely to have affected the volcanic arc protoliths. Furthermore, seafloor weathering known to effect "normal" oceanic basalt as a plate moves away from a spreading centre (e.g. Staudigel et al. 1996; Kelley et al. 2003), is unlikely to affect volcanic arc basalts. Consequently, VAB protoliths are not likely to be analogous to AOB basalts with respect to initial H_2O

concentrations. It is also unlikely that the VAB protoliths had initail H_2O contents high enough for cause significant dehydration during metamorphism to eclogite facies. It follows that the geochemical evolution of the VAB protoliths during HP-LT metamorphism to ~2.4GPa cannot be used to reliably evaluate recycling models (as outlined in Section 9.7.1).

9.7.2 TECTONIC SETTING OF PROTOLITH PETROGENESIS 2: PROTOLITHS OF THE NORTH QILIAN SHAN

Two contrasting tectonic settings have been proposed for the origin of North Qilian Shan blueschists and eclogites: 1) back arc basin; 2) attenuated continental crust, perhaps at a continental margin.

9.7.2.1 PROTOLITHS ORIGINATING FROM A BACK ARC BASIN

The metamorphic rocks with back-arc basin basalt protoliths are generally associated with the low-grade blueschist belt, and their relationship with the protoliths is unclear (i.e., were they metamorphosed at the same subduction zone?). Ocean crust and lithosphere formed at a BAB is generally analogous to "normal" oceanic crust and lithosphere, in that it is composed of a basaltic layer overlying a succession of sheeted dikes, gabbros and ultramafic rocks. Furthermore, the crust formed at a BAB spreading centre would be analogous to normal MORB crust in that it forms relatively deep bathymetry, i.e. compared to bathymetric highs such as oceanic islands, seamounts, oceanic large igneous provinces etc.

It is noteworthy, however, that sheeted dykes are not observed in the HP-LT rocks of the low grade blueschist belt. The implication is that the BAB protoliths did not originate from crust and lithosphere analogous to normal oceanic crust and lithosphere (in the context outlined above). This would be true unless the basaltic layer was preferentially removed from the rest of the crust and lithosphere during its incorporation into the accretionary prism. However, separation of the basaltic crust from the sheeted dike complex is unlikely as these layers are continuous, i.e. the sheeted dike complex is composed of dikes which feed lavas to the basaltic layer. Thus there is unlikely to be a zone of weakness separating the sheeted dikes from the basalt layer which can be exploited during incorporation of BAB lithosphere into the accretionary prism.

It may be the case that the BAB protoliths originated from a bathymetric high, such as a seamount, or other thickened crust. Bathymetric highs may be easier to incorporate into accretionary prisms because they are susceptible to dismemberment during collision with the material of an accretionary prism (e.g. Figure 9.8). Thus bathymetric highs have a greater "preservation potential" in accretionary prisms compared to the lower-lying normal oceanic crust.

Back-arc basins contain spreading centres akin to those at Mid-Ocean Ridges, and so there is similar potential for hydrothermal alteration of BAB crust as there is MOR crust. However, if the BAB protoliths did originate from a bathymetric high the potential for pervasive hydrothermal alteration may be reduced, although, apart from the lack of sheeted dykes and gabbros, there is little evidence to support this.

9.7.2.2 PROTOLITHS ORIGINATING FROM ATTENUATED CONTINENTAL CRUST

Meta-basalts from the high-grade blueschist belt of the North Qilian Shan were shown to have protoliths with trace element chemistries similar to some basalts formed during crustal attenuation. From the tectonic model for North Qilian Shan prior to collision orogenesis (Figure 9.9A-D), protoliths of the high and low-grade blocks erupted in the Southern Terrane (ST). However, if the protoliths of the low-grade blueschist belt were in fact from a back-arc basin, the model of Figure 9.9A-D is inconsistent. This is because the only back-arc basin known to exist in the North Qilian Shan is identified in the Northern Terrain. Further geological mapping is required to solve this apparent paradox. Particular attention should be paid to the movement of rocks along faults, so that the original associations between the blueschist belts, ophiolites, volcanic arcs and continental blocks can be reconstructed.

Regardless of their actual location of eruption in the paleo-North Qilian Shan, a Continental Margin (CM) is the likely tectonic setting for eruption of the high-grade protoliths. Basalts erupted on CMs, are not erupted through mid ocean ridges with well developed hydrothermal convection cells. There are therefore differences in the igneous petrogenesis and the potential for hydrothermal alteration between basalts erupted on CMs and those erupted at MOR. In particular, at CMs basalt often erupts in large quantities which flow away from the fissure, producing "seaward dipping reflectors." Consequently basalts erupted at CMs are unlikely to be effected by seafloor or hydrothermal alteration to the same extent as some basalts produced at mid ocean ridges.

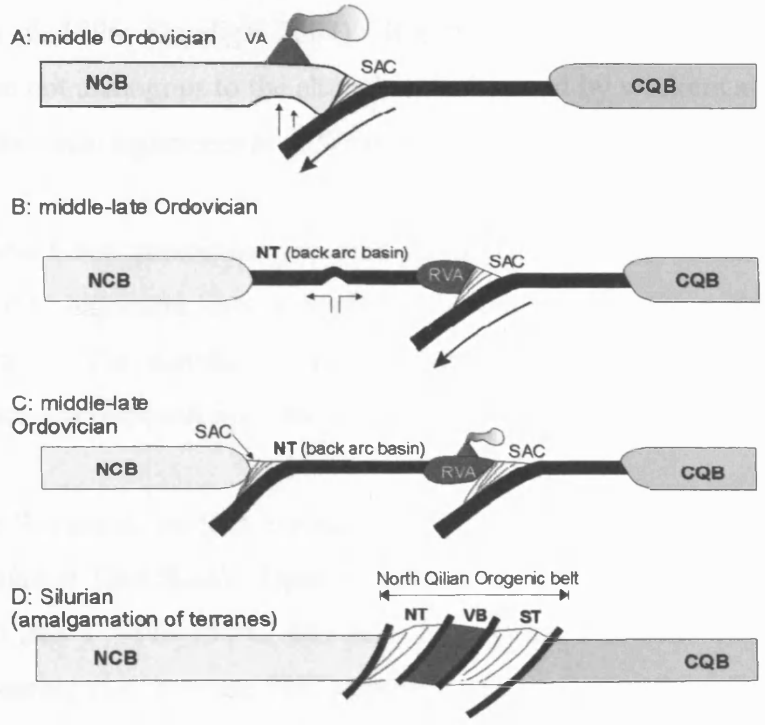


Figure 9.9 A-D. Schematic diagrams showing the tectonic evolution of the North Qilian Mountains, and likely locations of the basaltic protoliths (modified after Wang et al. 2005). SAC, Subduction accretionary complex; VA, volcanic arc; RVA, rifted volcanic arc; NT, Northern Terrane; ST, Southern Terrane, VB, volcanic rock belt; NCB, North China block; CQB, Central Qilian Block.

If the tectonic setting of the protoliths is correct, and faulting has not adjusted the relative positions of the belts, the tectonic model does not explain the locations of the high and low-grade blueschist belts. Both belts exist in the Southern Terrane, however, the back arc basin (the likely provenance of the low-grade protoliths) is in the Northern Terrane. Further geological mapping is required to establish the relationship of the blueschist belts to the tectonic evolution of the North Qilian Shan prior to collision orogenesis.

From the evidence discussed above, protoliths of the high-grade meta-basalts from the North Qilian Shan are not analogous to the rocks (i.e. AOB) invoked by recycling models to explain OIB genesis.

9.7.3 IMPLICATIONS OF THE EVIDENCE FROM PROTOLITHS

It has been shown that the protoliths of the collected HP-LT metamorphic rocks were not likely to have been analogous to AOB, in terms of either bulk rock composition or initial H_2O content. This is because the protoliths were formed at settings unlikely to have deep seated hydrothermal convection cells capable of pervasively altering large bodies of rock, as found at MOR. It is therefore unlikely that the protoliths were pervasively hydrothermally altered. Such a hypothesis is supported by the lack of U enrichment in the metamorphic rocks, which is a characteristic feature of AOB (e.g. Staudigel et al. 1996; Staudigel 2004). It is therefore possible to conclude that the protoliths are not analogous to the altered rocks invoked by workers aiming to explain HIMU geochemical signatures (e.g. Weaver 1991; Hofmann 1997).

If it is assumed that protoliths were not pervasively altered, the lack of a residual subduction zone signature may be explained by the fact that the rocks never reached H_2O-saturation. The corollary is that the rocks never dehydrated and so soluble elements were not removed from the rocks.

To illustrate this point, we turn to rocks with evidence for LILE mass loss (i.e. Group 1a of the Chinese Tian Shan). These rocks were shown to have metamorphosed at P~ 1.9-2.0 GPa and T ~440-550°C, and have an average LOI 2.26 wt% despite being carbonate-bearing (i.e. average H_2O contents will be below the LOI). Figure 9.10 shows that, at similar P-T conditions to those experienced by Group 1a, H_2O concentrations can be 2.3-3.8 wt% in meta-basalts of MORB-like composition. As the LOI in Group 1a is generally less than that that of a saturated basalt under the conditions outlined above, it likely that the rocks never reached saturation. Therefore it is unlikely that there was any fluid loss accompanying metamorphism, and thus mass transfer of chemical elements never took place.

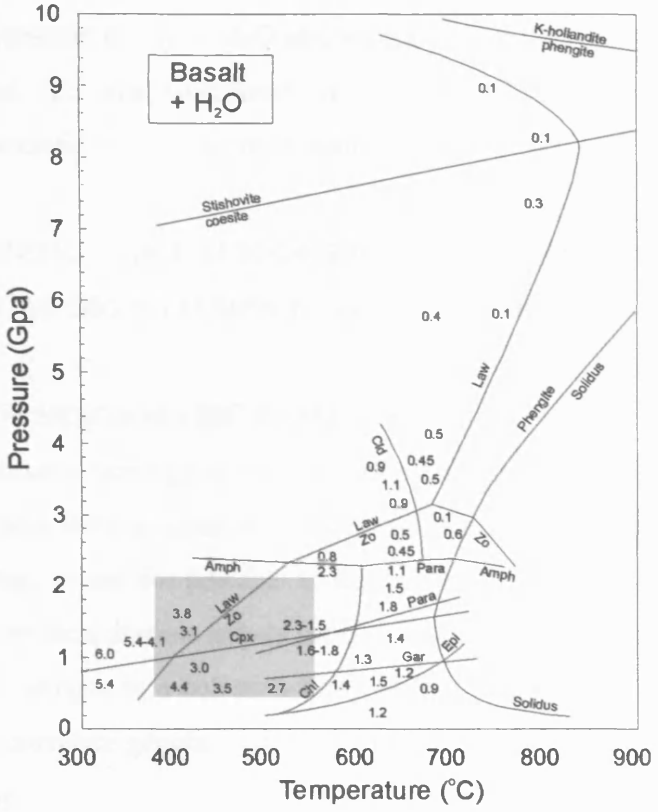


Figure 9.10. Major phase stability boundaries in MORB saturated with H_2O. Numbers refer to amount of H_2O stored in hydrous phases (in wt%), after Schmidt and Poli 1998). Grey square approximates the upper-P conditions underwhich the blueschists and eclogites metamorphosed under (based on the Tian Shan rocks, see Chapter 5).

Phase petrology may also be able to explain why the meta-sedimentary rocks do not show clear evidence for mass transfer. Phase petrology studies (e.g. Schmidt and Poli 2004, see also Chapter 2) have shown that significant sediment dehydration (after pore fluids have been expelled) is likely to take place at pressures greater than those necessary for meta-basalt dehydration. Therefore, it may also be the case that the meta-sedimentary rocks collected for this work have not fully dehydrated, and so fluid mobile elements have not been removed by a mobile phase.

It is generally thought that magma genesis at subduction zones is thought to be related to dehydration of the subducting slab (see Chapters 1 and 2). It follows that the lack of evidence for protolith dehydration, and associated chemical differentiation, has important implications for our understanding of magma genesis at subduction zones. However, as noted for the case of OIB petrogenesis models, the rocks collected for this thesis cannot be used to evaluate magma genesis at subduction zones. This is

because the protoliths were not geochemically analogous to actual subducting slabs, particularly with respect to initial H_2O abundance. Thus the response of the protoliths to metamorphism (i.e. the likelihood of dehydration reactions) differs from the response of the oceanic crust of actual subducting slabs.

9.8 EXPLAINING THE LACK OF RESIDUAL SUBDUCTION ZONE CHEMICAL SIGNATURES 2: OTHER EVIDENCE

9.8.1 LACK OF SYSTEMATIC SAMPLING

The sample selection strategy aimed at collecting metamorphic rocks that were relatively fresh and homogenous from various locations throughout the blueschist belts. By so doing, it was not possible to identify and systematically sample features at outcrop, such as dehydration haloes around large high pressure veins, shear zones or mineralogical changes in a cohesive body of HP/LT rock etc. It has therefore not been possible to correlate geochemistry with mineralogical changes which are known to exist at outcrop.

Future work should aim to identify features such as mineralogical differences between the core and rim of pillow basalt, or haloes surrounding veins or shear zones. By so doing, uncertainties relating to the protolith composition will be minimised, which should allow the assessment of even subtle chemical changes.

9.8.2 PROBLEMS WITH THE BEHAVIOUR OF LILEs

LILEs are easily mobilised in fluids, and so it is difficult to precisely determine the composition of the protolith with regard to these elements (particularly if the protolith was altered prior to subduction). Consequently, the potential for accurate prediction of the mobility of LILE during HP-LT metamorphism is significantly reduced. A further problem is the potential for redistribution of these elements during retrogression, assuming fluid is able to flow through these rocks.

9.8.3 NONE OF THE COLLECTED ROCKS UNDERWENT UHP METAMORPHISM

A severe limitation to the outcomes of this project has been the absence of UHPM eclogites. In fact, true eclogites are rare from both field locations and are often

intercalated with blueschists, indicating they must have followed identical P-T paths (e.g. Gao et al. 1999). It follows that the sampled rocks have not been metamorphosed to similar conditions as the rocks subducted back into the deep mantle. Thus the rocks collected are not analogues to the material that is proposed to be recycled by mantle plumes.

9.9 SUMMARY

This Chapter has not identified clear evidence for there being a residual subduction signature in the rocks collected from either Chinese Tian Shan or the North Qilian Shan. Some rocks do show evidence for being depleted in certain LILE elements, but such LILE depletion can be explained by variation in the protoliths. Further work should use Sr isotopes to assess the pre-metamorphic alteration of blueschists and eclogites. Furthermore, there is no evidence for systematic differences in the composition of blueschists and eclogites. Thus metamorphic grade has not affected the composition of LILE in the collected rocks.

To explain the lack of residual subduction zone signatures, this chapter examined the geological setting of the meta-basaltic protoliths to investigate whether the pre-metamorphic evolution of the rocks was analogous to AOB. In most cases it was speculated that in terms of hydrothermal alteration history, the protoliths were not likely to be analogous to AOB. It is likely that the protoliths had initial H_2O abundance less than AOB. In consequence, the protoliths may never have dehydrated because H_2O contents did not approach saturation. This may be true even at the maximum P-T conditions experienced by the collected rocks.

Another potential explanation for the lack of residual subduction signatures is the fact that the collected rocks did not undergo UHPM, as initially expected for the Chinese Tian Shan eclogites. With further subduction, dehydration should take place, and so assuming that the evolved fluid is able to escape, there remains the potential for chemical modification of the collected rocks.

CHAPTER 10

THESIS CONCLUSIONS

10.1 INTRODUCTION

The principal conclusions of this thesis are relevant to four areas of study:

1) methods for identifying immobile elements and chemically analogous samples in altered and/or metamorphosed rocks;
2) the petrogenetic history (i.e. pre-metamorphic and metamorphic petrogenesis) of the rocks collected from the Chinese Tian Shan blueschist belt;
3) the petrogenetic history of the rocks collected from the North Qilian Shan blueschist belts;
4) the geochemical effects of subduction zone metamorphism in the context of oceanic crust recycling models.

This Chapter aims to provide a summary of the conclusions made in this thesis relevant to each of the four areas of study outlined above.

10.2 IDENTIFYING IMMOBILE ELEMENTS AND SAMPLES CHEMICALLY ANALOGOUS TO PROTOLITHS

In the course of interpreting the data for the Tian Shan HP-LT rocks, approaches for identifying immobile elements and identifying analogous samples have been developed. In the following sections, conclusions on the effectiveness of these methods, and information about the pre-metamorphic and metamorphic petrogenesis of the Tian Shan blueschists and eclogites are presented.

10.2.1 IDENTIFYING IMMOBILE ELEMENTS IN ROCKS WITH HETEROGENEOUS PROTOLITHS

It has been shown in Chapter 7 that immobile elements could be identified in metamorphic rocks with chemically heterogeneous, cogenetic protoliths by using

"correlation diagrams." Investigating the correlation of elements with Nb is particularly useful as Nb is the most incompatible of the elements commonly found to be immobile. When the difference between the KD of a given element and Nb increases, so the correlation co-efficient decreases. It follows that poor correlation caused by igneous processes results in a smooth, leftward-dipping slope on Nb-correlation diagrams. Such leftward-dipping slopes can be identified on a number of Nb-correlation diagrams for the various chemical groups identified in the Tian Shan and Qilian Shan data sets.

Chapter 7 shows that, in addition to Nb-correlation diagrams, correlation between any elements can be effectively investigated with correlation diagrams. This has been demonstrated by the investigation of correlation between La and the other LREE, HFSE and REE in gabbroic eclogites from Zambia. By using La-correlation diagrams, it has been shown that the LREE are not decoupled (or mobilised) from HREE and HFSE, as originally proposed by John et al. (2004).

An additional advantage of the correlation diagrams is that they can be used to present correlations between a large number of elements on relatively few diagrams. However, correlations between elements should also be investigated in scatter diagrams to identify "outliers" or multiple trends, as these would otherwise reduce the apparent correlation coefficient.

10.2.2 IDENTIFYING FRESH ROCKS WITH SIMILAR COMPOSITIONS TO PROTOLITHS

After identifying immobile elements, Chapter 7 developed a method (the ΣD^2 method) for identifying fresh samples with compositions similar to protoliths. The ΣD^2 method has been successfully employed to identify a number of analogue samples for the geochemical groups identified in the rocks collected from the two paleo-subduction zones. These analogues have been used to complement petrogenetic information from multi-element and tectonic discrimination diagrams. The analogues also provided a baseline to which the geochemistry of metamorphic rocks could be compared, in order to identify the geochemical effects of HP-LT metamorphism.

10.3 PETROGENETIC HISTORY OF THE CHINESE TIAN SHAN HP-LT ROCKS

10.3.1 PRE-METAMORPHIC PETROGENESIS

The meta-basaltic protoliths of the Chinese Tian Shan HP-LT rocks are compositionally heterogeneous. A number of compositionally distinct groups have been identified, as well as a small number of samples not fitting any of these groups. These groups are as follows:

1) Group 1a: oceanic transitional-alkali basalts, with enriched trace element signatures originating from a seamount (or positive seafloor bathymetry), perhaps close to a continental margin;
2) Group 1b: sub-alkalic enriched oceanic basalts (although not as enriched as Group 1a) originating from a similar setting to Group 1a;
3) Group 2a: sub-alkalic volcanic arc basalts, with low Zr and Hf abundance;
4) Group 2b: sub-alkalic basalts, similar to Group 2a but without low Zr and Hf abundance;
5) Group 3: highly depleted, clinopyroxene-phyric, sub-alkalic basalts originating either from a back-arc basin or a seamount-like setting;
6) Group 2c: sub-alkalic basalts with N-MORB-like trace element abundance, but enriched in Th, which may be indicative of eruption through a continental margin.

Comparison of the geochemistry of meta-igneous rocks with analogue samples and the expected effects of seafloor alteration shows some evidence for sea-floor alteration prior to subduction. The LILE elements are generally decoupled from the more immobile elements, such as Nb, which may indicate mobilisation during sea-floor alteration. However, the interpretation of LILE mobilisation is not unique, with the following also being possible explanations: 1) mobilisation during dehydration reactions, and; 2) mobilisation during retrogression (perhaps resulting from fluid infiltration during exhumation). During seafloor alteration U, is added quantitatively (Staudigel 2004), leading to enhanced U abundance in altered rocks. However, U abundance in the meta-

basalts was shown to be indistinguishable from that of the protoliths, indicating that seafloor alteration was neither extensive nor pervasive.

The possibility of gaining detailed information about the protoliths of meta-sedimentary rocks is discussed at length in Chapter 7. It has been shown in Chapter 7 that the pre-metamorphic petrogenesis of sedimentary rocks is not conducive to detailed investigations into protolith geochemistry. The conclusion about the pre-metamorphic petrogenesis of meta-sedimentary rocks was therefore general, in that protoliths were similar to clastic sediments outboard of many subduction zones.

10.3.2 METAMORPHIC PETROGENESIS OF THE CHINESE TIAN SHAN HP-LT ROCKS

In the current literature, the issue of whether eclogites from the Chinese Tian Shan HP-LT belt have experienced UHPM is highly contentious. This work has contributed to the debate by showing that eclogites collected for this work were not likely to have metamorphosed to ultra-high pressure conditions. Based on the analysis of phase assemblages, and by using calibrated geothermobarometers, the peak P-T conditions were likely to have been T = 441-552°C and P = 1.91 – 2.01GPa. The P-T path initially followed a relatively cool trajectory through the Lawsonite-Blueschist facies, before temperature increase, perhaps coupled with pressure decrease, replaced lawsonite with zoisite + paragonite.

Comparison of the geochemistry of the metamorphic rocks with analogue samples does not reveal any systematic evidence for chemical modification coupled with metamorphism. In explaining this, the following observations were used:

1) the metamorphic rocks had not fully dehydrated, as shown by the ubiquitous presence of hydrous minerals (e.g. paragonite, clino-zoisite, phengite etc);
2) the metamorphic rocks are unlikely to have dehydrated during their metamorphic evolution, as shown by LOI values, which for many (even carbonate-bearing) rocks are below that of H_2O-saturated MORB under the relevant P-T conditions.

Essentially, no chemical modification took place because no mobile phases were generated. In the absence of mobile phases, no chemical transport could take place and hence no chemical modification.

10.4 PETROGENETIC HISTORY OF ROCKS FROM THE NORTH QILIAN SHAN HP-LT BELTS

The methods employed during the interpretation of the Tian Shan HP-LT rocks were also successfully used during the interpretation of the Qilian Shan HP-LT rocks. However, an additional problem relevant to the Qilian Shan samples could be addressed, as it was uncertain whether the high- and low-grade blueschist belts originated from the same paleo-subduction zone.

10.4.1 PRE-METAMORPHIC PETROGENESIS

Protolith compositions for the North Qilian Shan HP-LT rocks have been found to be highly heterogeneous, as found for the protoliths of the Chinese Tian Shan, and shown by other works (e.g. Spandler et al. 2004). A number of geochemical groups for the Qilian Shan meta-basaltic rocks have been defined:

1) Group Q1: sub-alkalic basalts originating from a back-arc basin;
2) Group Q1a: sub-alkalic basalts originating from volcanism associated with continental crust attenuation;
3) Group Q1b: sub-alkalic basalts originating from volcanism associated with continental crust attenuation or from a back-arc basin;
4) Group Q2: sub-alkalic basalts originating from volcanism associated with continental crust attenuation.

Based on geochemistry, it is likely that rocks from the high- and low-grade blueschist belts did not originate from the same subduction zone. Such a conclusion is also supported by evidence from the phase assemblages of rocks from the high- and low-grade blueschist belts (see below).

Protoliths of meta-sedimentary rocks were interpreted according to the arguments presented in Chapter 7, where it was shown that sedimentary rock petrogenesis is not conducive to detailed investigations into the protolith compositions. The general conclusion about the meta-sedimentary rocks is that their protoliths were similar to clastic sediments outboard of many subduction zones.

10.4.2 METAMORPHIC PETROGENESIS

Chapter 5 showed that rocks from the low-grade belt contain lawsonite, an index mineral not present in the high-grade belt (where epidote is the principal hydrous Ca-Al-silicate phase). It is unlikely that rocks from the above blueschist belts originated from the same paleosubduction zone. This is because lawsonite forms under relatively cool P-T paths, whereas epidote forms only under hotter P-T paths.

Rocks from the low-grade blueschist belt did not reach eclogite facies, peaking in the early Lawsonite-Blueschist facies (based on the continued presence of prehnite and pumpellyite). True eclogites are rare in the high-grade blueschist belts of the North Qilian Shan. Previous estimates of peak P-T conditions predict conditions of 0.9-0.95GPa (e.g. Wu et. al. 1993), which were considered "on the high side." However, P-T estimates using calibrated geothermobarometers on an eclogite collected for this work gave upper limits of 2.2GPa and 700°C, respectively. These P-T conditions are significantly greater than previous estimates.

10.5 EVIDENCE FOR CHEMICAL RECYCLING IN SUBDUCTION ZONES: CONCLUSIONS

Based on the likely tectonic origin of the protoliths, the geochemistry of the metamorphic rocks and metamorphic P-T history the following conclusions can be made:

1) the studied rocks are not analogous to Altered Oceanic Basalt (as required by "recycling models" that aim to explain OIB geochemistry) in terms of initial H_2O content or bulk rock geochemistry;
2) it is unlikely that the samples in this study dehydrated as a result of subduction zone metamorphism;

3) a mobile phase (i.e. hydrous fluid) capable of transferring mobile elements did not develop, or, if a mobile phase did develop, it was not effective in transporting mobile elements;
4) the rocks are not UHP eclogites, and require further subduction to >>2.5 GPa to reach H_2O-saturation, and hence begin to dehydrate.

Based on these conclusions, the rocks collected for this work cannot reliably be used to evaluate recycling models that aim to explain the geochemistry of Ocean Island Basalts. Similarly, the results of this work cannot be used to evaluate models of magma genesis at subduction zones. Furthermore, the processes that incorporate the oceanic basaltic protoliths into an accretionary wedge favour positive bathymetry (such as seamounts). It is therefore likely that basaltic blueschists/eclogites in B-type blueschist belts originating from positive bathymetry are relatively common, whereas metamorphosed AOBs (i.e. altered N-MORB) are relatively rare. Consequently, any future work analysing rocks from B-type blueschist belts to evaluate the geochemical effects of subduction zone metamorphism and "recycling models," should take many samples and carefully evaluate the nature of the protolith.

10.6 FURTHER WORK

As already noted, protoliths from B-type subduction zones are not likely to be analogous to AOB, a condition required for evaluation of recycling models that aim to explain OIB geochemistry. However, the presence of metamorphosed AOB in B-type subduction zones cannot be ruled out. To increase the chance of sampling metamorphosed AOB, it is advised that large sample sets be collected from a blueschist belt. Furthermore, this practise is advantageous because protolith compositions in paleo-subduction zones are heterogeneous (as indicated by this work), and so large numbers of rocks are required to obtain representative sample sets.

Although the rocks do not show clear evidence for having dehydrated, the existence of high-pressure veins in some HP/LT rocks attests to the existence of a free hydrous phase during subduction zone metamorphism. If it can be shown that these veins were part of a

hydrothermal system operating during prograde metamorphism, they should allow for a detailed study of the behaviour of elements in fluids at high P/T conditions. Furthermore, by comparing the host rock isotopic composition with that of the vein, any isotopic fractionation could be identified. Future work should therefore aim to systematically sample high pressure veins, any surrounding alteration haloes, and the host rock. By so doing, ambiguity associated with the actual protolith composition is also minimised, as any rock showing evidence for hydrothermal alteration at high P/T conditions can be compared with its immediately adjacent un-altered equivalent.

It is necessary to characterise the geochemistry of protoliths to evaluate chemical changes during metamorphism. However, the possibility of hydrothermal alteration prior to metamorphism complicates evaluation of protolith compositions. Analysis of Sr isotopes should provide evidence independent of trace element geochemistry to evaluate the degree of seafloor alteration prior to metamorphism (assuming dehydration reactions have not reset Sr isotope systematics). Future work on HP-LT rock geochemistry should benefit by analysing Sr isotopes.

In the absence of sampling metamorphosed AOB from blueschist belts, experimentation should provide the clearest evidence for the geochemical effects of subduction zone metamorphism. Experimentation under controlled conditions will allow for control over the modelled subducted material, as well as the P-T conditions. Experimentation should not be conducted on natural metamorphic samples unless it is clear that the rocks are H_2O saturated (and have been during their prograde history). Experimentation on natural AOB (or composites) may also be useful. However, reaction kinetics are typically too slow for laboratory study.

Apart from addressing "global" geodynamic issues, blueschist and eclogite geochemistry could be useful for understanding tectonic processes that took place during a particular orogenesis. In this context, future work should aim at sampling large numbers of samples from blueschist belts, to obtain representative sample sets from potentially geochemically heterogeneous rocks.

Further mapping in the North Qilian Shan is also required to determine the structural relationships between the high and low-grade belts. Furthermore, more extensive sampling and chemical analysis is required to confirm whether the high- and low-grade blueschist belts originate from the same subduction zone. Age constraints may also provide a significant contribution in understanding the relationship between these belts.

APPENDIX 1

PREPARATION OF SAMPLES FOR ANALYSIS BY INDUCTIVELY-COUPLED PLASMA (ICP) OPTICAL EMISSION SPETROMETRY (OES) AND ICP-MASS SPECTROMETRY (MS)

A1.1 PREPARATION OF SAMPLE POWDERS

To prepare sample powders, hand specimens were first cut to size and ground on a diamond wheel, to remove saw marks and weathered surfaces. After rinsing with de-ionised water and drying, the hand specimens were crushed by a clean jaw crusher, and powdered using either an agate Tema mill or agate ball mills. Sample handling was kept to a minimum, and, when prepared, powders were transferred to clean plastic vials for storage.

A1.2 LOSS ON IGNITION (LOI) ANALYSIS

Sample powders were weighed into clean ceramic vials and placed in a furnace at 900°C for 2 hours. The ignited powders were allowed to cool sufficiently to be placed in a dessicator, before re-weighing and calculating LOI.

A1.2 SAMPLE PREPARATION FOR (ICP-OES) ANALYSIS

The abundance of major elements (i.e. Si, Al, Fe, Mg, Ca, Na, K, Ti, Mn and P) were measured by the Jobin Yvon Ultima 2 instrument at Cardiff University, operated by Ms E. De Vos.

Dried, sample powders that had been used for analysis of LOI were dissolved using the following method:

1) 0.1g (±0.005g) was mixed with 0.4g (±0.005g) of 100% lithium tetraborate flux in acid-washed platinum crucibles;
2) 8 or 9 drops of lithium iodide non-wetting agent was added to the sample/flux mixture, which was then fused;

3) the liquid flux/sample mixture was poured into 30ml of 10% HNO_3 and 20ml de-ionised water (18.2MΩ);
4) After the quenched glass shards had dissolved, the solution was spiked with 1ml of 100ppm Rh solution, and diluted to 100ml with de-ionised water.

A1.3 SAMPLE PREPARATION FOR ICP-MS ANALYSIS

Solutions of samples and rock standards were analysed on the x7 series Thermo-Elemental spectrometer in 2003/2004, operated Dr Iain McDonald. Two sample preparation methods were used to prepare the samples for analysis: 1) HF-HNO_3 dissolution, and; 2) lithium tetraborate fusion. The method for lithium tetraborate fusion is outlined in Section 4.6.4 of Chapter 4. The method of sample dissolution using HF-HNO_3 is given below. Results of the ICP-MS analysis are given in full in Table 4.4, Chapter 4.

A1.3.1 DISSOLUTION OF SAMPLES BY THE HF-HNO_3 METHOD

Samples were prepared by following the standard acid digestion method of Cardiff University:

1) 0.1 ±0.005g of sample powder was weighed into a nalgene vial;
2) 0.5mls concentrated HNO_3 was added to the vial, and, after any reaction had ceased, 4 ml HF of concentrated was added. The vials were then heated for at least 24 hrs on a hot plate set at 125°C;
3) After cooling, the solution was evaporated from the vials until a clear fluid with a plastic consistency remained;
4) 1 ml of concentrated HNO_3 was then added to the vials, and the resulting solution evaporated. This procedure was carried out twice;
5) After evaporating for a second time, 5ml of 5M HNO_3 was added to the vials to dissolve any residue;
6) The resulting solution was spiked with 1ml 2500ppb mixed Rh-Re standard solution, and made up to 50ml volume with de-ionised water.

APPENDIX 2

MINERAL CHEMICAL ANALYSES AND FORMULAE

	TS02-01		TS02-02		TS02-3a		TS02-04		TS02-05		TS02-6		TS02-09		TS02-11	
	Core	Rim	Core	Rim	Core	Rim	Core	Rim	Core	Rim	Core	Rim	Core	Rim	Core	Rim
Wt%																
SiO_2	36.79	36.81	36.49	36.53	36.80	37.41	36.76	36.71	37.11	37.76	36.35	36.77	36.48	36.68	36.17	36.47
TiO_2	0.00	0.00	0.23	0.00	0.00	0.00	0.29	0.00	0.00	0.00	0.20	0.00	0.00	0.00	0.00	0.00
Al_2O_3	20.27	20.44	19.91	20.72	20.67	21.12	20.51	20.77	20.36	20.78	20.08	20.04	20.20	20.76	20.32	20.59
FeO^*	30.48	30.59	30.03	33.36	34.19	30.31	33.79	33.75	32.05	29.70	33.38	33.06	30.12	32.51	29.39	28.84
MnO	2.90	3.72	5.69	0.29	0.56	0.27	1.86	0.74	1.22	0.97	1.00	0.81	4.57	0.83	3.66	0.42
MgO	2.20	2.80	0.88	1.71	1.19	3.01	0.97	1.44	2.75	3.82	1.20	1.22	0.89	1.53	1.05	1.39
CaO	7.68	5.94	7.37	7.88	7.08	8.67	7.10	7.34	6.76	7.70	8.13	8.52	7.96	8.45	9.26	11.69
Na_2O	0.00	0.00	0.00	0.00	0.00	0.00	0.00	0.00	0.00	0.00	0.00	0.00	0.00	0.00	0.00	0.00
K_2O	0.00	0.00	0.00	0.00	0.00	0.00	0.00	0.00	0.00	0.00	0.00	0.00	0.00	0.00	0.00	0.00
Cr_2O_3	0.00	0.00	0.00	0.00	0.00	0.00	0.00	0.00	0.00	0.00	0.00	0.00	0.00	0.00	0.00	0.00
Total	100.32	100.30	100.59	100.49	100.49	100.78	101.27	100.76	100.25	100.72	100.34	100.42	100.22	100.75	99.85	99.41
Si	5.93	5.93	5.93	5.89	5.94	5.93	5.92	5.91	5.96	5.97	5.90	5.95	5.93	5.90	5.89	5.90
Ti	0.00	0.00	0.03	0.00	0.00	0.00	0.04	0.00	0.00	0.00	0.02	0.00	0.00	0.00	0.00	0.00
Al	2.89	2.91	2.86	2.95	2.95	2.96	2.92	2.96	2.89	2.90	2.88	2.87	2.90	2.95	2.92	2.94
Fe^{2+}	2.05	2.06	2.04	2.25	2.31	2.01	2.27	2.27	2.15	1.96	2.27	2.24	2.05	2.19	2.00	1.95
Mn	0.20	0.25	0.39	0.02	0.04	0.02	0.13	0.05	0.08	0.06	0.07	0.06	0.31	0.06	0.25	0.03
Mg	0.26	0.34	0.11	0.21	0.14	0.36	0.12	0.17	0.33	0.45	0.15	0.15	0.11	0.18	0.13	0.17
Ca	0.66	0.51	0.64	0.68	0.61	0.74	0.61	0.63	0.58	0.65	0.71	0.74	0.69	0.73	0.81	1.01
Na	0.00	0.00	0.00	0.00	0.00	0.00	0.00	0.00	0.00	0.00	0.00	0.00	0.00	0.00	0.00	0.00
K	0.00	0.00	0.00	0.00	0.00	0.00	0.00	0.00	0.00	0.00	0.00	0.00	0.00	0.00	0.00	0.00
Cr	0.00	0.00	0.00	0.00	0.00	0.00	0.00	0.00	0.00	0.00	0.00	0.00	0.00	0.00	0.00	0.00

Table A2.1. Results of SEM-EDS analysis of the core and rims of garnets. Oxygen measured by stoichiometry. Formula calculation based on 12 oxygens. *Total iron as FeO.

	TS02-12		TS02-13		TS02-14		TS02-15A		TS02-15B		TS02-16		TS02-17b		TS02-18	
	Core	Rim	Core	Rim	Core	Rim	Core	Rim	Core	Rim	Core	Rim	Core	Rim	Core	Rim
Wt%																
SiO_2	36.58	36.63	36.12	36.66	36.60	37.34	36.34	36.87	36.56	37.21	36.28	37.00	36.42	37.27	36.34	37.61
TiO_2	0.00	0.21	0.00	0.00	0.00	0.00	0.21	0.00	0.20	0.00	0.24	0.00	0.00	0.00	0.18	0.00
Al_2O_3	20.55	20.72	20.83	20.37	20.68	20.93	20.58	21.11	20.56	20.73	20.15	20.52	20.41	21.19	20.70	21.03
FeO^*	32.72	32.21	36.41	36.56	35.96	28.60	35.01	32.63	32.51	33.67	32.74	32.80	32.33	30.35	35.74	30.37
MnO	0.88	0.95	1.64	0.68	0.87	0.34	0.37	0.43	4.65	0.00	2.44	0.27	3.38	0.27	2.52	0.00
MgO	2.13	2.13	2.49	2.38	1.94	1.67	1.22	2.52	1.12	1.88	0.48	1.64	0.97	3.27	1.26	1.59
CaO	7.50	7.05	3.14	3.34	4.60	11.85	7.30	7.34	5.52	7.77	7.95	7.98	6.84	8.10	4.77	10.25
Na_2O	0.00	0.00	0.00	0.00	0.00	0.00	0.00	0.00	0.00	0.00	0.00	0.00	0.00	0.00	0.00	0.00
K_2O	0.00	0.00	0.00	0.00	0.00	0.00	0.00	0.00	0.00	0.00	0.00	0.00	0.00	0.00	0.00	0.00
Cr_2O_3	0.00	0.00	0.00	0.00	0.00	0.00	0.00	0.00	0.00	0.00	0.00	0.00	0.00	0.00	0.00	0.00
Total	100.37	99.89	100.63	100.00	100.64	100.72	101.03	100.90	101.12	101.26	100.29	100.21	100.34	100.45	101.51	100.84
Si	5.90	5.91	5.86	5.96	5.92	5.93	5.87	5.89	5.91	5.94	5.91	5.96	5.92	5.92	5.87	5.97
Ti	0.00	0.03	0.00	0.00	0.00	0.00	0.03	0.00	0.02	0.00	0.03	0.00	0.00	0.00	0.02	0.00
Al	2.93	2.96	2.99	2.93	2.96	2.94	2.94	2.98	2.94	2.93	2.90	2.92	2.93	2.97	2.96	2.95
Fe^{2+}	2.21	2.17	2.47	2.49	2.43	1.90	2.36	2.18	2.20	2.25	2.23	2.21	2.20	2.01	2.41	2.02
Mn	0.06	0.06	0.11	0.05	0.06	0.02	0.03	0.03	0.32	0.00	0.17	0.02	0.23	0.02	0.17	0.00
Mg	0.26	0.26	0.30	0.29	0.23	0.20	0.15	0.30	0.13	0.22	0.06	0.20	0.12	0.39	0.15	0.19
Ca	0.65	0.61	0.27	0.29	0.40	1.01	0.63	0.63	0.48	0.66	0.69	0.69	0.60	0.69	0.41	0.87
Na	0.00	0.00	0.00	0.00	0.00	0.00	0.00	0.00	0.00	0.00	0.00	0.00	0.00	0.00	0.00	0.00
K	0.00	0.00	0.00	0.00	0.00	0.00	0.00	0.00	0.00	0.00	0.00	0.00	0.00	0.00	0.00	0.00
Cr	0.00	0.00	0.00	0.00	0.00	0.00	0.00	0.00	0.00	0.00	0.00	0.00	0.00	0.00	0.00	0.00

Table A2.1. Continued.

	TS02-19		TS02-20		TS02-21a		TS02-23		TS02-26		TS02-26	TS02-27		TS02-28		TS02-29
	Core	Rim	Core	Rim	Core	Rim	Core	Rim	Core	Rim	Core	Core	Rim	Core	Rim	Core
Wt%																
SiO_2	36.49	36.90	37.43	37.31	36.24	37.37	37.22	38.34	37.22	38.17	37.62	36.75	37.90	36.63	37.92	36.99
TiO_2	0.00	0.00	0.00	0.29	0.00	0.00	0.00	0.00	0.00	0.00	0.00	0.00	0.00	0.00	0.00	0.00
Al_2O_3	20.63	20.62	20.65	21.14	20.50	21.00	21.22	21.79	20.77	21.93	21.29	20.65	21.59	20.69	21.35	20.83
FeO^*	33.37	32.51	33.15	31.61	33.85	29.30	31.80	26.89	29.45	26.29	30.11	31.70	27.29	30.92	26.78	32.47
MnO	1.93	0.31	0.27	0.28	3.42	0.28	1.21	0.38	2.57	0.49	0.59	2.34	0.23	0.94	0.27	1.93
MgO	1.63	1.87	2.56	3.22	1.07	2.27	2.99	5.96	1.98	6.16	4.38	2.00	5.31	2.83	6.20	2.26
CaO	5.64	7.66	7.30	7.78	5.41	10.18	7.02	8.05	8.57	7.91	6.96	7.33	8.41	8.14	7.93	6.42
Na_2O	0.00	0.00	0.00	0.00	0.00	0.00	0.00	0.00	0.00	0.00	0.00	0.00	0.00	0.00	0.00	0.00
K_2O	0.00	0.00	0.00	0.00	0.00	0.00	0.00	0.00	0.00	0.00	0.00	0.00	0.00	0.00	0.00	0.00
Cr_2O_3	0.00	0.00	0.00	0.00	0.00	0.00	0.00	0.00	0.00	0.00	0.00	0.00	0.00	0.00	0.00	0.00
Total	99.70	99.87	101.36	101.62	100.50	100.41	101.46	101.41	100.57	100.94	100.95	100.77	100.73	100.17	100.45	100.90
Si	5.94	5.96	5.95	5.88	5.90	5.94	5.89	5.92	5.95	5.90	5.92	5.91	5.91	5.88	5.91	5.92
Ti	0.00	0.00	0.00	0.03	0.00	0.00	0.00	0.00	0.00	0.00	0.00	0.00	0.00	0.00	0.00	0.00
Al	2.97	2.94	2.90	2.95	2.95	2.95	2.97	2.97	2.94	3.00	2.96	2.93	2.98	2.94	2.94	2.95
Fe^{2+}	2.27	2.19	2.20	2.08	2.31	1.95	2.11	1.74	1.97	1.70	1.98	2.13	1.78	2.08	1.75	2.17
Mn	0.13	0.02	0.02	0.02	0.24	0.02	0.08	0.02	0.17	0.03	0.04	0.16	0.02	0.06	0.02	0.13
Mg	0.20	0.22	0.30	0.38	0.13	0.27	0.35	0.69	0.24	0.71	0.51	0.24	0.62	0.34	0.72	0.27
Ca	0.49	0.66	0.62	0.66	0.47	0.87	0.60	0.67	0.73	0.66	0.59	0.63	0.70	0.70	0.66	0.55
Na	0.00	0.00	0.00	0.00	0.00	0.00	0.00	0.00	0.00	0.00	0.00	0.00	0.00	0.00	0.00	0.00
K	0.00	0.00	0.00	0.00	0.00	0.00	0.00	0.00	0.00	0.00	0.00	0.00	0.00	0.00	0.00	0.00
Cr	0.00	0.00	0.00	0.00	0.00	0.00	0.00	0.00	0.00	0.00	0.00	0.00	0.00	0.00	0.00	0.00

Table A2.1. Continued

	TS02-29	TS02-30	TS02-32		TS02-33		TS02-34		TS02-35		TS02-36	TS02-38		TS02-41		TS02-42
	Rim	Core	Core	Rim	Core	Rim	Core	Rim	Core	Rim	Core	Core	Rim	Core	Rim	Core
Wt%																
SiO_2	38.35	37.68	36.59	36.94	36.79	37.18	36.32	36.93	36.89	37.33	36.08	36.80	37.25	36.49	37.04	36.99
TiO_2	0.17	0.00	0.00	0.00	0.00	0.00	0.22	0.00	0.00	0.00	0.00	0.00	0.00	0.31	0.00	0.00
Al_2O_3	21.56	21.39	20.51	20.71	20.79	21.05	20.38	20.73	20.65	20.82	20.07	20.35	20.93	20.24	20.78	20.27
FeO^*	27.43	28.88	34.13	33.55	28.79	25.64	34.01	30.80	33.75	32.56	34.51	33.10	31.55	33.55	33.14	32.45
MnO	0.49	0.43	0.74	0.00	3.06	0.46	1.01	0.76	0.79	0.00	1.54	2.03	0.52	0.49	0.74	0.47
MgO	5.63	5.24	1.56	2.39	0.47	3.83	2.56	2.80	1.20	2.20	1.95	1.08	2.67	0.92	1.84	1.95
CaO	7.44	7.22	6.76	6.99	11.07	10.65	4.85	8.06	7.80	8.08	5.75	7.59	8.06	8.51	7.35	8.28
Na_2O	0.00	0.20	0.00	0.00	0.00	0.00	0.00	0.00	0.00	0.00	0.00	0.00	0.00	0.00	0.00	0.00
K_2O	0.00	0.00	0.00	0.00	0.00	0.00	0.00	0.00	0.00	0.00	0.00	0.00	0.00	0.00	0.00	0.00
Cr_2O_3	0.00	0.00	0.00	0.00	0.00	0.00	0.00	0.00	0.00	0.00	0.00	0.00	0.00	0.00	0.00	0.00
Total	101.08	101.04	100.29	100.58	100.97	98.81	99.35	100.08	101.08	101.00	99.88	100.94	100.98	100.50	100.90	100.40
Si	5.95	5.89	5.93	5.93	5.90	5.93	5.92	5.92	5.93	5.95	5.90	5.94	5.92	5.91	5.94	5.95
Ti	0.02	0.00	0.00	0.00	0.00	0.00	0.03	0.00	0.00	0.00	0.00	0.00	0.00	0.04	0.00	0.00
Al	2.96	2.96	2.94	2.94	2.95	2.97	2.94	2.94	2.93	2.93	2.90	2.90	2.94	2.90	2.94	2.88
Fe^{2+}	1.78	1.89	2.31	2.25	1.93	1.71	2.32	2.06	2.27	2.17	2.36	2.23	2.10	2.27	2.22	2.18
Mn	0.03	0.03	0.05	0.00	0.21	0.03	0.07	0.05	0.05	0.00	0.11	0.14	0.04	0.03	0.05	0.03
Mg	0.65	0.61	0.19	0.29	0.06	0.46	0.31	0.33	0.14	0.26	0.24	0.13	0.32	0.11	0.22	0.23
Ca	0.62	0.61	0.59	0.60	0.95	0.91	0.42	0.69	0.67	0.69	0.50	0.66	0.69	0.74	0.63	0.71
Na	0.00	0.02	0.00	0.00	0.00	0.00	0.00	0.00	0.00	0.00	0.00	0.00	0.00	0.00	0.00	0.00
K	0.00	0.00	0.00	0.00	0.00	0.00	0.00	0.00	0.00	0.00	0.00	0.00	0.00	0.00	0.00	0.00
Cr	0.00	0.00	0.00	0.00	0.00	0.00	0.00	0.00	0.00	0.00	0.00	0.00	0.00	0.00	0.00	0.00

Table A2.1. Continued.

	TS02-42	TS02-43		TS02-46		TS02-47	TS02-48		TS02-50B		TS02-51B		TS02-52		TS02-53	TS02-54
	Rim	Core	Rim	Core	Rim	Core	Core	Rim	Core	Rim	Core	Rim	Core	Rim	Core	Core
Wt%																
SiO_2	37.53	36.66	37.14	36.45	37.11	36.85	36.46	37.79	37.17	37.55	37.61	37.29	36.66	36.76	37.37	36.36
TIO_2	0.00	0.00	0.00	0.00	0.00	0.00	0.00	0.00	0.00	0.00	0.00	0.00	0.00	0.00	0.00	0.00
Al_2O_3	20.93	19.93	21.07	20.65	20.93	20.84	20.40	21.09	20.80	21.44	21.11	21.38	20.39	20.83	20.77	20.43
FeO^*	30.29	25.34	30.49	30.50	31.57	32.39	31.19	29.53	30.38	29.84	25.68	28.39	34.30	33.07	32.86	31.13
MnO	0.37	6.82	0.43	4.67	1.24	1.16	3.87	0.20	1.36	0.89	0.63	0.79	0.57	0.21	2.12	1.25
MgO	2.85	0.34	1.59	1.32	1.86	1.76	1.04	2.94	1.85	2.67	2.01	4.00	2.14	3.70	1.66	1.62
CaO	9.07	11.35	9.98	7.22	8.25	8.14	7.09	9.20	8.97	8.97	13.74	8.71	5.58	4.98	6.11	9.21
Na_2O	0.00	0.00	0.00	0.00	0.00	0.00	0.00	0.00	0.00	0.00	0.00	0.24	0.00	0.00	0.00	0.00
K_2O	0.00	0.00	0.00	0.00	0.00	0.00	0.00	0.00	0.00	0.00	0.00	0.00	0.00	0.00	0.00	0.00
Cr_2O_3	0.00	0.00	0.00	0.00	0.00	0.00	0.00	0.00	0.00	0.00	0.00	0.00	0.00	0.00	0.00	0.00
Total	101.03	100.44	100.71	100.80	100.97	101.13	100.04	100.76	100.53	101.37	100.78	100.81	99.64	99.55	100.89	100.00
Si	5.94	5.94	5.92	5.89	5.93	5.90	5.93	5.97	5.95	5.92	5.93	5.88	5.96	5.92	5.99	5.89
Ti	0.00	0.00	0.00	0.00	0.00	0.00	0.00	0.00	0.00	0.00	0.00	0.00	0.00	0.00	0.00	0.00
Al	2.93	2.85	2.97	2.95	2.95	2.95	2.93	2.94	2.94	2.99	2.94	2.98	2.93	2.97	2.94	2.92
Fe^{2+}	2.00	1.72	2.03	2.06	2.11	2.17	2.12	1.95	2.03	1.97	1.69	1.87	2.33	2.23	2.20	2.11
Mn	0.02	0.47	0.03	0.32	0.08	0.08	0.27	0.01	0.09	0.06	0.04	0.05	0.04	0.01	0.14	0.09
Mg	0.34	0.04	0.19	0.16	0.22	0.21	0.13	0.35	0.22	0.31	0.24	0.47	0.26	0.44	0.20	0.20
Ca	0.77	0.98	0.85	0.62	0.71	0.70	0.62	0.78	0.77	0.76	1.16	0.74	0.49	0.43	0.52	0.80
Na	0.00	0.00	0.00	0.00	0.00	0.00	0.00	0.00	0.00	0.00	0.00	0.02	0.00	0.00	0.00	0.00
K	0.00	0.00	0.00	0.00	0.00	0.00	0.00	0.00	0.00	0.00	0.00	0.00	0.00	0.00	0.00	0.00
Cr	0.00	0.00	0.00	0.00	0.00	0.00	0.00	0.00	0.00	0.00	0.00	0.00	0.00	0.00	0.00	0.00

Table A2.1. Continued.

	TS02-54	TS02-55		TS02-56		TS02-57		TS02-58A		TS02-62		105-1		106-14		106-3
	Rim	Core	Rim	Core	Rim	Core	Rim	Core	Rim	Core	Rim	Core	Rim	Core	Rim	Core
Wt%																
SiO_2	37.52	36.46	36.90	37.02	37.12	37.04	37.79	36.34	37.83	36.77	37.26	36.54	37.19	36.54	37.23	36.82
TiO_2	0.00	0.00	0.00	0.00	0.00	0.00	0.00	0.00	0.00	0.00	0.00	0.24	0.00	0.23	0.00	0.00
Al_2O_3	21.09	20.67	20.62	20.68	21.28	20.82	21.44	20.75	20.98	20.64	21.30	20.11	20.77	20.63	20.86	20.42
FeO^*	27.57	31.51	30.90	29.56	27.77	30.37	28.27	31.49	27.12	33.53	33.68	31.97	29.52	31.99	30.64	28.02
MnO	0.64	2.64	0.46	2.11	2.75	1.31	0.43	1.82	0.64	3.77	0.69	2.34	0.00	1.35	0.55	3.09
MgO	2.23	1.40	2.27	1.38	0.96	2.46	4.83	1.03	2.25	1.64	3.18	1.18	3.32	1.00	1.37	1.13
CaO	11.59	7.72	8.88	9.69	11.04	8.75	8.20	9.02	12.25	4.55	5.00	7.77	8.80	8.74	10.48	10.49
Na_2O	0.00	0.00	0.00	0.00	0.00	0.00	0.00	0.00	0.00	0.00	0.00	0.00	0.00	0.00	0.00	0.00
K_2O	0.00	0.00	0.00	0.00	0.00	0.00	0.00	0.00	0.00	0.00	0.00	0.00	0.00	0.00	0.00	0.00
Cr_2O_3	0.00	0.00	0.00	0.00	0.00	0.00	0.00	0.00	0.00	0.00	0.00	0.00	0.00	0.00	0.00	0.00
Total	100.65	100.40	100.03	100.44	100.92	100.76	100.96	100.45	101.07	100.90	101.11	100.14	99.60	100.49	101.13	99.96
Si	5.94	5.90	5.93	5.94	5.91	5.91	5.91	5.88	5.96	5.94	5.92	5.93	5.94	5.90	5.93	5.94
Ti	0.00	0.00	0.00	0.00	0.00	0.00	0.00	0.00	0.00	0.00	0.00	0.03	0.00	0.03	0.00	0.00
Al	2.95	2.95	2.93	2.93	3.00	2.94	2.96	2.97	2.92	2.95	2.99	2.89	2.93	2.94	2.94	2.91
Fe^{2+}	1.82	2.13	2.08	1.98	1.85	2.03	1.85	2.13	1.79	2.26	2.24	2.17	1.97	2.16	2.04	1.89
Mn	0.04	0.18	0.03	0.14	0.19	0.09	0.03	0.12	0.04	0.26	0.05	0.16	0.00	0.09	0.04	0.21
Mg	0.26	0.17	0.27	0.17	0.11	0.29	0.56	0.12	0.26	0.20	0.38	0.14	0.40	0.12	0.16	0.14
Ca	0.98	0.67	0.76	0.83	0.94	0.75	0.69	0.78	1.03	0.39	0.43	0.68	0.75	0.76	0.89	0.91
Na	0.00	0.00	0.00	0.00	0.00	0.00	0.00	0.00	0.00	0.00	0.00	0.00	0.00	0.00	0.00	0.00
K	0.00	0.00	0.00	0.00	0.00	0.00	0.00	0.00	0.00	0.00	0.00	0.00	0.00	0.00	0.00	0.00
Cr	0.00	0.00	0.00	0.00	0.00	0.00	0.00	0.00	0.00	0.00	0.00	0.00	0.00	0.00	0.00	0.00

Table A2.1. Continued.

	106-3	110-3		117-1		984-1	Q98-120		Q98-126		Q98-127		Q98-128		Q98-138	Q98-143
	Rim	Core	Rim	Core	Rim	Core	Core	Rim	Core	Rim	Core	Rim	Core	Rim	Core	Core
Wt%																
SiO_2	37.46	36.68	37.07	36.58	36.87	36.98	36.75	37.88	37.45	37.58	37.05	37.09	36.79	37.66	36.38	36.73
TiO_2	0.00	1.21	0.00	0.00	0.00	0.00	0.00	0.00	0.00	0.00	0.00	0.00	0.30	0.00	0.00	0.00
Al_2O_3	20.96	20.16	20.55	20.41	20.79	20.25	20.71	21.51	20.26	20.84	20.57	20.57	20.80	21.14	19.45	20.67
FeO^*	30.51	30.88	33.33	32.30	28.02	29.68	31.09	27.66	26.71	29.16	28.37	29.13	28.15	27.52	24.38	27.37
MnO	0.70	1.70	0.38	1.16	0.45	1.09	2.18	0.19	4.73	1.60	3.14	1.45	3.35	0.36	11.59	6.88
MgO	3.35	2.53	2.97	1.57	1.30	1.53	2.46	5.98	1.72	2.31	2.17	2.94	1.92	4.92	0.78	0.53
CaO	7.29	8.10	6.55	8.60	12.83	10.27	7.32	7.52	10.11	9.79	9.46	8.95	9.22	8.16	6.84	8.67
Na_2O	0.00	0.00	0.00	0.00	0.00	0.00	0.00	0.00	0.00	0.00	0.00	0.00	0.00	0.00	0.00	0.00
K_2O	0.00	0.00	0.00	0.00	0.00	0.00	0.00	0.00	0.00	0.00	0.00	0.00	0.00	0.00	0.00	0.00
Cr_2O_3	0.00	0.00	0.00	0.00	0.00	0.00	0.00	0.00	0.00	0.00	0.00	0.16	0.00	0.00	0.74	0.00
Total	100.28	101.25	100.84	100.63	100.27	99.79	100.51	100.73	100.98	101.29	100.74	100.29	100.54	99.76	100.16	100.85
Si	5.96	5.85	5.93	5.90	5.90	5.96	5.90	5.90	5.97	5.95	5.92	5.92	5.89	5.94	5.95	5.92
Ti	0.00	0.15	0.00	0.00	0.00	0.00	0.00	0.00	0.00	0.00	0.00	0.00	0.04	0.00	0.00	0.00
Al	2.95	2.84	2.90	2.91	2.94	2.89	2.94	2.96	2.86	2.91	2.91	2.90	2.94	2.95	2.81	2.95
Fe^{2+}	2.03	2.06	2.23	2.18	1.87	2.00	2.09	1.80	1.78	1.93	1.90	1.95	1.88	1.82	1.67	1.85
Mn	0.05	0.11	0.03	0.08	0.03	0.07	0.15	0.01	0.32	0.11	0.21	0.10	0.23	0.02	0.80	0.47
Mg	0.40	0.30	0.35	0.19	0.16	0.18	0.29	0.69	0.20	0.27	0.26	0.35	0.23	0.58	0.10	0.06
Ca	0.62	0.69	0.56	0.74	1.10	0.89	0.63	0.63	0.86	0.83	0.81	0.77	0.79	0.69	0.60	0.75
Na	0.00	0.00	0.00	0.00	0.00	0.00	0.00	0.00	0.00	0.00	0.00	0.00	0.00	0.00	0.00	0.00
K	0.00	0.00	0.00	0.00	0.00	0.00	0.00	0.00	0.00	0.00	0.00	0.00	0.00	0.00	0.00	0.00
Cr	0.00	0.00	0.00	0.00	0.00	0.00	0.00	0.00	0.00	0.00	0.00	0.02	0.00	0.00	0.07	0.00

Table A2.1. Continued.

	Q98-143	Q98-149		Q98-150		Q98-152		Q02-02		Q02-05		Q02-08		Q02-10A	
	Rim	Core	Rim	Core	Rim	Core	Rim	Core	Rim	Core	Rim	Core	Rim	Core	Rim
Wt%															
SiO_2	35.98	36.96	36.75	36.63	36.59	37.20	37.42	37.26	37.96	37.19	37.73	37.64	37.60	36.70	37.84
TiO_2	0.00	0.00	0.00	0.00	0.00	0.00	0.00	0.18	0.00	0.00	0.00	0.00	0.00	0.25	0.00
Al_2O_3	19.46	20.40	20.52	20.42	20.49	20.53	20.38	21.14	21.52	20.96	21.45	21.10	21.32	20.13	20.98
FeO^*	24.58	28.86	30.04	30.84	31.10	32.13	31.76	25.88	26.37	26.22	25.40	29.05	28.04	25.85	28.78
MnO	12.53	4.27	1.97	1.51	0.36	1.82	1.12	2.91	0.34	1.54	2.14	3.20	1.75	8.87	0.51
MgO	0.70	1.91	2.40	1.01	1.33	1.66	2.05	2.82	5.15	3.30	4.83	2.93	3.99	1.54	5.22
CaO	5.91	8.36	8.59	9.88	10.13	8.06	8.07	10.13	9.36	10.43	8.81	7.32	8.09	7.40	6.84
Na_2O	0.00	0.00	0.00	0.00	0.00	0.00	0.00	0.00	0.00	0.00	0.00	0.00	0.00	0.00	0.00
K_2O	0.00	0.00	0.00	0.00	0.00	0.00	0.00	0.00	0.00	0.00	0.00	0.00	0.00	0.00	0.00
Cr_2O_3	1.29	0.17	0.00	0.00	0.00	0.00	0.00	0.00	0.00	0.00	0.00	0.24	0.18	0.00	0.16
Total	100.44	100.93	100.27	100.30	100.01	101.39	100.80	100.33	100.69	99.65	100.37	101.49	100.97	100.73	100.34
Si	5.90	5.92	5.91	5.92	5.91	5.94	5.98	5.91	5.92	5.92	5.92	5.94	5.91	5.92	5.95
Ti	0.00	0.00	0.00	0.00	0.00	0.00	0.00	0.02	0.00	0.00	0.00	0.00	0.00	0.03	0.00
Al	2.82	2.89	2.91	2.92	2.93	2.90	2.88	2.96	2.96	2.95	2.97	2.94	2.96	2.87	2.92
Fe^{2+}	1.68	1.93	2.02	2.08	2.10	2.15	2.12	1.72	1.72	1.75	1.67	1.92	1.84	1.74	1.89
Mn	0.87	0.29	0.13	0.10	0.02	0.12	0.08	0.20	0.02	0.10	0.14	0.21	0.12	0.61	0.03
Mg	0.09	0.23	0.29	0.12	0.16	0.20	0.24	0.33	0.60	0.39	0.56	0.34	0.47	0.19	0.61
Ca	0.52	0.72	0.74	0.86	0.88	0.69	0.69	0.86	0.78	0.89	0.74	0.62	0.68	0.64	0.58
Na	0.00	0.00	0.00	0.00	0.00	0.00	0.00	0.00	0.00	0.00	0.00	0.00	0.00	0.00	0.00
K	0.00	0.00	0.00	0.00	0.00	0.00	0.00	0.00	0.00	0.00	0.00	0.00	0.00	0.00	0.00
Cr	0.13	0.02	0.00	0.00	0.00	0.00	0.00	0.00	0.00	0.00	0.00	0.02	0.02	0.00	0.01

Table A2.1. Continued.

	TS02-02	TS02-04		TS02-12	TS02-15A	TS02-16	TS02-17b	TS02-20		TS02-23	TS02-26			TS02-28	TS02-29	
Wt%																
SiO_2	54.85	56.04	55.94	55.88	55.39	54.68	55.68	55.91	54.93	55.67	55.57	55.63	55.13	55.76	56.08	56.10
TiO_2	0.00	0.00	0.00	0.00	0.00	0.23	0.00	0.00	0.00	0.00	0.00	0.00	0.00	0.00	0.00	0.00
Al_2O_3	8.37	10.93	11.87	12.27	9.01	7.05	9.04	9.80	6.99	8.47	8.45	10.15	9.67	10.17	9.57	9.53
FeO*	9.20	5.94	5.61	5.37	8.79	8.58	6.63	4.23	10.56	6.63	6.20	4.54	5.19	4.53	8.22	7.57
MnO	0.00	0.00	0.00	0.00	0.00	0.00	0.00	0.00	0.00	0.00	0.00	0.00	0.00	0.00	0.17	0.00
MgO	7.19	7.11	6.59	6.77	7.09	8.64	8.07	9.27	7.23	8.91	9.36	8.60	8.59	8.54	6.64	7.43
CaO	13.29	12.65	12.01	11.62	13.25	15.34	13.98	14.73	14.24	14.80	15.16	13.88	13.52	13.60	11.99	12.61
Na_2O	7.44	8.17	8.39	8.57	7.56	5.98	7.27	6.99	6.86	6.76	6.60	7.24	7.09	7.12	8.20	7.84
K_2O	0.00	0.00	0.00	0.00	0.00	0.00	0.00	0.00	0.00	0.00	0.00	0.00	0.00	0.00	0.00	0.00
Cr_2O_3	0.00	0.00	0.00	0.00	0.00	0.00	0.00	0.00	0.00	0.00	0.00	0.00	0.00	0.18	0.00	0.00
Total	100.33	100.84	100.41	100.48	101.10	100.49	100.68	100.92	100.81	101.25	101.34	100.03	99.18	99.90	100.88	101.08
Si	4.00	3.99	3.99	3.97	4.00	3.99	4.00	3.97	4.03	3.99	3.97	3.98	3.99	3.99	4.03	4.02
Ti	0.00	0.00	0.00	0.00	0.00	0.01	0.00	0.00	0.00	0.00	0.00	0.00	0.00	0.00	0.00	0.00
Al	0.54	0.69	0.75	0.77	0.58	0.45	0.57	0.61	0.45	0.54	0.53	0.64	0.62	0.64	0.61	0.60
Fe^{2+}	0.28	0.18	0.17	0.16	0.27	0.26	0.20	0.13	0.32	0.20	0.19	0.14	0.16	0.14	0.25	0.23
Mn	0.00	0.00	0.00	0.00	0.00	0.00	0.00	0.00	0.00	0.00	0.00	0.00	0.00	0.00	0.01	0.00
Mg	0.39	0.38	0.35	0.36	0.38	0.47	0.43	0.49	0.39	0.48	0.50	0.46	0.46	0.46	0.36	0.40
Ca	0.52	0.48	0.46	0.44	0.51	0.60	0.54	0.56	0.56	0.57	0.58	0.53	0.52	0.52	0.46	0.48
Na	0.26	0.28	0.29	0.30	0.26	0.21	0.25	0.24	0.24	0.23	0.23	0.25	0.25	0.25	0.29	0.27
K	0.00	0.00	0.00	0.00	0.00	0.00	0.00	0.00	0.00	0.00	0.00	0.00	0.00	0.00	0.00	0.00
Cr	0.00	0.00	0.00	0.00	0.00	0.00	0.00	0.00	0.00	0.00	0.00	0.00	0.00	0.01	0.00	0.00

Table A2.2. SEM EDS results of clinopyroxenes. Oxygen by stoichiometry. Clinopyroxene formula calculation based on six oxygens. FeO* - total Fe as FeO.

	TS02-30		TS02-32		TS02-33		TS02-35	TS02-38	TS02-41		TS02-42	TS02-43	TS02-46		TS02-47	TS02-48
Wt%																
SiO_2	55.18	56.79	54.41	56.07	55.84	54.23	54.31	54.33	54.26	54.11	55.22	55.19	54.72	55.57	56.02	54.97
TiO_2	0.00	0.00	0.00	0.00	0.00	0.00	0.00	0.00	0.00	0.18	0.00	0.00	0.00	0.00	0.00	0.00
Al_2O_3	8.66	10.98	7.99	10.20	10.14	7.90	6.99	6.16	8.40	9.04	6.19	8.58	8.18	8.57	10.50	9.50
FeO*	7.36	3.09	7.63	3.44	3.37	7.53	12.01	9.85	12.14	12.28	8.37	7.31	8.28	6.21	7.32	9.08
MnO	0.00	0.00	0.00	0.00	0.00	0.00	0.00	0.00	0.00	0.00	0.00	0.00	0.23	0.00	0.00	0.00
MgO	8.17	8.74	7.95	9.00	9.37	8.56	6.49	8.38	5.26	4.63	9.29	8.29	7.38	8.70	7.15	5.98
CaO	13.85	13.46	14.26	14.79	14.69	14.39	13.33	14.83	11.76	10.46	16.17	14.67	13.37	14.35	11.47	11.59
Na_2O	6.98	7.28	6.81	6.67	6.63	6.66	6.96	6.38	7.81	8.81	5.65	6.66	7.13	7.07	8.57	8.07
K_2O	0.00	0.00	0.00	0.00	0.00	0.00	0.00	0.00	0.00	0.00	0.00	0.00	0.00	0.00	0.00	0.00
Cr_2O_3	0.00	0.00	0.00	0.00	0.00	0.00	0.00	0.18	0.00	0.00	0.00	0.00	0.00	0.42	0.00	0.00
Total	100.20	100.33	99.05	100.19	100.04	99.26	100.08	100.11	99.63	99.51	100.88	100.70	99.29	100.89	101.03	99.19
Si	4.00	4.01	4.00	3.99	3.98	3.98	4.03	4.01	4.03	4.02	4.02	3.98	4.02	3.99	4.00	4.03
Ti	0.00	0.00	0.00	0.00	0.00	0.00	0.00	0.00	0.00	0.01	0.00	0.00	0.00	0.00	0.00	0.00
Al	0.55	0.68	0.52	0.64	0.64	0.51	0.46	0.40	0.55	0.59	0.40	0.55	0.53	0.54	0.66	0.62
Fe^{2+}	0.22	0.09	0.23	0.10	0.10	0.23	0.37	0.30	0.38	0.38	0.25	0.22	0.25	0.19	0.22	0.28
Mn	0.00	0.00	0.00	0.00	0.00	0.00	0.00	0.00	0.00	0.00	0.00	0.00	0.01	0.00	0.00	0.00
Mg	0.44	0.46	0.44	0.48	0.50	0.47	0.36	0.46	0.29	0.26	0.50	0.45	0.40	0.47	0.38	0.33
Ca	0.54	0.51	0.56	0.56	0.56	0.57	0.53	0.59	0.47	0.42	0.63	0.57	0.53	0.55	0.44	0.46
Na	0.25	0.25	0.24	0.23	0.23	0.24	0.25	0.23	0.28	0.32	0.20	0.23	0.25	0.25	0.30	0.29
K	0.00	0.00	0.00	0.00	0.00	0.00	0.00	0.00	0.00	0.00	0.00	0.00	0.00	0.00	0.00	0.00
Cr	0.00	0.00	0.00	0.00	0.00	0.00	0.00	0.01	0.00	0.00	0.00	0.00	0.00	0.02	0.00	0.00

Table A2.2. continued.

	TS02-48	TS02-50B		TS02-51b		TS02-53		TS02-54		TS02-57	TS02-58A		106-3		117-1	106-14	
Wt%																	
SiO_2	55.11	55.92	56.17	56.61	55.55	55.31	55.73	55.28	54.44	56.13	56.45	55.47	55.44	55.46	55.24	44.26	56.08
TiO_2	0.00	0.00	0.00	0.00	0.00	0.00	0.00	0.00	0.00	0.00	0.00	0.00	0.00	0.00	0.00	0.00	0.23
Al_2O_3	9.45	10.00	10.75	10.04	10.30	8.32	8.91	9.35	6.54	10.86	11.45	10.23	8.79	9.27	9.08	22.06	10.98
FeO*	10.13	8.19	5.68	5.08	5.40	11.33	9.51	10.50	11.94	3.51	5.43	7.75	6.50	6.04	7.96	7.39	11.08
MnO	0.00	0.00	0.00	0.00	0.00	0.00	0.00	0.00	0.00	0.00	0.00	0.00	0.00	0.00	0.00	0.00	0.00
MgO	5.52	6.18	7.46	8.33	7.77	5.75	6.52	5.61	7.05	8.43	6.85	6.47	8.34	8.50	7.43	2.21	11.11
CaO	11.24	11.30	12.66	13.73	12.77	11.71	11.65	11.16	12.98	13.36	12.09	12.21	13.57	14.01	13.59	20.02	2.79
Na_2O	8.62	8.88	7.76	7.62	7.80	8.27	8.51	8.51	7.37	7.52	8.47	8.06	7.28	7.14	7.27	3.95	7.05
K_2O	0.00	0.00	0.00	0.00	0.00	0.00	0.00	0.00	0.00	0.00	0.00	0.00	0.00	0.00	0.00	0.00	0.00
Cr_2O_3	0.00	0.00	0.00	0.00	0.00	0.00	0.00	0.00	0.00	0.00	0.00	0.00	0.00	0.00	0.00	0.00	0.00
Total	100.07	100.45	100.50	101.40	99.59	100.70	100.83	100.41	100.32	99.82	100.73	100.19	99.91	100.43	100.56	99.89	99.32
Si	4.03	4.04	4.00	4.00	4.00	4.05	4.04	4.03	4.03	4.00	4.01	4.01	4.01	3.99	4.00	3.27	4.02
Ti	0.00	0.00	0.00	0.00	0.00	0.00	0.00	0.00	0.00	0.00	0.00	0.00	0.00	0.00	0.00	0.00	0.01
Al	0.61	0.64	0.68	0.63	0.66	0.54	0.57	0.60	0.43	0.68	0.72	0.65	0.56	0.59	0.58	1.44	0.70
Fe^{2+}	0.31	0.25	0.17	0.15	0.16	0.35	0.29	0.32	0.37	0.10	0.16	0.23	0.20	0.18	0.24	0.23	0.33
Mn	0.00	0.00	0.00	0.00	0.00	0.00	0.00	0.00	0.00	0.00	0.00	0.00	0.00	0.00	0.00	0.00	0.00
Mg	0.30	0.33	0.40	0.44	0.42	0.31	0.35	0.31	0.39	0.45	0.36	0.35	0.45	0.46	0.40	0.12	0.59
Ca	0.44	0.44	0.48	0.52	0.49	0.46	0.45	0.44	0.52	0.51	0.46	0.47	0.53	0.54	0.53	0.79	0.11
Na	0.31	0.31	0.27	0.26	0.27	0.29	0.30	0.30	0.26	0.26	0.29	0.28	0.26	0.25	0.25	0.14	0.24
K	0.00	0.00	0.00	0.00	0.00	0.00	0.00	0.00	0.00	0.00	0.00	0.00	0.00	0.00	0.00	0.00	0.00
Cr	0.00	0.00	0.00	0.00	0.00	0.00	0.00	0.00	0.00	0.00	0.00	0.00	0.00	0.00	0.00	0.00	0.00

Table A2.2. continued

	TS02-01	TS02-02		TS02-3a		TS02-04	TS02-05					TS02-6		TS02-12		TS02-13
Wt%																
SiO_2	56.57	57.03	56.46	57.19	51.64	48.71	57.02	56.78	57.83	49.63	48.51	52.69	46.56	52.43	57.59	57.41
TiO_2	0.00	0.00	0.00	0.00	0.20	0.30	0.00	0.00	0.00	0.24	0.29	0.00	0.34	0.20	0.00	0.00
Al_2O_3	6.91	10.65	10.80	11.03	8.21	9.56	10.34	10.42	10.04	9.35	10.25	10.01	9.82	6.36	9.88	11.60
FeO*	14.55	11.59	11.10	10.17	12.39	15.27	10.07	10.24	9.72	14.75	14.78	18.07	20.76	11.09	11.07	10.49
MnO	0.00	0.00	0.00	0.00	0.00	0.00	0.00	0.18	0.00	0.00	0.00	0.00	0.00	0.00	0.00	0.00
MgO	10.60	9.69	10.31	10.46	13.34	11.53	11.12	11.31	11.83	11.61	11.43	7.00	7.87	14.98	10.53	9.32
CaO	0.12	0.60	0.98	0.45	8.03	8.78	1.57	1.57	1.16	7.92	8.71	1.69	5.36	9.69	0.81	0.00
Na_2O	7.44	7.63	7.33	7.62	3.96	3.88	7.15	6.93	7.08	4.13	3.85	7.13	5.81	2.74	7.48	7.59
K_2O	0.00	0.00	0.00	0.00	0.20	0.32	0.00	0.00	0.00	0.22	0.39	0.00	0.34	0.10	0.00	0.00
Cr_2O_3	0.00	0.00	0.00	0.00	0.00	0.00	0.00	0.00	0.00	0.00	0.00	0.00	0.00	0.00	0.00	0.00
Total	96.19	97.19	96.97	96.93	97.97	98.35	97.27	97.43	97.65	97.86	98.20	96.59	96.87	97.60	97.35	96.40
Si	8.10	7.95	7.88	7.93	7.38	7.09	7.90	7.87	7.95	7.21	7.05	7.70	7.06	7.48	7.99	7.99
Ti	0.00	0.00	0.00	0.00	0.02	0.03	0.00	0.00	0.00	0.03	0.03	0.00	0.04	0.02	0.00	0.00
Al	1.17	1.75	1.78	1.80	1.38	1.64	1.69	1.70	1.63	1.60	1.76	1.72	1.76	1.07	1.62	1.90
Fe^{2+}	1.74	1.35	1.30	1.18	1.48	1.86	1.17	1.19	1.12	1.79	1.80	2.21	2.63	1.32	1.28	1.22
Mn	0.00	0.00	0.00	0.00	0.00	0.00	0.00	0.02	0.00	0.00	0.00	0.00	0.00	0.00	0.00	0.00
Mg	2.26	2.01	2.14	2.16	2.84	2.50	2.30	2.34	2.42	2.51	2.48	1.53	1.78	3.19	2.18	1.93
Ca	0.02	0.09	0.15	0.07	1.23	1.37	0.23	0.23	0.17	1.23	1.36	0.26	0.87	1.48	0.12	0.00
Na	2.07	2.06	1.98	2.05	1.10	1.09	1.92	1.86	1.89	1.16	1.08	2.02	1.71	0.76	2.01	2.05
K	0.00	0.00	0.00	0.00	0.04	0.06	0.00	0.00	0.00	0.04	0.07	0.00	0.07	0.02	0.00	0.00
Cr	0.00	0.00	0.00	0.00	0.00	0.00	0.00	0.00	0.00	0.00	0.00	0.00	0.00	0.00	0.00	0.00

Table A2.3. Results of SEM EDS analysis of amphibole. Oxygen by stoichiometry. Amphibole formulae calculations based on 23 oxygens. FeO* - total Fe as FeO.

	TS02-14			TS02-15A							TS02-15B				TS02-16	
Wt%																
SiO_2	57.24	48.83	56.93	57.00	47.03	47.22	46.47	51.34	56.09	48.22	55.17	48.34	56.40	49.64	55.42	49.23
TiO_2	0.00	0.00	0.00	0.00	0.23	0.00	0.00	0.00	0.00	0.00	0.00	0.29	0.00	0.00	0.00	0.00
Al_2O_3	11.26	9.56	11.26	10.18	10.30	8.97	10.54	4.17	10.72	6.26	10.06	9.67	10.29	7.54	1.32	5.25
FeO*	12.18	13.85	12.46	12.89	17.69	17.35	17.56	15.23	11.97	20.77	16.68	17.02	14.04	17.73	10.60	21.29
MnO	0.00	0.00	0.00	0.00	0.00	0.00	0.00	0.00	0.00	0.27	0.00	0.00	0.00	0.00	0.00	0.00
MgO	9.04	11.77	8.41	9.19	9.72	10.09	9.48	13.45	9.40	9.66	7.18	10.01	8.89	10.86	17.83	9.07
CaO	0.00	8.61	0.00	0.47	8.75	8.90	8.49	10.45	0.76	9.65	1.42	8.24	0.80	8.32	10.50	10.71
Na_2O	7.77	3.47	7.66	8.00	3.89	3.50	3.79	1.90	7.34	2.96	7.05	3.73	7.30	3.68	1.54	1.81
K_2O	0.00	0.14	0.00	0.00	0.28	0.34	0.33	0.16	0.00	0.29	0.00	0.23	0.00	0.19	0.22	0.14
Cr_2O_3	0.00	0.00	0.00	0.00	0.00	0.00	0.00	0.00	0.00	0.00	0.00	0.00	0.00	0.00	0.00	0.00
Total	97.49	96.23	96.72	97.72	97.89	96.37	96.65	96.69	96.28	98.07	97.57	97.52	97.72	97.97	97.43	97.51
Si	7.95	7.18	7.98	7.96	6.97	7.10	6.97	7.57	7.91	7.25	7.87	7.13	7.91	7.31	7.89	7.43
Ti	0.00	0.00	0.00	0.00	0.03	0.00	0.00	0.00	0.00	0.00	0.00	0.03	0.00	0.00	0.00	0.00
Al	1.84	1.66	1.86	1.68	1.80	1.59	1.86	0.72	1.78	1.11	1.69	1.68	1.70	1.31	0.22	0.93
Fe^{2+}	1.41	1.70	1.46	1.51	2.19	2.18	2.20	1.88	1.41	2.61	1.99	2.10	1.65	2.18	1.26	2.69
Mn	0.00	0.00	0.00	0.00	0.00	0.00	0.00	0.00	0.00	0.03	0.00	0.00	0.00	0.00	0.00	0.00
Mg	1.87	2.58	1.76	1.91	2.15	2.26	2.12	2.96	1.98	2.17	1.53	2.20	1.86	2.38	3.79	2.04
Ca	0.00	1.36	0.00	0.07	1.39	1.43	1.36	1.65	0.11	1.56	0.22	1.30	0.12	1.31	1.60	1.73
Na	2.09	0.99	2.08	2.17	1.12	1.02	1.10	0.54	2.01	0.86	1.95	1.07	1.99	1.05	0.43	0.53
K	0.00	0.03	0.00	0.00	0.05	0.07	0.06	0.03	0.00	0.06	0.00	0.04	0.00	0.04	0.04	0.03
Cr	0.00	0.00	0.00	0.00	0.00	0.00	0.00	0.00	0.00	0.00	0.00	0.00	0.00	0.00	0.00	0.00

Table A2.3. continued.

	TS02-16	TS02-16	TS02-17b			TS02-18	TS02-19	TS02-20	TS02-21a			TS02-23		TS02-26	TS02-27	
Wt%																
SiO_2	55.35	55.13	57.19	57.79	51.41	56.71	56.98	54.64	49.08	49.03	48.63	56.36	53.05	54.94	52.35	52.59
TiO_2	0.00	0.21	0.00	0.00	0.00	0.00	0.00	0.00	0.26	0.23	0.28	0.00	0.00	0.00	0.00	0.00
Al_2O_3	1.66	1.69	10.71	10.98	6.26	11.54	11.14	4.19	8.53	8.77	9.34	1.35	6.42	3.42	6.33	6.28
FeO*	12.15	13.29	8.04	8.30	11.39	14.32	11.91	9.76	14.26	14.39	14.55	6.99	10.22	7.78	10.81	10.91
MnO	0.00	0.00	0.00	0.00	0.00	0.00	0.00	0.00	0.00	0.00	0.00	0.22	0.20	0.00	0.00	0.00
MgO	16.93	16.26	11.81	11.43	14.98	7.58	8.37	16.96	12.44	12.37	12.08	19.98	15.67	18.94	15.76	15.19
CaO	10.03	10.28	1.33	0.76	10.21	0.40	0.00	10.42	9.68	9.29	9.57	12.86	9.13	10.74	9.64	9.49
Na_2O	1.96	1.83	7.09	7.56	2.55	7.49	7.70	2.36	2.77	2.93	2.80	0.60	3.11	1.87	2.55	2.88
K_2O	0.18	0.20	0.00	0.00	0.00	0.00	0.00	0.00	0.14	0.20	0.22	0.00	0.00	0.00	0.00	0.09
Cr_2O_3	0.00	0.00	0.00	0.00	0.00	0.19	0.00	0.00	0.00	0.00	0.00	0.00	0.00	0.00	0.00	0.00
Total	98.26	98.88	96.18	96.82	96.80	98.22	96.11	98.34	97.15	97.20	97.47	98.36	97.80	97.68	97.44	97.42
Si	7.87	7.84	7.93	7.95	7.43	7.90	8.01	7.68	7.18	7.17	7.10	7.84	7.52	7.71	7.47	7.51
Ti	0.00	0.02	0.00	0.00	0.00	0.00	0.00	0.00	0.03	0.03	0.03	0.00	0.00	0.00	0.00	0.00
Al	0.28	0.28	1.75	1.78	1.07	1.90	1.85	0.69	1.47	1.51	1.61	0.22	1.07	0.57	1.06	1.06
Fe^{2+}	1.44	1.58	0.93	0.96	1.38	1.67	1.40	1.15	1.74	1.76	1.78	0.81	1.21	0.91	1.29	1.30
Mn	0.00	0.00	0.00	0.00	0.00	0.00	0.00	0.00	0.00	0.00	0.00	0.03	0.02	0.00	0.00	0.00
Mg	3.59	3.44	2.44	2.34	3.23	1.57	1.75	3.55	2.71	2.70	2.63	4.14	3.31	3.96	3.35	3.23
Ca	1.53	1.57	0.20	0.11	1.58	0.06	0.00	1.57	1.52	1.46	1.50	1.92	1.39	1.61	1.47	1.45
Na	0.54	0.50	1.91	2.02	0.71	2.02	2.10	0.64	0.79	0.83	0.79	0.16	0.85	0.51	0.71	0.80
K	0.03	0.04	0.00	0.00	0.00	0.00	0.00	0.00	0.03	0.04	0.04	0.00	0.00	0.00	0.00	0.02
Cr	0.00	0.00	0.00	0.00	0.00	0.02	0.00	0.00	0.00	0.00	0.00	0.00	0.00	0.00	0.00	0.00

Table A2.3. continued.

	TS02-28			TS02-30		TS02-33	TS02-35		TS02-36	TS02-38	TS02-42	TS02-43		TS02-46		TS02-47
Wt%																
SiO_2	52.98	52.74	57.30	52.79	52.05	53.31	57.74	58.16	57.04	56.89	58.02	55.46	57.76	57.85	49.91	55.45
TiO_2	0.00	0.17	0.00	0.17	0.00	0.00	0.00	0.00	0.00	0.00	0.00	0.00	0.00	0.00	0.21	0.00
Al_2O_3	6.50	6.85	11.28	6.10	6.09	4.67	10.80	11.25	8.73	10.05	10.18	1.02	10.93	10.93	8.00	11.50
FeO^*	9.34	9.15	6.40	10.60	10.39	8.93	11.71	10.09	12.57	10.91	10.19	13.22	11.52	9.53	11.85	11.65
MnO	0.00	0.00	0.00	0.00	0.00	0.00	0.00	0.00	0.00	0.00	0.00	0.00	0.00	0.00	0.00	0.00
MgO	16.13	15.90	13.17	15.41	15.60	16.97	9.96	11.00	10.90	10.48	11.64	16.39	10.20	10.68	13.62	10.03
CaO	9.46	9.10	1.70	9.50	9.69	10.08	0.57	0.59	0.97	0.64	1.01	11.04	0.64	0.29	9.52	2.12
Na_2O	3.09	3.24	7.17	2.83	2.89	2.31	7.73	7.77	7.38	7.13	7.69	1.16	7.44	7.49	3.12	7.14
K_2O	0.11	0.00	0.00	0.11	0.12	0.11	0.00	0.00	0.00	0.00	0.00	0.11	0.00	0.00	0.15	0.00
Cr_2O_3	0.00	0.00	0.00	0.16	0.00	0.00	0.00	0.00	0.00	0.00	0.00	0.00	0.00	0.00	0.00	0.00
Total	97.61	97.16	97.01	97.66	96.83	96.37	98.52	98.86	97.60	96.10	98.73	98.42	98.49	96.77	96.39	97.90
Si	7.50	7.48	7.83	7.51	7.48	7.63	7.94	7.91	7.98	7.98	7.92	7.91	7.93	7.99	7.27	7.72
Ti	0.00	0.02	0.00	0.02	0.00	0.00	0.00	0.00	0.00	0.00	0.00	0.00	0.00	0.00	0.02	0.00
Al	1.08	1.15	1.82	1.02	1.03	0.79	1.75	1.80	1.44	1.66	1.64	0.17	1.77	1.78	1.37	1.89
Fe^{2+}	1.11	1.09	0.73	1.26	1.25	1.07	1.35	1.15	1.47	1.28	1.16	1.58	1.32	1.10	1.44	1.36
Mn	0.00	0.00	0.00	0.00	0.00	0.00	0.00	0.00	0.00	0.00	0.00	0.00	0.00	0.00	0.00	0.00
Mg	3.40	3.36	2.68	3.27	3.34	3.62	2.04	2.23	2.27	2.19	2.37	3.49	2.09	2.20	2.96	2.08
Ca	1.43	1.38	0.25	1.45	1.49	1.55	0.08	0.09	0.15	0.10	0.15	1.69	0.09	0.04	1.49	0.32
Na	0.85	0.89	1.90	0.78	0.81	0.64	2.06	2.05	2.00	1.94	2.04	0.32	1.98	2.01	0.88	1.93
K	0.02	0.00	0.00	0.02	0.02	0.02	0.00	0.00	0.00	0.00	0.00	0.02	0.00	0.00	0.03	0.00
Cr	0.00	0.00	0.00	0.02	0.00	0.00	0.00	0.00	0.00	0.00	0.00	0.00	0.00	0.00	0.00	0.00

Table A2.3. continued.

	TS02-48		TS02-52						TS02-53		TS02-55			TS02-57		
Wt%																
SiO_2	57.10	56.68	57.85	46.17	56.73	50.21	58.50	47.45	56.50	55.37	53.69	55.13	55.12	53.71	52.77	57.70
TiO_2	0.00	0.00	0.00	0.00	0.00	0.00	0.00	0.00	0.00	0.00	0.00	0.00	0.00	0.00	0.00	0.00
Al_2O_3	11.48	11.64	11.60	8.09	11.11	7.99	11.10	6.03	11.22	11.38	3.80	2.09	1.79	5.84	5.54	11.66
FeO^*	10.08	8.81	10.05	21.16	12.11	14.48	8.88	24.72	12.36	12.86	8.55	9.42	9.10	9.60	10.66	6.22
MnO	0.00	0.00	0.00	0.00	0.00	0.00	0.00	0.33	0.00	0.00	0.00	0.00	0.19	0.00	0.00	0.00
MgO	10.58	11.03	10.70	8.45	9.31	12.26	11.31	6.92	9.49	9.47	17.41	18.30	18.22	16.24	15.65	12.85
CaO	0.98	1.37	0.63	10.29	0.95	8.99	0.51	7.91	1.04	1.88	10.92	11.07	11.42	10.18	9.79	1.33
Na_2O	7.27	7.51	7.58	2.53	7.68	3.04	7.91	3.33	7.85	6.99	1.70	1.36	1.08	2.51	2.72	7.46
K_2O	0.00	0.00	0.00	0.22	0.00	0.00	0.00	0.23	0.00	0.00	0.00	0.00	0.00	0.00	0.00	0.00
Cr_2O_3	0.00	0.00	0.00	0.00	0.00	0.00	0.00	0.00	0.00	0.00	0.00	0.00	0.00	0.00	0.27	0.00
Total	97.48	97.04	98.42	96.91	97.90	96.98	98.22	96.92	98.45	97.95	96.07	97.37	96.90	98.09	97.40	97.22
Si	7.87	7.83	7.89	7.05	7.88	7.33	7.96	7.34	7.83	7.74	7.69	7.81	7.84	7.56	7.54	7.85
Ti	0.00	0.00	0.00	0.00	0.00	0.00	0.00	0.00	0.00	0.00	0.00	0.00	0.00	0.00	0.00	0.00
Al	1.87	1.90	1.87	1.46	1.82	1.38	1.78	1.10	1.83	1.88	0.64	0.35	0.30	0.97	0.93	1.87
Fe^{2+}	1.16	1.02	1.15	2.70	1.41	1.77	1.01	3.20	1.43	1.50	1.02	1.12	1.08	1.13	1.27	0.71
Mn	0.00	0.00	0.00	0.00	0.00	0.00	0.00	0.04	0.00	0.00	0.00	0.00	0.02	0.00	0.00	0.00
Mg	2.17	2.27	2.18	1.92	1.93	2.67	2.29	1.60	1.96	1.97	3.72	3.87	3.87	3.41	3.33	2.61
Ca	0.14	0.20	0.09	1.68	0.14	1.41	0.07	1.31	0.15	0.28	1.68	1.68	1.74	1.54	1.50	0.19
Na	1.94	2.01	2.01	0.75	2.07	0.86	2.09	1.00	2.11	1.89	0.47	0.37	0.30	0.69	0.75	1.97
K	0.00	0.00	0.00	0.04	0.00	0.00	0.00	0.05	0.00	0.00	0.00	0.00	0.00	0.00	0.00	0.00
Cr	0.00	0.00	0.00	0.00	0.00	0.00	0.00	0.00	0.00	0.00	0.00	0.00	0.00	0.00	0.03	0.00

Table A2.3. continued.

	TS02-57	TS02-62					105-1		106-3			984-1		110-3	117-1	106-3
Wt%																
SiO_2	57.90	58.82	46.24	57.79	47.50	56.17	56.86	53.20	56.96	49.88	52.38	50.66	50.52	57.60	52.43	50.71
TiO_2	0.00	0.00	0.00	0.00	0.32	0.00	0.00	0.00	0.00	0.24	0.00	0.00	0.18	0.00	0.00	0.00
Al_2O_3	11.58	11.14	11.34	11.50	11.37	11.14	11.33	4.81	10.93	8.96	6.72	7.45	8.09	8.77	3.72	8.86
FeO^*	6.91	8.93	14.57	9.93	14.67	13.83	8.17	7.84	11.08	12.98	11.01	13.05	13.31	11.32	16.48	12.63
MnO	0.00	0.00	0.00	0.00	0.00	0.00	0.00	0.00	0.00	0.00	0.00	0.00	0	0.00	0.00	0.00
MgO	12.45	10.95	11.47	10.22	11.25	8.20	11.37	17.27	9.78	12.59	14.90	13.48	12.94	12.11	14.33	13.04
CaO	1.04	0.00	8.04	0.26	7.67	0.68	0.86	10.33	0.95	8.52	9.09	9.00	8.71	1.53	10.85	8.69
Na_2O	7.50	7.83	4.77	7.73	4.90	7.37	7.43	2.31	7.45	3.46	2.99	3.14	3.73	7.25	0.77	3.68
K_2O	0.00	0.00	0.43	0.00	0.32	0.00	0.00	0.00	0.00	0.14	0.10	0.00	0	0.00	0.00	0.15
Cr_2O_3	0.00	0.00	0.00	0.00	0.00	0.00	0.00	0.00	0.00	0.00	0.19	0.00	0	0.00	0.00	0.00
Total	97.36	97.68	96.86	97.44	98.01	97.39	96.02	95.78	97.15	96.75	97.38	96.77	97.49	98.58	98.57	97.76
Si	7.88	8.02	6.85	7.95	6.92	7.89	7.89	7.62	7.92	7.25	7.48	7.37	7.31	7.94	7.59	7.29
Ti	0.00	0.00	0.00	0.00	0.04	0.00	0.00	0.00	0.00	0.03	0.00	0.00	0.02	0.00	0.00	0.00
Al	1.86	1.79	1.98	1.86	1.95	1.84	1.85	0.81	1.79	1.54	1.13	1.28	1.38	1.42	0.63	1.50
Fe^{2+}	0.79	1.02	1.80	1.14	1.79	1.63	0.95	0.94	1.29	1.58	1.32	1.59	1.61	1.30	1.99	1.52
Mn	0.00	0.00	0.00	0.00	0.00	0.00	0.00	0.00	0.00	0.00	0.00	0.00	0.00	0.00	0.00	0.00
Mg	2.53	2.23	2.53	2.10	2.44	1.72	2.35	3.69	2.03	2.73	3.17	2.92	2.79	2.49	3.09	2.79
Ca	0.15	0.00	1.28	0.04	1.20	0.10	0.13	1.59	0.14	1.33	1.39	1.40	1.35	0.23	1.68	1.34
Na	1.98	2.07	1.37	2.06	1.38	2.01	2.00	0.64	2.01	0.98	0.83	0.89	1.05	1.94	0.22	1.03
K	0.00	0.00	0.08	0.00	0.06	0.00	0.00	0.00	0.00	0.03	0.02	0.00	0.00	0.00	0.00	0.03
Cr	0.00	0.00	0.00	0.00	0.00	0.00	0.00	0.00	0.00	0.00	0.02	0.00	0.00	0.00	0.00	0.00

Table A2.3. continued.

	106-3	Q02-02			Q02-08	Q02-10A	Q02-22						Q02-34B		Q98-120	
Wt%																
SiO_2	57.48	58.44	57.95	47.52	57.83	57.26	55.92	56.21	55.68	55.28	55.73	53.85	57.56	55.56	57.72	56.83
TiO_2	0.00	0.00	0.00	0.00	0.00	0.00	0.00	0.18	0.00	0.00	0.00	0.00	0.00	0.00	0.00	0.00
Al_2O_3	10.96	11.32	11.64	8.84	10.19	10.93	8.37	9.74	10.61	7.68	11.38	11.20	9.40	10.10	10.95	10.89
FeO*	9.56	6.05	5.51	15.98	9.43	11.00	15.95	14.10	13.96	16.33	12.71	15.70	14.91	14.60	8.57	11.94
MnO	0.00	0.00	0.00	0.28	0.00	0.00	0.00	0.00	0.00	0.00	0.00	0.16	0.00	0.00	0.00	0.00
MgO	11.23	13.54	13.65	11.52	12.01	10.45	8.82	8.91	8.22	8.90	8.75	7.20	8.45	8.88	11.94	9.80
CaO	1.22	1.06	1.59	10.51	1.18	0.61	0.55	0.29	0.57	0.58	0.95	1.61	1.37	1.44	0.79	0.64
Na_2O	7.29	7.41	7.16	2.67	7.53	7.55	7.52	7.75	7.53	7.36	7.45	6.99	7.08	6.84	7.86	7.63
K_2O	0.00	0.00	0.00	0.30	0.00	0.00	0.00	0.00	0.00	0.00	0.00	0.10	0.00	0.00	0.00	0.00
Cr_2O_3	0.00	0.00	0.00	0.00	0.00	0.00	0.00	0.00	0.00	0.00	0.00	0.00	0.00	0.00	0.00	0.37
Total	97.73	97.81	97.49	97.62	98.17	97.80	97.12	97.17	96.56	96.14	96.97	96.80	98.77	97.42	97.83	98.10
Si	7.90	7.89	7.84	7.03	7.92	7.91	7.99	7.94	7.91	8.01	7.84	7.74	8.02	7.86	7.89	7.87
Ti	0.00	0.00	0.00	0.00	0.00	0.00	0.00	0.02	0.00	0.00	0.00	0.00	0.00	0.00	0.00	0.00
Al	1.77	1.80	1.86	1.54	1.64	1.78	1.41	1.62	1.78	1.31	1.89	1.90	1.54	1.68	1.76	1.78
Fe^{2+}	1.10	0.68	0.62	1.98	1.08	1.27	1.91	1.67	1.66	1.98	1.50	1.89	1.74	1.73	0.98	1.38
Mn	0.00	0.00	0.00	0.04	0.00	0.00	0.00	0.00	0.00	0.00	0.00	0.02	0.00	0.00	0.00	0.00
Mg	2.30	2.72	2.75	2.54	2.45	2.15	1.88	1.88	1.74	1.92	1.83	1.54	1.75	1.87	2.43	2.02
Ca	0.18	0.15	0.23	1.67	0.17	0.09	0.08	0.04	0.09	0.09	0.14	0.25	0.20	0.22	0.12	0.09
Na	1.94	1.94	1.88	0.77	2.00	2.02	2.08	2.12	2.07	2.07	2.03	1.95	1.91	1.88	2.08	2.05
K	0.00	0.00	0.00	0.06	0.00	0.00	0.00	0.00	0.00	0.00	0.00	0.02	0.00	0.00	0.00	0.00
Cr	0.00	0.00	0.00	0.00	0.00	0.00	0.00	0.00	0.00	0.00	0.00	0.00	0.00	0.00	0.00	0.04

Table A2.3. continued.

	Q98-126		Q98-127						Q98-128		Q98-143		Q98-149		Q98-148		Q98-150		Q98-152	
Wt%																				
SiO_2	57.32	57.12	56.57	56.26	50.64	53.00	56.84	54.02	56.91	56.35	55.30	54.65	56.27	56.26	55.96	55.92	55.80	55.78	56.57	55.62
TiO_2	0.00	0.00	0.00	0.00	0.00	0.00	0.00	0.00	0.00	0.00	0.00	0.25	0.00	0.00	0.00	0.00	0.00	0.00	0.00	0.17
Al_2O_3	10.45	10.19	10.05	10.43	6.36	5.10	10.33	2.54	10.98	10.11	10.61	9.43	8.04	7.58	8.23	7.51	11.55	10.27	8.86	8.07
FeO*	8.35	11.15	9.61	6.62	12.31	10.95	8.66	12.61	5.80	8.06	18.39	19.96	13.60	13.70	16.81	18.40	14.49	12.28	13.47	14.42
MnO	0.00	0.00	0.00	0.00	0.00	0.00	0.00	0.29	0.00	0.00	0.22	0.00	0.00	0.00	0.00	0.29	0.00	0.00	0.00	0.00
MgO	12.90	11.01	11.57	13.34	14.00	15.54	12.01	16.62	13.40	12.43	5.46	5.44	11.10	11.01	8.23	7.81	7.35	9.54	10.30	10.27
CaO	1.63	1.11	0.92	1.98	8.63	9.61	1.05	11.67	1.48	1.29	0.32	0.60	2.25	1.94	0.30	0.39	0.52	0.96	1.14	1.78
Na_2O	7.32	7.39	7.39	6.96	2.97	2.68	7.07	1.15	7.33	7.07	7.61	7.37	6.70	6.46	7.57	7.42	7.39	7.06	7.27	6.88
K_2O	0.00	0.00	0.00	0.00	0.20	0.00	0.00	0.00	0.00	0.00	0.00	0.00	0.00	0.00	0.00	0.00	0.00	0.00	0.00	0.00
Cr_2O_3	0.00	0.00	0.00	0.00	0.00	0.00	0.00	0.00	0.00	0.00	0.00	0.00	0.00	0.00	0.00	0.00	0.00	0.00	0.00	0.00
Total	97.98	97.99	96.11	95.58	95.11	96.89	95.97	98.90	95.90	95.31	97.91	97.69	97.96	96.94	97.10	97.74	97.09	95.88	97.60	97.20
Si	7.84	7.90	7.92	7.83	7.47	7.61	7.92	7.68	7.85	7.90	7.91	7.91	7.91	7.98	8.02	8.04	7.88	7.92	7.95	7.91
Ti	0.00	0.00	0.00	0.00	0.00	0.00	0.00	0.00	0.00	0.00	0.00	0.03	0.00	0.00	0.00	0.00	0.00	0.00	0.00	0.02
Al	1.68	1.66	1.66	1.71	1.11	0.86	1.70	0.43	1.79	1.67	1.79	1.61	1.33	1.27	1.39	1.27	1.92	1.72	1.47	1.35
Fe^{2+}	0.96	1.29	1.12	0.77	1.52	1.31	1.01	1.50	0.67	0.94	2.20	2.42	1.60	1.63	2.02	2.21	1.71	1.46	1.58	1.72
Mn	0.00	0.00	0.00	0.00	0.00	0.00	0.00	0.03	0.00	0.00	0.03	0.00	0.00	0.00	0.00	0.04	0.00	0.00	0.00	0.00
Mg	2.63	2.27	2.41	2.77	3.08	3.33	2.49	3.52	2.76	2.60	1.16	1.17	2.33	2.33	1.76	1.67	1.55	2.02	2.16	2.18
Ca	0.24	0.16	0.14	0.30	1.36	1.48	0.16	1.78	0.22	0.19	0.05	0.09	0.34	0.29	0.05	0.06	0.08	0.15	0.17	0.27
Na	1.94	1.98	2.01	1.88	0.85	0.75	1.91	0.32	1.96	1.92	2.11	2.07	1.83	1.78	2.10	2.07	2.02	1.94	1.98	1.90
K	0.00	0.00	0.00	0.00	0.04	0.00	0.00	0.00	0.00	0.00	0.00	0.00	0.00	0.00	0.00	0.00	0.00	0.00	0.00	0.00
Cr	0.00	0.00	0.00	0.00	0.00	0.00	0.00	0.00	0.00	0.00	0.00	0.00	0.00	0.00	0.00	0.00	0.00	0.00	0.00	0.00

Table A2.3. continued.

	TS02-01	TS02-02	TS02-3a	TS02-04		TS02-05		TS02-6		TS02-10		TS02-12	TS02-13	TS02-14	TS02-17b	TS02-18
	parag	pheng	pheng	pheng	pheng	pheng	pheng	pheng	pheng	pheng	parag	parag	pheng	parag	parag	pheng
Wt%																
SiO_2	46.96	49.46	51.26	50.40	50.11	50.86	50.33	48.31	48.90	50.13	45.72	45.88	50.31	46.64	45.87	49.39
TiO_2	0.00	0.33	0.42	0.55	0.53	0.29	0.42	0.36	0.34	0.33	0.25	0.00	0.23	0.00	0.00	0.59
Al_2O_3	39.31	28.02	24.59	26.80	27.07	26.89	27.53	25.12	24.73	27.72	38.73	39.03	26.59	38.84	38.15	28.39
FeO*	0.99	3.25	2.18	2.39	2.64	2.26	2.48	4.83	5.08	3.48	0.29	0.41	2.95	0.29	0.43	3.55
MnO	0.00	0.00	0.00	0.00	0.00	0.00	0.00	0.00	0.00	0.00	0.00	0.00	0.00	0.00	0.00	0.00
MgO	0.00	2.95	4.24	3.33	3.03	3.68	3.49	2.62	2.85	2.38	0.00	0.19	3.19	0.00	0.20	2.37
CaO	0.20	0.00	0.00	0.00	0.00	0.00	0.00	0.00	0.00	0.00	0.00	0.11	0.00	0.00	0.15	0.00
Na_2O	7.13	0.68	0.35	0.64	0.74	0.59	0.70	0.29	0.21	0.42	7.37	7.38	0.45	7.17	7.07	0.65
K_2O	0.53	10.13	10.78	9.96	9.53	9.78	10.35	9.88	10.03	10.11	0.60	0.66	10.25	0.81	0.49	10.11
Cr_2O_3	0.00	0.00	0.00	0.00	0.16	0.00	0.00	0.00	0.00	0.00	0.00	0.00	0.00	0.00	0.00	0.00
Total	95.11	94.82	93.82	94.07	93.81	94.35	95.29	91.40	92.14	94.94	92.96	93.67	93.97	93.76	92.35	95.05
Si	6.02	6.67	6.96	6.80	6.78	6.83	6.73	6.81	6.85	6.76	5.98	5.97	6.82	6.05	6.04	6.65
Ti	0.00	0.03	0.04	0.06	0.05	0.03	0.04	0.04	0.04	0.03	0.02	0.00	0.02	0.00	0.00	0.06
Al	4.45	3.34	2.95	3.20	3.24	3.19	3.25	3.13	3.06	3.30	4.48	4.49	3.19	4.45	4.44	3.38
Fe^{2+}	0.05	0.18	0.12	0.13	0.15	0.13	0.14	0.28	0.30	0.20	0.02	0.02	0.17	0.02	0.02	0.20
Mn	0.00	0.00	0.00	0.00	0.00	0.00	0.00	0.00	0.00	0.00	0.00	0.00	0.00	0.00	0.00	0.00
Mg	0.00	0.30	0.43	0.34	0.31	0.37	0.35	0.28	0.30	0.24	0.00	0.02	0.32	0.00	0.02	0.24
Ca	0.01	0.00	0.00	0.00	0.00	0.00	0.00	0.00	0.00	0.00	0.00	0.01	0.00	0.00	0.01	0.00
Na	0.44	0.04	0.02	0.04	0.05	0.04	0.05	0.02	0.01	0.03	0.47	0.47	0.03	0.45	0.45	0.04
K	0.02	0.44	0.47	0.43	0.41	0.42	0.44	0.44	0.45	0.43	0.03	0.03	0.44	0.03	0.02	0.43
Cr	0.00	0.00	0.00	0.00	0.01	0.00	0.00	0.00	0.00	0.00	0.00	0.00	0.00	0.00	0.00	0.00

Table A2.4. Results of SEM EDS analysis of mica. Oxygen by stoichiometry. Mica formula calculation based on 11 oxygens. Pheng = phengitic mica; Parag = paragonite mica. FeO- total Fe as FeO.

	TS02-19		TS02-20			TS02-21a	TS02-23	TS02-26		TS02-28		TS02-29		TS02-30		TS02-32a
	pheng	pheng	pheng	pheng	parag	pheng	parag	parag	parag	parag	parag	parag	pheng	parag	pheng	pheng
Wt%																
SiO_2	49.66	49.11	49.61	49.74	46.29	50.13	45.57	46.96	46.51	45.73	45.97	46.46	54.27	46.17	53.89	48.86
TiO_2	0.36	0.30	0.46	0.00	0.00	0.41	0.00	0.16	0.00	0.00	0.00	0.00	0.00	0.00	0.34	0.00
Al_2O_3	26.89	26.51	27.81	27.71	39.66	27.77	39.14	38.90	39.38	38.94	38.90	39.44	23.15	39.30	22.85	29.53
FeO^*	2.51	2.92	1.97	2.37	0.39	2.42	0.28	0.59	0.40	0.21	0.46	0.31	1.58	0.28	1.56	1.61
MnO	0.00	0.00	0.00	0.00	0.00	0.00	0.00	0.00	0.00	0.00	0.00	0.00	0.00	0.00	0.00	0.00
MgO	3.18	3.32	3.44	3.23	0.00	3.20	0.00	0.00	0.00	0.00	0.00	0.00	5.07	0.00	4.96	2.93
CaO	0.00	0.00	0.00	0.00	0.20	0.00	0.29	0.24	0.28	0.29	0.32	0.30	0.00	0.34	0.00	0.00
Na_2O	0.56	0.64	0.89	0.87	7.60	0.77	7.94	7.58	6.99	7.07	7.14	6.19	0.34	6.48	0.36	1.13
K_2O	9.95	9.85	9.83	9.84	0.40	10.27	0.54	1.02	0.55	0.77	0.59	0.77	9.87	0.62	9.05	9.75
Cr_2O_3	0.00	0.00	0.00	0.00	0.00	0.00	0.00	0.00	0.00	0.00	0.00	0.00	0.00	0.00	0.00	0.00
Total	93.12	92.65	94.01	94.23	94.54	94.96	93.76	95.45	94.10	93.01	93.37	93.49	94.28	93.19	93.01	94.45
Si	6.78	6.76	6.70	6.73	5.96	6.72	5.93	6.02	6.00	5.98	5.99	6.02	7.24	6.01	7.25	6.60
Ti	0.04	0.03	0.05	0.00	0.00	0.04	0.00	0.02	0.00	0.00	0.00	0.00	0.00	0.00	0.03	0.00
Al	3.25	3.23	3.32	3.31	4.51	3.29	4.51	4.41	4.49	4.50	4.48	4.52	2.73	4.52	2.72	3.52
Fe^{2+}	0.14	0.17	0.11	0.13	0.02	0.14	0.02	0.03	0.02	0.01	0.03	0.02	0.09	0.02	0.09	0.09
Mn	0.00	0.00	0.00	0.00	0.00	0.00	0.00	0.00	0.00	0.00	0.00	0.00	0.00	0.00	0.00	0.00
Mg	0.32	0.34	0.35	0.33	0.00	0.32	0.00	0.00	0.00	0.00	0.00	0.00	0.50	0.00	0.50	0.29
Ca	0.00	0.00	0.00	0.00	0.01	0.00	0.02	0.02	0.02	0.02	0.02	0.02	0.00	0.02	0.00	0.00
Na	0.04	0.04	0.06	0.06	0.47	0.05	0.50	0.47	0.44	0.45	0.45	0.39	0.02	0.41	0.02	0.07
K	0.43	0.43	0.42	0.42	0.02	0.44	0.02	0.04	0.02	0.03	0.02	0.03	0.42	0.03	0.39	0.42
Cr	0.00	0.00	0.00	0.00	0.00	0.00	0.00	0.00	0.00	0.00	0.00	0.00	0.00	0.00	0.00	0.00

Table A2.4. continued.

	TS02-32a	TS02-33		TS02-34	TS02-35		TS02-36		TS02-38	TS02-41	TS02-42		TS02-46		TS02-47	
	pheng	pheng	pheng	parag	parag	pheng	parag	pheng	pheng	pheng	pheng	pheng	parag	pheng	parag	pheng
Wt%																
SiO_2	49.34	47.61	49.92	44.87	46.65	50.72	45.74	49.05	51.42	52.38	52.56	51.44	46.05	47.92	46.86	50.50
TiO_2	0.25	0.37	0.30	0.00	0.00	0.51	0.00	0.00	0.34	0.32	0.33	0.33	0.00	0.39	0.00	0.49
Al_2O_3	26.96	27.47	26.53	37.93	39.05	28.42	38.06	26.83	23.37	22.38	21.12	23.22	39.01	28.56	39.30	27.27
FeO^*	1.92	3.27	1.79	0.38	0.76	2.73	0.96	3.50	3.70	3.62	3.18	3.14	0.00	2.26	0.28	1.49
MnO	0.00	0.00	0.00	0.00	0.00	0.00	0.00	0.00	0.00	0.00	0.00	0.00	0.00	0.00	0.00	0.00
MgO	3.43	2.93	3.58	0.00	0.15	3.06	0.00	3.04	4.03	4.10	4.86	4.28	0.00	2.76	0.00	3.52
CaO	0.00	0.00	0.00	0.31	0.13	0.00	0.00	0.00	0.00	0.00	0.00	0.00	0.21	0.00	0.19	0.00
Na_2O	0.63	0.41	0.70	6.10	6.53	0.66	6.74	0.65	0.19	0.00	0.00	0.26	7.45	0.80	7.68	0.84
K_2O	9.60	8.28	10.17	0.71	0.88	9.54	0.79	9.98	10.01	10.48	11.09	11.06	0.78	9.99	0.31	9.88
Cr_2O_3	0.00	0.00	0.00	0.00	0.00	0.00	0.00	0.00	0.00	0.00	0.00	0.00	0.00	0.00	0.00	0.00
Total	92.48	90.33	93.00	90.30	94.16	95.64	92.29	93.45	93.06	93.29	93.14	93.72	93.50	92.68	94.61	93.99
Si	6.78	6.67	6.81	6.03	6.03	6.72	6.04	6.74	7.06	7.17	7.23	7.04	5.99	6.59	6.02	6.79
Ti	0.03	0.04	0.03	0.00	0.00	0.05	0.00	0.00	0.04	0.03	0.03	0.03	0.00	0.04	0.00	0.05
Al	3.27	3.40	3.20	4.50	4.46	3.33	4.44	3.26	2.83	2.71	2.57	2.81	4.49	3.47	4.46	3.24
Fe^{2+}	0.11	0.19	0.10	0.02	0.04	0.15	0.05	0.20	0.21	0.21	0.18	0.18	0.00	0.13	0.02	0.08
Mn	0.00	0.00	0.00	0.00	0.00	0.00	0.00	0.00	0.00	0.00	0.00	0.00	0.00	0.00	0.00	0.00
Mg	0.35	0.31	0.36	0.00	0.01	0.30	0.00	0.31	0.41	0.42	0.50	0.44	0.00	0.28	0.00	0.35
Ca	0.00	0.00	0.00	0.02	0.01	0.00	0.00	0.00	0.00	0.00	0.00	0.00	0.01	0.00	0.01	0.00
Na	0.04	0.03	0.05	0.40	0.41	0.04	0.43	0.04	0.01	0.00	0.00	0.02	0.47	0.05	0.48	0.05
K	0.42	0.37	0.44	0.03	0.04	0.40	0.03	0.44	0.44	0.46	0.49	0.48	0.03	0.44	0.01	0.42
Cr	0.00	0.00	0.00	0.00	0.00	0.00	0.00	0.00	0.00	0.00	0.00	0.00	0.00	0.00	0.00	0.00

Table A2.4. continued.

	TS02-48	TS02-50B		TS02-51b		TS02-52		TS02-53	TS02-54		TS02-55		TS02-56			TS02-57
	parag	parag	parag	parag	parag	parag	parag	parag	parag	parag	parag	parag	pheng	pheng	parag	parag
Wt%																
SiO_2	46.67	45.96	46.22	45.99	46.50	46.97	47.06	46.39	44.98	46.17	45.49	45.40	49.77	49.79	46.45	46.41
TiO_2	0.00	0.00	0.00	0.00	0.00	0.00	0.00	0.00	0.00	0.00	0.00	0.00	0.44	0.31	0.00	0.00
Al_2O_3	39.71	39.15	39.40	39.22	39.59	39.05	39.63	39.47	38.85	38.93	38.61	38.38	27.45	27.21	39.53	38.90
FeO^*	0.24	0.31	0.32	0.33	0.27	0.43	0.51	0.53	0.34	0.51	0.18	0.24	2.68	2.73	0.34	0.26
MnO	0.00	0.00	0.00	0.00	0.00	0.00	0.00	0.00	0.00	0.00	0.00	0.00	0.00	0.00	0.00	0.00
MgO	0.00	0.00	0.00	0.00	0.00	0.00	0.00	0.00	0.00	0.00	0.00	0.00	2.99	2.91	0.00	0.29
CaO	0.25	0.30	0.22	0.29	0.21	0.21	0.24	0.22	0.29	0.14	0.20	0.19	0.00	0.00	0.20	0.30
Na_2O	6.76	7.88	7.75	7.74	8.00	7.30	7.54	7.45	6.71	7.69	7.26	7.26	0.74	0.63	7.59	7.26
K_2O	0.43	0.38	0.42	0.46	0.49	0.78	0.81	0.46	0.42	0.49	0.60	0.34	10.09	10.29	0.26	1.02
Cr_2O_3	0.00	0.00	0.00	0.16	0.00	0.00	0.00	0.00	0.00	0.32	0.00	0.16	0.00	0.00	0.00	0.00
Total	94.06	93.98	94.34	94.18	95.07	94.75	95.79	94.52	91.58	94.25	92.35	91.99	94.15	93.87	94.36	94.44
Si	6.01	5.96	5.97	5.96	5.96	6.04	5.99	5.98	5.96	5.98	5.99	6.00	6.73	6.76	5.98	6.00
Ti	0.00	0.00	0.00	0.00	0.00	0.00	0.00	0.00	0.00	0.00	0.00	0.00	0.04	0.03	0.00	0.00
Al	4.52	4.49	4.50	4.49	4.49	4.44	4.46	4.50	4.55	4.46	4.50	4.48	3.28	3.27	4.50	4.44
Fe^{2+}	0.01	0.02	0.02	0.02	0.01	0.02	0.03	0.03	0.02	0.03	0.01	0.01	0.15	0.16	0.02	0.01
Mn	0.00	0.00	0.00	0.00	0.00	0.00	0.00	0.00	0.00	0.00	0.00	0.00	0.00	0.00	0.00	0.00
Mg	0.00	0.00	0.00	0.00	0.00	0.00	0.00	0.00	0.00	0.00	0.00	0.00	0.30	0.29	0.00	0.03
Ca	0.02	0.02	0.02	0.02	0.01	0.01	0.02	0.02	0.02	0.01	0.01	0.01	0.00	0.00	0.01	0.02
Na	0.42	0.50	0.49	0.49	0.50	0.45	0.47	0.47	0.43	0.48	0.46	0.46	0.05	0.04	0.47	0.45
K	0.02	0.02	0.02	0.02	0.02	0.03	0.03	0.02	0.02	0.02	0.03	0.01	0.44	0.45	0.01	0.04
Cr	0.00	0.00	0.00	0.01	0.00	0.00	0.00	0.00	0.00	0.02	0.00	0.01	0.00	0.00	0.00	0.00

Table A2.4. continued.

	TS02-57	105-1		106-3		106-14	110-3		117-1	984-1		984-1	Q02-02	Q02-05		Q02-08
	parag	pheng	parag	pheng	pheng	parag	pheng	pheng	parag	parag	parag	pheng	pheng	pheng	pheng	pheng
Wt%																
SiO_2	45.98	49.89	46.12	49.86	50.27	45.60	50.24	54.25	46.37	45.21	45.32	51.92	49.36	49.37	49.48	49.85
TiO_2	0.00	0.49	0.21	0.46	0.27	0.00	0.31	0.22	0.00	0.00	0.00	0.20	0.36	0.29	0.23	0.00
Al_2O_3	38.51	25.29	38.80	25.38	27.42	38.39	26.63	21.76	39.01	37.78	38.42	27.65	27.90	26.70	26.86	26.31
FeO^*	0.32	1.64	0.23	2.59	2.40	0.50	2.78	3.42	0.43	0.39	0.25	2.59	1.89	1.81	1.75	2.78
MnO	0.00	0.00	0.00	0.00	0.00	0.00	0.00	0.00	0.00	0.00	0.00	0.00	0.00	0.00	0.00	0.00
MgO	0.31	3.97	0.00	3.86	3.47	0.16	3.63	5.14	0.00	0.00	0.00	3.02	3.20	3.41	3.62	3.44
CaO	0.27	0.00	0.18	0.00	0.16	0.14	0.00	0.00	0.17	0.15	0.22	0.00	0.00	0.00	0.00	0.17
Na_2O	6.85	0.47	7.53	0.39	0.69	6.89	0.60	0.22	7.54	7.64	7.52	1.45	0.56	0.64	0.61	0.72
K_2O	0.44	10.43	0.50	10.59	9.94	0.85	10.46	11.00	0.48	0.40	0.25	10.21	10.23	9.83	9.76	10.06
Cr_2O_3	0.17	0.00	0.00	0.19	0.00	0.00	0.00	0.00	0.00	0.20	0.00	0.00	0.00	0.00	0.21	0.00
Total	92.86	92.18	93.57	93.32	95.08	92.52	94.66	96.01	94.01	91.77	91.99	97.03	93.52	92.05	92.53	93.34
Si	6.01	6.88	6.00	6.83	6.74	6.00	6.78	7.23	6.01	6.01	5.99	6.81	6.70	6.79	6.77	6.81
Ti	0.00	0.05	0.02	0.05	0.03	0.00	0.03	0.02	0.00	0.00	0.00	0.02	0.04	0.03	0.02	0.00
Al	4.45	3.08	4.46	3.07	3.25	4.47	3.18	2.56	4.47	4.44	4.49	3.21	3.35	3.25	3.25	3.18
Fe^{2+}	0.02	0.09	0.01	0.15	0.13	0.03	0.16	0.19	0.02	0.02	0.01	0.14	0.11	0.10	0.10	0.16
Mn	0.00	0.00	0.00	0.00	0.00	0.00	0.00	0.00	0.00	0.00	0.00	0.00	0.00	0.00	0.00	0.00
Mg	0.03	0.41	0.00	0.39	0.35	0.02	0.37	0.51	0.00	0.00	0.00	0.30	0.32	0.35	0.37	0.35
Ca	0.02	0.00	0.01	0.00	0.01	0.01	0.00	0.00	0.01	0.01	0.02	0.00	0.00	0.00	0.00	0.01
Na	0.43	0.03	0.47	0.03	0.04	0.44	0.04	0.01	0.47	0.49	0.48	0.09	0.04	0.04	0.04	0.05
K	0.02	0.46	0.02	0.46	0.43	0.04	0.45	0.47	0.02	0.02	0.01	0.43	0.44	0.43	0.43	0.44
Cr	0.01	0.00	0.00	0.02	0.00	0.00	0.00	0.00	0.00	0.02	0.00	0.00	0.00	0.00	0.02	0.00

Table A2.4. continued.

	Q02-08	Q02-10A	Q02-11	Q02-22		Q98-120	Q98-126	Q98-127		Q98-143	Q98-150	Q98-152
	pheng	pheng	pheng	pheng	pheng	pheng	pheng	pheng	pheng	pheng	pheng	pheng
Wt%												
SiO_2	48.49	50.97	50.11	48.46	49.68	49.58	50.24	48.82	50.14	51.94	51.81	49.59
TiO_2	0.00	0.29	0.29	0.24	0.35	0.00	0.00	0.30	0.34	0.23	0.23	0.42
Al_2O_3	25.98	23.67	26.55	27.45	27.73	27.65	27.29	26.23	26.04	28.97	27.48	25.88
FeO^*	2.10	2.81	3.22	3.27	3.28	2.78	2.70	3.60	2.18	3.82	3.19	4.66
MnO	0.00	0.00	0.00	0.00	0.00	0.00	0.00	0.00	0.00	0.00	0.00	0.00
MgO	3.62	4.26	3.37	2.51	2.69	3.04	3.46	3.10	3.73	2.49	3.39	3.00
CaO	0.00	0.00	0.00	0.00	0.00	0.00	0.00	0.00	0.00	0.00	0.00	0.00
Na_2O	0.62	0.27	0.97	0.71	0.48	0.63	0.61	0.41	0.68	0.44	0.57	0.37
K_2O	9.96	10.53	10.40	10.25	10.51	10.23	10.45	10.36	10.67	10.81	10.42	10.62
Cr_2O_3	0.00	0.00	0.00	0.00	0.00	0.00	0.00	0.00	0.00	0.00	0.00	0.00
Total	91.18	92.80	94.92	92.89	94.72	94.23	94.75	92.83	93.78	98.70	97.08	94.54
Si	6.79	7.01	6.77	6.68	6.71	6.73	6.76	6.75	6.82	6.73	6.81	6.77
Ti	0.00	0.03	0.03	0.02	0.04	0.00	0.00	0.03	0.03	0.02	0.02	0.04
Al	3.22	2.88	3.17	3.35	3.31	3.32	3.25	3.21	3.13	3.32	3.19	3.12
Fe^{2+}	0.12	0.16	0.18	0.19	0.19	0.16	0.15	0.21	0.12	0.21	0.18	0.27
Mn	0.00	0.00	0.00	0.00	0.00	0.00	0.00	0.00	0.00	0.00	0.00	0.00
Mg	0.38	0.44	0.34	0.26	0.27	0.31	0.35	0.32	0.38	0.24	0.33	0.31
Ca	0.00	0.00	0.00	0.00	0.00	0.00	0.00	0.00	0.00	0.00	0.00	0.00
Na	0.04	0.02	0.06	0.05	0.03	0.04	0.04	0.03	0.04	0.03	0.04	0.02
K	0.45	0.46	0.45	0.45	0.45	0.44	0.45	0.46	0.46	0.45	0.44	0.46
Cr	0.00	0.00	0.00	0.00	0.00	0.00	0.00	0.00	0.00	0.00	0.00	0.00

Table A2.4. continued.

	TS02-01		TS02-02	TS02-05		TS02-6	TS02-11	TS02-13	TS02-16	TS02-17b	TS02-23		TS02-26	TS02-27	TS02-27	TS02-28
	zoisite	zoisite	zoisite	zoisite	zoisite	zoisite	zoisite	zoisite	zoisite	zoisite	zoisite	zoisite	zoisite	zoisite	zoisite	zoisite
Wt%																
SiO_2	36.94	37.29	37.32	37.72	37.86	36.92	38.80	37.41	37.56	38.35	38.91	39.21	38.31	39.09	37.21	38.13
TiO_2	0.00	0.00	0.00	0.00	0.00	0.00	0.24	0.20	0.21	0.00	0.00	0.00	0.20	0.00	0.00	0.25
Al_2O_3	23.39	22.83	26.06	24.80	25.91	23.18	28.07	26.31	25.41	26.25	32.31	32.07	28.91	32.30	23.94	28.45
FeO^*	13.74	13.30	9.03	10.65	9.24	12.69	6.59	7.57	10.30	8.55	1.47	1.98	5.83	1.54	11.06	5.72
MnO	0.00	0.00	0.00	0.00	0.00	0.00	0.00	0.00	0.00	0.00	0.00	0.00	0.00	0.00	0.00	0.00
MgO	0.00	0.00	0.00	0.00	0.00	0.00	0.00	0.00	0.00	0.00	0.00	0.00	0.22	0.00	0.00	0.00
CaO	22.64	22.63	23.41	23.47	24.19	23.02	24.53	23.95	23.62	24.18	25.38	25.12	24.21	25.26	23.86	24.02
Na_2O	0.00	0.00	0.00	0.00	0.00	0.00	0.00	0.00	0.00	0.00	0.00	0.00	0.00	0.00	0.00	0.00
K_2O	0.00	0.00	0.00	0.00	0.00	0.00	0.22	0.00	0.00	0.00	0.00	0.00	0.00	0.00	0.00	0.00
Cr_2O_3	0.00	0.00	0.00	0.00	0.00	0.00	0.18	0.00	0.00	0.00	0.00	0.00	0.00	0.00	0.00	0.00
Total	96.71	96.05	95.82	96.64	97.20	95.81	98.63	95.44	97.09	97.33	98.07	98.38	97.68	98.19	96.07	96.57
Si	5.96	6.05	5.98	6.03	6.00	6.00	6.00	6.00	5.97	6.04	5.94	5.97	5.95	5.96	6.01	5.99
Ti	0.00	0.00	0.00	0.00	0.00	0.00	0.03	0.02	0.03	0.00	0.00	0.00	0.02	0.00	0.00	0.03
Al	3.33	3.27	3.69	3.50	3.63	3.33	3.84	3.73	3.57	3.66	4.36	4.31	3.97	4.35	3.42	3.95
Fe^{2+}	1.25	1.22	0.82	0.96	0.83	1.16	0.57	0.69	0.92	0.76	0.13	0.17	0.51	0.13	1.01	0.51
Mn	0.00	0.00	0.00	0.00	0.00	0.00	0.00	0.00	0.00	0.00	0.00	0.00	0.00	0.00	0.00	0.00
Mg	0.00	0.00	0.00	0.00	0.00	0.00	0.00	0.00	0.00	0.00	0.00	0.00	0.03	0.00	0.00	0.00
Ca	1.96	1.97	2.01	2.01	2.05	2.00	2.03	2.06	2.01	2.04	2.08	2.05	2.02	2.06	2.06	2.02
Na	0.00	0.00	0.00	0.00	0.00	0.00	0.02	0.00	0.00	0.00	0.00	0.00	0.00	0.00	0.00	0.00
K	0.00	0.00	0.00	0.00	0.00	0.00	0.00	0.00	0.00	0.00	0.00	0.00	0.00	0.00	0.00	0.00
Cr	0.00	0.00	0.00	0.00	0.00	0.00	0.02	0.00	0.00	0.00	0.00	0.00	0.00	0.00	0.00	0.00

Table A2.5. Results of SEM EDS analysis of epidote group minerals. Oxygen by stoichiometry. Epidote or clinozoisite/zoisite formula calculation based on 12.5 oxygens. FeO- total Fe as FeO.

	TS02-28	TS02-29	TS02-32		TS02-34	TS02-35		TS02-36	TS02-38	TS02-41	TS02-42	TS02-43	TS02-46	TS02-47	TS02-48	TS02-50B
	zoisite	zoisite	zoisite	zoisite	zoisite	zoisite	zoisite	zoisite	zoisite	zoisite	zoisite	zoisite	zoisite	zoisite	zoisite	zoisite
Wt%																
SiO_2	37.99	38.57	38.44	38.73	38.70	38.25	38.67	37.42	37.58	37.07	37.58	38.39	38.05	38.28	38.46	38.16
TiO_2	0.31	0.19	0.00	0.00	0.00	0.00	0.00	0.00	0.27	0.00	0.00	0.27	0.00	0.26	0.31	0.00
Al_2O_3	28.69	29.62	31.81	32.21	30.92	25.64	27.33	24.31	26.04	25.65	25.69	27.93	29.56	27.75	29.08	27.26
FeO^*	6.01	5.29	1.31	1.35	1.83	10.14	8.85	11.91	9.08	9.15	9.39	6.01	4.58	6.92	5.28	7.88
MnO	0.00	0.00	0.00	0.00	0.00	0.00	0.00	0.00	0.00	0.00	0.00	0.00	0.00	0.00	0.00	0.00
MgO	0.00	0.00	0.00	0.00	0.00	0.00	0.00	0.00	0.00	0.00	0.00	0.00	0.00	0.00	0.00	0.00
CaO	24.08	24.32	24.62	25.02	24.47	23.60	23.95	23.18	23.59	23.08	23.77	24.04	24.21	24.26	24.29	23.89
Na_2O	0.00	0.00	0.00	0.00	0.00	0.00	0.00	0.00	0.00	0.00	0.00	0.00	0.00	0.00	0.00	0.00
K_2O	0.00	0.00	0.00	0.00	0.00	0.00	0.00	0.00	0.00	0.00	0.00	0.00	0.00	0.00	0.00	0.00
Cr_2O_3	0.00	0.00	0.00	0.00	0.27	0.00	0.00	0.00	0.00	0.00	0.00	0.00	0.00	0.00	0.00	0.00
Total	97.08	97.99	96.18	97.31	96.19	97.63	98.80	96.82	96.56	94.95	96.43	96.64	96.40	97.47	97.42	97.19
Si	5.94	5.96	5.97	5.95	6.02	6.03	5.99	5.99	5.98	6.00	6.00	6.03	5.96	5.99	5.98	6.00
Ti	0.04	0.02	0.00	0.00	0.00	0.00	0.00	0.00	0.03	0.00	0.00	0.03	0.00	0.03	0.04	0.00
Al	3.97	4.05	4.37	4.37	4.25	3.57	3.74	3.44	3.66	3.67	3.62	3.88	4.10	3.84	4.00	3.79
Fe^{2+}	0.53	0.46	0.11	0.12	0.16	0.90	0.77	1.08	0.82	0.84	0.85	0.53	0.41	0.61	0.46	0.70
Mn	0.00	0.00	0.00	0.00	0.00	0.00	0.00	0.00	0.00	0.00	0.00	0.00	0.00	0.00	0.00	0.00
Mg	0.00	0.00	0.00	0.00	0.00	0.00	0.00	0.00	0.00	0.00	0.00	0.00	0.00	0.00	0.00	0.00
Ca	2.02	2.01	2.05	2.06	2.04	1.99	1.99	1.99	2.01	2.00	2.03	2.02	2.03	2.03	2.02	2.01
Na	0.00	0.00	0.00	0.00	0.00	0.00	0.00	0.00	0.00	0.00	0.00	0.00	0.00	0.00	0.00	0.00
K	0.00	0.00	0.00	0.00	0.00	0.00	0.00	0.00	0.00	0.00	0.00	0.00	0.00	0.00	0.00	0.00
Cr	0.00	0.00	0.00	0.00	0.02	0.00	0.00	0.00	0.00	0.00	0.00	0.00	0.00	0.00	0.00	0.00

Table A2.5. continued.

	TS02-50B	TS02-51b	TS02-52		TS02-54		TS02-55		TS02-57		TS02-58A		TS02-62		105-1	
	zoisite	zoisite	zoisite	zoisite	zoisite	zoisite	zoisite	zoisite	zoisite	zoisite	zoisite	zoisite	zoisite	zoisite	zoisite	zoisite
Wt%																
SiO_2	38.22	38.47	37.79	38.35	38.11	38.69	38.31	37.80	38.06	38.09	37.49	38.30	37.18	37.05	37.58	38.49
TiO_2	0.00	0.28	0.18	0.00	0.00	0.21	0.20	0.18	0.17	0.40	0.22	0.00	0.20	0.00	0.00	0.17
Al_2O_3	27.56	29.43	26.74	26.82	28.56	28.98	31.94	29.18	29.16	29.26	28.43	28.50	23.35	24.83	28.56	29.10
FeO^*	7.26	5.29	8.67	8.53	6.26	5.84	1.40	4.69	5.01	4.75	6.17	6.17	12.02	10.29	5.47	5.09
MnO	0.00	0.00	0.00	0.00	0.00	0.00	0.00	0.00	0.00	0.00	0.00	0.00	0.00	0.00	0.00	0.00
MgO	0.00	0.00	0.00	0.00	0.00	0.00	0.00	0.00	0.00	0.00	0.00	0.00	0.00	0.00	0.00	0.00
CaO	24.09	24.52	23.37	23.52	23.86	24.38	25.02	24.41	24.67	24.63	24.22	24.34	22.98	23.78	23.72	23.91
Na_2O	0.00	0.00	0.00	0.00	0.00	0.00	0.00	0.00	0.00	0.00	0.00	0.00	0.00	0.00	0.00	0.00
K_2O	0.00	0.00	0.00	0.00	0.00	0.00	0.00	0.00	0.00	0.00	0.00	0.00	0.00	0.00	0.00	0.00
Cr_2O_3	0.00	0.00	0.17	0.00	0.21	0.19	0.24	0.00	0.00	0.29	0.00	0.00	0.00	0.00	0.00	0.00
Total	97.13	97.99	96.92	97.22	97.00	98.29	97.11	96.26	97.07	97.42	96.53	97.31	95.73	95.95	95.33	96.76
Si	6.00	5.95	5.97	6.03	5.97	5.98	5.91	5.95	5.95	5.93	5.91	5.98	6.03	5.97	5.97	6.01
Ti	0.00	0.03	0.02	0.00	0.00	0.02	0.02	0.02	0.02	0.05	0.03	0.00	0.02	0.00	0.00	0.02
Al	3.83	4.02	3.74	3.73	3.95	3.96	4.36	4.06	4.03	4.03	3.96	3.94	3.35	3.54	4.01	4.02
Fe^{2+}	0.64	0.46	0.77	0.76	0.55	0.51	0.12	0.42	0.44	0.42	0.55	0.54	1.10	0.94	0.49	0.45
Mn	0.00	0.00	0.00	0.00	0.00	0.00	0.00	0.00	0.00	0.00	0.00	0.00	0.00	0.00	0.00	0.00
Mg	0.00	0.00	0.00	0.00	0.00	0.00	0.00	0.00	0.00	0.00	0.00	0.00	0.00	0.00	0.00	0.00
Ca	2.03	2.03	1.98	1.98	2.00	2.02	2.07	2.06	2.06	2.05	2.05	2.04	2.00	2.05	2.02	2.00
Na	0.00	0.00	0.00	0.00	0.00	0.00	0.00	0.00	0.00	0.00	0.00	0.00	0.00	0.00	0.00	0.00
K	0.00	0.00	0.00	0.00	0.00	0.00	0.00	0.00	0.00	0.00	0.00	0.00	0.00	0.00	0.00	0.00
Cr	0.00	0.00	0.02	0.00	0.02	0.02	0.02	0.00	0.00	0.03	0.00	0.00	0.00	0.00	0.00	0.00

Table A2.5. continued.

	106-3	106-3	110-3		117-1	984-1	Q02-02		Q08-08		Q02-10A		Q02-22		Q98-120	Q98-126
	zoisite	zoisite	zoisite	zoisite	zoisite	zoisite	epidote	epidote	epidote	epidote	epidote	epidote	epidote	epidote	epidote	epidote
Wt%																
SiO_2	38.29	37.35	38.00	38.18	38.36	38.02	37.46	37.54	37.72	37.78	24.70	38.06	37.33	37.42	37.69	38.60
TiO_2	0.22	0.00	0.00	0.00	0.34	0.19	0.00	0.00	0.00	0.00	0.00	0.00	0.00	0.00	0.00	0.00
Al_2O_3	28.83	25.90	26.07	26.62	26.81	28.44	27.09	26.82	23.55	26.04	7.55	27.59	24.06	24.85	25.86	28.30
FeO^*	5.93	8.63	10.02	9.38	8.49	5.79	7.02	6.97	11.90	9.16	6.84	7.03	11.53	10.58	9.25	7.20
MnO	0.00	0.00	0.00	0.00	0.00	0.19	0.00	0.00	0.25	0.00	0.00	0.00	0.00	0.00	0.00	0.00
MgO	0.00	0.00	0.00	0.00	0.00	0.00	0.00	0.00	0.00	0.43	5.36	0.00	0.00	0.00	0.00	0.00
CaO	24.22	23.65	23.53	23.96	23.96	24.14	23.94	23.48	23.47	22.17	2.89	23.79	23.46	23.75	23.45	23.95
Na_2O	0.00	0.00	0.00	0.00	0.00	0.00	0.00	0.00	0.00	0.17	0.00	0.00	0.00	0.00	0.00	0.00
K_2O	0.00	0.00	0.00	0.00	0.00	0.00	0.00	0.00	0.00	0.00	0.00	0.00	0.00	0.00	0.00	0.00
Cr_2O_3	0.00	0.00	0.00	0.00	0.00	0.00	0.00	0.00	0.30	0.37	0.00	0.22	0.00	0.19	0.26	0.00
Total	97.49	95.53	97.62	98.14	97.95	96.77	95.51	94.81	97.19	96.12	47.35	96.69	96.38	96.79	96.53	98.04
Si	5.96	6.00	5.99	5.98	6.00	5.97	5.99	6.03	6.04	6.02	7.57	6.00	6.01	5.98	6.00	5.99
Ti	0.03	0.00	0.00	0.00	0.04	0.02	0.00	0.00	0.00	0.00	0.00	0.00	0.00	0.00	0.00	0.00
Al	3.97	3.68	3.63	3.68	3.71	3.95	3.83	3.81	3.33	3.67	2.05	3.84	3.42	3.51	3.64	3.88
Fe^{2+}	0.52	0.78	0.89	0.83	0.75	0.51	0.63	0.63	1.07	0.82	1.18	0.63	1.05	0.95	0.83	0.63
Mn	0.00	0.00	0.00	0.00	0.00	0.01	0.00	0.00	0.02	0.00	0.00	0.00	0.00	0.00	0.00	0.00
Mg	0.00	0.00	0.00	0.00	0.00	0.00	0.00	0.00	0.00	0.05	1.22	0.00	0.00	0.00	0.00	0.00
Ca	2.02	2.04	1.99	2.01	2.01	2.03	2.05	2.02	2.01	1.89	0.47	2.01	2.02	2.03	2.00	1.99
Na	0.00	0.00	0.00	0.00	0.00	0.00	0.00	0.00	0.00	0.00	0.00	0.00	0.00	0.00	0.00	0.00
K	0.00	0.00	0.00	0.00	0.00	0.00	0.00	0.00	0.00	0.01	0.00	0.00	0.00	0.00	0.00	0.00
Cr	0.00	0.00	0.00	0.00	0.00	0.00	0.00	0.00	0.03	0.03	0.00	0.02	0.00	0.02	0.02	0.00

Table A2.5. continued.

	Q98-127		Q98-128	Q98-149	Q98-150	Q08-152	
	epidote	epidote	epidote	epidote	epidote	epidote	epidote
Wt%							
SiO_2	37.18	36.00	36.63	37.48	37.31	37.90	37.41
TiO_2	0.21	0.00	0.23	0.25	0.00	0.22	0.00
Al_2O_3	24.81	21.48	25.69	24.16	26.20	24.15	23.56
FeO*	11.10	13.55	8.97	11.10	8.25	12.02	12.81
MnO	0.00	0.17	0.00	0.48	0.00	0.00	0.00
MgO	0.00	0.00	0.00	0.00	0.00	0.00	0.00
CaO	23.52	23.18	23.21	23.56	23.49	23.76	23.35
Na_2O	0.00	0.00	0.00	0.00	0.00	0.00	0.00
K_2O	0.00	0.00	0.00	0.00	0.00	0.00	0.00
Cr_2O_3	0.17	0.00	0.00	0.00	0.18	0.00	0.00
Total	97.00	94.38	94.73	97.02	95.42	98.05	97.13
Si	5.94	5.99	5.95	6.00	5.99	6.00	6.00
Ti	0.03	0.00	0.03	0.03	0.00	0.03	0.00
Al	3.50	3.16	3.69	3.42	3.72	3.38	3.34
Fe^{2+}	1.00	1.27	0.82	1.00	0.75	1.07	1.16
Mn	0.00	0.01	0.00	0.03	0.00	0.00	0.00
Mg	0.00	0.00	0.00	0.00	0.00	0.00	0.00
Ca	2.01	2.07	2.02	2.02	2.02	2.02	2.01
Na	0.00	0.00	0.00	0.00	0.00	0.00	0.00
K	0.00	0.00	0.00	0.00	0.00	0.00	0.00
Cr	0.02	0.00	0.00	0.00	0.02	0.00	0.00

Table A2.5. continued.

REFERENCES

Ague, J. J., 2003. Fluid flow in the deep crust, pp. 195-228. In. The Crust (ed Rudnick, R. L.) Vol. 3 treatise on Geochemistry (eds Holland, H. D. and Turekian, K. K.) Elsevier-Pergamon, Oxford

Allègre, C. J., Hamelin, B., Provost, A. & Dupre, B., 1987. Topology in isotopic multispace and origin of the mantle chemical heterogeneities. Earth Planet. Sci. Lett. 81, 319-337.

Allen, M.B., Windley, B.F., Zhang, C., 1992. Palaezoic collisional tectonics and magmatism of the Chinese Tian Shan, central Asia. Tectonophysics 220, 89-115.

Alt, J.C., 1995. Subseafloor processes in mid-ocean ridge hydrothermal systems. In Seafloor Hydrothermal Systems: Physical, Chemical, Biological and Geological Interactions ed. SE Humphries, RE Zierenberg, LS Mullineaux, RE Thomson. Geophys. Monogr. Ser. 91:85-114. Am. Geophys Union, Washington DC. (N)

Arculus, R.J., Lapierre, H., Jaillard, E., 1999. Geochemical window into subduction and accretion processes: Rapas metamorphic complex, Ecuador. Geology 27, 547-550.

Bailey, E.H., Ragnarsdottir, K.V., 1994. Uranium and thorium solubilities in subduction zone fluids. EPSL 124, 119-129.

Barnicoat, A.C., Fry, N., 1986. High-pressure metamorphism of the Zermatt-Saas ophiolite zone, Switzerland. J. Geol. Soc. (London) 143, 607-618.

Barrett, T.J., and Jarvis, I., 1988. Rare Earth Element geochemistry of metalliferous sediments from DSDP Leg 92: The East Pacific Rise. Chemical Geology 67, 249-259.

Batiza, R., 1982. Abundances, distribution and sizes of volcanoes in the Pacific Ocean and implications for the origin of non-hotspot volcanoes. EPSL 60, 195-206.

Bebout, G.E., 1995. The impact of subduction zone metamorphism on mantle-ocean cycling. Chemical Geology 126, 191-218.

Bebout, G.E., 1997. Nitrogen isotope tracers of high-temperature fluid-rock interactions: Case study of the Catalina schist, California. EPSL 151, 77-90.

Bebout, G.E., Barton, M.D., 1989. Fluid flow and metasomatism in a subduction zone hydrothermal system: Catalina Schist terrane, California. Geology 17, 976-980.

Bebout, G.E., Barton, M.D., 1993. Metasomatism during subduction: products and possible paths in the Catalina Schist, California. Chemical Geology 108, 61-92.

Bebout, G.E., Ryan, J.G, Leeman, W.P., 1992. B-Be systematics in subduction-related metamorphic rocks: Charcterization of the subducted component. Geochim. Cosmochim. Acta 57, 2227-2237.

Bebout, G.E., Ryan, J.G., Leeman, W.P., Bebout, A.E., 1999. Fractionation of trace elements by subduction-zone metamorphism- effect of convergent-margin thermal evolution. EPSL 171, 63-81.

Bebout, G.E., and Barton, M.D., 2002, Tectonic and metasomatic mixing in a high-T, subduction zone melange- Insights into the geochemical evolution of the slab-mantle interface: Chemical Geology, v. 187, p. 79–106.

Becker, H., 2000. Re-Os fractionation in eclogites and blueschists and the implications for recycling of oceanic crust into the mantle. EPSL 177, 287-300.

Becker, H., Jochum, K.P, Carlson, R.W., 1999. Constraints from high-pressure veins in eclogites on the composition of hydrous fluids in subduction zones. Chemical Geology 160, 291-308.

Becker, H., Jochum, K.P., Carlson, R.W., 2000. Trace element fractionation during dehydration of eclogites from high-pressure terranes and the implications for element fluxes in subductiuon zones. Chemical Geology 163, 65-99.

Ben Othman, D., White, W.M., Patchet, J., 1989. The geochemistry of marine sediments, island arc magma genesis, and crust-mantle recycling. EPSL 94, 1-21.

Bhatia, M., Crook, K.A.W., 1986. Trace element characteristics of grawackes and tectonic discrimination of sedimentary basins. Contrib. Mineral Petrol 92, 181-193.

Bohrson, W.A., Reid, M.R., 1995. Petrogensis of alkaline basalts from Socorro Island, Mexio: Trace element evidence for contamination of ocean island basalt in the shallow ocean crust. J. Geophys. Res 100,

24555-24576.

Boutelier, D., Chemenda, A., Burg, J-P., 2003. Subduction Versus Accretion of Intra-Oceanic Volcanic Arcs: Insight from Thermo-Mechanical Analogue Experiments. EPSL 212, 31-45.

Breeding, C.M., Ague, J.J., Broker, M., 2004. Fluid-metasedimentary rock interactions in subduction-zone melange: Implications for the chemical composition of arc magmas. Geology 32, 1041-1044.

Brenan, J.M., Ryerson, F.J., Shaw, H.F., 1998. The role of aqueous fluids in the slab-to-mantle transfer of boron, beryllium, and lithium during subduction: Experiments and models. Geochim.Cosmochim.Acta 62 No. 19/20, 3337-3347. (N)

Brenan, J.M., Shaw, H.F., Phinney, D.L., Ryerson, F.J., 1994. Rutile-aqueous fluid partitioning of Nb, Ta, Hf, U and Th: Implications for high field strength element depletions in island-arc basalts. EPSL 128, 327-339.

Brenan, J.M., Shaw, H.F., Ryerson, F.J., Phinney, D.L., 1995. Mineral-aqueous fluid partitioning of trace elements at 900°C and 2.0GPa: Constraints on the trace element chemistry of deep crustal fluids. Geochim.Cosmochim.Acta 59, 3331-3350.

Brooking, D.G., Rehacek, J., Morris, G., 1999. Data Report: Major and Trace Element Composition, Strontium, Neodymium, and Oxygen Isotope Ratios, and Mineral Compositions of Samples. Proc. Ocean Drill. Program Scient. Results 163, 113-117.

Brunsman, A., Franz, G., Erzinger, J., 2001. REE mobilization during small-scale high-pressure fluid-rock interaction and zoisite/fluid partioning of La to Eu. Geochim.Cosmochim.Acta 65, 559-570.

Burtman, V. S., 1975. Structural geology of the Variscan Tien Shan, USSR. American Journal of Science, 275A, 157–186.

Burrett, C. F., 1974. Plate tectonics and the fusion of Asia. Earth and Planetary Science Letters, 21, 181–189.

Busigny, V., Cartigny, P., Philippot, P., Ader, M., Javoy, M., 2003. Massive Recycling of Nitrogen and other fluid-mobile elements (K, RB, Cs, H) in a cold slab environment: Evidence from HP to UHP oceanic metasediments of the Schistes Lustres Nappe (Western Alps, Europe). EPSL 215, 27-42.

Cann, J.R., 1970. Rb, Sr, Y, Zr and Nb in some ocean floor basaltic rocks. EPSL 10, 7-11.

Carroll, A.R., Liang, Y., Graham, S., Xiao, X., Hendrix, M.S.. Chu, J., McKnight, C.L., 1990. Junggar basin, northwest China: trapped Late Paleozoic ocean. Tectonophysics 186, 1-14.

Carswell, D. A. (1990). Eclogites and the eclogite facies: definitions and classification. In: Carswell, D. A. (ed.) Eclogite Facies Rocks. New York: Chapman & Hall, pp. 1–13.

Castelli, D., Rubatto, D., 2002. Stability of Al- and F-rich titanite in metacarbonate: petrologic and isotopic constraints from a polymetamorphic eclogitic marble of the internal Sesia Zone (Western Alps). Contrib. Mineral Petrol 142, 627-639.

Chalot-Prat, F., Ganne, J., Lombard, A., 2003. No Significant Element Transfer from the Oceanic plate to the mantle Wedge during Subduction and Exhumation of the Tethys Lithosphere (Western Alps). Lithos 69, 69-103.

Chauvel, C., Hofmann, A.W., Vidal, P., 1992. HIMU-EM: The French Polynesian connection. EPSL 110, 99-119.

Chopin, C., 1984. Coesite and pure pyrope in high grade pelitic blueschists of the western Alps. Journal of Petrology 22, 628-650.

Cingolani, C.S., Manassero, M., Abre, P., 2003. Composition, provenance, and tectonic setting of Ordovician siliciclastic rocks in the San Rafael block: Southern extension of the Precordillera crustal fragment, Argentina. Journal of South American Earth Sciences 16, 91-106.

Cloos, M., 1982. Flow melanges: numerical modelling and geologic constraints on their origin in the Franciscan subduction complex, California. Geological Society of America Bulletin 93, 330-345.

Cloos, M., 1993. Lithospheric Buoyancy and Collisional Orogenesis: Subduction of Oceanic Plateaus, Continental Margin, Island Arcs, Spreading Ridges and Seamounts. Geological Society of America Bulletin 105, 715-737.

Coleman, R.G., Lee, D.E., Beatty, L.G., Branok, W.E., 1965. Eclogites and eclogites- their differences and similarities. Geological Society of America Bulletin, 76, 483-508.

Conrey, R.M., Sherrod, D.R., Hooper, P.R., Swanson, D.A., 1997. Diverse primative magmas in the Cascades Arc, Northern Oregon and Southern Washington. Can. Mineral. 35, 367-396.

Cruciani, G., Franceschelli, M., Marchi, M., Zucca, M., 2002. Geochemiistry of metabasites from NE Sardinia, Italy:nature of the protoliths, magmatic trend, and geotectonic setting. Mineralogy and Petrology 74, 25-47.

Cullers, R.L., 2000. The geochemistry of shales, siltstones and sandstones of Pennsylvanian-Permian age, Colorado, USA: implications for provenance and metamorphic studies. Lithos 51, 181-203.

Dickin, Alan P., 1995. Radiogenic Isotope Geology, Cambridge University Press

Diegor, W., Longerich, H., Abrajano, T., Horn, I., 2001. Applicability of a high pressure digestion technique to the analysis of sediment and soil samples by inductively coupled plasma-mass spectrometry. Analytica Chimica Acta 431, 195-207.

Dobretsov, N.L., 2000. Collision Processesin Paleozoic Foldbelts of Asia and Exhumation Mechanisms. Petrology 8(5), 451-476.

Domanik, K.J., Hervig, R.L., Peacock, S.M., 1993. Beryllium and born in subduction zone minerals - an ion microprobe study. Geochim.Cosmochim.Acta 57 (21-22), 4997-5010.

Domanik, K.J., Holloway, J.R., 1996. The stability and composition of phengitic muscovite and associated phases from 5.5 to 11GPa: implications for deeply subducted sediments. Geochim.Cosmochim.Acta 60, 4133-4150.

Domanik, K.J. and Holloway, J.R., 2000. Experimental synthesis and phase relations of phengitic muscovite from 6.5 to 11 GPa in a calcareous metapelite from the Dabie Mountains, China. Lithos, 52, 51-77.

Doucet, S., Weis, D., Scoates, J.S., Nicolaysen, K., Frey, A., Giret, L., 2002. The Depleted Mantle Component in Kerguelen Archipelago Basalts: Petrogenesis of Tholeiitic-Transitional Basalts from the Loranchet Peninsula. Journal of Petrology 43, 1341-1366.

Dupre, B., Lambret, B, Allegre, C.J., 1982. Isotopic variations within a single oceanic island – The Terceira case. Nature, 299, 620-622

Elderfield, H., and Greaves, M.J., 1982. The rare earth elements in seawater. Nature 296, 214-219.

Ellam, R.M., Upton, B.G.J., Upton, J.G., 1998. Petrogenesis of late stage magmatism at Hold with Hope, East Greenland. Contrib. Mineral Petrol 133, 51-59.

Ellis, D.J., and Green, D.H., 1979. An experimental study of the effect of Ca upon garnet-clinopyroxene Fe-Mg exchange equilibria. Contrib. Min. Petrol., 71: 13-22.

Elliott, T., Plank, T., Zindler, A., White, W., Bourdon, B., 1997. Element transport from slab to volcanic front at the Mariana arc. J. Geophys. Res 102, 14991-15019.

El-Shazly, A.K., Sisson, V.B., 1999. Retrograde evolution of eclogite facies rocks from NE Oman: Evidence from fluid inclusions and petrological data. Chemical Geology 154, 193-223.

Ernst, W.G., 1988. Tectonic history of subduction zones from retrograde blueschist *P-T* paths. Geology, 16, 1081–1084.

Eskola, P., 1921. The mineral facies of rocks. Nor. Geol. Tidsskr. 6, 142-194.

Eskola, P., 1939. Die Entstehung der Gesteine. Julius Springer, Berlin.

Evans, B. W., 1990. Phase relations of epidote-blueschists. Lithos, 25, 3–23.

Ewart, A., Collerson, K.D., Regelous, M., Wendt, J.I., Niu, Y., 1998. Geochemical evolution within the Tonga-Kermadec Lau arc back arc systems: the role of varying mantle wedge composition in space and time. Journal of Petrology 39 (3), 331-368.

Feng, Y.M., He, S.P., 1995. Basic characteristics of tectonics in the Qilian Mountains and its neighbouring areas- on genetic environments of Early Palaeozoic marine volcanics. Northwest Geoscience 16, 92-103. (in Chinese with English abstract)

Finlow-Bates, T., Stumpfl, E.F., 1981. The Behavoir of so-called immobile elements in hydrothermally altered rocks associated with volcanogenic submarine-exhalative ore deposits. Mineral Deposita 16, 319-328.

Foley, S.F., Matthias, G.B., Jenner, G.A., 1999. Rutile/melt partition coefficients for trace elements and an assessment of the influence of rutile on the trace element characteristics of subduction zone magmas.

Geochim.Cosmochim.Acta 64, 933-938.
Forneris, J.F. Holloway, J,R., 2003. Phase equilibria in subducting basaltic crust: Implications for H_2O release from the slab. EPSL 214, 187-201.
Franz, G., Selverstone, J., 1992. An empirical phase diagram for the clinozoisite-zoisite transformation in the system $Ca_2Al_3Si_3O_{12}(OH)$-$Ca_2Al_2Fe^{3+}Si_2O_{12}(OH)$. American Mineralogist 77, 631-642.
Fretzdorff, S., Livermore, R.A., Devey, C.W., Leat, P.T., Stoffers, P., 2002. Petrogenesis of the Back-arc East Scotioa Ridge, South Atlantic Ocean. Journal of Petrology 43, 1435-1467.
Frey, F.A., Weis, D., Borisova, A.Y., Xu, G., 2002. Involvement of Continental Crust in the Formation of the Cretaceous Kerguelen Plateau: New Perspectives from ODP Leg 120 Stites. Journal of Petrology 43, 1207-1239.
Fryer, P., Wheat, C.G., Mottl, M.J., 1999. Mariana blueschist mud volcanism: Implications for conditions within the subduction zone. Geology 27, 103-106.
Fu, B., Touret, J.L.R., and Zheng, Y.-F. (2001) Fluid inclusions in coesite-bearing eclogites and jadeite quartzite at Shuanghe, Dabie Shan (China). Journal of Metamorphic Geology, 19, 531.547.
Fu, B., Zheng, Y.F., Touret, J.L.R., 2002. Petrological, isotopic and fluid inclusion studies of eclogites from Sujiahe, NW Dabie Shan (China). Chemical Geology 187, 107-128.
Ganguly, J., Cheng, W., Tirone, M., 1996. Thermodynamics of aluminosilicate garnet solid solution: New experimental data, an optimised model, and thermometry applications. Contrib. Mineral Petrol 126, 137-151.
Gao, J., Guoqi, H., Xiao, X., Yaoqing, T., Wang, J., Min, Z., 1995. The mineralogy, petrology, metamorphic PTt trajectory and exhumation mechanism of blueschists, south Tianshan, northwestern China. Tectonophysics 250, 151-168.
Gao, J., Klemd, R., 2001. Primary fluids entrapped at blueschist to eclogite transition: evidence from the Tianshan meta-subduction complex in northwestern China. Contrib. Mineral Petrol 142, 1-14.
Gao, J., Klemd, R., 2003. Formation of HP-LT rocks and their tectonic implications in the western Tianshan Orogen, NW China: geochemical and age constraints. LITHOS 66, 1-22.
Gao, J., Klemd, R., Zhang, L., Wang, Z., Xiao, X., 1999. P-T path of high-pressure/low-temperature rocks and tectonic implications in the western Tianshan mountains, NW China. J. metamorphic Geol. 17, 621-636.
Gao, J., Li, M., Xiao, X., Tang, Y., He, G., 1997. Paleozoic tectonic evolution of the Tianshan Orogen, northwestern China. Tectonophysics 287, 213-231.
German, C.R., Barreiro, B.A., Higgs, N.C., Nelson, T.A., Ludford, E.M., Palmer, M.R., 1995. Seawater-metasomatism in hydrothermal sediments (Escanaba Trough, northeast Pacific). Chemical Geology 119, 175-190.
Giaramita, M.J., Sorensen, S.S., 1994. Primary fluids in low-temperature eclogites: evidence from two subduction complexes (Dominican Republic and California, USA). Contrib. Mineral Petrol 117, 279-292.
Gill, J.B., 1986. Orogenic andesite and plate tectonics. Springer-Verlag, New York.
Godard, G., 2001. Eclogites and their geodynamic interpretaion: A history. Journal of Geodynamics 32, 165-203.
Grant, J.A., 1986. The isocon diagram- a simple solution to Gresens' equation for metasomatic alteration. Economic Geology 81, 1976-1982.
Green, D.H., Ringwood, A.E., 1967. An experimental investigation of the gabbro to eclogite transformation and its petrological application. Geochim.Cosmochim.Acta 31, 767-833.
Green, T. H., 1994. Experimental studies of trace-element partitioning applicable to igneous petrogenesis Sedona 16 years later, Chem. Geol., 117, 1–36.
Green, T.H., 1995. Significance of Nb/Ta as an indicator of geochemical processes in the crust-mantle system. Chemical Geology 120, 347-359.
Green, T.H., Adam, J., 2002. Experimentally-Determined Trace Element Characteristics of Aqueous Fluid from Partially Dehydrated Mafic Oceanic Crust at 3.0GPA, 650-700oC. Eur. J. Mineral. 15, 815-830.
Gresens, R. L., 1967. Composition–volume relationships of metasomatism: Chemical Geology 2, 47–65.

Griffin, W.L., Brueckner, H.K., 1985. REE, Rb-Sr and Sm-Nd studies of Norwegian eclogites. Chemical Geology 52, 249-271.

Griffiths, R.W., Campbell, I.H., 1990. Stirring and structure in mantle starting plumes, EPSL, 99, 66-78.

Griggin, W.L., Brueckner, H.K., 1985. REE, Rb-Sr and Sm-Nd studies of Norwegian eclogites. Chemical Geology 52, 249-271.

Haase, K.M., Worthington, T.J., Stoffers, P., Garbe-Schonberg, D., Wright, I., 2002. Mantle Dynamics, Element Recycling, and Magma Genesis beneath the Kermadec Arc-Havre Trough. Geochem. Geophys. Geosys. 3(11), Paper Number: 2002GC000335.

Hacker, B.R., 1996. Eclogite formation and the rheology, buoyancy seismicity and H_2O content of the oceanic crust. In: Subduction: Top to Bottom. (Eds: Bebout,GE, Scholl,D, Kirby,S, Platt,JP) American Geophysical Union, American Geophysical Monograph 96, 337-346.

Halliday, A.N., Lee, D., Tommasini, S., Davies, G.R., Paslick, C.R., Fitton, J.G., James, D.E., 1995. Incompatible trace elements in OIB and MORB and source enrichment in the sub-oceanic mantle. EPSL 133, 379-395.

Hanan, B.B., Graham, D.W., 1996. Lead and Helium evidence from oceanic basalts for a common deep source mantle. Science 272, 991-995.

Hart, S.R., and Nalwalk, A.J., 1970. K, Rb, Sr, Ba Cs and Sr relationships in submarine basalts from the Puerto Rico trench. Geochim Cosmochim Acta 34, 145-155

Hart, S. R., 1988. Heterogeneous mantle domains: signatures, genesis and mixing chronologies. Earth Planet. Sci. Lett. 90, 273-296.

Hart, S.R., Hauri, E.H., Oschmann, L.A., Whitehead, J.A., 1992. Mantle plumes and entrainment: Isotopic evidence. Science 256, 517-520.

Hart, S.R, and Staudigel, H., 1989. Isotopic characterisation and identification of recycled components. NATO ASI Series, C: Math and Phys. Sci. 258, 15-28.

Hauri E. H., Hart S. R., 1993. Re-Os isotope systematics of HIMU and EMII oceanic island basalts from the south Pacific Ocean. Earth Planet. Sci. Lett. 114, 353–371.

Hawkesworth, C.J., Lighfoot, P.C., Fedorenko, V.A., Blake, S., Naldrett, A.J., Doherty, W., Gorbachev, N.S., 1995. Magma Differentiation and Mineralisation in the Siberian Continental Flood Basalts. Lithos 34, 61-88.

Heinrich, C.A., 1982. Kyanite-eclogite to amphibolite facies evolution of hydrous mafic and pelitic rocks, Adula nappe, central Alps. Contrib. Mineral Petrol 81, 30-38.

Heinrich, W. & Althaus, E., 1988. Experimental determination of the reaction 4 lawsonite+1 albite=1 paragonite+2 zoisite+2 quartz+6 H2O and 4 lawsonite+1 jadeite= 1 paragonite+2 zoisite+1 quartz+6 H2O. Neues Jahrbuch fu¨r Mineralogie Monatshefte, 11, 516–528.

Hekinian, R., Cheminee, J.L., Dubois, J., Stoffers, P., Scott, S., Guivel, C., Garbe-Schönberg, D., Devey, C., Bourdon, B., Lackschewitz, K., McMurtry, G., Le Drezen, E., 2003. The Pitcairn hotspot in the South Pacific: distribution and composition of submarine volcanic sequences. Journal of Volcanolgy and Geothermal Research 121, 219-245.

Hellman, P.L., Smith, R.E., Henderson, P., 1979. The mobility of the rare earth elements: Evidence and implications from selected terrains affected by burial metamorphism. Contrib. Mineral Petrol 71, 23-44.

Hemingway, B. S., Bohlen, S. R., Hankins, W. B., Westrum, E. F. & Kuskov, O. L., 1998. Heat capacity and thermodynamic properties for coesite and jadeite, reexamination of the quartz–coesite equilibrium boundary. American Mineralogist, 83, 409–418.

Henry, C., Burkhard, M., Goffe, B., 1996. Evolution of Synmetamorphic Veins and their Wallrocks through a Western Alps Transect: No Evidence for Large-Scale Fluid Flow. Stable Isotope, Major- and Trace-Element Systematics. Chemical Geology 127, 81-109.

Hermann, J., 2002. Allanite: Thorium and Light Rare Earth Element Carrier in Subducted Crust. Chemical Geology 192, 289-306.

Hermann, J. , and Green, D. H. 2001. Experimental constraints on high pressure melting in subducted crust. Earth and Planetary Science Letters, 188, 149–168.

Hofmann, A.W., 1988. Chemical differentiation of the Earth: the relationship between mantle, continental crust, and oceanic crust. EPSL 90, 297-314.

Hofmann, A.W., 1997. Mantle geochemistry: the message from oceanic volcanism. Nature 385(Jan), 219-229.

Hofmann, A.W., 1997. Early Evolution of Continents. Science 275, 498-499.

Hofmann, A.W., Jochum, K.P., Seufert, M., White, W.M., 1986. Nb and Pb in oceanic basalts: new contraints on mantle evolution. EPSL 79, 33-45.

Hofmann, A.W., White, M.W., 1982. Mantle plumes from ancient oceanic crust. EPSL 57 (421-436).

Holland, T.J.B., 1979. Experimental-determination of the reaction Paragonite=Jadeite+kyanite+H_2O, and internally consistent thermodynamic data for part of the system Na_2O=Al_2O_3-SiO_2-H_2O, with applications to eclogites and blueschists. Contributions to Mineralogy and Petrology 68, 293-301

Holland, T.J.B., 1983. The experimental-determination of activities in disordered and short-range ordered jadeitic pyroxenes. Contributions to Mineralogy and Petrology 82, 214-220

Holland, T.J.B., 1990. Activities of components in omphacite solid solutions. Contrib. Mineral Petrol 105, 446-453.

Holland, T. J. B., Powell, R., 1990. An enlarged and updated internally consistent thermodynamic dataset with uncertainties and correlations: The system K2O–Na2O–CaO–MgO–MnO–FeO–Fe2O3–Al2O3–TiO2–SiO2–C–H2–O2. Journal of Metamorphic Geology, 8, 89–124.

Holland, T. J. B., Powell, R., 1998. An internally-consistent thermodynamic dataset for phases of petrological interest. Journal of Metamorphic Geology, 16, 309–343.

Huang, T.K., Ren, J.S., Jiang, C.F., Chang, Ch.M., Qin, D. L.Y., 1980. The geotectonic evolution of China. Geological Publishing House, Beijing.

Humphris, S.E., Alt, C.A., Teagle, D.A.H., Honnorez, J.J., 1998. Geochemical changes during hydrothermal alteration of basement in the stockwork beneath the active TAG hydrothermal mound. Proc. ODP, Sci. Results, 158: College Station, TX (Ocean Drilling Program), pp. 255-276

Ingle, S., Weis, D., Scoates, J.S., Frey, F.A., 2002. Relationship between the Early Kerguelen Plume and Continental Flood Basalts of the Paleo-Eastern Gondwanan Margins. EPSL 197, 35-50.

Iwamori, H., 1998. Transportation of H_2O and melting in subduction zones. EPSL 160, 65-80.

Jenkins, D.M., Newton, R.C., Goldsmith, J.R., 1985. Relative stability of Fe-free zoisite and clinozoisite. Geology 93, 663-672.

Jenner, G.A., Foley, S.F., Jackson, S.E., Green, T.H., Fryer, B.J. and Longerich, H.P., 1993. Determination of partition coefficients for trace elements in high pressure-temperature experimental run products by laser ablation microprobe-inductively coupled plasma-mass spectrometry (LAM-ICP-MS). Geochimica et Cosmochimica Acta 57(23-24): 5099-5103.

Jensen, L.S., 1976. A new cation plot for classifying subalkalic volcanic rocks. Ontario Div. Mines. Misc. Pap. 66

John, T., Schenk, V., 2003. Partial eclogisation of gabroic rocks in a Late Precambrian subduction zone (Zambia): Prograde metamorphism triggered by fluid infiltration. Contrib. Mineral Petrol 146, 174-191.

John, T., Scherer, E.E., Haase, K., Schenk, V., 2004. Trace element fractionation during fluid-induced eclogisation in a subducting slab: Trace element and Lu-Hf-Sm-Nd isotope systematics. EPSL 227, 441-456.

Johnson, M.C., Plank, T., 1999. Dehydration and melting experiments constrain the fate of subducted sediments. Geochem. Geophys. Geosys. 1, Paper number 1999GC000014.

Jun, G., Klemd, R., Shengwei, L., 2000. Eclogization of glaucophanites by fluid infiltration. Science in China (Series D) 43, 144-155.

Kamber, B.S., Collerson, K.D., 2000. Role of 'hidden' deeply subducted slabs in mantle depletion. Chemical Geology 166, 241-254.

Kamber, B.S., Collerson, K.D., 2000. Zr/Nb systematics of ocean island basalts reassessed-the case for binary mixing. Journal of Petrology 41, 1007-1021.

Keith, M., 2001. Evidence for a plate tectonics debate. Earth Sci. Rev. 55, 235-336.

Kelley, K.A., Plank, T., Ludden, J., Staudigel, H., 2003. Composition of altered oceanic crust at ODP Sites

801 and 1149. Geochem. Geophys. Geosys. 4(6), Article number 2002GC00435.
Keller, R.A., Fisk, M.R., Smellie, J.L., Strelin, J.A., Lawver, L.A., 2002. Geochemistry of back arc basin volcanism in Bransfield Strait, Antarctica: Subducted contributions and along-axis variations. Journal Geophysical Research- Solid Earth, 107 (B8) art. no. 2171
Kennedy, G.C., Wasserberg, G.J., Heard, H.C., Newton, R.C., 1962. The upper three-phase region in the system SiO_2-H_2O. Am. J. Sci. 260, 501-521.
Keppler, H., 1996. Constraints from partitioning experiments on the composition of subduction-zone fluids. Nature 380(3571, 21 Mar), 237-240.
Kerr, A.C., Pamela, D.K., Thompson, R.N., 1995. Crustal Assimilation during turbulent magma ascent (ATA), new isotopic evidence from the Mull Tertiary lava succesion, N.W. Scotland. Contrib. Mineral Petrol 119, 142-154.
Kerrick, D.M., Connolly, J.A.D., 2001a. Metamorphic devolatilisation of subducted oceanic metabasalts: Implications for seismicity, arc magmatism and volatile recycling. EPSL 189, 19-29.
Kerrick, D.M., Connolly, J.A.D., 2001b. Metamorphic devolatilization of subducted marine sediments and the transport of volatiles into the Earth's mantle. Nature 411((6835), 17 May), 293-296.
Kiminami, K., Ishihama, S., 2003. The parentage of low-grade metasediments in the Sanbagawa Metamorphic Belt, Shikoku, southwest Japan, based on whole-rock geochemistry. Sedimentary Geology 159, 257-274.
Klemd, R., 2003. Ultrahigh-Pressure Metamorphism in Eclogites from the Western Tianshan High-Pressure Belt (Xinjiang, Western China)-Comment. American Mineralogist 88, 1153-1156.
Klemd, R., Schroter, F.C., Will, T.M., Gao, J. 2002. P-T Evolution of Glaucophane-Omphacite Bearing HP-LT Rocks of the Western Tianshan Orogen, NW China: New Evidence for 'Apine-Type' Tectonics. J. metamorphic Geol. 20, 239-254.

Kogiso, T., Tatsumi, Y., Nakano, S., 1997a. Trace element transport during dehydration processes in the subducted oceanic crust: 1. Experiments and implications for the origin of ocean island basalts. EPSL 148, 193-205.
Kogiso, T., Tatsumi, Y., Shimoda, G., Barsczus, H.G., 1997b. High μ (HIMU) ocean island basalts in southern Polynesia:New evidence for whole mantle scale recycling of subducted oceanic crust. J. Geophys. Res 102, 8085-8103.
Krogh, E. J., 1988. The garnet-clinopyroxene Fe-Mg geothermometer: a reinterpretation of existing experimental data. Contributions to Mineralogy and Petrology, 99, 44–48.
Kullerud, M., Stephens, M.B., Zachrisson, E., 1990. Pillow lavas as protoliths for eclogites: Evidence from a Late Precambrian-Cambrian continental margin, Seves Nappes, Scandinavian Caledonides. Contrib. Mineral Petrol 105, 1-10.
Larson, L.M., Fitton, G., Saunders, A.D., 1999. Composition of volcanic rocks from the Southeast Greenland Margin, Leg 163: Major and trace element geochemistry. Proc. Ocean Drill. Program Scient. Results 163, 63-75.
Leake, B.E., Woolley, A.R., Arps, C.E.S., Birch, W.D., Gilbert, M.C., Grice, J.D., Hawthorne, F.C., Kato, A., Kisch, H.J., Krivovichev, V.G., Linthout, K., Laird, J., Mandarino, J.A., Maresch, W.V., Nickel, E.H., Rock, N.M.S., Schumacher, J.C., Smith, D.C., Stephenson, N.C.N., Ungaretti, L., Whittaker, E.J.W., and Youshi, G. (1997) Nomenclature of amphiboles: Report of the subcommittee on amphiboles of the International Mineralogical Association, Commission on new minerals and mineral names. American Mineralogist, 82, 1019–1037.
Le Fèvre, B., Pin, C., 2001. An extraction chromatography method for Hf seperation prior to isotopic analysis using multiple collection ICP-mass spectrometry. Analytical Chemistry 73, 2453-2460
Le Pichon, X.L., Henry, P., Lallemant, S., 1993. Accretion and erosion in subduction zones: The role of fluids. Annual Review of Earth and Planetary Sciences 21, 307-331.
Li, X.P., Zhang, L.F., Al, Y,L., 2003. Discovery and geological implication of rodingites derived from eclogites of ophiolites at Changawuzi, western Tianshan, China. Progress in Natural Science. 13, 901-907.

Li, C.Y., Liu, Y.W., Zhu, B.C., Feng, Y.M., Wu, H.Q., 1978. Structural evolutions of Qinling and Qilian. In: Scientific papers on Geology for International Exchange. (Eds Editorial Office of Chinese Geological Bureau), pp174-189. Geological publishing House Beijing. (in Chinese with English abstract). (N)

Li, R., Li, S., Jin, F., Wan, Y., Zhang, S., 2004. Provenance of Carbonifereous sedimentary rocks in the northern margin of Dabie Mountains, central China and the tectonic significance: constraints from trace elements, mineral chemistry and SHRIMP dating of zircons. Sedimentary Geology 166, 245-264.

Liebscher, A., 2004. Decoupling of Fluid and Trace Element release in Subducting Slab? Comment on "Redistribution of Trace Elements During Prograde Metamorphism from Lawsonite Blueschist to Eclogite Facies, Implications for Deep Subduction-Zone Processes" by C. Spandler et al. (Contrib Mineral Petrol 145:205-222, 2003). Contrib. Mineral Petrol 148, 502-505.

Lightfoot, P.C., Naldrett, A.J., Gorbachev, N.S., Doherty, W., Fedorenko, V.A., 1990. Geochemistry of the Siberian Trap of the Noril'sk area, USSR, with implications for the relative contributions of crust and mantle to flood basalt magmatism. Contrib. Mineral Petrol 104, 631-644.

Lightfoot, P.C., Hawkesworth, C.J., Olshefsky, K., Green, T., Doherty, W., Keays, R.R., 1997. Geochemistry of tertiary tholeiites and picrites from Qeqertarssuaq (Disko Island) and Nuussuaq, West Greenland with implications for the mineral potential of comagmatic intrusions. Contributions to Mineralogy and Petrology 128, 139-163.

Lilley, R., Pearce, J.A., Styles, M., MacCleod, C., (in prep) Geochemical evolution of the northern Oman – UAE ophiolite. PhD thesis, Cardiff University.

Liou, J.G., Tsumjimori, T., Zhang, R.Y., Katayama, I., Maruyama, S. 2004. Global UHP Metamorphism and Continental Subduction/Collision: The Himalayan Model. Int. Geol. Rev. 46, 1-27.

Liu, J., Bohlen, S.R., Ernst, W.G., 1996. Stability of hydrous phases in subducting oceanic crust. EPSL 143, 161-171.

Loubert, M., Sassi, R., Di Donato, G., 1988. Mantle heterogeneities: a combined isotopic and trace element approach and evidence for recycled materials in some OIB sources. EPSL 89, 299-315.

Luth, R.W., 2001. Experimental determination of the reaction aragonite + magnesite = dolomite at 5 to 9 GPa. Contrib. Mineral Petrol 141, 222-232.

MacLean, W.H., Kranidiotis, P., 1987. Immobile elements as monitors of mass transfer in hydrothermal alteration: Phelps Dodge Sulfide Deposit, Matagami, Quebec. Economic Geology 82, 951-962.

MacLean, W.H., 1990. Mass change calculations in altered rock series. Mineralium Deposita 25, 44-49.

Manning, C.E., 2004. The chemistry of subduction zone fluids. EPSL 223, 1-16.

Manning, C.E., 1998. Fluid composition at the blueschist - eclogite transition in the model system Na_2O-MgO-Al_2O_3-SiO_2-H_2O-HCl. Schwiz. Mineral. Petrogr. Mitt. 78 (2), 225-242.

Maruyama, S., Cho, M., Liou, J.G., 1986. Experimental investigations of blueschist-greenschist transition equilibria: Pressure dependence of Al_2O_3 contents in sodic amphiboles - a new geobarometer.- Geol. Soc. Amer. Memoir, 164, 1-16

Maruyama, S., Liou, J.G., Terabayashi, M., 1996. Blueschists and eclogites of the world and their exhumation. Int. Geol. Rev. 38, 484-593.

Maruyama, S., Liou, J.G., Terabayashi, M., 1997. Blueschists and eclogites of the world and Their Exhumation. Int. Geol. Rev. 38, 485-563.

McCulloch, M.T., Gamble, J.A., 1991. Geochemical and geodynamical constraints on subduction zone magmatism. EPSL 102, 358-374.

McDonough, W.F., 1991. Partial melting of subducted oceanic crust and isolation of its residual eclogitic lithology. Phil. Trans. R. Soc. Lond. 335, 407-418.

McInnes, B.I.A., Gregoire, M., Binns, R.A., Herzig, P.M., Hannington, M.D., 2001. Hydrous metasomatism of oceanic sub-arc mantle, Lihir, Papua New Guinea: Petrology and geochemistry of fluid-metasomatised mantle wedge xenoliths. EPSL 188, 169-183.

McKenzie, D., O'Nions, K., 1995. The source regions of ocean island basalts. Journal of Petrology 36, 133-159.

McLennan, S.M., Hemming, S., McDaneil, D.K., Hanson, G.N., 1993. Geochemical approaches to sedimentation, provenance and tectonics. In: Hohnsson M.J., Basu A (Eds), Processes Controlling the Composition of Clastic Sediments, Geological Society of America, Special Papers 285, pp21-40.

Meisel, T., Schoner,N., Paliulionyte, V., Kahr, E., 2001. Determination of rare earth elements Y, Th, Zr, Hf Nb and Ta in geological reference materials G-2, G-3 Sco-1 and WGB-1 by sodium peroxide sontering and inductively coupled plasma-mass spectrometry. Geostandards Newsletter 26, 53-61.

Mibe, K., Yoshino, T., Ono, S., Yasuda, A., Fujii, T., 2003. Connectivity of aqueous fluid in eclogite and its implications for fluid migration in the Earth's interior. Journal of geophysical Reseach-Solid Earth. 108 (B6): art. no. 2295

Miller, C., Thöni, M., 1995. Origin of eclogites from the Austroalpine Ötztal basement (Triol, Austria): Geochemistry and Sm-Nd vs. Rb-Sr isotope systematics. Chemical Geology 122, 199-225.

Milward, P.W., Massonne, H.J., 1980. The low-high quartz and quartz-coesite transition to 40kbar to 600° and 1600°C and some reconnaissance data on the effect of $NaAlO_2$ component on the low quartz-coesite transition. Journal Geophysical Research 85, 6983-6990

Miyashiro, A., 1961. Evolution of metamorphic belts. Journal of Petrology 2, 277-311.

Miyashiro, A., 1994. Metamorphic Petrology. UCL Press Limited, University College London, London, 404.

Morimoto, N., 1988. Nomenclature of pyroxenes. Contributions to Mineralogy and Petrology, 39, 55-76.

Molina, J.F., Poli, S., 2000. Carbonate stability and fluid composition in subducted oceanic crust: an experimental study on H_2O-CO_2-bearing basalts. EPSL 176, 295-310.

Moreira, M., Kurz, M.D., 2001. Subducted oceanic Lithosphere and the origin of the "high μ" basalt helium signature. EPSL 189, 49-57.

Morgan, J.P., Morgan, W.J., 1999. Two-stage melting and the geochemical evolution of the mantle: A recipe for mantle plum-pudding. EPSL 170, 215-239.

Morgan, W.J., 1971. Convection plumes in the lower mantle. Nature 230, 42-43.

Mosenfelder, J.L., Bohlen, S.R., 1997. Kinetics of the coesite to quartz transformation. Earth Planet. Sci. Lett., 153, 133–147.

Mottl, M.J., Wheat, C.G., Fryer, P., Gharib, J., Martin, J.B., 2004. Chemistry of springs across the Mariana forearc shows progressive devolatilization of the subducting plate. Geochim.Cosmochim.Acta 68, 4915-4933.

Mountain, BW, Williams-Jones, A.E., 1995. Mass transfer and the path of metasomatic reactions in mesothermal cold deposits: An example from Flambeau Lake, Ontario. Economic geology and the Bulletin of the Society of Economic Geologists 91, 302-321.

Münker, C., Weyer, S., Scherer, E., Mezger, K., 2001. Seperation of high field strength elements (Nb, Ta, Zr Hf) and Lu from rock samples for MC-ICPMS measurements. Geochem. Geophys. Geosys. 2 (Paper number: 2001/GC000183).

Nagasaki, A., Enami, M., 1998. Sr-bearing zoisite and epidote in ultra-high (UHP) metamorphic rocks from the Su-Lu province, eastern China: An important Sr reservoir under UHP conditions. American Mineralogist 83 (3-4), 240-247.

Naumann, T., Geist, D., Kurz, M., 2002. Petrology and geochemistry of Volcán Cerro Azul: Petrologic diversity among the western Galapagos volcanoes. Journal of Petrology 43, 859-883.

Newton, R.C., Manning, C.E., 2000. Quartz solubility in H_2O-NaCl and H_2O-CO_2 solutions at deep crust-upper mantle pressures and temperatures: 2-15kbar and 500-900°C. Geochim.Cosmochim.Acta 64, 2993-3005.

Niu, Y., 2004. Bulk-rock Major and Trace Element Compositions of Abyssal Peridotites: Implication for Mantle Melting, Melt Extraction and Post-melting Processes Beneath Mid-Ocean Ridges. Journal of Petrology 45, 2423-2458.

Niu, Y., Batiza, R., 1997. Trace element evidence from seamounts for recycled oceanic crust in the eastern Pacific mantle. EPSL 148, 471-483.

Niu, Y., Collerson, K.D., Batiza, R., Wendt, J.I., Regelous, M., 1999. Origin of enriched-type mid-ocean ridge basalt at ridges far from mantle plumes: the East Pacific Rise at 11°20'N. J. Geophys. Res 104,

7067.
Niu, Y., Langmuir, C.H., Kinzler, R.J., 1997. The origin of abyssal peridotites: a new perspective. EPSL 152, 251-265.
Niu, Y., Lesher, C.M., 1991. Hydrothermal alteration of mafic metavolcanic rocks and genesis of Fe-Zn-Cu sulphide deposits, Stone Hill district, Alabama. Economic Geology 86, 983-1001.
Niu, Y., O'Hara, M.J., 2003. Origin of ocean island basalts: A new perspective from petrology, geochemistry, and mineral physics considerations. J. Geophys. Res 108, .
Niu, Y., O'Hara, M.J., Pearce, J.A., 2003. Initiation of subduction zones as a consequence of lateral compostional buoyancy contrast within the lithosphere: A petrological perspective. Journal of Petrology 2003, 851-866.
Niu, Y., Regelous, M., Wendt, I.J., Batiza, R., O'Hara, M.J., 2002. Geochemistry of near-EPR seamounts: Importance of source vs. process and the origin of enriched mantle component. EPSL 199, 327-345.
Noll, P.D., Newsom, H.E., Leeman, W.P., Ryan, J.G., 1995. The role of hydrothermal fluids in the production of subduction zone magmas: Evidence from siderophile and chalcophile trace elements and boron. Geochim.Cosmochim.Acta 60 No. 4, 587-611.
Okamoto, K., Maruyama, S., 1999. The High-Pressure Synthesis of Lawsonite in the MORB + H_2O System. American Mineralogist 84, 362-373.
Ono, S., 1998. Stability limits of hydrous minerals in sediment and mid-ocean ridge basalt compositions: Implications for water transport in subduction zones. J. Geophys. Res., 103, 18253-18267.
Palacz, Z. A. and Saunders, A. D. (1986). Coupled trace element and isotope enrichment in the Cook-Austral-Samoa islands, southwest Pacific. Earth Planet. Sci. Lett. 79, 270-280.
Pascal, P., Agrinier, P., Scambelluri, M., 1998. Chlorine cycling during subduction of altered oceanic crust. EPSL 161, 33-44.
Patchett, P.J., White, W.M., Feldmann, H., Kielinczuk, S., Hofmann, A.W., 1984. Hafnium/rare earth element fractionation in the sedimentary system and crustal recycling into the Earth's mantle. EPSL 69, 365-378.
Peacock, S.M., 1992. Blueschist-facies metamorphism, shear heating, and P-T-t paths in subduction shear zones. J. Geophys. Res 97, 17693-17707.
Peacock, S.M., 1993. The importance of blueschist to eclogite dehydration reactions in subducting oceanic crust. Geological Society of America Bulletin 105, 684-694.
Peacock, S.M., 1996. Thermal and petrologic structure of subduction zones, in: G.E Bebout, D.W Scholl, S.H Kirby, J. P. PLatt (eds), Subduction Top to Bottom pp. 119-113. AGU, Washington DC.
Pearce, J.A., 1982. Trace element characteristics of lavas from destructive plate boundaries. In: Andesites: Orogenic andesites and related rocks. (Ed: Thorpe, R.S.) John Wiley & Sons, Milton Keynes, 525-548. (N)
Pearce, J.A., 1996. A user's guide to basalt discrimination diagrams. In: Trace element geochemistry of volcanic rocks: Applications for massive suphide exploration. (Ed: Wyman, D.A.) Geological Association of Canada, Short Course notes, v. 12, 79-113.
Pearce, J.A., Cann, J.R., 1973. Tectonic setting of basic volcanic rocks determined using trace element analysis. EPSL 19, 290-900.
Pearce, J.A., Peate, D.W., 1995. Tectonic implications of the composition of volcanic arc basalts. Annual Review of Earth and Planetary Sciences 23, 251-285.
Pearson, D.G., Carlson, R.W., Shirley, S.B., Boyd, F.R., Nixon, P.H., 1995. Stabilisation of Archaean lithospheric mantle, a Re-Os isotope study of peridotite xenoliths from the Kaapvaal craton. EPSL 134, 341-357.
Peate, D.W., Hawkesworth, C.J., 1996. Lithospheric to asthenospheric transition in low-Ti flood basalts from southern Parana, Brazil. Chemical Geology 127, 1-24.
Philippot, P., Chevallier, P., Chopin, C., Budessy, J., 1995. Fluid composition and evolution in coesite-bearing rocks (Dora-Maira massif, Western Alps): implications for element recycling during subduction. Contrib. Mineral Petrol 121, 29-44.
Philippot, P., Selverstone, J., 1991. Trace-element-rich brines in eclogitic veins: Implication for fluid composition and transport during subduction. Contrib. Mineral Petrol 106, 417-430.

Philippot, P., Agrinier, P., Scambelluri, M., 1998. Chlorine cycling during subduction of altered oceanic crust. Earth and Planetary Science Letters, 161, 33-44.

Philpotts, J.A., Schneltzler, C.C., Hart, S.R., 1969. Submarine basalts: some K, Rb, Sr, Ba, rare earth, H_2O and CO_2 data bearing on their alteration, modification by plagioclase and possible source materials. EPSL 7 293-299

Pickett, E.A., Robertson, A.H.F., 1996. Formation of the Late Palaeozoic Early Mesozoic Karakaya Complex and related ophiolites in NW Turkey by Palaeotethyan subduction-accretion. Journal of the Geological Society 153, 995-1009

Plank, T., Langmuir, C.H., 1988. An evaluation of the global variations in the major element chemistry of arc basalts. EPSL 90, 349-370.

Plank, T., Langmuir, C.H., 1993. Tracing trace elements from sediment input to volcanic output at subduction zones. Nature 362(22 April), 739-743.

Plank, T., Langmuir, C.H., 1998. The chemical composition of subducting sediment and its consequences for the crust and mantle. Chemical Geology 145, 325-394.

Poli, S., Schmidt, M.W., 1995. H_2O transport and release in subduction zones - Experimental constraints on basaltic and andesitic systems. J. Geophys. Res. Solid Earth 100 (B11), 22299-22314.

Poli, S., Schmidt, M.W., 1997. The high-pressure stability of hydrous phases in orogenic belts: An experimental approach on eclogite-forming. Tectonophysics 273, 169-184.

Poli, S., Schmidt, M.W., 1998. The high pressure stability of zoisite and phase relationships of zoisite-bearing assemblages. Contrib. Mineral Petrol 130, 162-175.

Poli, S., Schmidt, M.W., 2002. Petrology of subducted slabs. Annual Review of Earth and Planetary Sciences 30, 207-235.

Prestvik, T., Goldberg, S., Karlsson, H., Gronvold, K., 2001. Anomalous strontium and lead isotope signatures in the off-rift Oraefajokull central volcano in southeast Iceland: evidence for enriched endmember(s) of the Iceland mantle plume? EPSL 190, 211-220.

Qian, Q., Zhang, Q., Wang, Y., 2001. Early Paleozoic North Qilian oceanic basin, and analogue to modern west Pacific: Evidence from geochemical characteristics of ophiolites. InteRidge News 10, 28-31.

Ravna, E.J.K., 2000. The garnet-clinopyroxene geothermometer - an updated calibration. J. metamorphic Geol. 18, 211-219.

Ravna, E.J.K., Terry, M.P., 2004. Geothermobarometry of UHP and HP eclogites and schists - an evaluation of equilibria among garnet-clinopyroxene-kyanite-phengite-coesite/quartz. Journal of Metamorphic geology 22, 579-592.

Ravna, E.J.K., 2004. Excel spreadsheet for P-T calculations Phe-Ky eclogites. <http://www.ig.uit.no/~erlingr/P-T%20CALC%20eclogite.xls>

Regelous, M., Collerson, K.D., Ewart, A., Wendt, J.I., 1997. Trace element transport rates in subduction zones: Evidence from Th, Sr and Pb isotopic data for Tonga-Kermadec arc lavas. EPSL 150, 291-302.

Regelous, M., Niu, Y., Wendt, J.I., Batiza, R., Greig, A., Collerson, K.D., 1999. Variations in the geochemistry of magmatism on the east pacific Rise at 10 30'N since 800ka . EPSL 168, 45-63.

Rehkämper, M., Hofmann, A.W., 1997. Recycled ocean crust and sediment in Indian ocean MORB. EPSL 147, 93-106.

Rubatto, D., Hermann, J., 2003. Zircon formation during fluid circulation in eclogites (Monviso, Western Alps): implications for Zr and Hf budget in subduction zones. Geochimica et Cosmochimica Acta, 67, 2173.187.

Rubie, D.C., van der Hilst, R.D., 2001. Processes and consequences of deep subduction: Introduction. Phys. Earth. Planet. Int. 127, 1-7.

Rudnick, R.L., 1995. Making continental crust. Nature 378(7 December), 571-578.

Rudnick, R.L., Fountain, D.M., 1995. Nature and composition of the continental crust: a lower crustal perspective. Reviews of Geophysics, 33: 267-309.

Ryan, J., Morris, J., Bebout, G., Leeman, B., 1996. Describing chemical fluxes in subduction zones: Insights from "depth profiling" studies of Arc and Forearc rocks. In: Subduction: Top to Bottom. (Eds:

Bebout,GE, Scholl,D, Kerby,S, Platt,JP) American Geophysical Union, American Geophysical Monograph 96, 263-268.

Sadofsky, S.J., Bebout, G.E., 2003. Record of forearc devolatilisation in low-T, high-P/T metasedimentary suites: Significance for models of convergent margin chemical cycling. Geochem. Geophys. Geosys. 4(4), Article number 2002GC00412.

Saunders, A.D., Kempton, P.D., Fitton, J.G., Larsen, L.M., 1999. Sr, Nd and Pb isotopes and trace element geochemistry of basalts from the southeast Greenland margin. *In* Larsen, H.C., Duncan, R.A., Allan, J.F., Brooks, K. (Eds.), *Proc. ODP, Sci. Results,* 163, 77-93

Scambelluri, M., Muntener, O., Hermann, J., Piccardo, G.B., Trommsdorff, V., 1995. Subduction of water into the mantle-History of an Alpine peridotite. Geology, 23, 459-462

Scambelluri, M., Bottazzi, P., Trommsdorff, V., Vannucci, R., Hermann, J., Gomez-Pugnaire, M.T., Vizcaino, V.L., 2001. Incompatible element-rich fluids released by antigorite breakdown in deeply subducted mantle. EPSL 192, 457-470.

Scambelluri, M., Giovanni, B.P., Philippot, P., Robbiano, A., Negretti, L., 1997. High slinity fluid inclusions formed from recycled water in deeply subducted alpine serpentinite. EPSL 148, 485-499.

Scambelluri, M., Pennachioni, G., Philippot, P., 1998. Salt-rich aqueous fluids formed during eclogitisation of metabasites in the Alpine continental crust (Austrialpine Mt. Emilius Unit, Italian Western Alps). Lithos 43, 151-167.

Scambelluri, M., Philippot, P., 2001. Deep fluids in subduction zones. Lithos 55, 213-227.

Scambelluri, M., Rampone, E., 1999. Mg-metasomatism of oceanic gabbros and its control on Ti-clinohumite formation during eclogitisation. Contrib. Mineral Petrol 135, 1-17.

Scambelluri, M., Rampone, E., Piccardo, G., 2001. Fluid and element cycling in subducted serpentinite: a trace-element study of the Erro-Tobbio high-pressure ultramafites (western Alps, NW Italy). Journal of Petrology 42, 55-67.

Schiffman, P., Staudigel, H., 1994. Hydrothermal alteration of a seamount complex on La Palma, Canary Islands: Implications for metamorphism in accreted terranes. Geology 22, 151-154.

Schmidt, M.W., 1996. Experimental constraints on recycling of potassium from subducted oceanic crust. Science 272, 1927-1930.

Schmidt, M.W., Poli, P., 1998. Experimentally based water budgets for dehydrating slabs and consequences for arc magma generation. EPSL 163, 361-379.

Schmidt, M.W., Poli, S., 1994. The stability of lawsonite and zoisite at high pressures: Experiments in CASH to 92 kbar and implications for the presence of hydrous phases in subducted Lithosphere. EPSL 124, 105-118.

Schmidt, M.W., Vielzuf, D., Auzanneau, E., 2004. Melting and dissolution of subducting crust at high pressures: The key role of white mica. EPSL 228, 65-84.

Schmidt, M.W., Poli, S., 2004. Generation of mobile components during subduction of oceanic crust, pp 517-591. In: The Crust (ed. Rudnick, R.L.) Vol. 3 Treatise on Geochemistry (eds. Holland, H.D., and Turekian, K.K.), Elsevier-Pergamon, Oxford.

Schneider, M.E., Eggler, D.H., 1986 Fluids in equilibium with peridotite minerals: Implications for mantle metasomatism. Geochim.Cosmochim.Acta 50, 711-724.

Schreyer, W., 1995. Ultradeep metamorphic rocks: The retrospective viewpoint. J. Geophys. Res., 100, 8353–8366.

Selverstone, J., Franz, G., Thomas, S., Getty, S., 1992. Fluid variability in 2GPa eclogites as an indicator of fluid behavior during subduction. Contrib. Mineral Petrol 112, 341-357.

Seyfried, W.E., Berndt, M.E., Seewald, J.S., 1988. Hydrothermal alteration processes at mid-ocean ridges: Constraints from diabase alteration experiments, hot spring fluids and composition of the oceanic crust. Can. Mineral. 26, 787-804.

Shatsky, V.S., Kozmenko, O.A., Sobolev, N.V., 1990. Behaviour of rare-earth elements during high-pressure metamorphism. Lithos 25, 219-226.

Shervais, J.W., 1992. Petrology, geochemistry, and origin of the Coast Range Ophiolite, California: American Association of Petroleum Geologists Bulletin, v. 76, no. 3, p. 430.

Silver, E., Kastner, M., Fisher, A., Morris, J., McIntosh, K., Saffer, D., 2000. Fluid flow in the middle

America trench and Costa Rica margin. Geology 28, 679-682.
Sinton, J.M., Ford, L.L., Chappell, B., McCulloch, M.T., 2003. Magma genesis and mantle heterogeneity on the Manus back-arc basin, Papua New Guinea. Journal of Petrology 44 Number 1, 159-195.
Sobolev, N. V., Dobretsov, N. L., Bakirov, L. B. & Shatshy, V.S., 1986. Eclogites from various types of metamorphic complexes in the USSR and the problems of their origin. In: Blueschists and Eclogites (eds Evans, B. W. & Brown, E. H.) Geological Society of America Memoir, 164, 349–363.
Sobolev, A.V., Chaussidon, M., 1996. H_2O concentrations in primary melts from supra-subduction zones and mid-ocean ridges: implications for H2O storage and recycling in the mantle. EPSL 137, 45-55.
Sobolev, A.V., Hofmann, A.W., Nikogosian, I.K., 2000. Recycled oceanic crust observed in "ghost plagioclase" within the source of Mauna Loa lavas. Nature 404(27 April), 986-989.
Song, S., 1996. Metamorphic geology of blueschists, eclogites and ophiolites in the North Qilian mountains. Geological Publishing House, Beijing, China, Beijing.
Sorensen, S.S., Grossman, J.N., 1989. Enrichment of trace elements in garnet amphibolites from a paeo-subduction zone: Catalina Schist, southern Californa. Geochim.Cosmochim.Acta 53, 3155-3177.
Sorensen, S.S., Grossman, J.N., 1993. Accessory minerals and subduction zone metasomatism: a geochemical comparison of two melanges (Washington and California, USA). Chemical Geology 110, 269-297.
Sorensen, S.S., Grossman, J.N., Perfit, M.R., 1997. Phengite-hosted LILE enrichment in eclogite and related rocks: Implications for fluid mediated mass transfer in subduction zones and arc magmas. Journal of Petrology 38, 3-34.
Soresen, S.S., Grossman, J.N., Perfit, M.R., 1997. Phengite-hosted LILE enrichment in eclogite and related rocks: Implications for fluid-mediated mass transfer in subduction zones and arc magma genesis. Journal of Petrology 38, 3-34.
Spandler, C., Hermann, J., Arculus, R., Mavrogenes, J., 2003. Redistribution of trace elements during prograde metamorphism from lawsonite blueschist to eclogite facies; Implications for deep subduction-zone processes. Contrib. Mineral Petrol 146, 205-222.
Spandler, C., Hermann, J., Arculus, R., Mavrogenes, J., 2004. Geochemical heterogeneity and element mobility in deeply subducted oceanic crust; Insights from high-pressure mafic rocks from New Caledonia. Chemical Geology 206, 21-42.
Spandler, C., Hermann, J., Arculus, R., Mavrogenes, J., 2004. Reply to comments on "redistribution of trace elements during prograde metamorphsim from lawsonite blueschist to eclogite facies: Implications for deep subduction zone processes". Contrib. Mineral Petrol 148, 506-509.
Spear, F. S., 1993. Metamorphic Phase Equilibria and Pressure-Temperature-Time Paths. Washington, D.C., Mineralogical Society of America Monograph, 799
Spinelli, G.A., Underwood, M.B., 2004. Character of sediments entering the Costa Rica subduction zone: Implications for partitioning of water along the plate interface. The Island Arc 13, 432-451.
Stalder, R., Foley, S.F., Brey, G.P., Horn, I., 1998. Mineral-aqueous fluid partitioning of trace elements at 900-1200°C and 3.0-5.7GPa: New experimental data for garnet, clinopyroxene, and rutile, and implications for mantle metasomatism. Geochim.Cosmochim.Acta 62, 1781-1801.
Staudigel, H., Plank, T., White, B., Schmincke, H-U., 1996. Geochemical fluxes during seafloor alteration of the basaltic upper oceanic crust: DSDP Sites 417 and 418. In: Subduction: Top to Bottom. (Ed: Bebout,G) American Geophysical Union, Geophysical Monograph 96 pp. 19-38.
Staudigel, H., 2004. Hydrothermal alteration processes in the oceanic crust, pp511-535 In: The Crust (ed. Rudnick, R.L.) Vol. 3 Treatise on Geochemistry (eds. Holland, H.D., and Turekian, K.K.), Elsevier-Pergamon, Oxford.
Stern, R.J. 2002. Subduction zones. Rev. Geophys 40, 10142 doi:10.1029/2001RG000108,2002 .
Stolper, E., Newman, S., 1994. The role of water in the petrogenesis of Mariana trough magmas. EPSL 121, 293-325.
Stosch, H.G., Lugmair, G.W., 1990. Geochemistry and evolution of MORB-type eclogites from the Münchberg Massif, southern Germany. EPSL 99, 230-249.
Stracke, A., Bizimis, M., Salters, J.M., 2003. Recycling oceanic crust: Quantitative constraints. Geochem. Geophys. Geosys. 4(Paper number: 2001/GC000223).

Straub, S.M., Layne, G.D., Schmidt, A., Langmuir, C.H., 2004. Volcanic glasses at the Izu arc volcanic front: New perspectives on fluid and sediment melt recycling in subduction zones. Geochem. Geophys. Geosys. 5(1), Paper number 2002GC00408.

Sun, S-S., McDonough, W.F., 1989. Chemical and isotopic systematics of oceanic basalts: Implications for mantle composition and processes. In: Magmatism in the ocean Basins. (Eds: Saunders, A.D., Norry, M.J.) Geological Society Special Publication No. 42 pp. 313-345.

Svensen, H., Jamtveit, B., Yardley, B.W., Engvik, A.K., Austrheim, H., Broman, C., 1999. Lead and bromine enrichment in eclogite facies fluids: extreme fractionation during lower crustal hydration. Geology 27, 467-470.

Tackely, P.J., 2000. Mantle convection and Plate Tectonics: Toward an integrated physical and chemical theory. Science 288, 2002-2007.

Tagiri, M., Yano, T., Bakirov, A., Nakajima, T., and Uchiumi, S., 1995. Mineral parageneses and metamorphic P-T paths of ultrahigh-pressure eclogites from Kyrghyastan Tien-Shan. The Island Arc, 4, 280–292.

Tankut, A., Dilek, Y., Önen., 1998. Petrology and geochemistry of the Neo-Tethyan volcanism as revealed in the Ankara melange, Turkey. Journal of Volcanolgy and Geothermal Research 74, 265-284.

Tatsumi, Y., Hamilton, D. L., Nesbitt, R.W., 1986. Chemical characteristics of fluid phase released from a subducted lithosphere and origin of arc magmas: evidence from high-pressure experiments and natural rocks. Journal of Volcanology and Geothermal Research 29, 293–309.

Tatsumi, Y., Eggins, S., 1995. Subduction zone magmatism. Blackwell, Cambridge.

Tatsumi, Y., Kogiso, T., 1997. Trace element transport during dehydration processes in the subducted oceanic crust: 2. Origin of chemical and physical characteristiocs in arc magmatism. EPSL 148, 207-221.

Tatsumoto, M., 1978. Isotopic composition of lead in oceanic basalt and its implication to mantle evolution. Earth Planet. Sci. Lett. 38, 63-87.

Thompson, R.N., Gibson, S.A., Dickin, A.P., Smith, P.M., 2001. Earth Cretaceous basalt and picrite dykes of the southern Etendeka region, NW Namibia: Windows into the role of the Tristan mantle plume in Parana-Etendeka magmatism. Journal of Petrology 42, 2049-2081.

Tiepolo, M., Bottazzi, P., Foley, S.F., Oberti, R., Vannucci, R., Zanetti, A., 2001. Fractionation of Nb and Ta from Zr and Hf at mantle depths: The role if titanian pargasite and kaersutite. Journal of Petrology 42, 221-232.

Totland,M, Jarvis,I, Jarvis,KE (1992): An assesment of dissolution techniques for the analysis of geological samples by plasma spectroscopy. Chemical Geology 95, 35-62.

Totland, M., Jarvis, I., Jarvis, K.E., 1995. Microwave digestion and alkali fusion procedures for the determination of the platinum-group elements and gold in geological samples by ICP-MS. Chemical Geology 124, 21-36.

Tribuzio, R., Messiga, G., Vannucci, B., Bottazzi, P., 1996. Rare earth element redistribution during high pressure-low-temperature metamorphism in ophiolitic Fe-gabbros (Liguria, northwestern Italy): Implications for light REE mobility in subduction zones. Geology 24, 711-714.

Tropper, P., Manning, C.E., 2004. Paragonite stability at 700 degrees C in the presence of H_2O-NaCl fluids: constraints on H_2O activity and implications for high pressure metamorphism. Contributions to mineralogy and Petrology 147, 740-749

Turner, F.J., 1981. Metamorphic petrology. McGraw-Hill, New York.

Turner, S., Foden, J., 2001. U, Th and Ra disequilibria, Sr, Nd and Pb isotope and trace element variations in Sunda arc lavas: Predominance of a subducted sediment component. Contrib. Mineral Petrol 142, 43-57.

Ulfbeck, D., Baker, J., Waight, T., Krogstad, E., 2003. Rapid sample digestion by fusion and chemical seperation of Hf for isotopic analysis by MC-ICPMS. Talanta 59, 365-373

Ulmer, P., Trommsdorff, V., 1995. Serpentine stability to mantle depths and subduction-related magmatism. Science, 268, 858–861.

van Westrenen, W., Blundy, J.D., Wood, B.J., 2001. High field strength element/rare earth element fractionation during partial melting in the presence of garnet: Implications for identification of mantle heterogeneities. Geochem. Geophys. Geosys. 2, . (Paper number 2000GC000133)

Vielzeuf, D., Schmidt, M.W., 2001. Melting relations in hydrous systems revisited: Application to metapelites, metagreywackes and metabasalts. Contrib. Mineral Petrol 141, 251-267.

Volkova, N.I., Budanov, V.I., 1999. Geochemical discrimination of metabasalt rocks of the Fan-Karatgin transitional blueschist/greenschist belt, south Tianshan: Seamount volcanism and accretionary tectonics. Lithos 47, 201-216.

von Huene, R., Scholl, D.W., 1991. Observations at convergent margins concerning sediment subduction, subduction erosion, and the growth of continental crust. Rev. Geophys 29, 279-316.

Wang, Q., Liu, X.Y., 1976. On Caledonian polycyclic paired metamorphic belts of Qilian mountains, northwest China. In: Contributions to tectonics of China and adjacent regions (eds Huang, T.K. and Li, C.Y.), pp. 92-101. Geological Publishing House, Beijing. (in Chinese with English abstract).

Wang, Y.Sh., Chen, J.N., 1987. Metamorphic zones and metamorphism in Qinghai Province and its adjacent areas. Geological Publishing House, Beijing, Beijing (in Chinese with English Abstract).

Wang, C.Y., Zhang, Q., Qian, Q., Zhou, M-F., 2005. Geochemistry of the early Paleozoic Baiyin volcanic rocks (NW China): Implications for the tectonic evolution of the north Qilian orogenic belt. The Journal of Geology 113, 83-94.

Waters, D.J., Martin, H.N., 1993. Geobarometry of phengite-bearing eclogites. Terra Abstracts 5, 410-411.

Waters, DJ., 2004. Practical aspects of mineral thermobarometry. <http://www.earth.ox.ac.uk/~davewa/pt/pt-start.html>

Weaver, B.L., Wood, D.A., Tarney, T. Joron, J.L., 1986. Role of subduted sediment in the genesis of ocean-island basalts- Geochemical evidence from South-Atlantic ocean islands. Geology 14, 275-278

Weaver, B.L., 1991. Trace element evidence for the origin of ocean-island basalts. Geology 19, 123-126.

Weaver, B.L., 1991. The origin of ocean island basalt end-member compositions: Trace element and isotopic constraints. EPSL 104, 381-397.

Wei, C.J., Powell, R., Zhang, L.F., 2003. Eclogites from the south Tianshan, NW China: Petrological characteristics and calculated mineral equilibria in the Na_2O-CaO-FeO-MgO-Al_2O_3-SiO_2-H_2O System. J. metamorphic Geol. 21, 163-179.

Wedepohl, K.H., 1995. The composition of the continental crust. Geochimica et Cosmochimica Acta 59: 1,217-1,239.

White, W.M., 1985. Sources of oceanic basalts: Radiogenic isotope evidence. Geology 13, 115-118.

Will, T., Okrusch, M., Scmädicke, E., Chen, G., 1998. Phase relations in the greenschist-blueschist-amphibolite-eclogite facies in the system Na_2O-CaO-FeO-MgO-Al_2O_3-SiO_2-H_2O (NCFMASH), with application to metamorphic rocks from Samos, Greece. Contrib. Mineral Petrol 132, 85-102.

Wilson, M 1989. Igneous Petrogenesis. Kluwer Academic Publishers, London.

Winchester, J.A., Floyd, P.A., 1977. Geochemical discrimination of different magma series and their differentiation products using immobile elements. Chem. Geol. 20, 325-343

Winchester, J.A., Park, R.G., Holland, J.G., 1980. The geochemistry of Lewisian semipelitic schists from the Gailoch District, Wester Ross. Scottish Journal of Geology 16, 165-179.

Windley, B.F., Allen, M.B., Zhang, C., Zhao, Z-Y., Wang, G-R., 1990. Paleozoic accretion and Cenozoic redeformation of the Chinese Tien Shan range, central Asia. Geology 18, 128-131.

Wood, D.A., 1980. The application of a Th-Hf-Ta diagram to problems of tectonomagmatic classification and to establish the nature of crustal contamination of basaltic lavas of the British Tertiary Volcanic Province. EPSL 50, 11-30.

Woodhead, J.D., McCulloch, M.T., 1989. Ancient seafloor signals in Pitcairn-Island lavas and evidence for large-amplitude, small length-scale mantle heterogeneities. EPSL 94, 257-273.

Woodhead, J.D., 1996. Extreme HIMU in an oceanic setting: the geochemistry of Mangaia Island (Polynesia), and temporal evolution of the Cook-Austral hotspot. Journal of Volcanolgy and Geothermal Research 72, 1-19.

Woodhead, J.D., Eggins, S.M., Johnson, R.W., 1998. Magma genesis in the New Britain Island Arc: Further insights into melting and mass transfer processes. Journal of Petrology 39, 1641-1668.

Woodhead, J.D., Greenwood, P., Harmon, R.S., Stoffers, P., 1993. Oxygen isotope evidence for recycled crust in the sourse of EM-type ocean island basalts. Nature 362(29 April), 809-813.

Woodhead, J.D., Hergt, J.P., Davidson, S.M., Eggins, S.M., 2001. Hafnium isotope evidence for 'conservative' element mobilty during subduction zone processes. EPSL 192, 331-346.

Wu, H.Q., Feng, Y., Song, S.G., 1993. Metamorphism and deformation of blueschist belts and their tectonic implications, North Qilian Mountains, China. J. Metamorphic Geol. 11, 523-536.

Xia, L-Q., Xia, Z-C., Xu, X-Y., 2003. Magmagenesis in the Ordovician backarc basins of the northern Qilian mountains, China. Geological Society of America Bulletin 115, 1510-1522.

Xiao, X.C., Chen, G.M., Zhu, Z.Z., 1974. Some knowledges about the paleo-plate tectonics of the Qilian mountains. Geological Sciencews and Technology, 3 73-78 (in Chinese with English Abstract).

Xiao, X.C., Chen, G.M., Zhu, Z.Z., 1978. A preliminary study on the tectonics on the tectonics of ancient ophiolites in the Qilian Mountains, northwest China. Acta Geological Sinica, 4, 279-295 (in Chinese with English Abstract).

Xiao, X.C., Li, T.D., Li, G.G. Chang, Ch.F., Yuan, X.Ch., 1988. Tectonic evolution of the lithosphere of the Himalayas- General review. Geological Publishing House, Beijing (in Chinese with English abstract).

Xiao, Y., Hoefs, J., Kerkhof, A.M., Fiebig, J., Zheng, Y., 2000. Fluid history of UHP metamorphism in Dabie Shan, China: A fluid inclusion and oxygen isotope study on the coesite-bearing eclogite from Bixiling. Contrib. Mineral Petrol 139, 1-16.

Xiao, X., Tang, Y., Feng, Y., Zhu, B., Li, J., Zhao, M., 1992. The tectonic evolution of North Xinjiang and it's adjacent regions. Geol. Pub]. House. Beijing, 190 pp. (in Chinese with English abstract).

Xu, Zh.Q., Xu, H.F., Zhang, J.X., Li, H.B., Zhu, Zh.Zh., Qu, J.Ch., Chen, D.Ch., Chen, J.L., Yang, K.Ch., 1994 The Zhoulangnshan Caledonian subductive complex in the northern Qilian mountains and its dynamics. Acta Geological Sinica, 68, 1-15 (in Chinese with English abstract).

Yamamoto, K., Asahara, Y., Maekawa, H., Sugitani, K., 1995. Origin of blueschist facies clasts in the Mariana fore-arc, westerm Pacific. Geochemical Journal 29, 259-275.

Yang, S.Y., Jung, H.S., Lim, D.I., Li, C.X., 2003. A review on the provenance discrimination of sediments in the Yellow Sea. Earth Sci. Rev. 63, 93-120.

Yardley, B.W.D., 1989, An introduction to metamorphic petrology: Longman Scientific and Technical, 248, New York.

Yaxley, G.M., Green, D.H., 1994. Experimental demonstration of refractory carbonate-bearing eclogite and siliceous melt in the subduction regime. EPSL 128, 313-325.

You, C-F., Castillo, P.R., Gieskes, J.M., Chan, L.H, Spivack, A.J., 1996. Trace element behaviour in hydrothermal experiments: Implications for fluid processes at shallow depths in subduction zones. EPSL 140, 41-52.

Yu, Z., Robinson, P., McGoldrick, P., 2001. An evaluation of methods for the chemical decomposition of geological materials for trace element determination by ICP-MS. Geostandards Newsletter 25, 199-217

Zack, T., Foley, S., Rivers, T., 1998. Trace element partitioning between hydrous minerals (phengites, zoisite, amphibole) and omphacite in eclogites: Clues for modelling dehydration reactions in subduction zones. 8th V.M. Goldschmidt Conference, Mineralogical Magazine 62A, 1679-1680.

Zack, T., Foley, S.F., Rivers, T., 2002a. Equilibrium and disequilibrium trace element partitioning in hydrous eclogites (Trescolmen, Central Alps). Journal of Petrology 43, 1947-1974.

Zack, T., Kronz, A., Foley, S.F., Rivers, T., 2002b. Trace element abundance in rutiles from eclogites and associated garnet mica schists. Chemical Geology 184, 97-122.

Zack, T., Rivers, T., Foley, S.F., 2001. Cs-Rb-Ba systematics in phengite and amphibole: an assessment of fluid mobility at 2.0 GPa in eclogites from Trescolmen, Central Alps. Contrib. Mineral Petrol 140, 651-669.

Zack, T., Tomascak, P.B., Rudnik, .R.L, Dalpé, C., McDonough, W.F., 2003. Extremely light Li in orogenic eclogites: The role of isotopic fractionation during dehydration in subducted oceanic crust. EPSL 208, 279-290.

Zanetti, A., Mazzucchelli, M., Rivalenti, G., Vannucci, R., 1999. The Finero phlogopite-peridotite massif: An example of subduction-related metasomatism. Contrib. Mineral Petrol 134, 107-122.

Zhang, L., Ellis, D.J., Jiang, W., 2002a. Ultrahigh-pressure metamorphism in western Tianshan, China: Part

1. Evidence from inclusions of coesite pseudomorphs in garnet and from quartz exsolution lamellae in omphacite in eclogites. American Mineralogist 87, 853-860.
Zhang, L., Ellis, D., Williams, S., Jiang, W., 2002b. Ultra-high pressure metamorphism in western Tianshan, China: Part II, Evidence from magnesite in eclogite. American Mineralogist 87, 861-866.
Zhang, L., Ellis, D., Williams, S., Jiang, W., 2003. Ultrahigh-pressure metamorphism in eclogites from the Western Tianshan, China- Reply. American Mineralogist 88, 157-1160.
Zhang, L., Ellis, D.J., Arculus, R.J., Jiang, W., Wei, C., 2003b. 'Forbidden Zone' subduction of sediments to 150km depth- the reaction of dolomite to magnesite + aragonite in the UHPM metapelites from western Tianshan, China. J. metamorphic Geol. 21, 523-529.
Zhang, L., Song, S., Liou, J.G., Al, Y., Li, X., 2005. Relict coesite exsolution in omphacite from western Tianshan eclogites, China. American Mineralogist 90, 181-186.
Zindler, A., Hart, S., 1986. Chemical geodynamics. Annual Review of Earth and Planetary Sciences 14, 493-571.

